PERFORMANCE-BASED METHODOLOGY *for* *the* FIRE SAFE DESIGN *of* INSULATION MATERIALS *in* ENERGY EFFICIENT BUILDINGS

JUAN P. HIDALGO-MEDINA

A thesis submitted for the degree of
Doctor of Philosophy

THE UNIVERSITY
of EDINBURGH

2015

PERFORMANCE-BASED METHODOLOGY *for* *the* FIRE SAFE DESIGN *of* INSULATION MATERIALS *in* ENERGY EFFICIENT BUILDINGS

by

JUAN P. HIDALGO-MEDINA

This thesis has been supervised by
Dr Stephen Welch
Prof José L. Torero

The examining committee consisted of
Dr Björn Sundström
Dr Rory M. Hadden

To Papá, Mamá and David

Declaration

This thesis and the work described within have been completed solely by Juan P. Hidalgo-Medina at the BRE Centre for Fire Safety Engineering at the University of Edinburgh, under the supervision of Dr Stephen Welch and Prof José L. Torero. Where others have contributed or other sources are quoted, references are given.

Juan P. Hidalgo-Medina

May 2015

Abstract

This thesis presents a methodology to determine failure criteria of building insulation materials in the event of a fire that is specific to each typology of insulation material used. This methodology is based on material characterisation and assessment of fire performance of the most common insulation materials used in construction. Current methodologies give a single failure criterion independent of the nature of the material – this can lead to uneven requirements when addressing materials of different characteristics. At present, fire safety codes establish that performance of different materials or assemblies is assumed to be "equivalent" when subject to the same test, where attainment of the unique failure criteria occurs after a required minimum time. Nevertheless, when using extremely different materials this may not be actually the case.

Building performance is currently defined in a quantitative way with respect to factors such as energy usage (i.e. global thermal transmittance), element weight (i.e. thickness and mass), space utilisation and cost of application. In the case of fire performance, only a threshold value is required, therefore a quantitative performance assessment is not conducted. As a result, the drivers are those associated with the variables that can be quantified, whereas the thresholds merely need to be met without any alternative for a better performance.

Factors such as shortage of fuel for energy generation and determination in reducing carbon dioxide emissions to the atmosphere pose a scenario in which a decrease of energy consumption is required to allow sustainable development. Since a large proportion of the energy is used in buildings, plans for improving their energy performance have been strongly encouraged worldwide. During the last decade, energy efficiency has become the main driver for building design, leading to significant changes in construction typologies and materials. Therefore, achieving quantifiable improvements in insulation capacity has become a strong driver in building design. The main consequence of this required higher energy performance is the need for increased levels of insulation materials in buildings.

Among the most common insulation materials, rigid polymeric (plastic) materials have demonstrated great potential for the built environment. These materials appear to optimise all current requirements in a scenario where cost, space usage and thermal conductivity are the only quantifiable and thus optimisable design variables.

An analysis of the hazards introduced by higher levels of insulation materials in buildings is presented, accompanied by an assessment of the limitations of standard fire testing as a mechanism to quantify their fire performance. Common specific failure modes associated to fire and insulation materials in construction are highlighted, leading to a redefinition of the failure criteria. A methodology is then developed to quantitatively assess fire performance. The objective is therefore to structure a testing procedure that enables quantitative comparison between the fire performance of very different materials.

An extensive testing plan serves as baseline to define this methodology and determine the failure criteria for the studied insulation materials, which correspond to rigid polyisocyanurate (PIR), rigid phenolic foam (PF), expanded polystyrene (EPS) and stone wool (SW). These materials are identified as the most common insulators used in construction over recent decades.

The identification of a failure criterion requires a fundamental understanding of the thermal degradation processes associated to the different materials. This understanding can only be achieved by studying the relevant materials at the fundamental material scale and the results acquired by increasing length scales until all fire related parameters are incorporated. The testing plan is therefore defined in a way such that different scales are revised, with the objective of isolating different levels of complexity and failure modes. For that purpose, experiments are sequentially based on thermogravimetry, differential scanning calorimetry, bench-scale flammability, combustibility and one-dimensional thermal analysis, intermediate-scale thermal analysis and real-scale tests. The established methodology takes into account the phenomena that govern the behaviour of insulation products in fire, i.e. heat transfer by conduction linked to thermal degradation processes triggered by transfer and accumulation of energy.

The current state-of-the-art allows for a fairly consistent analysis or definition of the thermal degradation processes that can include reactions in the solid phase as well as gas phase and heat and mass transfer processes. While this might be a desirable approach in some cases, this infers a high level of complexity and great uncertainty in the definition of input parameters, becoming a tedious task where compensation errors play an important role. Thus, the aim of this work is to establish the critical failure modes that determine the performance of the materials in their application. The methodology presented demonstrates that for the definition of the failure criteria of insulation materials, only a simple heat transfer model that assumes inert conditions in the solid phase is required. This enables a much simpler approach to be followed.

This work opens the door to a performance-based-design methodology that takes into account fire performance as an optimisation variable for the building design, to be used with all other quantifiable variables. An added advantage is that the numerical tool required embraces a low level of complexity. As a result, the possibility for any insulation product to achieve quantifiable and acceptable fire safety levels for required energy efficiency targets is established. As a final remark, an application of the performance assessment methodology that introduces fire safety as a quantifiable variable is presented.

Lay Summary

This thesis presents a methodology to determine failure criteria of building insulation materials in the event of a fire that is specific to each typology of insulation material used. This methodology is based on material characterisation and assessment of fire performance of the most common insulation materials used in construction. Current methodologies give a single failure criterion independent of the nature of the material – this can lead to uneven requirements when addressing materials of different characteristics. At present, fire safety codes establish that performance of different materials or assemblies is assumed to be "equivalent" when subject to the same test, where attainment of the unique failure criteria occurs after a required minimum time. Nevertheless, when using extremely different materials this may not be actually the case.

Building performance is currently defined in a quantitative way with respect to factors such as energy usage (i.e. global thermal transmittance), element weight (i.e. thickness and mass), space utilisation and cost of application. In the case of fire performance, only a threshold value is required, therefore a quantitative performance assessment is not conducted. As a result, the drivers are those associated with the variables that can be quantified, whereas the thresholds merely need to be met without any alternative for a better performance.

This work opens the door to a performance-based-design methodology that takes into account fire performance as an optimisation variable for the building design, to be used with all other quantifiable variables. An added advantage is that the numerical tool required embraces a low level of complexity. As a result, the possibility for any insulation product to achieve quantifiable and acceptable fire safety levels for required energy efficiency targets is established. As a final remark, an application of the performance assessment methodology that introduces fire safety as a quantifiable variable is presented.

Acknowledgments

First of all, I would like to express my gratitude to my supervisors Dr Stephen Welch and Prof José Torero for their great support, guidance and advice during these three years of hard work. Their optimism and wide knowledge in this field have always been an inspiring example for me.

I would also like to thank Dr Guillermo Rein for opening the doors of the fire group to me, encouraging me to take this academic path at the BRE Centre for Fire Safety Engineering in Edinburgh, from which I have largely enjoyed and learned, and of course I will always be grateful.

Thanks to Prof Luke Bisby for his advice and support in many occasions during the PhD, for those marvellous Christmas dinners and for encouraging continuously my work and the work of any of my PhD colleagues.

Thanks to Prof Simeoni for our long talks and discussions, for that enthusiasm injected into the fire group since his arrival as the new BRE Chair of Fire Safety Engineering.

Thanks to Birgitte Messerschmidt for her patience and support as industrial supervisor, and especially for her complete trust in my work. Thanks to *Rockwool International A\S* for sponsoring my PhD scholarship and for their help during the first stage of the degree, introducing me to the world of insulation materials. I also would like to thank Prof Richard Hull from the Univerisity of Central Lancashire and Dr Grunde Jomaas from the Technical University of Denmark for inviting me to participate in the large-scale fire experiments carried out in Chorley.

Thanks to my colleagues at the Universitat Politècnica de València, Toni, Josemi, Vicente, Jose Vicente, Hector, Carmen, Figue and Juan Jaime, who encouraged me to come to Edinburgh so as to keep learning about fire science.

Thanks to Ati for starting the Edinburgh adventure with me and for being the best flatmate I will ever have. Thanks for our unconditional friendship, for his help during the first months in Edinburgh and for so many fantastic moments.

Thanks to all my good friends in Edinburgh, who have made my life so enjoyable during the last three years. Special thanks go to Ime, Martyn, Liming, Payam, Zafiris, Shaun and Brian, who became my first office mates and friends. Thanks for having taught me so much and having such a great patience. Thanks to Cristián, for being such a great friend and work colleague, for our long discussions about fire engineering, for his constructive negativity and example of unceasing hard work. Thanks to Ryan, who became my step brother during that long time at BRE Watford. Thanks to Emma and Ieuan for so many funny moments, for teaching me little by little how the British humour works. Thanks to the Simeoni's clan, Eric, Mo and Chris for such good moments and stories, especially behind the bars. In general, thanks to all the Juanmurians, for making our workplace such a nice environment.

Thanks to Cecilia and Adam for their wonderful friendship, continuous guidance and trust in me during the large-scale fire experiments at BRE Watford and Lisbon for the Tall Buildings project.

Thanks to Michal, the best lab colleague and best technician that any group could have, for being always there to help me with my experiments and crazy ideas in the fire lab.

Thanks to Ahmad for being such a good flatmate and friend and for his help with my thesis.

Thanks to Qing for his help in the lab during the last moments of the PhD.

Thanks to Liesa for sharing her wonderful home for six months during our stay in Studham for the Tall Buildings project, for so many great stories and keeping us sane during the difficult moments.

Thanks to all my friends in Valencia for being always there, for those 'Ave Marias' during your party nights that made me feel home. Special thanks go to Mario, for teaching me what an 'unconditional friendship' means.

Thanks to Elena for being my best friend, for believing in me more than anyone else, for being my third supervisor, for teaching me patience and being so patient with me, for being always there for me, for your kindness and your endless support.

And finally and more importantly, thanks to Papá, Mamá and David, for always having believed blindly in me, my work and my dreams, for teaching me that there are no limits for what you want to do, for your endless support and help. Thanks to my grandmas' Amparo and Maria, who left us while I wasn't at home. You have been and will always be for me the best example of sacrifice, hard work, love and kindness.

Contents

List of Figures

List of Tables

Nomenclature, Acronyms and Terminology

a	Polynomial coefficient for the spline (2nd degree)
A	Pre-exponential factor /s^{-1} or surface area /m^2
b	Polynomial coefficient for the spline (1st degree)
c	Polynomial coefficient for the spline (independent term)
d	Diameter /m
Bi	Biot number/-
c_p	Specific heat capacity at constant pressure /$J \cdot kg^{-1} \cdot K^{-1}$
erf	Gaussian error function
$erfc$	Complementary Gaussian error function
exp	Exponential function
E	Heat release per mass unit of oxygen consumed /$J \cdot kg^{-1}$
E_a	Energy of activation /$J \cdot mol^{-1}$
F	Array with the difference between modelled and experimental outputs
g	Gravity acceleration /$m \cdot s^{-2}$
Fo	Fourier number /-
Gr	Grashof number /-
h	Heat transfer coefficient /$W \cdot m^{-2} \cdot K^{-1}$
$\Delta H_{c,eff}$	Effective heat of combustion /$kJ \cdot g^{-1}$
J	Jacobian matrix
k	Thermal conductivity /$W \cdot m^{-1} \cdot K^{-1}$
$k\rho c$	Thermal inertia /$W^2 \cdot s \cdot \cdot K^{-2} m^{-4} \cdot$
L	Characteristic length or thickness /m
L_v	Energy of gasification /$J \cdot kg^{-1}$
m	Mass /kg
$\dot{m}$	Mass flow /$kg \cdot s^{-1}$
$\dot{m}''$	Mass flow rate per unit area /$kg \cdot m^{-2} \cdot s^{-1}$
M	Molecular mass /$g \cdot mol^{-1}$
Nu_L	Nusselt number/-
$\dot{q}''$	Heat flux /$kW \cdot m^{-2}$
$\dot{Q}$	Heat release rate /kW
R	Universal gas constant /$J \cdot mol^{-1} \cdot K^{-1}$
Ra	Rayleigh number /-
S	Fitness function
T	Temperature /K or /°C
t	Time /s
u	Internal energy /J
U	Thermal transmittance / $W \cdot m^{-2} \cdot K^{-1}$
x	Space /m
v	velocity / $m \cdot s^{-1}$
V	Volume / m^3
X	Mol fraction /- or optimisation variables
Y	Objective variables

Z	Constraint variables

Greek letters

α	Absorptivity /- or volumetric expansion factor for calorimetry /- or normalised mass for thermogravimetry
β	Film temperature /K or °C
δ	Differential
Δ	Incremental
ε	Emissivity /-
η	Non-dimensional parameter $\frac{x}{\sqrt{4\kappa t}}$ /-
θ	Non-dimensional parameter $\frac{h_T \cdot t^{1/2}}{\sqrt{k\rho c}}$ /-
ϑ	Stoichiometric coefficients of the combustion reaction
κ	Thermal diffusivity /$m^2 \cdot s^{-1}$
λ	Damping factor /-
μ	Dynamic viscosity /Pa·s
$\boldsymbol{\varphi}$	Porosity /-
$\boldsymbol{\phi}$	Oxygen depletion factor /-
Φ	Flame spread parameter /$kW^2 \cdot m^{-3}$
ρ	Density /$kg \cdot m^{-3}$
σ	Stefan–Boltzmann constant /$W \cdot m^{-2} \cdot K^{-4}$
τ	Duration of the fire /s
υ	Kinematic viscosity /$m^2 \cdot s^{-1}$

Superscripts

0	before ignition
A	Measured value by the analyser
$j-1$	Previous time step
j	Current time step
$j+1$	Next time step

Subscripts

0	initial
a	of the air or incoming flow of air
air	of the air
b	of the thermal barrier or bottom
$burner$	of the burner
c	of convection, characteristic or centre
$chem$	chemical
$cond$	of conduction
$conv$	of convection
cr	critical
d	of the interior of the exhaust duct of the Cone Calorimeter/FPA
e	external or of the exhaust flow
eff	effective
end	at the end of the test
exp	of the experiment

f	of the furnace walls
fire	of the fire
g	of the gas
i	of insulation or iteration counter
in	incoming
inc	radiant incident
ig	of ignition
l	of the lateral
loss	of losses
model	of the model
net	net
out	leaving
P	of pyrolysis
paint	of the coating paint
plate	of the metallic plate
r	of radiation
s	of sample or surface
st	stored
skin	of the metal skin from a sandwich panel
T	total
t	total assuming complete combustion
w	of the test sample/wall
∞	of the ambient or gas-phase

Acronyms

ASTM	American Society for Testing and Materials
BC	Boundary condition
BRE	Building Research Establishment
BS	British Standards
BSI	British Standards Institution
CDG	Carbon dioxide generation
CFC	Chlorofluorocarbon agent
CFD	Computational fluid dynamics
CHF	Critical heat flux
CN	Crank-Nicolson
CO	Carbon monoxide
CO_2	Carbon dioxide
dev	Deviation
DSC	Differential scanning calorimetry
DTU	Technical University of Denmark
DTG	Differential thermogravimetric analysis
E	Integrity
EN	European standard
EPS	Expanded polystyrene foam
ETICS	External thermal insulation composite system
ETFT	Edinburgh Travelling Fire Tests

EU	European Union
EWI	External wall insulation
FPA	Fire propagation apparatus
FPI	Fire propagation index
FM	Factory Mutual
FRS	Fire Research Station
F-S	Fraser-Suzuki regression
GB	Gas Burner
HCFC	Hydrochlorofluorocarbon agent
HFC	Hydrofluorocarbon agent
HRR	Heat release rate
HRRPUA	Heat release rate per unit area
H-TRIS	Heat-Transfer Rate Inducing System
I	Thermal insulation
ICF	Insulating concrete formwork
IM	Inverse modelling
ISO	International Organization for Standardization
IPS	Insulated panel system
IWI	Internal wall insulation
LIFT	Lateral Ignition and Flame Spread Test
LMA	Levenberg-Marquardt algorithm
LOI	Limiting oxygen index
LSF	Lightweight steel frame system
MDI	Methylene di-phenyl di-isocyanate
MLR	Mass loss rate
MW	Mineral wool
N_2	Nitrogen
NFPA	National Fire Protection Association
nZEB	Nearly zero-energy buildings
pHRR	Peak of heat release rate
O_2	Oxygen
OC	Oxygen consumption
ODP	Ozone depleting factor
PB	Plasterboard
PCS	Gross heat of combustion ($MJ \cdot kg^{-1}$)
PF	Phenolic Foam
PIR	Rigid polyisocyanurate foam
PS	Polystyrene
PUR	Rigid polyurethane foam
QMC	Queen Mary College
R	Load bearing capacity
RP	Radiant panels
SBI	Single burning item
SIP	Structural insulated panel
std	Standard

SPT	Sandwich Panel Tests
SW	Stone wool
TA	Thermal analysis
TC	Thermocouple
TDI	Toluene di-isocyanate
TG	Thermogravimetry
TGA	Thermogravimetric analysis
TRP	Thermal response parameter ($kW \cdot s^{1/2} \cdot m^{-2}$)
TSC	Thin skin calorimeter
UCLAN	The University of Central Lancashire
WC	Wood crib
XPS	Extruded polystyrene foam

Chapter 1.

Introduction

1.1 Background to the project

During the last decades, sustainability has been introduced as the main driver in the built environment, leading to several changes in the construction practices and the society. New disciplines such as *sustainability science* have been defined [1], which consider sustainability as a problem with three different aspects: global, social and human. Whereas the global aspect refers to the preservation of the planet and therefore the human survival (energy, climate, ecosystems, etc.), the social aspect considers the political, economic and technological factors from society. The third aspect considers human factors such as lifestyle, values or security, which are related to the human culture and are intrinsically linked to the other two aspects. A schematic representation of this concept of global sustainability is presented in Figure 1.1.

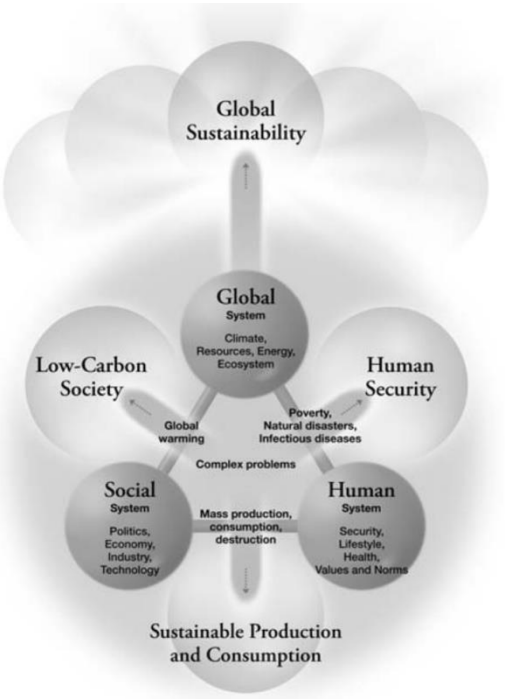

Figure 1.1. Schematic representation of the different aspects and relationships established by the discipline "*sustainability science*". Extracted from [1]

The established relationships between the different aspects by *sustainability science* serve as a clear baseline to understand the context of insulation materials in the built environment. Insulation materials are no longer required only for satisfying human comfort in buildings, but also for controlling other issues such as fuel shortage in the planet and the global warming from carbon dioxide emissions. Indeed, a common solution to overcome these problems and satisfy the aforementioned issues is to reduce the levels of energy consumption. *Rockwool International A\S* provided relevant data for this framework in a survey presented in 2011 [2], showing the distribution of energy consumption by different sectors. The results from this survey indicated that the energy consumed in buildings represents approximately 41% of the total consumption, while the transport and industry sectors represent 33% and 26%

respectively. Along with the frameworks set for industries and transportation for the reduction of energy consumption, there is also a clear need to develop control measures in buildings. Insulation materials represent the main control measure in order to reduce the heat losses or gains through the external partitions of the building; therefore, the use of insulation materials is expected to increase significantly in the built environment in order to meet the goals established by these frameworks and governmental policies on this front. An example of this is evident in the European Union, with the approval of the *Energy Performance of Building Directive* (EPBD) [3] in 2010. National plans are required towards the objective of *nearly Zero Energy Buildings* in the EU Member States by 2020.

As a result, energy performance has become the main driver in construction during the last decade. However, this is not the only criterion to be considered in the design of buildings, but one among several others such as cost, space-usage, accessibility, human comfort, structural design or fire safety. Indeed, the building design can be conceived as a multi-objective problem in which a global optimum is aimed in relation to the combination of each of the considered criteria. The use of multi-objective optimisation techniques requires the application of quantitative analyses in which an objective or target function can be 'measured'. This sets the baseline for performance-based designs, which require quantifiable variables so as to be applied.

Most of these criteria can be quantified as a function of specific variables. However, fire safety is usually conceived as a prescriptive approach in which codes define strict specifications to achieve safety requirements. Today, current methods for the fire safe design of buildings are based on the use of harmonised standard fire tests and code prescriptions. The aim of these tests is to assess the fire hazards from construction materials, products and systems in the building. Standard tests provide ratings that are used to evaluate fire performance in the event of a fire. However, these ratings only provide information in relation to the behaviour observed for these test conditions. Indeed, as described by *Brannigan* at the *FireSeat* conference in 2008 "*performance tests can only be used to 'score' materials in the specified test*" [4], which is consistent with *Drysdale*'s statement at the *Fire and cellular polymers* conference in 1986: "*The results of these tests are specific to the apparatus and the procedure, and need to be interpreted very carefully before decisions are made about the end use of the material/composite*"[5].

A series of issues are anticipated with regard to fire safety and insulation materials, which lie on how the fire safety framework and building design methods are established at present. Fire safety cannot be integrated as a quantifiable variable in the design of buildings since the performance assessment from standard testing is only relevant to the conditions of the test. As a result, the design is expected to be biased by materials that provide better energy performance due to demanding energy efficiency policies. This is the case of plastic insulation products which generally show lower thermal conductivities. However, despite their flammability, the only fire safety requirement is to comply with the established standard testing framework.

Several concerns [6, 7] have been raised during the last decade due to this 'technological innovation' possibly including inherent fire risks into the built environment. Main concerns relate to the flammability and combustibility of some of these materials and the effect on the fire due to their characteristic thermal properties. However, the main question remains on whether there is a fundamental consistency between the fire safety framework, based on standard tests, and the hazards from the intense use of insulation materials.

At present, the clear challenge for designers is that, while it is recognised that the actual material behaviour does not necessarily replicate other than the one observed during the test, no tools are available to quantify the fire risks from the use of insulation materials. A rigorous analysis of the fire performance of elements should recognise the limitations of a specific test, and more importantly not being biased by the particular interests of the industry.

Therefore, recommendations and tools are urgently required for designers. These tools seem necessarily to lie on material characterisation, so as assessments to unlimited fire scenarios can be approached and quantitative designs can be developed.

1.2 Aims of the research

The main aims of the research presented in this thesis is to assess the fire performance of the main insulation materials used in construction, identify the fire hazards associated to the use of these materials in buildings, and eventually present a methodology for the quantifiable and safe design under fire conditions. In order to fulfil these aims, a series of goals need to be pursued:

- **Identification of the main insulation materials and wall typologies used in the market.**
- **Review of the criteria for the design of insulation systems in buildings at present.**
- **Review of the fire performance of insulation materials and drivers for the development of combustible insulation materials.**
- **Identification of the inadequacies of current fire safety methods for the design of insulation systems in buildings.**
- **Failure criteria redefinition based on material characterisation.**
- **Characterisation of the main insulation materials at different scales**.
- **Development of a methodology for the fire safe design of insulation systems in buildings based on quantifiable parameters.**

1.3 Outline of chapters

This thesis contains nine chapters, as well as a number of appendices. A brief description of these chapters, aside from the current introductory chapter, is presented below.

Chapter 2

Literature Review

A review on the current criteria for the design of buildings is undertaken; highlighting that from the large number of criteria, fire safety is a non-quantifiable criterion due to the prescriptive approach used at present. An extensive review of the main insulation materials and wall typologies used for construction is presented. Current fire safety methods for the design of insulation systems in buildings and different frameworks such as the one applied in the European Union and the NFPA framework commonly applied in America are also presented. Finally, an investigation on the fire performance of insulation materials found in literature is presented.

Chapter 3

Moving from Compliance Testing to a Performance-Based Design Methodology

The inadequacy of current fire safety methods for the design of insulation systems in buildings is discussed, highlighting what is being measured and quantified by the EU framework of reaction-to-fire tests and the fire-resistance test. A redefinition of the failure criteria for the design of insulation systems is proposed, which is based on the identification of the main hazards associated to the use of combustible insulation materials. A methodology based on the control of the main fire hazard, i.e. the onset of pyrolysis, is proposed. The aim of this methodology is to provide a quantifiable assessment that could be included in performance-based designs of insulation systems. A series of inputs from material properties and performance are required. An extended experimental plan is presented in order to verify the identified hazards' map and fill the gaps required for the application of this methodology.

Chapter 4

Identification of Main Solid Phase Thermal Degradation Processes: Pyrolysis and Oxidation

The experimental work based on thermogravimetric analyses of the studied insulation materials is presented in this chapter. Pyrolysis and oxidation reactions are explored under different conditions. An analysis on the complexity of the thermal degradation for each of the insulation materials is presented. Quantification of the critical temperature for the design methodology based on the kinetics of the pyrolysis reactions is discussed.

Chapter 5

Fire Performance of Insulation Materials in Bench-Scale Testing: A Qualitative Approach

The experimental work based on the use of the Cone Calorimeter [8] for the flammability and combustibility assessment of the studied insulation materials is presented. Values of critical heat flux, ignition temperature, thermal inertia, heat release rate, effective heat of combustion and gas analyses are provided. The combustion dynamics and behaviour from the different materials are explored, as well as the effect of the sample boundary condition at the exposed face (foiled protective layer commonly used by rigid plastic foams). Classic regressions for the determination of the thermal inertia are discussed. Results obtained by thermogravimetry are correlated to the obtained ignition temperatures, and quantification of the critical temperature for the design methodology is established.

Chapter 6

Assessment and Characterisation of the Thermal Evolution of Insulation Materials

The experimental work based on the use of an external radiant heat source without pilot igniter, and measurement of in-depth temperatures in the solid-phase is presented. The thermal degradation processes experienced by the insulation materials are correlated to temperature measurements and gas analyses. A novel method based on the use of a thin metallic plate is introduced in the experimental plan in order to reduce the uncertainty in the heat transfer analysis and reduce the oxidation rate for charring materials. A numerical method for the prediction of the thermal evolution of insulation materials when exposed to severe conditions of heat is applied. This model is based on the resolution of a one-dimensional conduction heat transfer equation under inert conditions, and the use of inverse modelling techniques. Values of thermal properties are provided, and the limitations of the undertaken approach are discussed.

Chapter 7

Large-Scale Testing: Performance and Hazards' Map Validation

Chapter 7 presents the experimental work based on two real-scale testing programmes (the Edinburgh Travelling Fire Tests carried out at BRE, Watford (UK) and the Sandwich Panel Tests carried out in Chorley (UK) in 2013) and an intermediate-scale testing programme using radiant panels. These represent opposite case scenarios for studying the onset of pyrolysis, due to the definition of thermally thick and thermally thin barriers. The intermediate-scale tests provide further validation of the fire hazards' map identified in previous chapters under a controlled environment. A simplified method for determining pyrolysis rates is presented.

Chapter 8

Design Tool for the Definition of Thermal Barriers for Insulation Materials

A tool for the design of thermal barriers for combustible insulation materials is developed and presented in this chapter, as well as the required inputs for the design of this tool. The two suggested approaches for the definition of input parameters from the fire are based on the definition of the heat flux as a characteristic parameter rather than a time-temperature curve. Non-dimensional charts that generalise the different possible solutions as a function of the barrier parameters (thermal properties and thickness), insulation parameters (critical temperature and thermal properties) and fire inputs (net heat flux or radiant heat flux with a cooling heat transfer coefficient) are provided.

Chapter 9

Conclusions and Further Work

The main conclusions from this thesis are highlighted, followed by a detailed summary of the developed work and extended conclusions. Recommendations for further work on the fire performance and design of insulation materials are also presented.

1.4 References

[1] H. Komiyama and K. Takeuchi, "Sustainability science: building a new discipline," *Sustainability Science*, vol. 1. pp. 1–6, 2006.

[2] M. Gilles and T. D. Jensen, "SRI roadshow Paris," 2011. [Online]. Available: http://www.rockwool.com/files/COM2011/Investor/Presentations/2011/20110610_Paris-SRI-Roadshow_BAML.pdf. [Accessed: 01-Feb-2015].

[3] EU, "Directive 2010/31/EU of the European Parliament and of the Council of 19 May 2010 on the energy performance of buildings," *Official Journal of the European Union*, pp. 13–35, 2010.

[4] V. M. Brannigan, "The regulation of technological innovation: the special problem of fire safety standards," in *FireSeat "Fire & Building Safety in the Single European Market,"* 2008, pp. 20–33.

[5] D. Drysdale, "Fundamentals of the fire behaviour of cellular polymers," in *Fire and cellular polymers*, 1986, pp. 61–75.

[6] B. Meacham, B. Poole, J. Echeverria, and R. Cheng, *Fire Safety Challenges of Green Buildings*. Springer New York, 2012.

[7] U. Krause, W. Grosshandler, and L. Gritzo, "The International FORUM of Fire Research Directors: A position paper on sustainability and fire safety," in *Fire Safety Journal*, 2012, vol. 49, no. 0, pp. 79–81.

[8] "BS 476-15, ISO 5660-1. Fire tests on building materials and structures. Method for measuring the rate of heat release of products." BSI, 1993.

Chapter 2.

Literature Review

2.1 Introduction to the problem

2.1.1 Quantifiable and non-quantifiable variables for building design

At present, the building design can be considered as a multi-objective optimisation technique, in which many criteria are considered for finding the most favourable solutions. Optimisation techniques are often applied to several criteria such as sustainability (energy consumption [1, 2], life cycle [3, 4] or durability), space-usage and lay-out [5, 6], human comfort (thermal [7, 8], acoustical or visual [9]) or structural design [10, 11]. These are some relevant factors among many others to be considered in the design of buildings.

Multi-objective optimisation techniques mean to reach a global maximum or minimum for the considered objectives or cost functions. However, a local optimum for each of the criteria does not imply a global optimum for the design. Certainly, two types of criteria can be found: those which are collaborative (i.e. while improving a certain criterion, another criterion is also improved) and those that are conflictive (i.e. improving a certain criterion implies deteriorating another criterion). These conflictive criteria lead to a range of optimum solutions that are defined as the 'Pareto frontier'. A schematic of a multi-objective Pareto frontier for two variables is shown in Figure 2.1 below. An extensive review on multi-objective techniques has been presented by *Coello et al.* [12, 13]. Apart from the above mentioned criteria which are highlighted for the construction industry, other engineering fields such as fire safety are at present also considered for the design of buildings.

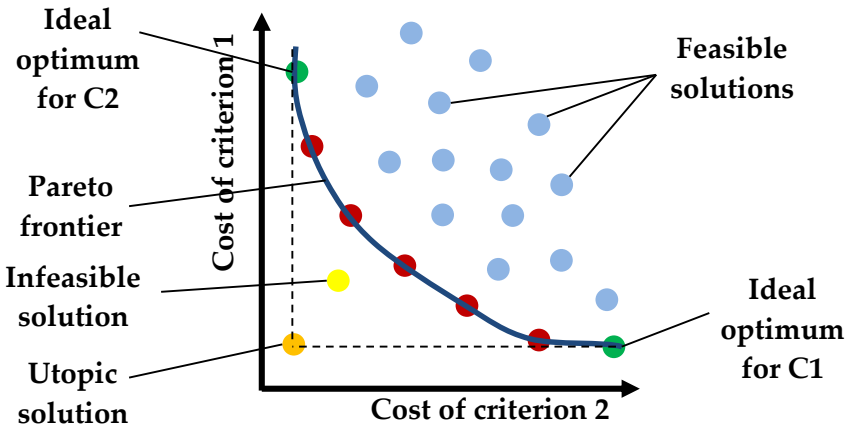

Figure 2.1. Schematic of the Pareto frontier for two criteria. Feasible and infeasible solutions respectively correspond to the points above and below the Pareto frontier, while the possible compromised solutions are represented as the Pareto frontier. The utopic solution would be represented as a point with minimum cost for C1 and C2

It is obvious that if a multi-objective design is to be carried out, the considered criteria must be quantifiable in order to be able to evaluate the cost of alternative solutions. Criteria such as energy performance, space usage, product life cycle or acoustics can be quantified as functions of certain parameters. For instance, energy efficiency can be measured as energy consumption per year per unit of floor area or

thermal transmittance, space usage can be quantified as a function of the thickness, surface or volume, life cycle can be quantified in terms of a functional unit, and acoustics can be quantified with parameters such as reverberation time. However, fire safety is not considered as a quantifiable parameter at present for the design of buildings. Indeed, fire safety is considered as a prescriptive approach in which a framework based on standard flammability testing for material classification and standard furnace testing for the design of compartmentalisation elements is used. Then, safety requirements are based on pass-fail thresholds that impede the evaluation of fire as a quantifiable approach (performance-based). Current methods of design based on this approach are detailed in the following sections, while its drawbacks will be discussed in Chapter 3.

Under this scenario, energy performance has become the main driver in construction during the last decades. Throughout Europe and worldwide, many design concepts and voluntary standards for energy efficient buildings or low-energy buildings have been developed. Some of the differences among these standards are the definition of energy efficient buildings (low-energy buildings, passive buildings, etc.), drivers to classify the energy savings (carbon dioxide emissions, $kWh \cdot yr \cdot m^{-2}$), several requirements for different kind of buildings (new or existing; residential or non-residential) or different techniques so as to reach the energy savings.

In Europe, requirements for *nearly Zero-Energy Buildings* (nZEB) are specified by the *Energy Performance of Building Directive* (EPBD) and the *Renewable Energy Directive*. A nearly Zero-Energy Building is defined as "*a building that has a very high energy performance. The nearly zero or very low amount of energy required should be covered to a very significant extent by energy from renewable sources, including energy from renewable sources produced on-site or nearby*" [14]. By the end of 2020 all new buildings[1] have to be *nearly Zero-Energy Buildings*, and the Member States shall set the targets and draw national plans for reaching this objective. Nevertheless, substantial differences on the existing low-energy building definitions are encountered among EU Member States [15]. Some of the steps and plans defined towards *nearly Zero-Energy Buildings* by different EU Member States are shown in Table 2.1

[1] Actions on existing buildings that undergo through major renovation are also indicated, depending on a series of factors such as useful floor area.

Table 2.1. National approaches to implement nZEB requirements. Extracted from [16]

Country	Steps towards 2020	2020 NZEB requirement
Belgium	(housing) 2012: ~ -12 to 22% (baseline 2011) 2014: ~ 25-45% (baseline 2011)	Zero Energy Buildings
Czech Republic	2012: ~20-30% 2015: ~20-30%	Passive house principle: 20 $kWh \cdot m^{-2} \cdot yr^{-1}$ (heating only)
Denmark	2010: - 25% (baseline 2006) 2015: - 57% (baseline 2006)	Energy frame: Dwellings: 20 $kWh \cdot m^{-2} \cdot yr^{-1}$ Offices etc.: 25 $kWh \cdot m^{-2} \cdot yr^{-1}$ Implemented as voluntary standard in building regulation
France	2010: - 20 % (baseline 2005) 2012: : 40-65 $kWh \cdot m^{-2} \cdot yr^{-1}$ (BBC level)	Energy positive buildings
Finland	2012: - 44 to 52% (baseline 2009) 2015: Public buildings Passive House Level	Passive house principle: 20 $kWh \cdot m^{-2} \cdot yr^{-1}$ (heating only)
Germany	2009: - 30% (baseline 2006) Stepwise strengthening towards NZEB – next changes scheduled for 2012	Climate Neutral
The Netherlands	2011 : - 25% (EPC) 2015 : - 33% (Passive House Level)	Energy Neutral Buildings
Norway	Not known	Passive House Standard
Sweden	Not known	In discussion 30-50 $kWh \cdot m^{-2} \cdot yr^{-1}$ (electrical heat.) 55-75 $kWh \cdot m^{-2} \cdot yr^{-1}$ other heat sources
United Kingdom	2010: - 25% (baseline 2006) 2013: - 44 % (baseline 2006) 2016: zero carbon houses 2019: zero carbon buildings	Zero Carbon Buildings

However, the main concepts and features for energy efficiency in buildings are similar among the EU Member States as well as the large amount of standards formulated worldwide. A summary of some of the main features and concepts for energy efficient buildings of these standards is presented below:

- High levels of insulation materials in the envelope of the building.
- Increased levels of air tightness.
- Efficient heat recovery of the ventilation in order to improve the performance of heating and cooling systems.
- Reduction of thermal bridging.
- Use of more efficient windows.

2.1.2 Side effects on a path towards *nearly Zero-Energy Buildings* (nZEB)

The most important measure towards more energy efficient buildings is represented by the use of high levels of insulation materials, which aim to reduce the heat losses or gains to the exterior of the building. These new targets have substantial implications in relation to the methods of construction typically used, and obviously in the final design of the building:

- **With regard to the effect on the construction methods:** classic methods of construction must be adapted to meet the new regulations if their use is to be continued. This implies new changes in the way these elements are constructed so as to reach an increased thermal performance. Systems which already use internal insulation will increase their thicknesses because of required lower transmittance values. This is the case of masonry cavity walls or framing boards which will be described in the following section. However, other systems without internal insulation will require the attachment of new layers of insulation materials. This is the case of refurbishment of existing masonry solid walls where the insulation is placed either on the outer leaf of the wall with a render or on the inner side with cladding materials such as plasterboards. Alternatively, innovative and new methods of construction are being developed, which can offer a solution of high performance in terms of energy efficiency and cost.
- **With regard to the effect on the final design of buildings:** a new challenging scenario is presented for designers. As noted by *Papadopoulos* [17], despite building construction is an important economic sector in Europe, it has eventually been a nationally and regionally fragmented market. The most common products used in each region have commonly been determined by the trends of the market. Nevertheless, as noted in the previous section, building design can be understood as an optimisation problem with multiple objective variables such as cost and space usage. A new scenario is posed, where higher requirements on the thermal performance of the building envelope are required. Indeed, products with lower thermal conductivity can offer an optimum minimum in terms of space usage and amount of material, which eventually may translate into lower cost. This optimised design is, however, obtained only by considering the energy efficiency criteria, but not fire safety which is presented as a pass-fail add-on in the design.

An example of an EU Member State is presented with regard to energy efficiency in buildings. In UK some actions have been taken and a solution for a regulation of domestic buildings is being formulated as a plan for the *Zero Carbon Buildings*. An analysis of different standards' proposals for these energy efficient dwellings has already been performed [15]. As a result of this survey, losses of 39 and 46 $kWh \cdot m^{-2} \cdot yr^{-1}$ seem to be the final target for new residential buildings. Specific values for non-residential buildings are still being studied [18]. As a result, the U-values for the different elements of the envelope of the building are specified in order to reach these energy consumption targets. A summary of these thermal

transmittances from British regulations for England and Wales are listed in Table 2.2 below.

Table 2.2. Current and expected U-values guidelines by British standards for new buildings[2]

Building element	Type of building	Current U-value range /W·m^{-2}·K^{-1} (2010 Standards) [19–22]	New U-value range /W·m^{-2}·K^{-1} (2020 Standards)
Wall	New dwellings	0.24	0.18
	New non-domestic buildings	0.24	Not defined yet
Floor	New dwellings	0.15	0.14 – 0.18
	New non-domestic buildings	0.20	Not defined yet
Roof	New dwellings	0.13 – 0.16	0.11 – 0.13
	New non-domestic buildings	0.16	Not defined yet
Window	New dwellings	1.5	1.3 – 1.4

This set of values serve as an orientation of the thermal performance required for building elements in new or refurbished energy efficient buildings. Focussing on walls, values of 0.18 W·m^{-2}·K^{-1} will be required, approximately 25% lower than the current required value.

A brief review of the most common insulation materials and boundary typologies used in the European market are presented in the following section. Current thicknesses of insulation from typical wall systems are insufficient while plastic (polymeric) materials with lower thermal conductivities represent an ideal optimum from the perspective of the energy performance criterion.

2.2 Review of the main insulation materials and boundary typologies in construction

The types of insulation materials that can be found in the market for the use in buildings are classically divided into four main groups of materials, depending on their characteristics. A classic classification proposed by *Papadopoulos et al.* [17, 23] is as follows:

- **Inorganic materials** such as foams (glass foam) or fibrous materials (glass wool and stone wool).
- **Organic materials** such as expanded foams (expanded polystyrene, extruded polystyrene, polyurethane, polyisocyanurate, phenolic, cork and melamine foams) or fibrous materials (sheep-wool, cotton-wool and cellulose).
- **Combined materials** (siliconated calcium, gypsum foam and wood-wool).
- **New technology materials** (transparent and dynamic materials like phase change materials).

[2] This study was carried out before the release of the latest editions of Approved Documents L1A and L2A published in 2013, coming into effect on 6 April 2014 [143]

According to *Papadopoulos et al.* in 2005, the most used insulators in the European market belong in the two first groups listed previously. Inorganic materials such as glass wool and stone wool account for 60% of the market and organic foams such as EPS, XPS and polyurethane for 27% of the market. The rest of materials represent less than 13%. A more recent study presented by *Rockwool International A\S* in 2011 [24] showed similar trends but with increased percentages for the plastic foams, from which stone wool was found to represent the 25-30% of the European market, while glass wool has the same representation and plastic foams represent the 40-45%.

As part of the ongoing PhD research at Glasgow Caledonian University into the effect of fire on thermally efficient walls containing polymeric insulation, a preliminary survey [25] was carried out in order to examine the type of insulation materials specified in 2000 and in 2011 for use in new timber framed wall constructions. In 2000 the dominant form of insulation was mineral wool; in 2011, this had changed strongly in favour of polymeric foam insulation. The data was extracted from Building Warrant approvals held in Stirling Council's archives, and relates to proposed construction work throughout the Stirlingshire area (United Kingdom).

The main typologies of external walls are identified herein. Specific insulation materials and wall suppliers are noted solely for the purposes of factual accuracy. These can be classified into two main groups: those corresponding to classic systems adapted to meet the new regulations (i.e. masonry cavity walls, framing boards and masonry solid walls) and innovative systems which are normally characterised for being composite elements and are becoming very popular as sustainable methods of construction (e.g. structural insulated panels (SIPs), insulated panel systems (IPS) and insulating concrete formworks (ICFs)).

The major part of these systems, or variations of them, can also be used as roofs, floors or inner walls. Furthermore, some of the techniques related to these systems not only can be used for new buildings, but also for refurbishments. A diagram of these main typologies identified for this thesis is shown in Figure 2.2. Some of the insulation materials, typically used for constructing these elements, are also indicated.

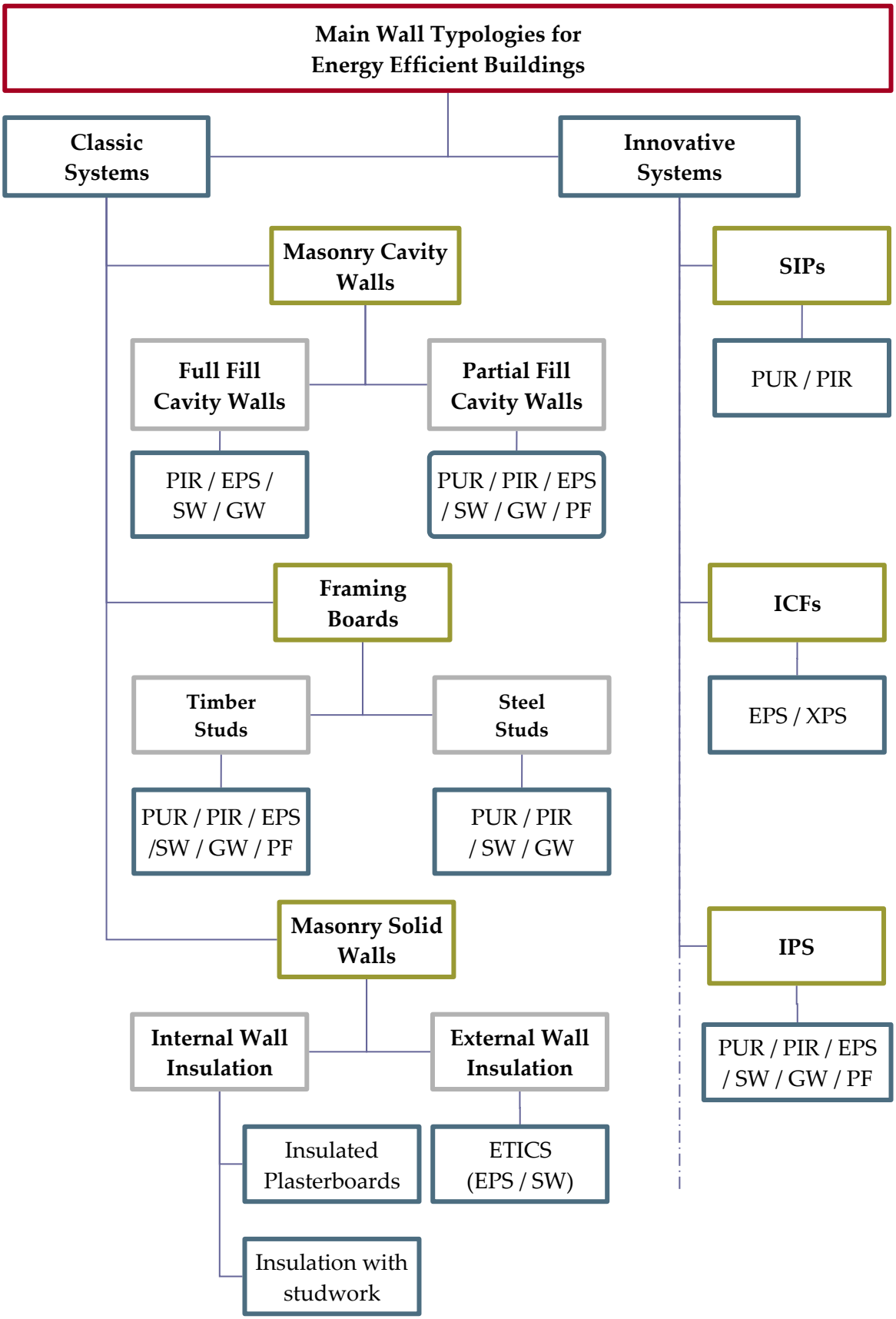

Figure 2.2. Schematic of wall typologies for energy efficient buildings

2.2.1 Classic wall systems

2.2.1.1 Masonry cavity walls

A masonry wall is a partition made of units disposed and bounded together by the use of mortar. The materials used to compound the wall are typically bricks, concrete blocks, ceramic blocks or stones. A cavity is made in the middle of the inner and outer leaves in order to place the insulation material. Wall ties are used to connect the two leaves of the wall so as to spread lateral loads. Masonry walls can be distinguished depending on whether the insulation material fills fully or partially the cavity. A brief description of these and values of thermal transmittances as a function of the insulation thickness are detailed below.

a. Full fill cavity walls

This kind of cavity wall is completely filled by the insulation material, with two main procedures for filling the cavity:

- By placing **solid insulation boards** into the cavity. Good practices recommend constructing the wall by rows in height. In each stage, the external leaf is constructed first, followed by placing the insulation board and finally the internal leaf. This process is repeated in stages using ties.
- By constructing the outer and inner leaves of the wall and **injecting the insulation material** through a hole in order to fill the cavity formed by the leaves of the wall.

Schematics of full fill cavity walls are shown in Figure 2.3, extracted from [26]. Different configurations are possible according to the U-value requirement and the different kind of bricks, cladding or internal finishes used (Table 2.3). Stone wool, rigid polyisocyanurate foam, expanded polystyrene and glass wool are the most typical insulation materials used for filling the cavity.

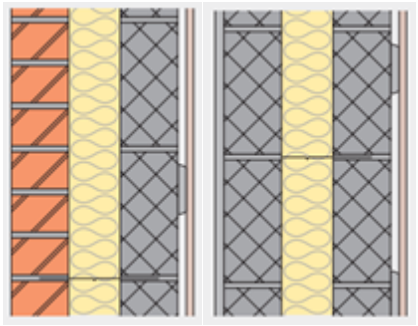

Figure 2.3. Examples of full fill cavity walls constructed by different outer leaves. Extracted from [26]

The typologies and data presented in Table 2.3 correspond to data extracted from common manufacturers with public access to technical data sheets of their products. Typical U-values that can be reached by different insulation thicknesses are presented. It must be noted that not only the insulation materials affect the final U-value of the wall, but also the thermal properties of the material used for the wall leaves and claddings.

Table 2.3. Typical full fill cavity wall typologies

Insulation material	Product type Thermal conductivity /W·m^{-1}·K^{-1}	U-value range /W·m^{-2}·K^{-1}	Insulation thickness range /mm	Wall description
PIR (Manufacturer 1) [27]	Board [28] 0.021	0.12 – 0.24	75 - 150	Similar configuration to stone wool configuration. PIR board has gas tight facings - with one additional face bonded to provide a drainage plane, directing moisture onto the outer leaf.
EPS (Manufacturer 1) [29]	Slab [30] 0.030	0.23 – 0.38	75 – 100	**External leaf:** 102.5 mm brickwork / 150 mm natural stone / 100 mm dense concrete block + 13 mm render / 100 mm dense concrete block + 13 mm render or tiles on batten finish **Internal leaf:** 100 mm dense concrete block / 100 mm lightweight block / 100 mm aerated concrete block **Internal finishes:** Fair-faced / 13 mm lightweight plaster / 12.5 mm plasterboard on dabs
EPS (Manufacturer 2) [31]	Injected in bead form [32] 0.033	0.14 – 0.29	100 – 200	**Configuration 1:** Render + dense block + injected EPS + dense block + plaster **Configuration 2:** Render + light block + injected EPS + dense block + plaster **Configuration 3:** Brick + injected EPS + dense block + plaster **Configuration 4:** Brick + injected EPS + dense block + plaster
Stone wool [33]	Slab [34] 0.037	0.15 – 0.30	75 – 235 (>150 2 layers)	**Construction 1:** 102 mm facing brick outer skin + stone wool slab + internal concrete block 100 mm + plaster/ plasterboard on dabs **Construction 2:** Render + 100 mm medium dense block outer skin + stone wool slab + internal concrete block 100 mm + plaster/plasterboard on dabs
	Blown [35] 0.039	0.20 – 0.30	85 - 175	**Construction 1:** 102 mm facing brick outer skin + stone wool blown + internal concrete block 100 mm + plaster **Construction 2:** Render + 100 mm medium dense block outer skin stone wool blown + internal concrete block 100 mm + plaster

Glass wool [36]	Blown [37] 0.037 - 0.040	0.25 – 0.55	50 – 100	Brick outer leaf + glass wool blown + 100 mm block inner leaf type + 12.5 mm plasterboard on dabs

b. Partial fill cavity wall

This kind of cavity wall includes a cavity that is not fully filled by the insulation, since this system provides an effective barrier to rain penetration, permits drainage of water or humidity and provides further ventilation. This system is used in more severe environments avoiding problems related to full fill cavity walls such as condensation. The insulation is attached to the inner leaf of the wall, as shown in the schematics presented in Figure 2.4 below, extracted from [26].

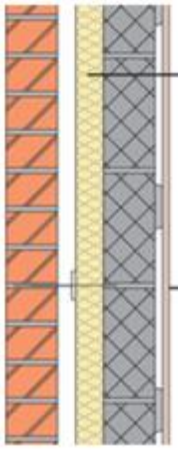

Figure 2.4. Example of partial fill cavity wall. Extracted from [26]

The width of the cavity is usually specified by the regulations of the country, and usually depends on the wall height and the severity of the area of exposition, while the thickness of this cavity is between 25 and 75 mm. The insulation materials typically used for partial filling of the cavity are rigid polyurethane foam, rigid polyisocyanurate foam, phenolic foam, expanded polystyrene foam and stone wool. The thermal performance achieved by different insulation manufacturers is presented in Table 2.4.

Table 2.4. Typical partial fill cavity wall typologies

Insulation material	Product type Thermal conductivity /W·m^{-1}·K^{-1}	U-value range /W·m^{-2}·K^{-1}	Insulation thickness range /mm	Common wall description
PIR (Manufacturer 1) [38]	Rigid board [39] 0.022	0.14 – 0.35	30 – 140	**Configuration 1:** 10 mm render polymer + 100 mm dense block outer + residual cavity + insulation +inner leaf fair faced blockwork + optional internal finish (3 mm skim coated 12.5 mm plasterboard or PF insulated plasterboard) **Configuration 2:** 102.5 mm brick outer leaf + residual cavity + insulation + inner leaf fair faced blockwork + optional internal finish (3 mm skim coated 12.5 mm plasterboard or PF insulated plasterboard)
PIR (Manufacturer 2) [27]	Rigid board [40] 0.021	0.13 – 0.29	50 – 150	Outer leaf + residual cavity (minimum of 25 mm) + insulation + inner leaf (AAC block / dense block)
PF (Manufacturer 1) [38]	Rigid board [41] 0.020 - 0.023	0.14 – 0.35	30 – 125	Similar to PIR (manufacturer 1)
PF (Manufacturer 2) [27]	Rigid board [42] 0.021 - 0.023	0.15 – 0.29	50 – 100	Similar to PIR (manufacturer 2)
EPS [31]	Rigid board [43] 0.037	0.20 – 0.27	100 – 140	Outer leaf + residual cavity + insulation + EPS board + inner leaf (AAC block / dense block)
Stone wool [33]	Semi-rigid [44] 0.034	0.20 – 0.30	80 - 150	102 mm facing brick outer skin + residual cavity + insulation + internal concrete block 100 mm (medium dense / aircrete) + plaster/ plasterboard on dabs

2.2.1.2 Masonry solid walls

Simple masonry solid walls do not contain a cavity where the insulation material is placed; therefore the thermal performance is clearly lower. This type of walls can be found on buildings built before the first half of the twentieth century or in regions with moderate climates. After that period, cavity walls became more common due to the need of better thermal performance and comfort.

In order to improve the thermal performance, two general methods can be used, which are based on adding new layers to the wall including an insulation layer in the

inner or outer face of the wall. Both systems have advantages and disadvantages with regard to factors such as durability, air tightness, vapour control or condensation [45]. These systems are mainly used for refurbishment, but they can also be found in new buildings.

a. Internal wall insulation (IWI)

This system is normally used when the external appearance of the façade needs to be preserved. The main advantage is that scaffolding tasks are not required since the work is done from the interior of the building. Some identified disadvantages are the reduction in the effective area of the internal floor or problems of interstitial condensation if the insulation is placed on a heavy masonry wall. Two common applications are based on the attachment of the insulation directly to the masonry wall covered by plasterboard, or using internal insulation with studwork. A brief description of these systems is presented below, with indicative U-values for different thicknesses noted in Table 2.5.

- **Insulated plasterboards.** These are typically composite walls where the insulation layer attached to plasterboard is jointed to the inner leaf of the masonry wall by using adhesive or continuous ribbons of plaster and mechanical fixings. Additional layers can be fitted depending on the risk of moisture penetration.

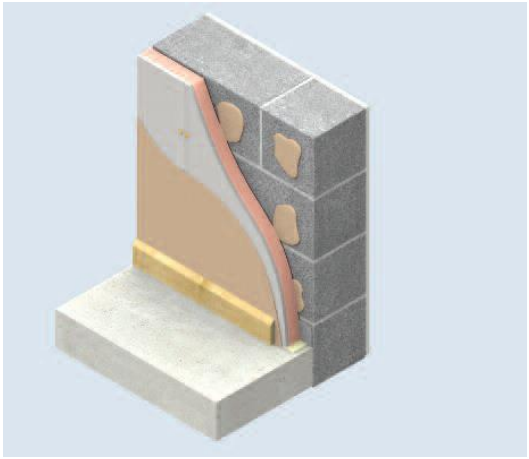

Figure 2.5. Example of insulated plasterboards for masonry solid wall. Extracted from [38]

- **Insulation with studwork.** Studs of timber or steel are attached to the inner leaf of the masonry wall and a layer of insulation with a vapour layer and plasterboard is placed between the studs. Studs can also include a layer of insulation in order to improve the thermal performance of this system, e.g. composite studs made of oriented strand board and rigid insulation.

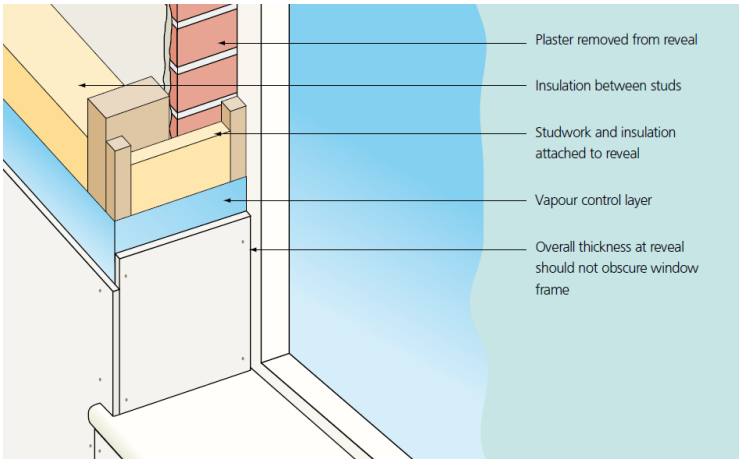

Figure 2.6. Example of studwork for masonry solid wall. Extracted from [46]

Table 2.5. Typical U-values for insulated plasterboard wall insulation [46]

Insulation material	Typical thermal conductivity /W·m^{-1}·K^{-1}	U-value range /W·m^{-2}·K^{-1}	Insulation thickness /mm
Phenolic foam	0.022	0.16 – 0.42	40 ⇒ 0.42 W·m^{-2}·K^{-1} 100 ⇒ 0.21 W·m^{-2}·K^{-1} 140 ⇒ 0.16 W·m^{-2}·K^{-1}
PUR/PIR	0.023	0.16 – 0.43	40 ⇒ 0.43 W·m^{-2}·K^{-1} 100 ⇒ 0.21 W·m^{-2}·K^{-1} 140 ⇒ 0.16 W·m^{-2}·K^{-1}
Stone wool	0.038	0.20 – 0.52	40 ⇒ 0.52 W·m^{-2}·K^{-1} 100 ⇒ 0.26 W·m^{-2}·K^{-1} 140 ⇒ 0.20 W·m^{-2}·K^{-1}
EPS/XPS	0.038	0.24 – 0.60	40 -> 0.60 W·m^{-2}·K^{-1} 100 -> 0.32 W·m^{-2}·K^{-1} 140 -> 0.24 W·m^{-2}·K^{-1}

Table 2.6. Typical U-values for studwork internal wall insulation [46]

Insulation material	Typical thermal conductivity /W·m^{-1}·K^{-1}	U-value range /W·m^{-2}·K^{-1}	Insulation thickness /mm
Phenolic foam	0.022	0.21 – 0.51	40 ⇒ 0.51 W·m^{-2}·K^{-1} 100 ⇒ 0.27 W·m^{-2}·K^{-1} 140 ⇒ 0.21 W·m^{-2}·K^{-1}
PUR/PIR	0.023	0.21 – 0.52	40 ⇒ 0.52 W·m^{-2}·K^{-1} 100 ⇒ 0.28 W·m^{-2}·K^{-1} 140 ⇒ 0.21 W·m^{-2}·K^{-1}
Stone wool	0.035	0.27 – 0.62	40 ⇒ 0.62 W·m^{-2}·K^{-1} 100 ⇒ 0.35 W·m^{-2}·K^{-1} 140 ⇒ 0.27 W·m^{-2}·K^{-1}
EPS	0.038	0.28 – 0.64	40 ⇒ 0.64 W·m^{-2}·K^{-1} 100 ⇒ 0.36 W·m^{-2}·K^{-1} 140 ⇒ 0.28 W·m^{-2}·K^{-1}

As presented in Table 2.5 and Table 2.6, U-values lower than 0.20 $W \cdot m^{-2} \cdot K^{-1}$ are rarely achieved with these indicated thicknesses. Therefore, combinations of internal and external insulation are likely required, or thicknesses higher than 140 mm in most of the cases. This implies the use of thicker studs and thus a cost increase. A common solution as lightweight studs is explained in the following section of framing boards.

b. External wall insulation (EWI)

In this system an insulation layer is attached to the outer leaf of the masonry wall by mechanical means or adhesively fixing. The insulation can be finally covered by a render or a cladding finish. A schematic example of this system is shown in Figure 2.7. The main disadvantages of this system are that scaffolding works and specialised workforce are required, as well as the significant change of the property appearance. However, the area of the inner floor remains unaffected and helps protecting the masonry wall from moisture and thermal stresses.

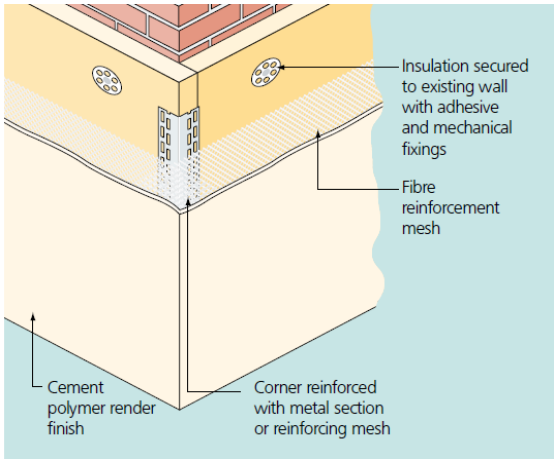

Figure 2.7. Example of external wall insulation for a masonry wall. Extracted from [46]

Insulation materials such as phenolic foam, polyisocyanurate foam, polyurethane foam, expanded polystyrene or stone wool can be used for this type of solution. An indicative range of thermal transmittances for different insulation materials is noted in Table 2.7.

Table 2.7. Typical U-values for external wall insulation [46]

Insulation material	Typical thermal conductivity /$W \cdot m^{-1} \cdot K^{-1}$	U-value range /$W \cdot m^{-2} \cdot K^{-1}$	Insulation thickness /mm
Phenolic foam	0.022	0.16 – 0.44	40 ⇒ 0.44 $W \cdot m^{-2} \cdot K^{-1}$ 100 ⇒ 0.21 $W \cdot m^{-2} \cdot K^{-1}$ 140 ⇒ 0.16 $W \cdot m^{-2} \cdot K^{-1}$
PUR/PIR	0.023	0.16 – 0.45	40 ⇒ 0.45 $W \cdot m^{-2} \cdot K^{-1}$ 100 ⇒ 0.22 $W \cdot m^{-2} \cdot K^{-1}$ 140 ⇒ 0.16 $W \cdot m^{-2} \cdot K^{-1}$
Stone wool and EPS	0.038	0.25 – 0.65	40 ⇒ 0.65 $W \cdot m^{-2} \cdot K^{-1}$ 100 ⇒ 0.33 $W \cdot m^{-2} \cdot K^{-1}$ 140 ⇒ 0.25 $W \cdot m^{-2} \cdot K^{-1}$

The external wall insulation system is also known as external thermal insulation composite system (ETICS) [47]. At present, the most common insulation materials being used are stone wool and expanded polystyrene. The three main components that an ETIC system consists of are:

- A layer of insulation material, usually stone wool boards or expanded polystyrene foam.
- Reinforcement such as plaster and a reinforcing mesh from glass fibres. The reinforcing mesh prevents any possible future crack formation.
- Top coat such as ceramic plaster or glazed bricks.

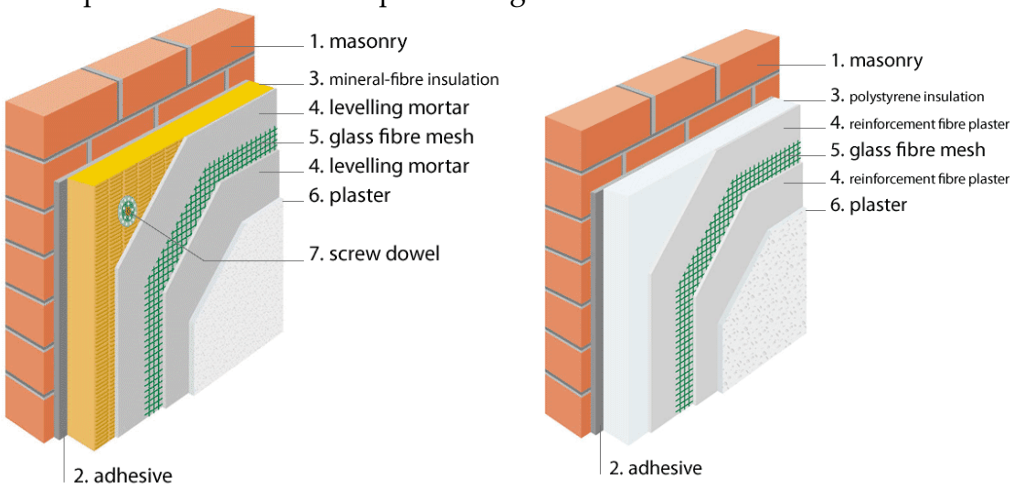

Figure 2.8. Examples of stone wool and EPS ETIC systems. Extracted from [47]

2.2.1.3 Framing boards

Framing boards are characterised for being lightweight systems of construction. This typology of wall represents a traditional method of construction that has also become very popular for sustainable construction, adapting its features for the new regulations in terms of thermal, fire and acoustic performance. These elements can be used as external walls as well as extensions, inner partitions or roofs.

The system is based on the use of studs, mainly of timber or steel, in order to create frames for the walls of the building compartments. Bricks, claddings, renders, internal finishes and insulation are used to complete the wall.

a. Timber framing system

Classic timber framing walls require the use of timber studs to create a gap where the insulation layer is fitted. Then, the gap with the insulation is covered by a sheathing board on the outer face and usually plasterboard on the inner face. As for partial fill cavity walls, a cavity is used between an external masonry leaf and the framing system. Therefore, a classical timber framing wall is made of the following layers, represented in Figure 2.9:

- Outer masonry leaf.
- 50 mm cavity.
- Breather membrane.

- Sheathing board (9 mm OSB).
- Insulation between the studs (usually 140 mm thick studs).
- Vapour control layer.
- Plasterboard layer.

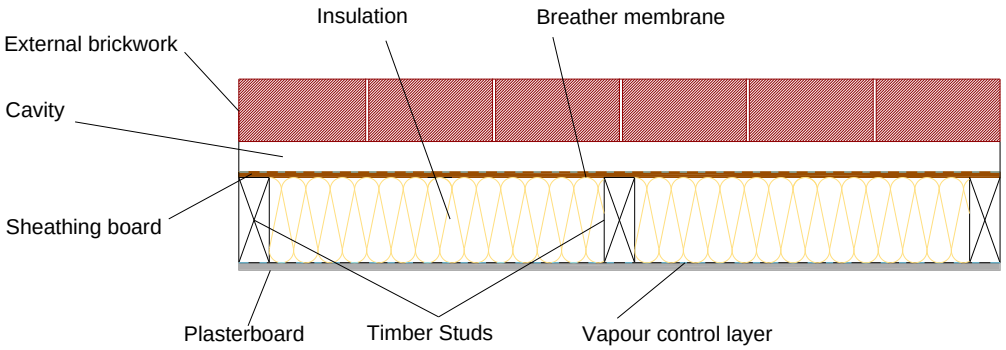

Figure 2.9. Scheme of a classic timber frame studs wall

The common insulation materials used for this type of wall are phenolic foam, stone wool, polyurethane foam (PUR) and polyisocyanurate foam (PIR). This system has been represented in Figure 2.9 with the insulation layer fully filling the gap between the sheathing board and the plasterboard, but other configurations are also possible. Since PIR and phenolic foam have a lower conductivity, for the same range of thicknesses framing, walls with PIR and phenolic foam have a better thermal performance than with stone wool. This implies the possibility of the insulation material not filling the cavity fully between the plasterboard and the sheathing board; thus, another air gap is present in the wall. This common representation for PIR and phenolic foam walls is presented in Figure 2.10a below. Additionally, there is also the possibility of constructing these walls with a service zone, normally a 25 mm battened void between the vapour layer and the internal finish (plasterboard).

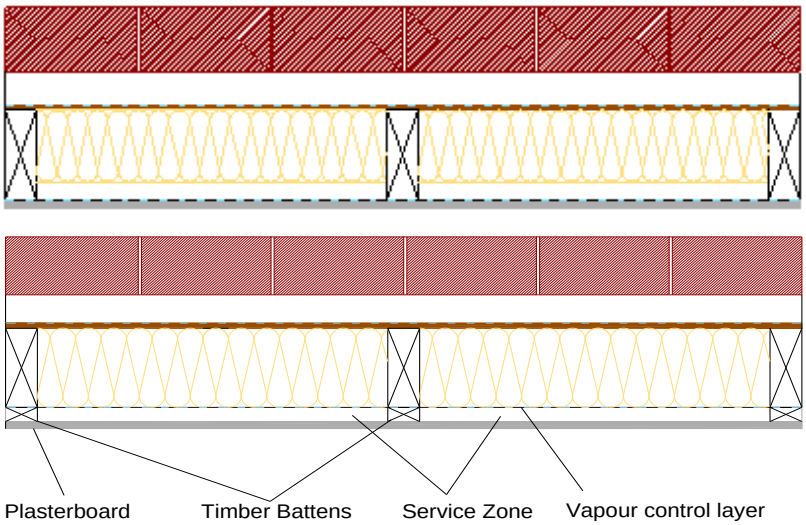

Figure 2.10. (a) Timber frame studs wall with the insulation layer not fully filling the gap (b) Timber frame studs wall with a service zone

The stud thickness of this timber frame wall is usually 140 mm. Other smaller sizes as 89 or 120 mm) can also be adapted, depending on the insulation material used.

Nevertheless, smaller sizes are not widely used anymore, since increased insulation thicknesses are required to reach lower thermal transmittance. Examples of the thermal performance of this system by using different insulation materials are presented in Table 2.8. The products have been selected from the main manufacturers of PIR, phenolic foam and stone wool in the UK.

Table 2.8. U-values achieved by classic timber frame walls

Insulation material	Typical thermal conductivity /W·m^{-1}·K^{-1}	Insulation thickness /mm	U-value range /W·m^{-2}·K^{-1}	Comments
PIR [38, 48]	0.022	50 – 120	0.15 – 0.34	U-values lower than 0.19 are achieved by the use of insulated plasterboards. Wall configuration similar to Figure 2.9 with 140 mm thick studs. The insulation does not fully fill the space between the sheathing board and the plasterboard.
Phenolic foam [38, 49]	0.020	45 – 120	0.15 – 0.35	
Stone wool [33, 50]	0.035 - 0.038	140	0.25 – 0.28	Wall configuration similar to Figure 2.9 with 140 mm thick studs.

As was noted in Table 2.2, U-values below 0.020 W·m^{-1}·K^{-1} are required for walls in refurbished or new energy efficient buildings, although this target cannot be achieved by typical timber stud walls. Therefore, in order to improve the thermal performance of these elements, alternative techniques are applied:

- **Use of additional plasterboards.** The thermal performance increase is not very significant, thus this technique should be used in combination with other solutions.
- **Use of insulated plasterboards instead of common plasterboards.** Insulated plasterboards are solutions commonly used for refurbishing solid masonry walls.
- **Use of double insulation layer.** The new insulation layer is placed within the cavity, attached to the sheathing board. This system is similar to partial fill cavity walls. Two examples of walls insulated by stone wool and phenolic foam are shown in Figure 2.11.
- **Increasing the thickness of insulation.** This implies an increase of the depth of the studs, thus making the system heavier and more expensive. This increase depends on the insulation material due to the variation of the thermal conductivity. A new type of lightweight timber studs can be used as shown in Figure 2.12, called I-section studs and consist of two squared in section flanges and a thin web. Thicknesses up to 220 mm can be achieved, and the main benefit of using these is the reduction of heat losses across the studs.

Figure 2.11. Schemes of timber frame studs walls with an additional insulation layer. Stone wool based system [26] (b) PIR based system [38, 49]

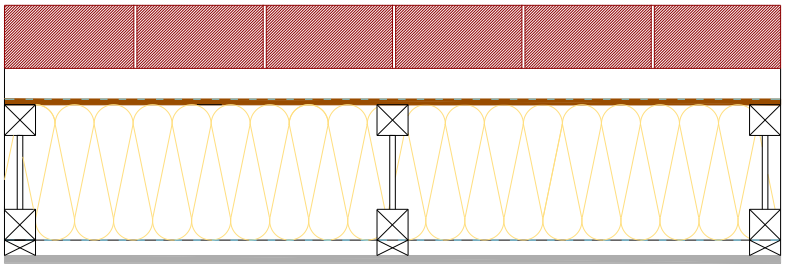

Figure 2.12. Schematics of a timber frame wall with a service zone using I-section studs

b. Steel framing system

The system used for these walls is also known as Lightweight Steel Frame systems (LSF). Loadbearing C studs from 75 mm to 150 mm wide are normally used and two types of LSF systems can be identified:

- **Warm frame construction.** The insulation is placed outside the steel frame; therefore, it is a similar configuration to external wall insulation. The range of thicknesses achieved by this system ranges from 250 mm to 450 mm. An example of this configuration would be the one made of the following layers:
  - Render finish.
  - Insulation.
  - Vapour control layer.
  - External sheathing board.
  - Steel studs.
  - Layers of plasterboard.
- **Hybrid construction.** The insulation is placed externally as a warm frame construction as well as between the steel studs. An example of this configuration consists of the following layers:
  - Render finish.
  - External insulation.
  - Breather membrane.
  - Steel studs full fill by the internal insulation.
  - Layers of plasterboard.

The latter system, i.e. hybrid construction, usually provides a better thermal performance. Therefore, the former system is rarely going to achieve the required thermal performance for future U-value targets, unless thicker layers of insulation are used. Another possible configuration for external walls is the same as these two configurations explained above, but including a cavity between the render and the external insulation. As mentioned before, this cavity allows reducing problems related to the rain and drainage of humidity. An alternative solution of hybrid LSF wall using drainage channels instead of a cavity is possible. Schematics of this are shown in Figure 2.13 below, extracted from [51].

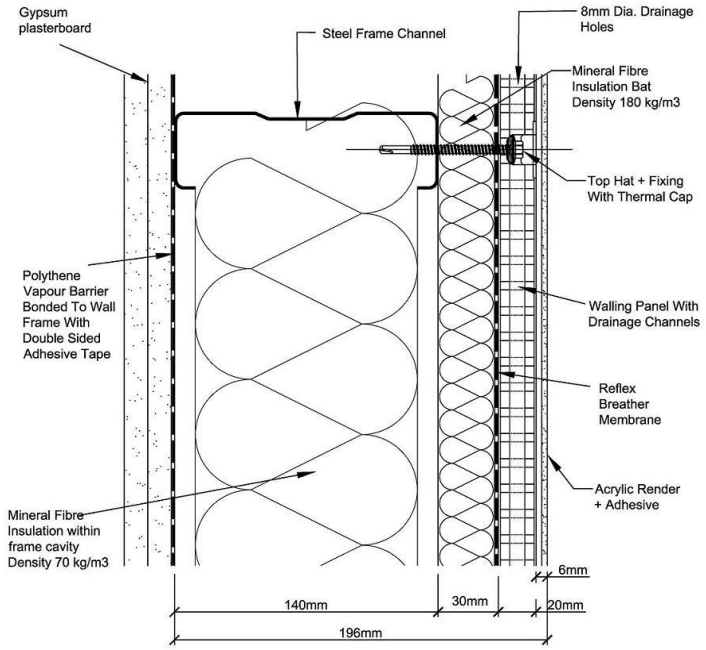

Figure 2.13. Example of hybrid LSF wall. Extracted from [51]

2.2.2 Innovative systems

2.2.2.1 Structural insulated panels (SIPs)

This system can be classified as a composite building material. According to the definition given by the Structural Insulated Panel Association [52], "*SIPs are a high performance building system for residential and light commercial construction. The panels consist of an insulating foam core sandwiched between two structural facings, typically oriented strand board (OSB).*" Oriented strand boards are boards made of strands of wood layered in specific orientations. Despite oriented strand boards are the main elements used as structural facings, other materials such as plywood, sheet of metals or cement can also be used.

SIPs can be used as exterior walls, inner partitions, roofs or floors. This system has a considerable load bearing capacity, thus reducing the necessity of internal studding. To achieve this good performance, the bond between the three layers (the two leaves of OSB and the foam core) must be very strong. This can also provide a good acoustic performance, which explains why it is usually used as an inner partition.

Regarding to the core foam of the structural insulated panels, the main insulation materials used are expanded polystyrene, extruded polystyrene, polyurethane foam and polyisocyanurate. As SIPs depend on the bond between the foam core and the outer sheeting, fibre insulation as stone and glass wool cannot be used due to delamination issues.

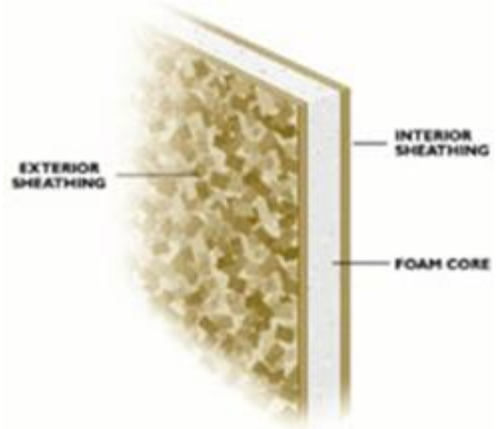

Figure 2.14. Example of structural insulated panel. Extracted from [52]

The two fundamental applications for SIPs are full structural and infill for concrete, steel or timber frames. Depending on the end use, SIPs can also be used for cavity walls as external walls, by attaching them to the inner leaf (vapour layer and lining finishes) and keeping a residual cavity between the SIP and the outer leaf (external cladding, render or bricks) to avoid problems related to rain penetration.

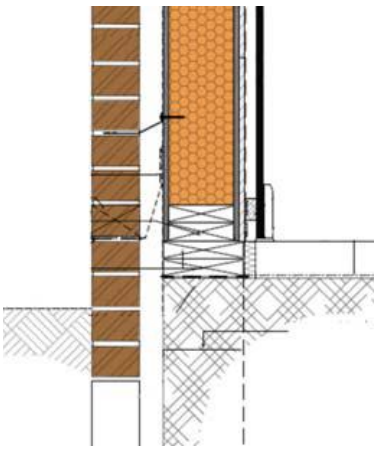

Figure 2.15. Example of structural insulated panel as external wall. Extracted from [53]

Typical U-values achieved by different thicknesses and insulation materials are shown in Table 2.9. Additionally, common wall configurations by different manufacturers are listed.

Table 2.9. U-values achieved by SIP systems from different manufacturers

Insulation material	Typical thermal conductivity /W·m^{-1}·K^{-1}	U-value range /W·m^{-2}·K^{-1}	SIP thickness range /mm	Common wall description
Polyurethane foam (Manufacturer 1) [54, 55]	0.023	Wall panels: 0.19 – 0.22	223 ⇒ 0.20 W·m^{-2}·K^{-1}	**Configuration 1:** Outer brick leaf + 50 mm cavity + breather membrane + SIP + 25 mm timber battens + 12.5 mm vapour check plasterboard **Configuration 2:** Render + calcium silicate board + 25 mm timber counter batten + breather membrane + SIP + 25 mm timber battens + 12.5 mm vapour check plasterboard **Configuration 3:** Brick slip system + 25 mm timber counter batten + breather membrane + SIP + 25 mm timber battens + 12.5 mm vapour check plasterboard Other possible configuration available
EPS (Manufacturer 2) [56]	~0.030	0.15 – 0.27	100 – 250	Facings of 9 and 11 mm OSB are **Standard configuration for external wall:** 102 mm brick outer leaf + 50 mm cavity + breather membrane + SIP + vertical timber strap + 12.5 mm vapour control plasterboard

2.2.2.2 Insulating concrete formwork (ICF)

This system consists of interlocking modular units without intermediate bedding materials, which create a cavity where the concrete is pumped and eventually the wall is formed. The modular units are made of insulation materials which provide a high thermal performance to the wall. The most common insulation material used is expanded polystyrene foam. Schematics from this system are presented in Figure 2.16.

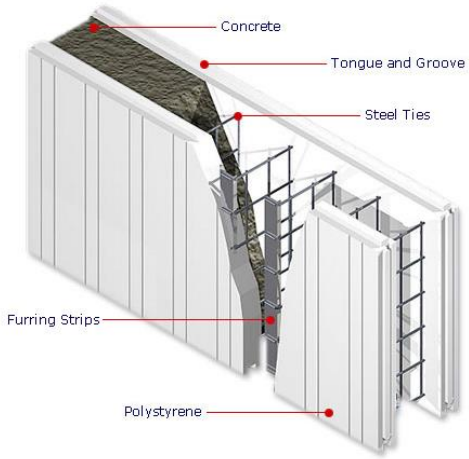

Figure 2.16. Example of insulating concrete formwork. Extracted from [57]

A common configuration for an insulating concrete formwork system could be:

- External render.
- External brick.
- EPS outer layer.
- Concrete core.
- EPS inner layer.
- Internal finishes such as plasterboards with dry-lined finish.

The approximate thermal performance of some ICF systems from different manufacturers is presented in Table 2.10.

Table 2.10. U-values achieved by ICF systems from different manufacturers

Manufacturer	Insulation material	U-value range /W·m^{-2}·K^{-1}	ICF thickness range /mm	Comments
1 [58]	EPS 1	0.20 – 0.23	242 – 394	Actual performance will depend on the finish used. Inner EPS is 70 mm thick.
	EPS 2	0.19 – 0.21	298	
	EPS 3	0.11 – 0.17	330 – 431	
2 [59]	EPS	0.11 – 0.19	250 – 335	Actual performance will depend on inner and outer finishes such as brick slip systems, timber cladding, render or commercial cladding systems
3 [31, 60]	EPS	0.19 – 0.20	300 – 350	Insulation thickness of 150 mm

2.2.2.3 Insulated panel systems (IPS)

Insulated panel systems (also called composite insulated panels (CIPs) or commonly referred as sandwich panels) are composite walls with a wide range of possible uses such as external walls, façades, roofs and inner partitions. Insulated panel systems are commonly used for new or refurbished non-residential constructions as industrial and commercial buildings. This system consists of two metal facings less than 1 mm thick with an insulation core and no air gaps between

them. The core of the panel is bonded by the use of adhesive materials or is automatically bonded by the self-adhesion of the insulation to the metal facings. IPS are pre-manufactured materials which are transported to the construction location and placed in-situ.

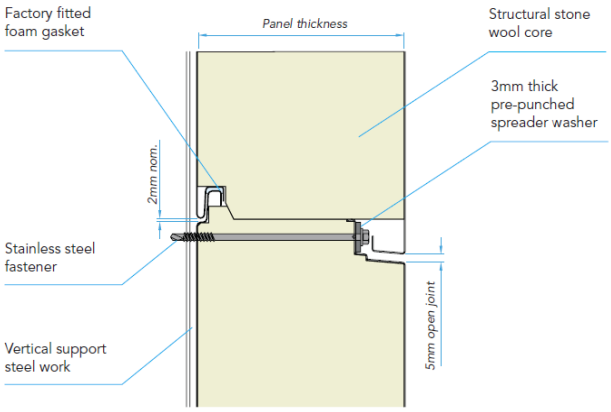

Figure 2.17. Example of insulating panel system of stone wool core. Extracted from [61]

Insulated panel systems are considered as non-structural systems but are strong units able to transfer wind or snow loads to the supporting structure of the building. The common insulation materials used for the core are polyisocyanurate foam, polyurethane foam, stone wool, polystyrene foams and phenolic foam.

The thermal performance depends on the thickness of the core used some rough calculations of which considering only the insulation are shown in Table 2.11.

Table 2.11. Approximate U-values achieved by different insulation materials

Insulation material	Typical thermal conductivity /W·m^{-1}·K^{-1} [43]	Thickness /mm U-value /W·m^{-2}·K^{-1}
PUR/PIR	0.022 – 0.028	50 ⇒ 0.44 – 0.56 100 ⇒ 0.22 – 0.28 150 ⇒ 0.15 – 0.19
Stone wool	0.034 – 0.044	50 ⇒ 0.68 – 0.88 100 ⇒ 0.34 – 0.44 150 ⇒ 0.23 – 0.29
EPS	0.031 – 0.038	50 ⇒ 0.62 – 0.76 100 ⇒ 0.31 – 0.38 150 ⇒ 0.21 – 0.25
Phenolic foam	0.021– 0.024	50 ⇒ 0.42 – 0.48 100 ⇒ 0.21 – 0.24 150 ⇒ 0.14 – 0.16

2.2.3 Common aspects from insulation systems

A series of facts can be identified in relation to the partition elements based on insulation materials:

- Insulation materials are normally installed covered under a lining or render avoiding the direct exposure of these. Common practices include insulation materials as composite elements.

- Insulation materials can be found totally embedded within the inner and outer leaves of the partition, or attached to one of the leaves from the partition leaving a cavity for the free circulation of air. Gaps for service areas can also be found.
- Rigid plastic insulators such as PUR/PIR or phenolic foams provide solutions that represent an optimum in terms of thermal transmittance and thicknesses, due to their low thermal conductivity.
- Inorganic materials such as glass wool and stone wool require thicker insulation boards, and even changes in the typology of construction for certain partition elements such as framing walls.
- As a result, the design of these construction elements is clearly dominated by the thermal performance.

2.3 Current methods of design for insulation systems in fire

As mentioned before, many criteria can be considered for the design of buildings, some of them being quantifiable, and others such as fire safety simply being considered as a prescriptive approach. Current methods for designing insulation systems in fire depend on the regulation framework where this is applied. The description presented herein is mainly focused on the EU regulation framework, although the framework based on the NFPA is briefly discussed as well.

2.3.1 Regulatory framework in EU

Two sets of fire related harmonised standards applicable for insulation materials and insulation-based products are compulsory in the EU at present: the reaction-to-fire [63] and fire-resistance [64] testing frameworks. The concept is based on the classical understanding of fire development in a compartment, commonly classified as pre-flashover and post-flashover compartment fires, the latter also referred as *Regime I* by *Thomas et al* [65].

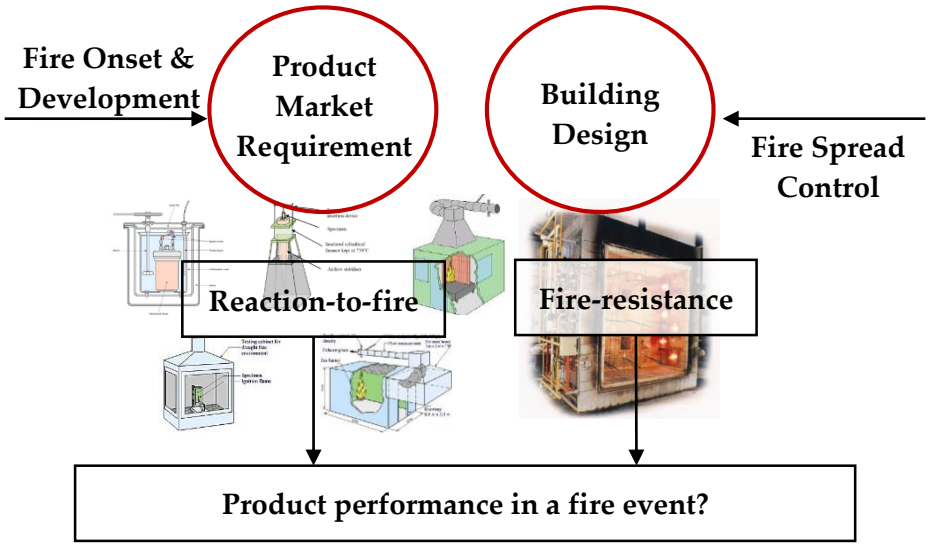

Figure 2.18. Fire safety framework based on standard testing in the EU

a. Reaction-to-fire framework

Reaction-to-fire type of standard testing aims in elucidate the likely contribution of materials or products to the fire in the stage previous to flashover (i.e. combustible-controlled fire previous to the fully-developed fire or ventilation-controlled fire), and therefore the likely contribution in accelerating the flashover. The current reaction-to-fire testing framework is used as a material/product classification which is used to assess any product to be used in the EU market, commonly known as Euroclasses [63]. Therefore, this can be understood as a product-type standardisation by which the flammability of the product is assessed and the material is eventually classified. This classification is extrapolated as the expected performance of the product in the event of a fire. Prescriptive design standards require the use of certain classes for specific uses. An example of this can be found in the use of insulation materials in cavity walls for high rise buildings[3] in Scotland, in which only non-combustible[4] materials can be used. An exception is made if the two leaves of the external cavity wall are at least 75 mm thick masonry or concrete walls and the external wall is provided with cavity barriers around all openings and top of the wall-head [66].

The fire classification of construction products and building materials (classified from A to F) proposed by BS EN 13501-1 [44] is briefly shown in Table 2.12.

Table 2.12. Euroclasses classification and description by BS EN 13501-1 [63]

Class	Description by BS EN 13501-1
A1	No contribution to fire in any stage.
A2	Satisfying the same criteria as class B for EN 13823 [48]. In addition, under conditions of fully developed fire they will not contribute significantly to the fire load and fire growth.
B	As class C but satisfying more stringent requirements.
C	As class D but satisfying more stringent requirements. Additionally under thermal attack by a single burning item they have a limited lateral flame spread [48].
D	Products satisfying criteria for class E and capable of resisting, for a longer period, a small flame attack without substantial flame spread [49]. In addition, they are also capable of undergoing thermal attack by a single burning item with sufficiently delayed and limited heat release [48].
E	Products capable of resisting, for a short period, a small flame attack without substantial fire spread. [49].
F	No tested or incapable of achieving Class E.

Materials may be classified as A1 and A2 if they pass **a non-combustibility test** [69] and the **heat of combustion** tested by BS EN ISO 1716 [70] is lower than a certain value (e.g. it shall be satisfied that the gross heat of combustion "PCS" for a construction products is PCS ≤ 3 $MJ \cdot kg^{-1}$). The non-combustibility test is based on a small furnace where the temperature is monitored continuously. The non-combustibility criterion lies in verifying whether there is significant temperature increase after the sample insertion. The heat of combustion test is determined by the amount of energy accumulated by the material and that can be released by a

[3] High rise buildings in Scotland are referred to buildings with any storeys at a high of more than eight metres above the ground.

[4] This term is referred to materials classified by the Euroclasses [63] as A1 and A2.

combustion reaction. The latter is a usual test used in fire science to assess combustibility of materials.

Materials or products classified as B, C, D or E should be tested by an **ignitability test** [68] and by the **single burning item (SBI)** test [67]. The ignitability test is based on the impingement of a flame on the surface or edge for 15-30 seconds, and verification of a subsequent ignition and flame spread. The SBI test evaluates the potential contribution of a product to the development of a fire, under a fire situation simulating a burning item in a room corner near to that product. The heat source is a fire of 30 kW at a corner where the product is placed. Parameters to measure smoke production (SMOGRA) and heat release rate/fire growth (FIGRA) [71] are used to characterise the performance.

b. Fire-resistance framework

Fire-resistance standard testing aims to elucidate the likely spread of the fire in the subsequent stage to flashover (i.e. during the fully-developed fire regime), and therefore represent the ability of the assembly to contain the fire within the compartment. Then, this is related to the compartmentalisation strategy, which is vital in fire safety designs to control the development and spread of a fire through a building. This type of testing can be understood as a system-design-type standardisation by which the compartmentalisation performance of the system is evaluated. Most of fire-resistance testing methods are based on the use of the furnace test BS EN 1363-1 [64]. Other standard tests have been developed for specific applications such as façades [53], curtain walls and cavity barriers [73]. Construction elements are exposed to the heat conditions resulting from monitoring the standard time-temperature curve [64] in the furnace, commonly controlled by gas burners; other technologies such as electrical furnaces are also under research [74]. The performance is evaluated by assessing three variables: load bearing capacity 'R', integrity 'E' and thermal insulation 'I', designated as a time measurement resulting from satisfying these criteria. This is commonly defined as the fire-resistance rating. The meaning of these different criteria is listed below:

- Load bearing capacity 'R' corresponds to the ability of the element to withstand certain load during the test. This is not relevant for most of insulation systems.
- Integrity 'E' corresponds to the ability of the element of not presenting flammable gases at the unexposed face. This is evaluated by locating a piece of cotton at the unexposed face and verifying if ignition is achieved. This is confirmed by observing whether flaming is achieved at the back or by verifying whether a gap gauge can be inserted.
- Thermal insulation 'I' which corresponds to the ability of the element of not presenting high temperatures on the unexposed face. The limit is set to an average increase of 140 K or a temperature increase at any location of 180 K.

2.3.2 Regulatory framework according to NFPA

The NFPA 5000 framework with regard to insulation materials, and more specifically to plastic foams, is based on three concepts: reduced flammability, thermal barrier and ignition barrier [75]. Similarly to the EU regulation framework, insulation materials must be classified with regard to their flammability. A thermal barrier needs to be used to protect the insulation material, which has to be tested according to a fire-resistance standard test, with the performance assessed as a thermal insulation criterion (I). The particular conditions to be met are:

- **Flammability:** foams must achieve a minimum rating of Class B, flame spread index from 26 to 75, and smoke developed index lower than 450, when tested according to the ASTM E84 [57].
- **Thermal barrier for the foam plastic:**
  a) Thermal barrier is tested over a thermal inert substrate. The temperature rise on an unexposed surface must not exceed 130°C after 15 minutes of exposure, when tested under the ASTM E119 time-temperature curve [77].
  b) Room-corner test [78] with specific requirements: "*(i) During the 40 kW flame exposure, flames shall not spread to the ceiling (ii) during the 160 kW flame exposure, flames shall not spread to the outer extremity of the sample on any wall or ceiling and flashover shall not occur; (iii) during the entire test, the peak rate of heat release shall not exceed 800 kW (iv) and the total smoke released shall not exceed 1,000 m²*."
- **Ignition barrier:** A barrier material that prevents total exposure of the foam must be used.

2.4 Insulation materials and fire safety in buildings: A perceptible problem

Energy performance in buildings is driving the construction industry towards a more intense use of thermal insulation materials, from which plastic materials seem to provide an optimum solution. However, plastic insulation materials are combustible[5] by definition, thus representing a potential issue with regard to the fire performance of buildings. Additionally, the intense use of insulation materials may modify the dynamics of the fire due to change in the energy balance from more insulated boundaries. These are however assumptions rather than facts, which need to be validated and quantified. Some of these issues relating sustainability and fire safety have already been recognised by *The International FORUM of Fire Research Directors* [79] and *Meacham et al.* [80].

A straightforward qualitative description of the likely different fire issues related to insulation materials is presented here. The author proposes a hazard classification from two perspectives, with regard to the fire dynamics inside and outside the

[5] The term combustible used in this thesis shall be interpreted as the ability of an organic compound (gas or solid) to oxidise rather than based on a formal material classification given by standard fire testing.

compartment. The former is related to the expected different behaviour of the fire inside a compartment, anticipated to be more severe due to:

- An increase of the combustible load due to higher amounts of materials in the boundaries, most of them being combustible materials. Increased amounts of combustible materials might imply **contribution to the energy released inside the compartment** and **longer-lasting fires** if these materials are involved in the combustion. Possible mechanisms of contribution could be represented as failure of the boundary/barrier element or transport of pyrolysis gases.
- A **reduction of the thermal losses** to the outside of the compartment, increasing the thermal feedback to burning fire load. This subject has been studied by different authors [81–84].

The intense use of combustible insulation materials within the boundaries could lead to potential issues with regard to the spread of fire hazards outside the compartment such as:

- **Internal fire spread** due to premature collapse of the boundaries acting as fire compartmentalisation elements, or spread through internal cavities.
- **External fire spread** due to collapse of external wall, external flaming through windows or flame spread through cavities.
- **Spread of toxic gases** released either by pyrolysis of insulation materials placed within the compartment divisions, or by combustion of these pyrolysates.

Meacham et al. performed a profound analysis in relation to the fire safety challenges of green buildings [80]. Similarly to the author's proposal, a series of fire hazards of green attributes with regard to rigid foam insulations have been recognised. Examples of these are: *"potential explosion hazard, poses potential toxicity hazard, readily ignitable, burn readily once ignited, contributes more fuel/increased HRR, material affects burning characteristics, faster fire growth rate, significant smoke production hazard, failure affects burning characteristics, material presents flame spread concern, may impact suppression effectiveness and relative risk level".*

While the philosophy for standard testing is to address these series of hazards, yet the challenges remain in answering aspects such as:

- whether the hazards from insulation materials are clearly identified and fundamentally understood,
- whether these hazards can be quantified, and
- whether the control measures and methods for designing insulation systems in fire are suitable.

2.5 Review of fire performance of insulation materials

The selection of insulation materials for this thesis is based on the two main groups of insulation materials found in the market: inorganic wools and organic plastic

foams. Stone wool (SW) is selected from the inorganic wools, while expanded rigid closed-cell foams such as isocyanurate-based polyurethane foam (PIR), phenolic foam (PF) and expanded polystyrene (ESP) are chosen from the group of plastics. Three types of PIR are chosen due to the uncertainty in the formulation of this material depending on the manufacturer. As a matter of fact, one of these products was initially obtained as a PUR denomination, but as will be discussed in further sections the distinction between PUR/PIR tends to be confusing. Indeed, at present PIR seems to have substituted PUR foams some of the EU markets, including the UK market.

A descriptive review of these materials is presented below, together with a more specific review of their thermal and fire properties. It should be noted that while many data parameters can be found in the literature, only a brief description is presented herein. Extended compilation of fire material properties can be found in Appendix B.

2.5.1 Stone wool (SW)

Stone wool is a fibrous material made of wool spun from mainly volcanic basalt and diabase rocks and organic binders. The process of manufacturing stone wool is based on melting volcanic stones and coke to later on generate spun fibres using spinning machines. Eventually, in order to create a wool shape product, the spun of fibres is cured and cut. In this process, a binder and oils are used to keep the fibres together and form the wool. The binder is normally a thermoset resin, and the content of this depends on the density of the wool, with typical contents of binder being a fraction of 2-3% of the total for low density wools [85].

The thermal decomposition of stone wool is commonly understood, following different steps as the temperature within the material is increased [86]:

- Initial decomposition of organic parts of the product such as the binder.
- Increase of the fibres' temperature up to high temperatures when the crystallization process takes place and the thickness of the material is reduced. During this process, physical properties of the wool change drastically, losing the wool shape.
- Once the fibres reach temperatures above 1,000°C, the fibres melt.

Stone wool can be manufactured with different densities depending on the end-use application. Typical stone wool used as insulation for construction has a density in the range of 22-180 $kg \cdot m^{-3}$ [62], with 40 $kg \cdot m^{-3}$ being a standard for frame systems and higher densities like 180 $kg \cdot m^{-3}$ being used as fire protection elements. The density of the wool is a key parameter that determines its thermal behaviour since stone wool is a heterogeneous material consisting of a gas phase (air) and a solid matrix (fibres) [87]. The permeable nature of this material determines its thermal properties and therefore the processes of heat transfer. As noted by *Dyrbøl* [87], the heat is transmitted within the material by different mechanisms: conduction in fibres and gas, radiation and convection. These processes are represented in Figure 2.19, in which a global thermal conductivity can be assumed as the sum of equivalent thermal conductivities from the different mechanisms involved in the transfer of heat.

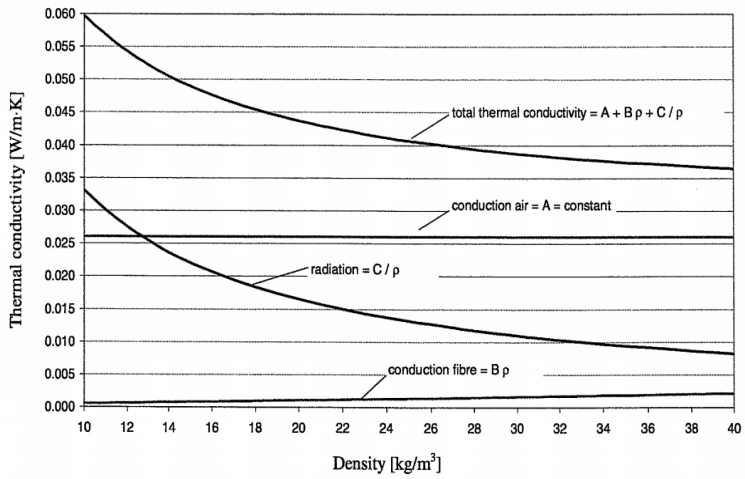

Figure 2.19. Contribution from conduction in air, conduction in fibres and radiation to the total thermal conductivity in mineral fibre insulation for building application at certain temperature according to Kumaran [88]. Extracted from [87]

From these different mechanisms, convection is normally assumed to be negligible, studied by *Dyrbøl et al.* [89]. *Dyrbøl et al.* showed the significant impact of the permeability of the wool in the heat transfer. Indeed, the convection is found to have a significant contribution on the total heat flow through the material when this is highly permeable (low density).

Typical values of thermal conductivity at low temperatures are in the range of 0.034-0.044 $W \cdot m^{-1} \cdot K^{-1}$ for wools with low density (e.g. 40 $kg \cdot m^{-3}$) [62]while for other densities, the conductivity may change. If the permeability is assumed to be low, the equivalent thermal conductivity assuming only a solid heat transfer phenomenon, the thermal conductivity of stone wool can be expressed by the following expression determined by *Bomberg and Klarsfeld* [90]:

$$\bar{k} = A + B \cdot \rho + \frac{C}{\rho} \tag{2.1}$$

where $\bar{k}$ is the equivalent thermal conductivity, ρ is the density of the wool, A is the thermal conductivity of air, B· ρ is the thermal conductivity of the stone wool fibre and C/ ρ is the radiative term. The usual values of parameters A, B and C that can be found in the literature, correspond to A = 0.02606 $W \cdot m^{-1} \cdot K^{-1}$, B = $5.48 \cdot 10^{-5}$ $W \cdot m^{2} \cdot K^{-1} \cdot kg^{-1}$ and C = 0.331 $W \cdot kg \cdot K^{-1} \cdot m^{-4}$ at a temperature of 10°C. Nevertheless, the coefficients noted above should not be assumed to be constant with temperature. If higher thermal severity is experienced, these factors need to be assumed as a function of the temperature.

The equation presented above can be characterised as a semi-empirical expression, since it represents the different mechanisms of heat transfer. This is suitable for calculating the conductivity for variable conditions of the density and temperature when adequate information about the composition of the material is available. Nevertheless, another possible approach for these materials is to obtain empirical expressions for different testing equipment. An example of this is the work performed by *Sjöström and Jansson* [91] using a Transient Pane heat Source [92], where stone wool

of density 140 kg·m^{-3} was reported to reproduce the thermal conductivity as a function of temperature as shown in Equation (2.2) below:

$$k = 3 \cdot 10^{-7} \cdot T_s^2 + 1 \cdot 10^{-4} \cdot T_s + 0.04 \quad (2.2)$$

where T_s is the solid temperature in Celsius degree. Additional values of thermal conductivity for a low density mineral wool were reported by *Jansson* [93], which are presented in Figure 2.20.

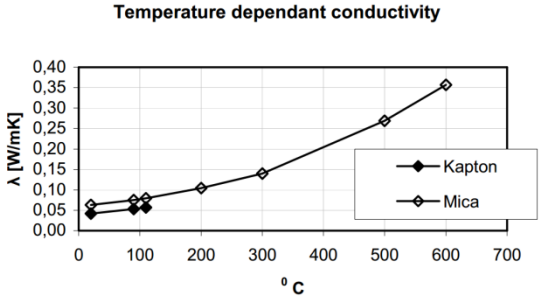

Figure 2.20. Thermal conductivity dependent with temperature for low density mineral wool. Extracted from [93]

Regarding the thermal degradation of stone wool, the main mechanisms are related to the pyrolysis or oxidation of the binder. Under the presence of oxygen the thermal decomposition of the binder is expected to be exothermic as shown in Figure 2.21, hence a certain amount of heat is released. Some additives such as magnesium hydroxide are commonly used to introduce endothermic reactions [94], which decomposes at a temperature above 200°C.

Differential Scanning Calorimetry (DSC) analyses performed by *Sjöström and Jansson* [91] showed the nature of the exothermicity of the thermal degradation associated to the binder. Furthermore, it is also observed that the crystallisation achieved at temperatures above 900°C indicate that this process is exothermic as well. These results are shown by the TGA-DSC data plotted in Figure 2.21 below. The authors also calculated a heat of combustion for the binder of 14.85 kJ·kg^{-1}.

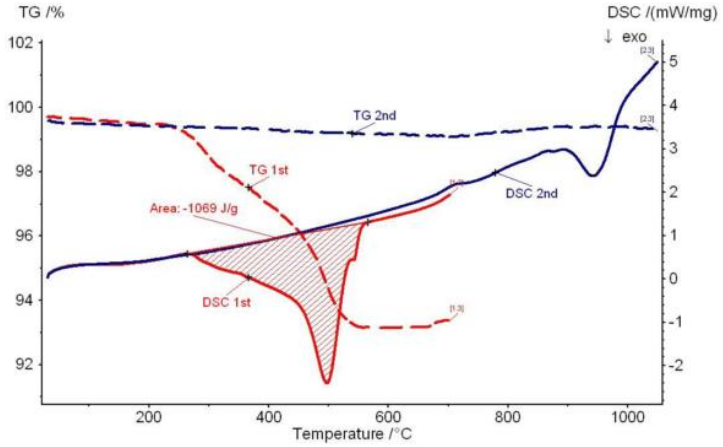

Figure 2.21. TGA (dashed) and DSC (solid) signals from TGA/DSC measurements in a 20% oxygen flow. Red curve: Heating up to 700°C. Blue curve: Heating up to 1050°C. Extracted from [91]

Additional data such as the constant pressure heat capacity of stone wool fibres is obtained from these experiments by using the sapphire procedure described later on. This data shows variation of the thermal capacity of stone wool being between 600 and 800 $J \cdot kg^{-1} \cdot K^{-1}$ at ambient temperature and increasing up to 1800 $J \cdot kg^{-1} \cdot K^{-1}$ at 900°C. This is presented in Figure 2.22 together with some results from *Rockwool International A/S*. Significant differences can be found between values of heat capacity obtained by SP and *Rockwool International A/S*.

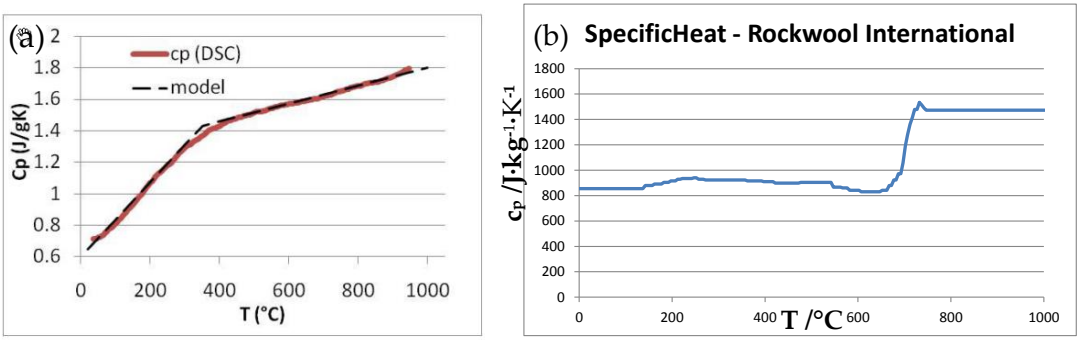

Figure 2.22. Temperature dependence of constant pressure heat capacity of stone wool measured by sapphire methodology using DSC.
(a) Extracted from [91] (b) Personal communication from *Rockwool International A/S*

2.5.2 Cellular polymers

Insulation materials such as polyurethane, polyisocyanurate, phenolic foam and expanded polystyrene are polymeric materials classified as plastics, i.e. organic polymers that have only partially reversible deformability. Among this category, plastic materials are divided into two main groups, thermoplastics and thermosets. These two types of plastics show complete different behaviour under conditions of severe heat exposure. Thermoplastics show a reversible deformation at high temperature, while thermosets do not. This behaviour is attributed to their different chemical structure and therefore expected different physical behaviour and thermal degradation.

Thermoplastics at low temperatures are presented as solids, which are characterised by their level of crystallinity. Once warmed up, two main processes are presented: glass transition and melting. After glass transition the thermo-physical properties of the material change drastically, achieving a rubbery state. Phase change is not achieved during glass transition, but at higher temperatures. Thermoplastics become fluid when the melting point is reached [95]. These processes are represented in Figure 2.23 below, where the different transitions are characterised by the deformability of the polymer.

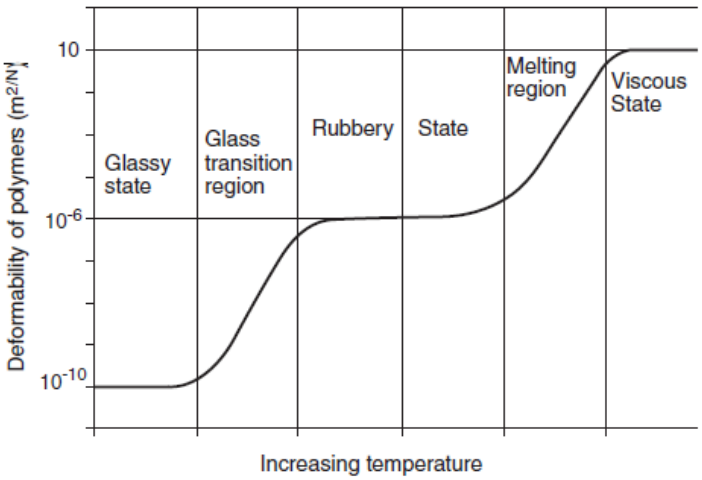

Figure 2.23. Deformability of thermoplastics with temperature. Extracted from [95]

In contrast to thermoplastics, no phase change is observed for thermosets before thermal degradation processes are triggered thus, thermosets do not become fluid (melting) due to a phase change.

While the classification of polymeric materials according to their chemical structure is fundamental to understand the fire performance of these materials, additional factors such as the manufacturing process play an important role in the behaviour of these materials. Plastics can be produced by the use of different processes which determine their physical properties. Materials such as EPS, PUR, PIR and PF used for the construction industry are manufactured as rigid closed-cell or cellular polymers by blowing a gas through the entire structure of the foam. A series of discrete pockets are formed using this technique, all of them being separated by solid material, thus eliminating the permeability of the foam. As will be discussed in the following sections, the cellular and rigid structure of these polymers has become one of the key parameters so as to improve their thermal performance.

During the last decades, new types of blowing agents have been used. Initially chlorofluorocarbon agents (CFCs) and hydrochlorofluorocarbons (HCFCs) were used as main blowing agents, while at present these are prohibited due to their ozone depleting potential (ODP) [96]. At present, mainly n-Pentane, iso-Pentane, cyclo-Pentane and hydrofluorocarbons (HFCs) that have zero ODP have are the best options [97]. Factors such as cost and availability drive towards a scenario where hydrocarbons are the ideal solution versus HFC [98] despite their higher flammability. Great efforts have been put in order to find ideal mixes of blowing agents that optimise cost, thermal and fire performance of cellular polymers [98–100]. Blowing agents determine the foam thermo-physical properties (density, thermal conductivity and heat capacity), uniformity, compressive strength, dimensional stability, friability and peel adhesion.

Since over 90% of the volume is gas (although in terms of mass represent 5% to 25% of the mass the reactive component in the case of isocyanate-based foams), the heat transfer within cellular polymers is significantly determined by the thermal

properties of the blowing agent (this concept should apply to low temperatures, before the blowing agent is released during the thermal degradation). Therefore, it is very important to know the thermal properties of the main blowing agents cited. A few studies on the thermal conductivity of n-Pentane and iso-Pentane can be found in the literature. *Dohrn et al.* studied the thermal conductivity of pure and binary systems of iso-Pentane and n-Pentane as a function of temperature and pressure [101]. Experimental values obtained for different mixtures are shown in Figure 2.24a, up to a temperature of 410 K. More results and extrapolated data points for extended ranges of temperature and pressure for n-Pentane were explored by *Carmichael et al.*, presented in Figure 2.24b.

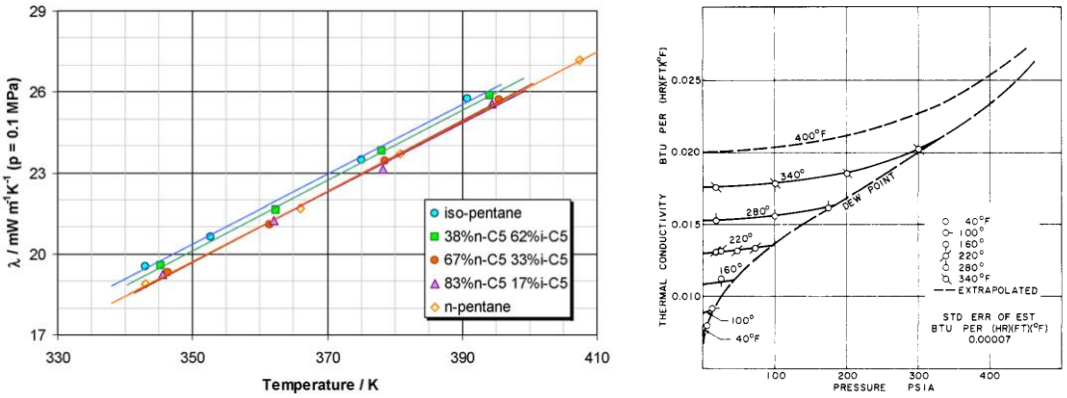

Figure 2.24. Temperature dependence of the thermal conductivity of (a n-Pentane, iso-Pentane and other mixtures at 0.1 MPa (Extracted from [101]) and (b) n-Pentane (Extracted from [102])

The heat capacities at constant pressure for a range of temperatures up to 427°C for n-Pentane, iso-Pentane and cyclo-Pentane are shown in Figure 2.25. The heats of combustion of n-pentane and iso-Pentane are 3,535.4 ± 0.96 kJ·mol^{-1} (49 MJ·kg^{-1}) and 3,528.4 ± 0.92 kJ·mol^{-1} (48.9 MJ·kg^{-1}) respectively [80].

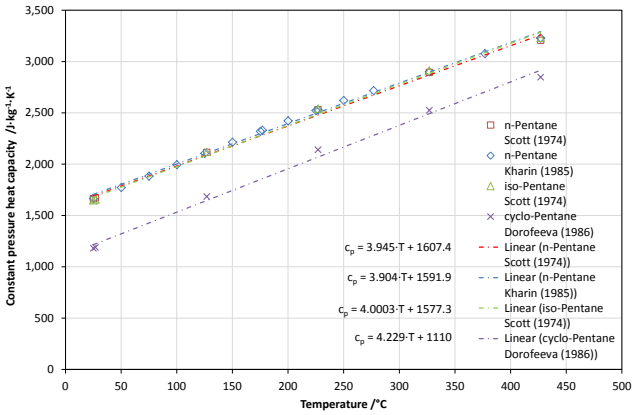

Figure 2.25. Temperature dependence of constant pressure heat capacity of n-Pentane, iso-Pentane and cyclo-Pentane [103]

An appropriate approach to understand the thermal degradation of polymers is to consider the different ways the polymer is decomposed in order to generate

volatiles. There are many different mechanisms but the main ones are denoted by *Beyler and Hirschler* [95]:

- **Chain scission of main chains**, a mechanism by which the bonds in the main polymer chain are broken. Depending on where the scission of the chain occurs, it can be classified as an end-chain or random-chain scission. Monomers are generated by end-chain scissions or 'unzipping', while monomers, oligomers and other species are obtained by random-chain scissions.
- **Cross-linking of main chains**, a mechanism by which a new bonds are created between two polymers, which occurs after the stripping of substituents. New structures with a high molecular weight are created by this mechanism, e.g. the char.
- **Elimination reaction**, a mechanism by which the side groups of the polymer are separated from the polymer chain by breaking the bonds. These side groups often react to other eliminated groups.
- **Cyclisation**, a mechanism by which adjacent side groups form new bonds creating a cyclic structure. This is an important process for char formation.

Whereas understanding the mechanisms by which the polymers break down may help to determine the nature of the volatiles, in reality this is not feasible for most of the cases due to the level of complexity and uncertainty in the polymer chains, requiring profound chemistry analysis. Much simpler approaches to understand the thermal degradation processes are normally applied, such as using thermogravimetric techniques (TGA). A simplistic approach to understand the thermal decomposition of polymers by which fuel vapours are generated from solids can be categorised by different modes presented in Figure 2.26.

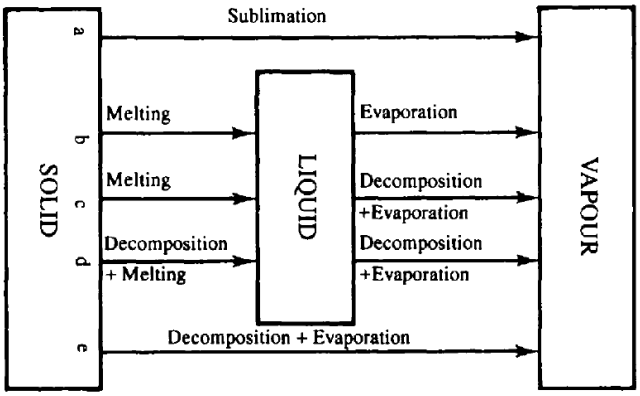

Figure 2.26. Different modes in which fuel vapour is generated from a solid. Extracted from [95]

The common mechanism for thermoplastics is chain scission of main chains which results in melting, followed by low molecular weight species being released by decomposition and evaporation. However, thermosets decompose producing volatiles and char. The carbonaceous char affects the thermal decomposition from the

material reducing the heat flow to the virgin material. The main characteristics of the char are density, continuity, coherence adherence, oxidation-resistance, thermal properties and permeability, which govern the eventual behaviour of it [104]. The volatiles obtained from the thermal decomposition of solids normally consist of a mixture of species of different molecular weight. These volatiles can be consumed by a flaming combustion. Otherwise, an aerosol smoke will be formed by the condensed liquid products when mixes with cool air [95]. Additionally, as noted by *Mouritz and Gibson* [105], the thermal decomposition of polymers may be affected by the presence of oxidants such as air. This effect complicates the determination of rates of thermal degradation, since it depends on the diffusion and concentration of oxygen to the surface of the material.

Whereas expanded polystyrene is a thermoplastic polymer, rigid polyurethane, polyisocyanurate and phenolic foams are thermosets. An aprioristic assessment of the materials anticipates that the behaviour of these materials will be significantly different under severe conditions of heat exposure. A review for each of the cellular polymers studied in this thesis is presented in the following sections.

2.5.2.1 Rigid polyurethane (PUR) and polyisocyanurate (PIR) foam

Rigid polyurethane foam (PUR) is an urethane-based foam, the formulation of which consists of an organic isocyanate component, originally toluene di-isocyanate (TDI), but at present methylene di-phenyl di-isocyanate (MDI) being more common, and an isocyanate-reactive component, normally a polyol. Rigid polyisocyanurate foam (PIR) is similar in formulation to rigid PUR, but PIR is an isocyanurate-based foam. Isocyanurate linkages are obtained by a cyclotrimerisation of the isocyanate radicals while the urethane linkages are obtained by the reaction of hydroxyl and isocyanate groups. Isocyanurate and urethane linkages are shown in Figure 2.27 below. Detailed reactions of how to produce these polymeric structures can be found in [106].

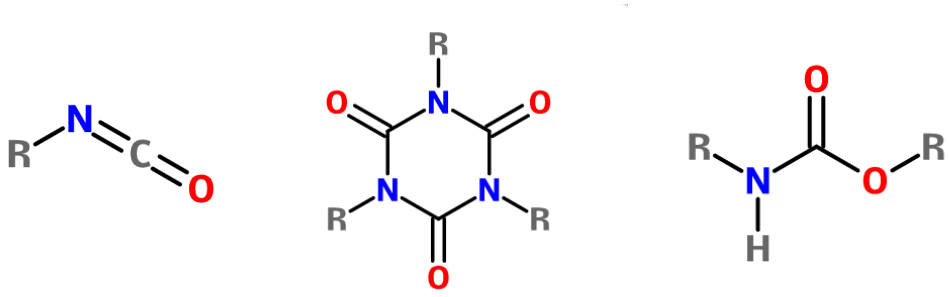

Figure 2.27. Left: Isocyanate group. Centre: Isocyanurate linkage. Right: Urethane linkage

Isocyanurate-based foams were introduced in the market in 1968 as an improved product of urethane-based foams with regard to flammability [107]. As it can be seen in Figure 2.27, an isocyanurate linkage is a crosslink, which is why it is more thermally stable than an urethane linkage. Indeed, urethane linkage breaks at temperatures around 200°C while isocyanurate linkage does at approximately 350°C [108]. Nevertheless, as indicated by *Dominguez-Rosado et al.* [109], pure polyisocyanurate

foam is friable, thus reducing the possible applicability of this product despite its better fire performance. This leads to combine urethane and isocyanurate linkages to optimise a product for both usability and fire performance.

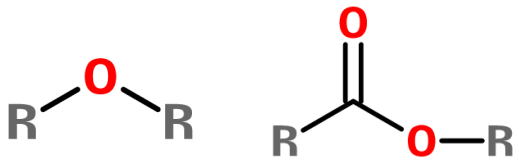

Figure 2.28. Left: Ether group. Right: Ester group

During the last decades, many attempts have been made in reducing the flammability of rigid PUR and PIR foams by improving their formulation. Several studies have focused on optimising the type and content of isocyanate-reactive component, i.e. the polyol element (alcohol containing multiple hydroxyl groups). Two types of compounds are normally used, polyether polyols and polyester polyols. Ether and ester generic structures are shown in Figure 2.28. Characterisation of these foams is normally indicated by the ratio isocyanate/polyol (NCO/OH) which determines their thermal stability and structure [109, 110]. Studies performed by *Cunningham et al.* [88]showed that if polyether polyols are used as the isocyanate-reactive component, a higher content of this would result in lower flammability. *Dominguez-Rosado et al.* [86] studied the thermal stability of urethane modified polyisocyanurate foams based on aromatic and aliphatic polyester polyols and polyether polyols of different molecular mass. This study showed that a high content of polyether polyol results in higher thermal stability than foams based on polyester polyols. Nevertheless, foams with low content of polyether polyol behave worse than polyester polyol foams.

Improvements on the formulation of PUR and PIR have led to the increase of thermal stability and reduction of flammability of these products by delaying the onset of thermal degradation and increasing the aromatic/cross-linkage nature of the polymer. Nevertheless, the removal of CFC and HCFC blowing agents became a challenge for the polyurethane industry. The best candidates to replace these blowing agents are hydrocarbons such as n-Pentane, iso-Pentane and cyclo-Pentane due to lower cost and good thermal properties, but at the expense of increasing their flammability. The polyurethane industry is therefore driven to include different additives and flame retardants that lead their products to meet regulations and pass standard fire tests. The main mechanisms by which flame retardants improve the fire performance of these polymers is mainly due to [112]:

- Promotion of endothermic reactions in the solid-phase.
- Generation of inert gases for the dilution of the oxygen supply.
- Formation of a char layer that interferes in the heat transfer of the solid-phase.

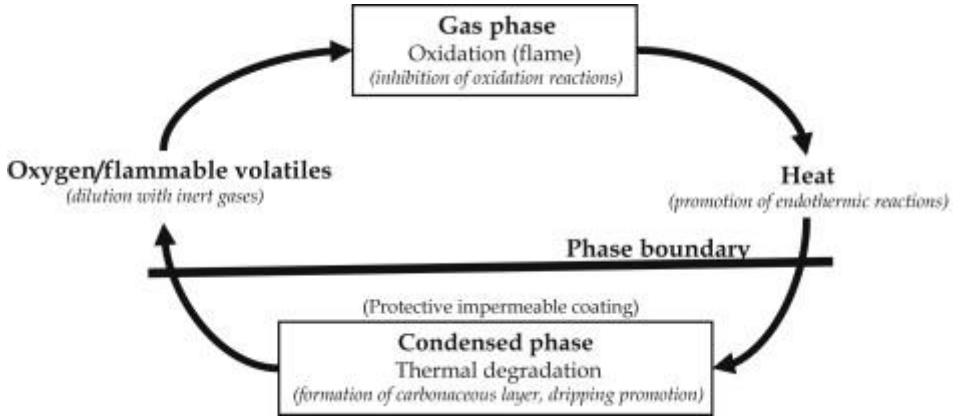

Figure 2.29. Combustion/flame retardation cycle. Extracted from [112]

PUR and PIR foam, as insulation for construction, typically present a density in the range of 30-80 $kg \cdot m^{-3}$ and a thermal conductivity in the range of 0.022-0.028 $W \cdot m^{-1} \cdot K^{-1}$ [62]. The European classification of reaction-to-fire [63] is usually D-E for PUR and C-D for PIR. Despite the extended use of PIR replacing PUR, main fire related literature found refers to PU or PUR. The main research that can be found corresponds to the chemical industry at material scale (e.g. use of TGA), which has been introduced above.

Extensive work on flame retardants in polyurethane and polyisocyanurate foams has been developed by *Modesti and Lorenzetti* [106, 113]. The results presented by *Modesti and Lorenzetti* showed reduced values of heat release rate and mass loss rate. They also found that the effectiveness of the char layers created by different flame retardants is not the same, with the concentration of these agents strongly affecting the results.

Vitkauskienė et al. studied several formulations of PIR [114], carrying out a series of thermogravimetric and Cone Calorimeter tests focusing in time to ignition, peak of heat release rate and smoke production.

Wiedermann [115] tested PUR and PIR foams at different scale tests, observing clear differences in behaviour between large and bench-scale testing for isocyanide based rigid foams.

As a final remark, the author would like to make a clarification with regard to the denomination used for these cellular plastics. Whereas one could imagine that polyurethane foams relate to only those urethane-based foams with no isocyanurate groups, commonly polyurethane foams are known to also include these. According to *Briggs* [116], a foam can be denominated as PIR if the conversion of MDI to isocyanurate linkage is over 60% and the weight retention in the Butler Chimney [117] is larger than 80%. However, this criterion is not clearly declared by the polyurethane industry at present. The denomination used in the market for PUR and PIR tends to be confusing and formulation of the available products is not public. PUR foams are known to behave worse in fire (since melting occurs). At present, no more rigid PUR foams but only PIR can be found as insulation for construction in the British market. Four types of isocyanurate-based foams are selected for this research.

The denominations used for the products studied in this thesis are those referred by the manufacturer. Nevertheless, the author encourages the reader to understand that, particularly for this field, main differences between products denominated PUR and PIR are strictly related to the degree of isocyanurate linkage in the polymer structure. Compiled data found in the literature is presented in Appendix B.

2.5.2.2 Rigid phenolic foam (PF)

Similarly to PIR, phenolic foam is an expanded closed-cell thermosetting polymer. Phenolic foam, as insulation for construction, typically has a density in the range of 30-40 $kg \cdot m^{-3}$ and a thermal conductivity in the range of 0.021-0.024 $W \cdot m^{-1} \cdot K^{-1}$ [62]. The European classification of reaction to fire [63] is usually B-C.

Different authors have studied the fire performance of phenolic foams, but scarce information is found in the literature, mainly in relation to the actual composition of this type of rigid foam. Some of these studies that are found in the literature are detailed below.

Scudamore et al. [118] tested three different types of phenolic foams by the Cone Calorimeter. The samples did not show clear flaming combustion up to 50 $kW \cdot m^{-2}$ of external radiant heat flux, with low values of heat release rate. Additionally, it was observed that the behaviour of foams with different densities was remarkable, with high density foams not showing significant deformation during the test, while the fire retardant grade foams showed spalling and expansion behaviour.

Paul [119, 120] studied the burning behaviour of polymeric materials such as phenolic foam. Modified versions of standard tests as the Limiting Oxygen Index [98] and the Setchkin Flash and Self-Ignition Test [122] were used. The results showed a large difference between the limits of flaming and smouldering combustion. Results also indicated the smouldering reaction propagated rapidly.

Auad et al. [123] compared the flammability properties of epoxy modified phenolic foams to pure phenolic foams and flame-retarded epoxy modified phenolic foams. The results showed lower flammability for the flame-retarded of epoxy modified phenolic foams. Pure phenolic foams showed lower flammability than epoxy modified phenolic foams without retardants.

Cleary and Quintiere [124] performed tests investigating the flammability properties on plastic foams by using the Cone Calorimeter and the LIFT . Phenolic foam showed a higher critical heat flux than other plastic materials such as EPS, PU and PIR.

Most of the quantifiable fire parameters of phenolic foam found in the literature are included in Appendix B. However, it should be noted that since no precise information exists with regard to the composition of the material, comparison to the results obtained could not be rigorous.

2.5.2.3 Expanded polystyrene (EPS)

Expanded polystyrene is a rigid and closed-cell thermoplastic polymer with an aromatic structure based on the styrene monomer. The chemical formula of the styrene monomer and its polymerisation process is presented in Figure 2.30 below. As other cellular polymers, expanded polystyrene is manufactured by blowing a gas through solid polystyrene.

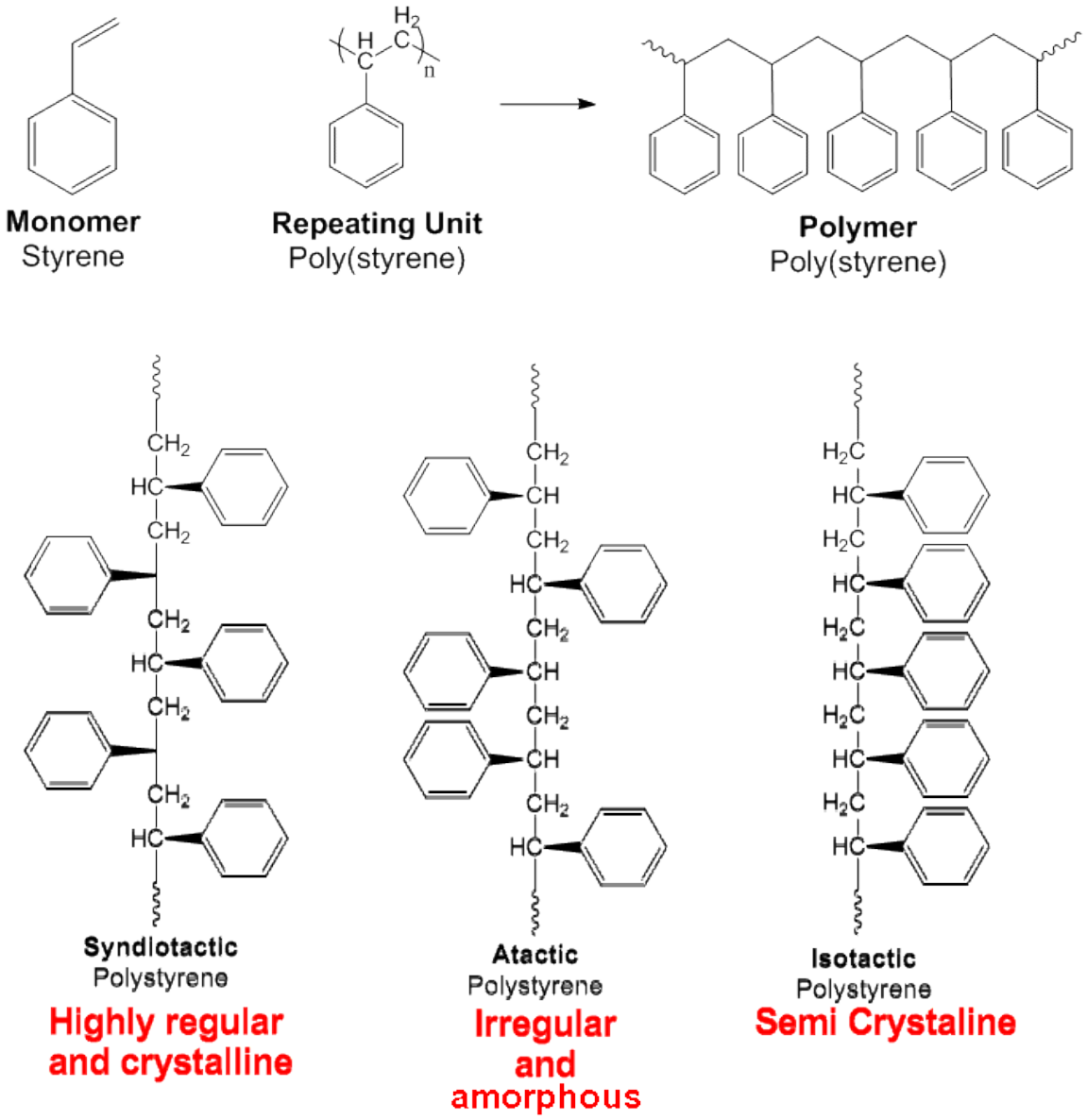

Figure 2.30. Process of polymerisation for EPS and its different structures. Extracted from ChemTube3D. The University of Liverpool [102]

Depending on the arrangement of the phenyl radicals on the polymeric backbone, polystyrene can be classified into three groups: atactic (phenyl groups randomly distributed), isoatactic (phenyl groups on the same side) and syndiotactic (phenyl groups on the same side) [126]. Melting points of isotactic and syndiotactic

polystyrene are 240°C and 270°C, respectively, while the glass transition temperatures for atactic and syndiotactic are 90°C and 100°C. *Beyler and Hirschler* [95] indicated that polystyrene has a low degree of crystallinity, with a glass transition temperature above 80°C, while the crystalline melting temperature is achieved at 230°C.

Expanded polystyrene as insulation for construction typically presents a density in the range of 10-50 $kg \cdot m^{-3}$ and a thermal conductivity in the range of 0.031-0.038 $W \cdot m^{-1} \cdot K^{-1}$ [62]. The European classification of reaction-to-fire [63] is usually E-F (combustible). As all thermoplastics, EPS softens when heated, reaching a rubbery-state when the glass transition is achieved [95]. In temperatures above 120°C (once reached the glass transition), the polymer becomes very soft [127], thus losing the blowing agent. When PS foams are exposed to heat, before ignition, their cell structure tends to collapse and a thin liquid film is produced, while after ignition, a thin coating is burning on the substrate. Because of this phenomenon, measuring the HRR of PS foams tends to be apparatus dependent; therefore determining the intrinsic response of the material is not an easy procedure. Set-up factors of the test, such as the specimen holder and edges conditions, affect the burning behaviour of the material.

Some authors have studied the flammability properties of EPS and XPS. Extruded PS foam of 50 mm of thickness and density of 26 $kg \cdot m^{-3}$ was tested by *Babrauskas et al.* [128] by using the Cone Calorimeter. The tests with polystyrene foam showed low repeatability with this material due to dependence to the apparatus. Furthermore, XPS foam was found to melt before ignition, thus reducing the volume occupied significantly. Instead of the foam itself, a thin coating on the inside of the sample holder was the burning material.

Scudamore et al.[118] carried out some tests on plastics using the Cone Calorimeter. 25 mm thick EPS samples of 15 $kg \cdot m^{-3}$ with and without fire retardants were tested. EPS melted before ignition and the molten polymer was exposed to a heat flux approximately 23% lower than the original heat flux that the sample was initially exposed to.

Cleary and Quintiere [124] studied the flammability of different density EPS and XPD foams with and without fire retardants using the Cone Calorimeter and the LIFT. As polystyrene foams melt, a modified method for testing was used. Aluminium foil pans were used as sample holders, while the distance between the heater and the regressing sample surface was kept at 25 mm.

Several studies about the fire performance of EPS have been recently done by *Collier and Baker* [129–131] as project for improving the performance of polystyrene insulated panels (PIP) in New Zealand. Although these sandwich panel tests did not show fire spread through the wall, melting and contribution to the heat release rate was observed. Regression rates of EPS were also studied as a function of the heat flux. Significant information about the flammability properties was collected for different configurations and types of EPS of 100 x 100 x 25 mm by using the Cone Calorimeter;

some of these are compiled in Appendix B, with most of the quantifiable fire parameters of polystyrene and EPS found in the literature.

2.5.3 Key note on the fire performance from cellular polymers

Fire performance of cellular polymers have been largely studied in the last decades due to the increase in production and extended usage of these materials in buildings. The main reference literature on cellular polymers and fire can be found in [132] as a compendium of the proceedings of a conference organised by QMC Wolfson Fire & Materials Centre (Queen Mary College) and the Fire Research Station in 1986. This conference was organised between the collaboration of governmental institutions, the industry, academics and professionals in order to review the state-of-the-art of the fire hazards of cellular polymers in the built environment, and find consensus on mitigation measures and regulatory actions. The main conclusions obtained by different authors are described below:

- *Buist* [107] presented a historical review of the development of cellular polymers and main description of these. A significant problem is identified on the performance of the different available flammability tests. These concerns were raised by authorities such as the Greater London Council which prohibited the use of many grades of PUR and highlighted the need of improving the fire performance of polymers such as PUR or PIR.
- *Woolley* [133] performed several experiments with different cellular polymers in order to identify the hazards imposed by these foams. Several inadequacies were found in terms of the testing methods, as these were not compatible with the properties of these materials, while it was recognised that improvements in the formulation of these materials and composites for their protection had been achieved. A hazards and risk map was proposed in relation to different testing scales. Higher severity in the standard testing was also proposed for evaluating the performance of composite elements.
- *Drysdale* [134] proposed an analysis based on the fundamental behaviour of the material when exposed to severe conditions of heat exposure. This analysis consisted of a heat transfer analysis highlighting the significant effect of the low thermal inertia of these materials in the onset of ignition. This analysis will be revisited in Chapter 3. It is also highlighted that results obtained from a test are specific to the apparatus and procedure, so conclusions with regard to the performance of these materials or composites need to be made carefully. This issue was highlighted by the work developed by *Abbot* [135].
- *Troitzsch* [136] performed a series of full-scale tests and concluded that these foams do not represent an unacceptable fire hazard, since they fulfilled the fire precautions of different countries for combustible materials in buildings.
- *Christian* [137] examined the development of standards for the fire safety regulatory framework in the UK. It was recognised the need of a test that

would enable judgement to be made by the authorities, so as to prohibit the use of materials extremely hazardous. The need to obtain this particular standard test by consensus from the different interested parts involved was also highlighted.

- *Briggs* [116] studied different cellular polymers at large-scale tests, showing that small laboratory experiments are not able to represent the complex chemical and physical phenomena when exposed to fire under real end-use conditions. The selection of proper material and composite engineering to reduce the fire hazards from these materials was also emphasised.

The research performed by the aforementioned authors showed clear uncertainty and controversy, with regard to the actual performance of cellular polymers. The use of these materials has been of high concern during the last 50 years, a concern that still remains. As a result main actions with regard to fire performance from the polymeric industry have been driven to formulate plastics with:

- **Reduced flammability** (with performance criteria on the basis of a series of standard tests enumerated below).
- **Higher thermal stability** (defined as increased char content and delay on the onset of thermal degradation).

The drivers that have led for these actions toward the production of materials with such characteristics are:

- The **introduction of legislation that required measurement of flammability of materials**. This impulses the design of testing methods such as FPA [138], Cone Calorimeter [139], LOI [121], LIFT [140], UL-94 [141, 142] among other several standard tests. Most of these tests are no longer referred by the regulatory framework, though they are used for research purposes. Legislation is geographically dependent and as presented in previous sections, two different paths for the definition of standardisation frameworks have been eventually established by the EU and the NFPA.
- The **necessity of understanding material performance and characterisation of thermal degradation processes for further material development**.
- Possibility of **wider applicability** for higher ranges of temperature and better physical properties.

As discussed by *Drysdale, Wooley* or *Briggs* the extrapolation of the performance observed from small-scale testing is hardly applicable to larger scale due to the combination of complex phenomena. While large efforts are made to reduce the flammability/combustibility of these materials, there is a misleading concept believing that the hazard is controlled by obtaining better ratings from standard testing. Harmonisation of standard testing intended to offer a plausible representation of the fire hazards from construction products. However, quantification of these hazards and risks associated to these remains as the main challenge. The work developed in this thesis is established on the basis of the lessons learnt from the extensive work developed during the last decades, and including

material performance into the design of quantitative tools, so as fire can be introduced as a quantifiable variable in the multi-objective design of buildings. This will be presented and largely discussed in the following chapters.

2.6 References

[1] M. Hamdy, A. Hasan, and K. Siren, "Applying a multi-objective optimization approach for Design of low-emission cost-effective dwellings," *Building and Environment*, vol. 46, no. 1, pp. 109–123, Jan. 2011.

[2] M. Fesanghary, S. Asadi, and Z. W. Geem, "Design of low-emission and energy-efficient residential buildings using a multi-objective optimization algorithm," *Building and Environment*, vol. 49, pp. 245–250, Mar. 2012.

[3] H. Islam, M. Jollands, S. Setunge, and M. A. Bhuiyan, "Optimization approach of balancing life cycle cost and environmental impacts on residential building design," *Energy and Buildings*, vol. 87, pp. 282–292, Jan. 2015.

[4] F. Asdrubali, C. Baldassarri, and V. Fthenakis, "Life cycle analysis in the construction sector: Guiding the optimization of conventional Italian buildings," *Energy and Buildings*, vol. 64, pp. 73–89, Sep. 2013.

[5] J. Damsky and J. Gero, "An evolutionary approach to generating constraint-based space layout topologies," *Proc. CAAD Futures*, vol. 1, no. Steadman 1983, pp. 855–864, 1997.

[6] X. Shi, "Design optimization of insulation usage and space conditioning load using energy simulation and genetic algorithm," *Energy*, vol. 36, no. 3, pp. 1659–1667, Mar. 2011.

[7] W. Yu, B. Li, H. Jia, M. Zhang, and D. Wang, "Application of multi-objective genetic algorithm to optimize energy efficiency and thermal comfort in building design," *Energy and Buildings*, vol. 88, pp. 135–143, Feb. 2015.

[8] C. Croitoru, I. Nastase, F. Bode, A. Meslem, and A. Dogeanu, "Thermal comfort models for indoor spaces and vehicles—Current capabilities and future perspectives," *Renewable and Sustainable Energy Reviews*, vol. 44, pp. 304–318, Apr. 2015.

[9] G. K. Oral, A. K. Yener, and N. T. Bayazit, "Building envelope design with the objective to ensure thermal, visual and acoustic comfort conditions," *Building and Environment*, vol. 39, no. 3, pp. 281–287, Mar. 2004.

[10] S. M. J. Spence and A. Kareem, "Data-Enabled Design and Optimization (DEDOpt): Tall steel building frameworks," *Computers & Structures*, vol. 129, pp. 134–147, Dec. 2013.

[11] G. Li and H. Hu, "Risk design optimization using many-objective evolutionary algorithm with application to performance-based wind engineering of tall buildings," *Structural Safety*, vol. 48, pp. 1–14, May 2014.

[12] C. A. C. Coello, "20 Years of Evolutionary Multi-Objective Optimization: What Has Been Done and What Remains To Be Done," in *Computational Intelligence: Principles and Practice*, G. Y. Yen and D. B. Fogel, Eds. IEEE Computational Intelligence Society, 2006, pp. 79–88.

[13] C. C. Coello, "Evolutionary multi-objective optimization: a historical view of the field," *IEEE Computational Intelligence Magazine*, vol. 1, no. February 2006, pp. 28–36, 2006.

[14] EU, "Directive 2010/31/EU of the European Parliament and of the Council of 19 May 2010 on the energy performance of buildings," *Official Journal of the European Union*, pp. 13–35, 2010.

[15] B. Atanasiu (editor), T. Boermans, K. E. Thomsen, J. Rose, S. Aggerholm, A. Hermelink, S. Schimschar, J. Grözinger, and M. Offermann, *Principles for Nearly Zero-Energy Buildings: Paving the way for effective implementation of policy requirements*. BPIE - Buildings Performance Institute Europe, 2011.

[16] "Rockwool factsheet. The way towards Nearly Zero Energy Buildings in EU." Rockwool International A/S Group Corporate Affairs, 2012.

[17] A. M. Papadopoulos, "State of the art in thermal insulation materials and aims for future developments," *Energy and Buildings*, vol. 37, no. 1, pp. 77–86, 2005.

[18] "Zero carbon non-domestic buildings. Phase 3 final report," Department for Communities and Local Government, 2011.

[19] HM Government, "The Building Regulations 2010," *Approved Document L1A: Conservation of fuel and power in new dwellings*, 2010. [Online]. Available: http://www.planningportal.gov.uk/uploads/br/BR_PDF_AD_L1A_2010_V2.pdf. [Accessed: 01-Feb-2015].

[20] HM Government, "The Building Regulations 2010," *Approved Document L2A: Conservation of fuel and power in new buildings other than dwellings*, 2010. [Online]. Available: http://www.planningportal.gov.uk/uploads/br/BR_PDF_AD_L2A_2010_V2.pdf. [Accessed: 01-Feb-2015].

[21] HM Government, "The Building Regulations 2010," *Approved Document L2B: Conservation of fuel and power in existing dwellings*. [Online]. Available: http://www.planningportal.gov.uk/uploads/br/BR_PDF_AD_L1B_2011.pdf. [Accessed: 01-Feb-2015].

[22] HM Government, "The Building Regulations 2010," *Approved Document L2B: Conservation of fuel and power in existing buildings other than dwellings*. [Online]. Available: http://www.planningportal.gov.uk/uploads/br/BR_PDF_AD_L2B_2011.pdf. [Accessed: 01-Feb-2015].

[23] A. M. Papadopoulos and E. Giama, "Design and Development of Innovative Stone-wool Products for the Energy Upgrading of Existing and New Buildings (SAPPEK)," Project Interim Report, Thessaloniki (Greece), 2004.

[24] M. Gilles and T. D. Jensen, "SRI roadshow Paris," 2011. [Online]. Available: http://www.rockwool.com/files/COM2011/Investor/Presentations/2011/20110610_Paris-SRI-Roadshow_BAML.pdf. [Accessed: 01-Feb-2015].

[25] D. A. Meikle, "Timber frame wall insulation: A survey of industry practice (2000 - 2011)." (Personal communication), 2014.

[26] Rockwool, "An introduction to Part L 2010," 2010. [Online]. Available: http://rwiumbracouknew.inforce.dk/media/270255/partl_u_values.pdf. [Accessed: 01-Feb-2015].

[27] "Xtratherm Ltd." [Online]. Available: http://www.xtratherm.com/. [Accessed: 01-Feb-2015].

[28] Xtratherm, "Technical Data Sheet of CavityTherm," 2013. [Online]. Available: http://www.xtratherm.com/wp-content/uploads/2013/12/Xtratherm-CT-PIR-12pp-12.13_LOW_RES.pdf. [Accessed: 01-Feb-2015].

[29] "Jablite." [Online]. Available: http://www.jablite.co.uk. [Accessed: 01-Feb-2015].

[30] Jablite, "Technical Data Sheet of Jabfill," *Jabfill in a Brick & Block Cavity Wall*, 2012. [Online]. Available: http://www.jablite.co.uk/products/show/jabfill-system. [Accessed: 08-Jan-2013].

[31] "Airpacks Ltd." [Online]. Available: http://www.kore-system.com/. [Accessed: 01-Feb-2015].

[32] Airpacks, "Technical Data Sheet of KORE Fill," 2012. [Online]. Available: http://cdn2.hubspot.net/hub/299572/file-313203405-pdf/pdf/kore_fill_technical.pdf?t=1422375502661. [Accessed: 08-Jan-2013].

[33] "Rockwool Limited." [Online]. Available: http://www.rockwool.co.uk.

[34] Rockwool, "Technical Data Sheet of Rocwool Cavity," 2011. [Online]. Available: http://www.rockwool.co.uk/products/u/2011.product/9838/building-insulation/rockwool%C2%AE-cavity. [Accessed: 08-Jan-2013].

[35] Rockwool, "Technical Data Sheet of Rockwool Energysaver," 2011. [Online]. Available: http://www.rockwool.co.uk/products/u/2011.product/9841/building-insulation/rockwool-energysaver%C2%AE. [Accessed: 08-Jan-2013].

[36] "Knauf Insulation Ltd." [Online]. Available: http://www.knaufinsulation.co.uk. [Accessed: 01-Feb-2015].

[37] KnaufInsulation, "Technical Data Sheet of Supafil," 2011. [Online]. Available: http://www.knaufinsulation.co.uk/en-gb/products/blown-mineral-wool.aspx#axzz3QslN7ugX. [Accessed: 08-Jan-2013].

[38] "Kingspan Insulation." [Online]. Available: http://www.kingspaninsulation.co.uk.

[39] Kingspan, "Technical Data Sheet of Thermawall TW50," 2011. [Online]. Available: http://www.kingspaninsulation.co.uk/getattachment/b08c2d53-474b-4bfd-ad44-d38eb4041dd2/Thermawall-TW50.aspx. [Accessed: 08-Jan-2013].

[40] Xtratherm, "Technical Data Sheet of Xtratherm Cavity-Plus XT/CWP," 2012. [Online]. Available: http://www.xtratherm.com/wp-content/uploads/2012/10/Thin-R-XT-CW-4pp-Web-1.pdf. [Accessed: 01-Feb-2015].

[41] Kingspan, "Technical Data Sheey of Kooltherm K8 Cavity Board," 2011. [Online]. Available: http://www.kingspaninsulation.co.uk/getattachment/61f60f6d-8e1f-459e-a533-51e186c775f3/Kooltherm-K8-Cavity-Board.aspx. [Accessed: 08-Jan-2013].

[42] Xtratherm, "Technical Data Sheet of Xtratherm Cavity-Plus SR/CW," 2012. [Online]. Available: http://www.xtratherm.com/wp-content/uploads/2012/06/Xtratherm-SR-CW-4pp-28.6.12.pdf. [Accessed: 01-Feb-2015].

[43] Airpacks, "Technical Data Sheet of KORE Key." [Online]. Available: http://cdn2.hubspot.net/hub/299572/file-312278167-pdf/pdf/kore_key_technical.pdf?t=1422375502661. [Accessed: 08-Jan-2013].

[44] Rockwool, "Technical Data Sheet of HP Partial Fill Cavity Walls," 2011. [Online]. Available: http://www.rockwool.co.uk/products/u/2011.product/9844/building-insulation/hp-partial-fill-cavity-slab. [Accessed: 08-Jan-2013].

[45] M. D. Gonçalves, "Insulating Solid Masonry Walls," *Building Envelope Forum*. [Online]. Available: http://www.cebq.org/documents/Insulatingsolidmasonrywalls-BEF_000.pdf. [Accessed: 01-Feb-2015].

[46] "Practical refurbishment of solid-walled houses (CE184)," Energy Saving Trust, 2006.

[47] "European Association for External Thermal Insulation Composite Systems." [Online]. Available: http://www.ea-etics.eu.

[48] Kingspan, "Technical Data Sheet of Thermawall TW55," 2011. [Online]. Available: http://www.kingspaninsulation.co.uk/getattachment/e02084f9-9c74-4695-97ea-7877b8e4ea12/Thermawall-TW55.aspx. [Accessed: 08-Jan-2013].

[49] Kingspan, "Technical Data Sheet of Kooltherm K12 Framing Board," 2011. [Online]. Available: http://www.kingspaninsulation.co.uk/getattachment/fd77d557-97b0-47c1-b0e9-5c12eb237861/Kooltherm-K12-Framing-Board.aspx. [Accessed: 08-Jan-2013].

[50] Rockwool, "Technical Data Sheet of Rockwool Flexi," 2011. [Online]. Available: http://www.rockwool.co.uk/products/u/2011.product/9908/building-insulation/rockwool-flexi%C2%AE. [Accessed: 08-Jan-2013].

[51] A. Amundarain, "Assesment of the Thermal Efficiency, Structure and Fire Resistance of Lightweight Building Systems for Optimised Design (Ph.D. thesis)," The University of Edinburgh. http://hdl.handle.net/1842/2128, 2007.

[52] "Structural Insulated Panel Association (SIPA)." [Online]. Available: http://www.sips.org.

[53] "SIPs Eco Panels Ltd." [Online]. Available: http://www.sipsecopanels.co.uk. [Accessed: 01-Feb-2015].

[54] "Kingspan TEK." [Online]. Available: http://www.tek.kingspan.com. [Accessed: 01-Feb-2015].

[55] Kingspan, "Technical Data Sheet of Kingspan TEK Building System," 2009. [Online]. Available: http://www.kingspantek.co.uk/Products/TEK-Building-System/TEK-Building-System/Introduction-to-TEK-Building-System. [Accessed: 08-Jan-2013].

[56] "Sips Industries Ltd.," *Our Strength is our Experience with Ten years in SIPs Manufacturing on three continents*, 2012. [Online]. Available: http://www.sipsindustries.com. [Accessed: 08-Jan-2013].

[57] "Insulating Concrete Formwork Association." [Online]. Available: http://www.icfinfo.org.uk.

[58] "Logix. UK." [Online]. Available: http://www.logix.uk.com.

[59] "ICF Tech Ltd.," *Insulating Concrete Form structural walling solutions*. [Online]. Available: http://www.icf-tech.com/download-brochure/. [Accessed: 08-Jan-2013].

[60] Airpacks, "Technical Data Sheet of KORE ICF," 2012. [Online]. Available: http://cdn2.hubspot.net/hub/299572/file-312283952-pdf/pdf/kore_icf_technical.pdf?t=1422375502661. [Accessed: 08-Jan-2013].

[61] "Eurobond Lamintes Ltd." [Online]. Available: http://www.eurobond.co.uk.

[62] L. Cody, "Fire Safety Considerations for a Green and Sustainable Future," in *IFE AGM and Conference*, 2011.

[63] "BS EN 13501-1. Fire classification of construction products and building elements. Part 1: Classification using data from reaction to fire tests." BSI, 2009.

[64] "BS EN 1363-1 . Fire resistance tests - Part 1: General Requirements." 2012.

[65] P. H. Thomas, A. J. Heselden, and M. Law, "Fully-developed compartment fires -two kinds of behaviour," *Fire Research Technical Paper No. 18. Ministry of Technology and Fire Offices Committee, Joint Fire Research Organisation, FRS, London, UK*, vol. 18, 1967.

[66] Scottish Government, "Building (Scotland) Regulations 2013: Technical Handbooks (Non Domestic) – Section 2 (Fire)." 2013.

[67] "BS EN ISO 13823. Reaction to fire tests for building products — Building products excluding floorings exposed to the thermal attack by a single burning item." 2010.

[68] "BS EN ISO 11925-2. Reaction to fire tests — Ignitability of products subjected to direct impingement of flame. Part 2: Single-flame source test." 2010.

[69] "BS EN ISO 1182. Reaction to fire tests for products — Non- combustibility test." BSI, 2010.

[70] "BS EN ISO 1716. Reaction to fire tests for products — Determination of the gross heat of combustion (calorific value)." 2010.

[71] B. Sundström, "The Development of a European Fire Classification System for Building Products Test Methods and Mathematical Modelling (Doctoral Thesis)," Lund University, 2007.

[72] "BS 8414-1. Fire performance of external cladding systems. Test methods for non-loadbearing external cladding systems applied to the face of a building." 2002.

[73] "BS EN 1364-4. Fire resistance tests for non-loadbearing elements. Curtain walling. Part configuration." 2014.

[74] R. Zhao and J. Sanjayan, "Test method for concrete spalling using small electric furnace," *Fire and Materials*, vol. 34, no. 4, pp. 189–201, 2009.

[75] "NFPA 5000 - Building Construction and Safety Code." 2015.

[76] "ASTM E84: Standard Test Method for Surface Burning Characteristics of Building Materials." ASTM International, West Conshohocken, PA, 2014.

[77] ASTM Standard E119, "Test Methods for Fire Tests of Building Construction and Materials." 2012.

[78] "ISO 9705. Fire tests -- Full-scale room test for surface products." 1993.

[79] U. Krause, W. Grosshandler, and L. Gritzo, "The International FORUM of Fire Research Directors: A position paper on sustainability and fire safety," in *Fire Safety Journal*, 2012, vol. 49, no. 0, pp. 79–81.

[80] B. Meacham, B. Poole, J. Echeverria, and R. Cheng, *Fire Safety Challenges of Green Buildings*. Springer New York, 2012.

[81] T. Z. Harmathy, "The role of Thermal Feedback in Compartment Fires," *Fire Technology*, vol. 11, no. 1, pp. 48–54, 1975.

[82] B. J. McCaffrey, J. G. Quintere, and M. F. Harkleroad, "Estimating room temperatures and likelihood of flashover using fire test data correlations," *Fire Technology*, vol. 17, no. 2, pp. 98–119, 1981.

[83] A. Poulsen and G. Jomaas, "Experimental Study on the Burning Behavior of Pool Fires in Rooms with Different Wall Linings," *Fire Technology*, vol. 48, pp. 419–439, 2012.

[84] A. Poulsen and A. C. Bwalya, "An Experimental Study of the Effect of Thermal Radiation Feedback on the Room-Burning Behaviour of Horizontal Slabs of Polyurethane Foam," *Research Report No. 309*. NRC Institute for Research in Construction, National Research Council Canada, 2011.

[85] A. Dunster, "Characterisation of Mineral Wastes, Resources and Processing technologies – Integrated waste management for the production of construction material." p. 17, 2007.

[86] "DIN 4102-17. Fire behaviour of building materials and elements. Determination of melting point of mineral fibre insulating materials. Concepts, requirements and testing." DIN, 1990.

[87] S. Dyrbøl, "Heat transfer in Rockwool modelling and method of measurement (Ph.D. thesis)," Technical University of Denmark (DTU), 1998.

[88] M. K. Kumaran, "Heat, Air and Moisture Transfer in Insulated Envelope Parts. Final Report, Volume 3, Task 3: Material Properties.," Belgium, 1996.

[89] S. Dyrbøl, S. Svendsen, and A. Elmroth, "Experimental investigation of the effect of natural convection on heat transfer in mineral wool," *Journal of Building Physics*, 2002.

[90] M. Bomberg and S. Klarsfeld, "Semi-Empirical Model of Heat Transfer in Dry Mineral Fiber Insulations," *Journal of Thermal Insulation*, vol. 6, 1983.

[91] J. Sjöström and R. Jansson, "Measuring thermal material properties for structural fire engineering," in *15th International Conference on Experimental Mechanics*, 2012.

[92] "ISO 22007-2. Plastics -- Determination of thermal conductivity and thermal diffusivity -- Part 2: Transient plane heat source (hot disc) method." International Organization for Standardization, Geneva (Switzerland), 2008.

[93] R. Jansson, "Measurement of thermal properties at elevated temperatures – Brandforsk project 328-031," 2004.

[94] K. M. Pedersen, "Man-made vitreous fibre products and their use in fire protection systems," EP 0936060 A1, 1999.

[95] C. L. Beyler and M. M. Hirschler, "Thermal Decomposition of Polymers," in *SFPE Handbook of Fire Protection Engineering*, 3rd ed., P. J. DiNenno, D.

Drysdale, C. L. Beyler, W. D. Walton, R. L. P. Custer, and J. M. Watts, Eds. Massachusetts, U.S.A.: National Fire Protection Association, 2002, pp. 1–110 to 1–131.

[96] G. Buxton, "The Montreal protocol on substances that deplete the ozone layer.," *International Negotiation*, vol. 1. pp. 231–246, 1988.

[97] S. Quinn, "Chemical blowing agents: providing production, economic and physical improvements to a wide range of polymers," *Plastics, Additives and Compounding*, vol. 3. pp. 16–21, 2001.

[98] R. Berrier, S. Singh, J. Costa, and V. Bonapersona, "Hydrocarbon Blown Rigid Polyurethane Foam for the Boardstock Industry—A Novel Approach," *Journal of Cellular Plastics*, 1999.

[99] S. N. Singh, S. B. Burns, J. S. Costa, and V. Bonapersona, "Method of increasing the solubility of hydrocarbons and HFCs in polyurethanes raw materials and the effects on the performance and processing characteristics of construction foams," *Cellular polymers*, vol. 16, no. 6, pp. 444–467.

[100] S. Singh, M. Ntiru-Karamagi, and M. Ritchie, "Optimizing polyiso blowing agents," in *Proceedings of Polyurethanes Expo*, 2005, pp. 402–408.

[101] R. Dohrn, J. M. Fonseca, R. Albers, J. Kušan-Bindels, and I. M. Marrucho, "Thermal conductivity of polyurethane foam cell gases: Improved transient hot wire cell – data of isopentane + n-pentane mixtures – Extended Wassiljewa-model," *Fluid Phase Equilibria*, vol. 261, no. 1–2, pp. 41–49, Dec. 2007.

[102] L. Carmichael, J. Jacobs, and B. H. Sage, "Thermal conductivity of fluids. n-pentane," *Journal of Chemical and Engineering Data*, vol. 14, no. 1, pp. 31–37, 1969.

[103] The National Institute of Standards and Technology, "The NIST Chemistry WebBook." [Online]. Available: webbook.nist.gov.

[104] Craig L. Beyler and M. M. Hirschle, "Thermal Decomposition of Polymers," in *SFPE Handbook of Fire Protection Engineering, 3rd Edition*, 3rd ed., P. J. DiNenno, D. Drysdale, C. L. Beyler, and W. D. Walton, Eds. Massachusetts, U.S.A.: National Fire Protection Association, Massachusetts, U.S.A., 2002, pp. 1–110 – 1–131.

[105] A. P. Mouritz and A. G. Gibson, *Fire Properties of Polymer Composite Materials*. 2006, p. 394.

[106] M. Modesti, A. Lorenzetti, F. Simioni, and M. Checchin, "Influence of different flame retardants on fire behaviour of modified PIR/PUR polymers," *Polymer Degradation and Stability*, vol. 74, no. 3, pp. 475–479, 2001.

[107] J. M. Buist, "Cellular Polymers," in *Fire and cellular polymers*, 1986, pp. 5–23.

[108] K. Ashida, K. Saiki, J. Goto, and K. Sasaki, "Polyisocyanurate foams modified by thermally stable linkages," in *ACS Symp Series*, 1997, pp. 669:81–100.

[109] E. Dominguez-Rosado, J. J. Liggat, C. E. Snape, B. Eling, and J. Pichtel, "Thermal degradation of urethane modified polyisocyanurate foams based on aliphatic and aromatic polyester polyol," *Polymer Degradation and Stability*, vol. 78, no. 1, pp. 1–5, Jan. 2002.

[110] Y. Zhang, S. Shang, and X. Zhang, "Influence of the composition of rosin-based rigid polyurethane foams on their thermal stability," *Journal of Applied Polymer Science*, pp. 1167–1171, 1996.

[111] A. Cunningham, B. Eling, and D. J. Sparrow, "A study of the low smoke potential, flame resistance and processibility of high index polyisocyanurate rigid foam," *Cellular polymers*, vol. 6, no. 6, pp. 42–59, 1987.

[112] P. Kiliaris and C. D. Papaspyrides, "Polymer Green Flame Retardants," in *Polymer Green Flame Retardants*, Elsevier, 2014, pp. 1–43.

[113] M. Modesti and A. Lorenzetti, "Improvement on fire behaviour of water blown PIR–PUR foams: use of an halogen-free flame retardant," *European Polymer Journal*, vol. 39, no. 2, pp. 263–268, 2003.

[114] I. Vitkauskienė, R. Makuška, U. Stirna, and U. Cabulis, "Thermal Properties of Polyurethane-Polyisocyanurate Foams Based on Poly (ethylene terephthalate) Waste," vol. 17, no. 3, pp. 2–6, 2011.

[115] R. Wiedermann, "Fire properties of isocyanate based rigid foams," in *Fire and cellular polymers*, 1986.

[116] P. J. Briggs, "Fire Behaviour of Rigid Foam Insulation Boards," in *Fire and cellular polymers*, 1986, pp. 117–133.

[117] "ASTM D3014. Standard test method for flame height, time of burning and loss of mass of rigid thermoset cellular plastics in vertical position." ASTM International, West Conshohocken, PA, 1999.

[118] M. J. Scudamore, P. J. Briggs, and F. H. Prager, "Cone calorimetry—a review of tests carried out on plastics for the association of plastic manufacturers in Europe," *Fire and Materials*, vol. 15, no. 2, pp. 65–84, 1991.

[119] K. T. Paul, "Characterization of the burning behaviour of polymeric materials," *Fire and Materials*, vol. 8, no. 3, pp. 137–147, 1984.

[120] K. T. Paul, "Burning characteristics of materials," *Fire and Materials*, vol. 3, no. 4, pp. 223–231, 1979.

[121] "ASTM D2863. Measuring the minimum oxygen concentration to support candle-like combustion of plastics (oxygen index)." ASTM International, West Conshohocken, PA, 2010.

[122] "ASTM D1929. Ignition properties of plastics." ASTM International, West Conshohocken, PA, 2011.

[123] M. L. Auad, L. Zhao, H. Shen, S. R. Nutt, and U. Sorathia, "Flammability properties and mechanical performance of epoxy modified phenolic foams," *Journal of Applied Polymer Science*, vol. 104, no. 3, pp. 1399–1407, 2007.

[124] T. G. Cleary and Quintiere, James G., "NISTIR 4664. Flammability Characterization of Foam Plastics," National Institute of Standards and Technology, 1991.

[125] N. Greeves, "ChemTube3D. The University of Liverpool." [Online]. Available: http://www.chemtube3d.com/polymer/_PolystyreneF.html. [Accessed: 01-Feb-2015].

[126] J. R. Wunsch, *Polystyrene – Synthesis, Production and Applications*. iSmithers Rapra Publishing, 2000, p. 15.

[127] H. Sehaqui, M. Salajková, Q. Zhou, and L. A. Berglund, "Mechanical performance tailoring of tough ultra-high porosity foams prepared from cellulose I nanofiber suspensions," *Soft Matter*, vol. 6. p. 1824, 2010.

[128] V. Babrauskas, W. H. Twilley, and W. J. Parker, "The effects of specimen edge conditions on heat release rate," *Fire and Materials*, vol. 17, no. 2, pp. 51–63, 1993.

[129] G. Baker, "Performance of expanded polystyrene insulated panel exposed to radiant heat," University of Canterbury, Christchurch, New Zealand, 2002.

[130] P. Collier and G. Baker, "Improving the fire performance of polystyrene insulated panel in New Zealand," NZFSC, Wellington, New Zealand, 2004.

[131] P. Collier and G. Baker, "The Influence of Construction Detailing on the Fire Performance of Polystyrene Insulated Panels," *Fire Technology*, pp. 1–17, 2011.

[132] J. M. Buist, S. J. Grayson, and W. D. Woolley, "Fire and Cellular Polymers," 1986.

[133] W. D. Woolley, "Are Foams a Fire Hazard?," in *Fire and cellular polymers*, 1986, pp. 61–75.

[134] D. Drysdale, "Fundamentals of the fire behaviour of cellular polymers," in *Fire and cellular polymers*, 1986, pp. 61–75.

[135] J. G. Abbott, "Standard Laboratory Tests: How Meaningful are they in Assessing Fire Performance of Insulation Materials?," in *Fire and cellular polymers*, 1986, pp. 199–218.

[136] J. H. Troitzsch, "How Do Foams Perform Under Fire Conditions?," in *Fire and cellular polymers*, 1986, pp. 77–91.

[137] S. D. Christian, "Legislation — Standards — Polymers," in *Fire and cellular polymers*, 1986, pp. 93–102.

[138] "ASTM E 2058. Standard Test Methods for Measurement of Synthetic Polymer Material Flammability Using a Fire Propagation Apparatus (FPA)." ASTM International, West Conshohocken, PA, 2009.

[139] "BS 476-15, ISO 5660-1. Fire tests on building materials and structures. Method for measuring the rate of heat release of products." BSI, 1993.

[140] "ASTM E1321. Standard Method for Determining Material Ignition and Flame Spread Properties." ASTM International, West Conshohocken, PA, 2009.

[141] "ASTM D635. Standard Test Method for Rate of Burning and/or Extent and Time of Burning of Plastics in a Horizontal Position." ASTM International, West Conshohocken, PA, 2014.

[142] "ASTM D3801. Standard Test Method for Measuring the Comparative Burning Characteristics of Solid Plastics in a Vertical Position." ASTM International, West Conshohocken, PA, 2010.

[143] HM Government, "Approved Document L - Conservation of fuel and power." [Online]. Available: http://www.planningportal.gov.uk/buildingregulations/approveddocuments/partl/approved#ApprovedDocumentL1A:ConservationoffuelandpowerNewdwellings. [Accessed: 01-Feb-2015].

Chapter 3.

Moving from Compliance Testing to a Performance-Based Design Methodology

3.1 Introduction

Current methods for the fire safe design of insulation systems in buildings were presented in Chapter 2. This chapter presents a qualitative study that demonstrates the incapability of these methods of design to reveal the intrinsic fire hazards related to the use of insulation materials in buildings. The onset of pyrolysis (or onset of thermal degradation) is proposed herein as the main failure mode to be included in a failure criteria framework.

To prove this hypothesis, an evaluation of these main failure modes is included herein. This study comprises a theoretical analysis of the expected performance of insulation materials from a heat transfer perspective and from the introduction of a highly instrumented case scenario, where the main failure mode can be identified. This is followed by the definition of a hazards map, which consists of a redefinition of the main set of failure criteria to be evaluated during design. The role that combustible and non-combustible insulation materials might play under the proposed set of failure criteria is explored.

As a final remark, a methodology is proposed as a possible solution for the future design of assemblies incorporating insulation materials in fire. This methodology intends to include fire safety of insulation materials in a quantitative way, so that this can be evaluated in a performance-based context. It is noted, however, that further work is needed with regard to reducing the uncertainty level related to unknown or undefined heat inputs from real fires.

A series of inputs based on material performance and properties are required for the proposed methodology, which requires a fundamental understanding of the thermal degradation processes associated with the different materials involved. This understanding can only be achieved by studying the behaviour of relevant materials at the material scale, and results acquired by increasing length scales until all relevant fire-related parameters are accounted for. The related experimental work is presented in Chapters 4 through 7, providing information regarding material performance under severe conditions of heat at different scales.

3.2 Inadequacies of standard fire tests on insulation materials

During the last decade much criticism and scepticism has been raised regarding standard testing methodologies for fire safety design of buildings. As already presented in Chapter 2, the current methodologies fail to provide fire safety as a quantifiable variable for use in building design, but simply give pass/fail criteria that any construction system must achieve if it is intended to be placed in a building. The main criticisms of standard fire testing are related to the fact that knowledge from first principles is, in general, not widely applied in the fire safe design of buildings. Instead, fire safety is applied through a prescriptive approach rather than a rational, quantified performance-based approach.

Many other drawbacks of the predominantly prescriptive methodology can be identified. The most important one, which has also been previously identified by many authors [1, 2] is that results from standard fire testing are not representative of real fires, and in some cases not even representative of the most onerous scenarios and failure modes that might be experienced in a real building. Indeed, many tests have shown that results obtained from a specific test are rarely widely applicable to other scenarios [3]. As recognised by *Drysdale* [4], results obtained by standard testing must be generalised and applied with care, since these strongly depend on the apparatus and procedures followed. Therefore, extrapolation of results requires fundamental understanding of the material from first principles. This is where standard testing often fails, since results from standard testing are extrapolated as being representative of the expected performance in real scenarios, with rating systems used in a prescriptive way for any type of building and material.

The research presented in this thesis seeks a fundamental understanding of various insulation materials; therefore, it is important to understand the current standard fire tests and what they are actually testing/measuring. In this section, the author attempts to highlight the different phenomena involved in the different standard tests used under the EU (reaction-to-fire and fire resistance) and NFPA 5000 fire testing standardisation framework, especially within the context of standard tests on insulation materials. The different standard tests for reaction-to-fire and fire resistance are explored.

3.2.1 Dissecting reaction-to-fire testing (Euroclasses)

As previously noted in Chapter 2, reaction-to-fire testing aims to classify materials according to their flammability, assessed through the non-combustibility test [5], the heat of combustion test [6], the ignitability test [7], and the single-burning-item (SBI) test [8].

Controversy is often raised on the application of this classification in terms of whether these tests should be on materials or on the complete 'systems' consisting of different materials. Material performance can be expected to be different from system or product performance due to the interactions between the test methods and the tested samples; this can generally be explained from first principles. However, the objective of this section is not to settle the controversy, but rather to try to set a baseline understanding of what the standard tests are actually measuring. It is only in this way that the incapability of current standardisation to credibly show the 'real' performance of insulation materials can be properly understood.

The non-combustibility test and the heat of combustion test are classic tests that show the presence of organic compounds in the material and the amount of energy released by their combustion. These are relevant basic data, however they fail to provide information on the dynamics of the different degradation reactions. The ignitability test and the single burning item test, experiments that are both used to quantify the potential contribution to flashover, are based on the development of fire spread on the surface of materials. The ignitability test can represent material ignition

and burning under a zero imposed heat flux environment, i.e. when the sample is only exposed to a high thermal gradient at a localised point. Although this procedure can provide qualitative information about the degree of reactiveness of a material, it is not very useful to correlate material properties with regard to fire spread. The SBI test is based on similar principles, however in this case the exposure represents a certain fire scenario that can impose a certain thermal stress on a predetermined area of the sample. The dynamics of a compartment fire, including smoke production and pyrolysates accumulation and transport, are not represented; thus the expected performance cannot be directly correlated to real compartments.

A common critique often raised regarding the use of these experiments is related to the lack of connection to scientific basis in the case of the ignitability test, and the isolated fire scenario not being representative of likely heat fluxes of real scenarios for the SBI. Whilst this may be true, it is important to note that these tests are designed to assess performance as a measurement of flame spread in a specific way (FIGRA index). Nevertheless, insulation materials are rarely exposed directly, but placed behind a non-combustible lining or render.[6] Thus, if the insulation is to contribute to the fire within a compartment, it would rarely if ever be by flame spread on the surface of the material, since a physical barrier is invariably placed in front of the insulation. Hence, mixing of oxygen and pyrolysis gases is not possible at the surface of the insulation in most practical applications. This is significant with regard to an insulation material flammability assessment, since these tests are performed in a controlled environment and the behaviour of the generated pyrolysis gases may not be representative of a real fire scenario. Indeed, the pyrolysis gas flammability problem is determined by the concentration of the pyrolysates effluent and the gas-phase temperature within the mixture. Thus, if the performance with regard to insulations' contribution to fire is to be evaluated, a fundamental understanding on the pyrolysis process and transport is necessary; unfortunately, reaction-to-fire standard tests are incapable of evaluating these phenomena.

3.2.2 Dissecting fire-resistance testing (Furnace testing)

The inability of standardised fire-resistance testing to address the intrinsic fire hazards of combustible insulation materials is related to the fact that the only failure modes associated with these materials are represented by heat transfer phenomena, i.e. to the 'E' and 'I' failure criteria described in Chapter 2. Indeed, satisfactory test results can be achieved if the temperature at the back face of the insulation does not exceed a given value, and provided that no flammable gases or flaming occur at the backside of the product layer, no matter what the condition of the exposed surface or core of the assembly experience. As a result, hazards related to the contribution of pyrolysates to the heat release rate (HRR), and other potentially important issues,

[6] This relates to general use of insulation products. The author recognises the potential issue of insulation in cavities. In that case, the behaviour is expected to be much more severe and complex. Performance observed by reaction-to-fire tests cannot be extrapolated to this scenario.

such as generation and transport of toxic species for instance, cannot be quantitatively evaluated.

An example of this deficiency has already been investigated and presented by *Smolka et al.* [9]. In this study, different insulation assemblies based on metal-faced sandwich panels, with cores of isocyanurate-based foam (PIR) or stone mineral wool (MW), were tested in a furnace according to BS EN 1363-1[10].

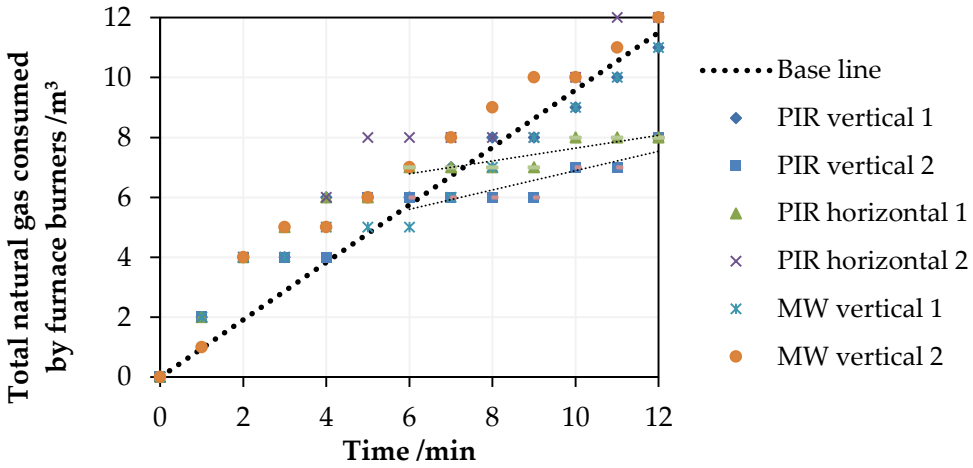

Figure 3.1. Fuel consumption from the furnace burners for experiments on wall panels with different insulation materials (PIR and SW) in the period 0 to 12 minutes. Extracted from [9]

Measurements of the total natural gas consumed by the furnace burners are shown in Figure 3.1. A considerably lower amount of fuel was required to follow the standard time-temperature curve for experiments where plastic foam insulation was used. This is indicative of the contribution from the pyrolysates generated by the foam to the total heat release inside the furnace. Indeed, two effects can be identified while testing combustible materials in the furnace due to the contribution of pyrolysis gases:

- reduction of the required energy introduced in the furnace to maintain the standard time-temperature curve, due to combustion of these pyrolysates; and
- endothermic processes within the insulation materials, likely delaying the progression of the thermal wave to the back of the material.

Since little fundamental understanding of the tested materials was used under the above framework, these two effects are not explicitly considered, and the insulations' contributions to the fire are not considered as failure modes. On the contrary, an inert material with higher thermal conductivity and experiencing no endothermic reactions would likely fail this specific test earlier than a reactive material. The temperature at the unexposed surface would achieve the failure temperature of thermal insulation criterion 'I' more rapidly.

Additionally, a central criticism of furnace testing is related to the uneven conditions of heat exposure for different materials or products, poor repeatability between furnaces, and non-uniformity of the heat exposure inside the furnace. The

latter was studied by *Welch and Rubini*, who suggested that significant variation of the sample surface temperature was predicted by CFD simulations [11]. The two first drawbacks mentioned above can be explained if a simplified heat transfer analysis is performed; already demonstrated by others [12, 13]. The main concern lies in the dependency between the tested sample and the amount of heat delivered into the furnace. The target during the test is to follow a specified time-temperature curve, by controlling the flow of fuel into the furnace. However, the gas-phase temperature, controlled by a series of thermocouples or plate thermometers [14] is a result of a balance between the energy inserted in the furnace and the energy absorbed by the furnace boundaries and the tested assembly. The absorbed energy by the boundaries (net heat fluxes) is dependent on the thermal conductivity in first instance, and eventually on the thermal diffusivity. Indeed, the thermal conductivity determines the net heat flux by Fourier's law and the thermal diffusivity determines the transfer of heat through the solid media. Therefore, the control variable of the test is intrinsically linked to the thermal properties of the tested material, so different values of inserted energy are expected within the furnace, in a sense imposing an arbitrary severity of heating.

The above issue can be illustrated using an energy balance in a control volume (furnace), as represented in Figure 3.2 and approximated by Equation (3.1):

$$\left(\dot{q}_{in,burner} - \dot{m}_{out} \cdot u_{out}\right) - \left(\dot{q}_f + \dot{q}_w\right) = V_g \cdot \rho_g \cdot c_{p,g} \cdot \frac{dT_g}{dt} \tag{3.1}$$

where $\dot{q}_{in,burner}$ is the energy input by the burner (equivalent to the HRR of the fire), $\dot{m}_{out}$ and u_{out} are the mass flow and internal energy of the gases leaving the furnace, $\dot{q}_f$ and $\dot{q}_w$ are the net heat fluxes on the surfaces of the furnace walls and the tested wall, respectively, V_g, ρ_g and $c_{p,g}$ are the volume, density and specific heat capacity of the gas inside the furnace, and $\frac{dT_g}{dt}$ is the variation of the gas phase temperature over time. The kinetic and potential energy terms linked to the transfer of mass are neglected for this approximate expression of the law of energy conservation.

Equation (3.1) can be expressed as Equation (3.2) considering that the net heat flux on the surface of the furnace and tested walls can be represented using Fourier's law, where S_f and S_w are the surface area, k_f and k_w are the thermal conductivity of the furnace walls and the tested wall respectively:

$$\begin{aligned} \dot{q}_{in,burner} &= f\left(T_g\right) + f(S_f \cdot k_f) + f(S_w \cdot k_w) = \\ &= V_g \cdot \rho_g \cdot c_{p,g} \cdot \frac{dT_g}{dt} + \left(-S_f \cdot k_f \cdot \left.\frac{\delta T}{\delta x}\right|_{f,front} - S_w \cdot k_w \cdot \left.\frac{\delta T}{\delta x}\right|_{w,front}\right) + \dot{m}_{out} \cdot u_{out} \end{aligned} \tag{3.2}$$

The term $V_g \cdot \rho_g \cdot c_{p,g} \cdot \frac{dT_g}{dt}$ in Equation (3.2) represents the change in the internal energy of the control volume, represented by the temperature change in the gas phase. This term is constrained by the time-temperature curve, and remains the same for any tested wall. If the tested material has much lower thermal conductivity, the net heat to the tested material is lower. This implies that the energy inserted in the furnace, which can be assumed to represent the HRR of the fire, is necessarily lower.

This proves that the severity of exposure in the furnace is intrinsically dependent on the tested material.

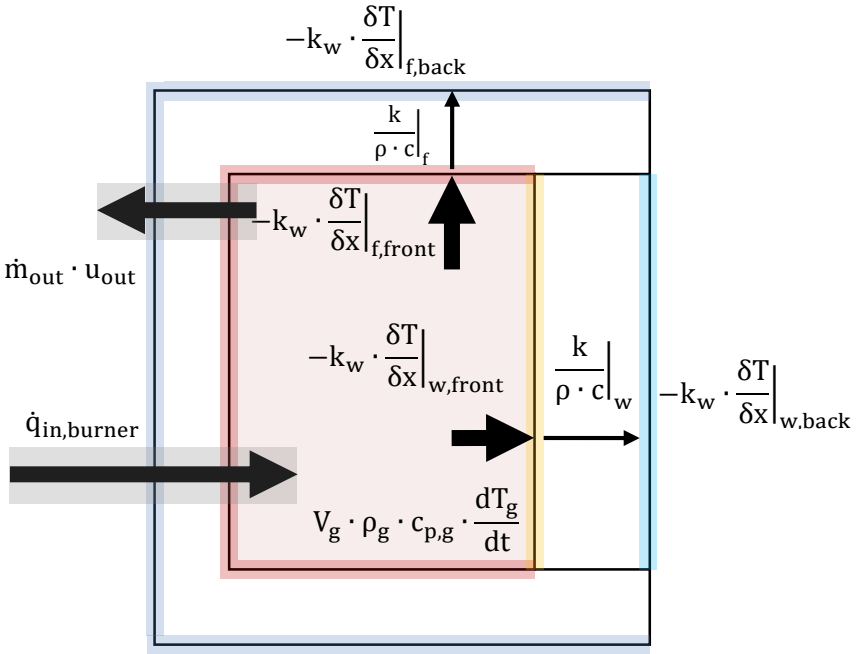

Figure 3.2. Schematic representation of the energy balance inside the furnace

3.2.3 Dissecting NFPA framework

The NFPA framework presents a better approach than the EU framework, since a thermal barrier is required for the use of plastic foams. However, the performance-based approach cannot be adopted. Similar inadequacies are considered with regard to the flammability classification, since the ASTM 84 test intends to measure flame spread on the material/product surface. Additionally, the prescription for the thermal barrier is based on the use of the furnace test so as to confirm that the temperature at the unexposed face does not exceed 130°C after 15 minutes. This prescription incurs in a series of incompatibilities with performance-based approaches:

- As detailed in the previous section, the severity of the heat exposure fire is related to the thermal properties of the tested material using this test. Therefore, the heat exposure is arbitrary.
- The selection of temperature at the unexposed face is totally independent of the insulation material behaviour and characteristics.
- The selection of time is arbitrary, especially considering that the severity of the heat exposure is arbitrary, depending on the barrier thermal properties.

Therefore, designers are unable of assessing the performance of plastic foams under different conditions to those presented in the test.

3.3 Redefinition of the failure criteria framework

3.3.1 Characteristics of insulation materials

A fundamental understanding of the characteristics of insulation materials is crucial to describe their fire performance. A detailed description based on an extensive experimental plan studying different testing scales is necessary in order to achieve this understanding. A description of this work, presented in Chapters 4 through 7, is not the purpose of this section. However, a brief analysis describing the expected behaviour of the insulation materials is presented. The baseline of this study is focussed on a heat transfer analysis already proposed by *Drysdale* [4], which was based on classical theories of ignition of solids. In this particular case, a finite difference model is used.

Insulation materials are characterised as low density materials with extremely low thermal conductivity. This is translated into a low thermal inertia; i.e. the product of thermal conductivity, density, and specific heat capacity (kρc). The thermal inertia of a material can be understood as its resistance to temperature change. High values of thermal inertia require larger heat flows to increase temperature. Therefore, low amounts of heat are able to achieve rapid increase of the temperature on the exposed solid surface of a low thermal inertia material. This is the case for insulation products. As a result, the temperature of pyrolysis, also commonly defined as piloted ignition temperature, may be achieved very fast if certain assumptions are met.

To prove the effect that low thermal inertia may have on the ignition onset of combustible insulation materials, a series of numerical analyses assessing time-to-ignition from a material exposed to a constant heat flux are presented. The problem to be solved is defined by the heat diffusion equation, as noted in Equation (3.3), and a boundary condition at the surface represented by a constant heat flux and heat losses by convection and radiation, as noted in Equation (3.4):

$$k \cdot \frac{\delta^2 T}{\delta x^2} = \rho \cdot c_p(T) \cdot \frac{dT}{dt} \tag{3.3}$$

$$\alpha \cdot \dot{q}''_{ext} - h_T(T_s) \cdot (T_s - T_\infty) = -k \cdot \left.\frac{\delta T}{\delta x}\right|_{x=0^+} \tag{3.4}$$

A generic typical insulation material of thermal properties k = 0.08 $W \cdot m^{-1} \cdot K^{-1}$, ρ = 40 $kg \cdot m^{-3}$ and c_p = 2000 $J \cdot kg^{-1} \cdot K^{-1}$, and absorptivity of α = 0.6 – 0.8 is assumed. The evolution of the surface temperature for different range of heat fluxes is presented in Figure 3.3. A global heat transfer coefficient of heat losses is assumed as noted in Equation (3.5):

$$h_T = 0.05 \cdot (T_s - T_\infty) + 12 \tag{3.5}$$

This is an arbitrary simplification assumed in order to represent a likely heat transfer coefficient in an apparatus such as the Cone Calorimeter [15] using a horizontal orientation; therefore, this should not be used for modelling purposes.

The variation of the surface temperature is presented for external heat fluxes of 10, 15 and 20 $kW \cdot m^{-2}$. If the assumed pyrolysis temperature is 350°C, this is achieved at

250 seconds for a heat flux of 15 kW·m^{-2}. If slightly larger external heat fluxes are used, this temperature is achieved very fast, for instance 11 seconds for the modelled heat flux of 20 kW·m^{-2}. Therefore, any heat flux larger than the critical heat flux implies extremely rapid temperature increase as presented in Figure 3.3. It should be noted that these external heat fluxes are illustrative, but essentially arbitrary due to the assumption taken for the value of the global heat transfer coefficient of heat losses in Equation (3.5).

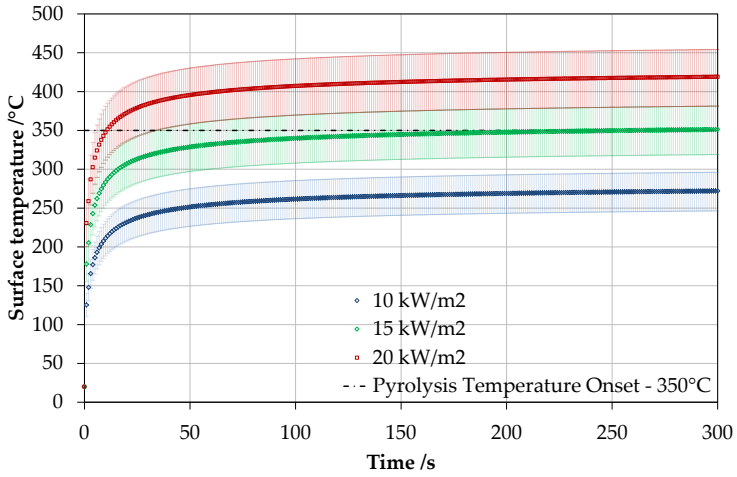

Figure 3.3. Surface temperature evolution at different external heat fluxes for a material with assumed properties k = 0.08 W·m^{-1}·K^{-1}, ρ = 40 kg·m^{-3} and c_p = 2000 J·kg^{-1}·K^{-1}. Error bars indicate the result obtained for values of absorptivity α = 0.6 – 0.8

Therefore, the main hazard from combustible insulation materials is the rapid response to any imposed heat, consequently achieving the onset of pyrolysis very rapidly. As noted some time ago by *Drysdale* [4] and reiterated here, "*these features, rather than the propensity to produce smoke and toxic gases, should be regarded as the principal hazard, and measures for their control urgently sought*".

3.3.2 Case study: Identification of the main failure mode

A series of highly instrumented experiments involving an insulation system based on metal-skin walls with a rigid isocyanurate-based foam core [16] is referenced as a case study to show that the crucial failure mode for insulation materials is strictly the onset of thermal degradation, with high production of pyrolysis gases.

The aim of the experimental program in question, carried out in Chorley (UK), was to evaluate the effect of 'damages' and increased fire load on the fire performance of sandwich panels. The essentially ad-hoc experiment consisted of a modified ISO 13784-1 [17] small room test with a sand gas burner in one corner. An essentially identical room made of panels with non-combustible core material (stone wool in this case) was also tested, with similar procedure and modifications (simulated 'damages'). The internal dimensions of the room were 2.4 m x 3.6 m x 2.4 m, and the walls and ceiling consisted of 100 mm thick metal-faced sandwich panels with a core of closed cell rigid isocyanurate-based foam (PIR). Measurements of gas-phase

temperature, gas species at the top of the opening, velocity measurements at the door, temperatures within the panels and video recording were taken for both experiments in similar positions. Precise details regarding instrumentation, test set-ups, and results can be found in [16, 18]. Additionally, configuration of the tests and selected instrumentation are presented in Chapter 7. Selected data and discussion on the obtained results are presented, focussing on the contribution to the HRR in the compartment with PIR core panels due to the contribution of pyrolysis gases to the combustion.

The average temperature and temperature profile inside the compartment for the first experiment, along with the calculated heat release rate inside the compartment based on oxygen consumption calorimetry [19, 20] are presented in Figure 3.4. The first steep increase of the compartment temperatures is produced between 7 and 8 minutes from the start of the test, followed by a steep growth of the temperature between 8 to 10 minutes, when a global peak is reached. These two steep increases correlate to the calculated heat release rates inside the compartment, slightly shifted by about 30 seconds due to the delay times on the gas analyser used. This shift can be evaluated by comparing the jump between the HRR calculated from the gas burner data (red line) and the calculated HRR with gas species data (grey region bounded by black dotted lines).

These two increases show that the thermal runaway is not produced suddenly. The contribution of extra fuel other than propane from the gas burner is inferred since no stabilisation on the temperature is observed for an input HRR of only 300 kW. This fact is supported by the calculated HRR, clearly being larger than the input. The contribution of extra fuel also appears not to be constant, since the temperature profile reduces after the largest peak at about 10 minutes.

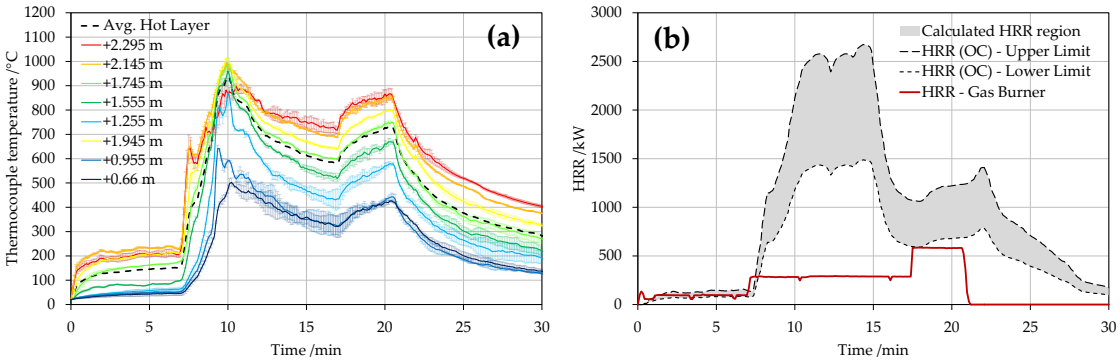

Figure 3.4. (a) Temperature profile over height of the compartment and average temperature in the hot layer (b) Calculated HRR inside the compartment. Error bars represent the standard deviation for two thermocouples at same height

As noted before, temperature measurements were taken within the wall panels of the compartment. The precise locations where these measurements were taken are presented in Chapter 7 in Figure 7.3. Locations with maximum temperature measurements until 30 minutes are selected and presented in Figure 3.5. These locations correspond to the closest monitoring positions to the gas burner, denoted W5t at top and W5b at bottom positions.

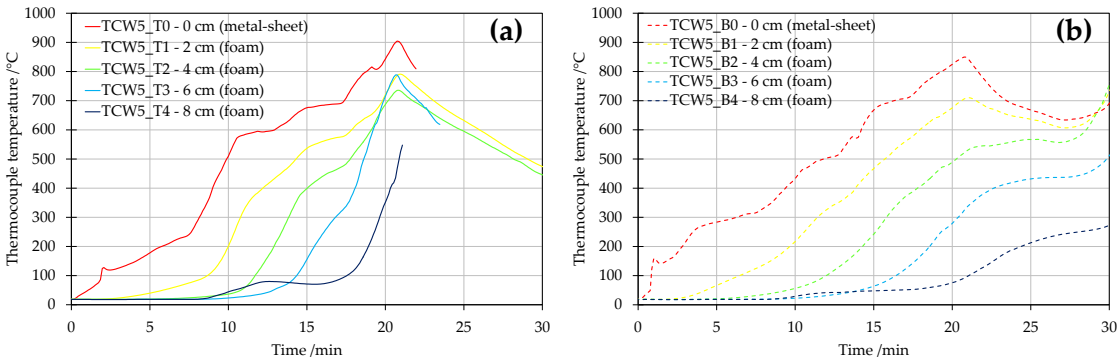

Figure 3.5. In-depth temperature measurements within the wall for positions (a) W5t and (b) W5b

As part of the work developed for this thesis, thermogravimetric analyses on the core of the insulated panels were also performed. Complete analysis, results and discussion of these are presented in Chapter 4. Normalised mass loss during TGA tests is processed and presented in its derivative form (Differential Thermal Analysis or DTG), so the different thermal degradation reactions can be highlighted. The thermal degradation kinetics of the core material are coupled to the in-depth temperature profile from position W5b for the times from the start of the test until 20 minutes. This is shown in Figure 3.6. The left hand graph represents DTG curves of PIR foam for different heating rates in a nitrogen atmosphere, while the right hand graph represents the temperature profile through thickness at Section W5b. The main region of pyrolysis is highlighted in red, corresponding to the range of temperatures between 250°C and 400°C. It is noteworthy that a first pyrolysis reaction is suggested in the DTG curve of PIR between 150°C and 250°C. However, the observed rate is relatively low compared to the region highlighted in red. Temperature profiles for the moment when the thermal runaway is observed (between 7 and 8 minutes) are plotted as a yellow and red line in the right hand graph of Figure 3.6.

Figure 3.6 indicates that at the time the gas-phase temperature and calculated HRR show a significant increase, a few millimetres depth in that section have already achieved temperatures within the main region of pyrolysis. This indicates that a range of pyrolysis gases have been released from the foam insulation for at least two to three minutes. These pyrolysis gases may have escaped the panel through its edges, or may have remained within the panel if panel sections near its edges remain intact and unaffected by heat. If pyrolysis gases are released from the core insulation, these could be transferred inside or outside the compartment, depending on the panel tightness, connection details, sealants, penetrations, voids, external cladding, etc. As a result of this, an accumulation of flammable gases might be expected at the top layer of the compartment and their ignition achieved under the right conditions of gas mixture and temperature. Under such circumstances, the problem is, in a sense, transformed into a flammability limit study for the generated pyrolysis gases.

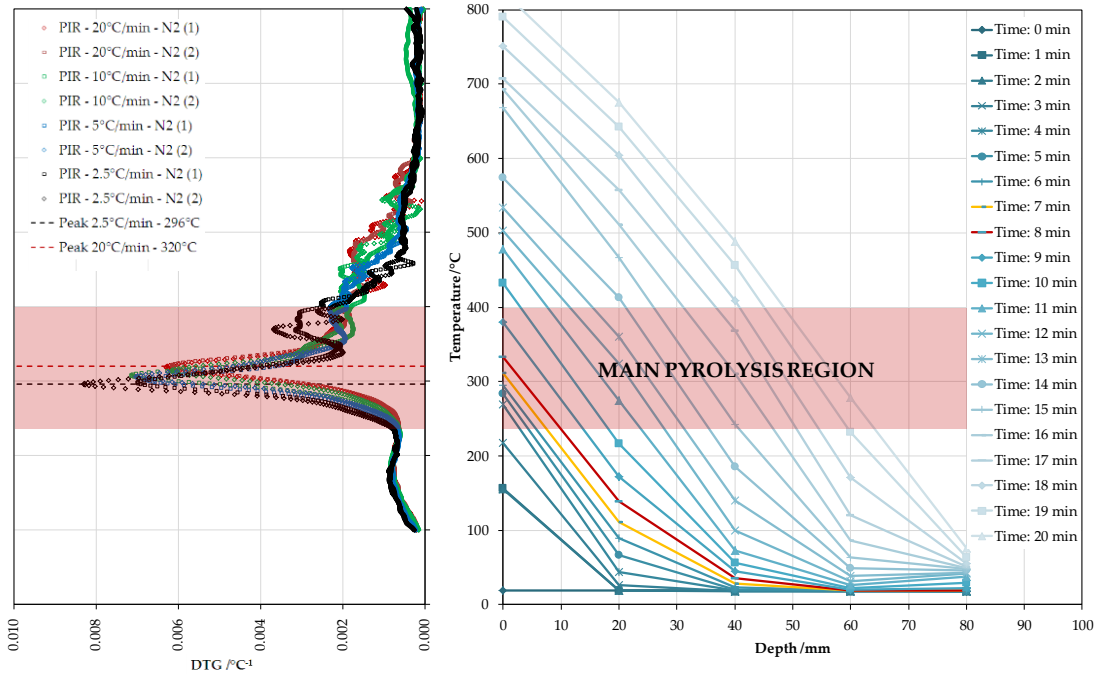

Figure 3.6. In-depth temperature measurements within the wall (right) and DTG analysis for PIR of the panels in nitrogen (left)

A complementary assessment to corroborate the contribution of the combustion of pyrolysis gases in the compartment is performed by analysing the ratio of carbon dioxide generated and the oxygen consumed, measured at the opening. This is presented in Figure 3.7, compared against values obtained for a similar test where non-combustible core was used (red line). The delay time from the analyser has been corrected. The stoichiometry ratio for complete combustion of propane is plotted as a dotted line. Additional results from bench-scale testing, presented in Appendix C, indicate that a ratio above 0.6 (approximately between 0.7-0.8) is expected from the combustion of the coating paint. The ratio for PIR pyrolysates is expected to be slightly below 0.6 (approximately between 0.5-0.6).

During the first ten minutes, some gentle increases and drops above and below 0.6 on the CO_2/O_2 show other fuel than propane contributing to the combustion. These might indicate scarce paint or PIR pyrolysates contributing to the combustion, but without any significant impact on the dynamics of the compartment fire. A steep drop of the CO_2/O_2 ratio just after seven minutes, when the burner HRR was turned up, indicates significant contributions from PIR pyrolysates to the combustion. This is consistent with the times for first steep increase in the gas-phase temperature and the calculated HRR in Figure 3.4. This first drop on the CO_2/O_2 ratio could be indicative of:

- Ignition of pyrolysates accumulated on the ceiling of the compartment when suitable conditions were achieved. In this case, some damage (described in [16]) to the test set-up could have helped the already generated pyrolysis gases to escape from the panels.
- Abrupt ignition of an effluent of pyrolysis gases being suddenly released. In this case, the increased HRR from the burner could have helped regions of the panels near the edges and damages to suddenly pyrolyse.

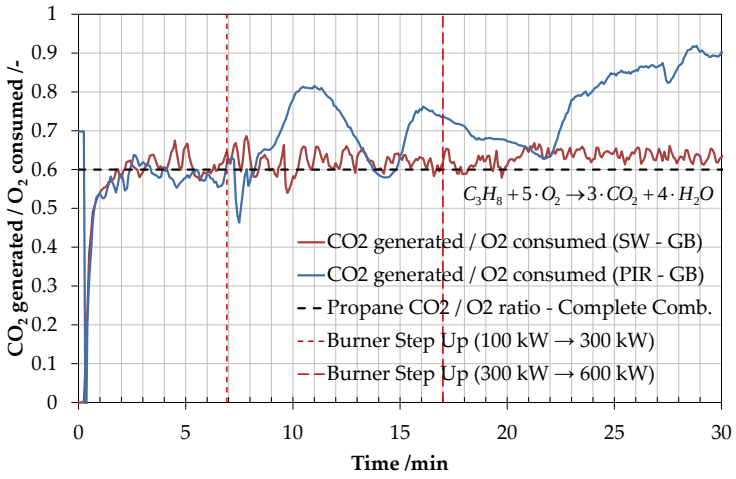

Figure 3.7. Generated carbon dioxide – consumed oxygen ratio during the experiment

After 7.5 minutes the CO_2/O_2 ratio continues to increase, reaching levels above 0.6, up to a maximum of 0.8. This indicates different fuels contributing to the combustion, presumably dominated by the burning of the coating paint. After 10-11 minutes it continues to decrease, presumably indicating larger contribution from PIR pyrolysates. In any case, pyrolysates are supplied in the compartment, with the representative temperature profile inside the panels given in Figure 3.6. The pyrolysis front is found to keep propagating in-depth; hence pyrolysis gases continue to be generated. The video footage taken inside the compartment demonstrated a contribution from pyrolysates from the panels and flame spread of the coating paint, which helped to sustain the heating conditions in the compartment. Additional visual observations from outside the compartment indicated a large amount of yellow smoke being released from the panels.

Visual observations given by the video footage is crucial for assessing the series of events. After the HRR of the burner was increased to 300 kW, the flame height of the burner was increased accordingly. This was followed by turbulent movement of certain sooty smoke on the ceiling, followed by burning of paint falling from the ceiling. One minute later, a deflagration is observed on the ceiling, which is consistent with the first increase in the HRR. However it is difficult to determine precisely whether this occurred due to previous release and accumulation or due to a sudden release of pyrolysates from the panel. The later deflagration is consistent with the second steep increase of temperature, followed by continuous flame spread of the paint and effluents of pyrolysates burning inside the compartment, also indicated by the CO_2/O_2 measurements. This sequence of images is presented in Figure 3.8 below.

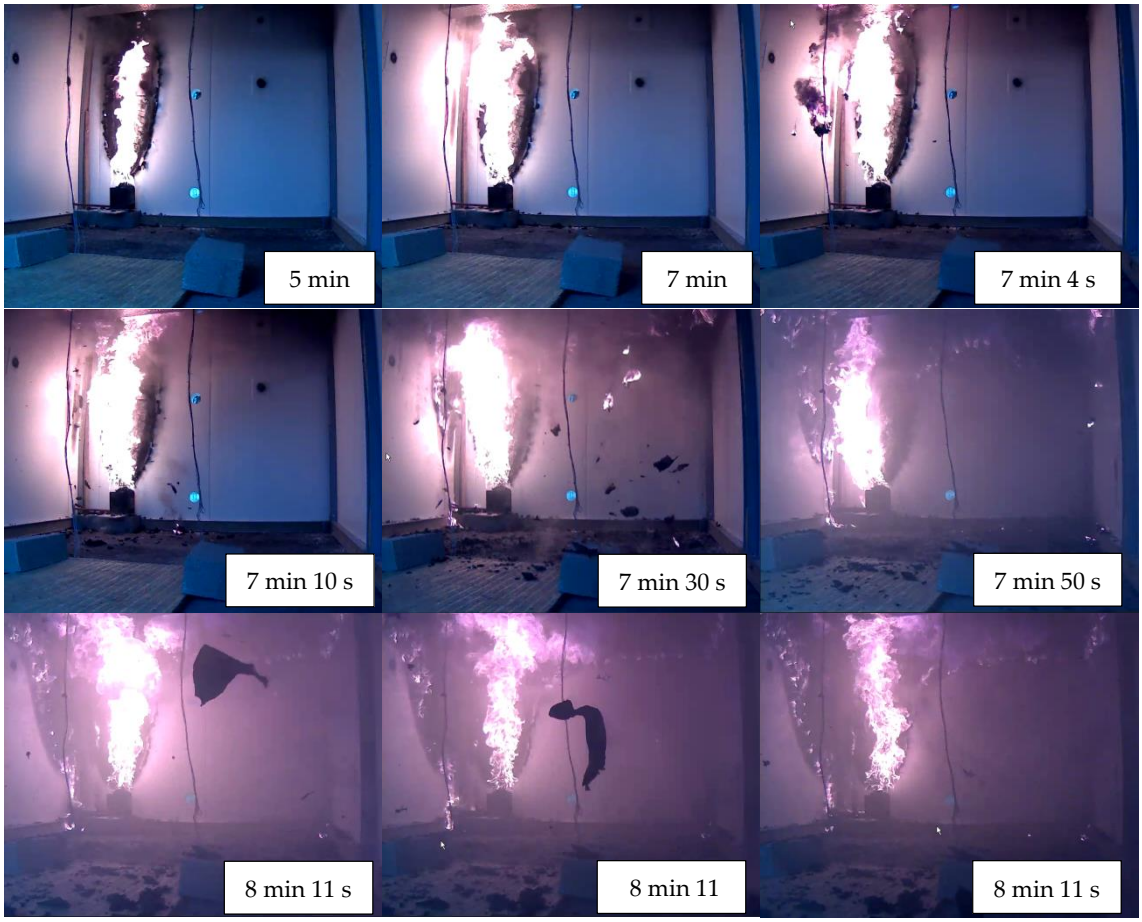

Figure 3.8. Images from video footage inside the compartment between 7 and 9 minutes

Therefore, it is quantifiably justified that the hazard from the use of insulation materials is related to the onset of pyrolysis and release of pyrolysis gases. The failure mode presented here is related to the flammability and contribution to the HRR of the fire. The ability of the pyrolysates to escape the wall assembly is vital for assessing these two hazards. Nevertheless, the understanding of this phenomenon based on transport of gases is extremely complex, since it depends on modifications, damages and installation techniques of the foam core panels. Unfortunately in this particular case, a clear assessment of the mechanisms involved is also complicated due to the additional burning dynamics of the coating paint.

3.3.3 Hazards' map determination

The origin of any hazard with regard to the use of combustible insulation materials is, in the opinion of the author, related to the onset of pyrolysis. Subsequent hazards such as flammability and generation and transport of toxic species can be avoided if the onset of pyrolysis is controlled or avoided. However, in some scenarios the designer can decide whether such hazards can be tolerated and if the risks are sufficiently low. Hence, it is necessary to map the different hazards related to the fire safety design of insulation systems if a credible risk analysis is to be carried out.

The original (initiating) hazard corresponds to the onset of pyrolysis, from which a series of flammable gases are released. The subsequent hazards linked to the release of pyrolysis gases are related to their ability to ignite and to the toxic species from those gases before ignition.

The ability of pyrolysis gases to ignite can be translated into an increased contribution of heat release inside or outside the compartment, depending on where these gases are transported. Their flammability is determined by the concentration above which they are able to ignite, i.e. the lower flammability limit, and the temperature associate with this limit. This is generically represented by Figure 3.9, where it is indicated that the lower flammability limit may be dependent on the temperature. A given concentration of pyrolysates can become flammable if the temperature is increased to a certain value [21], represented by line CD in Figure 3.9. Therefore, control measures should focus on maintaining the concentrations of pyrolysates below the flammability limit and the temperatures in the gas-phase at low levels. Additional control measures may be assigned to the manufacturers, for instance the addition of flame retardants to increase the concentration and temperature of the lower flammability limit. This technique is however typically at the expense of increasing the toxic species from the pyrolysis gases.

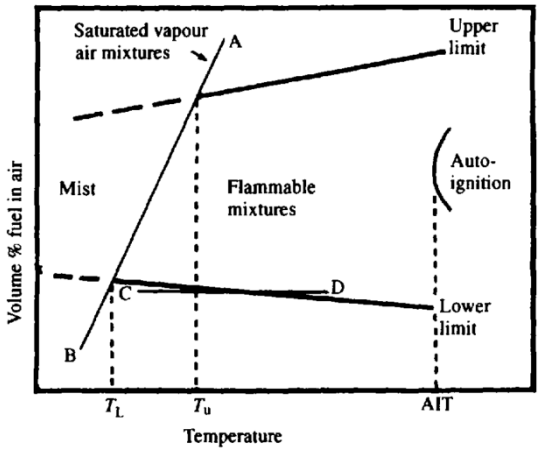

Figure 3.9. Effect of initial temperature on the limits of flammability of a flammable vapour/air mixture at a constant initial pressure [22]. Extracted from [21]

A subsequent hazard to the onset of the pyrolysis is the intrinsic toxicity of the vapours generated, before they are ignited and/or after ignition of the resulting gas mixture. The nature of the products before and after ignition may be very different, and toxic species may be generated once flaming combustion is achieved. This is the case of typical toxic effluents such as carbon monoxide, hydrogen cyanide, and hydrogen chloride.

Once all of these phenomena occur, the thermal wave will travel through the material and can lead to displacement of the pyrolysis front in the material at the back of the insulation system, and as a result compartmentalisation may be threatened. It is noteworthy that compartmentalisation may also be threatened if the pyrolysates are transported to the outside of the compartment due to leaks or gaps generated by

thermal degradation of the material accompanied by thermal stresses in the system, or due to bad practice in constructing, joining, or the sealing of the installation.

All of the hazards discussed herein are schematically represented in Figure 3.10; this can be studied in depth and valuable information can be incorporated into design strategies. The work presented in Chapters 4 through 7 is intended to provide an understanding and quantification of some of these hazards, particularly focusing on flammability, combustibility and thermal evolution of, and within, the insulation materials.

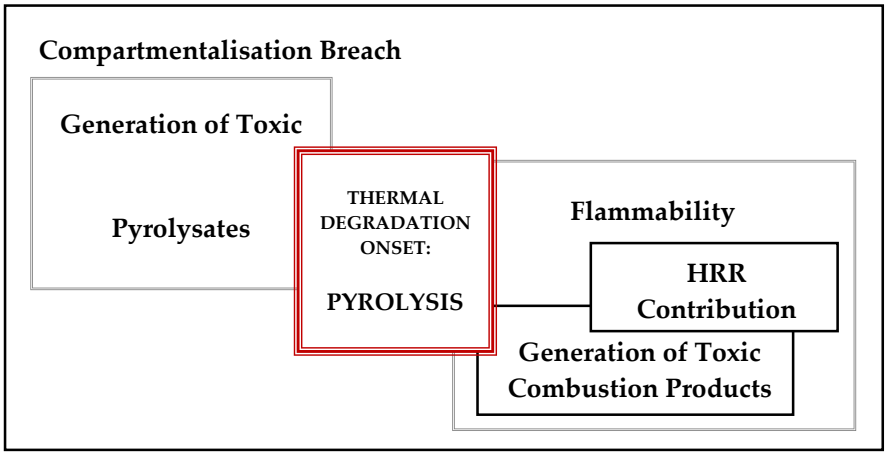

Figure 3.10. Schematic of hazards associated with combustible insulation materials under fire conditions

A list with proposed control measures for reducing the risks associated with the hazards given in Figure 3.10 is presented in Table 3.1. Quantifiable parameters for a performance-based assessment of these hazards are also included.

Table 3.1. Control measures for reduction of associated risks and quantifiable variables for performance-assessment

ID	Hazard	Control Measures	Quantifiable Variable for Performance Assessment
A1	Thermal degradation onset (Pyrolysis)	Design of a thermal barrier	(a) Time to achieve critical temperature on the exposed face of the insulation (b) Barrier thermal properties (c) Barrier thickness
B1	Generation and transport of toxic pyrolysates	Control hazard [A1] Design a gas tightness system	(a) Production rate of pyrolysates (b) Material species ratio (c) Critical concentration of toxic species
B2.1	Flammability (HRR contribution)	Control hazard [A1] Design a gas tightness system Reduce heat of combustion of material (use of flame retardants)	(a) Production rate of pyrolysates (b) Material heat of combustion (c) Critical HRR contribution
B2.2	Flammability (Generation and transport of toxic combustion products)	Control hazard [A1] Design a gas tightness system Reduce toxicity of material (less use of flame retardants)	(a) Production rate of pyrolysates (b) Combustion species ratio (c) Critical concentration of toxic species
C	Compartmentalisation breach	Control hazards [A1], [B1] and [B2] Design required insulation thickness	(a) Time to achieve critical temperature on the back face (b) Barrier thermal properties (c) Barrier thickness (d) Insulation thickness

The increased thermal feedback in insulated compartments is often referenced as a likely hazard that may accelerate the occurrence of flashover. A common misleading concept in the community is to relate fire performance to U-values of assemblies. Although U-values are commonly used to assess energy performance of assemblies, this variable has only a meaning in a steady-state regime. This assumption may be valid for low temperature calculations, where the time scale of the heat transfer is much larger. This is not the case of a fire scenario, in which the time scale tends to be much shorter, thus transient regimes becoming much more important.

Several authors have discussed the effect of insulated assemblies on the fire behaviour of liquids and solids [23–26]. While the effect is shown to be in general larger on liquid fuels than on solids, presumably due to higher Spalding number [27], this is found to be significant when the insulation is uncovered in compartments of reduced geometry (the quasi-cubic small enclosure). Since the thermal conductivity of insulation materials is very low, the net heat on the surface of the assembly is

expected to be much lower (Fourier's law) and thus more energy remains in the compartment. This was experimentally correlated by *McCaffrey et al.* [24] showing that different values of heat release rate were necessary to reach the flashover in a small compartment of 4 m x 6 m x 2.4 m height with different types of fuel. Indeed, when the insulation is placed as lining, the required HRR to reach the flashover was significantly low. On the contrary, if other lining is used or the insulation material is covered by a lining, the effects are expected to be less significant. This can be explained due to the larger thermal conductivity of the lining, thus increasing the net heat flux. Additionally, the lining is capable of absorbing much higher amounts of heat due to the significantly larger thermal inertia. Nevertheless, these correlations are expected not to apply for larger compartments and other configurations of the fuel.

The reality is that such a problem is far from being solved since it is required precise characterisation of the energy distributions within the compartment fire. Clear limitations are encountered because many factors affect the dynamics of the fire, e.g. the compartment dimensions, the fuel type, the ventilation and the compartment boundaries [28, 29].

In any case, if combustible insulation materials are installed uncovered, the real and main hazard is not the effect that the insulation might have on the fire behaviour due to reduced thermal losses, but the effect due to the contribution to the HRR by release of pyrolysis gases, which is expected to be rapid under these circumstances.

3.3.4 The role of combustibility under failure criteria framework

As noted in previous sections, if fire safety is to be incorporated as a quantitative variable in design, fundamental knowledge of material performance is required. A performance-based design methodology requires the prediction of a series of critical events that determine the system behaviour in case of fire. The existing fire-resistance framework identifies criteria such as resistance 'R', integrity 'E' and isolation 'I' as key events for the evaluation of the fire performance of construction elements as a function of time. The definition of these events is based on an understanding of the heat transfer problem that governs the thermal behaviour of the particular element being studied. On the contrary, the analysis with regard to contribution to HRR by the reaction-to-fire framework lies on a classification that is poorly applicable in a quantitative analysis.

If contribution to HRR, also identified in the literature as "contribution to flashover", is to be incorporated into a performance-based design, an additional key event that needs to be included is the "onset of pyrolysis". This is determined by the moment at which the material releases large amounts of pyrolysates which mixture

could be above the lower flammability limit. It is thus vital to understand the role that both combustible[7] and non-combustible materials play in the design process.

An approach that incorporates the quantification of performance of a given system as a series of events is schematically presented in Figure 3.3, where t_P is the time to achieve the "onset of pyrolysis", t_R is the time at which the system loses its load-bearing capacity and t_{EI} is the time at which compartmentalisation is breached. In the case that a non-combustible material is used, t_P becomes infinite since no significant thermal degradation accompanied by release of pyrolysates is expected, and no contribution to the HRR is expected. Despite the simplicity of this concept, it is important to highlight the implications for a design process. As noted in Chapter 2, combustible materials are typically able to provide the most attractive option in a multi-objective optimisation design with regard to building energy performance. The fact that non-combustible materials present an infinitely large time of thermal degradation onset (t_P), introduces a competitive scenario where an optimum can be found including both energy performance and fire performance as quantitative parameters.

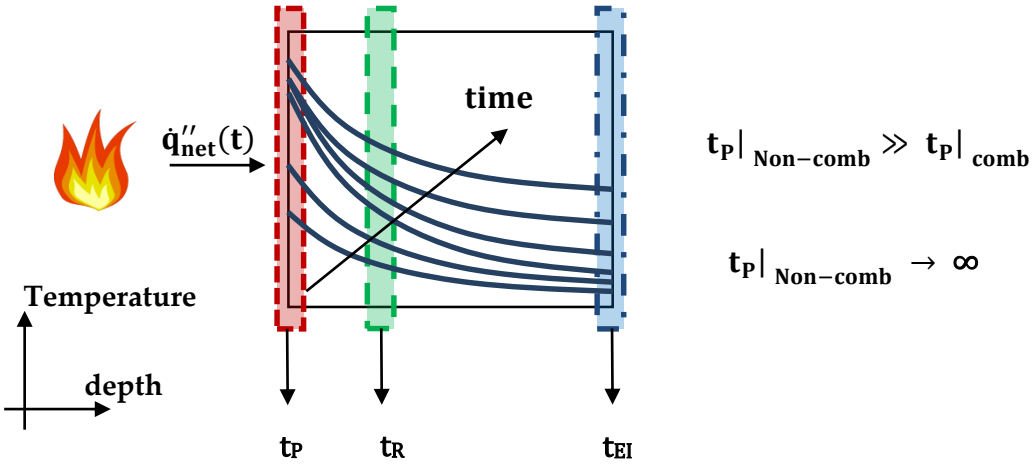

Figure 3.11. Schematic of an in-depth thermal profile for representative solid media during a fire

3.4 Methodology

The methodology proposed by the author is based on controlling the main failure mode and origin of any of the fire hazards related to insulation materials: i.e. the onset of pyrolysis. The temperature at which this is achieved is defined herein as the critical temperature, T_{cr}.

Information from material properties such as thermal conductivity, density and specific heat capacity, and critical temperature are required for the proposed methodology. This information can be obtained experimentally. For instance, values of thermal conductivity and heat capacity can be obtained by the use of the transient

[7] The term combustible used in this thesis shall be interpreted as the ability of an organic compound (gas or solid) to oxidise rather than based on a formal material classification given by standard fire testing.

hot plate [30] and differential scanning calorimetry analyses [31, 32], respectively. These properties can also be correlated by inverse modelling of the heat transfer within a solid medium, provided that the boundary condition can be properly defined. The critical temperature can be obtained by thermogravimetric analyses (TGA) or flammability analyses carried out with the Cone Calorimeter [15], or similar instruments such as the Fire Propagation Apparatus [33] or an ad-hoc radiant panel based system [34]. As shown in the previous section, the former technique can provide valuable information about the pyrolysis process of materials. The definition of the critical temperature will be discussed in Chapters 4 and 5.

If the onset of pyrolysis is to be controlled, a thermal barrier is required since, as discussed previously, very low thermal inertia leads to a rapid increase of insulation temperature. Therefore, the design of suitable lining for insulation assemblies becomes crucial; this is the philosophy presented by the NFPA framework for plastic foams. However, as noted previously, a performance-based approach is not possible under the NFPA framework, and no fundamental understanding in the performance of the insulation material is considered.

The simple approach suggested herein is based on solving the heat transfer equation for a solid medium assuming inert behaviour. This is defined by Equation (3.6) below:

$$\frac{\partial\left(k(T)\cdot\frac{\delta T}{\delta x}\right)}{\partial x}=\rho\cdot c_p(T)\cdot\frac{dT}{dt} \tag{3.6}$$

If a series of heat exposures are assumed, defined as a net heat flux into the assembly or as an external incident heat flux with defined heat losses, the failure mode can be obtained as the instant when the interface of the thermal barrier (lining) and the insulation board achieves the critical temperature of the insulation material. This approach is schematically represented in Figure 3.12 below.

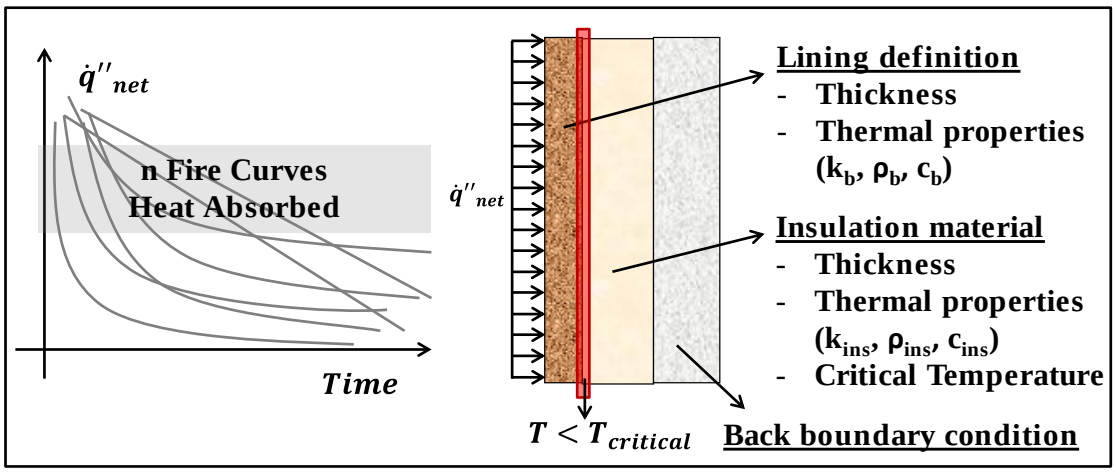

Figure 3.12. Scheme of the methodology for designing insulation systems in buildings

Assuming inert behaviour of the lining and the insulation material, the associated one-dimensional heat transfer problem is defined using:

$$\dot{q}''_{net}(t) = -k_b(T) \cdot \left.\frac{\delta T}{\delta x}\right|_{x=0^-} \qquad \text{For } x = 0 \qquad (3.7)$$

$$\frac{\partial\left(k_b(T) \cdot \frac{\delta T}{\delta x}\right)}{\partial x} = \rho_b \cdot c_{p,b}(T) \cdot \frac{dT}{dt} \qquad \text{for } 0 < x < L_b \qquad (3.8)$$

$$-k_b(T) \cdot \left.\frac{\delta T}{\delta x}\right|_{x=L_b^-} = -k_i(T) \cdot \left.\frac{\delta T}{\delta x}\right|_{x=L_b^+} \qquad \text{for } x = L_b \qquad (3.9)$$

$$\frac{\partial\left(k_i(T) \cdot \frac{\delta T}{\delta x}\right)}{\partial x} = \rho_{ins} \cdot c_{p,i}(T) \cdot \frac{dT}{dt} \qquad \text{for } L_b < x < L_b + L_i \qquad (3.10)$$

$$-k_i(T) \cdot \left.\frac{\delta T}{\delta x}\right|_{x=L_b+L_i} = \dot{q}''_{loss}(t) \qquad \text{for } x = L_b + L_i \qquad (3.11)$$

where $\dot{q}''_{net}(t)$ is the net heat flux to the surface of the thermal barrier, $k_b(T)$, ρ_b and $c_{p,b}(T)$ are the thermal conductivity, density and specific heat capacity of the thermal barrier, $k_i(T)$, ρ_i and $c_{p,i}(T)$ are the thermal conductivity, density and specific heat capacity of the insulation material, L_b is the thickness of the lining, L_i is the thickness of the insulation and $\dot{q}''_{loss}(t)$ is the heat losses at the back face of the insulation. The domain definition of the heat transfer problem defined by the equations above is represented in Figure 3.13.

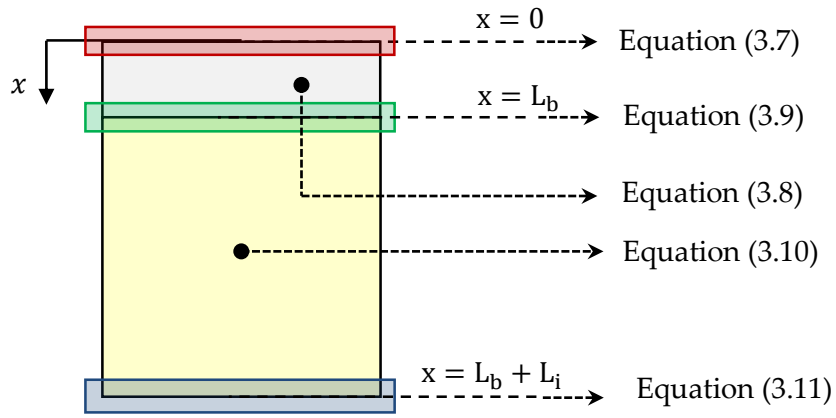

Figure 3.13. Domain definition of the one-dimensional heat transfer problem with a thermal barrier (grey) and the insulation material (yellow)

The back boundary condition is dependent on whether the back layer of insulation is attached to another material or is directly exposed to the air. The heat losses will be significantly affected by this condition; however, the expected impact on the time to achieve the critical temperature is low since the thermal inertia and diffusivity of the insulation material are low and the thermal wave takes a comparatively long time to arrive to the back of the insulation material. In any case, the assumption of an adiabatic boundary condition, i.e. $\dot{q}''_{loss}(t) = 0$, will always be a conservative scenario.

Optimised thermal barriers can be designed by selection of materials according to their thermal inertia and thickness. The state-of-the-art in fire modelling can provide inputs as heat exposure for the application of this methodology. However, this

approach carries a series of limitations such as high computational cost and inaccurate modelling of under-ventilated fires. Further research is required to reduce the uncertainty of heat inputs from real fires.

If simplified and efficient design tools are to be used, a characterisation of the fire severity, understood as potential damage from the fire to the compartment boundary is urgently required. *Harmathy and Mehaffey* [35] introduced the concept of the normalised heat load as an assessment of the fire severity in order to evaluate barriers' performance, rather than the approach based on the time-temperature history. This classic concept appears promising and should be revisited.

The main advantage of this methodology is the simplicity of the numerical tool required. This allows a performance-based methodology or probabilistic approaches to be used for the design of insulation systems in buildings, so fire safety related to the intrinsic hazards of insulation materials can be addressed in a multi-objective optimisation design. The primary steps towards the definition of this tool, as well as an example of application will be presented in Chapter 8.

3.5 Conclusions

Current methods of design for combustible insulation systems in fire are incapable of revealing the hazards related to their use in buildings. Reaction-to-fire standard tests seek to characterise the likely contribution from insulation systems to the fire by the assessment of flame spread, which does not apply to the configuration of insulation materials in buildings. A fire-resistance framework based on furnace testing is also unsuitable due to the severe interaction between the furnace and the tested material, especially for materials that pyrolyse and combust.

An in-depth analysis performed on a series of heavily instrumented tests demonstrated that the main failure mode associated with combustible insulation materials is related to the onset of thermal degradation, followed by high production of pyrolysis gases. This represents the main fire hazard related to the use of insulation materials. Since insulation materials are characterised for their low thermal inertia, control measures must depend on the use of a thermal barrier as a protective element. A redefined set of failure criteria has been proposed for the performance assessment of insulation systems.

A performance-based design methodology for the fire safe of insulation systems in energy efficient buildings has also been proposed. This is based on controlling the onset of pyrolysis, which can be represented for combustible insulation products by a critical temperature. This can be obtained by thermal analysis or flammability studies, which is presented and discussed in following Chapters.

Information regarding material properties is required for the application of this methodology. Work presented in Chapters 4 through 7 provides relevant material information at different scales. Introduction of a potential design-tool based on this methodology is presented in Chapter 8. However, further work is required to define heat inputs from real fires. Despite the current use of standard testing as pass-fail

criteria does not provide means for performance-based designs, the use of further instrumentation in these testing methods, accompanied with a rational assessment of the material behaviour and properties, could provide valuable sets of data points for particular heat inputs for the methodology validation.

3.6 References

[1] L. Bisby, J. Gales, and C. Maluk, "A contemporary review of large-scale non-standard structural fire testing," *Fire Science Reviews*, vol. 2, p. 1, 2013.

[2] C. Wade, "Future directions in fire testing of building products," in *Building for a Global Future – Australia's Built Environment*, 2003.

[3] J. M. Buist, S. J. Grayson, and W. D. Woolley, "Fire and Cellular Polymers," 1986.

[4] D. Drysdale, "Fundamentals of the fire behaviour of cellular polymers," in *Fire and cellular polymers*, 1986, pp. 61–75.

[5] "BS EN ISO 1182. Reaction to fire tests for products — Non- combustibility test." BSI, 2010.

[6] "BS EN ISO 1716. Reaction to fire tests for products — Determination of the gross heat of combustion (calorific value)." BSI, 2010.

[7] "BS EN ISO 11925-2. Reaction to fire tests — Ignitability of products subjected to direct impingement of flame. Part 2: Single-flame source test." BSI, 2010.

[8] "BS EN ISO 13823. Reaction to fire tests for building products — Building products excluding floorings exposed to the thermal attack by a single burning item." BSI, 2010.

[9] M. Smolka and Y. Suurenbroek, "Smoke and heat emissions as measures for interaction of tested elements with test environment in fire resistance testing," in *Proceedings of the 13th International Interflam Conference*, 2013.

[10] "BS EN 1363-1 . Fire resistance tests - Part 1: General Requirements." BSI, 2012.

[11] S. Welch and P. Rubini, "Three-dimensional Simulation Of A Fire-resistance Furnace," *Fire Safety Science*, vol. 5. pp. 1009–1020, 1997.

[12] A. Amundarain, "Assesment of the Thermal Efficiency, Structure and Fire Resistance of Lightweight Building Systems for Optimised Design (Ph.D. thesis)," The University of Edinburgh. http://hdl.handle.net/1842/2128, 2007.

[13] A. Jowsey, "Fire Imposed Heat Fluxes for Structural Analysis (Ph.D. thesis)," The University of Edinburgh. http://hdl.handle.net/1842/1480, 2006.

[14] U. Wickström, "Adiabatic Surface Temperature and the Plate Thermometer for Calculating Heat Transfer and Controlling Fire Resistance Furnaces," *Fire Safety Science*, vol. 9, pp. 1227–1238, 2008.

[15] "BS 476-15, ISO 5660-1. Fire tests on building materials and structures. Method for measuring the rate of heat release of products." BSI, 1993.

[16] R. J. Crewe, J. P. Hidalgo, M. X. Sørensen, S. Molyneus, M. McLaggan, G. Joomas, S. Welch, J. L. Torero, A. A. Stec, and T. R. Hull, "Fire performance of sandwich panels in a modified ISO 13784-1 small room test: the effect of damage and increased fire load," *Fire Technology (submitted)*.

[17] "ISO 13784-1. Reaction to fire test for sandwich panel building systems. Part 1: Small room test." International Organization for Standardization, Geneva (Switzerland), 2014.

[18] J. P. Hidalgo, M. McLaggan, S. Welch, and J. L. Torero, "Characterisation of fire dynamics in a modification to the Small room test, ISO 13784-1," *(in preparation)*, 2015.

[19] W. M. Thornton, "The relation of oxygen to the heat of combustion of organic compounds," *Philosophical Magazine Series*, vol. 33, pp. 196–203, 1917.

[20] M. L. Janssens, "Measuring rate of heat release by oxygen consumption," *Fire Technology*, vol. 27, no. 3, pp. 234–249, 1991.

[21] D. Drysdale, "Limits of Flammability and Premixed Flames," in *An Introduction to Fire Dynamics*, John Wiley & Sons, Ltd, 2011, pp. 83–119.

[22] M. G. Zabetakis, "Flammability characteristics of combustible gases and vapours," *US Bureau of Mines. Bulletin 627*, 1965.

[23] T. Z. Harmathy, "The role of Thermal Feedback in Compartment Fires," *Fire Technology*, vol. 11, no. 1, pp. 48–54, 1975.

[24] B. J. McCaffrey, J. G. Quintere, and M. F. Harkleroad, "Estimating room temperatures and likelihood of flashover using fire test data correlations," *Fire Technology*, vol. 17, no. 2, pp. 98–119, 1981.

[25] A. Poulsen and G. Jomaas, "Experimental Study on the Burning Behavior of Pool Fires in Rooms with Different Wall Linings," *Fire Technology*, vol. 48, pp. 419–439, 2012.

[26] A. Poulsen and A. C. Bwalya, "An Experimental Study of the Effect of Thermal Radiation Feedback on the Room-Burning Behaviour of Horizontal Slabs of Polyurethane Foam," *Research Report No. 309*. NRC Institute for Research in Construction, National Research Council Canada, 2011.

[27] D. B. Spalding, "Combustion of liquid fuel in gas stream," *Fuel*, vol. 29, no. 1, pp. 2–7, 1950.

[28] J. L. Torero, A. H. Majdalani, C. Abecassis-Empis, and A. Cowlard, "Revisiting the Compartment Fire," in *11th International Symposium on Fire Safety Science*, 2014.

[29] A. H. Majdalani, "Compartment Fire Analysis for Contemporary Architecture (Ph.D. thesis)," The University of Edinburgh, 2014.

[30] S. E. Gustafsson, "Transient plane source techniques for thermal conductivity and thermal diffusivity measurements of solid materials," *Review of Scientific Instruments*, vol. 62, pp. 797–804, 1990.

[31] M. O'neill, "Measurement of Specific Heat Functions by Differential Scanning Calorimetry.," *Analytical Chemistry*, vol. 38, no. 10, pp. 1331–1336, 1966.

[32] "ASTM E1269. Standard Test Method for Determining Specific Heat Capacity by Differential Scanning Calorimetry." 2011.

[33] "ASTM E 2058. Standard Test Methods for Measurement of Synthetic Polymer Material Flammability Using a Fire Propagation Apparatus (FPA)." ASTM International, West Conshohocken, PA, 2009.

[34] C. Maluk, "Development and Application of a Novel Test Method for Studying the Fire Behaviour of CFRP Prestressed Concrete Structural (Ph.D. thesis)," The University of Edinburgh, 2014.

[35] T. Z. Harmathy and J. R. Mehaffey, "Normalized heat load: A key parameter in fire safety design," *Fire and Materials*, vol. 6, no. 1, pp. 27–31, Mar. 1982.

Chapter 4.

Identification of Main Solid-Phase Thermal Degradation Processes: Pyrolysis and Oxidation

4.1 Introduction

Characterisation of material performance under severe conditions of heat exposure requires fundamental understanding of the different thermal degradation processes the material experiences at high temperatures. Flammability and thermal stability of materials can be interpreted if details on the thermal decomposition are known. Techniques such as thermogravimetric analysis (TGA), also defined as thermogravimetry (TG) or thermal analysis (TA), are usually applied to quantify this decomposition, which are based on the determination of mass loss with respect to temperature increases.

Solid materials may experience two types of thermal degradation processes: pyrolysis and thermal oxidation. Pyrolysis is normally understood as an endothermic chemical reaction by which solid material thermally decomposes into lower molecular weight products. These generated volatiles, or pyrolysates, are normally characterised for being flammable hydrocarbon molecules of different molecular weight, i.e. from simple molecules such as hydrogen or ethylene up to really complex products of high molecular weight that are only gas phase at high temperatures [1]. Pyrolysates generated from the surface of a material can react with oxygen from the air and then sustain an exothermic chemical reaction, flaming combustion. The generated heat is used to produce more pyrolysis gases from the solid media. Thermal oxidation of solids, commonly denominated as smouldering combustion, is considered as an oxygen diffusion-controlled heterogeneous reaction characterised for being strongly exothermic [2]. Thermal oxidation is a much more complex phenomenon than pyrolysis due to its exothermicity and heterogeneity [3]. In comparison to pyrolysis, thermal oxidation does not only depend on the chemical composition of the material and the kinetics of the reaction, but also on the diffusion of oxygen [4].

Thermal degradation processes of materials may proceed in two different regimes: kinetic regime or heat-transfer-controlled regime. The former is controlled by the rate of the chemical reaction, thus the heat transfer time scales are not limiting as these are assumed to be very fast. This is typically the case for small samples. On the contrary, thermal degradation under a heat-transfer-controlled regime is limited by the amount of heat transferred to the material, this being slower than the rate of the chemical reaction [3]. This regime is normally used for explaining the behaviour of materials under fire conditions.

Thermogravimetry can offer really valuable information to assess the behaviour of materials under fire conditions; however, this is normally assessed as a kinetic regime [5]. Extrapolation of the information obtained by thermogravimetry must be used carefully and the actual behaviour needs to be observed in a larger scale. For that purpose, it is very important to understand the energy balance within the solid phase and the thermodynamics of the different reactions. This is commonly assessed in parallel to thermogravimetric techniques by using differential scanning calorimetry

(DSC), which allows measuring heat flows related to the thermal degradation processes [6].

This chapter presents experimental work mainly based on the application of thermogravimetric analyses. Unfortunately, the equipment used for the experiments showed to be incapable of providing repeatable and reliable DSC results. Therefore, no assessment of the enthalpy of the different reactions is presented. Information extracted from the results presented in this chapter is extremely valuable for the definition and characterisation of the behaviour of insulation materials under fire conditions, described in the subsequent chapters.

4.2 Aim

The aim of this chapter is to explore the different thermal degradation processes experienced by the studied insulation materials in a kinetic regime. This information is fundamental in order to understand and extrapolate the behaviour of materials under fire conditions. Although it has been recognised that the regime of thermal decomposition for these conditions is a heat-transfer-controlled regime, it is necessary to step back to a kinetic regime to understand the different processes that characterise the thermal degradation of materials.

The pyrolysis and thermal oxidation reactions which are characteristic of these materials under different atmospheres by thermogravimetric analyses are explained herein, so as the different reactions can be isolated. In order to determine the different thermal degradation reactions, the mass loss of each material is expressed by the differential form of this (DTG), so the rates of mass loss representative of each thermal degradation reaction can be presented.

While modelling of thermal degradation reactions in a kinetic regime by Arrhenius law is a common approach followed by the scientific community, this is not generally applied for all materials in this chapter. The anticipated high complexity of the thermal degradation of some of the materials studied converts this into a really complex task which is out of the scope of this thesis.

4.3 Experimental set-up

The thermogravimetric analyses were performed using a METTLER-TOLEDO TGA/DSC 1 apparatus, which is commonly used for material characterisation. The TGA/DSC apparatus consists of a furnace with a horizontal arm with a load cell for the reference and sample crucible. The cell for the reference crucible is used to control the heating rate programs defined by the user. In addition, a heat flux gauge is provided in order to measure the heat flows experienced by the sample crucible. A gas controller is installed in the apparatus, so the concentration of oxygen in the atmosphere inside the furnace chamber can be controlled. Two types of gas flow can be set in the original apparatus: air or nitrogen. The crucibles, or sample holders, used for this research are made of alumina (aluminium oxide) and are of 70 μL capacity. The TGA/DSC apparatus works automatically due to a robotic arm controlling the

sample insertion, removal and correct positioning of this. Schematics of the apparatus and the combustion chamber are presented in Figure 4.1 below.

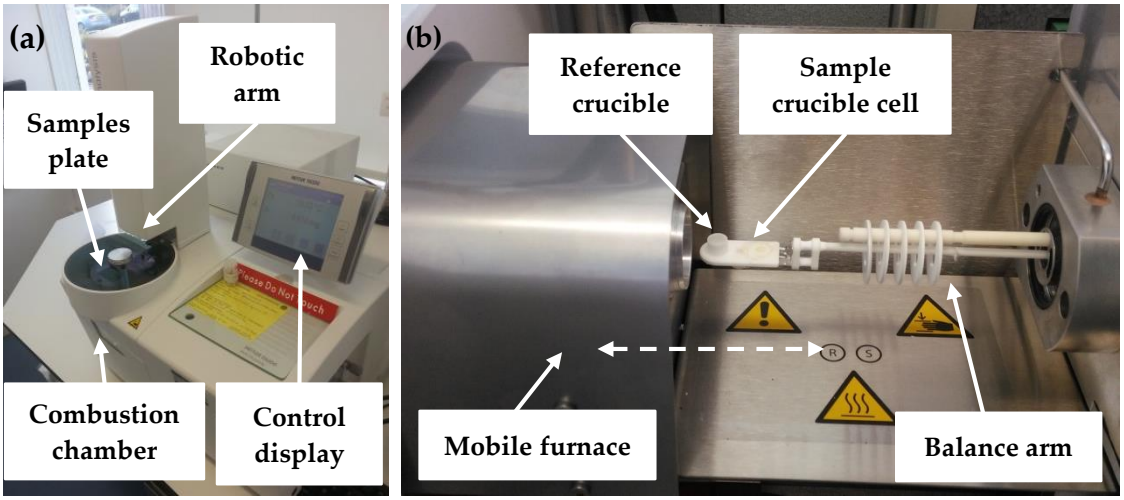

Figure 4.1. (a) External view of the TGA/DSC apparatus. (b) Schematics from the combustion chamber

A total of seven types of material are selected for the thermogravimetric analyses, with these being stone wool (SW), expanded polystyrene (EPS), phenolic foam (PF) and four types of isocyanurate-based foams from different manufacturers (PIRa, PIRb, PIRc, PIRd[8]).

Each material is tested under two different atmospheric conditions, air and nitrogen at 50 ml·min^{-1}, and under four different heating rates: 2.5, 5, 10 and 20 °C·min^{-1}. Experiments are repeated twice in order to check the repeatability of the results. The nominal sample size is 2 mm x 2 mm x 2 mm for plastic foams and 3 mm diameter by 2 mm for stone wool. Since these materials are characterised by very low density (<40kg·m^{-3}), this sample size is translated to a mass lower than 1 mg for plastic foams and a mass lower than 25 mg for stone wool. Small sample sizes and low masses are required for achieving good results since a kinetic regime is pursued. Thus, the sample is expected not to present a significant thermal gradient within itself. The samples from plastic foams are prepared by cutting small pieces of the original material, since the material is relatively homogeneous. On the contrary, since stone wool is a heterogeneous material, the SW samples are prepared by mixing a bunch of fibres extracted from the original wool and introducing them into the crucible. A more homogeneous sample is expected by proceeding with this technique.

[8] PIRd corresponds to the PIR foam extracted from sandwich panels used in large-scale experiments presented by *Crewe et al.* [16].

A list of the total number of experiments is listed in Table 4.1 below. As general practice, experiments run from 25°C up to 800°C.

Table 4.1. List of general TGA experiments

Material	Sample configuration	Heating rate /°C·min^{-1}	Atmospheric condition	Temperature range
SW	**Nominal sample size:** Ø3 mm x 2 mm **Nominal initial mass:** < 25 mg	20, 10, 5, 2.5 (2 repetitions)	(a) 50 ml·min^{-1} of N_2 (b) 50 ml·min^{-1} of air	25 – 800 °C
PIRa	**Nominal sample size:** Cut 2 mm x 2 mm x 2 mm **Nominal initial mass:** < 1 mg			
PIRb				
PIRc				
PIRd				
PF				
EPS	**Nominal sample size:** (a) 2 mm x 2 mm x 2 mm (b) 2 mm x 2 mm x 2 mm from warmed up and shrunk EPS* **Nominal initial mass:** (a) < 1 mg (b) 2.76 ± 0.22 mg* * repeated (x4) air experiments at 10°C·min^{-1}			

Measurements of DSC curves from these thermogravimetric experiments have been found to be erratic, presumably due to inappropriate calibration and low sensitivity of the DSC gauge, low sample size, contamination of the crucibles, not good surface contact between the bottom of the crucible and the sample and drifts in the DSC gauge. This drawback was expected due to warnings from the apparatus manufacturer. Therefore, values of enthalpy for the different reactions are not presented.

4.4 Results

4.4.1 Stone wool (SW)

Mass loss experienced by stone wool samples due to thermal degradation processes is presented in Figure 4.2. Mass loss is expressed as a normalised variable, being a ratio between the measured value and the total mass at the beginning of the experiment, i.e. the initial mass sample. Figure 4.2a presents the normalised mass in a nitrogen atmosphere. The total mass loss for most of the heating rates is lower than 1% at the reference temperature of 800°C. Only one experiment run with a heating rate of 2.5°·C^{-1} presents a total mass loss of approximately 2% at 800°C. All mass loss curves show a main drop of mass between 200°C and 350°C, while no trends are shown between different heating rates. Figure 4.2b presents the normalised mass in an air atmosphere. The total mass loss for all the heating rates is between 1% and 1.5% at the reference temperature of 400°C. A plateau in mass is observed between 500°C

and 700°C, with a slight increase of mass from 700°C, while no clear trends are observed among the different heating rates.

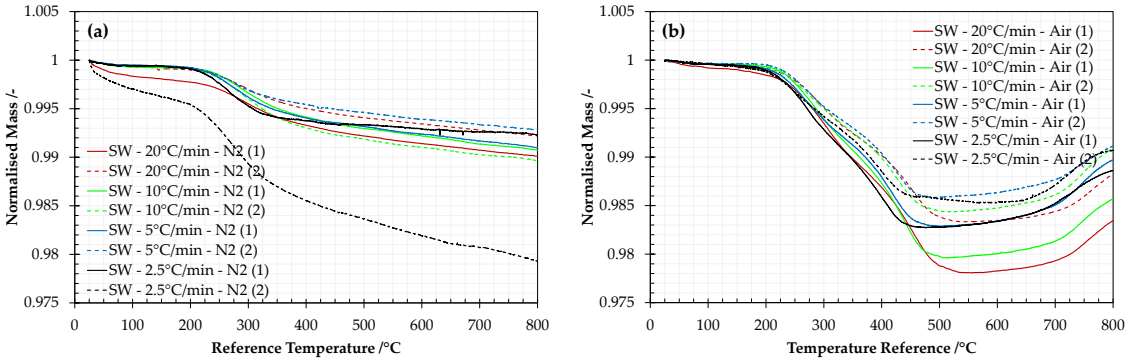

Figure 4.2. Thermal decomposition of stone wool under different heating rates in nitrogen (a) and air (b) atmospheres at 50 ml·min^{-1}

Differential forms of TGA curves from Figure 4.2 are presented in Figure 4.3. The differential form of a TGA curve (DTG) is obtained by calculating the first derivative of the normalised TGA curve. The DTG curves presented in this chapter are obtained by calculating the first derivative as the ratio between the increment of the normalised TGA value for a temperature step and the temperature step. Mass loss is indicated by positive DTG values, while negative DTG values indicate mass gain. The curves generated by this technique implicitly carry a low signal-to-noise ratio, i.e. significant noise disturbance in the measurement. For illustrative purposes, these curves have been adjusted and smoothed by using locally weighted scatterplot smoothing (LOESS) [7, 8].

Identification of main thermal decomposition reactions can be assessed by interpreting the peaks of mass loss rate, i.e. peaks in the DTG curve. These are normally presented and characterised as a log-normal function, also denominated as Fraser-Suzuki (F-S) function [9, 10]:

$$y = a_0 \cdot \exp\left\{-\ln(2) \cdot \left[\frac{\ln(1 + 2 \cdot a_3 \cdot \frac{x - a_1}{a_2})}{a_3}\right]\right\} \quad (4.1)$$

where y is the dependent term, x is the independent term, and a_0, a_1, a_2 and a_3 are respectively the amplitude/height, centre, width and asymmetry of the peak.

As noted in following sections, the reactions may overlap, making difficult to assess the actual number of reactions and lost mass by this reaction. In any case, the identification of the peaks is relevant information to understand qualitatively the temperature region with highest mass loss.

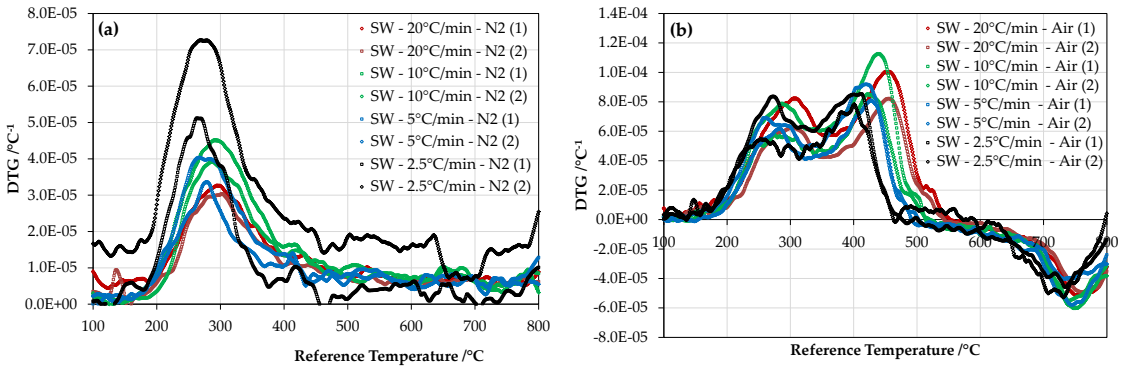

Figure 4.3. Differential thermogravimetric curves (DTG) of stone wool under different heating rates in nitrogen (a) and air (b) atmospheres at 50 ml·min^{-1}

Figure 4.3a shows the DTG curves for different heating rates in a nitrogen atmosphere. As for the TGA curve, a main peak of mass loss is presented between 200°C and 350°C. The peak of the curve increases and displaces to lower temperatures with lower heating rates. Peak properties for the two first peaks under different heating rates are noted in Table 4.2, presented as average and standard deviation values. Figure 4.3b shows the DTG curves for different heating rates in an air atmosphere. Two peaks of mass loss are observed, the first being between 250°C and 350°C and the second being between 400°C and 500°C, with the height of the second peak being larger than first one for all heating rates. Peaks from lower heating rates are shifted to lower temperatures. A third peak of mass gain is observed between 700°C and 800°C, indicating the interaction of oxygen in the chemical process taking place, potentially crystallisation.

Table 4.2. Main peaks properties of nitrogen and air in DTG curves for SW

Atmosphere	Heating rate /°C·min^{-1}	1st Peak		2nd Peak	
		Peak temperature /°C	Peak height /°C^{-1}	Peak temperature /°C	Peak height /°C^{-1}
Nitrogen	20	299.0 ± 4.0	3.1e-05 ± 1.1e-06	-	-
	10	289.5 ± 2.5	4.2e-05 ± 3.0e-06	-	-
	5	273.0 ± 6.0	3.7e-05 ± 3.4-06	-	-
	2.5	266.0 ± 3.0	6.2e-05 ± 1.1-05	-	-
Air	20	305.0 ± 2.0	4.2e-05 ± 9.9e-06	456.0 ± 1.0°C	9.1e-05 ± 9.1-06
	10	280.0 ± 6.0	6.8e-05 ± 1.0e-05	430.5 ± 8.5°C	9.9e-05 ± 1.4-05
	5	271.0 ± 12.0	6.5e-05 ± 3.8-06	423.5 ± 4.5°C	8.6e-05 ± 5.5-06
	2.5	263.0 ± 10.0	6.9e-05 ± 1.5-05	406.5 ± 5.5°C	8.2e-05 ± 3.6-06

Residues from nitrogen and air experiments are shown in Figure 4.4 below, with those obtained from tests in a nitrogen atmosphere being black and those tested in air

being brown. Both residues seem to have lost the flexible behaviour from the original wool.

Figure 4.4. Examples of stone wool residue after TGA tests in a nitrogen atmosphere (top) and air (bottom)

4.4.2 Isocyanurate-based polyurethane foam (PIR)

Mass loss results due to thermal degradation processes in a nitrogen atmosphere for four different heating rates and four different isocyanurate-based foams are presented in Figure 4.6. PIRa, PIRb and PIRc show a total mass loss of approximately 76% at a reference temperature of 800°C, while for PIRd the total mass loss is 79% at that temperature. The residues after the experiments present a typical char structure, black and porous. Examples of these residues in the alumina crucibles are presented in Figure 4.5 and average values for different heating rates are shown in Table 4.3.

Table 4.3. Remaining char residue at 800°C in a nitrogen atmosphere for PIR foams

Heating rate /°C·min^{-1}	PIRa	PIRb	PIRc	PIRd
20	28.0% ± 1.3%	25.9% ± 0.2%	26.1% ± 0.6%	22.6% ± 0.5%
10	26.2% ± 0.5%	27.6% ± 0.7%	23.5% ± 0.4%	21.8% ± 1.4%
5	26.7% ± 0.5%	16.9% ± 5.6%	19.8% ± 2.1%	22.1% ± 1.5%
2.5	14.4% ± 1.1%	27.3% ± 1.7%	29.2% ± 0.2%	17.7% ± 1.9%
Average	23.8% ± 5.2%	24.4% ± 5.0%	24.6% ± 3.4%	21.1% ± 2.2%

From Figure 4.6 it can be identified that the main mass loss step is produced between 250°C and 450°C for four foams. In general, noticeable patterns can be observed between the different heating rates and the mass loss. Lower heating rates present higher mass loss than higher heating rates for same reference temperatures. These patterns are not followed after the main drop in mass, during the plateau up to 800°C, resulting in slightly different mass residues (Table 4.3). This is associated to the error in the measurement of mass when small sample sizes are used. Nevertheless, good repeatability is found between tests with same heating rate. Repeated tests are plotted in order to show the magnitude of the expected error in the measurement;

therefore no error bars are presented in order to facilitate the reader's interpretation of the different graphs.

Figure 4.5. Examples of remaining char after TGA tests in a nitrogen atmosphere

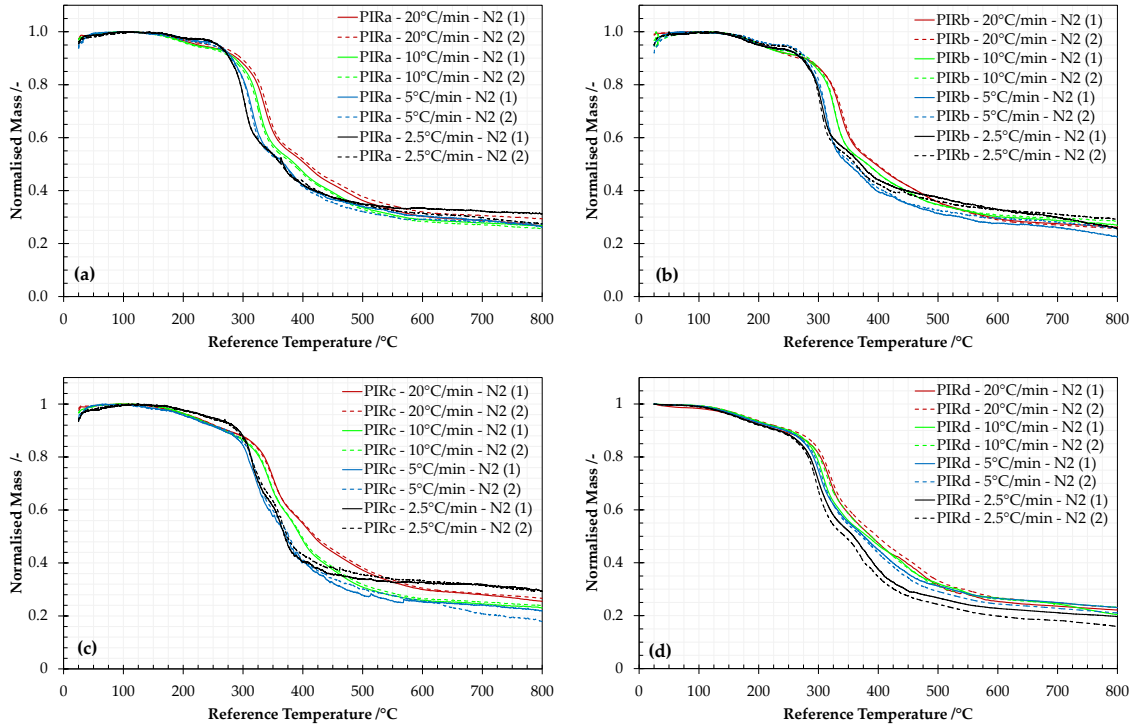

Figure 4.6. Thermal decomposition of (a) PIRa, (b) PIRb, (c) PIRc and (d) PIRd under different heating rates in a nitrogen atmosphere (50 ml·min^{-1})

Mass loss due to thermal degradation processes in an air atmosphere for four different heating rates and four different isocyanurate-based foams is presented in Figure 4.7. The mass loss curves for the four types of foam mainly consist of two steps. The first steep drop of mass is presented between 250°C and 350°C approximately, following a gentle drop of mass after 150°C, while the second steep drop of mass is presented between 350°C and 600-700°C, depending on the heating rate. In general, a pattern of curves from lower heating rates being displaced to lower temperatures is observed. PIRa, PIRb and PIRd show similar behaviour up to 350°C, presenting the steepest mass loss steps and achieving an approximate average of remaining mass of 64%, 59% and 64% respectively at this temperature. On the contrary, PIRc presents a gentler mass loss drop up to 350°C, achieving an average of remaining mass of 72%. Exact average and standard deviation values of mass remaining for each foam at 350°C are presented in Table 4.4, with the quantification obtained in a nitrogen and air atmosphere.

Table 4.4. Average of remaining mass at 350°C in a nitrogen and air atmosphere

Atmosphere	PIRa	PIRb	PIRc	PIRd
Nitrogen	56.8% ± 3.8%	55.5% ± 3.8%	64.9% ± 5.1%	55.5% ± 3.3%
Air	63.8% ± 1.5%	59.4% ± 2.8%	71.7% ± 3.2%	63.9% ± 3.7%

It can be seen that the mass loss is slightly larger in a nitrogen atmosphere than in air at a reference temperature of 350°C after the first main drop of mass. This is consistent for the four foams studied, with the difference being in the range 4-9%.

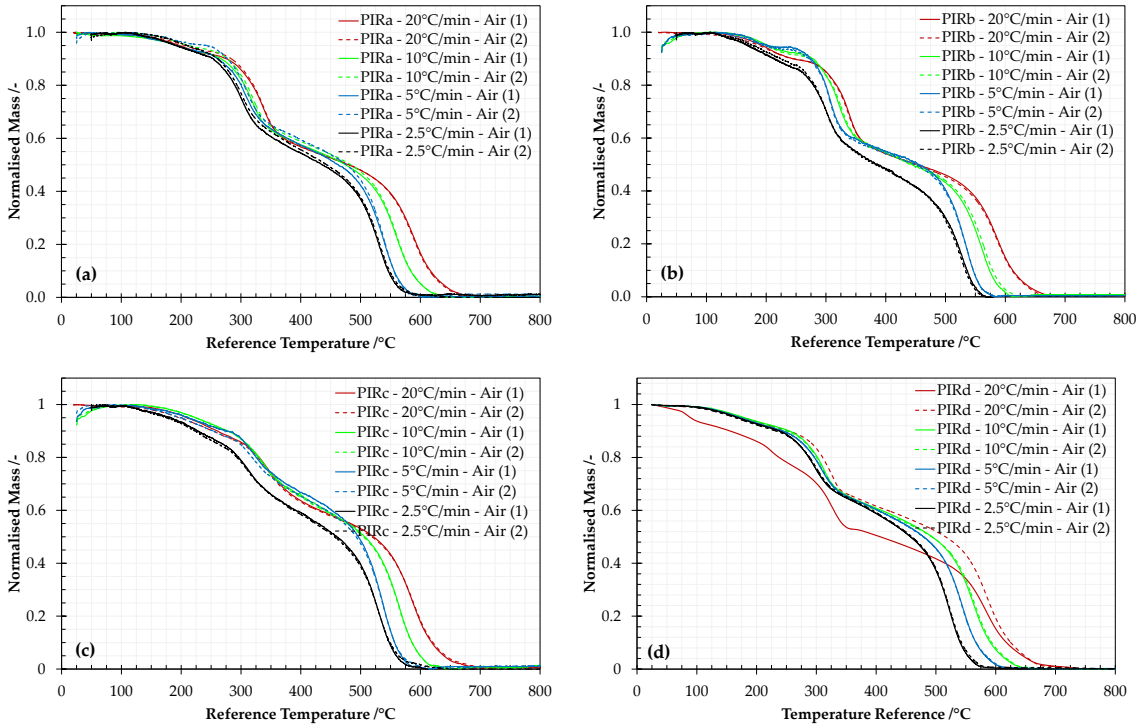

Figure 4.7. Thermal decomposition of (a) PIRa, (b) PIRb, (c) PIRc and (d) PIRd under different heating rates in an air atmosphere (50 ml·min^{-1})

Differential forms of TGA curves from Figure 4.6 and Figure 4.7 are presented in Figure 4.8 and Figure 4.9, respectively. Figure 4.8 shows the quantification of the main reactions of thermal degradation in a nitrogen atmosphere for the four PIR foams under four different heating rates. DTG curves of PIRa, PIRb and PIRd present similar shapes. An initial small peak is observed between 150°C and 200°C, which is followed by the largest peak observed between 250°C and 350°C. A series of overlapping peaks are observed after this main degradation process, between 350°C and 550°C. On the other hand, the DTG curve for PIRc has a similar behaviour below 250°C. This is followed by two large peaks observed in the range of 250°C to 450°C, depending on the heating rate. The first of these large peaks from PIRc is smaller than the main one observed for PIRa, PIRb and PIRd between 250°C and 350°C. The second largest peak showed by PIRc is in magnitude larger than that observed for PIRa, PIRb and PIRd in that range of temperatures, 350°C-450°C. For simplicity, quantification of the first three main thermal degradation processes for PIRa in a nitrogen atmosphere is presented in Table 4.5. As noted later in the discussion section, this quantification

should not be interpreted as single peaks that represent single thermal degradation reactions, but as lumped thermal degradation processes occurring at the same range of temperatures.

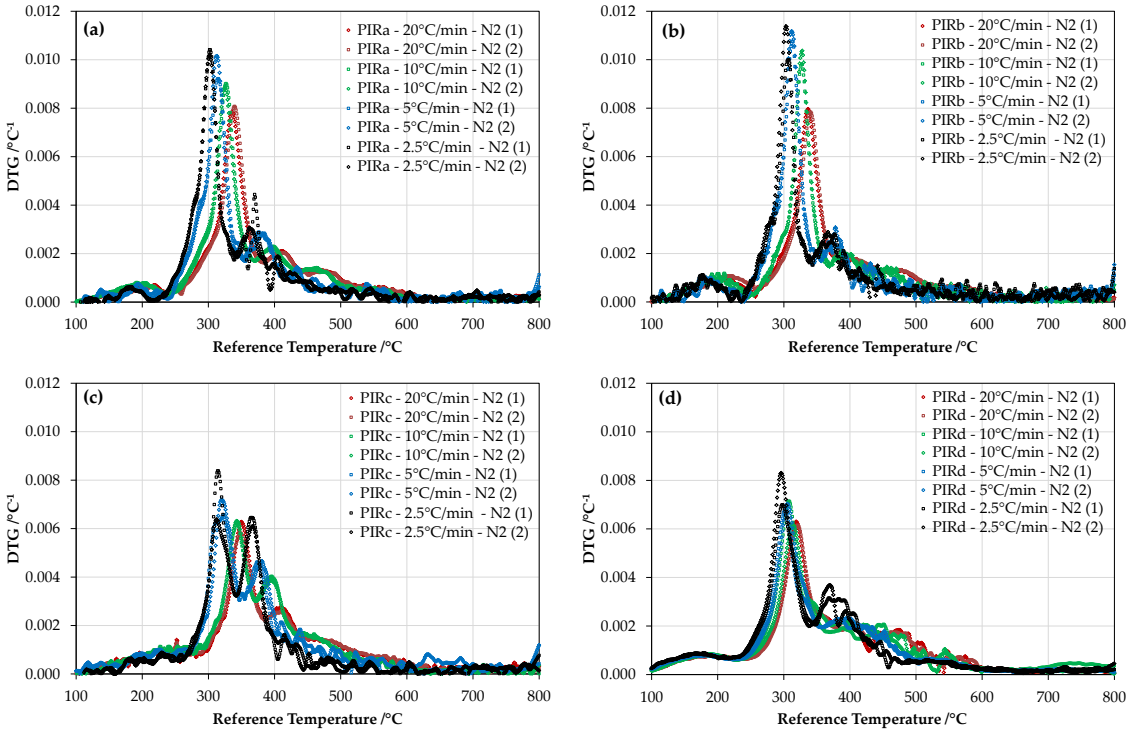

Figure 4.8. Differential thermogravimetric curves (DTG) of (a) PIRa, (b) PIRb, (c) PIRc and (d) PIRd under different heating rates in a nitrogen atmosphere at 50 ml·min^{-1}

Table 4.5. Properties of main lumped peaks for nitrogen and air atmospheres at different heating rates from DTG curves for PIRa

Atmosphere	Heating rate /°C·min^{-1}	1st Peak		2nd Peak		3rd Peak	
		Peak Temperature /°C	Peak Height /°C^{-1}	Peak Temperature /°C	Peak Height /°C^{-1}	Peak Temperature /°C	Peak Height /°C^{-1}
Nitrogen	20	211 ± 6	0.0007 ± 3e-05	338 ± 2	0.0080 ± 0.0001	412.5 ± 0.5	0.0021 ± 3e-05
	10	199 ± 7	0.0008 ± 9e-06	326 ± 1	0.0089 ± 0.0001	398 ± 0	0.0022 ± 5e-05
	5	191 ± 3	0.0007 ± 7e-05	314 ± 1	0.0097 ± 0.0005	379 ± 3	0.0029 ± 3e-05
	2.5	182.5 ± 0.5	0.0006 ± 3e-05	332 ± 0	0.0103 ± 0.0001	366 ± 4	0.0038 ± 0.0007
Air	20	208 ± 0	0.0009 ± 6e-05	337 ± 0	0.0055 ± 3e-05	589 ± 0	0.0055 ± 6e-05

	10	197 ± 2	0.0008 ± 4e-05	319.5 ± 0	0.0052 ± 1e-05	560 ± 0	0.0065 ± 5e-05
	5	180.5 ± 0.5	0.0008 ± 3e-05	306.5 ± 1.5	0.0051 ± 1e-04	540 ± 1	0.0077 ± 3e-04
	2.5	185.5 ± 0.5	0.0010 ± 4e-05	301.5 ± 0.5	0.0049 3e-05	530 ± 0	0.0070 ± 2e-05

Figure 4.9 presents the quantification of the main thermal degradation in an air atmosphere. In general, similar behaviour is observed for the four PIR foams. Three main peaks of mass loss rate can be identified. The first and smaller peak is observed as in a nitrogen atmosphere, between 150°C and 250°C, while the second and third peaks are observed in the range of 250-400°C and 450-700°C respectively, depending on the heating rate. These peaks tend to displace to lower temperatures with slower heating rates. Similarly, the third peak at 450°C-700°C slightly increases with the exception of a heating rate of 5°C·min^{-1} for PIRa, PIRb and PIRc. However, the second peak at 250°C-400°C decreases in magnitude with slower heating rates, with the exception of a heating rate of 5°C·min^{-1} for PIRb. An irregularity is found for PIRd in the first of the 20°C·min^{-1} heating rate, showing a small peak at 220°C, probably attributed to impurities in the crucible that was not cleaned suitably. Quantification of the peak properties for the thermal degradation of PIRa are shown in Table 4.5.

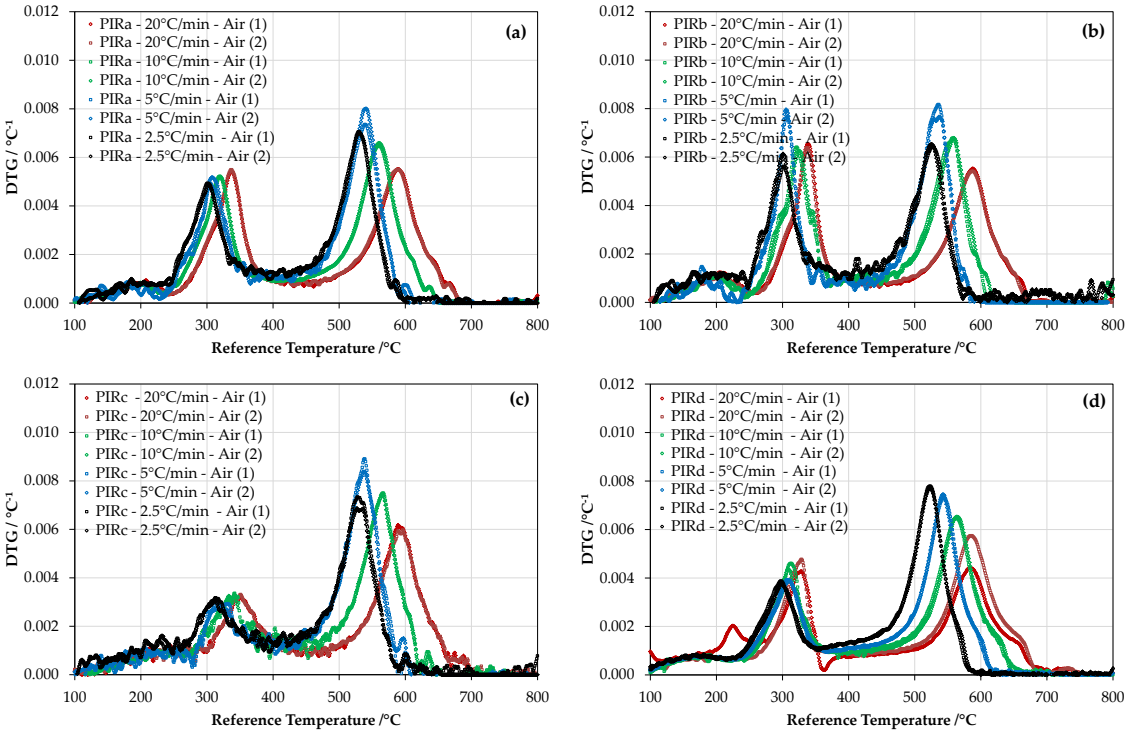

Figure 4.9. Differential thermogravimetric curves (DTG) of (a) PIRa, (b) PIRb, (c) PIRc and (d) PIRd under different heating rates in an air atmosphere at 50 ml·min^{-1}

Figure 4.10 presents a particular case of the average TGA curves obtained for PIRd with a heating rate of 5°C·min^{-1} in nitrogen and air atmospheres (blue diamonds and red squares, respectively). Residues from tests in a nitrogen atmosphere are later tested in air with the same heating rate (green triangles). This case is representative of the rest of isocyanurate-based foams and shows that thermal degradation proceeds

at same regime up to a reference temperature of 300°C. From this point, thermal degradation proceeds at different rate in nitrogen and air atmospheres. It is found that a steepest mass loss in nitrogen atmospheres occurs from 300°C up to 500°C. From that temperature, a plateau with no significant mass loss from 500°C to 800°C is observed for the mass in nitrogen. On the contrary, in an air atmosphere, mass loss from 500°C up to approximately 600°C presents a sudden drop until all mass is finally consumed. The residue obtained from the sample tested initially in nitrogen and later in air, presents a single drop from 400°C up to 600°C, with all the mass finally being consumed at the latter temperature.

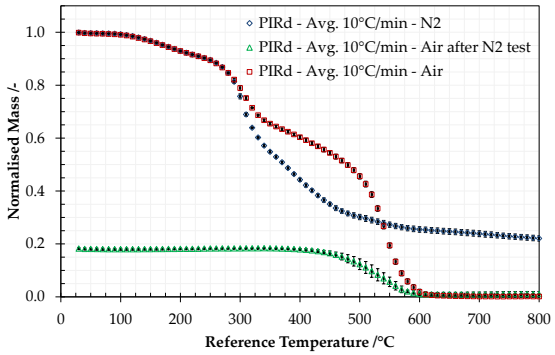

Figure 4.10. Average TGA curves of PIRd under heating rate of 10°C·min^{-1}. Blue diamonds: Nitrogen atmosphere; Green triangles: Residue of nitrogen atmosphere tests in an air atmosphere; Red squares: Air atmosphere. Error bars represent standard deviation between two repeated tests

4.4.3 Phenolic foam (PF)

Mass loss due to thermal degradation processes experienced by the phenolic foam samples is presented in Figure 4.11. Figure 4.11a presents the mass loss of phenolic foam in a nitrogen atmosphere Two main steps of mass loss can be identified: the first approximately between 200°C and 350°C, and the second and steepest step between 350°C and 500°C, followed by a plateau with low mass loss until 800°C. The total mass loss at a reference temperature of 800°C is approximately 63%. The remaining residue for each heating rate is presented in Table 4.6. A good agreement is observed among the different heating rates, with slightly higher mass loss achieved for faster heating rates.

Table 4.6. Remaining char residue of phenolic foam at 800°C in a nitrogen atmosphere

Heating rate /°C·min^{-1}	20	10	5	2.5	Average
Residue	44.6% ± 0.8%	46.4% ± 1.1%	45.9% ± 3.0%	50.2% ± 0.2%	46.8% ± 2.7%

Figure 4.11b shows the mass loss of phenolic foam in an air atmosphere. Two main steps of mass loss can be identified: the first between 200°C and 300°C, followed by very sharp mass loss from 350°C up to 500-600°C, depending on the heating rate. All the mass gets consumed after 600°C. Experiments with a heating rate of 2.5°C·min^{-1} show a final mass loss of 15% between 500°C and 600°C. This could indicate a last residue eventually being consumed. Rest of experiments do not present this drop of mass, likely due to an error in the normalisation of the mass loss. In general, good

agreement is found between different heating rates. Slower heating rates show steeper mass loss in the second step. However, this is not observed for first step of mass loss.

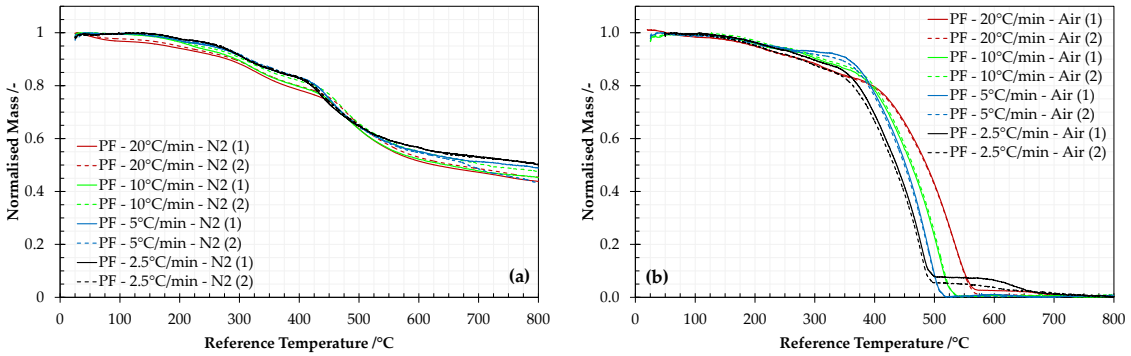

Figure 4.11. Thermal decomposition of phenolic foam under different heating rates in nitrogen (a) and air (b) atmospheres at 50 ml·min^{-1}

Differential form of TGA curves in Figure 4.11 is presented in Figure 4.12. Figure 4.12a presents three peaks of mass loss rate in nitrogen, where the first and second peaks are observed between 150°C and 250°C, and between 250° and 350°C, respectively. The third and largest peak is observed between 400°C and 600°C. Good repeatability is observed for experiments with the same heating rate, while clear trends are found between peak properties and heating rates, with peak temperatures being displaced to lower temperatures with slower heating rates. A slight increase in the magnitude of the peak is generally observed for slower heating rates. Figure 4.12b presents the mass loss rates in air, where two small peaks can be observed at lower temperatures, as found in nitrogen. Subsequently, two peaks overlap from 300°C up to 500-575°C, with the latter reference temperature being dependent on the heating rate. Clear patterns are observed for the large peaks, which increase in magnitude and are displaced to lower temperatures as the heating rate is reduced, as the TGA curves shown previously. Good repeatability for same heating rates is observed. Average main properties of the different lumped peaks for nitrogen and air are noted in Table 4.7.

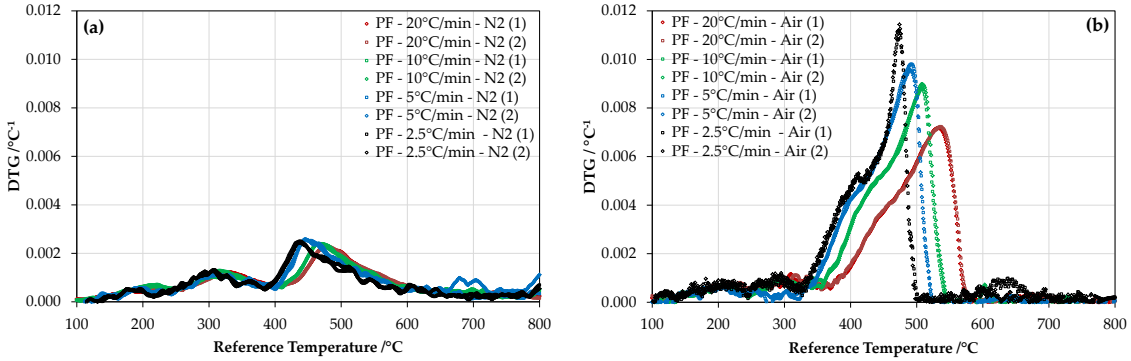

Figure 4.12. Differential thermogravimetric curves (DTG) of phenolic foam under different heating rates in nitrogen (left) and air (right) atmospheres at 50 ml·min^{-1}

Table 4.7. Properties of main lumped peaks of phenolic foam in nitrogen and air atmospheres at different heating rates from DTG curves

Atmosphere	Heating rate /°C·min^{-1}	1st Peak		2nd Peak		3rd Peak	
		Peak temperature /°C	Peak height /°C^{-1}	Peak temperature /°C	Peak height /°C^{-1}	Peak temperature /°C	Peak height /°C^{-1}
Nitrogen	20	250 ± 0.0	0.00055 ± 1.6e-05	327.5 ± 5.5	0.00118 ± 3.3e-05	478.0 ± 2.0	0.00227 ± 1.0e-05
	10	219.5 ± 2.5	0.00068 ± 3.3e-05	318.5 ± 2.5	0.00118 ± 1.1e-04	468.0 ± 2.0	0.00239 ± 0.8e-05
	5	194.5 ± 4.5	0.00057 ± 0.3e-05	310.5 ± 1.5	0.00118 ± 2.6e-05	445.0 ± 0.0	0.00256 ± 1.2e-05
	2.5	186.0 ± 10.0	0.00052 ± 0.7e-05	307.0 ± 1.0	0.00129 ± 0.8e-05	437.5 ± 0.5	0.00246 ± 3.0e-05
Air	20	217.0 ± 4.0	0.00079 ± 1.7e-05	313.5 ± 3.5	0.00113 ± 2.1e-05	534.0 ± 2.0	0.00720 ± 2.9e-05
	10	208.5 ± 1.5	0.00068 ± 1.3e-05	296.0 ± 1.0	0.00092 ± 8.6-05	508.0 ± 0.0	0.00889 ± 9.0e-05
	5	207.5 0 ± 0.5	0.00065 ± 2.7e-05	-	-	491 ± 1.0	0.00968 ± 1.21e-04
	2.5	201.0 ± 20.0	0.00090 ± 6.6e-05	298.0 ± 3.0	0.00111 ± 8.6-05	474 ± 0.0	0.01131 ± 1.3e-04

Figure 4.13 presents a particular case of the average TGA curves obtained for phenolic foam with a heating rate of 10°C·min^{-1} in nitrogen and air atmospheres (blue diamonds and red squares, respectively). Residues from tests in a nitrogen atmosphere are later tested in air with the same heating rate (green triangles). It is observed that thermal degradation proceeds at same regime up to a reference temperature of 325°C. Afterwards, thermal degradation proceeds at different rate in nitrogen and air atmospheres. Initially, Mass loss in a nitrogen atmosphere is slightly larger than in air, but at 400°C a steep mass loss in air atmosphere is observed. From that temperature, mass in nitrogen continues to decrease gentler until a plateau with no significant mass loss from 600°C to 800°C. In an air atmosphere, mass loss from 400°C up to approximately 550°C presents a sharp drop to leave a residue around 15% of the original mass. The residue obtained from the test in nitrogen, approximately 40% of the original mass, is later tested in air, which presents a single step of mass loss from 425°C up to 550°C, with a small proportion of mass of approximately 10% of the original mass remaining. The repeatability for nitrogen and original air experiment is good. However, the residues after testing in a nitrogen atmosphere present some discrepancy in their quantification. This is probable due to oxidation during the cooling phase of the residue. Indeed, the residue has different

weight after finishing the experiment in nitrogen and starting the experiment in air. In any case, the drop of mass is obtained between 450°C and 550°C for both cases.

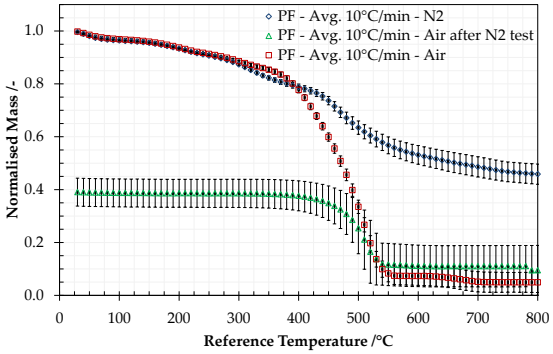

Figure 4.13. Average TGA curves of phenolic foam under heating rate of 10°C·min^{-1}. Blue diamonds: Nitrogen atmosphere; Green triangles: Residue of nitrogen atmosphere tests in an air atmosphere; Red squares: Air atmosphere. Error bars represent standard deviation between two repeated tests

4.4.4 Expanded polystyrene (EPS)

Mass loss due to thermal degradation processes experienced by the expanded polystyrene foam samples is presented in Figure 4.14. Figure 4.14a shows the mass of samples in a nitrogen atmosphere. A single main drop of mass is observed between 350°C and 450°C-475°C, with all mass being consumed at the latter reference temperature; therefore, no significant residue is found after the tests were ended at 800°C. Good repeatability is found between the different tests run at the same heating rate. A clear pattern is observed between the mass loss obtained for different heating rates, where the big drop of mass being displaced to lower temperatures for slower heating rates. An increase of mass is observed at the lower temperatures, which is attributed to the error on mass measurement due to low sample mass and blank subtraction technique. Figure 4.14b presents the loss of mass in an air atmosphere. Apparently a single mass loss drop is observed for all heating rates from 300°C to 425°C, but with non-uniform slope between them. All mass is consumed after this single mass drop, with no apparent residue being found after 800°C. The repeatability of the tests is found poor in comparison with the tests run in nitrogen.

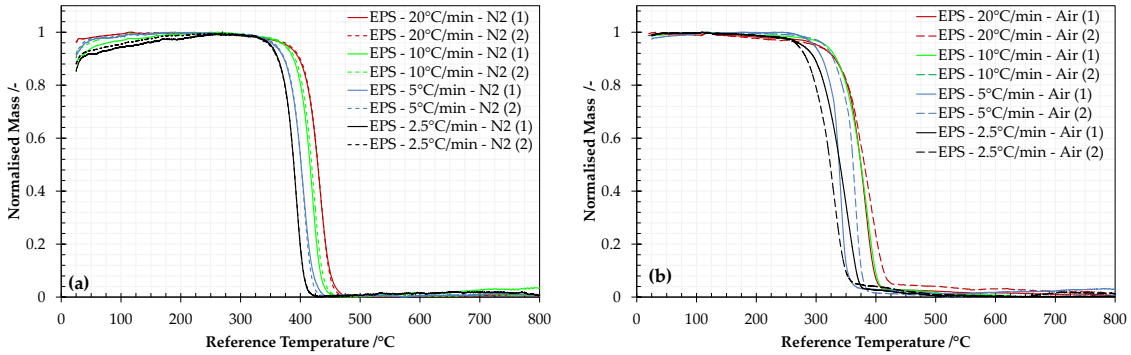

Figure 4.14. Thermal decomposition of EPS under different heating rates in nitrogen (a) and air (b) atmospheres at 50 ml·min^{-1}

Differential forms of TGA curves from Figure 4.14 are presented in Figure 4.15 below. Figure 4.15a presents the mass loss rates for different heating rates in nitrogen. As for the TGA curves, a single clear peak is observed for each experiment. A clear trend can be observed between heating rates and peak properties, with peak temperatures being displaced to lower temperatures and larger amplitudes for slower heating rates. Average values of main peak properties are presented in Table 4.8. Figure 4.15b presents the mass loss rate for different heating rates in air. The obtained curves are not representative of a single kinetic reaction. Indeed, mass loss rate for all curves seems to severely increase after a gentle increase of mass loss rate. However, a lack of good repeatability is found for even same heating rates. Onset of the reaction seems to be displaced to lower temperatures as the heating rate is reduced, but peak temperatures do not show this displacement very consistently.

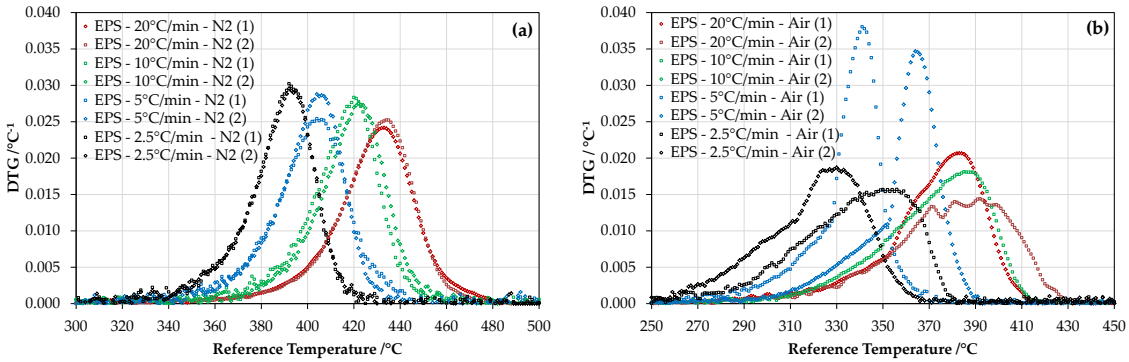

Figure 4.15. Differential thermogravimetric curves (DTG) of EPS under different heating rates in nitrogen (a) and air (b) atmospheres at 50 ml·min^{-1}

Since the repeatability of the results in an air atmosphere was found poor, a series of four tests were carried out using larger sample size with a heating rate of 10°C·min^{-1}. The samples are shown Figure 4.16, which were obtained by warming up the original EPS cells what led to increase its density.

Table 4.8. Peak properties of nitrogen and air DTG curves for EPS

Atmosphere	Heating rate /°C·min^{-1}	Peak value /°C^{-1}	Peak temperature /°C
Nitrogen	20	0.0247 ± 0.0005	433.5 ± 0.5
	10	0.0279 ± 0.0004	421 ± 1
	5	0.0271 ± 0.0017	404 ± 0
	2.5	0.0299 ± 0.0003	392 ± 0
Air	20	0.01754 ± 0.0031	387.5 ± 4.5
	10	0.0181 0.0161± 0.0004 (repeated tests)	385 374 ± 4
	5	0.0364 ± 0.0017	352.5 ± 11.5
	2.5	0.0172 ± 0.0015	343 ± 13

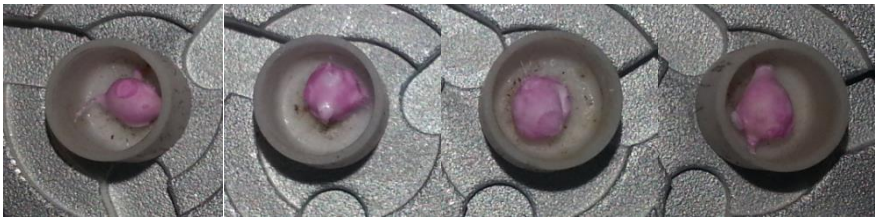

Figure 4.16. EPS samples with larger mass

Figure 4.17 presents the average TGA and DTG curves for the four repeated experiments, with error bars indicating the standard deviation. Good repeatability is observed and results are similar in shape to the ones presented in Figure 4.14b. Figure 4.17a shows the drop of all the mass is obtained in a step between 300°C and 400°C. However, Figure 4.17b shows two likely overlapping reactions of mass loss, despite only one peak is clearly identified at 374°C.

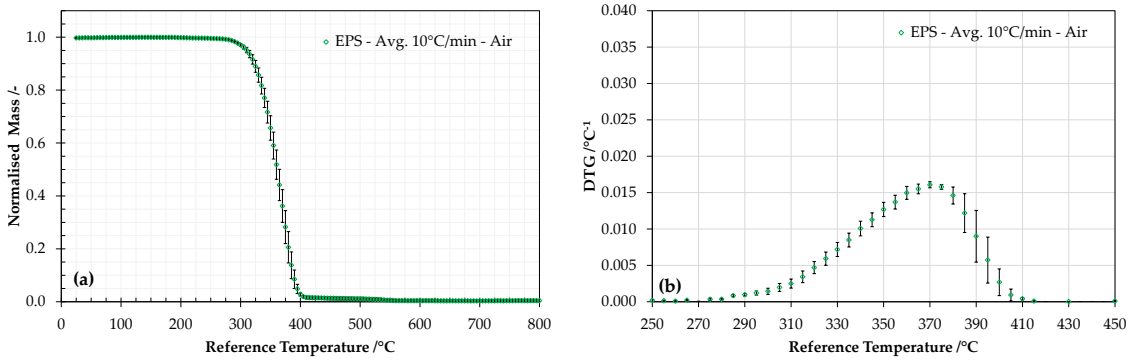

Figure 4.17. TGA (a) and DTG (b) curves at a heating rate of 10°C·min^{-1} in an air atmosphere at 50 ml·min^{-1} for four repeated tests of larger sample size (2.76 ± 0.22mg). Error bars: standard deviation obtained by the four repeats

4.5 Discussion of results

4.5.1 Effect of the heating rate

The peak properties height and temperature under nitrogen atmospheres are found for most of the cases to be larger and displace towards lower temperatures with lower heating rates. This is a common concept well-known in thermogravimetry, which lies on the different speed at which certain mass is consumed during its thermal degradation. The rate of mass loss experienced by a material during a thermal degradation reaction can be expressed by an Arrhenius' type expression:

$$\frac{d\alpha}{dt} = A \cdot \exp\left(-\frac{E_a}{RT}\right) \cdot f(\alpha) \qquad (4.2)$$

where $\frac{d\alpha}{dt}$ is the rate of mass loss (s^{-1}), A is the s the Arrhenius pre-exponential factor (s^{-1}) E_a is the activation energy (kJ·mol^{-1}), R is the universal gas constant (kJ·mol^{-1}·K^{-1}), T is the temperature and f(α) is the conversion function, which according to *Pérez-Maqueda et al.* [11] can be expressed as:

$$f(\alpha) = c \cdot (1-\alpha)^n \cdot \alpha^m \qquad (4.3)$$

It should be noted that Equation (4.2) provides the normalised rate of mass loss. If the total mass consumed by the reaction is Δm_0, the mass loss rate ($g \cdot s^{-1}$) can be calculated as:

$$\frac{dm}{dt} = \Delta m_0 \cdot \frac{d\alpha}{dt} \tag{4.4}$$

If the mass loss rate is expressed versus temperature (DTG curve) and it is assumed unicity of the parameters A, E_a, c, n and m that define the kinetics of the reaction, this can be expressed as follows:

$$\frac{d\alpha}{dT} = \frac{1}{dT/dt} \cdot A \cdot \exp\left(-\frac{E_a}{RT}\right) \cdot f(\alpha) \tag{4.5}$$

where dT/dt is the heating rate used for TGA experiments ($°C \cdot s^{-1}$).

According to Equation (4.5), smaller values of heating rate would be represented as larger values of the $\frac{d\alpha}{dT}$ curve for temperatures during the increase of mass loss rate, i.e. while $\frac{d\alpha}{dT}$ is increasing monotonically. Therefore, the peak of a $\frac{d\alpha}{dT}$ curve is expected to be displaced to lower temperatures and present larger magnitude with lower heating rates.

4.5.2 Effect of the atmospheric conditions

Differential thermogravimetric curves (DTG) obtained from tests in nitrogen atmospheres reveal the pyrolysis reactions that materials experience at the range of temperatures being studied. However, materials tested in air atmospheres tend to present a more complicated behaviour since pyrolysis and oxidation reactions may occur, sometimes simultaneously. DTG curves obtained for each material at a specific heating rate for both nitrogen and air atmosphere are studied herein.

A deconvolution technique [12] based on Fraser-Suzuki regression [9, 10] is used in order to identify the potential degradation reactions for each material. As noted by *Perejón et al.* [13], deconvolution techniques using F-S regressions can be used to evaluate complex thermal degradation processes, that later can be characterised by finding the respective kinetic parameters of each reaction, e.g. by using combined kinetics analysis [11, 14]. The use of F-S regression has been demonstrated to provide better fitting than classic approaches such as Lorentzian and Gaussian fittings due to the asymmetry of kinetic curves [13]. However, as noted in previous sections, the determination of kinetic parameters is out of the scope of this thesis. Therefore, the fitting functions presented below shall be interpreted as a mean to identify the effect of oxidative atmospheres in the pyrolysis of these materials. Peak properties from F-S regression can be found in Appendix C.

4.5.2.1 Stone wool (SW)

As shown in Figure 4.18a, stone wool presents a single reaction of pyrolysis in a nitrogen atmosphere, likely representative of the pyrolysis of binders or additives as noted in Chapter 2. Similar peak is presented in an air atmosphere at same range of temperatures, although of larger amplitude. This could indicate the tested sample in

air has larger mass of binder or the pyrolysis is enhanced in an oxidative atmosphere. Figure 4.18b shows two additional reactions, the former indicating the oxidation of the residue from previous pyrolysis and the latter indicating likely adhesion of the oxygen to the structure of the stone wool fibres.

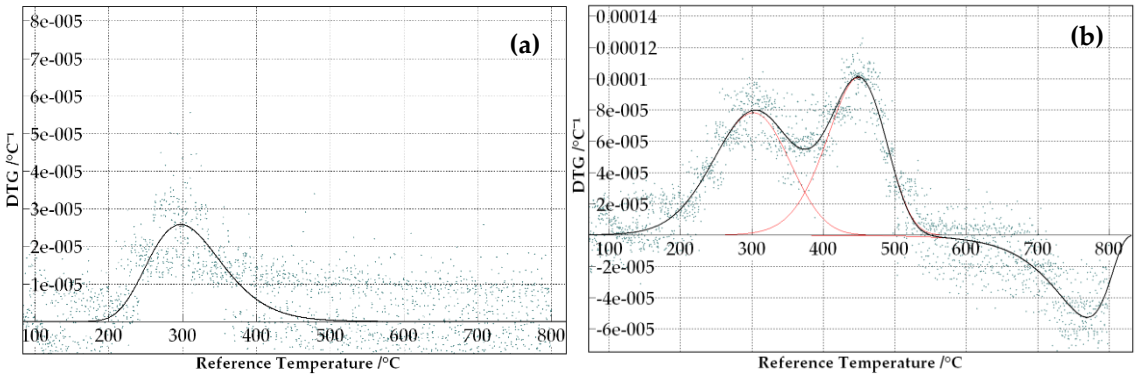

Figure 4.18. Fraser-Suzuki fitting for SW at 20°C·m^{-2} (a) N_2 (b) Air

4.5.2.2 Isocyanurate-based polyurethane foam (PIR)

Figure 4.19a shows that the pyrolysis of PIR is a complex process, potentially with at least six different reactions represented by the red F-S curves. As shown in Figure 4.19b, two first reactions seem to proceed in the same way in an oxidative atmosphere. As noted in Chapter 2, the former could correspond to the breakage of the urethane linkage, while the latter could be related to the isocyanurate linkage breakage. This is however difficult to assess due to the unknown chemistry of the specific products being studied. Third and fourth reactions are presented in the same range of temperatures in nitrogen and air, but with lower amplitude in air. This is indicative of the effect of the oxygen to these pyrolysis reactions. After 450°C, the thermal degradation processes look completely different in nitrogen and air, indicating that the residues from previous pyrolysis processes follow different paths. A series of light pyrolysis reactions are observed in a nitrogen atmosphere, while two strong oxidation reactions are inferred from the DTG shape in air.

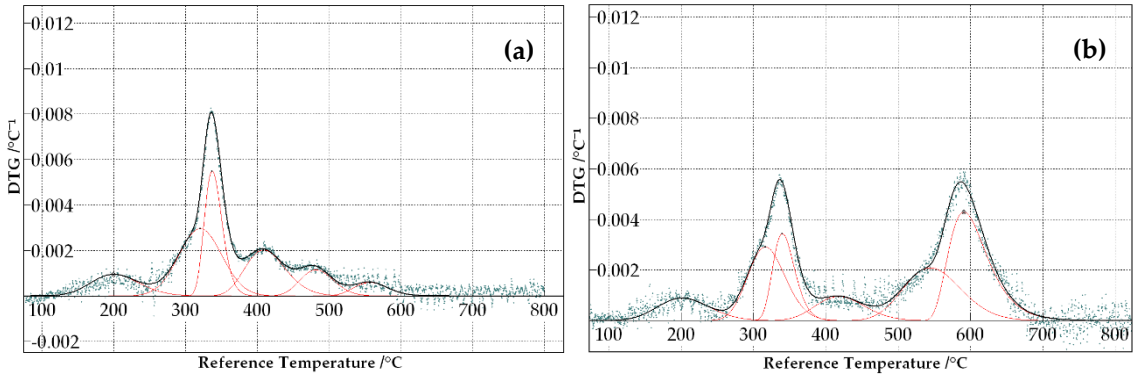

Figure 4.19. Fraser-Suzuki fitting for PIRa at 20°C·m^{-2} (a) N_2 (b) Air

Figure 4.9 showed that the peak around 300°C in air tends to reduce its amplitude with lower heating rates, contrarily to the usual mechanism explained in previous section. The third peak is found to change between nitrogen and air, indicating an effect on this pyrolysis reaction in an oxidative atmosphere. Despite the pyrolysis

process of PIR seems to be affected by oxygen, two clear domains of pyrolysis and oxidation are observed within different ranges of temperature.

4.5.2.3 Phenolic foam (PF)

Figure 4.20a shows that the pyrolysis of PF is also a complex process, potentially consisting of six reactions. Two first reactions are also found in an air atmosphere as shown in Figure 4.20b. Third reaction, which is the main pyrolysis reaction, is also observed in an air atmosphere, although its amplitude is larger than in nitrogen. The pyrolysis reactions found in nitrogen present lower amplitude from 450°C. This contrasts with the oxidation reactions observed in air after 450°C, being significantly larger than the main pyrolysis peak at 350°C and 450°C. As opposed to PIR, the main pyrolysis and oxidation domain are found to appear in a close range of temperatures.

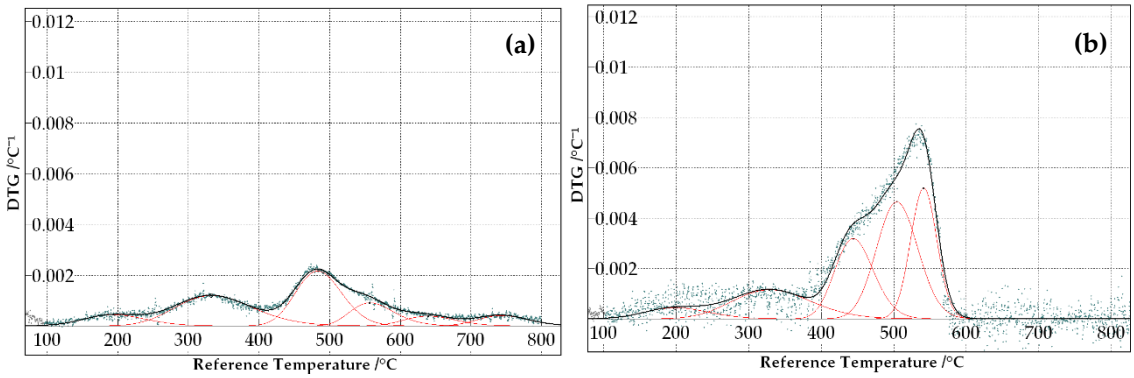

Figure 4.20. Fraser-Suzuki fitting for PF at 20°C·m^{-2} (a) N_2 (b) Air

4.5.2.4 Expanded polystyrene (EPS)

Figure 4.21a shows that the pyrolysis of EPS without oxidants proceeds as a single reaction. Thermal degradation of EPS in air is found to present different behaviour, with the onset of pyrolysis clearly displaced to lower temperatures. Additionally, Figure 4.21b shows that the process of degradation does not occur as a single reaction, but likely as two or more different mechanisms.

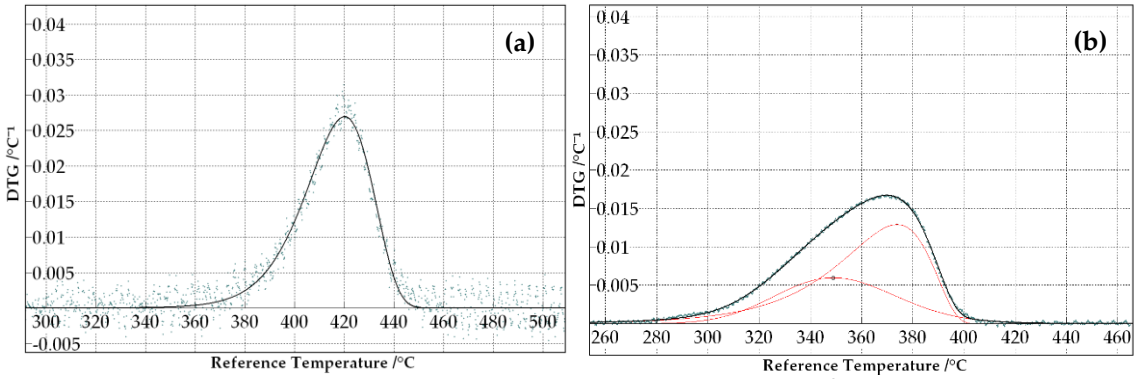

Figure 4.21. Fraser-Suzuki fitting for EPS at 20°C·m^{-2} (a) N_2 (b) Air

4.5.3 Material properties for the design methodology

As noted in Chapter 3, the proposed methodology for the design of insulation systems in buildings requires the definition of a series of material properties in relation to the insulation product. The most relevant parameter is the critical temperature, which is intended to represent the real hazard from these materials, i.e. the onset of thermal degradation with large release of combustible gases from the solid material.

Experimental work presented in this chapter provides fundamental understanding of the thermal degradation processes, pyrolysis and oxidation, of the main insulation materials. Therefore, the results presented above provide crucial information with regard to the definition of the critical temperature. However, the rigorous definition of this parameter lies on the flammability concept of flashpoint, i.e. the temperature of the solid surface at which sufficient amount of volatiles are generated and reach the lower flammability limit [15]. It should be noted that despite the firepoint is normally used for assessing the flammability of solids, i.e. temperature at which flaming at the surface is self-sustained, the hazard lies on the availability of pyrolysates to combust. Indeed, as demonstrated in previous chapter, contribution to the HRR of a fire does not necessarily require pyrolysates to combust at the surface of the insulation product.

Instinctively it could be inferred that the critical temperature corresponds to the temperature at which highest rates of pyrolysates are released, i.e. the temperature of the first main DTG peak. Nevertheless, this information cannot easily be extrapolated from TGA-DTG data; therefore, a flammability study is required to prove this assumption, which is discussed in Chapter 5.

4.6 Concluding remarks

Identification of pyrolysis and oxidation reactions for SW, EPS, PF and three types of PIR is presented. Thermogravimetric experiments are carried out under different heating rates and two atmospheric conditions, nitrogen and air.

Results indicate that organic compound from SW are below 2% of the total mass. Thermal degradation of these compounds proceeds as a single pyrolysis reaction between 200°C and 350°C in the absence of oxygen. Two additional reactions are observed if oxygen is available, first oxidation between 350°C and 550°C and later crystallisation from 600°C approximately.

Results from four different PIR foams indicate qualitatively similar results among them, mainly varying the rate of mass loss during pyrolysis. PIR achieves an approximate mass loss of 75-80% up to 800°C in a nitrogen atmosphere. Pyrolysis under an oxidative atmosphere is observed in the same range of temperatures, but appears to be more moderate in air. Oxidation processes appear from 500°C to 650°C. Pyrolysis and oxidation domains are clearly presented in two different regions of temperature.

PF achieves an approximate mass loss of 55% up to 800°C in a nitrogen atmosphere. Pyrolysis behaviour seems not to change drastically in an oxidative atmosphere up to 450°C. In comparison to PIR, PF rates of mass loss due to pyrolysis are clearly more moderate. Oxidation processes appear from 450°C, overlapping with the main peak of pyrolysis. Approximately all mass gets consumed once reached 600°C.

Results from EPS are in agreement with the classic literature on polystyrene thermal degradation. Pyrolysis in a nitrogen atmosphere is observed as a single reaction between 350°C and 450°C. Oxidative atmospheres accelerate the pyrolysis, displacing it towards lower temperatures, 280°C-400°C. Mechanism of thermal degradation appears to consist of more than a single reaction.

Differential thermogravimetry analyses reveal high level of complexity in relation to the different mechanisms of thermal degradation from PIR and PF. On the contrary, SW and EPS presented simpler mechanisms of thermal degradation.

Future work is required for the full characterisation of the thermal degradation of insulation materials. Further experimental steps to this full characterisation comprise the use of different oxygen concentrations in the atmosphere and advanced gas analyses on the generated pyrolysates. Determination of kinetic parameters requires the verification under different heating rates of the reactions obtained by deconvolution techniques.

Definition of the critical temperature from insulation materials for the design methodology proposed in Chapter 3 requires a flammability assessment, which is presented in next chapter. Mapping of the thermal degradation processes presented in this chapter is essential for validating the hypothesis of using the main peak temperature of pyrolysis as critical temperature.

4.7 References

[1] D. Drysdale, "Fire Science and Combustion," in *An Introduction to Fire Dynamics*, John Wiley & Sons, Ltd, 2011, pp. 1–34.

[2] G. Rein, "Smouldering Combustion Phenomena in Science and Technology," *International Review of Chemical Engineering*, vol. 1, pp. 3–18, 2009.

[3] R. Aseeva, B. Serkov, and A. Sivenkov, *Fire Behavior and Fire Protection in Timber Buildings*. Dordrecht: Springer Netherlands, 2014.

[4] E. Bar-Ziv and I. I. Kantorovich, "Mutual effects of porosity and reactivity in char oxidation," *Progress in Energy and Combustion Science*, vol. 27, no. 6, pp. 667–697, Jan. 2001.

[5] P. Gabbot, *Principles and Applications of Thermal Analysis*. Blackwell Publishing Ltd., 2008, p. 484.

[6] M. J. O'Neill, "Measurement of Specific Heat Functions by Differential Scanning Calorimetry.," *Analytical Chemistry*, vol. 38, pp. 1331–1336, 1966.

[7] W. S. Cleveland, S. J. Devlin, and S. Cleveland, "Locally Weighted Regression: An Approach to Regression Analysis by Local Fitting," *Journal of the American Statistical Association*, vol. 83, no. 403, pp. 596–610, 1988.

[8] W. S. Cleveland, "Robust Locally Weighted Regression and Smoothing Scatterplots," *Journal of the American Statistical Association*, vol. 74, no. 368, pp. 829–836, 1979.

[9] R. D. B. Fraser and E. Suzuki, "No Title," *Analytical Chemistry*, vol. 41, p. 37, 1969.

[10] R. D. B. Fraser and E. Suzuki, "No Title," *Analytical Chemistry*, vol. 38, p. 1770, 1966.

[11] L. A. Pérez-Maqueda, J. M. Criado, and P. E. Sanchez-Jiménez, "Combined kinetic analysis of solid-state reactions: a powerful tool for the simultaneous determination of kinetic parameters and the kinetic model without previous assumptions on the reaction mechanism.," *The journal of physical chemistry. A*, vol. 110, no. 45, pp. 12456–62, Nov. 2006.

[12] M. Wojdyr, "Fityk: a general-purpose peak fitting program," *Journal of Applied Crystallography*, vol. 43, no. 5, pp. 1126–1128, Sep. 2010.

[13] A. Perejón, P. E. Sánchez-Jiménez, J. M. Criado, and L. a Pérez-Maqueda, "Kinetic analysis of complex solid-state reactions. A new deconvolution procedure.," *The journal of physical chemistry. B*, vol. 115, no. 8, pp. 1780–91, Mar. 2011.

[14] P. E. Sánchez-Jiménez, L. a. Pérez-Maqueda, a. Perejón, and J. M. Criado, "Combined kinetic analysis of thermal degradation of polymeric materials under any thermal pathway," *Polymer Degradation and Stability*, vol. 94, no. 11, pp. 2079–2085, Nov. 2009.

[15] D. Drysdale, "Ignition: The Initiation of Flaming Combustion," in *An Introduction to Fire Dynamics*, John Wiley & Sons, Ltd, 2011, pp. 225–275.

[16] R. J. Crewe, J. P. Hidalgo, M. X. Sørensen, S. Molyneus, M. McLaggan, G. Joomas, S. Welch, J. L. Torero, A. A. Stec, and T. R. Hull, "Fire performance of sandwich panels in a modified ISO 13784-1 small room test: the effect of damage and increased fire load," *Fire Technology (submitted)*.

Chapter 5.

Fire Performance of Insulation Materials in Bench-Scale Testing: A Qualitative Approach

5.1 Introduction

As noted in Chapter 2, the study of material performance under fire conditions can be assessed by using several standard tests, so comparison exercises and classification can be performed. However, the material behaviour observed during the experiment is intrinsically linked to the test nature. Extrapolation of results to different conditions tends to be complex, and unexpected behaviour can be observed in real conditions if standard test results are blindly used as guideline for design. Therefore, it is very important to understand the phenomena behind the nature of a fire test and its coupled behaviour to the tested material. This can only be achieved if the material performance is understood from first principles.

The Cone Calorimeter [1] and equivalent FM Global Fire Propagation Apparatus (FPA) [2] are typical tests used to understand the performance of materials from first principles. Flammability and combustibility of solid materials can be assessed by using these apparatuses, based on classical theories of ignition and calorimetry of solids. Additionally, information from burning dynamics and material properties such as thermal inertia and effective heat of combustion can be evaluated.

In the present chapter, a classical approach for characterising the flammability and combustibility of materials is used to study the fire behaviour of the insulation materials selected for this thesis. The approach is mainly based on the use of the Cone Calorimeter. Furthermore, the effect of the coatings for foamy materials is studied. The information obtained from these experiments shall be interpreted sensibly, and as noted before, extrapolation of results must be done carefully.

As a final remark, estimated ignition temperatures are compared to thermogravimetric analyses. A series of critical temperature values related to each of the studied materials are proposed for the design methodology introduced in Chapter 3.

5.2 Aim

The aim of this chapter is to assess the flammability and combustibility from insulation materials by using classic analysis methods. A particular interest is focused on the determination of the critical temperature on the basis of the flammability assessment and correlation to thermogravimetric analyses. A summary of the goals pursued in this chapter is presented below:

- Qualitative assessment of the material performance under several conditions of heat exposure.
- Determination of critical heat flux and ignition temperature.
- Assessment of the thermal properties based on a flammability assessment.
- Determination of combustibility (HRR) and effective heat of combustion.
- Assessment of the different regimes of burning by analyses based on calorimetry, gas species correlations and mass loss.

5.3 Methodology

5.3.1 Experimental set-up

The materials selected for these experiments are stone wool (SW), expanded polystyrene (EPS), rigid phenolic foam (PF) and three types of rigid isocyanurate-based foams (PIR) from different manufacturers. Samples are prepared with dimensions of nominal surface area 0.090 m x 0.090 m and thickness 100 mm. The ideal dimensions for bench-scale testing using the Cone Calorimeter, or similar type of instrument, have been determined to be 0.1 m x 0.1 m as noted in the experimental methods review presented in Appendix A, which are nominal dimensions for this type of standard tests. Slightly narrower samples are prepared since additional tests using the FPA are performed in a parallel project focused on the smouldering behaviour of PIR foams [3]. Standard dimensions in the FPA did not allow achieving mass loss measurements due to the combustion chamber size and sample holder set-up. Thickness is selected to represent real end-use conditions of insulation products in construction. As noted in Appendix A, the thickness might have an effect on the time-to-ignition. However, this is not expected to be significant for materials of low thermal inertia and thermal diffusivity such as the studied ones. This was analytically demonstrated in Chapter 3. Additionally, 50 mm thick samples of EPS are tested in order to correlate the shrinking effect and explore the time-to-ignition versus heat flux plots of this material.

Samples are wrapped in aluminium foil, leaving only the top surface exposed, and then wrapped by two layers of ceramic paper at sides and bottom. The aluminium foil is used to prevent gas flow leaving or getting in the sample from the sides. This has an important effect if the behaviour observed during these tests is to be extrapolated to real conditions. Indeed, oxygen diffusion through the sides of the sample can significantly affect the rate of oxidation of the material, which is not expected to occur if larger sizes are exposed to heat. Additionally, it is ideal to keep one-dimensional conditions from a heat transfer perspective. This is normally achieved by adding a more insulating material on the sides of the sample. However, this is an impossible task for the present work, since the tested materials are less conductive than the insulation material typically used as holder in Edinburgh's fire laboratory, i.e. ceramic paper. Nevertheless, two layers of 3 mm thickness are used since melting behaviour is expected from one of the studied materials and same testing conditions are preferred for comparison purposes. This sample set-up is presented in Figure 5.1 below.

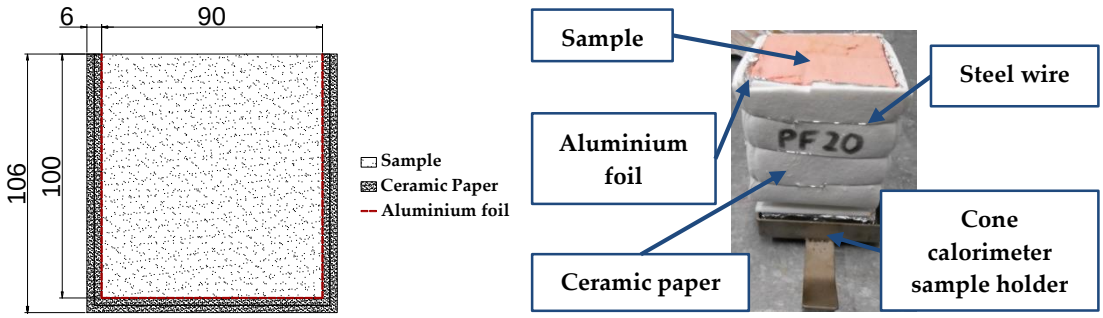

Figure 5.1. Sample preparation for flammability and combustibility tests (Dimension units in millimetres)

Materials such as PIR and PF are normally distributed with a protective layer on the surface. This is expected to have some impact in the observed performance during the tests. In order to correlate this, samples with and without protective layer on the surface are used for studying both flammability and combustibility. A summary of the different test configurations is presented in Table 5.1. Material samples without protective layer and prior to being prepared for testing are shown in Figure 5.2 below.

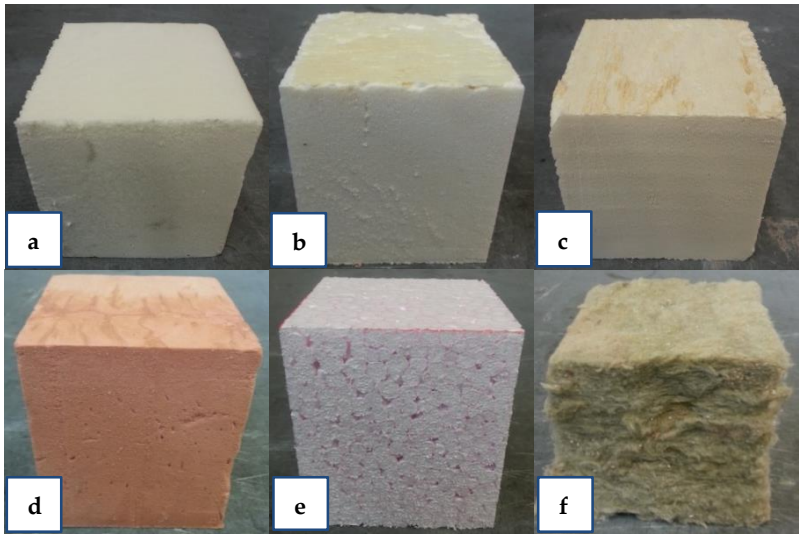

Figure 5.2. Samples of tested insulation materials. (a) PIR.a (b) PIR.b (c) PIR.c (d) PF (e) EPS (f) SW

As shown in Figure 5.1, the used sample orientation is horizontal. Despite this is expected to introduce larger uncertainty in the evaluation of convection, this orientation is found to be more suitable due to the melting behaviour of EPS.

Figure 5.3 below shows the Cone Calorimeter apparatus used for the performed experiments at the University of Edinburgh. The spark igniter has been used for all the experiments.

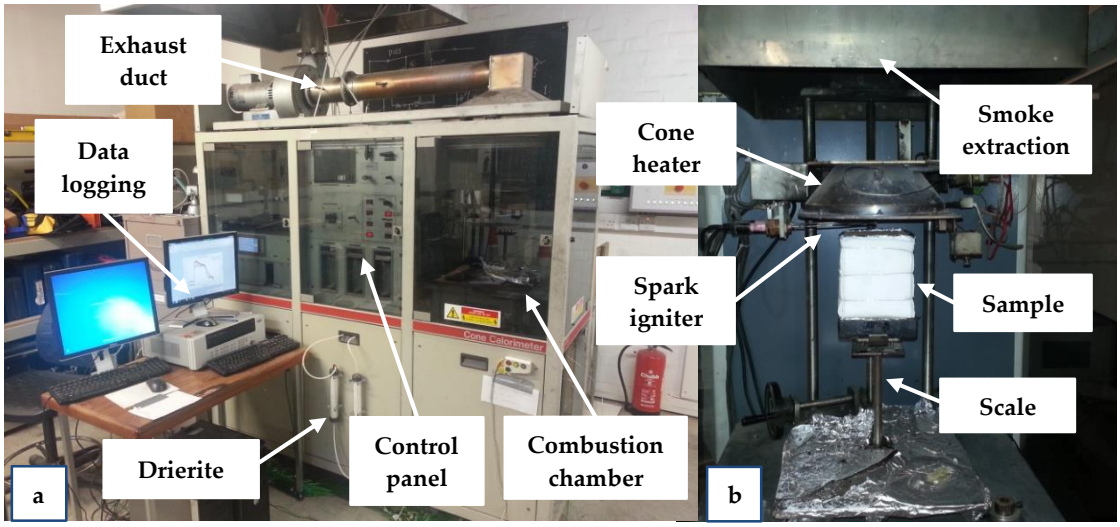

Figure 5.3. (a) Cone calorimeter apparatus. (b) Combustion chamber

Table 5.1. Summary of test conditions

Material	Configuration	Incident radiative heat flux range /kW·m^{-2}	Measured parameters
PIRa PIRb PIRc PF	**Nominal sample size:** 90 mm x 90 mm x 100 mm **Exposed surface:** (a) With protective layer (b) Without protective layer **Wrapping:** 2 layers of ceramic paper + 1 layer of foil **Back boundary condition:** Ceramic board (25 mm) **Orientation:** Horizontal	From CHF to 65 (2 repetitions)	(1) Time to ignition (2) O_2, CO_2 and CO gas species (3) Mass loss
EPS	**Nominal sample size:** (a) 90 mm x 90 mm x 100 mm (b) 90 mm x 90 mm x 50 mm **Exposed surface:** No protective layer **Wrapping:** 2 layers of ceramic paper + 1 layer of foil **Back boundary condition:** Ceramic board (25 mm) **Orientation:** Horizontal		
SW	**Nominal sample size:** 90 mm x 90 mm x 100 mm **Rest of the configuration as EPS**	Up to 88	

5.3.2 Method for the flammability assessment

The classic approach for assessing flammability parameters for solid media is based on a heat transfer analysis for the infinite plate. This has been largely studied by many authors, and a brief of which is detailed by *Janssens et al.* [4]. The particular solution used hereby is noted by *Long et al.* [5]. The temperature of pyrolysis can be obtained by Equation (5.1) below, which corresponds to the exact solution for the surface temperature evolution of the infinite plate when exposed to a constant radiant heat flux:

$$T_P - T_\infty = \frac{\alpha \cdot \dot{q}_e''}{h_T} \cdot \left[1 - e^{t_P/t_c} \cdot \mathrm{erfc}\left(\left(\frac{t_P}{t_c}\right)^{1/2}\right)\right] \tag{5.1}$$

where T_P is the pyrolysis temperature, T_∞ is the ambient temperature, α is the absorptivity of the exposed surface, $\dot{q}_e''$ is the external radiant heat flux, h_T is the global heat transfer coefficient of losses, t_P is the time to achieve the pyrolysis temperature and t_c is the characteristic time defined as a function of the thermal inertia $k\rho c$, erfc is the complementary Gaussian error function and the global heat transfer coefficient of losses h_T:

$$t_c = \frac{k\rho c}{(h_T)^2} \tag{5.2}$$

If a first-order Taylor series expansion is applied to Equation (5.1), two simplified equations can be obtained for different domains. In first domain it is assumed that the pyrolysis time is much smaller than the characteristic time ($t_p/t_c \to 0$), therefore the external heat flux is proportional to the inverse square root of the pyrolysis time as noted in Equation (5.3) below:

$$t_P^{-\frac{1}{2}} = \frac{2}{\sqrt{\pi}} \cdot \frac{\alpha}{\sqrt{k\rho c}} \cdot \frac{\dot{q}_e''}{(T_P - T_\infty)} \tag{5.3}$$

Otherwise, if the characteristic time is much smaller than the pyrolysis time ($t_p/t_c \to \infty$), the expression includes the global heat transfer coefficient for heat losses term h_T, and is defined as follows:

$$t_P^{-\frac{1}{2}} = \frac{\sqrt{\pi} \cdot h_T}{\sqrt{k\rho c}} \cdot \left[1 - \frac{h_T \cdot (T_P - T_\infty)}{\alpha \cdot \dot{q}_e''}\right] \tag{5.4}$$

In general, Equation (5.3) is commonly applied for high values of incident heat flux, while Equation (5.4) should be used for low values. Further discussion on the range of validity of these expressions is presented in the discussion section of this chapter.

A regression analysis is commonly used in order to determine the thermal inertia of the material by using Equations (5.3) and (5.4). This quantification of thermal inertia should be interpreted carefully, as it is assumed to be constant with temperature and the formulation assumes the material remains inert until the pyrolysis temperature is achieved. Additionally, determination of the thermal inertia requires quantification of the absorptivity and the temperature of pyrolysis if

Equation (5.3) is used, and additionally the global heat transfer coefficient of heat losses if Equation (5.4) is used.

The ignition temperature, here assumed to be the pyrolysis temperature since the mixing period and the induction time are assumed to be negligible, sometimes can be measured if a thermocouple is positioned close to the surface. This is however a tricky task that unfortunately may not be applied for any material. This is the case of the studied materials due to several reasons such as:

- brittle nature of the foams,
- large thermal gradient expected at the surface due to low conductivity,
- slower response from thermocouples in comparison to the rate of temperature variation of the surface temperate, and
- expected heat losses through the thermocouple inserted in an insulated medium.

If temperature measurements are not feasible, the ignition temperature can be calculated assuming the quasi steady-state is achieved for the heat balance at the surface. For this case, the heat losses through the thickness of the material $\dot{q}''_{net}$ can be neglected, i.e:

$$\dot{q}''_{net} = -k \cdot \frac{\delta T}{\delta x} = 0 \tag{5.5}$$

where k is the conductivity of the material and $\frac{\delta T}{\delta x}$ is the thermal gradient at the surface. Then, the heat balance at the surface can be expressed as:

$$\alpha \cdot \dot{q}''_{cr} - h_c \cdot \left(T_{ig} - T_\infty\right) - \varepsilon \cdot \sigma \cdot \left(T_{ig}^4 - T_\infty^4\right) = -k \cdot \frac{\delta T}{\delta x} = 0 \tag{5.6}$$

where h_c is the convective heat transfer coefficient, ε is the emissivity of the surface, σ is the constant of Stefan–Boltzmann constant, T_{ig} is the temperature of the surface at the time of ignition. A simplified expression can be obtained if the heat losses are lumped into a single variable, previously introduced as global heat transfer coefficient of losses and defined as follows:

$$h_T = h_c + h_r = h_c + \varepsilon \cdot \sigma \cdot \frac{\left(T_{ig}^4 - T_\infty^4\right)}{\left(T_{ig} - T_\infty\right)} = h_c + \varepsilon \cdot \sigma \cdot \left(T_{ig}^2 + T_\infty^2\right) \cdot \left(T_{ig} + T_\infty\right) \tag{5.7}$$

The ignition temperature can be calculated quantifying the value of the convective heat transfer coefficient, the emissivity and absorptivity, and solving Equation (5.6). Therefore, the expression to calculate the ignition temperature can be written as follows:

$$T_{ig} = T_\infty + \frac{\alpha \cdot \dot{q}''_{cr}}{h_T} \tag{5.8}$$

Estimated values for the convective, radiative and global heat transfer coefficient up to 450°C are presented in Figure 5.4. The definition of the convective heat transfer coefficient is based on the estimation of the Nusselt number for a horizontal plate [6], as noted in Equations (5.9) and (5.10):

$$\overline{Nu}_L = 0.54 \cdot Ra_L^{1/4} \tag{5.9}$$

$$\overline{Nu}_L = \frac{h_c \cdot L}{k} \tag{5.10}$$

with k the fluid conductivity and Ra_L the Rayleigh number, defined as a function of the gravity acceleration g, the inverse of the film temperature β, the surface temperature T_s, the fluid temperature T_∞, the characteristic length L, the fluid kinematic viscosity υ and thermal diffusivity α:

$$Ra_L = \frac{g \cdot \beta \cdot (T_s - T_\infty) \cdot L^3}{\upsilon \cdot \alpha} \tag{5.11}$$

Figure 5.4 shows that the global heat transfer coefficient is very linear for the selected range of temperatures, so a linear regression could be used for its definition. It should be noted that the main uncertainty lies on the right quantification of the convective coefficient. However, it is crucial to provide a set of values for ignition temperature that, although arbitrary, are comparable and are in the correct order of magnitude. Comparison between these values and results from thermogravimetric analyses is presented in the following sections.

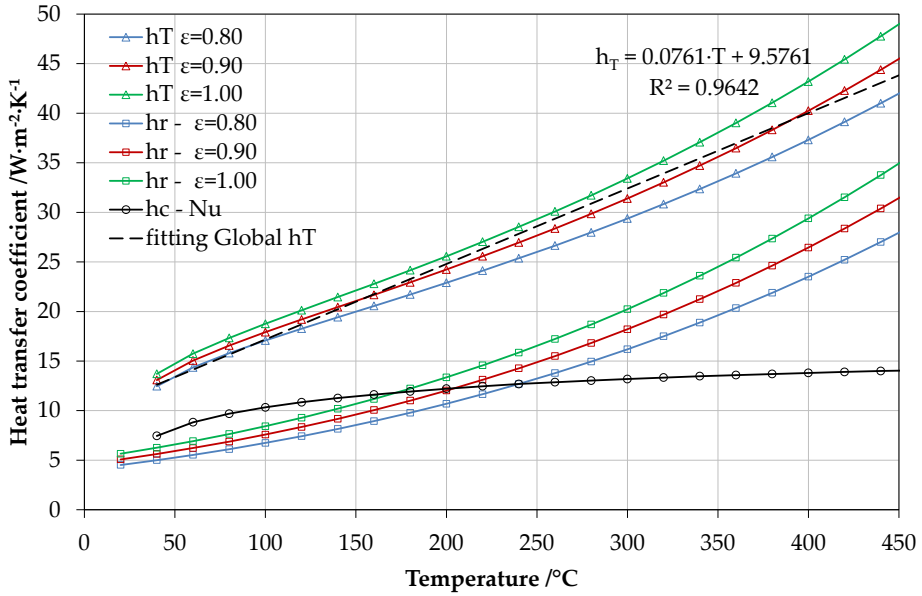

Figure 5.4. Estimation of global, radiative and convective heat transfer. Linear regression for the global heat transfer coefficient

5.3.3 Method for the combustibility assessment

Several calorimetry methods for the estimation of heat release from materials can be found in the literature. The most common methods have been largely described and analysed by *Biteau* [7]. Despite the large amount of methods compared by *Biteau*, feasible approaches to be followed are the species evolution and mass loss approach if an instrument such as the Cone Calorimeter is used. Since an in-depth review on these two approaches can be found in Appendix A, only a brief discussion justifying the followed methodology is provided below.

Mass loss calorimetry is an approach that relies on the accurate measurement of mass during the experiment and the definition of the effective heat of combustion of the studied material. This is a suitable approach if the used materials correspond to typical materials which calorimetry has been largely studied. Nevertheless, the studied materials are known to have largely been subjected to optimisation processes in order to achieve reduced flammability and combustibility. As noted in Chapter 2, this is normally accomplished by altering the composition of the polymer or adding flame retardants. Therefore, despite values of heat of combustion have been identified in the literature (noted in Appendix B), this approach is not followed due to large uncertainty on the chemistry of these compounds.

The species approach considers two potential methods to measure heat release rate, which are based on oxygen consumption (OC) [8] and carbon dioxide generation (CDG) [9] calorimetry. Oxygen consumption rather than carbon dioxide generation calorimetry is used to correlate the heat release rate of the experiments due to two main reasons:

- The filtering and desiccation system of the gas analysers is based on calcium sulphate, material commercially known as *drierite*®. Calibration experiments show that *drierite*® tends to absorb carbon dioxide when anhydrous, and therefore affect the shape of the measured curve of carbon dioxide. This effect is much more significant when test time scales are short. As a result of this, peaks are shifted and smoothed, leading to incorrect values of heat release rate if CDG is used.
- Variability of energy coefficients for CDG tends to be larger than OC. If the chemistry of the materials being tested is unknown, CDG would lead to larger error bars in the estimation of heat release rate.

Then, the formulation considered for the experiments corresponds to OC calorimetry, noted in Equation (5.12) below, which was originally proposed by *Janssens* [10]. This expression takes into account a correction to HRR due to inefficiency in the combustion, with generation of carbon monoxide:

$$\mathrm{HRR}^{\mathrm{OC}} = \left(\mathrm{E}_{\mathrm{O}_2} \cdot \phi - \left(\mathrm{E}_{\mathrm{CO}\rightarrow\mathrm{CO}_2} - \mathrm{E}_{\mathrm{O}_2}\right) \cdot \frac{1-\phi}{2} \cdot \frac{\mathrm{X}_{\mathrm{CO}}}{\mathrm{X}_{\mathrm{O2}}}\right) \cdot \frac{\dot{\mathrm{m}}_{\mathrm{e}}}{1+\phi\cdot(\alpha-1)} \cdot \frac{\mathrm{M}_{\mathrm{O}_2}}{\mathrm{M}_{\mathrm{air}}} \cdot \mathrm{X}_{\mathrm{O}_2}^{0} \qquad (5.12)$$

where $\mathrm{E}_{\mathrm{O}_2}$ is the energy released per mass unit of oxygen consumed, $\mathrm{E}_{\mathrm{CO}_2\rightarrow\mathrm{CO}_2}$ is the energy released per mass unit of oxygen consumed for the combustion of carbon

monoxide, $\dot{m}_e$ is the mass flow in the exhaust, α is the volumetric expansion factor, M_{O_2} and M_{air} are the molecular weight of oxygen and air respectively, and ø is the oxygen depletion factor defined as:

$$ø = \frac{X_{O_2}^0 \cdot (1 - X_{CO_2} - X_{CO}) - X_{O_2} \cdot (1 - X_{CO_2}^0)}{(1 - X_{O_2} - X_{CO_2} - X_{CO}) \cdot X_{O_2}^0} \tag{5.13}$$

with $X_{O_2}^0$ and $X_{CO_2}^0$ the measured concentration of oxygen and carbon dioxide before the start of the test, X_{O_2} the measured concentration of oxygen, X_{CO_2} the measured concentration of carbon dioxide and X_{CO} the measured concentration of carbon monoxide.

Further information on the derivation of Equation (5.12), and estimation of the parameter mass flow $\dot{m}_e$ can be found in Appendix A.

5.4 Results

5.4.1 Summary of results

A summary of the experimental data from flammability and combustibility tests is presented in Appendix C. Detailed results are presented and discussed in the following sections. It should be noted that PIR results in terms of HRR, mass loss and gas species is only presented for one type of PIR in following sections, since results are qualitatively and quantitatively similar. These are included in Appendix C as well.

5.4.2 Visual observations

The three types of PIR are found to behave similarly, with a very fast ignition for every external heat flux larger than the critical. This is followed by a small flame which continues to be reduced until the flame is only observed by the edges of the sample. PIR tends to expand slightly at early stages of the heat exposure. After flaming, a black char layer remains which tends to glow if the external heat flux is high. The char continues to get consumed by oxidation and its thickness starts to reduce at different rate, depending on the external heat flux. Flaming at edges is sporadically observed. Figure 5.5 shows a summary of the remains from PIRa samples tested under different heat exposures and different boundary conditions at the surface, as noted in Table 5.1. The remaining char from PIR is very soft and light. Discoloration of the PIR samples is observed, changing from yellow to orange-brown and finally black colour during the process of thermal degradation. Additionally, it is shown that the effectivity of the protective layer at surface is overcome for external heat fluxes higher than 35 kW·m^{-2}. This result is found to be similar for PIRb and PIRc. As it is presented in following sections and can be observed in Figure 5.5, the presence of the protective layer at high heat fluxes is negligible.

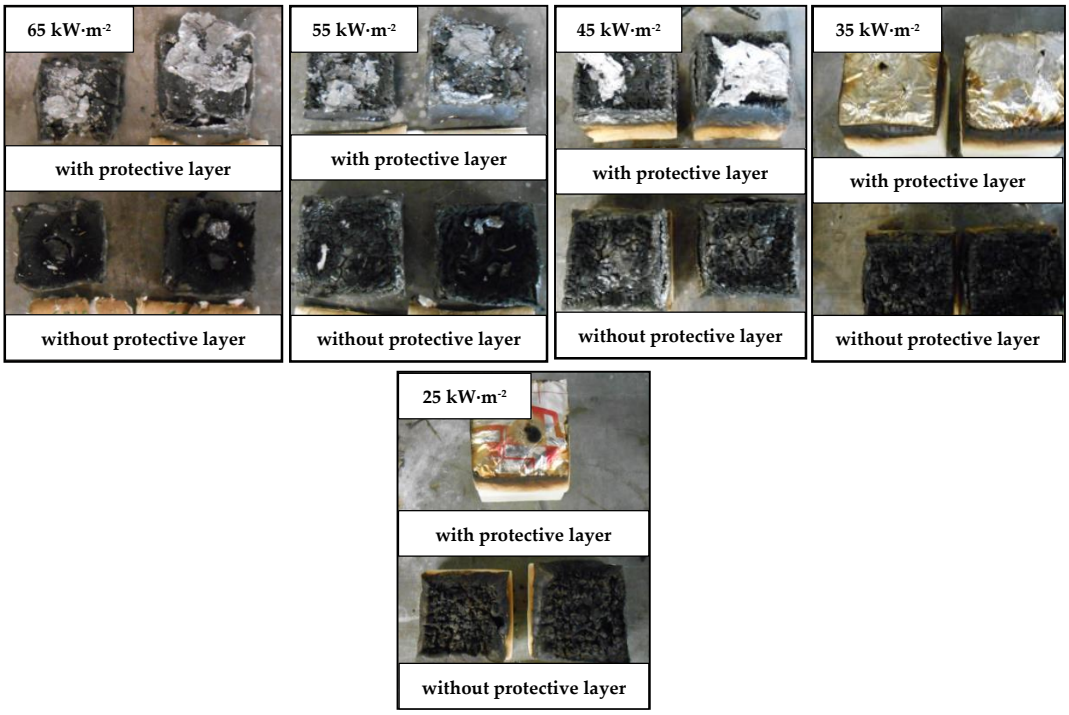

Figure 5.5. PIRa samples after exposure of 1500-2000 seconds. Top samples: foil layer at the surface. Bottom samples: no foil layer at the surface

Phenolic foam is found to have a similar behaviour to PIR, proceeding to char formation after flaming and to smoulder after flame out at the surface. However, as it is described in further sections, the critical heat flux for ignition is larger than PIR but its regression after ignition is much faster. Additionally, the protective layer at surface is found to be less effective than the ones attached on PIR surfaces, and to present higher thermal degradation. PF tends to spall and crack very easily during heat exposure and presents a more brittle behaviour. Popping and snapping sounds can be heard during testing. Discoloration is observed, changing from pink-brown to yellow and finally black colour during the process of thermal degradation. This is correlated in Chapter 6.

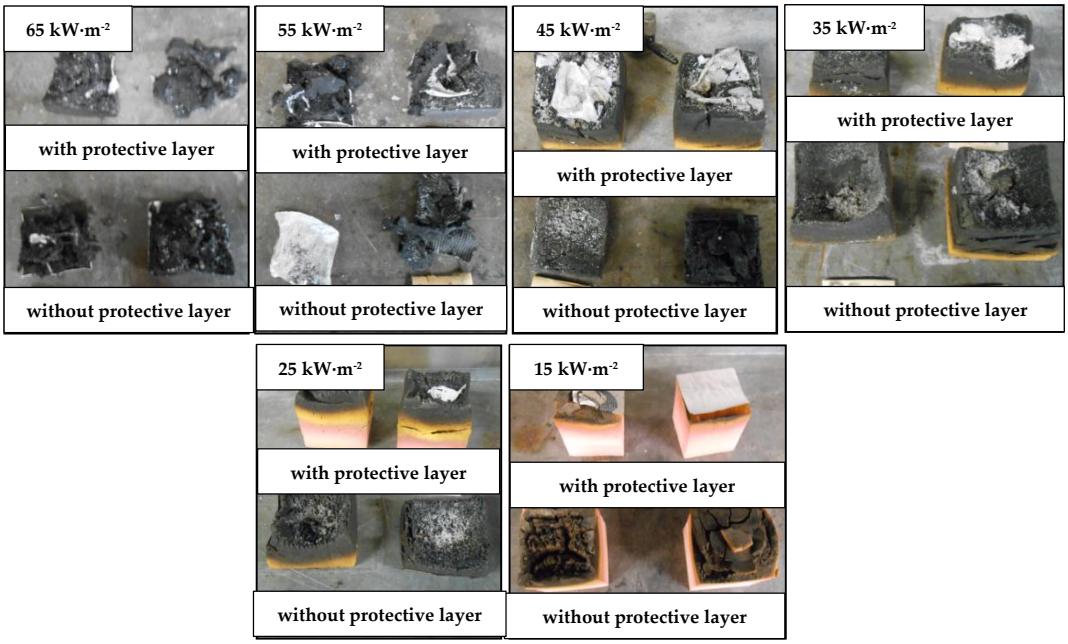

Figure 5.6. PF samples after exposure of 1500-2000 seconds. Top samples: foil layer at the surface. Bottom samples: no foil layer at the surface

Expanded PS presented a much different behaviour than PIR and PF. Shrinking is observed right after being exposed to radiation from the Cone and its density is increased. The cells of polystyrene that form the expanded foam start contracting, followed by reduction of the thickness of the foam. This transition is presented in Figure 5.7a. After complete regression, the sample melts and becomes a viscous fluid. An example of the residue after melting is presented in Figure 5.7b. This residue continues to volatilise and suddenly ignites after melting. The burning of EPS produces a sooty and larger flame than the one observed for PIR or PF.

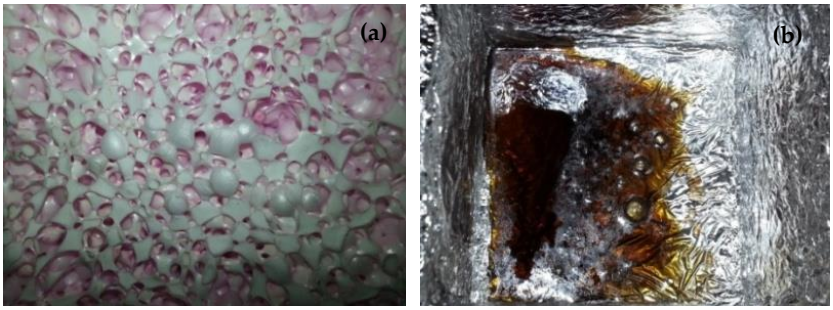

Figure 5.7. EPS residues: (a) Heat flux < 4 kW·m^{-2} (b) 10 kW·m^{-2}

SW was tested up to 88 kW·m^{-2} and no ignition was observed. Different grades of discoloration were observed, indicating a series of thermal degradation processes. This is consistent with the results presented in the previous chapter. However, further analysis is presented in Chapter 6, correlated to temperature measurements within the solid media.

5.4.3 Critical heat flux and time-to-ignition regressions

Table 5.2 shows the values of critical heat flux (CHF) below which the different insulation materials do not proceed to ignite with the horizontal set-up in the Cone Calorimeter. The three types of PIR show different values of critical heat flux, with PIRa being the most prone to ignite with a CHF of 10 kW·m^{-2}, while PIRb and PIRc show higher CHF of 12 and 15 kW·m^{-2} respectively. PF shows the highest CHF for the plastic foams, with a CHF of 22 kW·m^{-2}. Stone wool did not ignite at any tested heat flux.

However, EPS requires a special consideration. Since EPS tends to shrink rapidly once exposed to radiation from the Cone, actual values of CHF do not strictly correspond to the nominal flux at which the samples are initially exposed. No ignition was achieved before complete shrinkage of the sample for any of the studied cases. CHF values of 16 and 15 kW·m^{-2} were obtained assuming the external heat flux does not reduce at lower positions. Measurements of heat flux at lower positions, closer to the bottom of the sample, indicate that these tend to reduce approximately 35% and 64% for positions 50 mm and 100 mm lower. This would indicate the actual CHF is 6 kW·m^{-2} and 9-10 kW·m^{-2} for 100 and 50 mm thick EPS, but this is unreliable and would lead to inconsistent values of ignition temperature if the followed methodology is the one indicated in the previous section. Indeed, many mechanisms normally not considered for the ignition theory such as pre-heating followed by shrinking or different and more complex mechanisms of cooling are here present.

Table 5.2. Critical heat flux obtained in the Cone Calorimeter

Critical heat flux / kW·m^{-2}					
PIRa	**PIRb**	**PIRc**	**PF**	**EPS**	**SW**
~10	~12	~15	~22	100 mm thick: ~16[9] equivalent to ~6 50 mm thick: ~15 equivalent to ~9-10	N/A

Scatter data of the inverse squared root of time-to-ignition versus external heat flux for the three types of PIR and PF are presented in Figure 5.8 and Figure 5.9. Linear regressions representing the approach for the range $t_p/t_c \rightarrow 0$, noted in Equation (5.3), are included in the charts from Figure 5.8. Non-linear regressions representing the approach for the range $t_p/t_c \rightarrow \infty$, noted in Equation (5.4), are included in charts from Figure 5.9 up to an external heat flux of 45 kW·m^{-2}.

Linear regressions ($t_p/t_c \rightarrow 0$) for PIR show better agreement for high heat fluxes rather than low heat fluxes for which agreement is presented to be very poor. However, the approach based on a non-linear regression ($t_p/t_c \rightarrow \infty$) seems to introduce a better fitting, at least for the range up to 45 kW·m^{-2}. It should be noted that times-to-ignition for high heat fluxes, presented in Appendix A, correspond to

[9] This value refers to the heat flux at the surface before EPS starts shrinking. Actual heat flux at the bottom of the material where material accumulates is expected to be between 6-10 kW·m^{-2}

values lower than five seconds. This implies that the error bars associated to regression techniques at high heat fluxes are expected to be very large.

For the case of PF, the scatter data shows two clear trends: presented as a growing function from 22 to 40 kW·m^{-2} and as a horizontal function from 40 to 65 kW·m^{-2}. Linear regression ($t_p/t_c \to 0$) for lower range of heat fluxes presents similar result to PIR, with a poor agreement. The fitting technique based on non-linear regression ($t_p/t_c \to \infty$) gives similar agreement, but however replicating lower heat fluxes in a better way.

The results indicate that early conclusions determining which of the regression analyses provide better agreement cannot easily be derived.

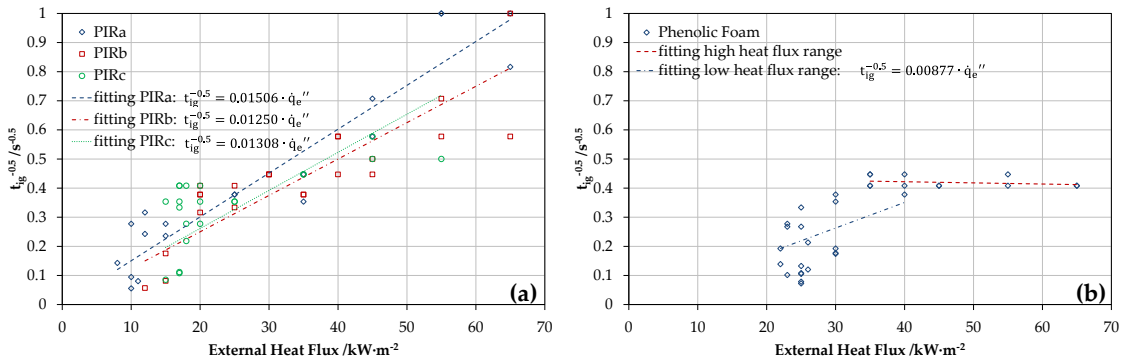

Figure 5.8. Time-to-ignition versus external heat flux of (a) three rigid isocyanurate-based foams and (b) phenolic foam based on Equation (5.3)

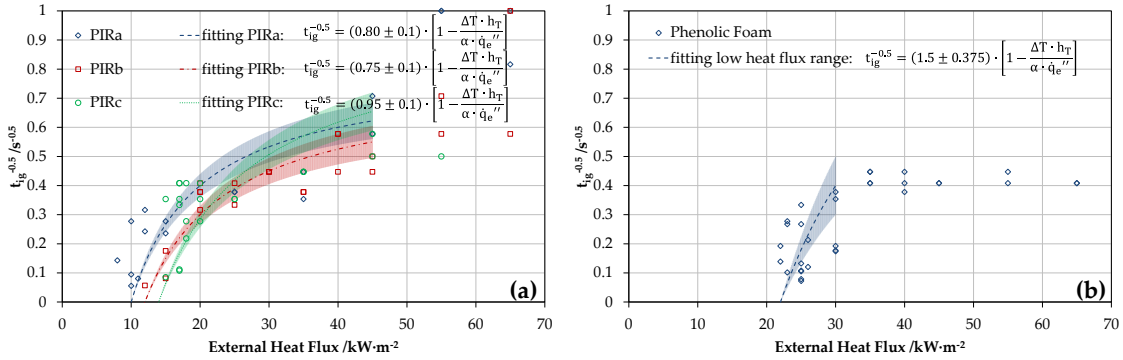

Figure 5.9. Time-to-ignition versus external heat flux of (a) three rigid isocyanurate-based foams and (b) phenolic foam based on Equation (5.4)

Scatter data of the inverse of time-to-ignition versus external heat flux for EPS are presented in Figure 5.10. Figure 5.10a presents the inverse of ignition times versus the nominal heat flux – considered as the heat flux at the surface of the material at the start of the test. Figure 5.10b presents the inverse of ignition times versus the corrected heat flux – considered as the heat flux measured at the height of the back face of the sample at the start of the test. Linear regressions are plotted for all data series. Interestingly, while one would expect the CHF to be different for shrinking samples of different thickness, this is not the case here. If the external heat flux is corrected, the regressions seem to be parallel but with very different CHF. In any of the cases, a linear regression provides a very good fitting.

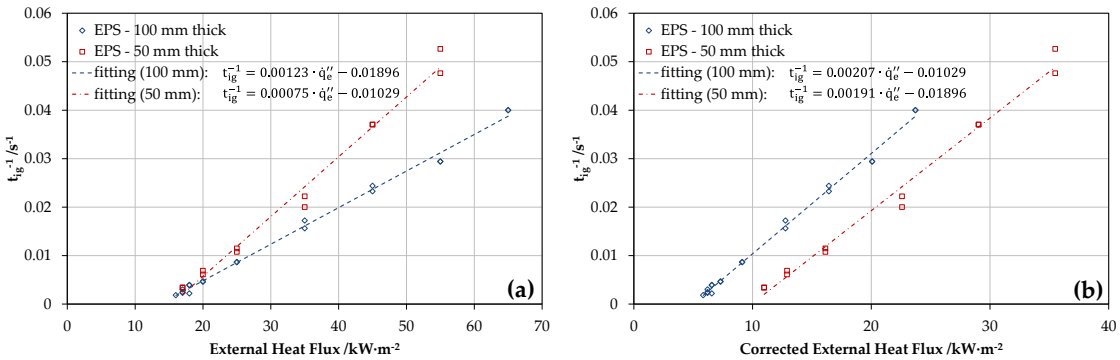

Figure 5.10. Time-to-ignition versus external heat flux of EPS. (a) Nominal heat flux (b) Corrected heat flux

5.4.4 Ignition temperature and thermal inertia

Ignition temperatures are calculated considering an emissivity of $\varepsilon = 0.9$ and the global coefficient of heat losses as a function of the temperature (Equation (5.7) and Figure 5.4). Calculated values for the different materials are presented in Table 5.3. The sensitivity of the ignition temperature calculation with regard to the uncertainty of the emissivity and the accuracy of the external heat flux measurement is indicated in Figure 5.11. Shaded regions are included in the plot, indicating variability with respect to the nominal value of assumed emissivity and heat flux. It is shown that the error related to these uncertainties is low.

Table 5.3. Calculated ignition temperature

Ignition temperature /°C					
PIRa	**PIRb**	**PIRc**	**PF**	**EPS**	**SW**
~306	~337	~377	~453	~305.9 - 389.4 (with CHF 10-16 kW·m^{-2})	N/A

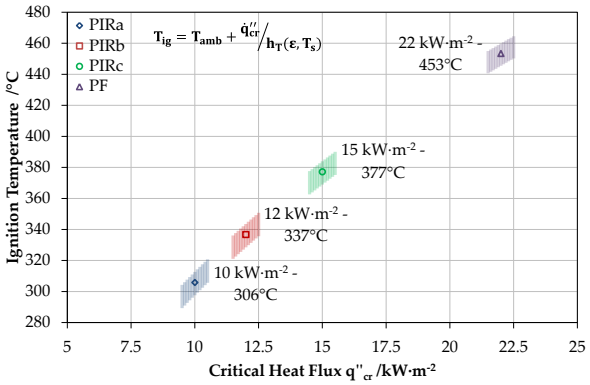

Figure 5.11. Calculated ignition temperature for PIR and PF. Shading indicates sensitivity of the calculated variable to $\varepsilon \pm 0.1$ and $\dot{q}''_{cr} \pm 0.5\ kW \cdot m^{-2}$

However, the highest uncertainty lies on the quantification of the convective heat transfer coefficient. Unfortunately, this cannot be easily assessed, and consistency of the obtained values will be evaluated by comparison with data obtained from thermogravimetric analyses. In any case, values of global heat transfer coefficient are consistent with the ones observed in the literature. Larger values for the convective

heat transfer coefficient were presented by *Steinhaus* [11], which are not used for this analysis. Estimated values for the heat transfer coefficient are noted in Table 5.3.

Table 5.4. Estimated heat transfer coefficients

Convective, radiative and global heat transfer coefficient / $W \cdot m^{-2} \cdot K^{-1}$					
PIRa	**PIRb**	**PIRc**	**PF**	**EPS**	**SW**
$h_c \approx 13.2$ $h_r \approx 19.1$ $h_T \approx 32.3$	$h_c \approx 13.4$ $h_r \approx 21.4$ $h_T \approx 34.8$	$h_c \approx 13.7$ $h_r \approx 24.9$ $h_T \approx 38.5$	$h_c \approx 14.1$ $h_r \approx 32.3$ $h_T \approx 46.4$	$h_c \approx 13.2 – 13.7$ $h_r \approx 19.1 – 26.0$ $h_T \approx 32.3 – 39.7$	N/A

Calculated values of thermal inertia obtained by the two different approaches introduced in previous sections are presented in Table 5.5. It is shown that the approach usually used for high heat fluxes ($t_p/t_c \rightarrow 0$) offers significantly large values of thermal inertia in comparison to the approach usually indicated for low heat fluxes ($t_p/t_c \rightarrow \infty$). The observed discrepancy is a 10 to 20 times. Values of thermal inertia for SW are not calculated since no ignition was achieved. Values of thermal inertia for EPS are not calculated since the material shrinks and melts becoming a thermally thin material; therefore, the calculation of thermal inertia using this methodology does not have any physical meaning.

Table 5.5. Nominal values for calculated thermal inertia

$k\rho c$ / $W^2 \cdot s \cdot K^{-2} \cdot m^{-4}$						
Range	**PIRa**	**PIRb**	**PIRc**	**PF**	**EPS**	**SW**
$t_p/t_c \rightarrow \infty$ Equation (5.4)	$5.1 \cdot 10^3$	$6.1 \cdot 10^3$	$5.2 \cdot 10^3$	$3.0 \cdot 10^3$	N/A	N/A
$t_p/t_c \rightarrow 0$ Equation (5.3)	$55 \cdot 10^3$	$66 \cdot 10^3$	$47 \cdot 10^3$	$71 \cdot 10^6$	N/A	N/A

The sensitivity of the calculation for $t_p/t_c \rightarrow \infty$ with regard to the uncertainty in the emissivity and the measurement of heat flux is presented as a shaded region in Figure 5.12a. Figure 5.12b indicates the sensitivity of the calculation related to the assumed error during the fitting in the coefficient $\frac{\sqrt{\pi} \cdot h_T}{\sqrt{k\rho c}}$ in Equation (5.4).

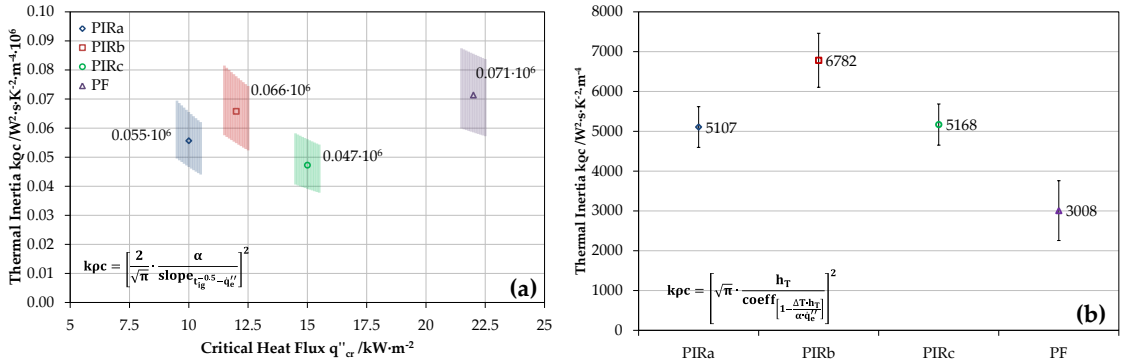

Figure 5.12. Calculated thermal inertia for PIR and PF. (a) Equation (5.3). (b) Equation (5.4). Shading indicates sensitivity of the calculated variable to $\varepsilon \pm 0.1$ and $\dot{q}''_{cr} \pm 0.5\ kW \cdot m^{-2}$. Error bars indicate sensitivity to error on coefficient $\frac{\sqrt{\pi} \cdot h_T}{\sqrt{k\rho c}}$ in Equation (5.4)

Estimated values of thermal conductivity for PIR and PF, assuming measured densities and a range of heat capacities provided by manufacturers, are presented in Figure 5.13. It can be noted that values obtained by the thermal inertia related to the regression that considers $t_p/t_c \to 0$, provide extremely large values of thermal conductivity. On the contrary, the regression that considers $t_p/t_c \to \infty$, gives values still higher than the ones claimed by the manufacturer, but within the same order of magnitude.

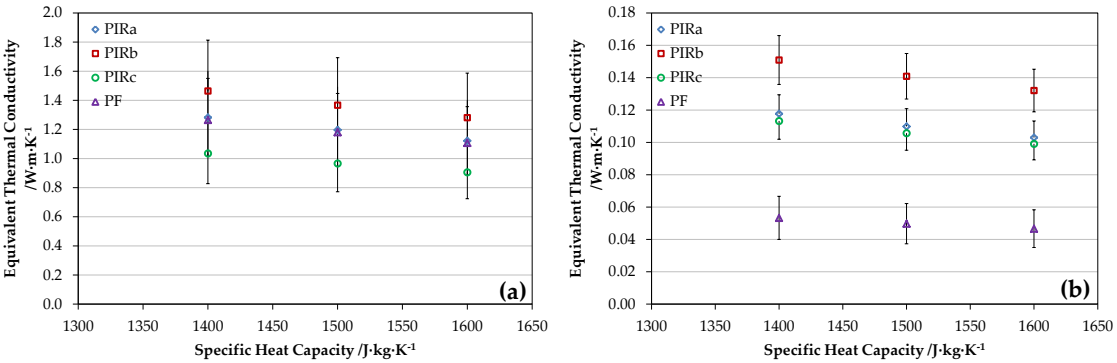

Figure 5.13. Estimated thermal conductivity for PIR and PF from calculated thermal inertia by (a) Equation (5.3) (b) Equation (5.4). Specific heat capacity assumed as c_p = 1400 – 1600 J·kg^{-1}·K^{-1}. Error bars indicate accumulated error from thermal inertia calculation

5.4.5 Heat release rate

Figure 5.14 to Figure 5.16 show the average heat release rate per unit area (HRRPUA) from two repetitions for PIR, PF and EPS. For PIR and PF, charts on the left and right respectively indicate the HRRPUA for samples with and without protective layer at surface. For EPS, charts on the left and right respectively indicate the HRRPUA for 100 mm and 50 mm thick samples.

The used energy coefficient for oxygen consumption calorimetry corresponds to the generic value $E_{O_2} = 13.1\ \text{kJ} \cdot g_{O_2}^{-1}$ for materials such as PIR and PF due to unknown chemistry of the material. A value of $E_{O_2} = 12.97\ \text{kJ} \cdot g_{O_2}^{-1}$ is used for EPS since *Hugget* reported values for another type of EPS [12]. Error bars indicating uncertainty with regard to the quantification of the energy coefficient are not shown for simplicity in the visual representation of the heat release rate curves. This is further discussed in the following section.

In general, PIR samples show the most reduced combustibility with lowest HRRPUA throughout the duration of the test, followed by phenolic foam. EPS presents a higher HRRPUA with a maximum value approximately between 4 to 5 times larger than the values for PIR and PF.

The burning behaviour of PIR and PF shows similar trend, with a large peak of HRRPUA right after ignition, followed by a progressive decay. This is generally correct for any PIR with and without protective layer at surface. However, PF shows a decay of HRRPUA after first peak, but an increase for high heat fluxes without protective layer at surface. Slightly larger peaks of HRRPUA are found for samples

with protective layer at surface. This might be indicative of a slightly contribution of the protective layer to the combustion.

The burning behaviour of EPS shows an initial increase of HRRPUA, followed by a maximum HRRPUA that remains in quasi steady-state for approximately 50 seconds, continuing to a progressive decay.

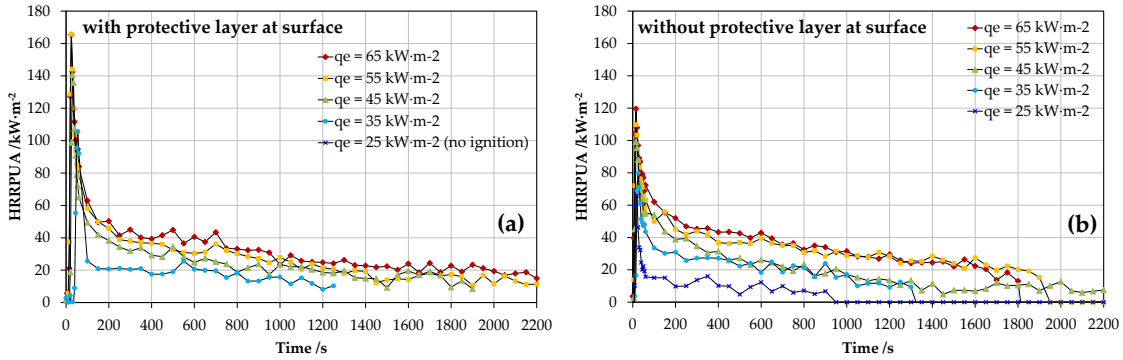

Figure 5.14. Heat release rate per unit area of 100 mm thick PIRc samples, with (a) and without (b) protective layer, at different external heat fluxes. ($E_{O_2} = 13.1\ kJ \cdot g_{O_2}^{-1}$). Average from two repetitions

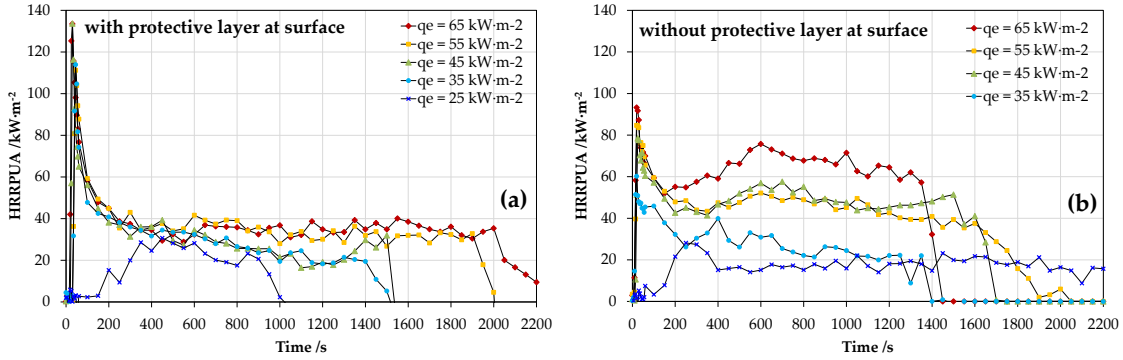

Figure 5.15. Heat release rate per unit area of 100 mm thick PF samples, with (a) and without (b) protective layer, at different heat fluxes. ($E_{O_2} = 13.1\ kJ \cdot g_{O_2}^{-1}$). Average from two repetitions

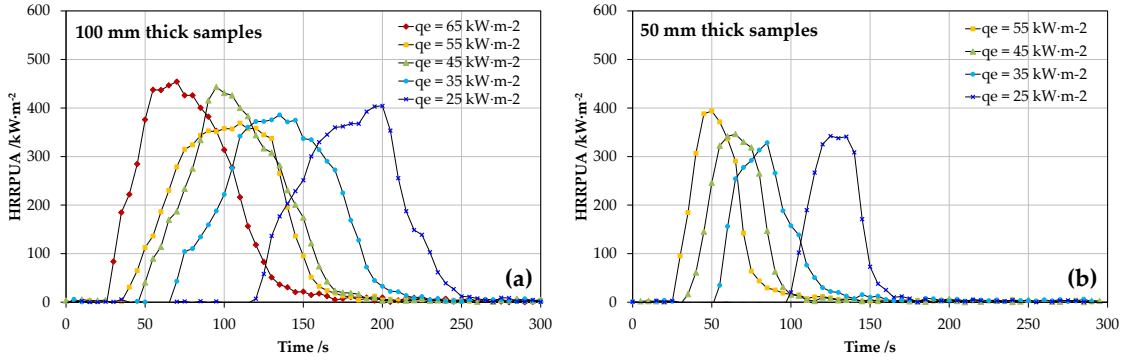

Figure 5.16. Heat release rate per unit area of 100 mm (a) and 50 mm (b) thick EPS samples at different heat fluxes ($E_{O_2} = 12.97\ kJ \cdot g_{O_2}^{-1}$ [12]). Average from two repetitions

5.4.6 Normalised mass loss

Figure 5.17 to Figure 5.19 show the average curves of normalised mass[10] from two repetitions for PIR, PF and EPS. It should be noted that mass loss rate is often used to represent the burning behaviour of the material. Then, the result is expected to be qualitatively similar to the obtained HRRPUA curves. Instead of this and for simplicity in the visual assessment of the different evolution of the tests, the mass loss data is presented as normalised mass.

PIR mass loss curves present different slope throughout the tests, indicating different mechanism of thermal degradation occurring at different rate. PF mass loss curves are more linear than the ones observed for PIR, while PF mass loss is also observed to be larger than PIR for same heat conditions. This is consistent with the visual observation and measured HRR curves presented in previous sections. EPS presents the most linear behaviour in mass loss, indicating a steady-state in the burning dynamics.

It can be observed that experiments without protective layer present steeper slope in the mass loss curves. PIR mass loss curves between tests with and without protective layer has a significant difference for heat fluxes lower than 35-45 kW·m^{-2}. In the case of PF, the effectivity of the protective layer is lower.

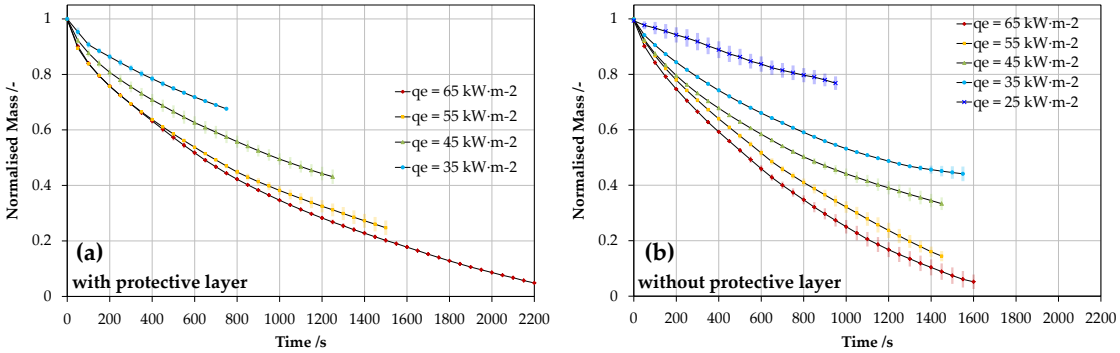

Figure 5.17. Normalised mass (m/m_0) of PIRc samples, with (a) and without (b) protective layer, at different heat fluxes. Shading indicates std. dev. from two repetitions

[10] Normalised mass refers to the ratio between the mass at present time and the original mass of the sample before start of test.

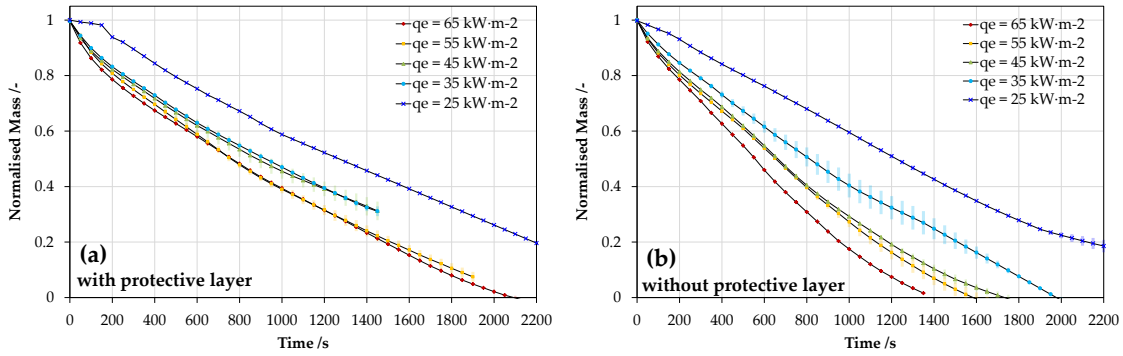

Figure 5.18. Normalised mass (m/m_0) of PF samples, with (a) and without (b) protective layer, at different heat fluxes. Shading indicates std. dev. from two repetitions

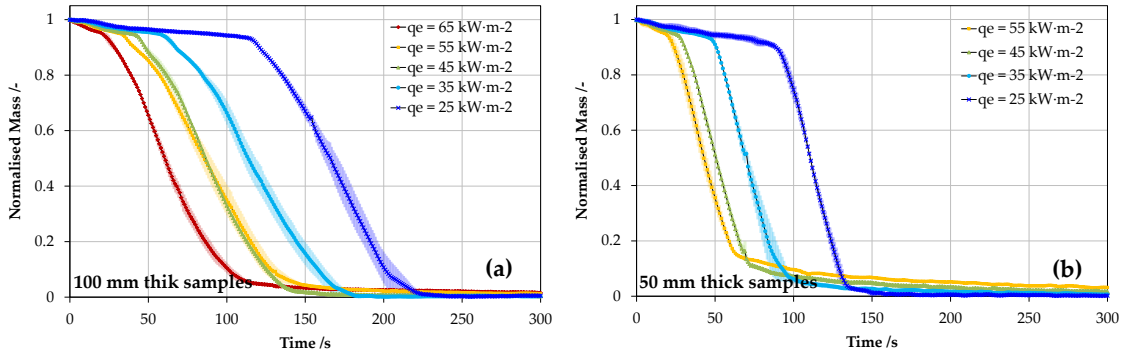

Figure 5.19. Normalised mass (m/m_0) of 100 mm (a) and 50 mm (b) thick EPS samples at different heat fluxes. Shading indicates std. dev. from two repetitions

5.4.7 Gas species correlations

Figure 5.20 to Figure 5.21 show a selection of gas species correlations of specific tests from PIR, PF and EPS. In general, high heat fluxes are selected to represent clearly the different phenomena taking place. Charts on the left indicate carbon dioxide and monoxide concentrations, while those on the right indicate ratio of generated carbon dioxide versus consumed oxygen, and ratio of generated carbon monoxide versus carbon dioxide.

These indicators help to demonstrate the different burning behaviour of the material. Applying CDG calorimetry principles, CO_2 concentration is equivalent in shape to the HRR. This is found to be generally correct for the cases presented below, with a peak of CO_2 and a progressive decay for PIR. From the HRRPUA curves, PF shows an initial decay, followed by further decay and then an increase which is again followed by a decrease. In the case of EPS, the shape is dissimilar due to the effect of absorption by *drierite*®.

The ratio of generated CO versus generated CO_2 indicates the different behaviour of burning and efficiency of the combustion. Higher efficiency is obtained when lower ratios are observed. For PIR and PF this ratio tends to increase largely throughout the duration of the test, suggesting a transition from flaming to smouldering combustion, with both phenomena occurring simultaneously during some periods of the test. In the case of EPS, the ratio presented in Figure 5.22 it is not reliable since the CO_2 curve is erratic. In any case, an approximate ratio can be derived by assessing the curve at

100 seconds, during the steady-state and peak of the CO_2 curve. A ratio between 0.05 and 0.15 is observed during flaming combustion for PIR and between 0.025 and 0.05 for PF. A constant value is difficult to be established since steady-state is not clearly observed. For EPS, an approximately value of 0.05 is derived.

The ratio of generated CO_2 versus consumed O_2 indicates the contribution of different species to the combustion. In general, a short steady-state is shown for PIR, suggesting only flaming combustion from PIR pyrolysates. This continues to decrease throughout the duration of the test indicating the transition to a different burning regime, probably with char being consumed by oxidation. Similar results are observed for PF, although the decrease occurring much earlier and followed by a transition to a quasi-steady-state. This might be indicative of oxidation of char and flaming of pyrolysis gases occurring simultaneously. At the final stage of the test, this gets reduced again, probably indicating just oxidation of char. In the case of EPS, the flaming can be easily identified by steady-state. After flame out, large values are observed for this ratio, indicating extreme low consumption of oxygen but still measurement of generated CO_2, which is an artefact due to CO_2 desorption by the drierite.

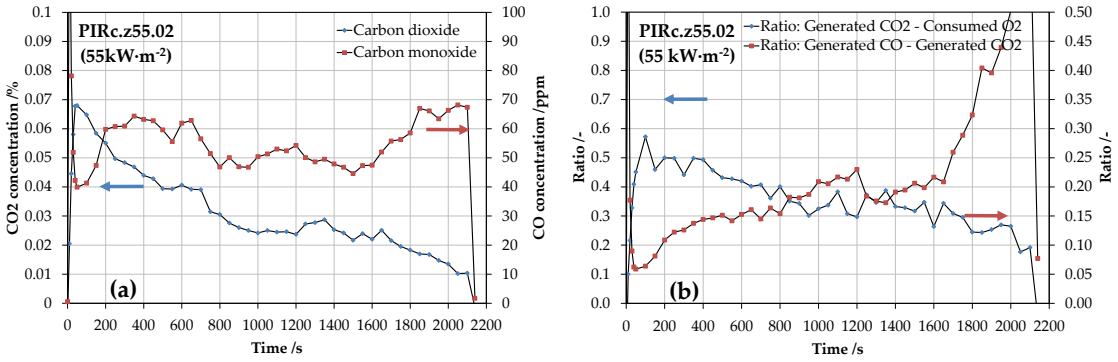

Figure 5.20. CO_2 and CO concentrations (left) and ratios of generated CO_2 vs. consumed O_2 and generated O_2 vs. generated CO (right) for PIRc at 55 kW·m^{-2} (test PIRc.z55.02)

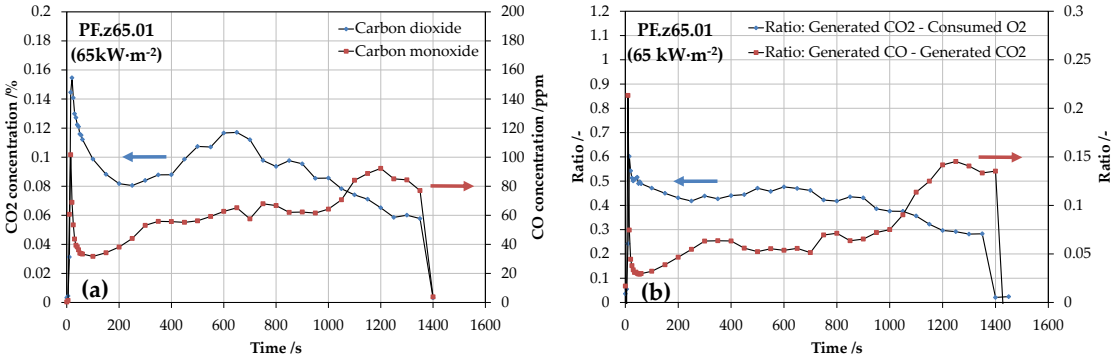

Figure 5.21. CO_2 and CO concentrations (a) and ratios of generated CO_2 vs. consumed O_2 and generated O_2 vs. generated CO (b) for PF at 65 kW·m^{-2} (test PF.z65.01)

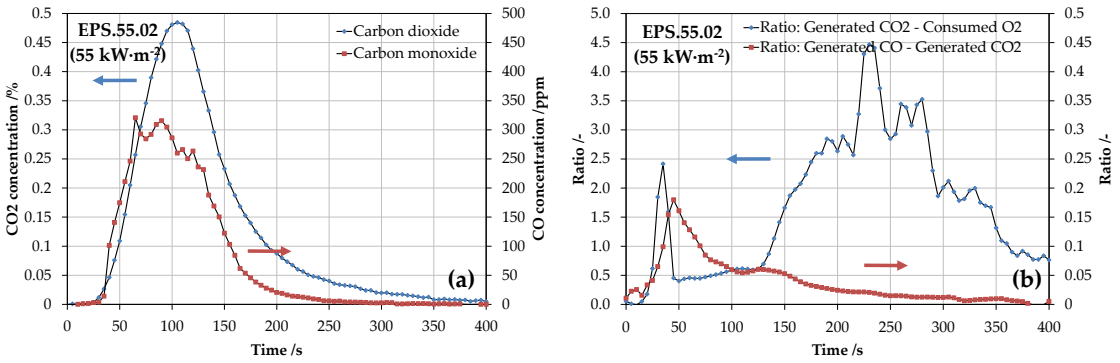

Figure 5.22. CO2 and CO concentrations (a) and ratios of generated CO2 vs. consumed O2 and generated O2 vs. generated CO (b) for EPS at 65 kW·m^{-2} (test PF.z65.01)

5.4.8 Estimation of effective heat of combustion

Table 5.6 shows the calculated values for the effective heat of combustion for plastic foams PIRa, PIRb, PIRc, PF and EPS. The approach followed for the calculation of these values is given by the following expression:

$$\Delta H_{c,eff} = \frac{\int_0^{t_{end}} HRR(t) \cdot dt}{m_{loss}} \tag{5.14}$$

where $\Delta H_{c,eff}$ is the effective heat of combustion, HRR(t) is the heat release rate calculated by oxygen consumption calorimetry, t_{end} is the end time of the test and m_{loss} is the total mass loss during the test.

The notation 'effective' relates to an average value obtained by the combustion of the material. However, the combustion process for most of these foams has been found to be non-uniform, with transition from flaming to smouldering for charring foams, and dependent on the magnitude of the external heat flux. Then, if Equation (5.14) is applied for the total test time, the obtained values of heat of combustion will represent a lumped value that considers both flaming and smouldering as a single process.

If values for the effective heat of combustion from pyrolysis gases are to be correlated for materials that char and experience smouldering, this analysis should be applied for periods of time when only flaming is produced. In order to get an estimation of this, an arbitrary period up to 200 seconds is used, which is sufficient for capturing the peak of HRR and decay before this gets a steady-state.

Table 5.6. Calculated effective heat of combustion for plastic foams

Effective Heat of Combustion / kJ·g^{-1}					
Integration time	**PIRa**	**PIRb**	**PIRc**	**PF**	**EPS**
Total test time (t_{end})	Protective layer: 19.65 ± 2.52 no protective layer: 19.09 ± 1.99	protective layer: 19.56 ± 2.09 no protective layer: 18.05 ± 2.48	protective layer: 21.41 ± 1.26 no protective layer: 20.52 ± 3.45	protective layer: 18.60 ± 3.54 no protective layer: 20.98 ± 6.01	100 mm: 31.67 ± 1.38 50 mm: 27.34 ± 0.96
Up to 200 s (initial flaming)	protective layer: 13.34 ± 0.56 no protective layer: 14.38 ± 0.68	protective layer: 12.94 ± 0.55 no protective layer: 13.22 ± 1.30	protective layer: 15.68 ± 0.98 no protective layer: 16.26 ± 0.84	protective layer: 14.30 ± 1.16 no protective layer: 15.35 ± 0.80	-

5.5 Discussion

5.5.1 Effect of the low thermal inertia

Two main effects can be highlighted due to the characteristic low thermal inertia of the studied materials. These effects relate to the time-to-ignition and the quantification of thermal inertia by using classic regressions noted in previous sections.

In Chapter 3 it was numerically demonstrated by classic ignition theories that low values of thermal inertia lead to low ignition times for any external radiant heat flux above the critical heat flux. This is consistently supported by the results of the experiments carried out on PIR and PF, with time-to-ignition falling below 20-30 seconds above the region of heat fluxes close to the critical heat flux. However, this is not the case for EPS, for which ignition times are higher. This can be explained since the material shrinks and melts before flaming, acting as a thermally thin material before ignition. Once melted, the thermal inertia is no longer the key factor that governs ignition, but the volumetric heat capacity as noted in Equation (5.15) below, which represents the heating process before ignition of a thermally thin material:

$$L \cdot \rho \cdot c_p \cdot \frac{dT}{dt} = \alpha \cdot \dot{q}_e'' - h_T \cdot (T - T_\infty) - \dot{q}_{cond,loss}'' \quad (5.15)$$

with L being the thickness of the film, $\rho \cdot c_p$ the volumetric heat capacity, T the temperature of the film and $\dot{q}_{cond,loss}''$ the conductive heat losses.

Significant discrepancies have been observed between the two thermal inertia quantifications based on the classical regression methods found in the literature, which were defined in Equations (5.3) and (5.4). In order to assess the source of this discrepancy, an auxiliary function $f(t_p)$ is defined, based on the non-dimensional solution of the surface temperature of the infinite plate as noted in Equation (5.1):

$$f(t_p) = \left[1 - \frac{(T_P - T_\infty) \cdot h_T}{\alpha \cdot \dot{q}_e''}\right] = e^{t_P/t_c} \cdot \mathrm{erfc}\left(\left(\frac{t_P}{t_c}\right)^{1/2}\right) \quad (5.16)$$

The evolution of $f(t_p)$ over time represents the exact solution for a specific characteristic time and therefore for a couple of specific values of heat transfer coefficient and thermal inertia. Regressions defined in Equations (3) and (5.4) can analogously be transformed to a series of auxiliary functions defined as the RHS term in Equation (5.16) above. These are respectively indicated below, with $f^{low}(t_p)$ the auxiliary function for $t_P/t_c \to 0$ and $f^{high}(t_p)$ the auxiliary function for $t_P/t_c \to \infty$:

$$f^{high}(t_p) = \left[1 - \frac{2 \cdot h_T}{\sqrt{k\rho c} \cdot \sqrt{\pi}} \cdot \sqrt{t_p}\right] \tag{5.17}$$

$$f^{low}(t_p) = \frac{\sqrt{k\rho c}}{h_T \cdot \sqrt{\pi}} \cdot \frac{1}{\sqrt{t_p}} \tag{5.18}$$

Results for the exact and auxiliary functions for a generic insulation material with low thermal inertia (noted in Table 5.11) and a cellulosic material with higher thermal inertia such as yellow pine are presented in Figure 5.23. These results indicate that the regression for $t_P/t_c \to \infty$ presents a good fitting from low times, while the regression $t_P/t_c \to 0$ only offers a good fitting for times lower than one second. On the contrary, regression for $t_P/t_c \to \infty$ does not offer a good fitting for a material such as yellow pine until times larger than 300 seconds are achieved. Again, the regression for $t_P/t_c \to 0$ presents a good fitting for short times, but the error significantly increases after 20 seconds.

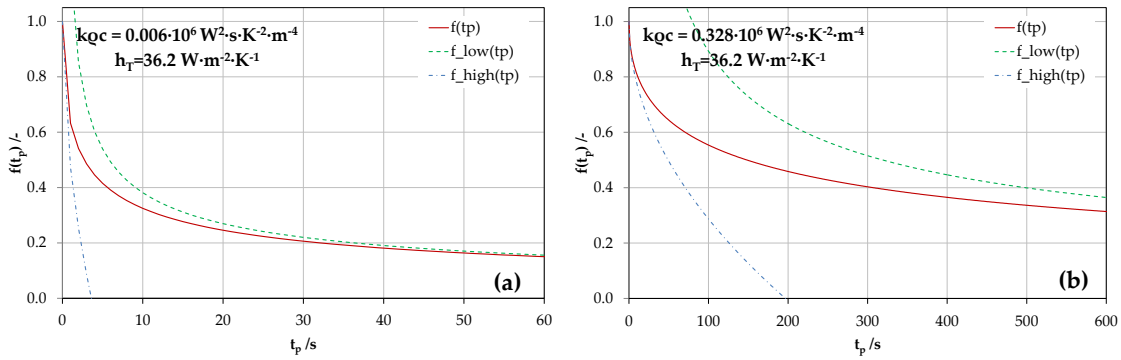

Figure 5.23. Evolution of function $f(t_p)$ and regression for low and high heat flux ranges. (a) Low $k\rho c$ (generic insulator Table 5.8). (b) high $k\rho c$ (yellow pine [13])

Since the materials being studied are known to have low thermal inertia, the error is expected to be much lower if the expression corresponding to $t_P/t_c \to \infty$ defined in Equation (5.4) is used. These correspond to the lower thermal inertia values noted in Table 5.5, which are in good agreement with values calculated by using thermal properties indicated by manufacturers. As expected, values obtained by using Equation (5.3) are presented to be much larger, since it has been demonstrated that the fitting is very inaccurate. Significant errors are attributed to the fact that ignition times are obtained extremely fast for high heat fluxes, auto-ignition being sometimes achieved instantaneously, therefore the mixing period dominating over the pyrolysis time.

Figure 5.24 shows the obtained data processed by the function $f(t_p) = \left[1 - \frac{(T_P - T_\infty)}{T_c}\right]$ versus ignition times for PIR and PF. A relatively good fitting for ignition times longer than ten seconds is shown, while the fitting below ten seconds is significantly poor, with dissimilar trends between the fitting and the experimental data. This disagreement is indicative of pyrolysis times near zero seconds, thus the mixing and induction time playing an important role; consequently, correlations of thermal inertia near this region are expected to provide erroneous quantification.

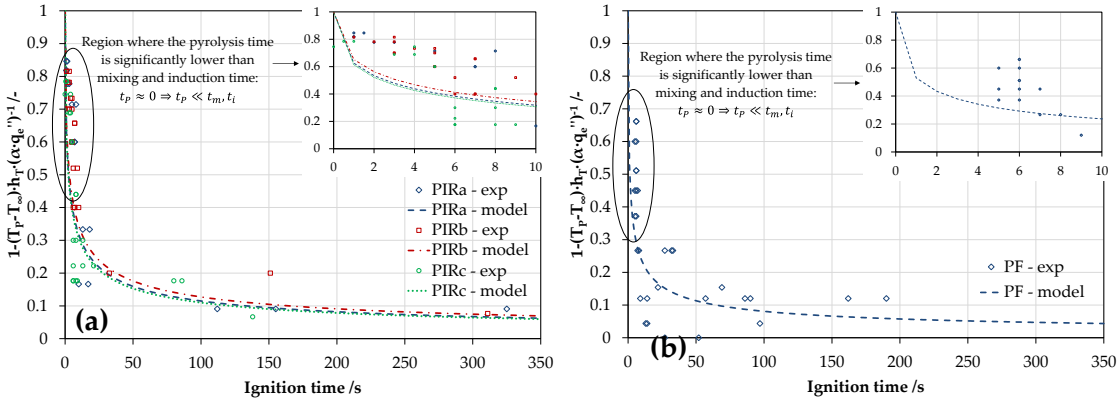

Figure 5.24. Time-to-ignition versus external heat flux of (a) three PIR foams and (b) PF based on Equation (5.16)

Table 5.7 presents the values of thermal inertia using this method compared to the values obtained by the regression considering $t_P/t_c \to \infty$. Consistent values of thermal inertia are obtained, confirming the erroneous assessment of thermal inertia for insulation materials if the regression considering $t_P/t_c \to 0$ is used.

Table 5.7. Nominal values for calculated thermal inertia

$k\rho c$ /W²·s·K⁻²·m⁻⁴				
Range	**PIRa**	**PIRb**	**PIRc**	**PF**
$t_p/t_c \to \infty$ Equation (5.4)	$5.1 \cdot 10^3$	$6.1 \cdot 10^3$	$5.2 \cdot 10^3$	$3.0 \cdot 10^3$
$f(t_p) = \left[1 - \frac{(T_P - T_\infty)}{T_c}\right]$ Equation (5.16)	$4.5 \cdot 10^3$	$6.5 \cdot 10^3$	$5.5 \cdot 10^3$	$4.5 \cdot 10^3$

5.5.2 Effect of the protective (foil) layer of rigid plastic foams

Experimental results provide evidence on the significant effect that the foil protective layer of rigid foams has on their observed flammability and combustibility. This is presented as a reduced rate of thermal degradation, understood as a slower mass loss.

The effect of the protective layer on the material performance throughout the experiments can be understood in four ways, in relation to:

- the mixing of pyrolysis gases and air,
- the rate of surface oxidation,
- the interaction with the radiant heat flux from the test procedure, and

- the combustibility.

Despite these effects are intrinsically linked, their relevance depends on the stage of the test. The protective layer is characterised by presenting a foil aspect, which leads to a lower emissivity of the exposed surface. Since the heating system of the test procedure is based on a radiative source such as the Cone Calorimeter, the exposed surface absorptivity of the tested material may have a significant effect on the thermal behaviour. In order to qualitatively evaluate the effect of a surface with low emissivity under similar conditions as the one observed in the Cone Calorimeter, a series of case studies are presented. Generic insulation foam with thermal properties as noted in Table 5.8 is assessed by a one-dimensional heat transfer analysis. The emissivity and external radiant heat flux are the variables altered, between 0.1 and 1 for the former, and between 10 and 60 $kW \cdot m^{-2}$ for the latter. These variables, together with the geometry and boundary conditions, are noted in Table 5.9 below.

Table 5.8. Thermal properties of generic insulation material

Thermal conductivity /$W \cdot m^{-1}K^{-1}$	Specific heat capacity /$J \cdot kg^{-1} \cdot K^{-1}$	Density /$kg \cdot m^{-3}$	Thermal diffusivity /$m^2 \cdot s^{-1}$	Thermal inertia /$W^2 \cdot s \cdot K^{-2} \cdot m^{-4}$
0.03	1500	40	5E-07	1800

Table 5.9. Geometry and boundary conditions

Emissivity /-	External radiant heat flux /$kW \cdot m^{-2}$	Dimensions /mm	Convective heat transfer coefficient formulation	Back surface condition
0.15 – 1	25 - 65	Surface: 90 x 90 Thickness: 100	$Nu_L = 0.54 \cdot Ra^{1/4}$ $h_c = \frac{k_{air} \cdot Nu_L}{L}$	Neumann B.C. Adiabatic $(\dot{q}''_{loss} = 0kW \cdot m^{-2})$

The heating period is limited to ten minutes, and the boundary condition at the exposed surface is defined by a Neumann boundary condition, i.e. as a net heat flux that is calculated as the balance between the external radiant heat flux and heat losses by convection and radiation. This boundary condition is defined as the term on the left of Equation (5.6). For simplicity, an adiabatic boundary condition is assumed at the back layer of the material.

Figure 5.26 shows the results of the performed numerical analyses. In general, as it would be expected, the main significant result is the discrepancy between low and high emissivity being approximately 100% and 40% larger at 25 and 65 $kW \cdot m^{-2}$ respectively for highest emissivity. Additionally, it is shown that the thermal gradient for 65 $kW \cdot m^{-2}$ and low emissivity is equivalent to the one showed for 25 $kW \cdot m^{-2}$ and high emissivity.

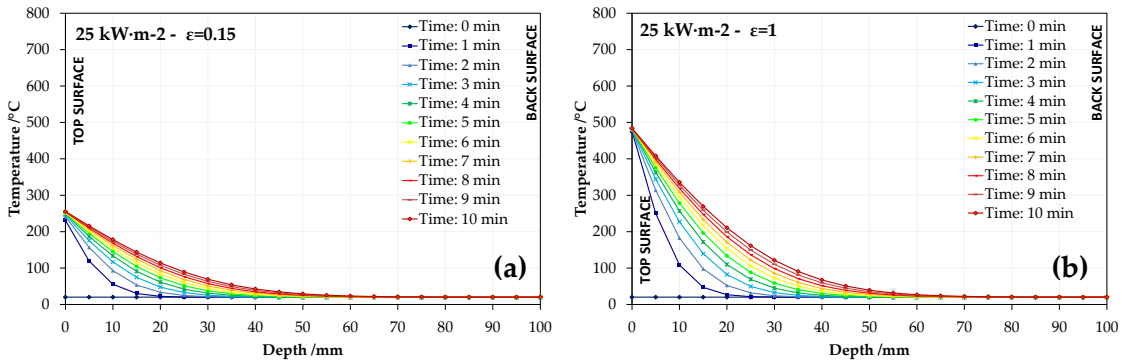

Figure 5.25. In-depth thermal profiles for a generic insulation foam at different times for $\dot{q}_i'' = 25\ kW \cdot m^{-2}$ and different emissivities. (a) $\varepsilon = 0.15$. (b) $\varepsilon = 1$.

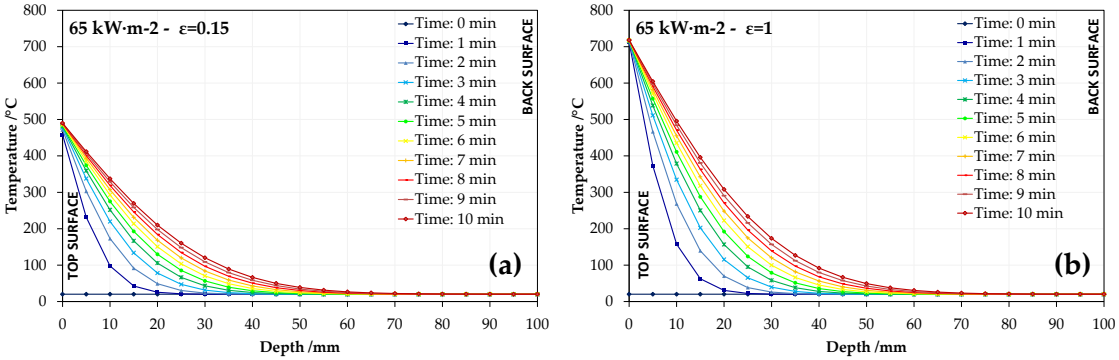

Figure 5.26. In-depth thermal profiles for a generic insulation foam at different times for $\dot{q}_i'' = 65\ kW \cdot m^{-2}$ and different emissivities. Left: $\varepsilon = 0.15$. Right: $\varepsilon = 1$.

Once the onset of pyrolysis is achieved, the protective layer delays the release of pyrolysis gases, trapped between the top layer and the surface of the foam. Once the rate of pyrolysation is high enough, these gases can escape by the edge of the samples or simply lifting, detaching or cracking the protective layer. Flaming occurs not uniformly at the surface of the sample since the mixing is obstructed. This behaviour is very dependent on the size of the sample and the quality of the bonding between the foam and the protective layer. Therefore, extrapolation of the observed behaviour with protective layer to higher scales must be addressed carefully, since this may differ.

The integrity of the protective layer has a significant impact in the oxidation of the char formed at the top and edges. If the protective layer gets detached or perforated, oxidation tends to occur if temperatures are sufficiently high. The oxidation rates and areas have been observed to be random. Indeed, oxidation is a diffused-controlled mechanism, which is much more complicated to model and therefore to predict [14].

Finally, it has been shown that larger peaks of HRR are achieved when testing the foams with protective layer. This indicates that the protective layer might slightly contribute to the combustion when ignition is produced.

5.5.3 Effect of the charring and shrinking-melting behaviour

Materials PIRa, PIRb, PIRc and PF have shown a charring behaviour after flaming was produced. On the contrary, EPS showed fast shrinking behaviour followed by melting before flaming. This material behaviour determines the rate of pyrolysation, and therefore the burning rate.

With regard to the shrinking nature, it has been observed that before ignition, EPS shrank completely until the generation of a thin film that became viscous after melting. The burning dynamics of the obtained bed of fuel are characteristic from a thermally thin material, or a liquid. This is reflected by the HRR and mass loss curve, with a steady-state region of burning.

With regard to the charring nature, the pyrolysis rate can be significantly reduced over the duration of the heat exposure. This effect is often attributed to the low conductivity of the created char. Nevertheless, the reduction of the pyrolysis rate is due to stability of the char layer rather than its thermal conductivity. Indeed, the rate of pyrolysis is determined by the ratio between the net energy at the pyrolysis front and the enthalpy of gasification L_v. This is represented by Equation (5.19) below and is an approach considered by several models [15, 16].

$$\dot{m}''_P = \frac{\dot{q}''_1 - \dot{q}''_2}{L_v} \tag{5.19}$$

Under this approach, the net energy at the pyrolysis front can be defined as the difference between the incoming energy from layers above $\dot{q}''_1$ and the energy lost by conduction to layers below $\dot{q}''_2$. For simplicity, the pyrolysis front can be defined as the layer of material at a given pyrolysis temperature. For charring materials, Equation (5.19) can be expressed as Equation (5.20) below:

$$-k_{char} \cdot \left.\frac{\delta T}{\delta x}\right|_{L^-} = -k_{virgin} \cdot \left.\frac{\delta T}{\delta x}\right|_{L^+} + \dot{m}''_P \cdot L_v \tag{5.20}$$

with k_{char} and k_{virgin} being the thermal conductivity of the charred and virgin material respectively, and $\left.\frac{\delta T}{\delta x}\right|_{L^-}$ and $\left.\frac{\delta T}{\delta x}\right|_{L^+}$ the thermal gradient at the pyrolysis front in the char layer and virgin layer. Figure 5.27 shows an example of two different stages for a charring material with the pyrolysis front at different positions. Then, the pyrolysis rate can be estimated by quantifying the thermal gradients at the pyrolysis front, thermal properties and enthalpy of gasification.

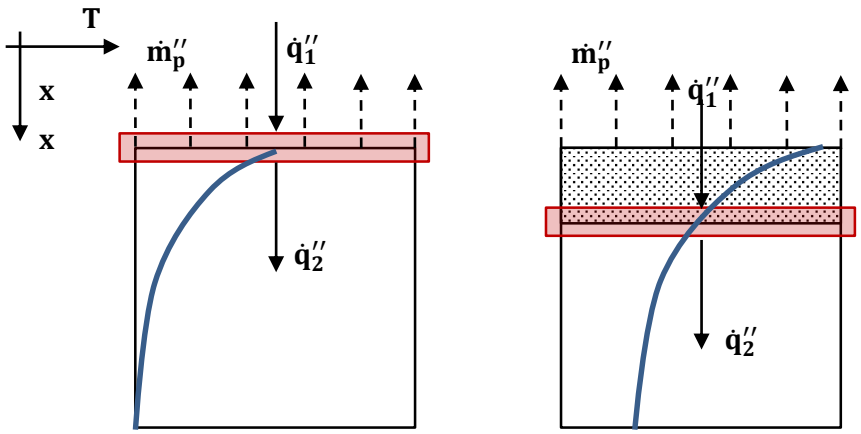

Figure 5.27. Thermal profile and pyrolysis front evolution for a charring material

As an example, if the thermal gradient presented at top right of Figure 5.26 is considered and is assumed that the pyrolysis temperature is given by 300°C, the history of the pyrolysis front position can be correlated. This is presented in Figure 5.28, together with the time history of the net energy at the pyrolysis front. Since the enthalpy of gasification can be assumed to be constant, the pyrolysis rate and therefore HRR should be proportional to the net energy at the pyrolysis front. This is observed to decrease exponentially and is consistent with the behaviour observed by PIR.

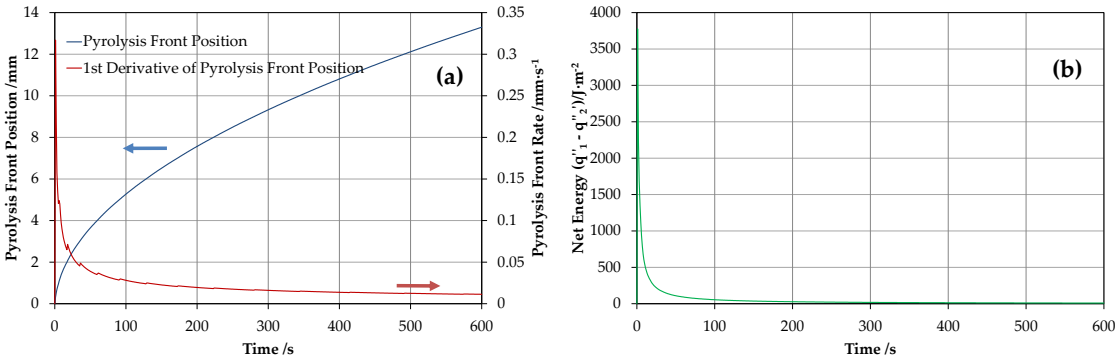

Figure 5.28. (a) Time history of pyrolysis front position and (b) net energy at the front

Flaming would proceed until a critical value of the flow of pyrolysates is achieved. This was originally proposed by *Rasbash* [17, 18], and expressed by the following expression:

$$(\phi \cdot \Delta H_c - L_v) \cdot \dot{m}''_{cr} + \dot{q}''_e - \dot{q}''_L = S \qquad (5.21)$$

where ϕ is a parameter related to the flammability of the pyrolysis gases, ΔH_c is the heat of combustion of the material, L_v is the heat of gasification, $\dot{q}''_e$ is the external heat flux, $\dot{q}''_L$ is the heat losses and S represents the energy balance. If $S \geq 0$ sustained flaming is achieved, while if $S < 0$, extinction of flames is obtained.

It should be noted that for this assessment, the char is assumed to remain unaffected. However, it has been experimentally observed that the char oxidation for PIR and PF is very significant, which plays an important role on the performance of

the material. Indeed, pyrolysis rates are expected to be larger as the char layer gets consumed.

Characterisation of the pyrolysis rates requires information regarding the time history of the in-depth temperature profile in the solid. This quantification is investigated in Chapters 6 and 7.

5.5.4 Uncertainties on heat release rate and effective heat of combustion calculations

Main sources of systematic errors related to the calculation of HRR by species analyses rely on three main parameters: mass flow in the exhaust, molar fractions for O_2 and CO_2, and energy coefficients.

Estimation of mass flow and measurements of molar fractions are errors related to the equipment, while the energy coefficients are related to the material properties. Due to the uncertainty of the chemistry of the material, the latter is considered as the main source of error. *Biteau* [7] summarised a variety of calculated energy coefficients for OC and CDG calorimetry from work developed by *Huggett* [12], *Babrauskas* [19], *Walters et al.* [20], *Janssens* [21]and *Tewarson* [9]. From this study, standard deviations of 1.86 $kJ \cdot g^{-1}$ and 2.17 $kJ \cdot g^{-1}$ were found for E_{O_2} and E_{CO_2}respectively, which corresponds to an error approximately from 14% to 17% in the HRR.

As noted by *Biteau*, if the chemistry of the material is unknown, a good evaluation of the right calorimetry can be assessed by comparing HRR curves obtained by OC and CDG. Figure 5.29 presents this evaluation for a PIR test, including error bars, which represent the standard deviation in the energy coefficients mentioned before. HRR based on OC is slightly larger than CDG, but within the uncertainty given by the quantification of the energy coefficient. Figure 5.29 also shows the effect that *drierite*® has on calorimetry based on CDG, smoothing the first peak of HRR after ignition.

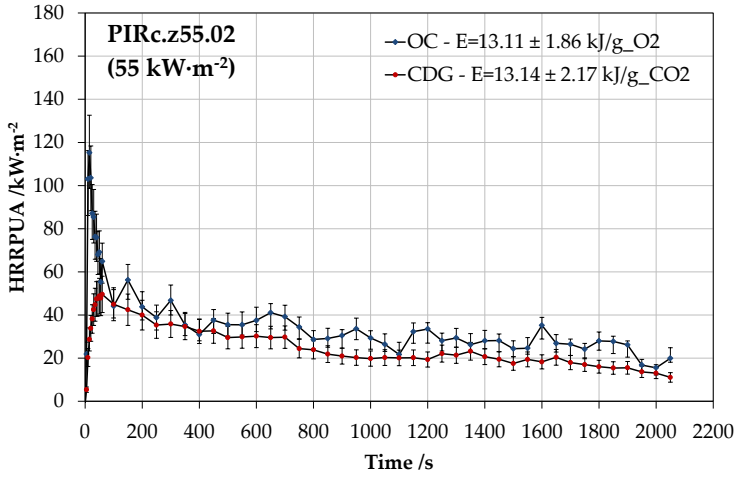

Figure 5.29. HRR based on OC and CDG for sample PIRc.z55.02. Error bars indicate the standard deviation of the energy coefficient given by *Biteau* [7]

5.5.5 Correlation with DTG analyses – critical temperature selection

Values of ignition temperature are compared to the peaks of mass loss rate from thermogravimetric analyses in Figure 5.30. In general, good correlations are found between the calculated ignition temperature and the range of temperatures where the main peak of pyrolysis were identified for any material. PIRa and PIRb ignition temperatures match very well the DTG data. On the contrary, PIRc ignition temperature seems to have been overestimated in comparison with the DTG data. PF ignition temperature is found to match well with the first peak observed in the DTG data, corresponding to the main DTG peak for nitrogen analyses shown in previous chapter. EPS ignition temperature is also in good agreement with the range of temperatures observed for the peak of mass loss by DTG analyses, despite the repeatability of these was found to be poor.

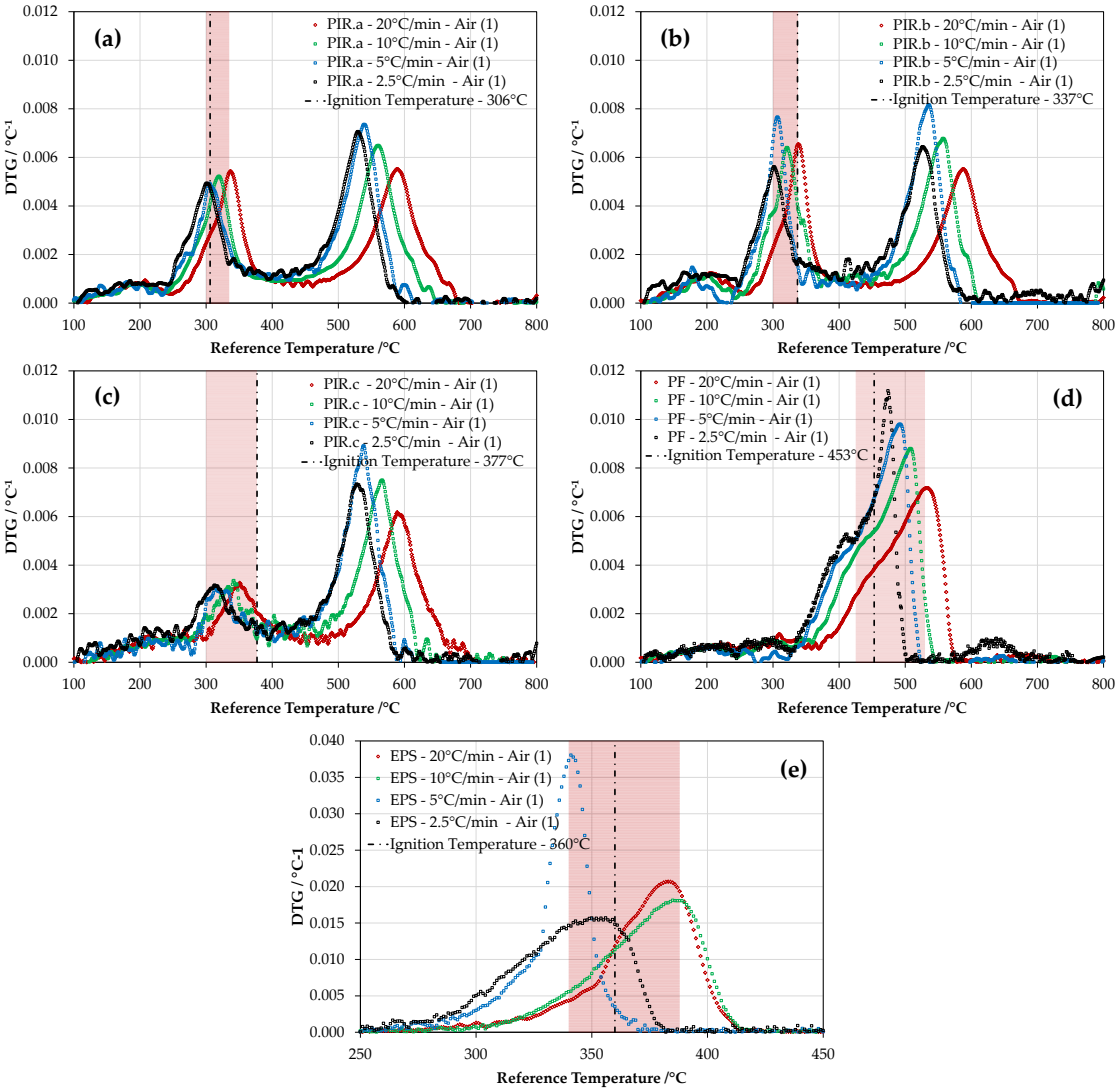

Figure 5.30. DTG for (a) PIRa (b) PIRb (c) PIRb (c) PIRc (d) PF (e) EPS. Red shading indicates region for peaks of mass loss rate in thermal analysis. Calculated ignition temperature noted as a dashed line

Flammability experiments have provided a series of ignition temperatures for rigid plastic that are indicative of the likely critical temperature representative of the pyrolysis onset hazard. The obtained ignition temperature represents an estimation of the *firepoint*, i.e. the point at which the mass flux of pyrolysis gases provides sufficient heat for the flame to survive (i.e. reach a critical Damköhler number) [22].

Nevertheless, the critical temperature, which is indicative of the maximum rate of gasification from the solid-phase, must necessarily be lower than the calculated ignition temperature. This is due to the fact that the latter incorporates the assumption of reaching the flammability limits, which depend on the mixing conditions. Then, an assessment of the temperature of maximum gasification is necessary, which can be achieved by evaluating the differential form of the thermogravimetric results presented above.

Despite the fact that the peak temperature in DTG does not directly indicate a property of the specific decomposition reaction, since it tends to shift to higher temperatures at higher heating rates, it can be used to define the critical temperature. Indeed, if a sufficiently low heating rate is chosen, the peak temperature in DTG then provides a conservative value of temperature with the highest rate of mass loss. The three different PIR foams have shown different pyrolysis behaviour, with PIRc showing a larger ignition temperature. However, a conservative generic value of the critical temperature may be indicated by 300°C, while the proposed conservative critical temperature for PF is 425°C. Expanded polystyrene, however, requires a special consideration due to its melting behaviour. Although a value of 330°C has been identified as the main peak of DTG in Figure 5.30, considering this temperature would not be conservative. Indeed, while the hazard from rigid foams such as PIR and PF is represented by the direct pyrolysis without experiencing melting (solid→ gas), the hazard from EPS is represented by the melt prior to pyrolysis (solid→melt→ gas), which could transport to the compartment. Therefore, a conservative critical temperature for EPS can be represented by its melting point. Unfortunately values of melting point could not be measured by the proposed experimental programme; thus, a value of 240°C given by Wunsch [23] is proposed.

Data obtained from thermogravimetric analyses also provides valuable information in conjunction with the performance observed in the Cone Calorimeter tests. As noted before, PIR is more prone to ignite than PF. This is reflected by an earlier peak in the DTG PIR curves. PF however shows faster deterioration than PIR, which is in agreement with the comparison between DTG curves from PIR and PF. Indeed, the oxidation of PIR char proceeds at temperatures higher than 500°C, while PF char's oxidation occurs right after the main peak of pyrolysis at 425°C. This behaviour explains the behaviour of PIR showing lower HRR and mass loss rate than PF after ignition and peak of HRR.

5.6 Concluding remarks

A robust analysis on flammability and combustibility of three types of isocyanurate-based polyurethane foam, phenolic foam, expanded polystyrene and stone wool is presented.

Material properties such as ignition temperature and thermal inertia are obtained by application of classic flammability theories for solids. The range of piloted ignition temperatures found for the different types of PIR is 306-377°C, while PF piloted ignition was estimated at 453°C. The range of ignition temperature of EPS was estimated between 306-389°C. SW did not ignite for any heat exposure. Discrepancy is found in the quantification of thermal inertia when using two of the regression models based on the direct solution for the surface temperature of the infinite plate. Better agreement is found between manufacturer's data and the regression that assumes $t_p/t_c \rightarrow \infty$, which is found to provide better fitting for low thermal inertia materials. The proposed method for assessing thermal inertia has provided a good agreement with the latter regression. Nominal values obtained from this assessment are 4500, 6500, 5500 and 4500 $W^2 \cdot s \cdot K^{-2} \cdot m^{-4}$ for PIRa, PIRb, PIRc and PF respectively. The proposed method for assessing thermal inertia is found to provide a good agreement with the regression

Burning dynamics of PIR and PF are characterised by an initial fast ignition, followed by flaming, sporadic flaming at edges, flame extinguishment and smouldering combustion from the produced char. Different mechanisms of combustion have been observed to occur simultaneously. EPS is characterised by fast shrinkage, followed by melting and eventual flaming combustion from a thermally thin film.

Reduction of HRR and subsequent flame extinguishment has been observed for bench-scale tests due to achievement of a critical mass flux of pyrolysates. Nevertheless, an evaluation of the total rate of pyrolysates is vital in a large-scale for certainty in the evaluation of HRR contribution. If the rate of the generation of pyrolysates and rate of char regression needs to be assessed for charring insulation materials such as PIR and PF, understanding on the time history of the in-depth thermal profile is necessary.

Future work needs to be focussed on the extension of the flammability assessment of the generated pyrolysates by the insulation material once reached the main pyrolysis temperature. Ignition theories based on the generation of a critical mass loss rate and concentration of volatiles for ignition seems a promising step towards this objective.

Critical temperature for the methodology reported in Chapter 3 can be assumed as the main peak of pyrolysis obtained by thermogravimetry for materials that do not melt such as PIR and PF, and the melting point for materials such as EPS. Conservative values suggested for PIR, PF and EPS are 300°C, 425°C and 240°C.

5.7 References

[1] "BS 476-15, ISO 5660. Fire tests on building materials and structures. Method for measuring the rate of heat release of products." BSI, 1993.

[2] "ASTM E2058. Standard Test Methods for Measurement of Synthetic Polymer Material Flammability Using a Fire Propagation Apparatus (FPA)." ASTM International, West Conshohocken, PA, 2009.

[3] A. Q. Maani, "Effects of Oxygen Concentration on the Smouldering Combustion of the Rigid PIR Insulation Material (M.Sc. thesis)," The University of Edinburgh, 2013.

[4] M. Janssens, J. Kimble, and D. Murphy, "Computer tools to determine material properties for fire growth modeling from cone calorimeter data," in *Fire and Materials. 8th International Conference8th International Conference*, 2003, pp. 377–387.

[5] R. T. Long, J. L. Torero, J. G. Quintiere, and A. C. Fernandez-Pello, "Scale and transport considerations on piloted ignition of PMMA," in *Sixth International Symposium on Fire Safety Science*, 1999, pp. 567–578.

[6] J. R. Lloyd and W. R. Moran, "Natural Convection Adjacent to Horizontal Surface of Various Planforms," *Journal of Heat Transfer*, vol. 96, no. 4. p. 443, 1974.

[7] H. Biteau, "Thermal and chemical behaviour of an energetic material and a heat release rate (Ph.D. thesis)," The University of Edinburgh. http://hdl.handle.net/1842/4620, 2009.

[8] W. M. Thornton, "The relation of oxygen to the heat of combustion of organic compounds," *Philosophical Magazine Series*, vol. 33, pp. 196–203, 1917.

[9] A. Tewarson, "Generation of Heat and Chemical Compounds in Fires," in *SFPE Handbook of Fire Protection Engineering*, 3rd ed., P. J. DiNenno, D. Drysdale, C. L. Beyler, W. D. Walton, R. L. P. Custer, and J. M. Watts, Eds. Massachusetts, U.S.A.: National Fire Protection Association, 2002.

[10] M. L. Janssens, "Measuring rate of heat release by oxygen consumption," *Fire Technology*, vol. 27, no. 3, pp. 234–249, 1991.

[11] T. Steinhaus, "Determination of Intrinsic Material Flammability Properties from Material Tests assisted by Numerical Modelling (Ph.D. thesis)," The University of Edinburgh. http://hdl.handle.net/1842/3273, 2010.

[12] C. Huggett, "Estimation of rate of heat release by means of oxygen consumption measurements," *Fire and Materials*, vol. 4, no. 2, pp. 61–65, 1980.

[13] D. Drysdale, "Heat Transfer," in *An Introduction to Fire Dynamics*, John Wiley & Sons, Ltd, 2011, pp. 35–82.

[14] L. Ma and R. Mitchell, "Modeling char oxidation behavior under Zone II burning conditions at elevated pressures," *Combustion and Flame*, vol. 156, pp. 37–50, 2009.

[15] S. R. Wasan, P. Rauwoens, J. Vierendeels, and B. Merci, "An enthalpy-based pyrolysis model for charring and non-charring materials in case of fire," *Combustion and Flame*, vol. 157, no. 4, pp. 715–734, 2010.

[16] S. R. Wasan, P. Rauwoens, J. Vierendeels, and B. Merci, "Application of a simple enthalpy-based pyrolysis model in numerical simulations of pyrolysis of charring materials," *Fire and Materials*, vol. 34, no. 1, pp. 39–54, 2010.

[17] D. J. Rasbash, "Relevance of firepoint theory to the assessment of fire behaviour of combustible materials," *International Symposium on Fire Safety of Combustible Materials*, pp. 169–178, 1975.

[18] D. J. Rasbash, "Theory in the evaluation of fire properties of combustible materials," *Proceedings of the 5th International Fire Protection Seminar (Karlsruhe, September)*, pp. 113–130, 1976.

[19] V. Babrauskas, "Related Quantities: (a) Heat of Combustion and Potential Heat," in *Heat Release in Fires*, V. Babrauskas and S. J. Grayson, Eds. New York: Elsevier Applied Science, 1992, pp. 207–223.

[20] R. N. Walters, S. M. Hackett, and R. E. Lyon, "Heats of combustion of high temperature polymers," *Fire and Materials*, vol. 24, pp. 245–252, 2000.

[21] M. Janssens and W. J. Parker, "Oxygen Consumption Calorimetry," *Heat Release in Fires, edited by V. Babrauskas and S.J. Grayson*, vol. Chapter 3, pp. 31–59, 1992.

[22] J. L. Torero, "Flaming ignition of solid fuels," in *SFPE Handbook of Fire Protection Engineering*, 4th ed., P. J. DiNenno, D. Drysdale, C. L. Beyler, W. D. Walton, R. L. P. Custer, and J. M. Watts, Eds. Massachusetts, U.S.A.: National Fire Protection Association, 2008.

[23] J. R. Wunsch, *Polystyrene – Synthesis, Production and Applications*. iSmithers Rapra Publishing, 2000, p. 15.

Chapter 6.

Assessment and Characterisation of the Thermal Evolution of Insulation Materials

6.1 Introduction

A non-dimensional thermal analysis defining the different thermal degradation reactions for the studied materials was presented in Chapter 4. The definition of these processes is obtained by simplifying the heat transfer phenomenon by reducing the size of the sample, so as a null thermal gradient could be assumed. Nevertheless, the extrapolation of these processes to real scale is not straightforward since the heating rates rarely represent real exposures and thus the heat transfer problem must be resolved.

In the previous chapter, a qualitative analysis on the performance of insulation materials when exposed to different conditions of heat was presented. This performance was evaluated in terms of flammability and calorimetry by analysing external variables to the solid-phase such as time-to-ignition, gas species and mass loss. However, the different thermal degradation processes in the solid-phase must be understood from an energy balance perspective. Indeed, if the performance of the insulation material is to be quantified, prediction of its thermal evolution is required, which is critical for the application of the design methodology presented in Chapter 3. This implies the solution of the heat transfer equation and determination of thermal properties that provide reasonable prediction for known heat exposures. This is however a difficult task since quantification of variables such as thermal conductivity and specific heat capacity cannot be measured directly.

In order to address this problem, a similar experimental approach to the previous chapter is presented in the following sections, including multiple temperature measurements in the solid-phase. Two series of experiments are carried out under the framework of the Cone Calorimeter [1], with the first one corresponding to bench-scale tests where samples are directly exposed to a radiant heat source without pilot igniter. For the second series of experiments, a different approach is followed for the transfer of heat. A thin metallic plate, exposed to the radiant heat and in contact with the sample, is used to transfer the heat to the sample by conduction. Temperature measurements are taken within the core of the samples and the thermal degradation is studied in relation to the thermal profile experienced by the samples.

Subsequently, the heat transfer formulation of the problem related to the experimental work undertaken is presented together with a numerical method for its solution. This is based on the application of an implicit and numerically stable finite difference method to solve the one-dimensional conduction heat equation. An inverse heat transfer model is then proposed for the determination of the thermal properties of the material under inert conditions, i.e. previous to the onset of thermal degradation reactions. Equivalent thermal properties after the onset of thermal degradation processes are explored.

6.2 Aim

The aim of this chapter is to assess and characterise the thermal evolution of insulation materials when exposed to severe conditions of heat exposure. In order to achieve this aim, the following goals are pursued:

- **Mapping of the thermal degradation processes in relation to temperature measurements within the solid-phase.** The evolution of the thermal profile experienced by the material determines its thermal degradation dynamics, which is correlated to results obtained by thermogravimetric analyses.
- **Determination of thermal properties for a simplified heat transfer model based on the conduction heat equation.** Characterisation of the time-history of the thermal profile for known heat exposures requires the introduction of modelling techniques able to predict its evolution. The design methodology proposed in Chapter 3 requires the definition of thermal properties before the onset of thermal degradation. However, the quantification of pyrolysis rates also requires the determination of equivalent thermal properties once this process is achieved.

6.3 Experimental set-up

6.3.1 Heat transferred by radiation

The materials selected for these experiments are stone wool (SW), phenolic foam (PF), expanded polystyrene (EPS) and three types of isocyanurate-based foams (PIR). Similarly to Chapter 5, samples with a surface area of 9 cm by 9 cm and 100 mm thick are tested.

The samples are wrapped with aluminium foil at bottom and lateral sides, with a 6 mm nickel 200 block at the bottom, and altogether wrapped in two 3 mm thick layers of ceramic insulation paper. As noted in the previous chapter, the aluminium foil is mainly used to prevent the air penetration in the sample from the sides and only allow it from the top. From a heat transfer perspective, the foil is transparent for the conducted heat due to its low thickness and high thermal diffusivity, thus acting as a thermally thin material. The two layers of ceramic paper are used in order to reduce the thermal gradient on the surface of the sample sides. It should be noted that an adiabatic boundary condition at the sides will always be unattainable with this set-up since the conductivity of the ceramic paper is higher than the materials tested[11]. The layers of ceramic paper also allow testing all materials under the same conditions, which is necessary especially for materials that shrink and melt like EPS.

A convenient procedure to characterise the thermal losses at the exposed surface is to test the samples vertically (as noted in Appendix A). However, in the previous chapter it was necessary to use a horizontal positioning since EPS melts and comparative results between materials were aimed. Therefore, the same positioning

[11] Thermal conductivity of ceramic paper: 0.08 and 0.11 $W \cdot m^{-1} \cdot K^{-1}$ at 600 and 800°C, respectively.

is used here. A horizontal set-up is also found to be more practical than the vertical due to the difficulty of keeping the sample with thermocouples stable on the load cell. This is because of the significant difference of weight between the metallic block and the sample. A schematic drawing of the set-up and real set-up are shown in Figure 6.1 and Figure 6.2.

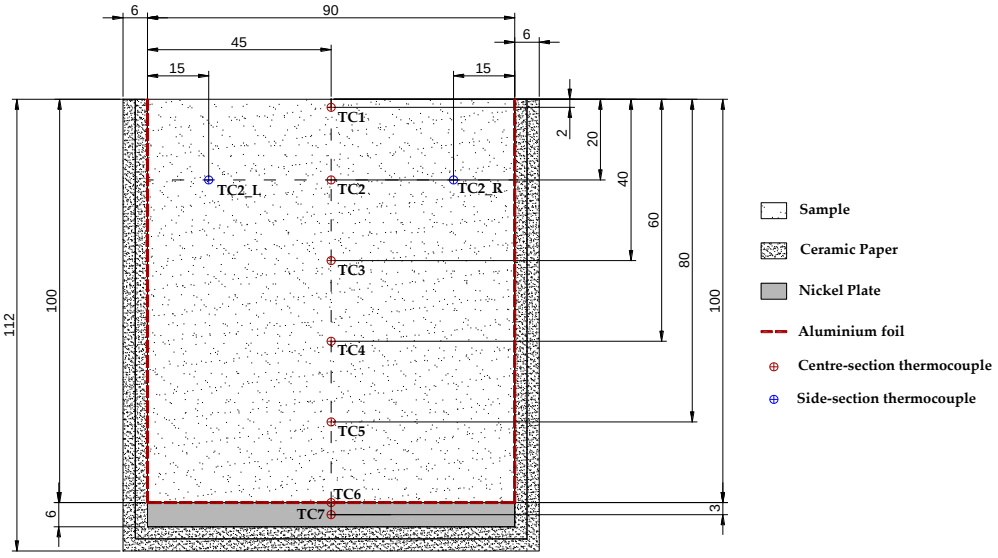

Figure 6.1. Schematics of sample preparation

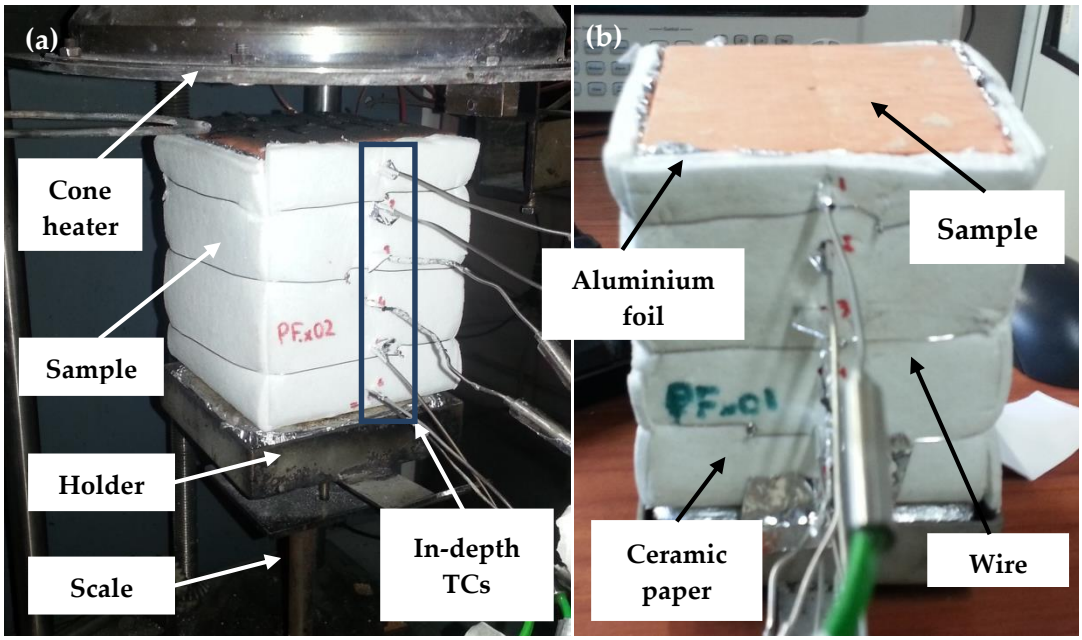

Figure 6.2. (a) Sample during testing (b) Sample prepared before testing

The characterisation of the boundary condition at the back face of the material is achieved by using the 6 mm Nickel 200 plate at the bottom of the samples. This approach is described by *Carvel et al.* [2] who recommend the use of a heat sink for material characterisation purposes.

As for the boundary condition at the exposed surface, several values of external heat flux from the radiant heater are used. The used heat fluxes are selected in such a way that mapping of the different thermal degradation processes is highlighted. The minimum heat flux for each material is selected to be a thermal exposure that does not trigger the onset of the thermal degradation. Specific values of external heat flux for each material are noted in Table 6.1.

Experiments are repeated at least twice in order to verify repeatability of the results. Additionally, for foamy materials such as PIR and PF, the tests are repeated for different configurations of the exposed surface. These materials are normally manufactured and installed in buildings within two layers of aluminium protective paper. As highlighted in the previous chapter, this boundary is expected to offer a different thermal performance when tested by radiative heaters. Therefore, tests are performed for three different configurations: with no protective layer, with a non-colourful and a colourful[12] protective layer attached to the surface.

Measurements of temperature are taken within the sample by using 1.5 mm bead K-type thermocouples. The temperature of the metallic plate at the back is also measured. Thermocouples are installed at the centre of the section and every 2 mm in-depth and in parallel to the exposed surface so the error in the thermocouple measurement is reduced, which is recommended for materials of particularly low conductivity [3, 4]. The first thermocouple is placed within a range of 2-3 mm from the surface. No temperature correction is considered by the heat losses introduced by the thermocouple. Additionally, two thermocouples are inserted 3 cm horizontally off the second in-depth thermocouple for some experiments. This procedure aims to clarify whether the heat transfer through the sample is behaving either one-dimensionally or two-dimensionally. The positioning of the thermocouples is shown in Figure 6.1. A summary of the conditions for all the performed experiments is presented in Table 6.1.

[12] The protective layer attached to the foam normally includes regions with a colourful logo of the manufacturer.

Table 6.1. List of performed experiments

Material	Configuration	Incident radiative heat flux range /kW·m^{-2}	Measured parameters
PIRa Manufacturer-claimed density: 31 - 34 kg/m^3 Average measured density: 31.2 ± 0.61 kg/m^3	**Nominal sample size:** 90 mm x 90 mm x 100 mm **Exposed surface:** (a) With protective layer (non-colourful) (b) With protective layer (colourful) (c) Without protective layer **Wrapping:** 2 layers of ceramic paper + 1 layer of aluminium foil **Back boundary condition:** Nickel 200 plate (6 mm) + Ceramic board (25 mm) **Orientation:** Horizontal **Pilot:** No pilot igniter	10, 25, 35 (2 repetitions)	(1) In-depth temperature (2) O_2, CO_2 and CO gas species (3) Mass loss
PIRb Manufacturer-claimed density: 32 kg/m^3 Average measured density: 33.0 ± 0.71 kg/m^3		5, 10, 25, 35 (2 repetitions)	
PIRc Manufacturer-claimed density: 30 - 32 kg/m^3 Average measured density: 33.5 ± 0.65 kg/m^3		5, 10, 25, 35 (2 repetitions)	
PF Manufacturer-claimed density: 35 kg/m^3 Average measured density: 38.1 ± 1.05 kg/m^3		5, 10, 15, 25 (2 repetitions)	
EPS Manufacturer-claimed density: 10 kg/m^3 Average measured density: 10.4 ± 0.2 kg/m^3	**Nominal sample size:** 90 mm x 90 mm x 100 mm **Exposed surface:** No protective layer **Wrapping:** 2 layers of ceramic paper + 1 layer of aluminium foil **Back boundary condition:** Nickel 200 plate (6 mm) + Ceramic board (25 mm) **Orientation:** Horizontal **Pilot:** No pilot igniter	2, 4, 10 (2 repetitions)	
SW Manufacturer-claimed density: 45 kg/m^3 Average measured density: 33.1 ± 1.91 kg/m^3		10, 25, 40, 60 (2 repetitions)	

6.3.2 Heat transferred by conduction by using metallic plate

For these series of experiments the used set-up is similar to the one described in the previous section. The only modification included is the use of a 6 mm thick Monel alloy 400 plate positioned on the surface of the tested sample. The temperature of the

plate is measured by inserting a thermocouple inside the plate. The plate is painted with a high temperature optical black coating of known absorptivity (α=0.92) from Medtherm Corporation®. A schematic drawing of this new set-up is represented in Figure 6.3 below.

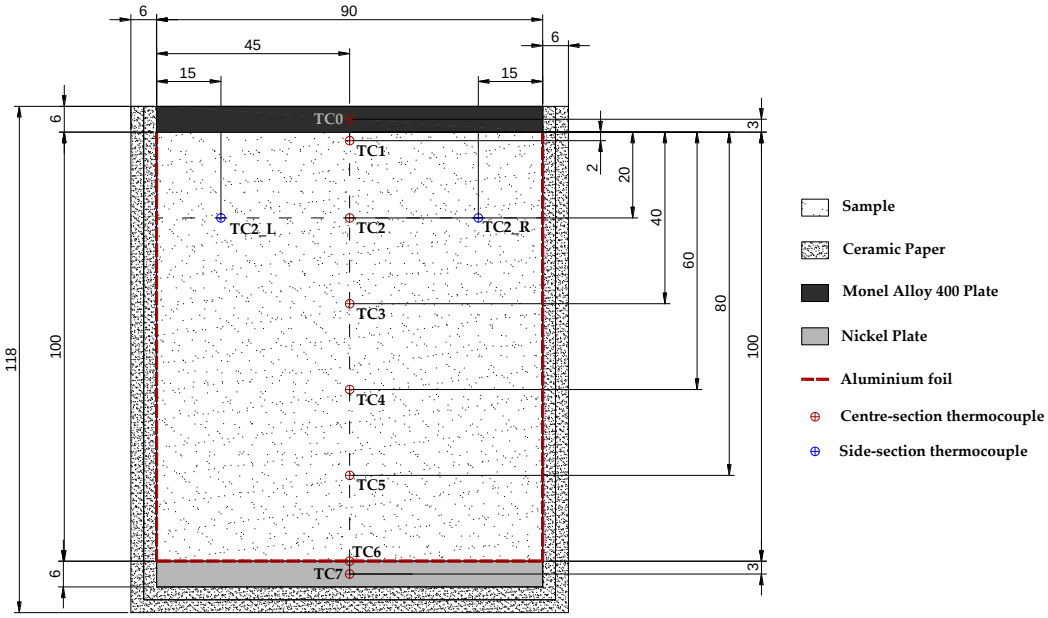

Figure 6.3. Sample design for experiments where the heat is transferred by conduction

Additionally, 1 mm bead N-type thermocouples are used for measuring temperature within the sample in order to improve the readings [5]. Moreover, rigid ceramic tubes are used as holder for the thermocouples to reduce the error in the positioning. This feature is added since the thermocouples tend to bend when getting inserted in the insulation material. An illustration of this set-up is shown in Figure 6.4 below.

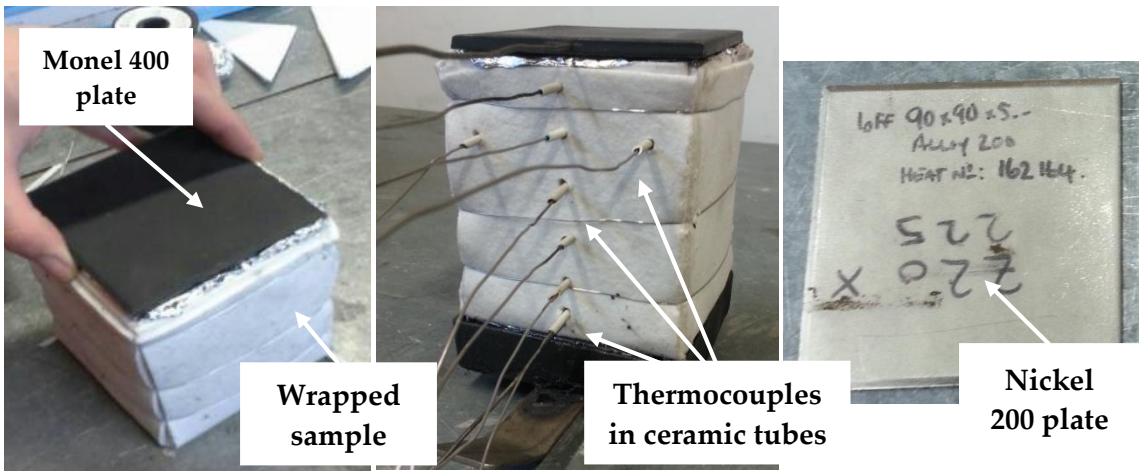

Figure 6.4. (a) Sample preparation (b) Thermocouples' distribution (c) Bottom plate

The use of the plate presents a case study representative of a common end-use condition of insulation materials, since these are rarely installed uncovered but

behind a lining. The oxidation rate is expected to be reduced or eliminated by using this methodology, therefore reducing the complexity for modelling purposes.

A summary of the experiments performed with this set-up is presented in Table 6.2 below. It should be noted that only rigid closed-cell insulation materials such as PIR and PF are tested. This methodology lies on the non-deformability of the material under certain period of the heating, which excludes EPS due to its shrinking behaviour and SW due to its flexibility.

Table 6.2. Summary of performed experiments

Material	Configuration	Incident radiative heat flux range /kW·m^{-2}	Measured parameters
PIRb	**Nominal sample size:** 90 mm x 90 mm x 100 mm **Top boundary condition:** Monel 400 plate (6 mm) + Ceramic board (25 mm) **Wrapping:** 2 layers of ceramic paper + 1 layer of aluminium foil **Back boundary condition:** Nickel 200 plate (6 mm) + Ceramic board (25 mm) **Orientation:** Horizontal **Pilot:** No pilot igniter	5, 25 (2 repetitions)	(1) In-depth temperature (2) O_2, CO_2 and CO gas species (3) Mass loss
PF			

6.4 Results

A large number of experiments has been performed for each of the materials being studied. Complete results from all experiments are not presented in this section, but only a selection of these in order to reach the objectives pursued. Extended results can be found in Appendix C.

The summary of results discussed herein consists of in-depth thermal profiles measured throughout the experiments, as well as visual observations and gas analyses in order to complement the temperature measurements. It should be noted that despite mass loss is measured, results are erratic due to the use of thermocouples. Visual observations mainly focus in assessing the thickness that experiences material degradation, indicated by discolouration from the virgin material. This is achieved by cutting a section of the sample through the vertical centre-line after the experiment. This technique also provides more accurate information about the thermocouple positioning[13]. Gas analyses based on carbon monoxide and carbon dioxide species qualitatively indicate the dynamics of the thermal degradation processes, i.e. whether

[13] Since insulation materials are soft, precise thermocouple insertion is a tricky task. Thermocouple wires tend to bend and displace from ideal location during the insertion.

oxidation has started and by which mechanism it is dominated (solid-phase or gas-phase oxidation). The upper edge of the temperatures envelope is quantitatively compared to the discolouration from the section of the sample. Change of discolouration from degradation is correlated to interpolated values of temperature from the thermal gradient within the solid, which are compared to thermogravimetric analyses.

6.4.1 Isocyanurate-based polyurethane foam (PIR)

Figure 6.5 shows the time history of the in-depth temperature profile for PIRa experiments tested at 10 $kW \cdot m^{-2}$ with (Figure 6.5a) and without (Figure 6.5b) protective layer at the surface. The in-depth temperature profile is presented for a series of time steps during the test (i.e. from 0 to 10 minutes using a time step of 2.50 minutes and from 10 to 30 minutes using a time step of 5 minutes). Vertical error bars show the standard deviation from two repetitions for each thermocouple position. Horizontal error bars indicate the estimated error in the thermocouple positioning. Figure 6.5a shows good repeatability in the experiments, while Figure 6.5b presents worse repeatability, especially for temperature measurements near the surface. This is attributed to the non-uniform thermocouple positioning for repeated experiments, which has larger impact for measurements near the surface due to low conductivity of the tested material.

Figure 6.5a shows a case study where no thermal degradation is observed. Temperature close to the surface achieves a quasi-steady state in early stages (from 2.5 minutes), with a maximum value of 123°C ± 4°C. The temperature profile achieves a quasi-steady state after 20-25 minutes, with a minor rate of temperature increase (<1°C·min^{-1}) for inner positions. The displacement of the thermal gradient towards higher temperatures for inner positions and with steady temperature at the surface is due to the back boundary layer; the metallic plate that is acting as a heat sink is slowly increasing temperature. Sample section in Figure 6.5a2 shows that no discolouration is produced in the foam and, consistently, no release of volatiles is observed during the tests.

Figure 6.5b presents a case study where thermal degradation is observed at the surface of the sample. Thermal gradients are significantly larger than those shown in Figure 6.5a, indicating the clear effect of the protective layer on the thermal performance. This is in agreement with the conclusions from the flammability and combustibility analysis presented in Chapter 5. Temperature close to the surface achieves a quasi-steady state after 5 minutes, with a maximum value of 323°C ± 20°C, while the temperature profile achieves a quasi-steady state after 20 minutes, with a minor rate of temperature increase (<1°C·min^{-1}) for inner positions. The sample section in Figure 6.5b2 shows three clear tonalities in the discolouration experienced by the sample. The discolouration is presented to be non-uniform, with higher degradation for regions near the centre-line than near the edge. This indicates that the heat transfer is not behaving perfectly in a one-dimensional regime. Some cracking is observed near the surface, where the discolouration is darker. Additionally, the

sample thickness appears to have increased by up to 1 cm. Significant release of volatiles was observed after 3-4 minutes, but with no ignition during the experiment. Measurements of carbon dioxide and carbon monoxide did not present noticeable concentrations compared to the start baseline, therefore these are not presented, which confirms that no significant oxidation was produced.

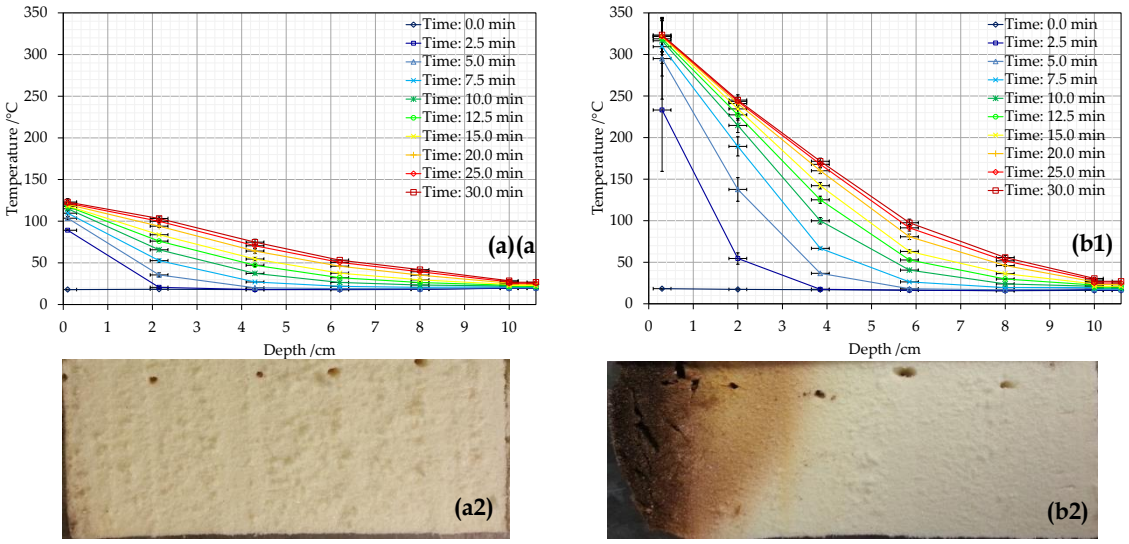

Figure 6.5. In-depth thermal profiles of PIRa at 10 kW·m^{-2} with (a1) and without protective layer (b1). Centre-section for the end of the tests (a2, b2) Horizontal error bars: estimated error of ±2mm in thermocouple positioning Vertical error bars: standard deviation between two repeated tests

Figure 6.6 shows the in-depth temperature profiles for PIRa experiments tested at 25 kW·m^{-2} with (Figure 6.6a) and without (Figure 6.6b) protective layer at the surface. Figure 6.6a shows good repeatability, with vertical error bars being noticeable only for the surface thermocouple. Figure 6.6b however presents worse repeatability, with the error bars being significantly larger for the three first thermocouples. This non-uniformity is attributed to the positioning and, more importantly, to the degradation processes forming cracks within the sample and likely different rate of surface oxidation. Significant differences are observed between the performance of the samples with and without protective layer, which is attributed to the effect that the protective layer has on the absorption of radiation due to its low emissivity and the blocking of air from contact with the surface.

Figure 6.6a presents a case study where small thermal degradation is observed. The temperature close to the surface achieves a quasi-steady state after 2.5-5 minutes, with a maximum value of 252°C ± 5°C, while the temperature gradient achieves a quasi-steady state after 30 minutes, with a minor rate of temperature increase (<0.5°C·min^{-1}) for inner positions. As noted previously, the slight displacement of the thermal gradient towards higher temperatures at inner positions is due to the back boundary condition. Two different tonalities are observed in the sample section, which seem to be uniform between the edge and the centre-line. This indicates that the heat transfer can be considered as a one-dimensional regime. Small cracks are observed near the surface. Darker tonalities are observed near the edge of the surface,

where the foil ends, which might be indicative of an edge effect with lower cooling, therefore presenting higher temperatures. Measurements of carbon dioxide and carbon monoxide did not show concentrations displaced from baseline, confirming no oxidation occurred. The sample appears to have slightly expanded by up to 0.3 cm.

Figure 6.6b shows a case study where severe thermal degradation is observed. Temperature close to the surface achieves a maximum value of 591°C ± 34°C at 7.5 minutes. The lack of measurements from the first thermocouple for next time steps indicates its detachment from the solid due to consumption of the surrounding material. No steady state is observed for the thermal gradient during the last steps, with the temperature increasing with a rate of 9-10°C·min^{-1} for inner positions. This rate of temperature increase indicates the consumption of material at the surface, thus moving the exposed boundary to lower positions. Three to four tonalities can be observed in the sample section: yellow (virgin material), orange-brown discolouration, and black (char). Small cracks are observed between the interface of virgin material and orange discolouration, while a series of large cracks are observed in the brown region, before the char. A thickness regression of approximately 1.5 cm is observed, indicating large amount of material is consumed due to surface oxidation.

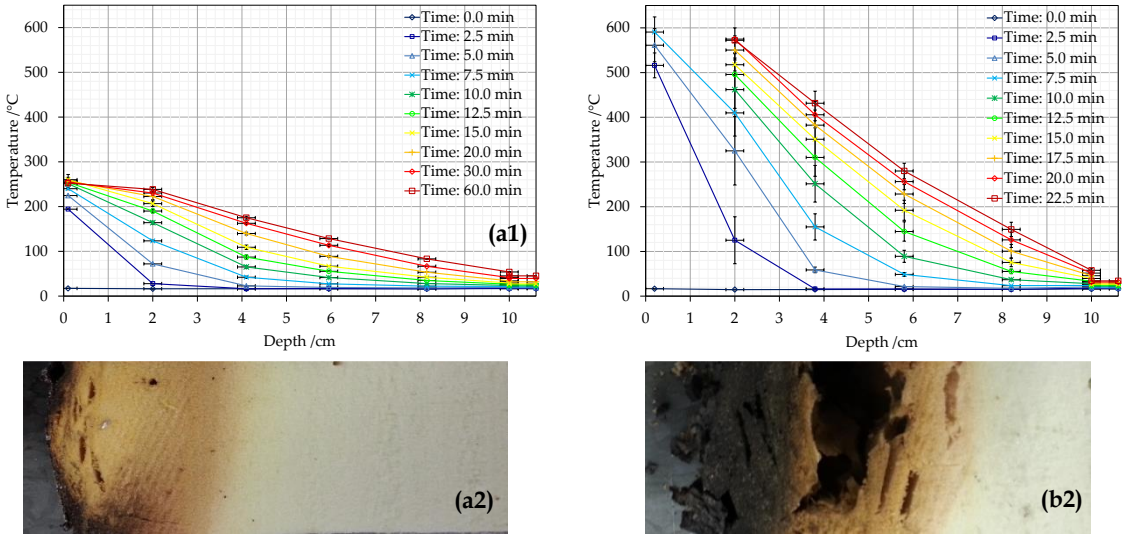

Figure 6.6. In-depth thermal profiles of PIRa at 25 kW·m^{-2} with (a1) and without protective layer (b1). Centre-section for the end of the tests (a2, b2)
Horizontal error bars: estimated error of ±2mm in thermocouple positioning
Vertical error bars: standard deviation between two repeated tests

Figure 6.7 shows the sample residue from different perspectives for the test presented in Figure 6.6b. The surface of the sample presents complex morphology characterised by craters formed by surface oxidation. It can be observed that the char at the edges and lateral sides of the sample presents a smooth morphology, indicating that oxidation has not taken place. This is consistent with the set-up that uses aluminium foil to prevent oxygen penetration through the sides, thus limiting oxidation to the top surface.

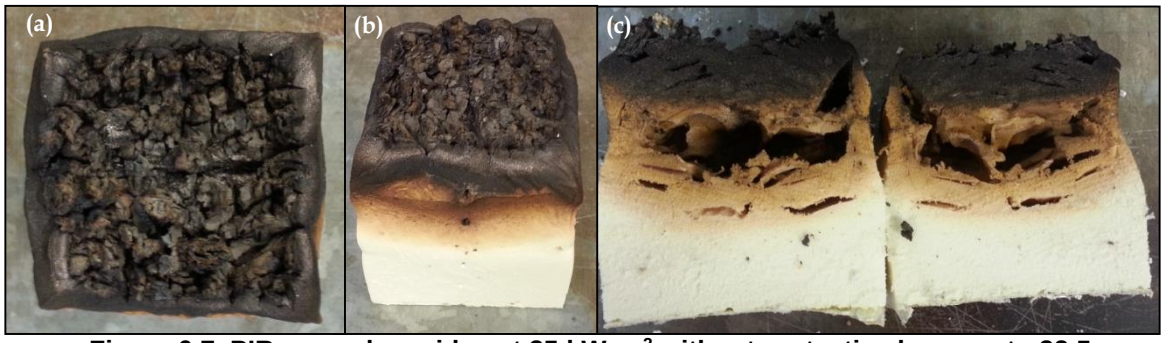

Figure 6.7. PIRa sample residue at 25 kW·m^{-2} without protective layer up to 22.5 minutes (a) Top view (b) Lateral view (c) Lateral view from section

Large amount of volatiles are released from the start of the test shown in Figure 6.6b and Figure 6.7, but ignition is not achieved. The release of volatiles continues to decrease after one minute. Measurements of carbon monoxide are presented in Figure 6.8a with the time-history of temperature measurements. The concentration of CO increases almost from the beginning, probably indicating generation of pyrolysates. The shape of CO curve changes slope from 2 to 3 minutes, when the CO generation remains approximately under a steady state during the rest of the test. A slight decrease between 10 and 15 minutes is also observed. These measurements are indicative of smouldering combustion (surface oxidation), with a high CO/CO_2 ratio between 0.8 and 1.2 as shown in Figure 6.8b. The concentration of CO_2 remains very low in comparison to the generation of CO_2 presented by flaming of PIR pyrolysates in Chapter 5. Additionally, it is shown that the smouldering is not self-sustained since the thermal gradient and CO generation drop significantly after removing the external heat source. This is due to the closed-cell structure of the foam that does not allow the free circulation of oxygen through the sample, limiting the oxidation to the top surface of the sample; therefore, the generation of heat being drastically reduced once the external heat source is removed.

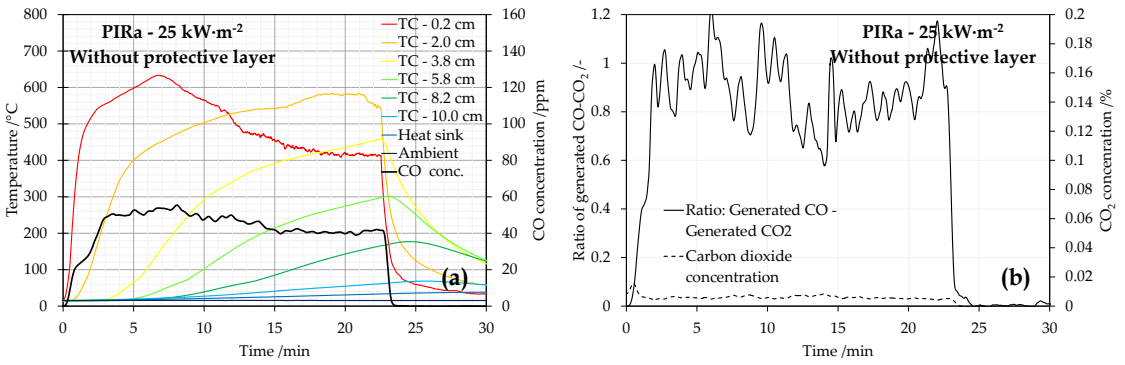

Figure 6.8. Time-history of temperatures within the solid-phase and CO concentration (a) and generated CO vs. generated CO_2 for PIRa with no protective layer at 25 kW·m^{-2}

A more severe case study is presented in Figure 6.9, corresponding to a PIRa sample tested at 35 kW·m^{-2} without protective layer. The sample auto-ignited after 5 seconds of heat exposure, introducing a different regime that was not observed previously. Figure 6.9a shows the time-history of temperatures within the solid-phase and the concentration of generated CO. Thermal evolution within the solid is similar

to Figure 6.8a, but with a faster heating rate. The generation of CO follows a different pattern due to flaming combustion, which is confirmed by the CO_2 concentration presented in Figure 6.8b. The CO/CO_2 ratio increases over time, indicating simultaneous flaming and smouldering. This is consistent with the behaviour presented in Chapter 5.

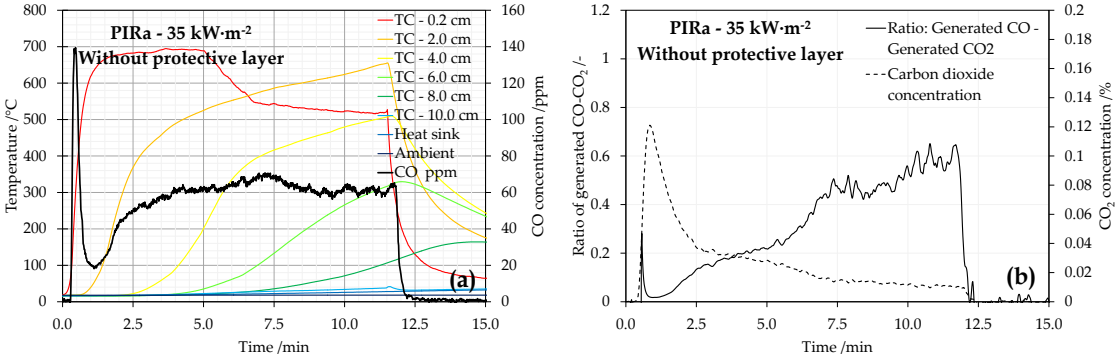

Figure 6.9. Time-history of temperatures within the solid-phase and CO concentration (a) and generated CO vs. generated CO_2 (b) for PIRa with no protective layer at 35 kW·m^{-2}

The behaviour from PIRb and PIRc foams is similar to the one presented above. The upper edge of the temperature envelopes for PIRa, PIRb and PIRc at 35 kW·m^{-2} is presented in Figure 6.10, with a section of the sample after the test. The temperature values are interpolated for the interface between the three main regions of discolouration (yellow, orange-brown and black). In general, the first interface is found between 220°C and 260°C, while the second interface is identified between 460°C and 520°C. The first set of temperatures is in agreement with the temperature before the onset of the main peak of pyrolysis observed in DTG analyses under nitrogen atmospheres in Chapter 4. The second set of temperatures corresponds to the temperature range in which no more significant pyrolysis is observed under nitrogen atmospheres. Maximum temperatures measured in the solid-phase in Figure 6.10 are near 700°C. TGA analyses showed that the full consumption of mass terminates below 600°C, which might indicate that the combustion of char is dominated by the diffusion of oxygen at the surface. However, further assessment is required to characterise the mechanisms that govern the combustion of this char.

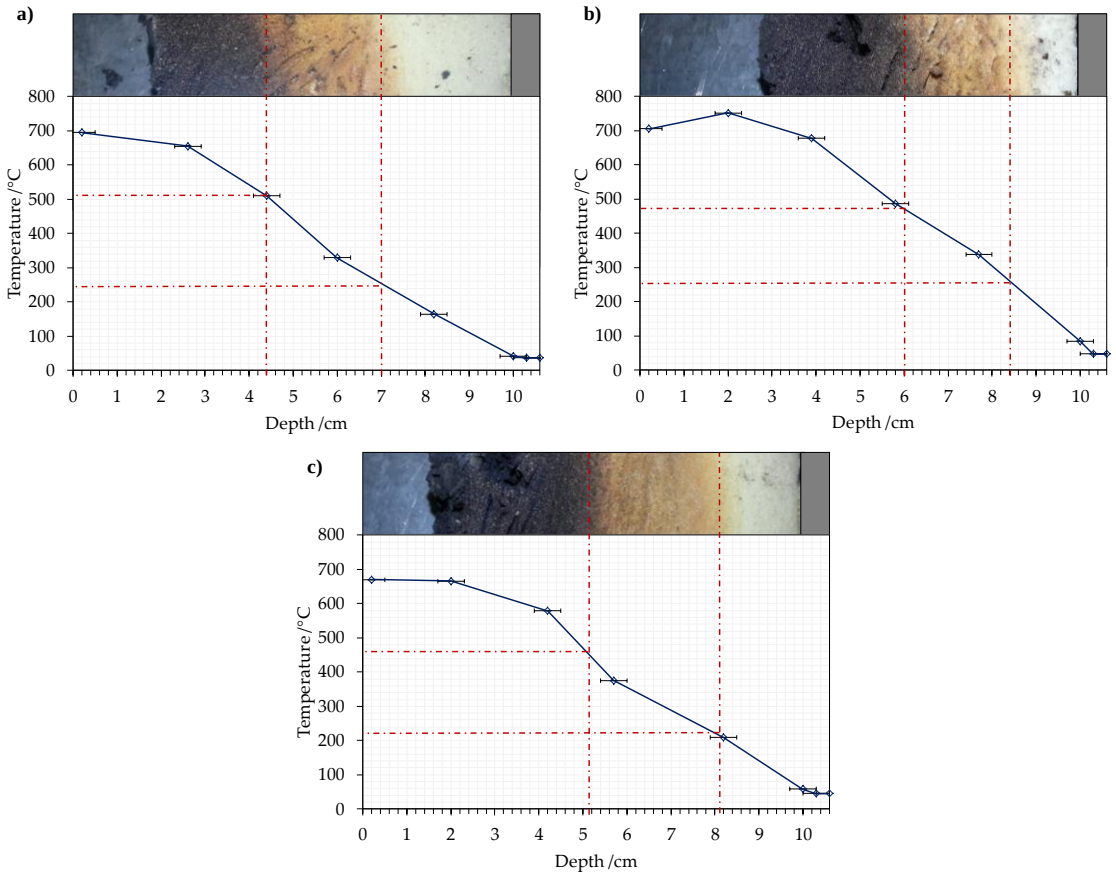

Figure 6.10. Maximum in-depth temperature profile of (a) PIRa, (b) PIRb and (c) PIRc at 35 kW·m^{-2} (no protective layer). Horizontal error bars: estimated error of ±2mm in thermocouple positioning

As a final remark, the ignition temperature obtained in Chapter 5 is compared to results observed in Figure 6.5b. The ignition temperature for PIRa was determined in the range 306°C ± 20°C, although it is found that the thermal degradation starts at lower temperatures. This supports the principle stating that ignition does not correspond to a specific value, but to a critical mass flow of pyrolysates from different layers at different temperature [6]. This approach however requires complex modelling tools. Indeed, a characteristic value of the surface temperature that represents the ignition hazard seems to be more appropriate from an engineering perspective, which is the approach suggested for the design methodology in Chapter 3.

6.4.2 Phenolic foam (PF)

Figure 6.11 shows the time history of the in-depth temperature profile for PF experiments tested at 10 kW·m^{-2} with (Figure 6.11a) and without (Figure 6.11b) protective layer at the surface. Figure 6.11a presents good repeatability in the experiments, while Figure 6.11b presents worse repeatability, especially for temperature measurements obtained by the two first thermocouples. This is attributed to the non-uniformity of the thermocouples positioning and especially to the thermal degradation observed, with char being detached from the surface.

Figure 6.11a presents a case study where no clear thermal degradation is observed. The temperature close to the surface achieves a quasi-steady state from 10 minutes, with a maximum value of 124°C ± 1°C. The temperature profile achieves a quasi-steady state from 15-20 minutes, with a minor rate of temperature increase (<1°C·min^{-1}) for inner positions. A change in the slope of the thermal profile is observed near the second thermocouple once the steady state is achieved. The sample section displayed in Figure 6.5a2 shows that some discolouration of a darker pink tonality is produced near the surface of the sample. Additionally, the sides and bottom of the section have different tonality than the centre, which indicates that material suffers from oxidation at ambient temperatures. No release of volatiles is observed during the tests.

Figure 6.11b presents a case study where clear thermal degradation is observed at the surface of the sample. Thermal gradients are significantly larger than the ones shown in Figure 6.11a, indicating again the clear effect of the protective layer on the thermal performance. The temperature close to the surface achieves a quasi-steady state after 10 minutes, with a maximum value of 296°C ± 44°C at this time step. The temperature profile achieves a quasi-steady state from 25 minutes, with a minor rate of temperature increase (<1°C·min^{-1}) for inner positions. The in-depth temperature profile during the steady state shows an interesting shape, with two different slopes converging at 78°C, indicating temperature dependency of the thermal properties or endothermic processes at lower temperatures. This is consistent with the change of slope observed in Figure 6.11a. Sample section in Figure 6.5b2 shows four clear tonalities in the discolouration experienced by the sample, which is non-uniform, with higher degradation for regions near the centre-line than near the edge. This indicates that the heat transfer is not behaving perfectly in a one-dimensional regime. Cracks and delamination is observed within the first 2 cm from the surface, in the char area, as shown in Figure 6.14. Delamination is probably due to spalling from the sample; popping and snapping sounds can be heard during the experiment. No significant surface regression or oxidation is observed, but measurements of carbon dioxide and carbon monoxide indicate low concentrations compared to the start baseline. This is indicative of minor oxidation from the delaminated pieces.

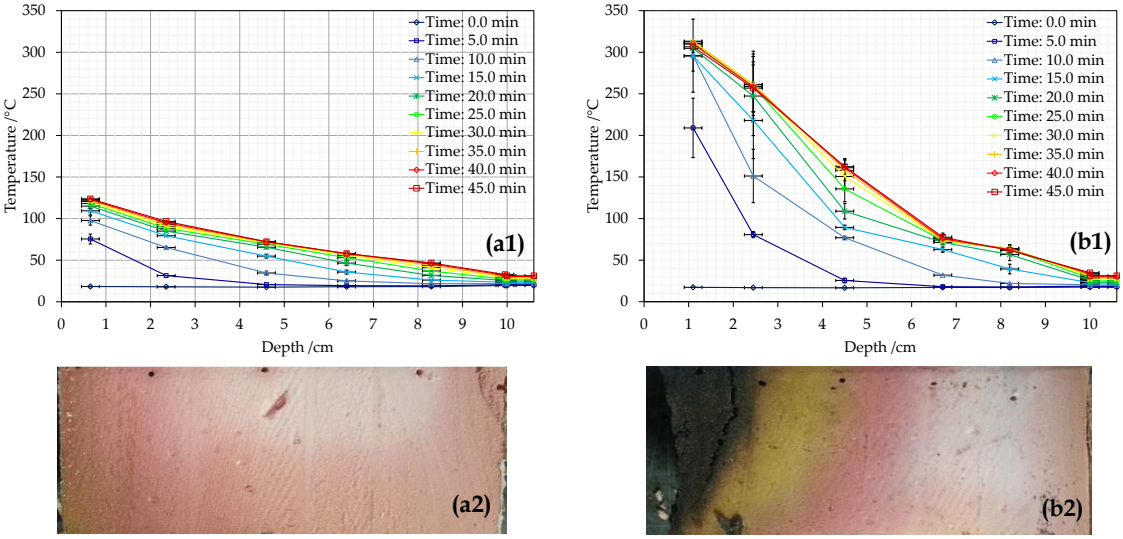

Figure 6.11. In-depth thermal profiles of PF at 10 kW·m^{-2} with (a1) and without protective layer (b1). Centre-section for the end of the tests (a2, b2) Horizontal error bars: estimated error of ±2mm in thermocouple positioning Vertical error bars: standard deviation between two repeated tests

Figure 6.12 shows the in-depth temperature profiles for PF experiments tested at 25 kW·m^{-2} with (Figure 6.12a) and without (Figure 6.12b) protective layer at the surface. Figure 6.12a and Figure 6.12b present good repeatability except for the first thermocouples. Slightly better performance is observed for the samples with a protective layer (Figure 6.12a) than those without (Figure 6.12b), with lower thermal gradients for same times of exposure. However, the protective layer does not prevent the onset of thermal degradation.

Figure 6.12a presents a case study where the effectiveness of the protective layer is lost after certain temperature and thermal degradation is eventually achieved. The temperature profile close to the surface shows a moderate rate of temperature increase around 30-50°C·min^{-1} until 5 minutes, achieving a temperature of 204°C ± 14°C, when the rate of increase rises severely, since the protective layer starts to detach and lift after 4 minutes of heat exposure. As a result, temperature near the surface achieves a maximum value below 600°C at around 9 minutes, when the thermocouple detaches from the initial position due to consumption of the surrounding material. Approximately 2 cm of material are consumed by the end of the tests. Four different uniform tonalities are observed in the sample section between the edge and the centre-line, indicating that the heat transfer can be considered as a one-dimensional regime. No cracks within the core of the sample are observed, but the top of the sample presents a rough surface with some random cracks. Measurements of carbon dioxide and carbon monoxide show concentrations displaced from baseline, confirming the occurrence of solid-phase oxidation. For simplicity, these results are not presented herein, but for the case shown in Figure 6.12b which is equivalent.

Figure 6.12b shows a case study where severe thermal degradation is observed from early times of the test (2.5 minutes). The temperature close to the surface

achieves a maximum value of 592°C ± 10°C at 5 minutes. No steady state is observed for the thermal gradient during the last steps, with temperature increasing with a rate of 9-10°C·min^{-1} for inner positions. This rate is only observed for positions with temperature higher than 100°C, indicating a clear endothermic effect at that temperature range. A high rate of temperature increase, without achieving the steady state, indicates the consumption of material at the surface, thus moving the exposed boundary to lower positions. The experienced thermal degradation is similar to that shown in Figure 6.12a. The surface of the material is presented in Figure 6.14c, showing crater morphology on the edges and rough surface and random long cracks expanding from the centre to the edges.

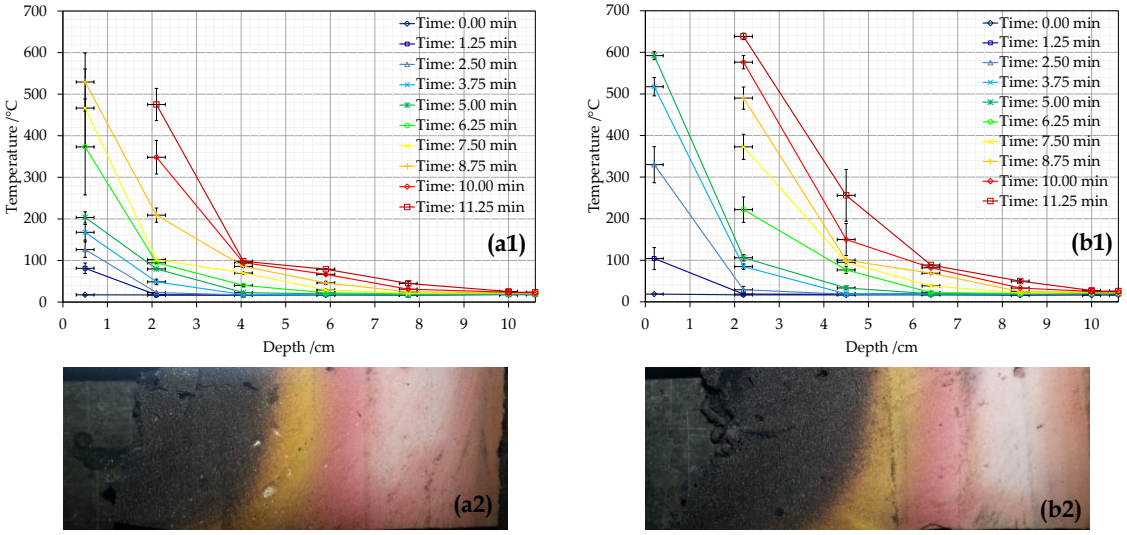

Figure 6.12. In-depth thermal profiles of PF at 25 kW·m^{-2} with (a1) and without protective layer (b1). Centre-section for the end of the tests (a2, b2) Horizontal error bars: estimated error of ±2mm in thermocouple positioning. Vertical error bars: standard deviation between two repeated tests

Measurements of carbon monoxide are presented in Figure 6.13a with the time-history of temperature measurements. The concentration of CO shows an increasing trend until 5 minutes, when it achieves a steady state around 150 ppm. These measurements are indicative of smouldering combustion (surface oxidation), suggesting a constant rate of oxidation. Similarly the CO/CO_2 ratio increases until 5 minutes as shown in Figure 6.13b, remaining approximately constant at around 0.2. The concentration of CO_2 remains very low in comparison to the generation of CO_2 presented for flaming of PF in Chapter 5. Additionally, it is shown that the smouldering is not self-sustained since the thermal gradient and CO generation drops significantly after removing the external heat source. This is due to the closed-cell structure of the foam that does not allow the free circulation of oxygen through the sample. Additionally, a plateau of temperatures is clearly observed below 100°C in Figure 6.13a, indicating an endothermic reaction probably due to water desorption in the polymer.

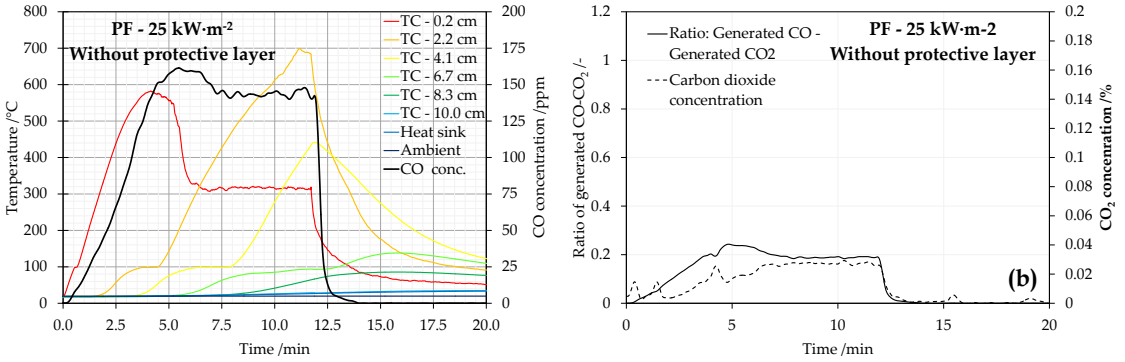

Figure 6.13. Time-history of temperatures within the solid-phase and CO concentration (a) and generated CO vs. generated CO_2 (b) for PF without protective layer at 25 kW·m^{-2}

Images from the surface of the remaining residue for PF experiments without protective layer at 10, 15 and 25 kW·m^{-2} are shown in Figure 6.14 below. Different patterns indicate the significance of surface oxidation. Figure 6.14a shows the occurrence of the delamination effect when the achieved temperatures are not high enough to trigger the oxidation of the char created. Figure 6.14b shows that the oxidation at the surface is not homogenous, indicating the high complexity of the oxidation mechanism, while Figure 6.14c shows the case of a smouldering process with fairly constant rate of surface regression as shown in Figure 6.13.

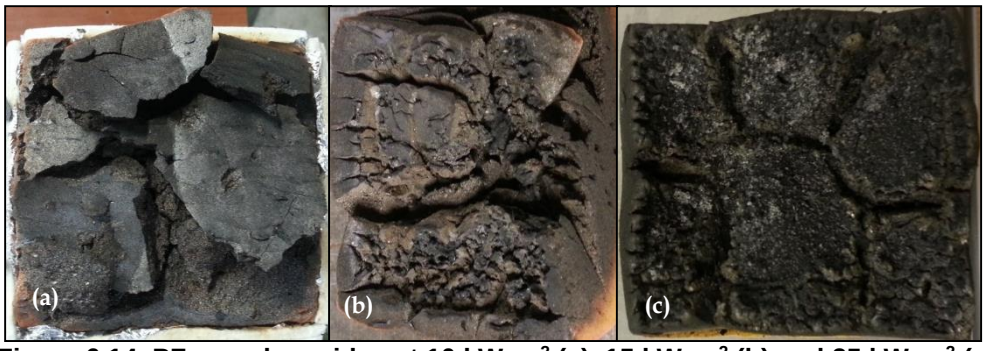

Figure 6.14. PF sample residue at 10 kW·m^{-2} (a), 15 kW·m^{-2} (b) and 25 kW·m^{-2} (c) without protective layer

The upper edge of the temperature envelopes for the experiments that showed different values of maximum temperature close to the surface are presented separately in Figure 6.15, together with a section of the sample after the test. Temperatures values are interpolated for the interface between the three main regions of discolouration (light pink, dark pink, orange-brown and black). In general, the first interface, which is observed as a plateau of temperature in Figure 6.13a, is around 100°C, near the change of slope in the thermal gradient. The second interface is identified between 125°C and 160°C, which is in agreement with the temperature before the first peak of pyrolysis observed in DTG analyses under nitrogen atmospheres in Chapter 4. The third interface is identified between 250°C and 300°C, which is in agreement with the temperature between the first and second peak of pyrolysis observed in DTG analyses under nitrogen atmospheres. Maximum temperatures measured in the solid-phase in Figure 6.15 are between 600°C and

700°C, while TGA analyses showed that all mass consumption ends below 600°C in an air atmosphere. This indicates that the combustion of char is probably dominated by the diffusion of oxygen at the surface.

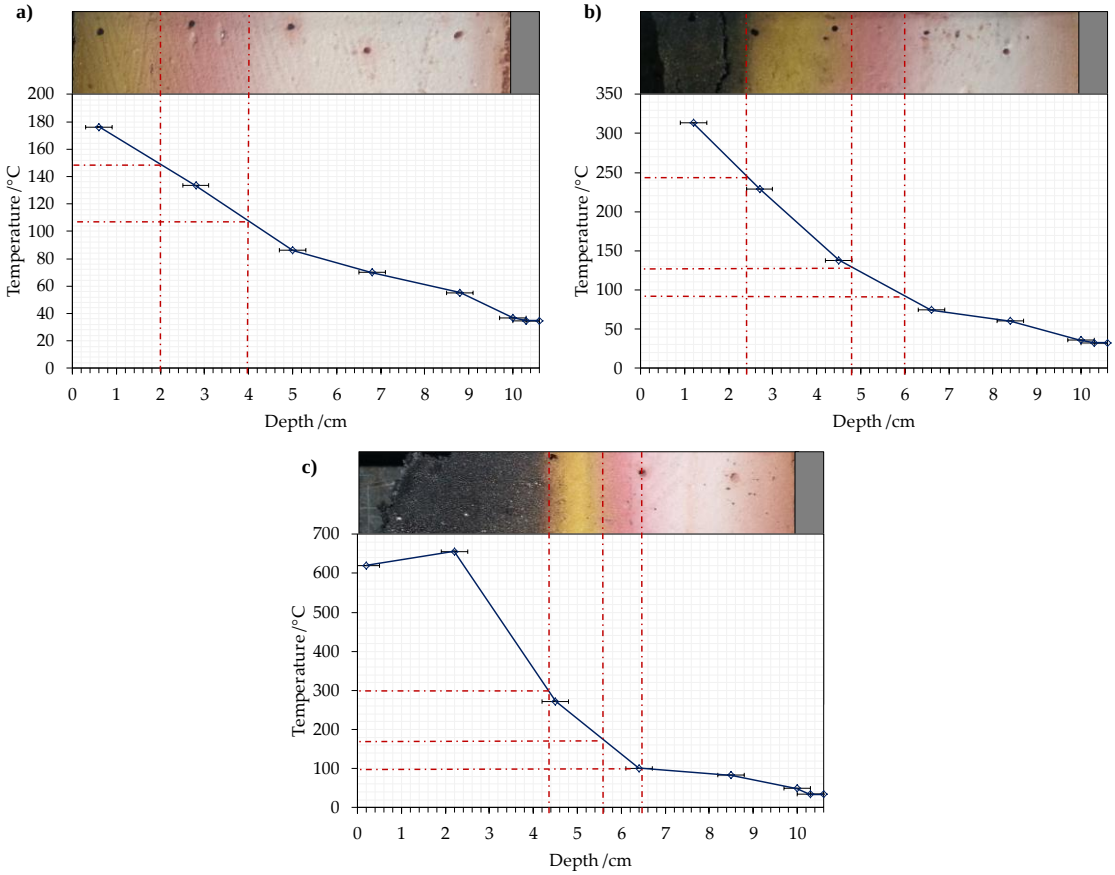

Figure 6.15. Maximum in-depth temperature profile of PF:
a) 15 kW·m^{-2} (foil) b) 10 kW·m^{-2} (no foil) c) 25 kW·m^{-2} (no foil)
Horizontal error bars: estimated error of ±2mm in thermocouple positioning

6.4.3 Expanded polystyrene (EPS)

EPS was found to shrink fast when exposed to severe conditions of heat. Therefore, measurements of in-depth temperature are only relevant for a short time frame. A couple of case studies are presented in Figure 6.17 as the time-history of temperature measurements within the solid at different positions. Smooth temperature curves indicate the thermocouple is inserted in the solid-phase, while noisy temperature curves indicate detachment from the solid-phase and provide gas-phase measurement (including radiation error from the radiation from the cone).

Figure 6.17a presents a case study of an EPS sample tested at 2 kW·m^{-2}. The maximum temperature, measured by the first thermocouple is approximately 110°C and was reached at 2-3 minutes, when the thermocouple detaches from the solid due to regression of the sample. As shown by the thermocouple at 2.7 cm, regression of the surface does not proceed since a steady state is achieved. This can be observed in Figure 6.16a where the section of EPS is compared to the upper edge of the temperature envelope. The regression temperature can be assumed to be in the range

of 100-120°C, which is slightly larger than the glass transition temperature of the material (between 90-100°C as noted in Chapter 2). It is observed that the EPS pellets at the surface have reduced diameter and acquire some hardness after cooling, indicating that the polystyrene has transitioned to a glass state once the blowing agent was eliminated and the temperature was reduced.

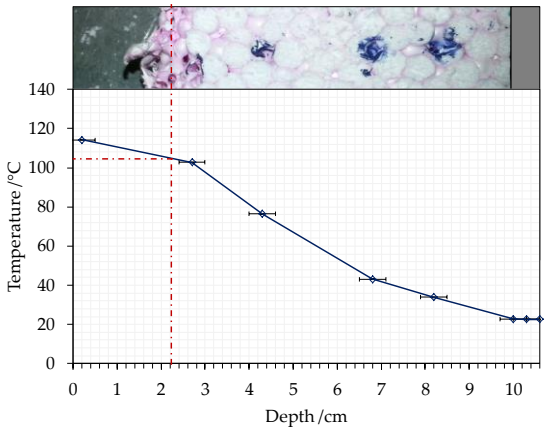

Figure 6.16. Maximum in-depth temperature profile of EPS at 2 kW·m^{-2}
Horizontal error bars: estimated error of ±2mm in thermocouple positioning

Figure 6.17b presents a case study of an EPS sample tested at 10 kW·m^{-2}. It is found that the sample shrinks completely after the first minute of heating, leaving a thin film of material at the bottom which is presented in Figure 6.18c. The maximum temperature measured in the solid-phase before regression is between 100°C and 150°C for the five first thermocouples. The thermocouples at the bottom and in the plate present significant discrepancy, although the trend is similar. Figure 6.18c shows that the film formed is not regularly distributed in the sample holder, which indicates that the temperature recorded by the thermocouple is not reliable.

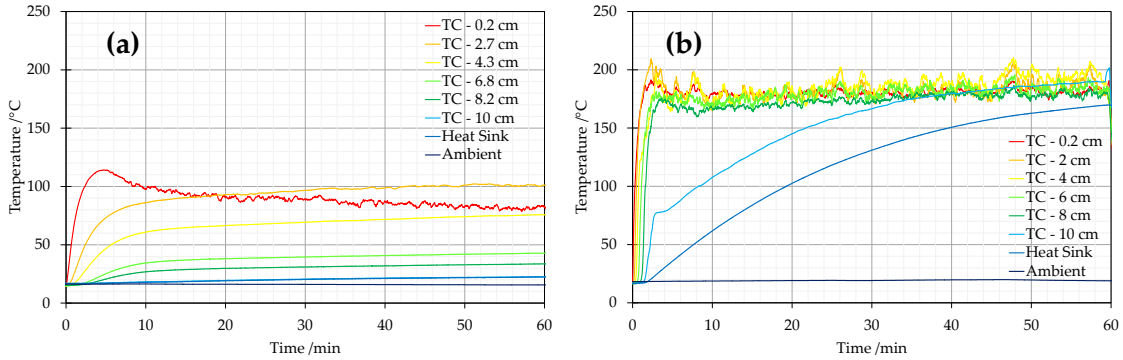

Figure 6.17. Time-history of temperatures within the solid-phase of EPS samples at (a) 2 kW·m^{-2} (b) 10 kW·m^{-2}

As shown in Figure 6.17, the regression rate of the foam depends on the temperature profile within the solid-phase. This regression is identified as a reduction of the density of the EPS pellets at a certain temperature, which corresponds to the loss of the blowing agent. This temperature has been found to correspond to values between 100°C and 120°C, which is in good agreement with the literature. Since the material presents a low thermal inertia, the surface rapidly achieves this temperature

for any heat exposure. Although thermal properties of the material can be determined, this behaviour implies that the material rapidly forms a thin film which will melt depending on the energy balance, i.e. once the melting temperature is achieved. This is verified by the performed experiments, for which the sample residues are presented in Figure 6.18 and correspond to external heat fluxes of 2, 4 and 10 kW·m^{-2}. It is shown that the level of regression is significant even for external heat fluxes of 2 and 4 kW·m^{-2}. However, no melting is observed since the temperature at the surface remains lower than the melting point (between 230°C and 270°C according to the literature). This seems to be achieved for the experiment at 10 kW·m^{-2} (Figure 6.18c), but the temperature measurement by the bottom thermocouple (presented in Figure 6.17b) shows lower values than the melting point noted above. In any case, this measurement of temperature is not reliable since the thermocouple is probably not in perfect contact with the film.

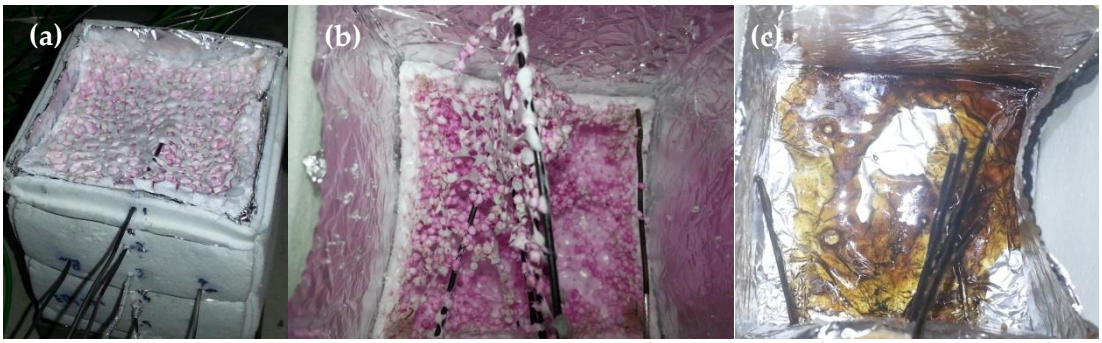

Figure 6.18. EPS sample residue at (a) 2 kW·m^{-2}, (b), 4 kW·m^{-2} and (c) 10 kW·m^{-2}

Results obtained by thermogravimetry cannot be compared to those presented in this section. Indeed, the melting point cannot be characterised by thermogravimetry but with differential scanning calorimetry. The EPS pyrolysis temperature in an oxidative atmosphere was found to be between 300°C and 400°C; however, this temperature cannot be easily measured due to the melting behaviour of the EPS and the used experimental methodology.

6.4.4 Stone wool (SW)

Figure 6.19 and Figure 6.20 show the in-depth temperature profiles for stone wool samples at different test times for external heat fluxes of 10, 25, 40 and 65 kW·m^{-2}. These profiles represent the average profile from two repeated tests. Horizontal error bars express an estimated error in the thermocouple positions, while vertical error bars express the standard deviation from average values. Excellent repeatability is observed for most of the studied cases.

Figure 6.19a presents a case study of samples tested at 10 kW·m^{-2}, where the maximum temperature close to the surface achieves a steady state value of 327°C ± 2°C below 2.5 minutes. The temperature profile achieves a quasi-steady state at 15 minutes, with a minor rate of temperature increase (<1°C·min^{-1}) for inner positions. The sample section in Figure 6.19a1 shows minor discolouration in regions close to the surface of the wool, with a yellow to brown transition. No release of volatiles is

observed during the tests, as well as the measurements of carbon monoxide and carbon dioxide do not show any increase of concentration.

Figure 6.19b presents a case study of samples tested at 25 kW·m^{-2}, where the maximum temperature close to the surface achieves a steady state value of 498°C ± 6°C below 2.5 minutes. The temperature profile achieves a quasi-steady state from 15 minutes, with a minor rate of temperature increase (<1°C·min^{-1}) for inner positions. The sample section in Figure 6.19a2 shows three regions of discolouration, changing from yellow (virgin material) to orange-brown and finally brown-grey. No release of volatiles is observed during the the tests, as well as the measurements of carbon monoxide and carbon dioxide do not show any increase of concentration.

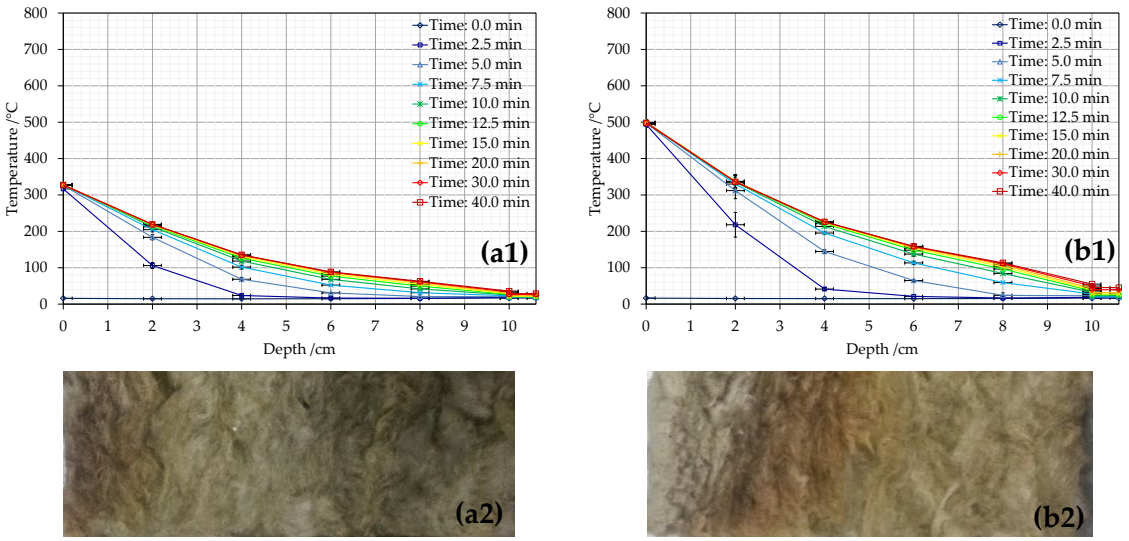

Figure 6.19. In-depth thermal profiles of SW at 10 kW·m^{-2} (a) and 25 kW·m^{-2} (b). Centre-section for the end of the tests (a2, b2)
Horizontal error bars: estimated error of ±2mm in thermocouple positioning
Vertical error bars: standard deviation between two repeated tests

Figure 6.20a and Figure 6.20b present the cases studies of the samples tested at 40 and 60 kW·m^{-2}, where the maximum temperature close to the surface achieves a steady state value of 621°C ± 10°C and 701°C ± 16°C below 2.5 minutes, respectively. Both temperature profiles achieve a quasi-steady state after 10 minutes, with a minor rate of temperature increase (<1°C·min^{-1}) for inner positions. Sample sections in Figure 6.20a2 and Figure 6.20b2 show the same pattern of discolouration as shown in Figure 6.19a2.

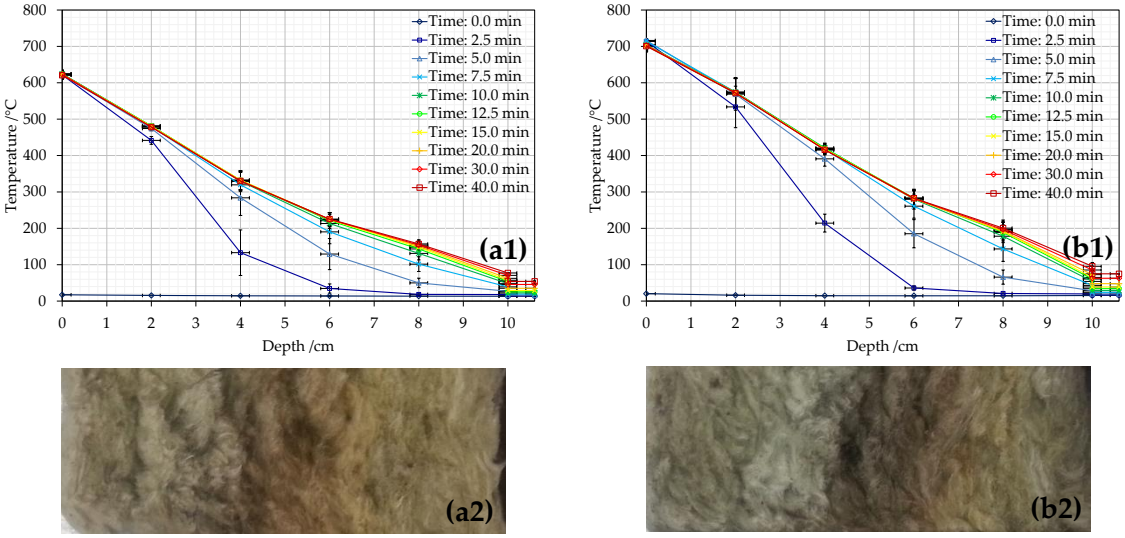

Figure 6.20. In-depth thermal profiles of SW at 40 kW·m^{-2} (a) and 60 kW·m^{-2} (b). Centre-section for the end of the tests (a2, b2) Horizontal error bars: estimated error of ±2mm in thermocouple positioning. Vertical error bars: standard deviation between two repeated tests

Measurements of carbon monoxide for experiments at 40 and 60 kW·m^{-2} are presented in Figure 6.21 with the time-history of temperature measurements. CO concentrations for 60 kW·m^{-2} increase until they reach a peak of 15 ppm and then follow a progressive reduction until 10-20 minutes, when the steady state is achieved and the CO concentration comes back to the base line. A similar trend and peak but with much lower amplitude is observed at 40 kW·m^{-2} (7 ppm). It should be noted that although these concentrations are insignificant, they indicate the combustion of some organic component in the wool (likely the binder). It was found by the TGA analyses that the binder content in the wool is below 2% of the total mass. Therefore, such low concentrations of CO are consistent with the expected low mass of binder in the wool. Additionally, peaks in the temperature that could represent the combustion of binder are not observed in the time-history of the temperature measurements. This was however observed by *Sjöström and Jansson* [7], who tested stone wool with higher content of binder, which is usually present in denser wools used for fire protection.

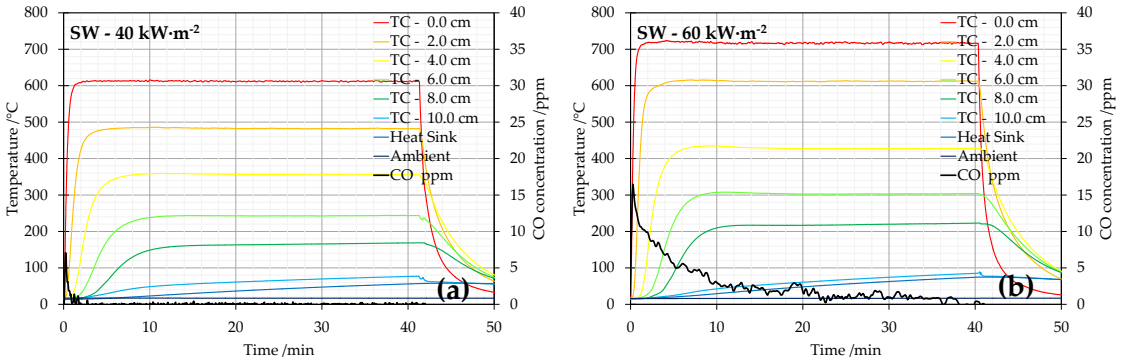

Figure 6.21. Time-history of temperatures within the solid-phase and CO concentration of SW at 40 kW·m^{-2} (a) and 60 kW·m^{-2} (b)

The upper edge of the temperature for an experiment at 40 kW·m^{-2} is presented in Figure 6.22 with a section of the sample after the test. Values of temperature are interpolated for the interface between the three main regions of discolouration. The first interface is identified around 200°C, while the second interface is identified at 340°C. These values of temperature are in agreement with the temperature previous to the peak of pyrolysis and temperature before the oxidation peak, both observed in DTG analyses under air atmospheres in Chapter 4.

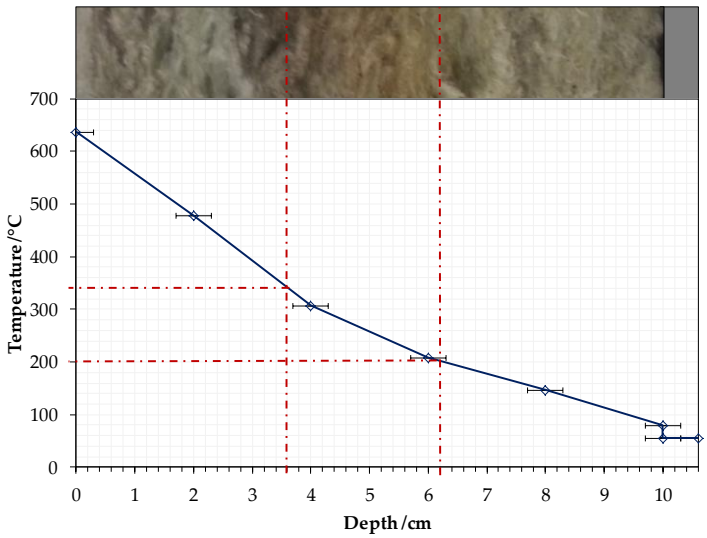

Figure 6.22. Maximum in-depth temperature profile of SW sample tested at 40kW·m^{-2} Horizontal error bars: estimated error of ±2mm in thermocouple positioning

6.4.5 Discussion

6.4.5.1 One-dimensionality of experiments

As noted previously, the main concern lies on whether the one-dimensional assumption is met for the experiments, since the studied materials present lower conductivity than the ceramic paper. Results from some experiments are presented in order to verify this assumption prior to introducing modelling tools.

Figure 6.23 shows the time-history of the temperature measurements within the solid-phase of three PIRb samples with different boundary conditions. Figure 6.23a and Figure 6.23b correspond to heat exposures of 5 kW·m^{-2} with and without protective layer on the surface, respectively. Figure 6.23c corresponds to a heat exposure of 25 kW·m^{-2} with a metallic plate on the surface. Additional measurements are taken at the same depth of the second centre-line thermocouple but horizontally displaced 1.5 cm, which are indicated as red dashed lines. In general, good agreement is found between lateral (dashed) and centre (straight) thermocouple measurements during the transient state. On the contrary, worse agreement is observed during the steady-state, with the average deviation[14] between the centre and the lateral

[14] Calculated as abs $\left(\frac{T_l - T_c}{T_c}\right)$, with T_l and T_c the steady-state value of the lateral and centre thermocouple reading, respectively.

thermocouples being proportional to the temperature during the steady sate. Indeed a deviation of 6.6% is observed for Figure 6.23a (54.6-58.8°C), while deviations for Figure 6.23b and Figure 6.23c are 15.5% (124.9-147.8°C) and 16.3% (345.8-413°C) respectively.

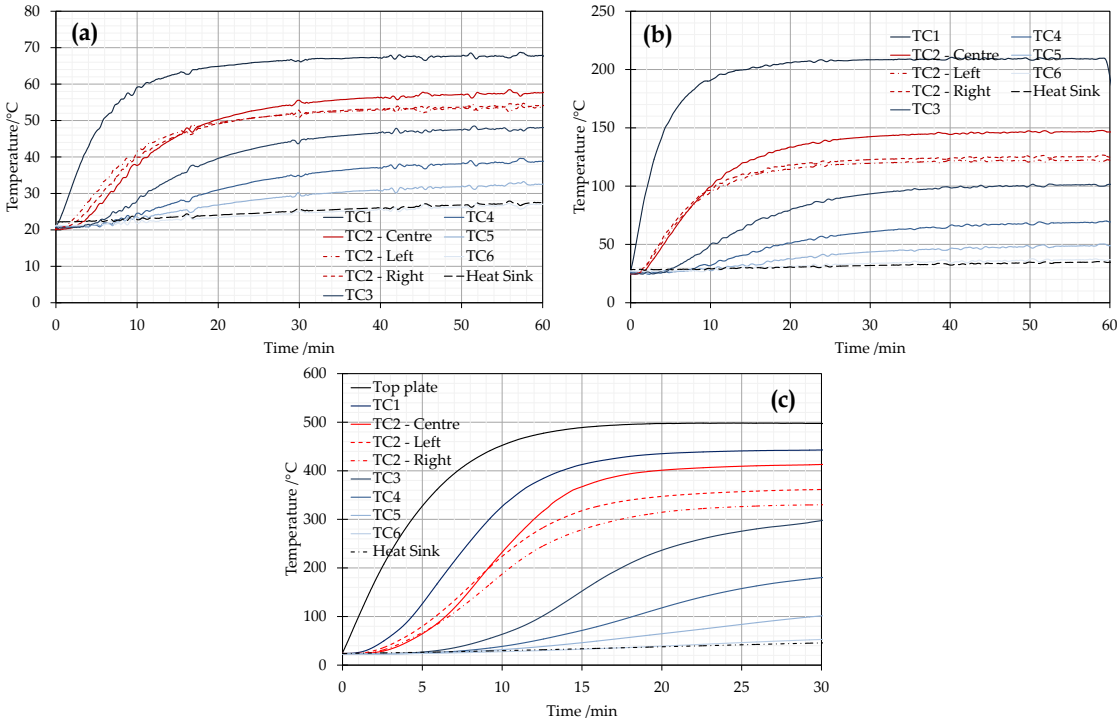

Figure 6.23. Time-history of temperatures within the solid-phase of PIRb at 5 kW·m^{-2} with (a) and without (b) protective layer, and (c) at 25 kW·m^{-2} with a metallic plate on top

Figure 6.24 shows a schematic representation of the temperature profile of an insulation sample, where the larger deviation for higher temperatures indicates that the heat losses through the sides of the sample are greater, as it is assumed that these are directly proportional to the temperature at the edge. A flatter profile is then expected for lower temperatures at the same depth, while a profile with higher temperature at the centre-line than at the sides is expected for depths with higher temperature. The former is representative of experiments with low heat fluxes, while the latter is representative of higher heat fluxes, depending on the configuration of the exposed surface.

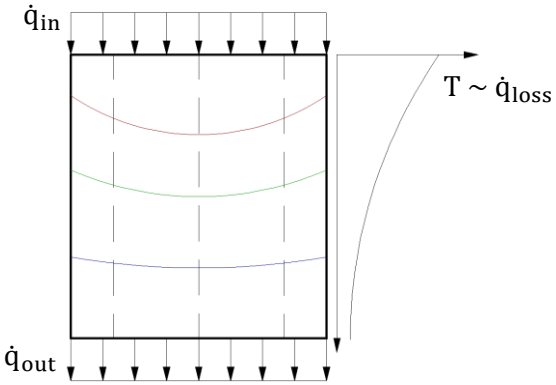

Figure 6.24. Time-history of temperatures within the solid-phase of PIRb at 5 kW·m^{-2} with (a) and without (b) protective layer

6.5 Thermal properties characterisation

6.5.1 Methodology definition: the inverse problem

The determination of approximated values of thermal properties for the insulation materials being studied is crucial for the design methodology presented in Chapter 3. Since a simplistic modelling approach is proposed, the thermal properties of the materials do not strictly correspond to the real values, but equivalent properties able to predict the thermal evolution by using the one-dimensional solid heat transfer equation under inert hypothesis. Despite there are experimental techniques that provide quantification of thermal conductivity [8] and specific heat capacity of materials [9], the challenge still remains in whether these values are able to provide good prediction of the thermal evolution when exposed to known heat conditions. Alternative approaches to direct measurement of thermal properties are based on the calculation of these properties by solving the heat transfer problem inversely, i.e. estimating the thermal properties and other unknown variables from the heat transfer formulation, given a series of measurements such as temperature or heat flux.

Figure 6.25 shows a logic diagram representative of the specific inverse problem where three series of variables can be identified. Optimisation variables (X) are the system variables that are unknown; objective variables (Y) are the variables that serve to evaluate the solution proposed by comparing experimental and numerical results; constraint variables (Z) are system variables that are fixed to certain values. Initially, the problem is solved with a proposed initial solution X_0. The objective variables obtained as output of the heat transfer solver are compared to the experimental ones. If good agreement is achieved, this is chosen as the best particular solution. Otherwise, the optimisation algorithm produces a new solution X_i that together with the constraint variables produces a new output by solving the heat transfer problem. This process is repeated in a loop until good agreement between the experimental and model results are met and a better solution cannot be found.

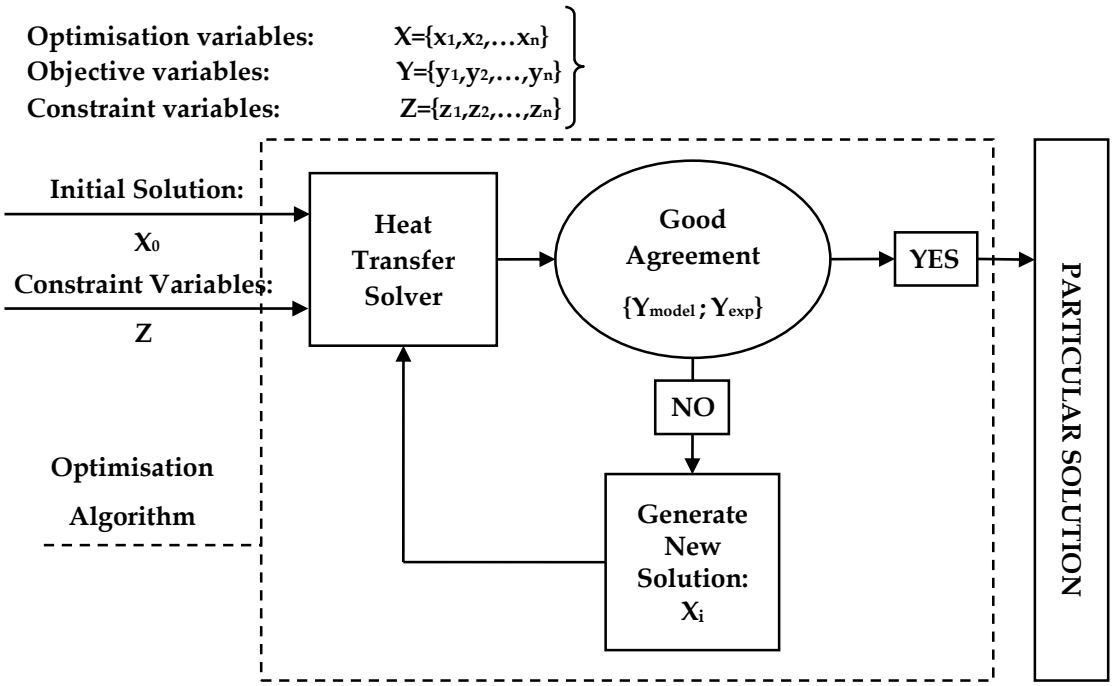

Figure 6.25. Methodology diagram for solving the inverse heat transfer problem

Most of the inverse modelling techniques follow the same approach (as shown in Figure 6.25). General optimisation algorithms aim to find a solution that minimises an error or cost function in an efficient way, so as the computational and time costs are reduced. A coarse solution may be found by running all the possible solutions that result from a combination of all different discretised values for each optimisation variable. This may be a suitable approach if the number of cases is reduced; otherwise, this technique is prohibitive.

The purpose of this section is to determine the thermal properties of the studied insulation materials and therefore these corresponding to the main optimisation variables. However, these are not the only parameters included as optimisation variables, since other parameters with high uncertainty also need to be quantified. A detailed description of these parameters is included in the following section together with the definition of the heat transfer problem for the particular cases representative of the experimental set-up.

6.5.2 Heat transfer formulation for the inverse problem

6.5.2.1 Governing equation

The heat transfer through the solid media is governed by the heat diffusion equation derived from Fourier's law and the law of energy conservation. The one-dimensional formulation is presented in Equation (6.1) below:

$$\frac{\partial\left(k(T)\cdot\frac{\delta T}{\delta x}\right)}{\partial x}=\rho(T)\cdot c_p(T)\cdot\frac{dT}{dt}+\dot{g}''' \tag{6.1}$$

where k(T), ρ(T), c_p(T) are the thermal conductivity, density and specific heat capacity of the material respectively and $\dot{g}'''$ is the volumetric generated/absorbed heat. The left-hand-side term represents the heat conducted through the material and the first right-hand-side term represents the heat stored by the material.

As noted in Chapter 2, many of the studied materials are not made of one single solid component but a multiphase solid-gas media for closed-cell foams or permeable media of fibres for stone wool. The definition of a fine model that represents all the phenomena attained to the nature of the problem would imply the use of computational fluid dynamics tools and radiation transfer equation (RTE) solvers. Although this approach might be suitable in some scenarios, the purpose of this work is not to get into advanced models of high complexity. Instead, a simpler approach that can represent the transient heat transfer with an acceptable level of precision is pursued.

Therefore, Equation (6.1) is taken as a framework for the analyses undertaken throughout this chapter, which implies a series of assumptions listed below:

- The heat is transferred one-dimensionally, assuming that the heat losses to the lateral boundaries of the samples studied are negligible.
- The thermal conductivity and specific heat capacity of the multiphase samples are lumped into equivalent thermal properties.

The domain of the problem, defined by Equation (6.1) and represented in Figure 6.26, is restricted by a series of boundary conditions that are described below. Since the analysis is restricted to a one-dimensional problem, the boundaries are in the range x = [0, L_i], with x = 0 being the surface at which the material is exposed to heat and x = L being the position corresponding to the thickness of the sample.

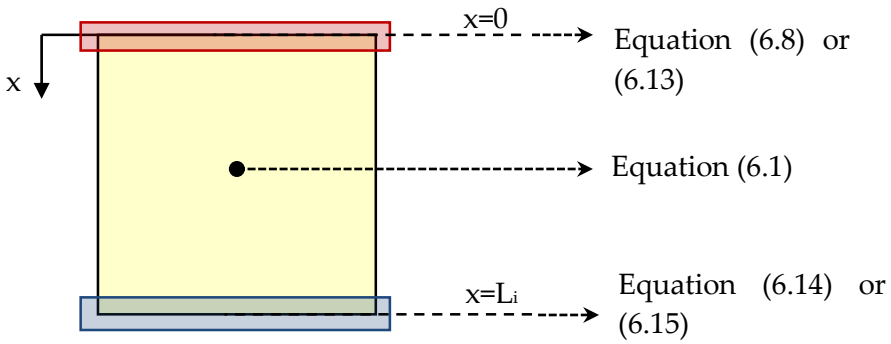

Figure 6.26. Domain definition of the one-dimensional heat transfer problem

6.5.2.2 Boundary condition: surface exposed to radiation

The energy balance at the exposed surface is represented by the heat entering the surface, which has to meet Fourier's law. During a fire, the amount of the net heat flux absorbed by an element may be represented as the sum of a net convective fraction and a net radiative fraction:

$$\dot{q}''_{net}(t) = \dot{q}''_c(t) + \dot{q}''_r(t) = -k \cdot \left.\frac{\delta T}{\delta x}\right|_{x=0^+} \quad (6.2)$$

where $\left.\frac{\delta T}{\delta x}\right|_{x=0^+}$ is the thermal gradient at the surface and, $\dot{q}''_c(t)$ and $\dot{q}''_r(t)$ are the convective and net radiative fractions of heat flux at the surface respectively. The convective heat flux and the net radiative heat flux can be defined as:

$$\dot{q}''_c(t) = h_c \cdot (T_\infty - T_s) \quad (6.3)$$

$$\dot{q}''_r(t) = \alpha \cdot \dot{q}''_e(t) - \varepsilon \cdot \sigma \cdot T_s^4 \quad (6.4)$$

with h_c being the convective heat transfer coefficient, T_s the surface temperature, T_∞ the fluid temperature, $\dot{q}''_e(t)$ the irradiance received at the exposed surface of the material, α and ε the absorptivity and emissivity of the surface respectively and σ the Stefan–Boltzmann constant. This formulation can also be applied for a controlled environment like a bench-scale test such as the Cone Calorimeter, or intermediate-scale testing by using radiant panels [10, 11]. For that case, the strict definition of the heat balance at the surface is written as:

$$\dot{q}''_{net}(t) = \alpha \cdot \dot{q}''_e(t) + \alpha_\infty \cdot \sigma \cdot T_\infty^4 + h_c \cdot (T_\infty - T_s) - \varepsilon \cdot \sigma \cdot T_s^4 = -k \cdot \left.\frac{\delta T}{\delta x}\right|_{x=0^+} \quad (6.5)$$

with α_∞ the absorptivity to the radiation from the surroundings. Although the term $\alpha_\infty \cdot \sigma \cdot T_\infty^4$ is negligible due to the low value of T_∞, if $\alpha_\infty$is assumed to be equal to ε, the formulation can be expressed as:

$$\dot{q}''_{net}(t) = \alpha \cdot \dot{q}''_e(t) + h_c \cdot (T_\infty - T_s) - \varepsilon \cdot \sigma \cdot (T_s^4 - T_\infty^4) = -k \cdot \left.\frac{\delta T}{\delta x}\right|_{x=0^+} \quad (6.6)$$

As noted in Chapter 5, a simplification can be assumed if a global heat transfer of heat losses is defined as noted below:

$$h_T = h_c + \varepsilon \cdot \sigma \cdot \frac{T_s^4 - T_\infty^4}{T_S - T_\infty} = h_c + h_r \quad (6.7)$$

Then, the boundary condition at the surface can be eventually defined as Equation (6.8) below:

$$\dot{q}''_{net}(t) = \alpha \cdot \dot{q}''_e(t) - h_T \cdot (T_s - T_\infty) = -k \cdot \left.\frac{\delta T}{\delta x}\right|_{x=0^+} \quad (6.8)$$

As mentioned in previous chapters, several studies have been carried out trying to characterise the convective coefficient of a horizontal hot surface as in the Cone Calorimeter [12]. Despite several correlations can be found, the quantification of the convective coefficient also depends on external factors such as the induced buoyant flow from the hot cone coil, which cannot be easily characterised. Since different external heat fluxes can result in different surface temperature due to variable absorptivity, the induced buoyant flow is not expected to be the same for any heat flux and material. Then, the quantification of the losses by convection entails a high level of uncertainty, not only because h_c is unknown, but also because the measurement of surface temperature is extremely complicated. The main advantage of using a global heat transfer coefficient h_T is that all the uncertainties linked to the

heat loss phenomena are lumped into a global variable. Clear limitations can be found when trying to define the boundary condition at larger scales, especially due to the high of uncertainty in defining the heat transfer coefficient of losses, since this depends on the conditions of the flow on the surface.

6.5.2.3 Boundary condition: metallic plate as interface

The use of a metallic plate as interface for the heat transfer to the tested sample is proposed in order to reduce the level of uncertainty with regard to the boundary condition at the exposed surface. The problem domain is as shown in Figure 6.27, with Equation (6.1) as governing equation for the solid phase (shown in grey and yellow). The governing equation for the interface of the plate and the sample, corresponding to the net heat absorbed by the sample, and considering the contact resistance as negligible, is as noted below:

$$\dot{q}''_{net,s} = -k_A \cdot \frac{\delta T}{\delta x}\Big|_{x=L^-_{plate}} = -k_B \cdot \frac{\delta T}{\delta x}\Big|_{x=L^+_{plate}} \quad (6.9)$$

where $\dot{q}''_{net,s}$ is the net heat absorbed by the sample, k_A and k_B are the thermal conductivity of the plate and the sample respectively, and L_{plate} is the thickness of the plate.

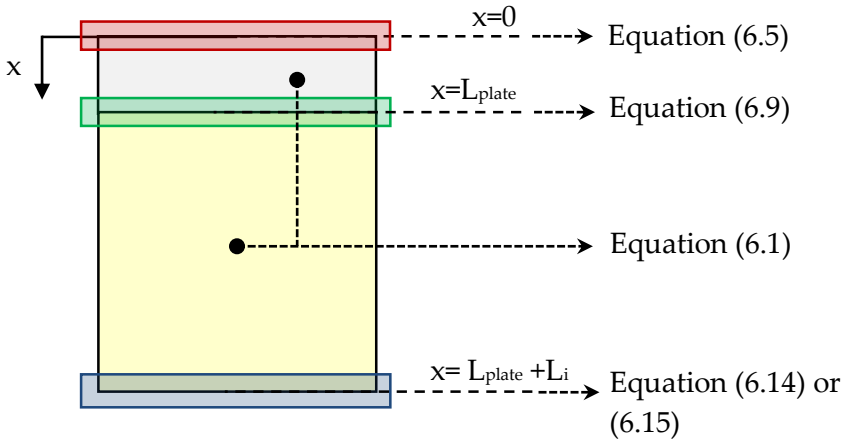

Figure 6.27. Domain definition of the one-dimensional heat transfer problem with a metallic plate on the sample material

The main advantage of using a material of high thermal diffusivity on the surface is that, if this is designed to be thermally thin, due to continuity, the surface temperature of the tested sample corresponds to the temperature of the plate. A minimum thickness is required in order to assure that the thermal gradient through the metallic plate is low, so as the errors related to measuring surface temperature are low as well. The equivalent requirement is to assure that the Biot number, defined in Equation (6.10), is strictly lower than 0.1 and therefore, a lump capacitance analysis is valid and may be applied to the plate.

$$Bi = \frac{h \cdot L_{plate}}{k_{plate}} < 0.1 \quad (6.10)$$

Assuming that a lump capacitance method is valid, the heat balance for the plate can be expressed as:

$$\dot{q}''_{net} = \dot{q}''_{st,plate} + \dot{q}''_{net,s} \tag{6.11}$$

where $\dot{q}''_{net}$ is the net heat absorbed at the surface of the metallic plate given by Equation (6.5), $\dot{q}''_{st,plate}$ is the heat stored by the plate and $\dot{q}''_{net,s}$ is the heat lost by the back surface of the plate or net heat to the sample. Considering that the heat stored by the plate can be defined as:

$$\dot{q}''_{st,plate} = L_{plate} \cdot \rho_{plate} \cdot c_{p_{plate}}(T) \cdot \frac{dT}{dt} \tag{6.12}$$

substituting Equation (6.12) into Equation (6.11) and rearranging terms, the net heat to the sample can be expressed as:

$$\dot{q}''_{net,s} = \alpha_{paint} \cdot \dot{q}''_{e} - h_T \cdot (T_s - T_\infty) - L_{plate} \cdot \rho_{plate} \cdot c_{p_{plate}}(T) \cdot \left.\frac{dT}{dt}\right|_{plate} \tag{6.13}$$

If a black coating paint is used at the exposed surface of the metallic plate, the absorptivity can be assumed to have a known value. Since the temperature at the surface is known, the only unknown at the right-hand-side of Equation (6.13) is the heat transfer coefficient h_T. Then, the heat transfer coefficient no longer needs to be assumed, but becomes the unknown variable of the boundary element.

6.5.2.4 Boundary condition: back face

Three common assumptions can be made with regard to the non-exposed surface or back boundary condition of the one-dimensional heat transfer:

- **Adiabatic boundary condition**, assuming that the back is perfectly insulated and thus, a Neumann boundary condition with the heat losses term being null.
- **Heat losses boundary condition,** calculating the heat losses from the back, i.e. Neumann boundary condition.
- **Isothermal boundary condition**, assuming that the temperature at the back remains as a known value throughout time, i.e. Dirichlet boundary condition.

An adiabatic boundary condition, i.e. $\dot{q}''_{loss}(t) = 0$, is typically assumed for material flammability testing in the Cone Calorimeter by attaching a low conductivity material under the sample. This is however a non-feasible procedure for the studied case for which thermal characterisation is pursued. Indeed, the thermal losses through the back surface of the material are never zero. Then, the assumption of an adiabatic boundary condition is only valid if exposure times are low enough to ensure that the thermal wave has not arrived to the back surface. This is the reason for attaching a metallic block under the sample in the bench-scale testing series presented in this chapter.

As noted in the previous sections, the metallic block of high thermal diffusivity acts as a heat sink for the present problem, allowing the last two approaches mentioned above to be considered. The first approach entails that the heat flux of

losses by the back surface is calculated for any time by Equation (6.14) below, and then the energy balance at the back surface of the sample is defined by Fourier's law:

$$\dot{q}''_{loss}(t) = \delta_{plate,b} \cdot \rho_{plate,b} \cdot c_{p_{plate,b}}(T_{plate,b}) \cdot \left.\frac{\Delta T}{\Delta t}\right|_{plate,b} = -k \cdot \left.\frac{\delta T}{\delta x}\right|_{x=L^-} \quad (6.14)$$

where $\dot{q}''_{loss}(t)$ is the heat flux lost by the back surface of the sample, $\delta_{plate,b}$ and $c_{p_{plate,b}}(T_{plate,b})$ are respectively the thickness and specific heat capacity, $\frac{\Delta T}{\Delta t}$ is the temperature gradient of the plate over time and L is the thickness of the sample.

The second approach entails the assumption of a Dirichlet boundary condition at the back, assuming that the temperature of the back surface of the material is equal to the temperature of the metallic plate by continuity. A material of low thermal properties shall be attached beneath the plate. Then, the governing equation is defined as:

$$T(x = L, t) = T_{plate,b}(t) \quad (6.15)$$

Since the wrapping material has higher conductivity than the tested samples, the thermal wave is expected to arrive earlier to the plate through the ceramic paper and the energy balance it is not correctly represented by Equation (6.14). Therefore, a Dirichlet boundary condition is applied for the analyses.

6.5.2.5 *Numerical method for solving the heat transfer problem*

The Crank-Nicolson method is the finite differences method chosen for solving the heat transfer problem. This method is a second-order method in time, and implicit in time and numerically stable. The formulation is based on building a system of N linear equations and N variables (i.e. temperatures of each node at the step j+1), based on Equation (6.16) below:

$$T_i^{j+1} = T_i^j + \frac{\Delta t}{2} \cdot \left(\left.\frac{dT}{dt}\right|_i^j + \left.\frac{dT}{dt}\right|_i^{j+1} \right) \quad (6.16)$$

where T_i^j and T_i^{j+1} are the temperature of the node i at the time step j and j+1 respectively, $\left.\frac{dT}{dt}\right|_i^j$ and $\left.\frac{dT}{dt}\right|_i^{j+1}$ are the time variation of the temperature of the node i at the time step j and j+1, and Δt is the time step.

The discretisation of a sample of thickness L is based on N elements, of thickness $\Delta x/2$ for nodes $i = 1$ and $i = N$ and thickness Δx for nodes $i = 2, \dots, N-1$. The discretisation of the domain is represented in Figure 6.28 below.

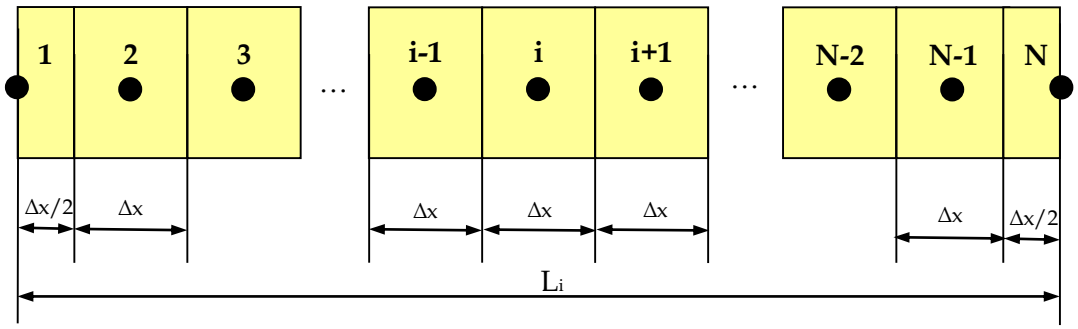

Figure 6.28. Discretisation for the domain of the one-dimensional heat transfer problem

The Crank-Nicolson method requires the derivation of the temperature variation over time $^{dT}/_{dt}$ for each element of the discretisation at time steps j and j + 1. The set of equations used to build the system of equations is noted below and the derivation of this is presented in Appendix D. The defined system of equations is a tridiagonal matrix system, which simplifies and reduces the computational cost of the model significantly. It should be noted that, since the temperature of the node N is known, the number of equations of the system is eventually N-1. A simplification is proposed by defining the Fourier number for each node i and time step j as:

$$Fo_i^j = \frac{k\left(T_i^j\right)\cdot \Delta t}{\rho\left(T_i^j\right)\cdot c_p\left(T_i^j\right)\cdot \Delta x^2} \tag{6.17}$$

where $k\left(T_i^j\right)$, $\rho\left(T_i^j\right)$ and $c_p\left(T_i^j\right)$ are respectively the thermal conductivity, density and heat capacity of the node i at the time step j, and Δt and Δx are the time step and the space discretisation of the finite difference method, respectively. It should be noted that the thermal properties are described as temperature dependent. This assumption is considered in order to derive the correct discretisation of the conduction heat transfer equation noted in Equation (6.1).

First element (1):

The discretised governing equation for the sample surface directly exposed to radiation is defined as noted in Equation (6.18). The terms are organised so as the unknown variables (marked in red colour) with their coefficients are placed on the left-hand-side of the equation, while the constant term is placed on the right-hand-side:

$$\begin{aligned} &\mathbf{T_1^{j+1}}\cdot\left[1+Fo_1^j+\frac{h_T\left(T_1^j\right)\cdot\Delta t}{\rho\left(T_1^j\right)\cdot c_p\left(T_1^j\right)\cdot\Delta x}\right]+\mathbf{T_2^{j+1}}\cdot\left[-Fo_1^j\right]= \\ &=T_1^j+Fo_1^j\cdot\left(T_1^j-T_2^j\right)+\frac{\alpha\cdot\Delta t}{\Delta x\cdot\rho\left(T_1^j\right)\cdot c_p\left(T_1^j\right)}\cdot\left(\dot{q}''^j_e+\dot{q}''^{j+1}_e\right) \\ &\quad+\frac{h_T\left(T_1^j\right)\cdot\Delta t}{\rho\left(T_1^j\right)\cdot c_p\left(T_1^j\right)\cdot\Delta x}\cdot\left(2\cdot T_\infty^j-T_1^j\right) \end{aligned} \tag{6.18}$$

If the metallic plate is used, T_1^{j+1} is no longer an unknown variable. Therefore, the discretised governing equation for the sample surface in contact to the metallic plate can be defined as noted in Equation (6.19), with h_T^{j+1} and T_2^{j+1} as the unknown variables:

$$\mathbf{h_T^{j+1}} \cdot \left[T_1^{j+1} - T_\infty\right] + \mathbf{T_2^{j+1}} \cdot \left[-\frac{k\left(T_1^{j+1}\right)}{\Delta x}\right] = \\ = \alpha \cdot \dot{q}''^{j+1}_e - \dot{q}''^{j+1}_{st,plate} - \frac{k\left(T_1^{j+1}\right)}{\Delta x} \cdot T_1^{j+1} - \frac{\Delta x \cdot \rho\left(T_1^j\right) \cdot c_p\left(T_1^{j+1}\right)}{2 \cdot \Delta t} \cdot \left(T_1^{j+1} - T_1^j\right) \quad (6.19)$$

Interior element (i):

The discretised governing equation for any interior element is defined as noted in Equation (6.20), with T_{i-1}^{j+1}, T_i^{j+1} and T_{i+1}^{j+1} being the three unknown variables:

$$\mathbf{T_{i-1}^{j+1}} \cdot \left[-\frac{Fo_i^j}{2}\right] + \mathbf{T_i^{j+1}} \cdot \left[1 + Fo_i^j\right] + \mathbf{T_{i+1}^{j+1}} \cdot \left[-\frac{Fo_i^j}{2}\right] = \\ = T_i^j + \frac{Fo_i^j}{2} \cdot \left(T_{i-1}^j - 2 \cdot T_i^j + T_{i+1}^j\right) + \frac{\delta k\left(T_i^j\right)}{\delta T} \cdot \left(\frac{T_{i+1}^j - T_{i-1}^j}{2 \cdot \Delta x}\right)^2 \cdot \frac{\Delta t}{\rho\left(T_i^j\right) \cdot c_p\left(T_i^j\right)} \quad (6.20)$$

Last element (N-1):

The discretised governing equation for the last element is defined as noted in Equation (6.21) below:

$$\mathbf{T_{N-2}^{j+1}} \cdot \left[-Fo_{N-1}^j\right] + \mathbf{T_{N-1}^{j+1}} \cdot \left[1 + Fo_{N-1}^j\right] = \\ = T_{N-1}^j + Fo_{N-1}^j \cdot \left(T_{N-2}^j - 2 \cdot T_{N-1}^j + T_N^j\right) + \\ + T_N^{j+1} \cdot \left[-Fo_{N-1}^j\right] + \frac{\delta k\left(T_{N-1}^j\right)}{\delta T} \cdot \left(\frac{T_{N-2}^j - T_N^j}{2 \cdot \Delta x}\right)^2 \cdot \frac{\Delta t}{\rho\left(T_{N-1}^j\right) \cdot c_p\left(T_{N-1}^j\right)} \quad (6.21)$$

6.5.2.4 Summary

A summary of the objective, constraint and optimisation variables are listed in Table 6.3 below.

Table 6.3. Summary of objective, constraint and optimisation variables

Type of variable	No plate on top	Plate on top
Objective variables (set of variables from the determined system of equations for the heat transfer problem)	{T_1, T_2, …, T_{N-1}}	{h_T, T_2, …, T_{N-1}}
Constraint variables	$\dot{q}''_e$, ρ, T_N, Δt, Δx	α, $\dot{q}''_e$, ρ, T_1, T_N, Δt, Δx
Optimisation variables	α, h_T, k, c_p	k, c_p

If the thermal conductivity and heat capacity are not dependent on temperature, four optimisation variables are needed for the approach without plate on the surface,

while if the metallic plate approach is followed, two optimisation variables are needed.

However, if a temperature dependency is assumed, the number of variables is increased. A general solution can be given by polynomial functions of degree m and n respectively:

$$k(T) = k_0 + k_1 \cdot T + k_2 \cdot T^2 + \cdots + k_m \cdot T^m \tag{6.22}$$

$$c_p(T) = c_{p,0} + c_{p,1} \cdot T + c_{p,2} \cdot T^2 + \cdots + c_{p,n} \cdot T^n \tag{6.23}$$

Another approach that could be considered is to assume that these variables are temperature dependent according to the following expressions, which is the approach implemented by the complex pyrolysis model *Gpyro* [13]:

$$k(T) = k_0 \cdot \left(\frac{T}{T_r}\right)^{k_n} \tag{6.24}$$

$$c_p(T) = c_{p_0} \cdot \left(\frac{T}{T_r}\right)^{c_{p_n}} \tag{6.25}$$

6.5.3 Optimisation method

Several optimisation algorithms are commonly used for solving inverse or fitting problems. Typical approaches are adopted by the use of genetic algorithms (GA) based on metaheuristic searches [14], or mathematical algorithms such as Levenberg-Marquardt (LMA) [15, 16] based on curve fitting. For the optimisation problem here, the Levenberg-Marquardt algorithm is used. LMA algorithm, commonly used to solve non-linear least square problems, is based on the minimisation of objective functions, e.g. fitness functions, by the use of the Jacobian matrix that represents the sensitivity of each optimisation variable to modify or improve the objective function in an iterative process. For a certain value of the optimisation variables defined in the array $\mathbf{X}$, if the values of the objective variable from the experiment and model are defined as array of values denominated $\mathbf{Y_{exp}}$ and $\mathbf{Y_{model}}(\mathbf{X})$ respectively, the fitness or objective function is defined as the sum of squares function:

$$S(\mathbf{X}) = \sum_{i=1}^{N_{points}} \left[\mathbf{Y_{model}}(\mathbf{X}) - \mathbf{Y_{exp}}\right]^2 \tag{6.26}$$

The aim of the LMA is to minimise the fitness function S, which can be expressed as follows:

$$S = \mathbf{F^T F} \tag{6.27}$$

where each element of the array $\mathbf{F}$ is defined as the difference between the model and the experimental value for certain point i:

$$F_i = Y_{model_i} - Y_{exp_i} \tag{6.28}$$

The Jacobian matrix, representative of the gradient of the solution $\mathbf{Y_{model}}(\mathbf{X})$ with respect to each optimisation variable X_j , is defined by the elements:

$$J_{ij} = \frac{\partial Y_{model_i}}{\partial X_j} \tag{6.29}$$

Then, the LMA is defined by the following formulation:

$$\left(\mathbf{J}^T\mathbf{J} + \lambda \text{diag}(\mathbf{J}^T\mathbf{J})\right)\boldsymbol{\delta} = \mathbf{J}^T\mathbf{F} \tag{6.30}$$

where λ is a damping factor and $\boldsymbol{\delta}$ is an array with the variation of the optimisation variables $\mathbf{X}$. A new set of values for the optimisation variables can be obtained for each iteration by the following expression extracted from (6.30):

$$\mathbf{X}^{n+1} = \mathbf{X}^n + \left(\mathbf{J}^T\mathbf{J} + \lambda \text{diag}\left(\mathbf{J}^T\mathbf{J}\right)\right)^{-1}\mathbf{J}^T\mathbf{F} \tag{6.31}$$

Fortunately, this algorithm is already implemented in MATLAB's framework [17], and the author has used this built-in algorithm for solving the particular inverse heat transfer problem defined in the previous section. The main disadvantage of the Levenberg-Marquardt algorithm is that it is able to find local minima, but not a global minimum. The conditioning of the inverse problem being studied is presented below.

6.5.3.1 The inverse problem conditioning

Absorptivity, global heat transfer coefficient of losses, thermal conductivity and specific heat capacity are the variables sought for the inverse problem if a metallic plate is not used. As noted in Equations (6.8), the triplet absorptivity, heat transfer coefficient and conductivity govern the net heat absorbed by the sample, while the thermal diffusivity determines the diffusion of heat within the material. All these together determine the singularity of the solution, i.e. a unique temperature profile history. However, the same temperature history can be obtained with these parameters being altered and maintaining the thermal conductivity – specific heat capacity ratio. An indication of this is presented by *Bal* [18], who demonstrated that compensation errors play an important role in the inverse problem of pyrolysis of solid materials, where the governing phenomena include a higher level of complexity than the problem defined here due to the number of variables.

A benchmark of the inverse model is pursued by generating a thermal profile history with a certain quantification of the optimisation variables and the constraint variables as shown in Table 6.4 and Table 6.5 respectively. The temperature profile associated to these variables, given for six points at 20 mm spacing within the material thickness is shown in Figure 6.29**.**

Table 6.4. Optimisation variables

Absorptivity	**Global heat transfer coefficient of losses:** $\mathbf{h_T = h_{T0} + h_{T1} \cdot (T_s - T_\infty)}$		**Thermal conductivity**	**Specific heat capacity**
α /-	h_{T0} /W·m^{-2}·K^{-1}	h_{T1} /W·m^{-2}·K^{-2}	k_0 /W·m^{-1}·K^{-1}	c_0 /J·kg^{-1}·K^{-1}
0.70	12.451	0.082	0.03	1500

Table 6.5. Constraint variables

External Heat Flux	Material Density	Ambient Temperature	Back Boundary Condition
$\dot{q}''_e$ /W·m^{-2}	ρ /kg·m^{-3}	T_∞ /°C	Known temperature profile given by a heat sink with an adiabatic boundary condition beneath it.
10000	32	20	

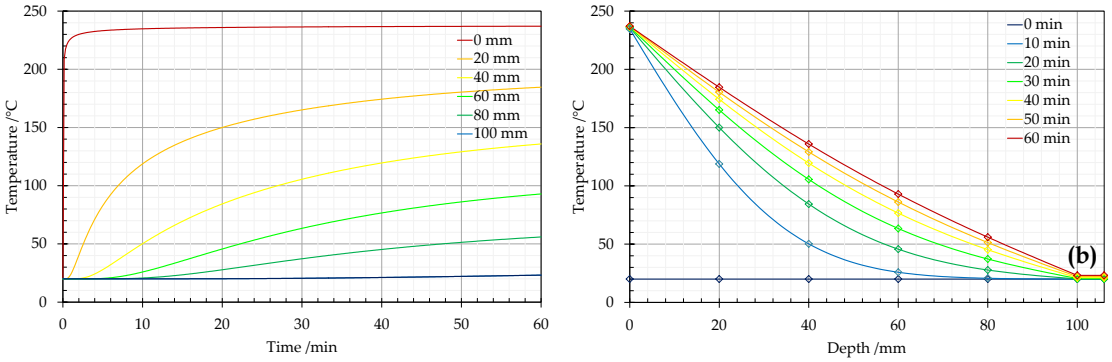

Figure 6.29. Temperature profile history within the thickness of the modelled material (a) Temperature-time history for the six positions (b) Temperature-thickness history

Initially, the thermal conductivity and heat capacity are fixed to different values, giving the same thermal diffusivity. The resulting values for the optimisation variables obtained by the inverse model are shown in Table 6.6 below. Figure 6.30 presents the net heat flux absorbed diverging from the original solution (#1). The ratio between any case and the original solution is equal to the ratio between the set thermal conductivity and the original one.

Table 6.6. Study cases

Case ID	Fixed Variables			Resulting optimisation variables			
	Thermal conductivity	Specific heat capacity	Thermal diffusivity	Absorptivity	Global heat transfer coefficient of losses:		Fitness function value (Residues)
	k_0	c_0	$k/\rho c_0$	α	h_{T0}	h_{T1}	
#1	0.03	1500	$2\cdot10^{-5}$	0.70	12.4508	0.0820	2.00759e-08
#2	0.01	500		0.233	4.1503	0.0273	2.00759e-08
#3	0.015	750		0.35	6.2254	0.0410	2.00759e-08
#4	0.06	3000		1.40	24.9014	0.1640	2.00806e-08
#5	0.09	4500		2.10	37.3522	0.2460	2.00785e-08

The fact that the temperature profile history remains the same indicates that the thermal gradient (δT/δx) at the surface is satisfied, and therefore the relation between the different net heat fluxes is indeed the ratio between the original conductivity and

the forced altered value of this ($-\frac{\delta T}{\delta x} = \dot{q}''_{net}/k$). Therefore, when performing an inverse heat transfer analysis, a perfect agreement in the temperature profile history does not necessarily mean that the result is correct, since the energy balance obtained may not be equal to the real one. If this approach is followed, only external data from material properties can identify whether reasonable values of the absorptivity and global heat transfer coefficients of heat losses are achieved within physical limits.

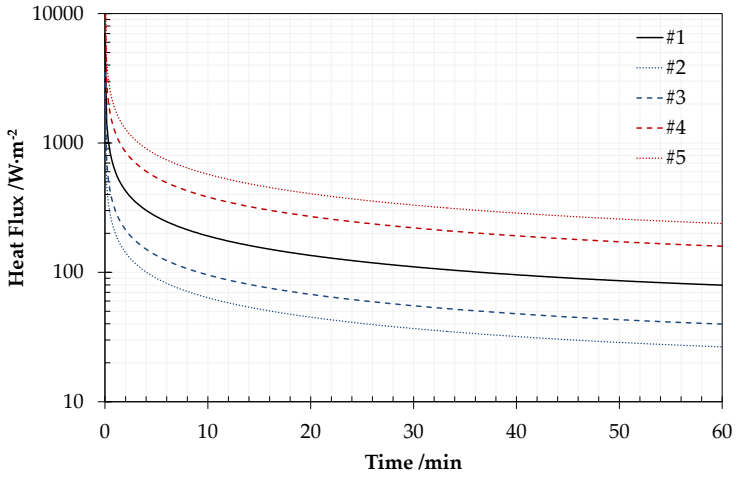

Figure 6.30. Net heat absorbed for the solved cases

If none of the optimisation variables are fixed, the inverse model might show a perfect agreement in the temperature profile, but the solution will be in the vicinity of the proposed initial solution. Additionally, if the actual positioning of the thermocouple is not defined correctly, the agreement would never be perfect, identifying a local minimum with a set of optimisation variables that satisfies a thermal diffusivity as the original one.

Therefore, the best approach for the determination of the thermal properties is to fix some of the parameters within limits with physical meaning; then, consider the obtained solution as a confidence region and verify its repeatability with several experiments. The approach with the metallic plate simplifies the problem and allows reducing the uncertainty during this process.

6.5.4 Modelling results

Inverse modelling techniques are applied with the extensive data obtained from the experiments carried out on plastic foams. As noted previously, two different approaches are taken in order to optimise the thermal properties, considering case studies with the heat transferred by radiation or with the heat transferred by a metallic plate. It has been demonstrated that infinite solutions may be found if none of the parameters included in the conduction equation are fixed. Thus, a range of values are considered for the specific heat capacity based on data from the literature. The benefit of fixing this parameter is that most of the materials present similar specific heat capacity. In any case, a range of uncertainty is considered.

Table 6.7 shows the fitted parameters by optimisation techniques by considering the measured density and the assumed specific heat capacity. Values of thermal inertia are calculated, so results obtained from Chapter 5 can be compared. The cases presented in Table 6.7 correspond to repeated experiments at a low range of radiant heat fluxes (10 $kW \cdot m^{-2}$ for PIRa, PIRb, PIRc and PF, and 2 $kW \cdot m^{-2}$ for EPS), so thermal degradation is not obtained. It should be noted that for different specific heat capacity values, different quantifications of the thermal conductivity are obtained, representing the range of uncertainty. These are presented as average values with the standard deviation from the considered experiments.

Table 6.7. Fitted thermal properties for temperatures below thermal degradation or shrinkage

Material	Thermal conductivity /$W \cdot m^{-1} \cdot K^{-1}$	Assumed density /$kg \cdot m^{-3}$	Assumed range of specific heat capacity /$J \cdot kg^{-1} \cdot K^{-1}$	Thermal inertia /$W^2 \cdot s \cdot K^{-2} \cdot m^{-4}$
	k (fitted)	ρ (measured)	c_p (literature)	kρc (calculated)
PIRa (foil faced)	0.040 ± 0.004 **0.060 ± 0.006** 0.080 ± 0.009	**31.2 ± 0.61**	1000 **1500** 2000	1248 **2808** 4992
PIRb (foil faced)	0.042 ± 0.006 **0.062 ± 0.010** 0.083 ± 0.013	**33.2 ± 0.71**	1000 **1500** 2000	1394 **3088** 5511
PIRc (foil faced)	0.024 ± 0.005 **0.035 ± 0.008** 0.047 ± 0.011	**33.5 ± 0.65**	1000 **1500** 2000	804 **1759** 3149
PF (foil faced)	0.038 ± 0.013 **0.057 ± 0.019** 0.077 ± 0.025	**38.1 ± 1.05**	1000 **1500** 2000	1448 **3258** 5867
EPS (before shrinking)	0.044 ± 0.001 **0.067 ± 0.001** 0.089 ± 0.002	**10.4 ± 0.2**	1000 **1500** 2000	458 1045 1851

Table 6.8 shows the fitted thermal conductivity by optimisation techniques for experiments carried out on PIRb and PF with a metallic plate at the surface. A higher radiant heat flux is used (25 $kW \cdot m^{-2}$), so as the pyrolysis reactions are considered. The use of the metallic plate controls the diffusion of air through the charred material, so smouldering is isolated from the thermal behaviour of the samples. Similarly to Table 6.7, the specific heat capacity is assumed to be in the range 1000-2000 $J \cdot kg^{-1} \cdot K^{-1}$, with 1500 $J \cdot kg^{-1} \cdot K^{-1}$ as nominal and recommended value from the literature. For simplicity, the thermal conductivity is considered as a temperature dependent linear function.

An approach based on fixing the specific heat capacity and defining a temperature dependent thermal conductivity is first proposed because a constant value of conductivity, with a temperature dependent specific heat capacity, did not provide acceptable trends in the prediction in-depth temperatures compared to experimental predictions. Indeed, a temperature dependent conductivity did not only provide a

better fitting, but better trends. This indicates that the approach used reflects the physical phenomena taking place.

Table 6.8. Fitted thermal properties up to 500°C by using the metallic plate (25 kW·m^{-2})

Material	Thermal conductivity /W·m^{-1}·K^{-1}	Density /kg·m^{-3}	Assumed range of specific heat capacity /J·kg^{-1}·K^{-1}
	k(T) with T in °C (fitted) *T<500°C*	ρ (measured)	c_p (literature)
PIRb	0.012 (±0.001) + T·8.3·10^{-5}(±8.3·10^{-6})	**33.2 ± 0.71**	1000
	0.018 (±0.001) + T·1.24·10^{-4}(±1.24·10^{-5})		**1500**
	0.025 (±0.001) + T·1.66·10^{-5}(±1.65·10^{-5})		2000
PF	0.029 (±0.0002) + T·2.33·10^{-5}(±3.1·10^{-6})	**38.1 ± 1.05**	1000
	0.044 (±0.0003) + T·3.49·10^{-5}(±4.6·10^{-6})		**1500**
	0.059 (±0.0004) + T·4.66·10^{-5}(±6.2·10^{-6})		2000

The author recognises that the specific capacity might actually experience a temperature variation due to (1) endothermic pyrolysis and (2) different molecular structure from the virgin material and the char. Nonetheless, since the density of the material is significantly low for insulation materials, the energy stored (dependent on the volumetric heat capacity) and endothermic reaction are expected to be very low compared to the conducted heat.

Additionally, the low conductivity of these materials is due to the blowing agent enclosed in their cells, since most of the volume is just gas. However, as shown in Chapter 2, the conductivity of gases tends to increase with temperature, Furthermore, once thermal degradation is achieved, the blowing agent is lost, with the pores being replaced for other gases with likely higher conductivity. These effects would justify the better fitting provided by an approach that considers a temperature dependence of the thermal conductivity.

Figure 6.31 shows two case studies where modelling techniques are applied to PIRb, while Figure 6.31a illustrates the time-history of temperatures within a sample tested under 10 kW·m^{-2} and with protective layer at the surface. The maximum temperature obtained at the surface is 100°C. Good agreement is observed when using constant thermal properties as noted in Table 6.7. Discrepancies are observed for the first and second thermocouple during the first period of the experiment, likely due to lateral heat losses not being considered in the model.

Figure 6.31b illustrates the time-history of temperatures within a sample tested under 25 kW·m^{-2} and using the metallic plate at the surface. The maximum temperature produced by the material is approximately 500°C, which is above the critical temperature of pyrolysis. Good agreement is observed between the model and the experimental results when using a temperature dependent thermal conductivity as shown in Table 6.8. The main discrepancies between the model and the experimental results are observed during the first period of the test in thermocouples at 4 mm and 20 mm, which represent a delay in the thermal wave probably due to the contact resistance at the interface plate-insulation. In any case, a good trend is

observed in the distribution of the thermal wave, and the use of the metallic plate provides a successful inhibition of the surface oxidation from the already pyrolysed material; otherwise, this simple modelling approach would not have been possible, since exothermic processes would be observed in the thermal gradient.

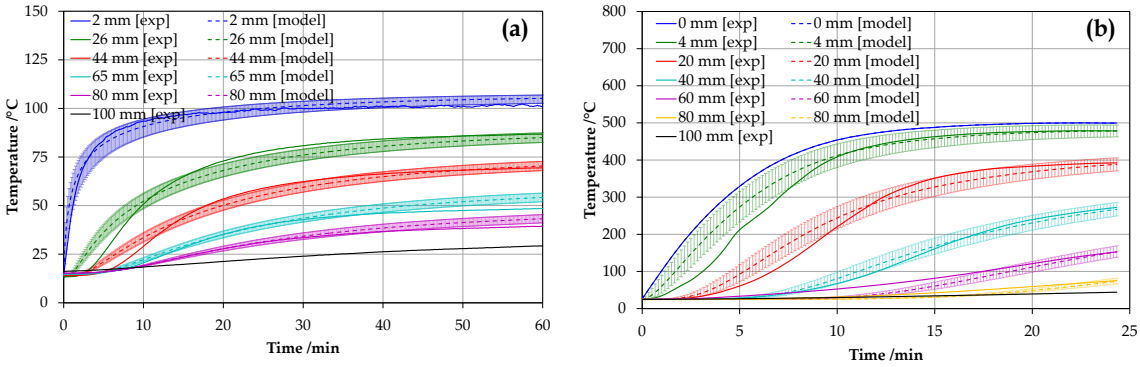

Figure 6.31. Experimental and modelled time-history of the temperature profile within PIRb (a) Low heat flux range: 10 kW·m^{-2} with protective layer (b) High heat flux range: 25 kW·m^{-2} with metallic plate

Two representative case studies where modelling techniques are applied to PF are shown in Figure 6.32. Error bars are included representing an error position of ±3 mm. Figure 6.32a presents the time-history of temperatures within a PF sample tested under 10 kW·m^{-2} and with protective layer at the surface, for which the maximum achieved temperature is approximately 125°C. Good agreement is observed between the model and the experimental results, although some discrepancies are identified. The surface temperature presents the main discrepancy, likely due to inaccurate positioning of the thermocouple. Thermocouples at 21 mm and 47 mm show faster temperature increase in the model than in the experiments, probably due to lateral thermal losses or endothermic reactions (moisture desorption) at 100°C below the surface. In any case, the trend observed for the thermal wave shows a good agreement between experimental and numerical values.

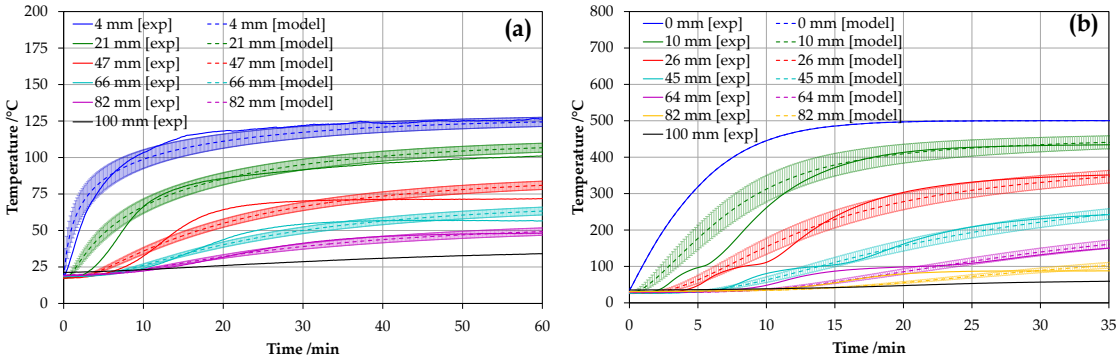

Figure 6.32. Experimental and modelled time-history of the temperature profile within PF (a) Low heat flux range: 10 kW·m^{-2} with protective layer (b) High heat flux range: 25 kW·m^{-2} with metallic plate

Figure 6.32b illustrates the time-history of temperatures within a PF sample tested under 25 kW·m^{-2} and with the metallic plate at the surface. The maximum temperature reached by the material at the surface is approximately 500°C. The model

prediction is obtained by considering a temperature dependent thermal conductivity as shown in Table 6.8. Worse agreement is observed between model and experiment, especially for thermocouples at the positions of 4 and 20 mm. Similarly to the other cases, these discrepancies may be produced because of the contact resistance at the interface, lateral heat losses and the endothermic reaction that PF experiences around 100°C. In any case, results show a fairly consistent distribution of the thermal wave with the used thermal properties.

Figure 6.33 shows a case study of EPS tested at 2 kW·m^{-2}. It should be noted that this low heat flux is required so as to isolate the shrinkage of the EPS for a certain period. Indeed, the temperature readings presented here are until 300 seconds, since shrinking was observed afterwards. Fairly good agreement is observed between the model and the experiments, with larger discrepancies being observed at the surface as would be expected. Larger values of radiant heat flux are not shown since shrinkage is observed almost immediately after the start of the experiments as mentioned in the previous sections. Then, the determined thermal properties are only valid for temperatures below the point where the blowing agent is lost (approximately 100°C). Indeed, values of conductivity are no longer of interest after shrinkage, since the governing phenomenon is not conduction but heat storage as a thermally thin element.

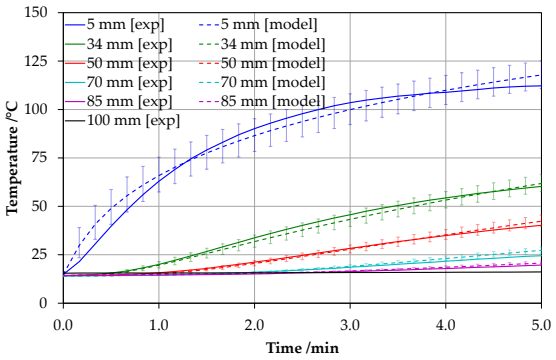

Figure 6.33. Experimental and modelled time-history of the temperature profile within EPS at 2 kW·m^{-2} before shrinking

6.5.5 Discussion

The simple modelling techniques proposed in this chapter show a series of limitations that do not allow considering phenomena such as lateral heat losses, endothermic reactions, and shrinkage/expansion of the material, or other mechanisms of heat transfer such as internal radiation or convection. However, this approach seems to provide reasonable predictions of the time-history of temperatures within rigid foams such as PIR and PF while oxidation reactions are isolated, and also for EPS before shrinking is obtained.

In any case, the results of these techniques are necessary for the design methodology proposed in Chapter 3, which requires the quantification of thermal properties from the insulation material until the onset of pyrolysis is reached.

The vulnerabilities of inverse modelling by which infinite solutions may be found if there is no understanding on the conditioning of the model, as well as the way that each of these parameters may interact have also been demonstrated herein. The simplest inverse heat transfer model may reach several solutions, thus fixing of some parameters was required since the definition of a reliable boundary condition is not easy. Additional factors such as positioning of temperature readings play an important role, especially at regions near the surface.

Surface oxidation was also been found to influence the thermal behaviour of the already pyrolysed material. However, significant oxidation is not expected until the integrity of the render or lining is violated. Thus, the use of a metallic plate as a boundary condition has allowed the characterisation of this behaviour under inert conditions, providing quantification of the thermal properties, which will be further assessed in Chapter 7.

6.6 Concluding remarks

A mapping of the thermal degradation processes linked to the thermal evolution of the solid-phase from each of the studied insulation materials has been presented. Additional modelling and optimisation techniques based on the solution of the one-dimensional heat diffusion equation have been proposed for characterising the thermal properties of the insulation materials.

A technique based on comparing the eventual thermal discolouration through the thickness of a sample has been correlated to the upper edge of the temperature envelopes during the test and the thermogravimetric results. Three clear domains are observed in the thermal evolution of PIR and PF, corresponding to the virgin material, pyrolysis region, and char. Stone wool shows patterns of discolouration indicating loss of the binder. Expanded polystyrene simply presents shrinkage of the surface as it reached the temperature at which the blowing agent was lost (glass transition ~110°C), and eventually melting.

During the pyrolysis process of PIR, the material is found to expand, creating a series of gaps within the structure of the foam. However, PF does not show a similar behaviour, but spalling due to the loss of the chemically bound water was evidenced by plateaus of temperature at 100°C. While the pyrolysis is clearly governed by the thermal evolution of the solid-phase for these charring materials, the rate of oxidation is clearly identified as a diffusion-controlled mechanism. Indeed, values of temperatures higher than those obtained by thermogravimetry are observed within the char. The rate of oxidation of the char is also found to be governed by the external heat flux, which also determines the evolution of the pyrolysis front.

The effect of the protective layer on the performance of PIR and PF when exposed to radiation is evidenced. The main effect is related to the reduction of the heat absorption due to low absorptivity/emissivity of this layer. The secondary main effect is the reduction of the surface oxidation (smouldering), avoiding the diffusion of air through the material already pyrolysed.

Simple modelling techniques based on a one-dimensional heat transfer approach have shown good prediction capabilities for experiments carried out at the ranges of heat flux where low temperatures (below thermal degradation) are observed. The inclusion of temperature dependence of the thermal properties in the model indicates an improvement in the fitting of experimental results with higher ranges of temperature. The relatively poor agreement found, indicates the two-dimensionality of the problem determined by the set-up as observed by temperature readings at the sides of the samples. This effect originates because of the low thermal properties of the studied materials in comparison to the sample wrapping, which represents the main limitation from this analysis technique, together with events such as surface oxidation or material shrinkage.

The use of the metallic plate has aided to the limitation of uncertainty in the analysis, mainly due to the direct determination of the surface temperature of the foam. Indeed, one of the biggest uncertainties in an inverse heat transfer model is related to the boundary condition, which is clearly conditioned in the model by the positioning of the first thermocouple. Additionally, the use of the metallic plate has eliminated the surface oxidation, thus allowing the application of the analysis to higher ranges of temperature for the charring materials.

6.7 References

[1] "BS 476-15, ISO 5660. Fire tests on building materials and structures. Method for measuring the rate of heat release of products." BSI, 1993.

[2] R. Carvel, T. Steinhaus, G. Rein, and J. L. Torero, "Determination of the flammability properties of polymeric materials: A novel method," *Polymer Degradation and Stability*, vol. 96, no. 3, pp. 314–319, 2011.

[3] J. V. Beck, "Thermocouple Temperature Disturbances in Low Conductivity Materials," *Journal of Heat Transfer*, vol. 84, no. 2, p. 124, 1962.

[4] P. Reszka, "In-Depth Temperature Profiles in Pyrolyzing Wood (Ph.D. thesis)," The University of Edinburgh. http://hdl.handle.net/1842/2602, 2008.

[5] N. A. Burley, "Nicrosil/Nisil Type N Thermocouples," *Omega complete temperature measurement handbook and encyclopedia*, vol. 28, pp. Z33–Z36, 1992.

[6] D. Drysdale, "Ignition: The Initiation of Flaming Combustion," in *An Introduction to Fire Dynamics*, John Wiley & Sons, Ltd, 2011, pp. 225–275.

[7] J. Sjöström and R. Jansson, "Measuring thermal material properties for structural fire engineering," in *15th International Conference on Experimental Mechanics*, 2012.

[8] S. E. Gustafsson, "Transient plane source techniques for thermal conductivity and thermal diffusivity measurements of solid materials," *Review of Scientific Instruments*, vol. 62, pp. 797–804, 1990.

[9] M. J. O'Neill, "Measurement of Specific Heat Functions by Differential Scanning Calorimetry.," *Analytical Chemistry*, vol. 38, pp. 1331–1336, 1966.

[10] A. Amundarain, "Assesment of the Thermal Efficiency, Structure and Fire Resistance of Lightweight Building Systems for Optimised Design (Ph.D. thesis)," The University of Edinburgh. http://hdl.handle.net/1842/2128, 2007.

[11] C. Maluk, "Development and Application of a Novel Test Method for Studying the Fire Behaviour of CFRP Prestressed Concrete Structural (Ph.D. thesis)," The University of Edinburgh, 2014.

[12] T. Steinhaus, "Determination of Intrinsic Material Flammability Properties from Material Tests assisted by Numerical Modelling (Ph.D. thesis)," The University of Edinburgh. http://hdl.handle.net/1842/3273, 2010.

[13] C. Lautenberger and C. Fernandez-Pello, "Generalized pyrolysis model for combustible solids," *Fire Safety Journal*, vol. 44, no. 6, pp. 819–839, 2009.

[14] X. S. Yang, *Engineering Optimization: An Introduction with Metaheuristic Applications*. 2010.

[15] D. Marquardt, "An Algorithm for Least-Squares Estimation of Nonlinear Parameters," *SIAM Journal on Applied Mathematics*, vol. 11, no. 2, pp. 431–441, 1963.

[16] K. Levenberg, "A Method for the Solution of Certain Non-Linear Problems in Least Squares," *Quarterly of Applied Mathematics*, vol. 2, pp. 164–168, 1944.

[17] The MathWorks Inc., "MATLAB and Optimization Toolbox R2014a." Natick, Massachusetts, United States.

[18] N. Bal, "Uncertainty and complexity in pyrolysis modelling (Ph.D. thesis)," The University of Edinburgh. http://hdl.handle.net/1842/6511, 2012.

Chapter 7.

Large-Scale Testing: Performance and Hazards' Map Validation

7.1 Introduction

The final step towards the full characterisation and understanding of the performance of insulation materials requires the assessment of large-scale experiments. For this thesis, two different programmes of large-scale experiments are carried out in collaboration with parallel research projects and institutions. Despite the different aims of these experimental programmes, they serve the purposes of this thesis. An additional programme of intermediate-scale experiments is performed in order to include case studies under controlled heating conditions.

The first programme of large-scale tests is denoted here as Sandwich Panels Tests' programme, which is performed in collaboration with The University of Central Lancashire, the Technical University of Denmark and If P&C Insurance Company Ltd. The aim of this collaborative research is to evaluate the effect of damages and the increase of fire load on the fire performance of sandwich panels. However, this thesis only focuses on the understanding of the behaviour of insulation materials in fire from first principles, which allows gaining a better understanding on the final effect that damages and increased fire load have in the result of a standard test. As presented in Chapter 3, this first programme of tests is used as a case scenario where the main failure criterion – the onset of pyrolysis – can easily be identified. Indeed, the used thermal barrier (metal skin) represents a worst case scenario, as the barrier acts as a thermally thin material not contributing significantly to the delay of the thermal wave.

The second programme of large-scale experiments corresponds to the "Edinburgh Tall Buildings Fire Tests", which is the first experimental programme of the research project "Real Fires for the Safe Design of Tall Buildings" carried out by The University of Edinburgh. The main aim of this research project is to develop a methodology that can be used to provide design fire inputs, which are representative of real fire dynamics in the large open plan compartments, typical of Tall Buildings and provide reliable data for modelling purposes. This experimental programme is used as a demonstration of the safe use of insulation materials, representing an opposite case scenario to the first experimental programme introduced before. Engineered boundaries, highly insulated and representing efficient thermal transmittances, are designed in order to control the main failure mode, i.e. the onset of thermal degradation.

The intermediate-scale programme corresponds to a series of radiant panel experiments on a typical wall assembly used in construction, which consists of plasterboard covering a layer of insulation. These experiments are designed to extend the results from bench-scale testing into more realistic end-use conditions. Additionally, these represent several case studies with a boundary element (plasterboard) that is in-between the two types of boundary elements used in the other experimental programmes (thin metal skin and aircrete brick).

A brief description of the experiments and main results are presented in the following sections. This is followed by an analysis based on the time history of the thermal profiles observed for the wall assemblies and the absorption of heat. Additionally, a simplified analysis for calculating pyrolysis rates based on thermal profiles and thermogravimetry is proposed.

Finally, a brief comparison on the behaviour of the boundary elements for the different experiments is presented, with the variable heat absorption as the key parameter to define the severity of the fire, which is considered as its destructive potential.

7.2 Aim

The aim of this chapter is to extend the conclusions from bench-scale testing to a large scale and validate the hazard analysis presented in Chapter 3. Therefore, a series of goals are set herein in order to meet this aim:

- Verification and comparison of the phenomena observed in bench-scale testing with real end-use conditions.
- Identification and prediction of the main failure criterion, i.e. the onset of thermal degradation, by an analysis of the thermal behaviour of the solid-phase.
- Introduction of a simplified method to estimate pyrolysis rates from the insulation.
- Evaluation of the heat absorption as a key parameter to assess the fire severity.

7.3 Experimental programmes' description

7.3.1 Sandwich Panels Tests' programme

Two types of metal-skin wall based on rigid isocyanurate-based foam (PIRd) and stone wool (SW) are used for this experimental programme. Two series of assemblies are designed for both wall systems, an ad-hoc ISO 13784-1 [1] compartment with approximate internal dimensions of 2.4 m width by 3.2 m length by 2.4 m height as presented in Figure 7.1. Experiments 1a and 1b are based on the use of a propane burner as the external fuel source, with a series of replicated damages being added to both set-ups. Experiments 2a and 2b include wooden cribs to the propane burner as external fuel source inside the compartment. The damages of experiments 2a and 2b are slightly modified. A detailed description of the series of damages is presented in [2, 3].

Table 7.1. Summary of experiments performed

ID	Barrier	Insulation core	Fuel source
1a	Painted steel 0.7mm	PIR (40 kg·m^{-3})	Propane burner
1b		Stone wool (140 kg·m^{-3})	Propane burner
2a		PIR	Propane burner + 169 kg wood crib
2b		Stone wool	Propane burner + 297 kg wood crib

A gas sand burner fed by propane gas is used as a fuel source for tests 1a and 1b. The mass flow of the burner is controlled to reproduce three different steps of heat

release inside the compartment of 100, 300 and 600 kW. The weight of the wooden crib in tests 2a and 2b are 169 kg and 297 kg, respectively.

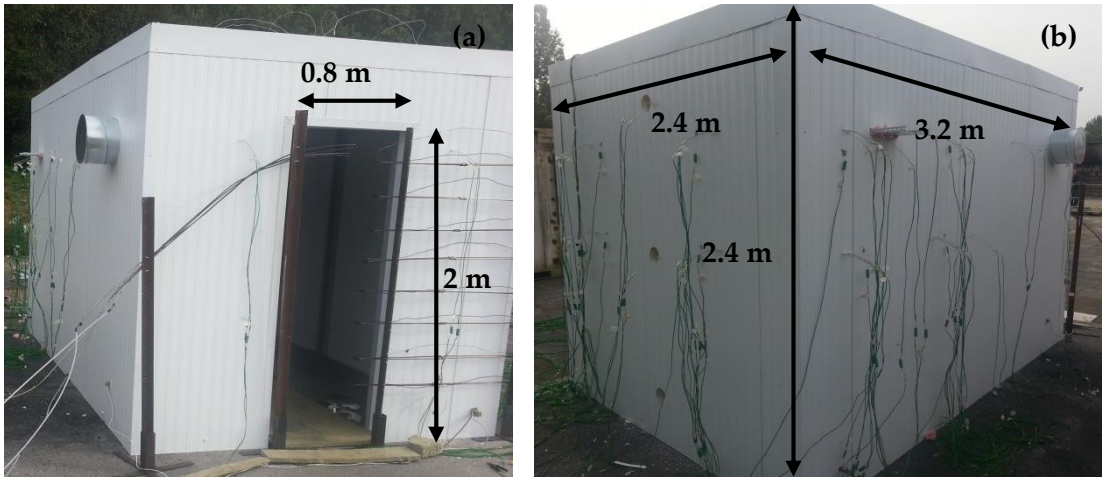

Figure 7.1. Highly instrumented modified ISO 13784-1 compartment. (a) Front view (b) Rear view

The gas flow of propane used for the different experiments, and corresponding heat release rates, are presented in Figure 7.2 below. It should be noted that identical input HRR curves are not followed due to complications while controlling the gas flow during the tests, and other safety reasons. The conversion of flow from standard litres per minute to heat release rate is obtained by considering a pressure of 1 bar, temperature of 298.15 K and a heat of combustion for propane of 2044 kJ·mol^{-1}.

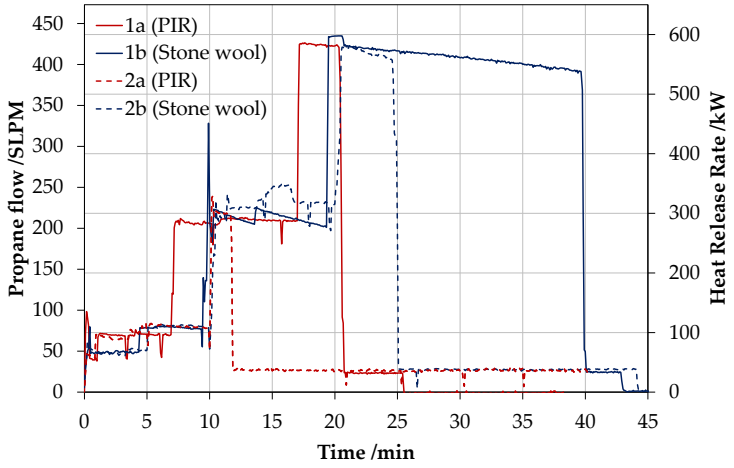

Figure 7.2. Gas flow and HRR of propane of the sand gas burner for each experiment

K-type Inconel-sheathed thermocouples (TCs) are inserted in certain positions of the wall and roof panels, which are more densely installed at locations closer to the gas burner. In particular, five thermocouples are distributed every 2 cm from the back of the inner metal-sheet of the panel close to the gas burner. The rest of locations are instrumented with two thermocouples separated 5 cm in-depth, with the first of them

being located behind the inner metal-sheet. Schematics of the of the thermocouple positioning are presented in Figure 7.3 below.

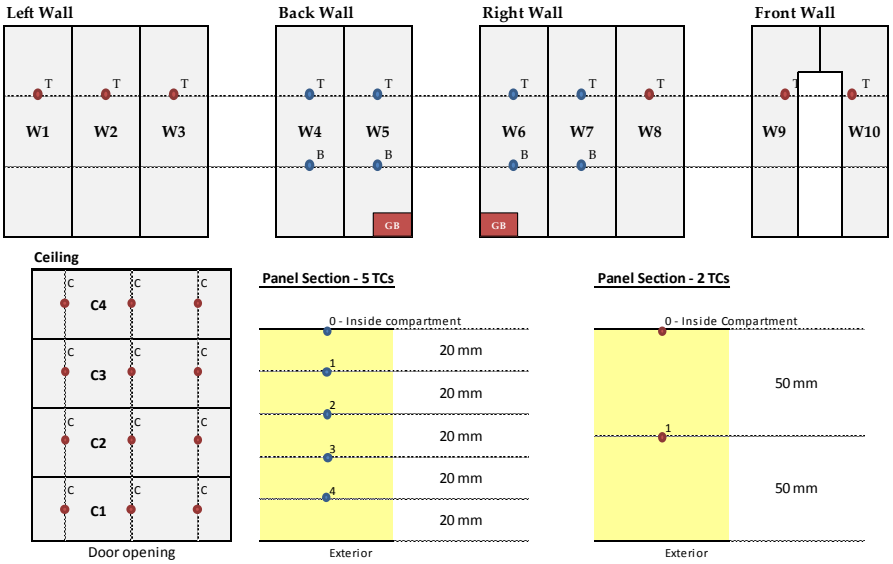

Figure 7.3. Monitoring locations for wall temperature measurements. Blue dots represent higher density of measurements (five thermocouples). Red dots represent lower density of measurements (two thermocouples). Relative position of the gas burner is represented by a red rectangle

The thermocouples are inserted from the back of the panel with a 15 mm lateral spacing in order to isolate the likely effect of heat sink introduced by the thermocouple wire and sheathing (Figure 7.4).

A series of non-standard thin skin calorimeters (TSCs) are installed 20 cm off the wall monitoring locations at walls W4, W5, W6 and W7. These TSCs consist of a 9.6 mm diameter and 1.3 mm thick 304b stainless-steel disc welded to two K-type thermocouple wires, and inserted on a layer of ceramic paper of nominal dimensions of 20 mm by 20 mm. This assembly is attached to the interior face of the panels with fire cement, and the wire goes through the panel to the exterior as shown in Figure 7.4 below.

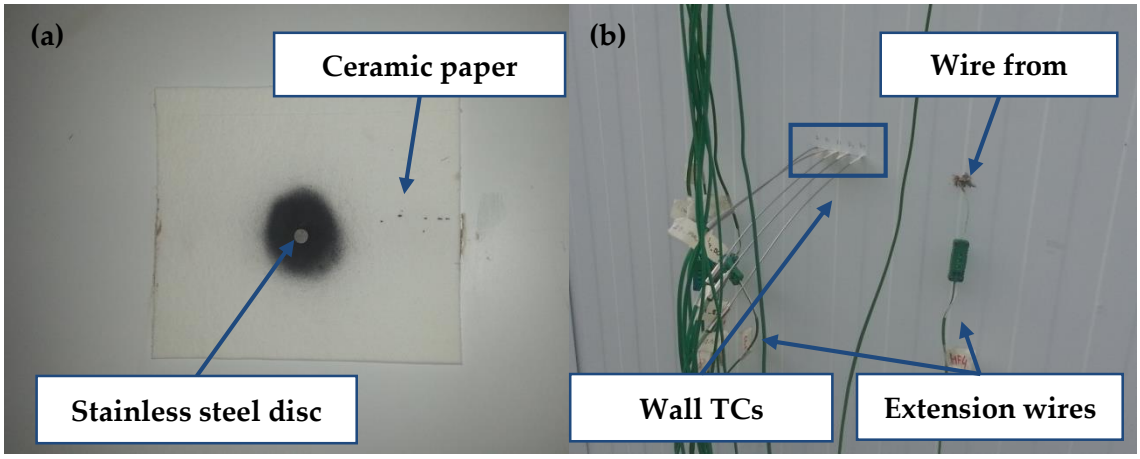

Figure 7.4. (a) Internal TSC (b) Wall TCs, wiring for TSC and extension wires

Measurements of gas-phase temperature, gas species and flow velocity are also taken, and the heat release rate in the compartment is estimated. However, these are not presented in detail in this chapter, but can be found in [2–4].

7.3.2 Edinburgh Tall Buildings Fire Tests' programme (ETFT)

A compartment of internal dimensions 17.8 m long by 4.9 m wide by 2.0 m high was constructed as shown in Figure 7.5. The compartment lays on a system of platforms 1 m over the ground in order to provide access from beneath. The total number of openings was fifteen, all of them located on a side of the compartment as shown in Figure 7.5, and each of them being 1.5 m high by 1.1 m wide. Precise details of the construction of the compartment can be found in [5]. The details presented below correspond to the walls which were instrumented for the purpose of this work.

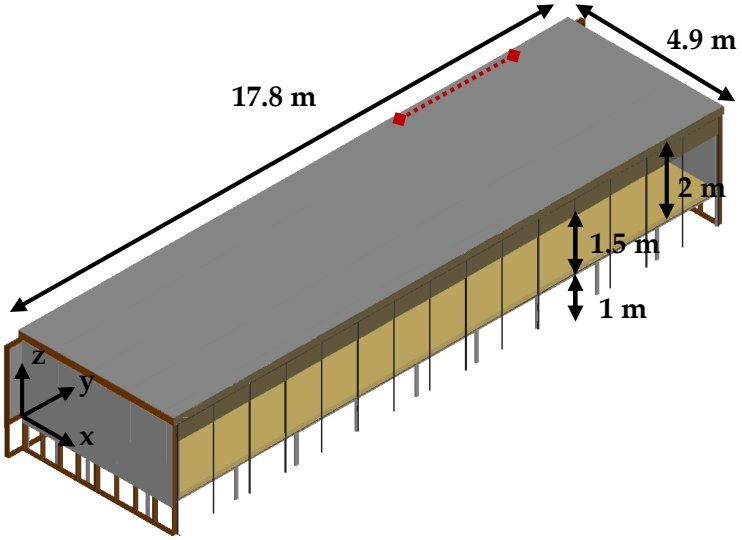

Figure 7.5. 3D schematics of the compartment design. Relative location of the instrumented walls is marked in red

The loadbearing walls consisted of timber frames and steel C-section profiles attached to the platform system and ground. The configuration of the standard wall system is illustrated in Figure 7.6 and detailed below from the inner face of the wall (interior of the compartment) to the outer face:

- 50 mm thick layer of aerated concrete bricks (aircrete).
- 50 mm thick layer of stone wool (lightweight insulation wool) between 50 mm wide steel C-section profiles.
- Timber frame wall of 145 mm thick studs, filled by stone wool (140 mm).
- 15 mm thick standard plasterboard.

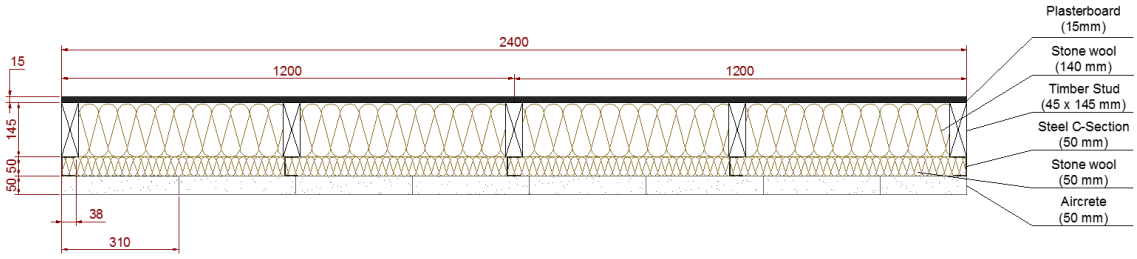

Figure 7.6. Schematics of the generic wall assembly

A series of frames are filled with other type of insulation, such as PIRb and PF, and a combination of these with stone wool. These sections are presented in Figure 7.7 previous to inserting the insulation. The location of these sections is on the right hand side of the compartment, near the location of the ignition area as shown in Figure 7.5 and Figure 7.8.

Figure 7.7. Sections prepared for inserting other insulation (a) before building up the aircrete wall - view from inside the compartment, and (b) after building the aircrete wall – view from outside

The thickness of each insulation material is presented in Table 7.2 below. It should be noted that although for the rest of the walls plasterboard is used to seal the exterior of the assembly, the instrumented walls presented above do not have plasterboard as the exterior element, in order to facilitate the insertion of thermocouples and examination of the state of these. The expected impact on the thermal performance of the samples from this technique is low due to the low thermal diffusivity of the insulation boards.

Table 7.2. Summary of insulation configurations

Section	Insulation core
1	50 mm SW + 140 mm SW
2	50 mm SW + 80 mm PF
3	50 mm SW + 90 mm PIRb
4	100 mm PF
5	50 mm PIRb + 60 mm PIRb

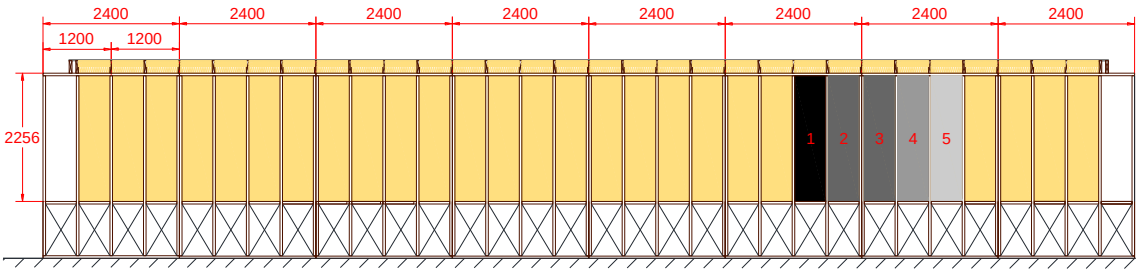

Figure 7.8. Section of the rear wall. The location of the instrumented wall sections is highlighted with different grey tonalities

Temperature readings are taken at different depths of each of the wall configurations at 400 mm, 1100 mm and 1800 mm over the floor of the compartment as shown in Figure 7.9. The thermocouples inserted in the insulation have a horizontal spacing of 15 mm in order to avoid the heat sink effect. Thin skin calorimeters are also used in order to provide heat flux measurements on the compartment boundaries. These consist of a 10 mm diameter, 0.5 mm thick 304b stainless steel disc, with a K type thermocouple welded to the centre of the unexposed face. The plate is embedded in a 80 mm diameter and 50 mm deep disc made of ceramic fibre (*ceraboard*®). The TSC positions on the instrumented wall are also shown in Figure 7.9.

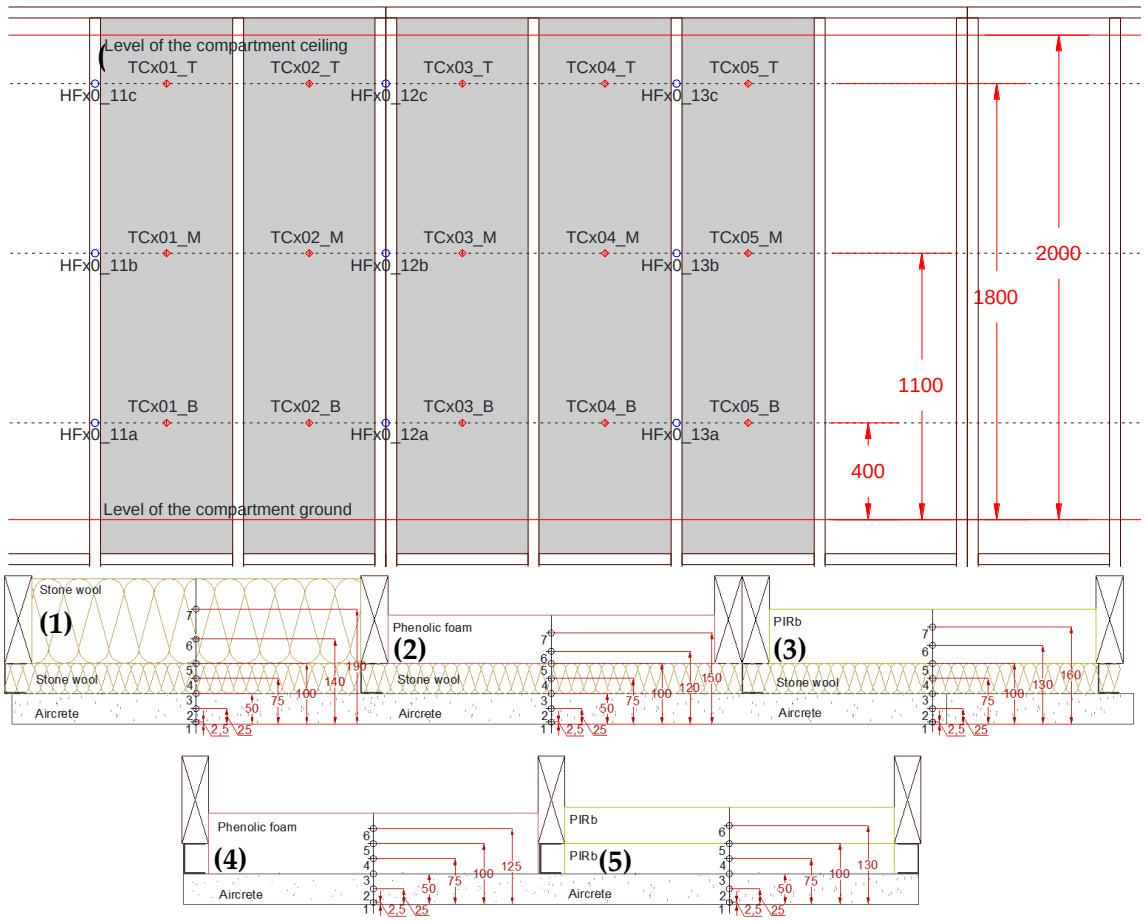

Figure 7.9. Thermocouple and TSC positioning for the instrumented walls. (a) Front section (b) Plan section

Two types of experiments are performed, based on sand gas burners (GB) and wood cribs (WC). The first set of experiments are designed to vary the fire behaviour (12 GB burning statically 2.5 MW, 2 GB travelling each of them burning 500 kW, or 2 GB being added to the previous ones and burning each of them 208 kW approximately) and the ventilation conditions (static ventilation with the fifteen openings, static ventilation with three openings, and variable ventilation). The experiments with wood cribs are performed with two types of ventilation, fully open and with only three openings. The wood crib is ignited linearly on the right-hand-side of the compartment. A summary of the performed experiments is listed in Table 7.3 below.

Table 7.3. Summary of experiments

Experiment ID	Type of fuel	Type of fire	Type of ventilation
GB_01_3	Propane (gas burners)	Static (12 burners)	Static – fully open
GB_01a GB_01b		Static (12 burners)	Static – fully open
GB_02		Static (12 burners)	Static – 3 openings (no.3,8,13)
GB_03b GB_03bii2 GB_03bii3		Travelling (2 burners - 2.5min)	Static - fully open
GB_03c GB_03c4		Spreading (2 burners - 2.5min)	
GB_04bii		Travelling (2 burners - 2.5min)	Static – 3 openings (no.3,8,13)
GB_04c		Spreading (2 burners - 2.5min)	
GB_05		Static (12 burners)	Variable - 1 shutter opens every 5 minutes
GB_06		Static (12 burners)	Variable - 1 shutter opens every 1 minute
GB_07 GB_07ii		Travelling (2 burners - 2.5min)	Variable - 1 shutter opens every 5 minutes
GB_08		Travelling (2 burners - 2.5min)	Variable - 1 shutter opens every 1 minute
GB_09		Travelling (2 burners)	
WC_01	Wood – (4 layer wood crib)		Static – fully open
WC_02			Static – 3 openings (no.3,8,13)

Figure 7.10. (a) Gas burners distributed in the compartment
(b) Wood cribs distributed in the compartment

7.3.3 Radiant Panel Tests' programme

A typical configuration of wall assembly typically found in buildings is explored, consisting of a layer of plasterboard onto a layer of insulation. As noted in Chapter 2, this configuration of wall can be found in types of walls such as timber or steel frame walls, or even cavity walls with the internal layer consisting of plasterboard.

Three insulation materials are studied: stone wool (SW), rigid isocyanurate-based polyurethane foam (PIRb) and rigid phenolic foam (PF). Expanded polystyrene is taken apart from the testing plan due to its tendency to shrink and melt when exposed to heat. The size of the insulation samples is approximately 450 mm by 760 mm and 100 mm thick. The insulation is cut to size and placed within a steel frame with the same internal dimensions, so as the insulation fits tightly into the frame. The system frame-insulation is covered by a 12.5 mm thick plasterboard leaf of dimensions 600 mm by 800 mm so as the insulation and frame remain covered during the experiments. The plasterboard is fixed on the frame with clamps that allow free expansion or contraction of the plasterboard, since the aim is to explore the behaviour of the insulation relying on the non-failure of the lining. The type of plasterboard is rated as type A and F according to BS EN 520 [6].

A picture of the sample holder and set-up is shown in Figure 7.11a and Figure 7.12. The sample consisting of the plasterboard leaf and the insulation board is exposed to a radiative heat source. The system used is H-TRIS [7], which is a system that allows moving the radiant panels onto different positions in order to represent a different heat exposure. Each position is calibrated to define a certain external/incident radiant heat flux. The radiant panels are fuelled by a mixture of propane-air. The process of calibration using a Schimdt-Boelter gauge [8] is shown in Figure 7.11b below.

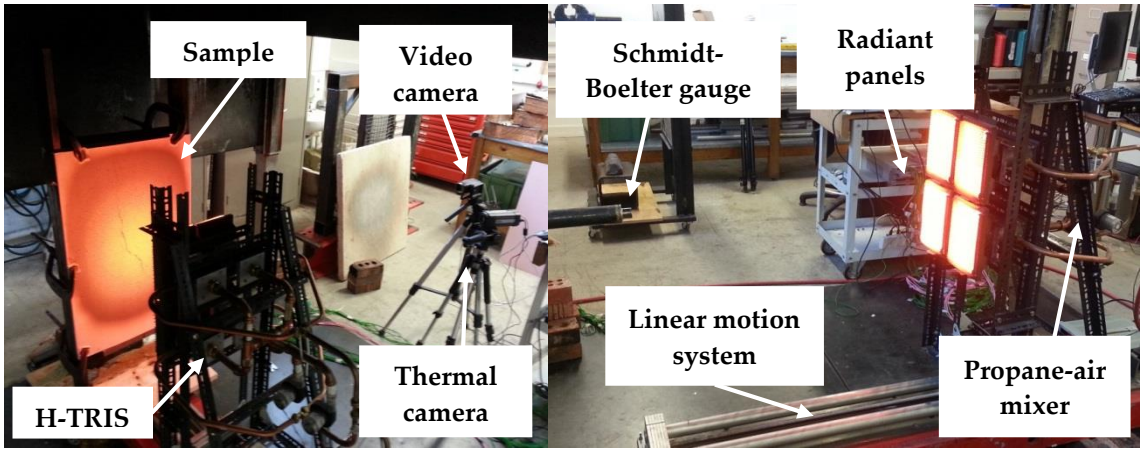

Figure 7.11. (a) Experimental set-up with sample, sample holder, H-TRIS and instrumentation (b) H-TRIS system during calibration

Every test is instrumented with several K-type thermocouples, and some N-type auxiliary thermocouples. The thermocouples are inserted in the core of the insulation material at three different positions and different depths from the back of the insulation, perpendicular to the exposed surface. The thermocouples are positioned at the plasterboard back surface, and every 20 mm in-depth from that position up to the back surface of the insulation. No thermocouples are inserted within the plasterboard so as not to damage the lining or produce any initial cracking. Instead, a thermal camera (FLIR® A320) is used to obtain an estimation of the surface temperature of the plasterboard.

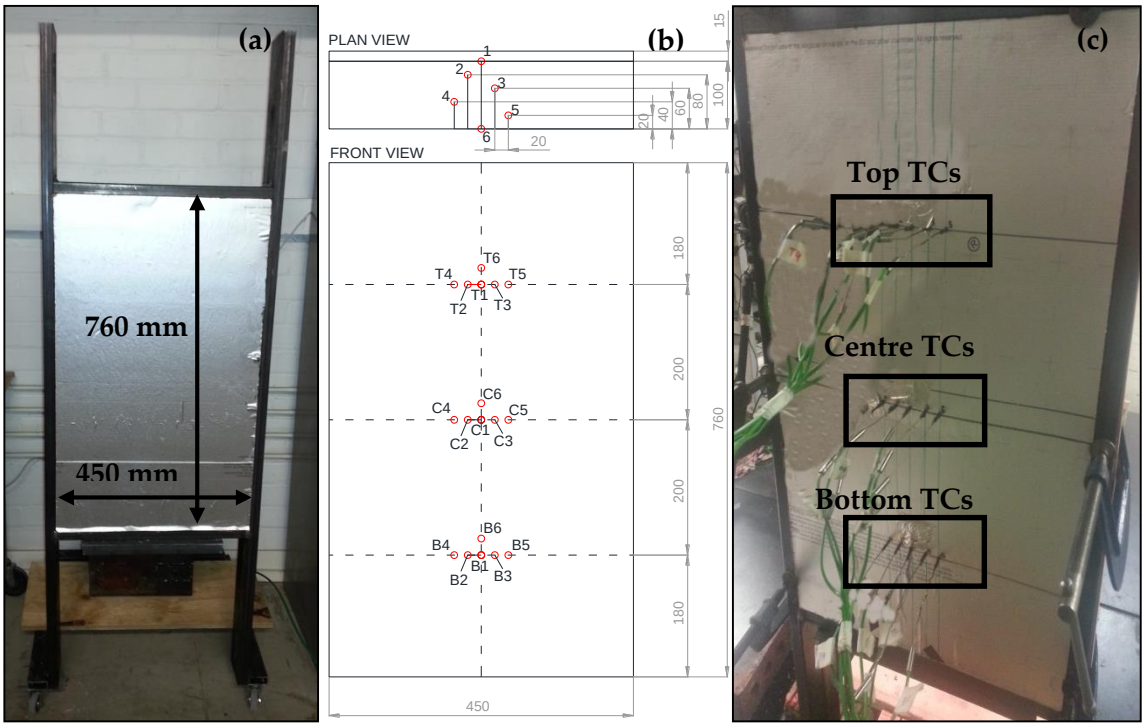

Figure 7.12. (a) Steel frame with embedded insulation board (b) Schematics of thermocouple positioning (c) In-depth thermocouples configuration

Additionally, gas measurements of oxygen, carbon monoxide and carbon dioxide are obtained from the effluent of gas extracted by the hood located above the sample. These measurements are taken in order to establish different regimes of combustion in case these take place. The analyser used for the measurements is a Servomex® 4100.

The heat exposures used for the tests are 15 kW·m^{-2}, 25 kW·m^{-2}, 65 kW·m^{-2} and a dynamic ramp up to 80 kW·m^{-2} described in Figure 7.13 below. The dynamic heating curve is an extrapolation of an equivalent incident heating curve for a material like aircrete in the furnace test exposed to an ISO-834 time-temperature curve [9]. This curve is provided by *Maluk* [7] and is computed by calculating the heat absorbed by the material from the experienced thermal profile during the test. Then, the heat absorbed is converted into an equivalent external radiant heat flux in an environment with heat losses represented by an infinite source at ambient temperature of approximately 20°C. Nevertheless, the dynamic heat flux curve in the experiments is limited up to 80 kW·m^{-2}, which is the limit of the radiant panels used for this set-up and calibration.

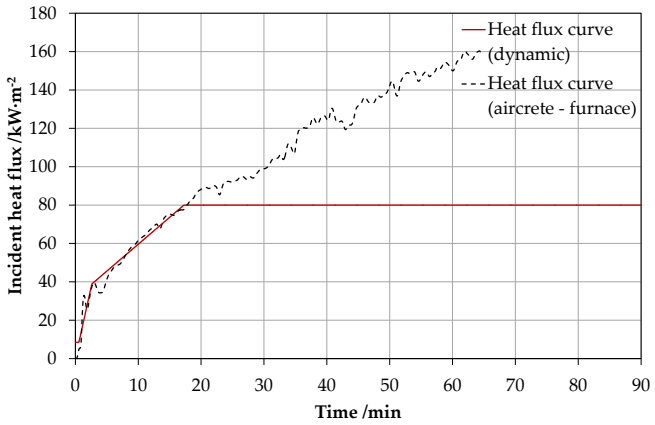

Figure 7.13. Equivalent incident heat flux for aircrete in the furnace [9] (calculated by Maluk [7] - dashed) and dynamic heat flux curve designed for experiments (solid)

A summary of the experimental plan is presented in Table 7.1. All the experiments are repeated at least twice for repeatability assessment. It should be noted that despite the nominal duration of the heat exposure is set to two hours, for some experiments the test duration is lower because either steady-state or the complete combustion of the insulation is achieved. Furthermore, the failure of the thermal camera during some of the experiments did not allow the recording of the surface temperature of the plasterboard.

Table 7.4. List of performed experiments

Material	Insulation dimensions	Plasterboard dimensions	Incident radiative heat flux range /kW·m^{-2}	Heat exposure duration /hours	Measured parameters
SW	450 mm x 760 mm x 100 mm	600 mm x 800 mm x 12.5 mm	15, 25, 65, dynamic (2 repetitions)	2	(1) In-depth temperature (2) O_2, CO_2 and CO gas species (3) Thermal camera
PIRb					
PF					

7.4 Analysis methodology

7.4.1 Boundary condition determination

As discussed in Chapter 6, the determination of the boundary condition is crucial for the correct evaluation and solution of the heat transfer problem within the solid phase of the materials exposed to severe heat conditions. Large uncertainties are addressed in the definition of the boundary condition in real-scale experiments where the heat exposure depends on the dynamics of the fire development. This uncertainty is however lower when performing experiments in a controlled environment such as a fire laboratory using calibrated radiant heaters. Indeed, measurements of irradiance can be used to evaluate the boundary condition of tested samples, while the main uncertainty remains on quantifying the cooling effects. If a finer boundary condition is required for real-scale experiments, the use of thin skin calorimeters (TSCs) can provide useful information about irradiance levels within a low margin of error. An uncertainty analysis can be found in [10]. However, the cooling or heating by convection should be evaluated as well.

Three different approaches are considered by the author, which refer to the definition of the boundary condition as noted in Equation (7.1) below, and allow evaluating the net heat absorption by the element in fire conditions. As will be shown in the subsequent sections, this variable is crucial to assess and compare the performance of insulation systems under severe conditions of heat exposure:

$$\dot{q}''_{net}(t) = \alpha \cdot \dot{q}''_e(t) + h_c \cdot (T_\infty - T_s) - \varepsilon \cdot \sigma \cdot T_s^4 = -k \cdot \left.\frac{\delta T}{\delta x}\right|_{x=0^+} \quad (7.1)$$

where $\dot{q}''_{net}(t)$ is the net heat flux, α is the absorptivity, $\dot{q}''_e(t)$ is the incident radiant heat flux, h_c is the convective coefficient, T_∞ is the gas-phase temperature, T_s is the surface temperature, ε is the emissivity, σ is the Stefan-Boltzmann constant, k is the thermal conductivity and $\left.\frac{\delta T}{\delta x}\right|_{x=0^+}$ is the thermal gradient at the surface.

a. Use of levels of irradiance from TSC

Thin skin calorimeters provide temperature measurements that can be converted to incident radiant heat fluxes. The governing equation that defines the incident radiant heat flux $\dot{q}''_e$ is noted in Equation (7.2), derived from a heat balance at the surface of the TSC presented in Figure 7.14, as a function of the emissivity of the disc ε_{TSC}, the heat conducted from the TSC disc to the back $\dot{q}''_{cond}$, the heat stored in the TSC disc $\dot{q}''_{st,TSC}$, the convective heat flux $\dot{q}''_c$ between the gas phase and the TSC disc, and the radiation emitted by the surface of the TSC disc $\dot{q}''_{rad,TSC}$:

$$\dot{q}''_e = \frac{\dot{q}''_{cond} + \dot{q}''_{st,TSC} + \dot{q}''_c + \dot{q}''_{rad,TSC}}{\alpha_{TSC}} \quad (7.2)$$

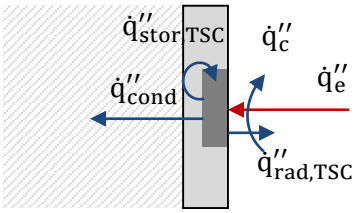

Figure 7.14. Heat balance at the surface of the thin skin calorimeter

The approach considered for the TSC is to assume that the heat of conduction is a fraction of the incident radiant heat flux considering $\dot{q}''_{cond} = C \cdot (\alpha_{TSC} \cdot \dot{q}''_{inc})$, with C as calibration factor. The quantification of this factor depends on the set-up of the TSC. Alston [11] reported a constant value of $C = 0.2$, while Amundarain [12] obtained calibration values as a function of the disc temperature, between 0.7 and 0.1 for a range between 100°C and 700°C.

The governing equation noted in Equation (7.2) can be expressed as:

$$\dot{q}''_e(T_s) = \frac{1}{\alpha_{TSC} \cdot (1 - C(T_s))}\left[\rho \cdot \delta \cdot c_P \cdot \frac{dT}{dt} + \varepsilon_{TSC} \cdot \sigma \cdot T_s^4 + h_c \cdot (T_s - T_\infty)\right] \quad (7.3)$$

where $\dot{q}''_{st,TSC} = \rho \cdot \delta \cdot c_P \cdot \frac{dT}{dt}$ is the heat stored, with ρ, δ, c_P and $\frac{dT}{dt}$ the density, thickness, specific heat capacity and temporal temperature variation of the disc, $\dot{q}''_{rad,TSC} = \varepsilon_{TSC} \cdot \sigma \cdot T_s^4$ is the radiation emitted by the surface of the disc, with σ Stefan–Boltzmann constant and T_s the temperature of the disc, and $\dot{q}''_c = h_c \cdot (T_s - T_\infty)$ is the convective heat flux, with h_c the convective heat transfer coefficient and T_∞ the gas-phase temperature.

Given the incident radiant heat flux, the net heat absorption in an element can be obtained as noted in Equation (7.1). However, values of gas phase temperature, convective coefficient and surface temperature must be known.

b. Use of a metallic plate

The specific type of wall used for the sandwich panels' experiments presents an opportunity for a simplified approach for the heat transfer analysis, similar to the one presented in Chapter 6 based on a metallic plate at the surface. Since thermocouples are placed at the back of the inner metal skin of the walls, a good approximation of the surface temperature is obtained. This is justified due to the low thickness of the

metal skin (approximately 0.7 mm thick stainless steel plate), which leads to Biot numbers lower than 0.1. Indeed, a thermal conductivity of 15 $W \cdot m \cdot K^{-1}$ at 25°C for stainless steel[15], with a thickness of 0.7 mm, would lead to convective coefficients of 2413 $W \cdot m^{-2} \cdot K^{-1}$ if Biot numbers higher than 0.1 are to be obtained. Then, it can be assumed that the thermal gradient through the metal skin can be neglected.

The energy balance at the surface of the sample beneath the metal skin can be obtained according to Fourier's law, which in a finite difference method is represented as Equation (7.4) in an implicit form:

$$\dot{q}''_{net,i}{}^{j+1} = k_i(T_1^{j+1}) \cdot \frac{T_1^{j+1} - T_2^{j+1}}{\Delta x} + \Delta x \cdot \rho_i \cdot c_{p_i}(T_1^{j+1}) \cdot \frac{T_1^{j+1} - T_1^{j}}{\Delta t} \tag{7.4}$$

where $\dot{q}''_{net,i}{}^{j+1}$ is the net heat at the step j+1, $k_i(T_1^{j+1})$ is the thermal conductivity, ρ_{ins} is the density, $c_{p_{ins}}(T_1^{j+1})$ is the specific heat capacity, T_1^{j+1} and T_1^{j} are the temperature of the element 1 at steps j and j+1, T_2^{j+1} is the temperature of element 2 at the step j+1, Δx is the space discretisation and Δt is the time discretisation.

Since the temperature of the element 1 is known, only two variables remain unknown: $\dot{q}''_{net}{}^{j+1}$ and T_2^{j+1}. Then, a system of N equations with N unknown variables can be set[16], with unknowns $\{\dot{q}''_{net,i}{}^{j+1}, T_2^{j+1}, \ldots, T_N^{j+1}, T_N^{j+1}\}$. The coefficient and constant terms matrix can be built as shown in Chapter 6 and Appendix D. Equation (7.4) can be arranged as follows for constructing the coefficients matrix:

$$\begin{aligned} &\mathbf{\dot{q}''_{net,i}{}^{j+1}} \cdot [1] + \mathbf{T_2^{j+1}} \cdot \left[\frac{k_i\left(T_1^{j+1}\right)}{\Delta x}\right] = \\ &= k_i(T_1^{j+1}) \cdot \frac{T_1^{j+1}}{\Delta x} + \Delta x \cdot \rho_i \cdot c_{p_i}(T_1^{j+1}) \cdot \frac{T_1^{j+1} - T_1^{j}}{\Delta t} \end{aligned} \tag{7.5}$$

If the net heat absorbed by the assembly is to be calculated, this can be obtained as:

$$\dot{q}''_{net}(t) = \dot{q}''_{net,i}(t) + \dot{q}''_{st,skin}(t) = \dot{q}''_{net,i}(t) + \rho_{skin} \cdot \delta_{skin} \cdot C_{P,skin} \cdot \left.\frac{dT}{dt}\right|_{skin} \tag{7.6}$$

where $\dot{q}''_{st,skin}(t)$ is the heat stored in the metal skin, ρ_{skin} and δ_{skin} are the density, thickness and specific heat capacity of the metal skin and $\left.\frac{dT}{dt}\right|_{skin}$ is the variation of temperature in the skin over time.

[15] Thermal conductivity of steel, k, obtained as a function of temperature, T, by the expression $k = 14.6 + 1.27 \cdot 10^{-2} \cdot T$, with temperature expressed in °C and thermal conductivity in $W \cdot m^{-1} \cdot K^{-1}$.

[16] Back boundary condition is defined by heat losses calculation considering losses by radiation and convection (convective heat transfer coefficient calculated by Nusselt number correlation).

c. Use of inverse modelling

If the lining does not correspond to a thermally thin element, and there is no information about irradiance levels and surface temperature, the determination of the net heat absorption is rather more complicated. An inverse model is then required in order to predict the time-history of the net heat absorbed by the assembly, given the time-history of the temperature profile of the solid-phase and its thermal properties. This has already been studied by *Maluk* [7] who proposed a methodology to define the external heat flux impinged to concrete elements given the thermal gradient through thickness.

A similar analysis is proposed here, but using an implicit method for solving the heat of conduction equation. An inverse model based on a Levenberg-Marquardt algorithm [13, 14] (detailed in Chapter 6) is used to optimise the function that defines the net heat absorbed. The total time scale of the experiment is divided in certain sets of data points and the inverse heat transfer model is run for each set of data points in order to provide the coefficients of a spline function for the net heat absorbed as shown in Equation (7.7). Eventually, the net heat absorbed is defined as a piecewise function for each of the intervals.

$$\dot{q}''_{net,i}(t) = a_i \cdot t^2 + b_i \cdot t + c_i \qquad (7.7)$$

It should be noted that since neither continuity nor derivability is required for the piecewise function, this is expected to include significant noise. Therefore, the functions defined as (7.7) shall be interpreted as data points of the actual $\dot{q}''_{net}(t)$, which need to be smoothed.

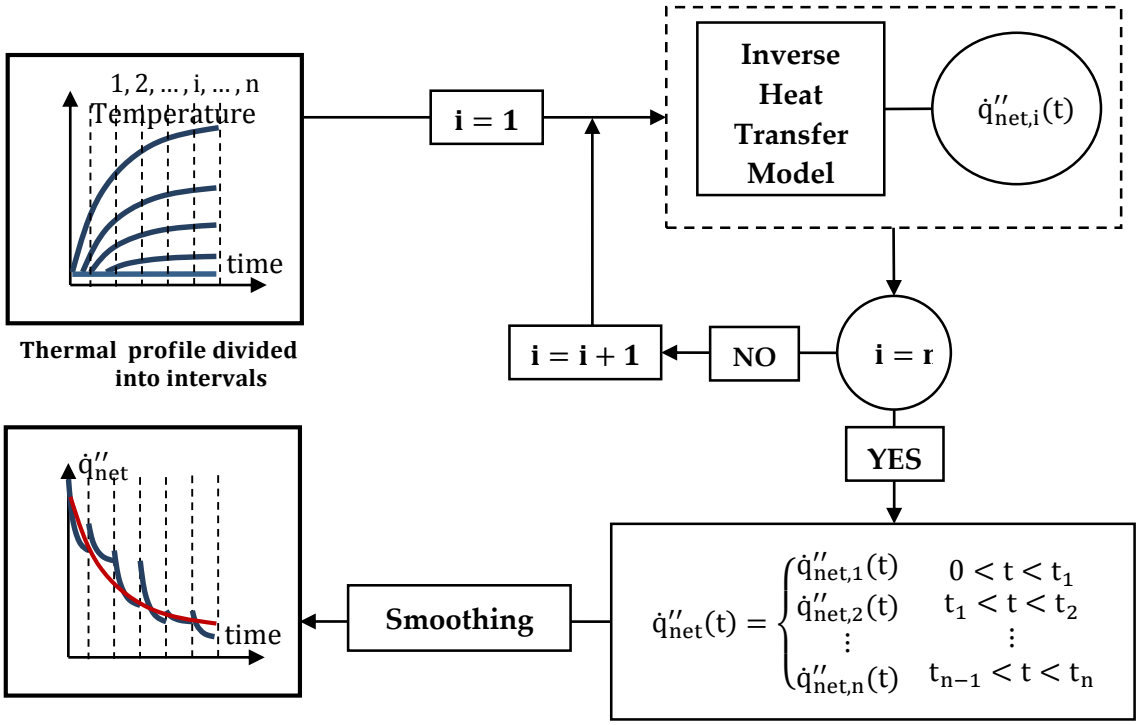

Figure 7.15. Conceptual definition for the inverse heat transfer model to estimate the net heat absorbed by a wall assembly given its temperatutime profile time-history

7.4.2 Thermal analysis: fraction of thermal degradation and pyrolysis rate

A simplified method is proposed in order to estimate the pyrolysis rate experienced by instrumented samples of insulation in the series of experiments presented in this chapter. This approach, which is schematically presented in Figure 7.16, is based on the use of thermogravimetric analyses and the time-history of the thermal profile through thickness.

Despite the fact that numerous pyrolysis models have been developed in the last decade [15, 16], the approach followed by the author is to present a pragmatic methodology of minimum complexity able to capture the rates of pyrolysis from closed-cell foams under non-oxidative conditions. The main justification for taking this approach is that the rates of pyrolysis can be obtained without having to solve the heat transfer problem (i.e. simply using experimental temperature measurements), and without having to consider the complex kinetics from the thermal degradation reactions. This approach allows for a qualitative assessment of the pyrolysis process, which is compared with visual observations during the experiment.

TGA profiles provide the fraction of remaining mass versus temperature, while temperature measurements through thickness can be interpolated and provide approximate thermal gradients experienced by the core of the insulation. The combination of this information allows the determination and quantification of the fraction of thermal degradation, i.e. the fraction of lost mass due to thermal degradation reactions experienced by the material.

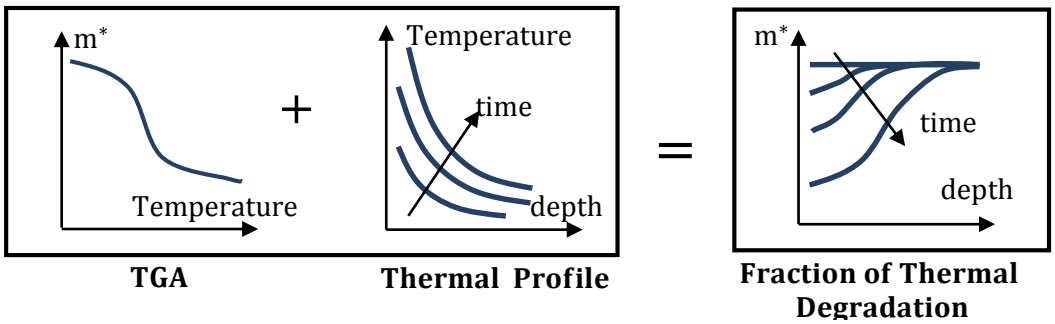

Figure 7.16. Conceptual definition for the thermal degradation fraction through thickness, based on thermogravimetric analyses (TGA) and measurement of thermal profile

The fraction of thermal degradation through thickness at a certain moment can be expressed as remaining mass per unit area $m''(kg \cdot m^{-2})$. Knowing the initial density of the insulation core ρ_0, and the thickness of the insulation core L, the virgin amount of mass per unit area can be defined as $m_0'' = \rho_0 \cdot L$. Plots from the fraction of thermal degradation versus thickness (RHS of Figure 7.16) can be integrated for the total thickness to provide the fraction of remaining mass per unit area as a function of time $m''(t)$. Applying differentiation over time, rates of pyrolysis from the insulation within the wall assemblies $\dot{m}''(t)$ can be approximated.

A series of uncertainties are identified for this simplified methodology, which are related to the precision of the measured thermal gradient, the heating rate and availability of oxygen during the thermal degradation process.

The precision of the thermal gradient through thickness depends on the number of thermocouples inserted within the core of the insulation, with the temperature at areas between thermocouples needing to be interpolated. For simplicity the chosen interpolation is linear. This technique is not precise for profiles near the exposed surface where thermal gradients are expected to be much higher, especially during transient regimes. On the contrary, this technique is expected to be precise enough for thermal gradients far from the exposed surface.

Thermogravimetric analyses on the studied insulation materials were presented in Chapter 4. These analyses were however performed on certain heating rates (2.5, 5, 10 and 20°C·min^{-1}), expected to be much lower than heating rates for regions near the exposed surface. It was demonstrated that higher heating rates lead to a shift on the thermal degradation process towards higher temperatures. Then, TGA curves with the highest heating rate are chosen for the determination of the fraction of mass pyrolysed within the core of the panels.

Thermogravimetric curves were processed in different atmospheres, nitrogen and air. The former indicates the thermal degradation processes when oxygen is not available, i.e. pyrolysis reactions, while the latter includes the combination of both pyrolysis and oxidation of solid-phase. When applying the approach noted above for the determination of the fraction of thermal degradation, there is an implicit uncertainty with regard to the conditions under which the insulation decomposes. This method is clearly limited to anaerobic conditions since oxidation is a diffusion-controlled reaction. Fortunately, the studied combustible materials are closed-cell polymers that do not allow the diffusion of air through its medium. Additionally, interaction with oxygen is not expected during the initial periods of the heating since the insulation boards are covered by a lining and the pressure within the wall is expected to be higher due to increased temperature.

Therefore, the proposed methodology is only applied for PIR and PF under the hypothesis that oxidation does not take place. This assumption is verified for the studied cases by analysing the temperature profile. However, this methodology is not applied for stone wool, since this is a porous material and air is expected within the core of the insulation. In any case, no significant impact is anticipated on the analysis, since the mass loss from stone wool tends to be extremely low as was demonstrated in Chapter 4, mainly depending on the content of binders and additives.

7.5 Results

7.5.1 Sandwich Panels Tests' programme

As noted previously, a total of four experiments were performed, with variations in the fuel source and damages. For simplicity, only the experiments that used a gas burner but no wooden cribs as main external fuel are discussed below. Conclusions from these series of experiments are similar to the series of experiments that included wood cribs since the main difference lies on different heating rates that can also be identified in different wall positions of the same test.

7.5.1.1 Stone wool compartment (experiment 1b)

Figure 7.17a shows the input heat release rate and the calculated heat release rate obtained inside the stone wool compartment for the experiment with the gas burner. The calculated HRR is defined by a confidence region due to the uncertainties in the used methodology. The upper limit of the calculated HRR appears to be larger than the input HRR due to the method uncertainty [4]; however, three clear steps of heat release rate can be identified, suggesting minor or null contribution from the panels to the fire. Indeed, the shapes of calculated and input HRR are equivalent, without clear patterns suggesting the sudden contribution of extra fuel. This is supported by the ratio of generated carbon dioxide (CO_2) and consumed oxygen (O_2) presented in Figure 7.17b below, which presents values close to the stoichiometry ratio for combustion of propane. Therefore, the heating to the panels is expected solely from the gas burner and no extra fuel, which is discussed below.

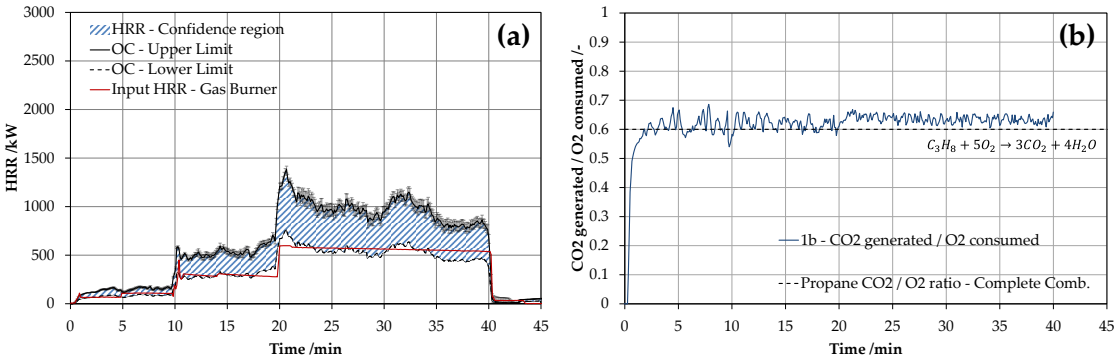

Figure 7.17. (a) Calculated heat release rate inside the compartment.Extracted from [4] (b) Ratio of CO_2 generation versus O_2 consumption

Figure 7.18 shows a selection of time-histories of temperature measurements within the monitoring positions W5t and W5b (panel next to the burner), and W7t and W7b (panel of the back wall on the opposite corner of the burner). The surface temperature for the four positions presents three clear trends, reflecting the three HRR inputs from the gas burner, which should be approximately equivalent to three steps of constant radiant heat flux. From these positions, position W5b corresponds to the location where higher thermal severity is observed, particularly at the first stages of the fire. A series of common patterns are found for the temperature profiles shown in Figure 7.18:

- During the heating period the thermal wave is clearly identified, showing similar delay in the propagation for most of the experiments. Uneven separations in some curves like the one shown by W7_B2 indicate that the thermocouple is displaced from its initial position.
- The thermal profile shows an endothermic plateau below 50°C, probably due to moisture in the wool, or increase of the thermal conductivity with temperature.
- No peaks indicating exothermicity are observed during the heating period below 40 minutes.
- After the gas burner is turned off, the thermal wave keeps propagating as would be expected. However, some temperature increase in Figure 7.18b and Figure 7.18d indicate the likely smouldering of organic compounds in the wool.

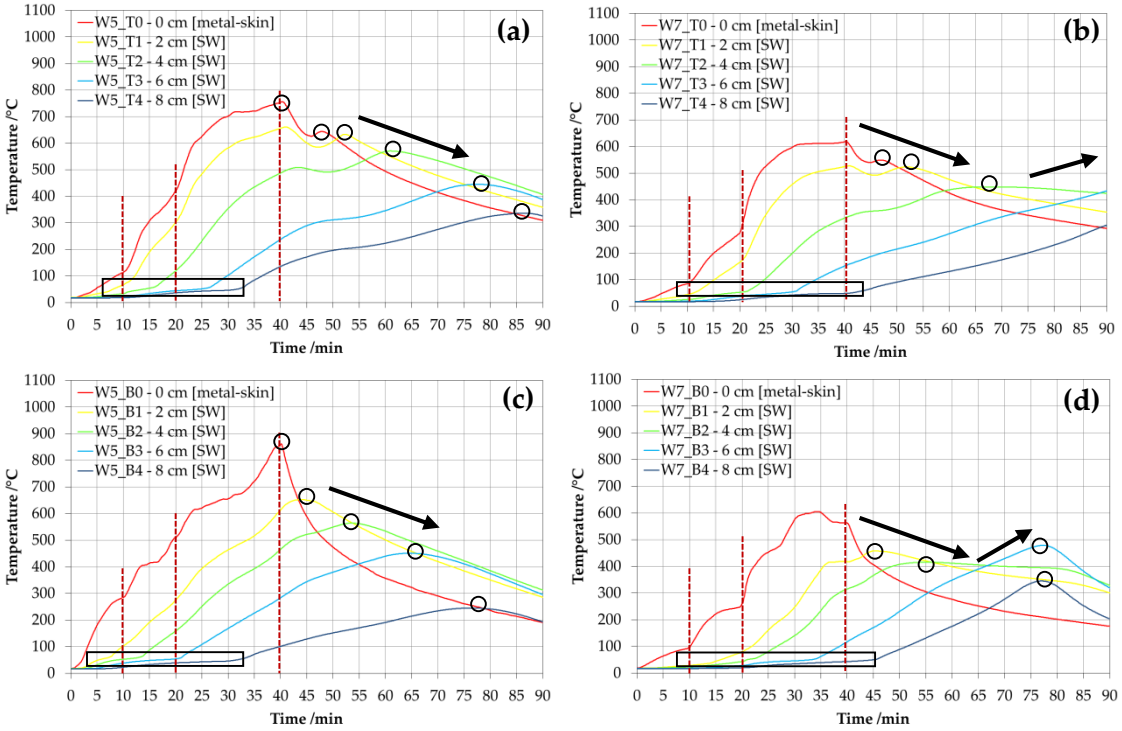

Figure 7.18. Wall temperatures for monitoring positions (a) W5t, (b) W7t, (c) W5b and (d) W7b for test 1b (stone wool panel with gas burner)

Modelling techniques described in previous sections have been applied in order to predict the time-history of temperature measurements within the stone wool panels. Two cases representing two opposite regimes (lowest and highest temperature histories) are presented in Figure 7.19 and Figure 7.20 below. It should be noted that, since the approach followed for this thesis is based on simple inert heat transfer models, the exothermic and endothermic events identified in the temperature profiles above cannot be represented. Therefore, only the period represented by the heating and first minutes of cooling are modelled.

Figure 7.19a shows the experimental and modelled temperatures for the monitoring position W4b, which corresponds to the position further to the gas burner.

The model prediction shows a very good agreement with the experimental results, giving a thermal diffusivity of $6.4 \cdot 10^{-7} m^2 s^{-1}$. The thermal properties are obtained by inverse modelling in order to find the best agreement. As noted in Chapter 6, one of the parameters of the model needs to be fixed if reasonable results are expected to be found. Thus, the heat capacity is assumed to be in the range of 800-1600 $J \cdot kg^{-1} \cdot K^{-1}$ which is in agreement with the respective values found in literature. As a result, conductivities of 0.072 and 0.143 $W \cdot m^{-1} \cdot K^{-1}$ are obtained for these values of specific heat capacity. It should be noted that the value of thermal conductivity is taken as the average value for the range of temperatures observed. The net heat flux that corresponds to the thermal profile shown in Figure 7.19a and these thermal properties is shown in Figure 7.19b. This net flux is the result of the heat stored by the metallic skin and the heat conducted to the stone wool core, with the latter being presented as dashed lines.

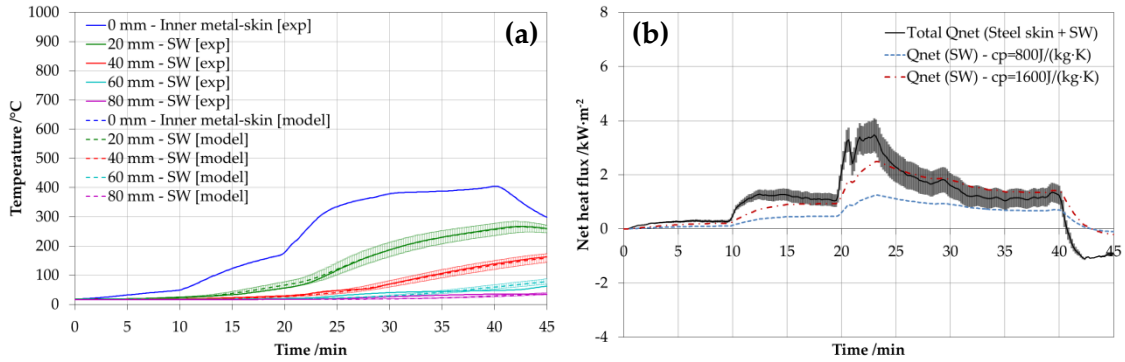

Figure 7.19. (a) Model prediction of temperatures and (b) net heat flux for W4b. Error bars indicate uncertainty in the specific heat capacity considered in the range {800-1600 $J \cdot kg^{-1} \cdot K^{-1}$}. Thermal diffusivity of $6.4 \cdot 10^{-7} m^2 s^{-1}$

Figure 7.20a shows the experimental temperatures and those obtained from the model for the monitoring position W6b, which presents the highest range of temperature measurements. The agreement between model and experimental data is also very good considering the simplicity of the model (inert behaviour). A temperature dependent thermal conductivity is assumed for this case in order to achieve a good agreement, considering a linear function for simplicity. The best fitting is given by a thermal conductivity of $k_{c_p=800 J \cdot kg^{-1} \cdot K^{-1}} = 0.029 + 2.116 \cdot 10^{-4} \cdot T$ (temperature in °C) for a density of 140 $kg \cdot m^{-3}$ and specific heat capacity of 800 $J \cdot kg^{-1} \cdot K^{-1}$. If the heat capacity is assumed to be 1600 $J \cdot kg^{-1} \cdot K^{-1}$, the thermal conductivity is given as $k_{c_p=1600 J \cdot kg^{-1} \cdot K^{-1}} = 0.058 + 4.240 \cdot 10^{-4} \cdot T$, double than $k_{c_p=800 J \cdot kg^{-1} \cdot K^{-1}}$ as would be expected. As a result, the thermal diffusivity can be considered as $\kappa = 2.625 \cdot 10^{-7} + 1.889 \cdot 10^{-9} \cdot T$ with $850°C > T > 20°C$. Finally, Figure 7.20b indicates the net heat flux absorbed by the wall, represented by the heat stored by the metallic skin and the heat conducted to the stone wool core.

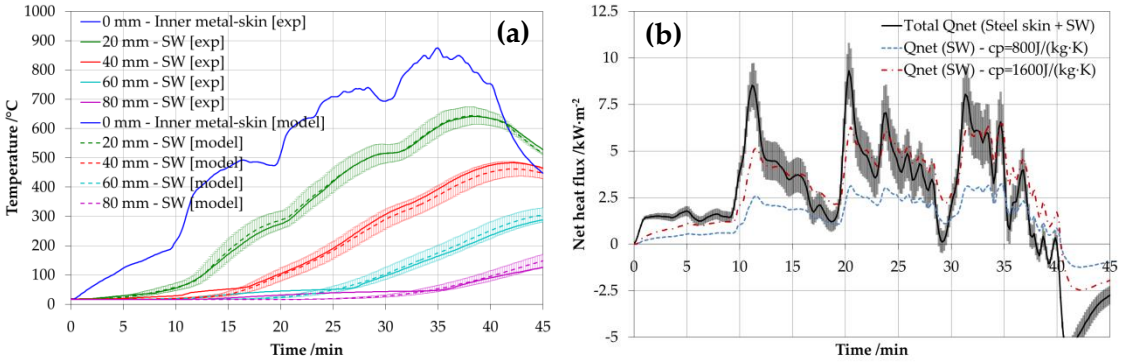

Figure 7.20. (a) Model prediction of temperatures and (b) net heat flux for W6b. Error bars indicate uncertainty in the specific heat capacity considered in the range {800-1600 J·kg^{-1}·K^{-1}}

7.5.1.2 PIR compartment (experiment 1a)

Figure 7.21a shows the input heat release rate and calculated heat release rate inside the compartment. Contribution to the release of energy is observed from 7-8 minutes, after the gas burner is turned up to 300 kW, with the calculated HRR being significantly larger than the input HRR. As discussed in Chapter 3 and in published papers from the author [2, 4], PIR pyrolysates released from the panel and the coating paint from interior skin are found to contribute to the fire. This is represented by the ratio CO_2/O_2 shown in Figure 7.21b, where a variable value after 7 minutes is observed, indicating non-uniform contribution from the different fuel sources. Indeed, a ratio between 0.5-0.6 was found for PIR pyrolysates, while a ratio between 0.7-0.9 was observed by bench-scale tests of the coating (Appendix C). As a result, the ratio CO_2/O_2 presents a clear variability, indicating the fraction of contribution to the total HRR from each heat source is not constant, with larger contributions of PIR and propane with ratios close to 0.6, and larger contribution of the coating with higher ratios during the heating. The generation and contribution of PIR pyrolysates are discussed below.

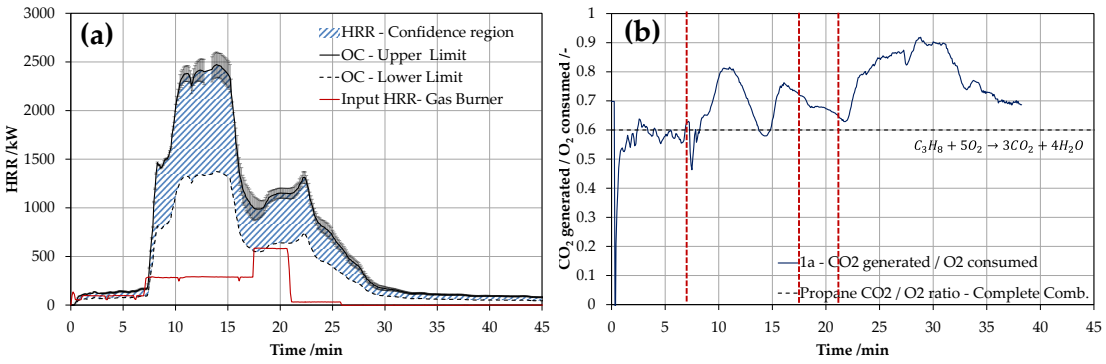

Figure 7.21. (a) Calculated and input heat release rate inside the compartment. Extracted from [4]
(b) Ratio of CO_2 generation versus O_2 consumption

Figure 7.22 shows a selection of time-histories of temperature measurements within the monitoring positions W5t and W5b (panel next to the burner) and W7t and W7b (panel of the back wall on the opposite corner of the burner). Position W5

corresponds to the location where higher thermal severity is observed, particularly at the first stages of the fire. The critical temperature of pyrolysis onset is indicated by purple shading from 300°C. To facilitate the interpretation of these results, the moments when the burner is stepped up are indicated as vertical dashed lines. The patterns of the curves observed in these graphs are discussed in detail below:

- A faster progression of the heat penetration, represented as the slope of the temperature measurements is observed for test 1a than for test 1b, indicating larger fire severity since the thermal conductivity and diffusivity of the PIR is lower than that for stone wool. This is consistent with the quantification of the heat release rate inside the compartment.
- The surface temperature of W5b and W5t indicate three clear trends in agreement with the three steps of the gas burners, indicating that the heat flux from the gas burner is the main contributor rather than the extra fuel. Nevertheless, the surface temperatures of W7b and W7t show this pattern only for the first step of the gas burner, with a large increase after the gas burner is stepped up to 300 kW. Then, the surface temperature indicates a profile similar in trend to the calculated heat release rate, with a peak at 12 minutes, followed by a decrease until the burner is stepped up to 600 kW. This is indicative of heat fluxes equivalent in trend to the total heat release, since this panel is further to the gas burner heat source.
- The temperature measurements show no endothermic plateaus of temperature during the heating period, which is in agreement with the results presented in Chapter 6.
- The temperature profiles during the heating period below 20 minutes do not present exothermic peaks indicating oxidation processes within the panel. However, temperature readings at different depths reach the critical temperature of pyrolysis onset sequentially, indicating release of pyrolysis gases. Indeed, the panel W5b has already reached this pyrolysis region before stepping the heat release rate of the gas burner up to 300 kW.
- Oxidation processes are clearly identified a few minutes after turning off the gas burner, by sudden increase of the temperature during the cooling process, or in the case of W5t during the last step of HRR from the gas burner from 20 minutes. These events are marked in Figure 7.22, from 30 minutes to 35 minutes for W5b and from 35 minutes to 45 minutes for W5t, suggesting that the process starts at the bottom of panel W5 by smouldering combustion of the remaining char from the pyrolysis of PIR. An increase of temperatures after cooling is observed for the first 4 cm of core in W5b, with a sudden increase at 30 minutes. This process seems to spread vertically and affect the remaining core of the top of the panel as shown in Figure 7.22a after 35 minutes. A similar process is observed for panel W7, with temperatures growing significantly from 60 minutes until 75 minutes at W7b, and with peaks from 75 to 80 minutes at W7t. This is produced after a gentle increase of temperature of the core from 60 to 75 minutes, likely due to the heating from the smouldering at the bottom. These events seem to be determined by the

diffusion of air through the panels after pyrolysing, which is a complex phenomenon to be predicted.

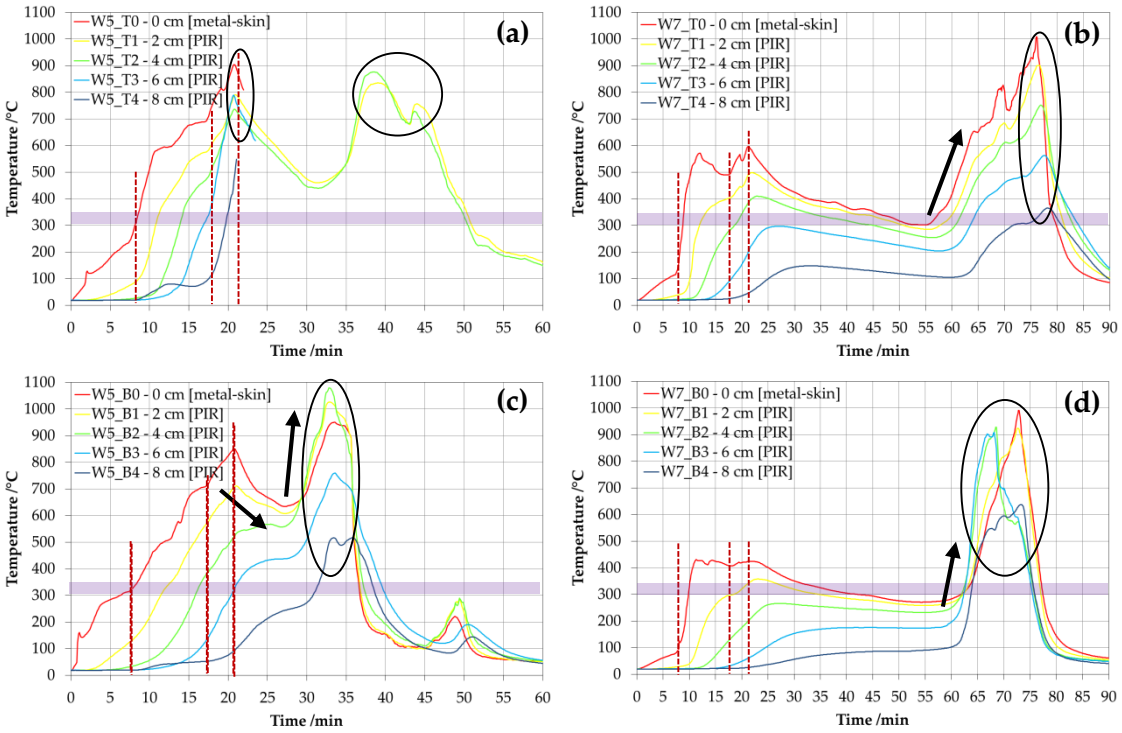

Figure 7.22. Wall temperatures for monitoring positions (a) W5t, (b) W7t, (c) W5b and (d) W7b for test 1a (PIR panel with gas burner)

The time-history of fraction of remaining mass over the depth of the insulation core for the monitoring position W5b (Figure 7.22a) is presented in Figure 7.23a. The fraction of remaining mass is plotted as a non-dimensional number, with a value of one reflecting no thermal degradation, and a value of zero reflecting that all mass is consumed. The curves shown in Figure 7.23a are based on thermogravimetry results from PIRd presented in Chapter 4. These curves are found not to achieve a zero value at any depth, which means that a char residue is left even if temperatures are higher than 800°C. As noted in previous sections, the late oxidation is not taken into account for the analysis, thus only pyrolysis rates are being calculated.

By applying this technique to the rest of the monitoring positions, the remaining mass per unit area is obtained as shown in Figure 7.23b. The results indicate a higher mass loss for earlier times by W5t and W5b, followed by regions at the top of the panels (W6t and W7t). Lower regions present a more moderate mass loss, which would be expected due to lower heat exposure at the cold layer.

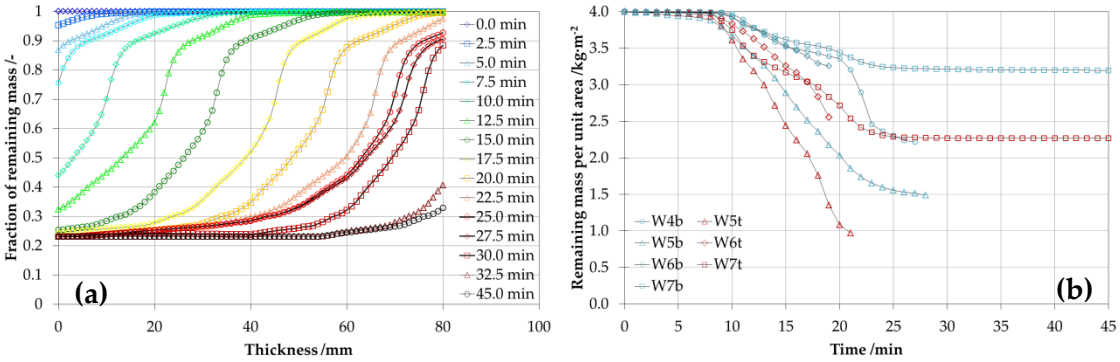

Figure 7.23. (a) Time history plots of the fraction of remaining mass versus thickness for monitoring position W5b (test 1a) (b) Remaining mass per unit area at the different monitoring positions

The first derivative of the mass loss measurements noted in Figure 7.23b is shown in Figure 7.24 below. The moment when the gas burner is stepped up and down is noted by vertical dashed lines. It is shown that when the burner is stepped up from 100 kW to 300 kW approximately at 7 min, when the panel W5b has been already pyrolysing. However, this generation appears not to be very significant. As noted in Chapter 3, the sudden increase of HRR in the compartment could be originated due to the accumulation of pyrolysis gases or the contribution from the coating paint, or even a combination of both. In any case, with the burner being stepped up to 300 kW, the rates of mass loss increase severely, especially for positions near the burner (W5b and W6b), and positions at the top panels (W6t and W7t). Despite not being possible to justify that the first increase is only due to the contribution of pyrolysates, good agreement is found with the times where a maximum heat release rate and significant pyrolysates are generated.

A quantitative approach can be applied, converting the rate of pyrolysates into values of heat release rate by multiplying it by the effective heat of combustion obtained in Chapter 5. For instance, if an average rate of mass loss is taken for the period of the second step of the gas burner (~2 $g \cdot m^{-2} \cdot s^{-1}$), taking the internal surface area of the panels (~32.96 m^2) and considering the effective heat of combustion as 15 $kJ \cdot g^{-1}$ (estimated in Chapter 5), a rate of heat release of approximately 1 MW is obtained. This analysis is however weak, since there is great uncertainty with regard to rates of pyrolysis from the ceiling and other panels, the transport of pyrolysates (many of which were released directly to the exterior) and calorimetry of pyrolysates at high gas-phase temperatures. In any case, it is demonstrated that the pyrolysis gases from the core of the insulation can contribute to the HRR of the fire, and a quantitative analysis is possible. Furthermore, the contribution from the coating is demonstrated, which is also critical for the fire performance of the panels.

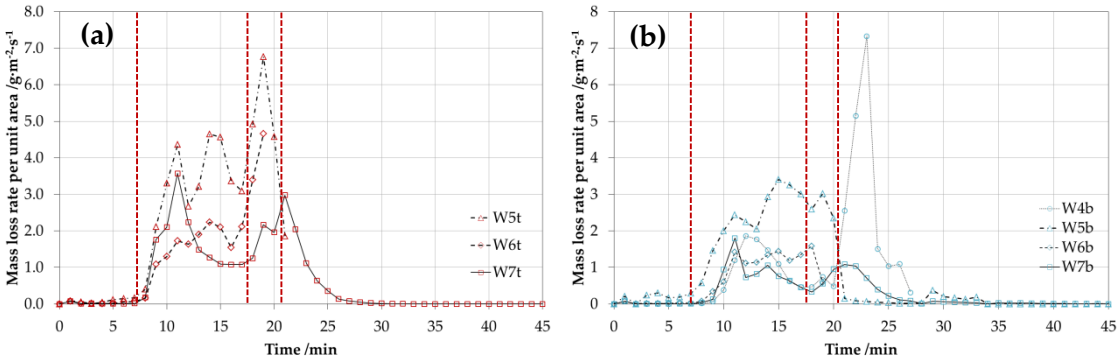

Figure 7.24. Mass loss rate per unit area for (a) top and (b) bottom monitoring positions (test 1a)

Numerical tools are applied in order to evaluate the prediction capabilities of the modelling approach denoted in previous sections, and quantify the net heat absorption. Two monitoring positions (W5b and W7b) corresponding to different range of achieved temperatures are presented in Figure 7.25 and Figure 7.26, where error bars indicating the expected error in the thermocouple position with a tolerance of ±3 mm are also included.

Figure 7.25a shows the experimental and modelled temperature profile for the monitoring position W5b, which achieves a maximum temperature above 800°C after 20 minutes. An inverse model is used in order to find the best fitting curve for a specific heat capacity $c_p = 1400 - 1600\ J \cdot kg^{-1} \cdot K^{-1}$. The thermal conductivity is assumed to be dependent on temperature as a linear function, and the density is modified, considering the mass loss by thermogravimetry and assuming no change in volume. A good agreement is found between the model and the experimental results, especially during the heating period. During the cooling phase, experimental measurements at depths of 20 and 40 mm indicate higher values than the inert model, suggesting the onset of exothermocity. The thermal conductivity functions obtained for a heat capacity of 1400 and 1600 $J \cdot kg^{-1} \cdot K^{-1}$ are $k_{c_p=1400J \cdot kg^{-1} \cdot K^{-1}} = 3.20 \cdot 10^{-4} \cdot T$ and $k_{c_p=1600J \cdot kg^{-1} \cdot K^{-1}} = 3.66 \cdot 10^{-4} \cdot T$ for the range $830°C > T > 20°C$ (temperature in °C). The total net heat flux absorbed by the wall is presented in Figure 7.25b, corresponding to the heat stored by the metallic skin and the conducted heat to the PIR core. The low amount of heat conducted to the PIR core in comparison with the heat stored by the metallic plate can also be seen in this graph.

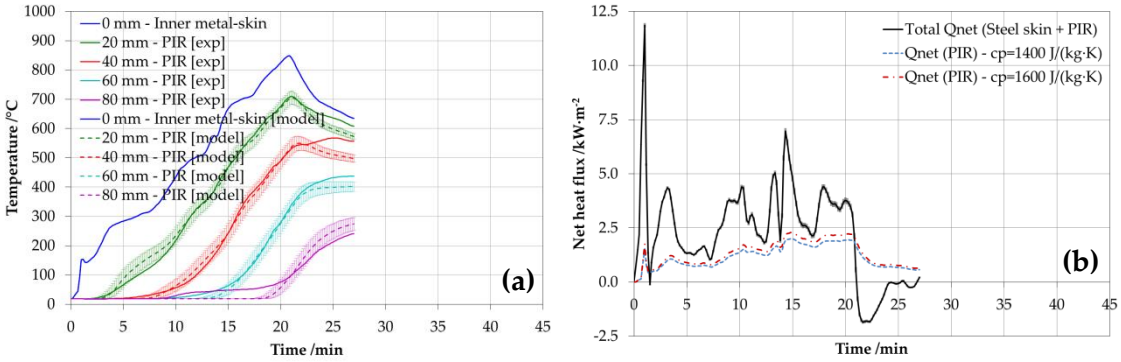

Figure 7.25. (a) Model prediction of temperatures and (b) net heat flux for W5b

Figure 7.26a shows the experimental and modelled temperature profile for the monitoring position W7b, which achieves a maximum temperature around 400°C after 10 minutes. The same assumptions as for the previous case are made here. A good agreement is found between the model and the experimental results. The thermal conductivity functions obtained for a heat capacity of 1400 and 1600 $J \cdot kg^{-1} \cdot K^{-1}$ are $k_{c_p=1400 J \cdot kg^{-1} \cdot K^{-1}} = 2.74 \cdot 10^{-4} \cdot T$ and $k_{c_p=1600 J \cdot kg^{-1} \cdot K^{-1}} = 3.14 \cdot 10^{-4} \cdot T$ for the range $425°C > T > 20°C$, which is in a good agreement with the results obtained for W5b. Figure 7.26b shows the total net heat flux to the wall, confirming the low flux conducted to the insulation in comparison to the metal skin.

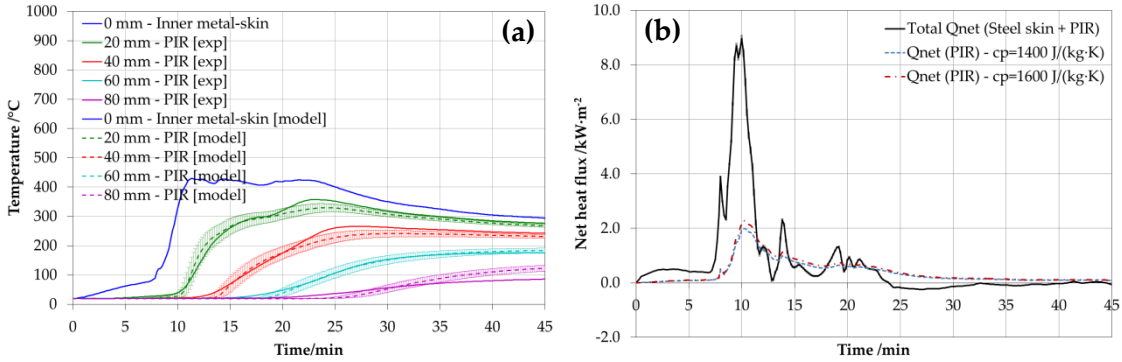

Figure 7.26. (a) Model prediction of temperatures and (b) net heat flux for W7b

7.5.2 Edinburgh Tall Buildings Fire Tests' programme

As noted in the previous sections, the number of performed experiments is very large. Therefore, a series of representative case scenarios of different heat transfer regimes are presented below for the configurations 1 (aircrete-SW), 4 (aircrete-PF) and 5 (aircrete-PIR).

Figure 7.27 shows the time-history of the temperature measurements registered in the top position of the walls 1, 4 and 5 for the experiment GB_05, a static fire of approximately of 2.5 MW in the compartment with all vents open. The surface temperature, approximately recorded by the thermocouple placed 0.25 cm deep in the aircrete, shows that a steady-state is achieved with a maximum temperature of 250°C, 276°C and 306°C for walls 1, 4 and 5 respectively. However, the steady-state is not achieved within the whole wall assembly, since the temperature within the

aircrete and the insulation boards continue to increase after the gas burners are turned off at 66 min. The interface layer between the aircrete and insulation achieves a maximum temperature of 165°C, 160°C and 194°C for walls 1, 4 and 5 respectively. These temperatures are clearly lower than the critical temperature for the onset of pyrolysis of the combustible insulations, indicating that the hazards are controlled. Therefore, no heat release contribution is obtained during the experiment.

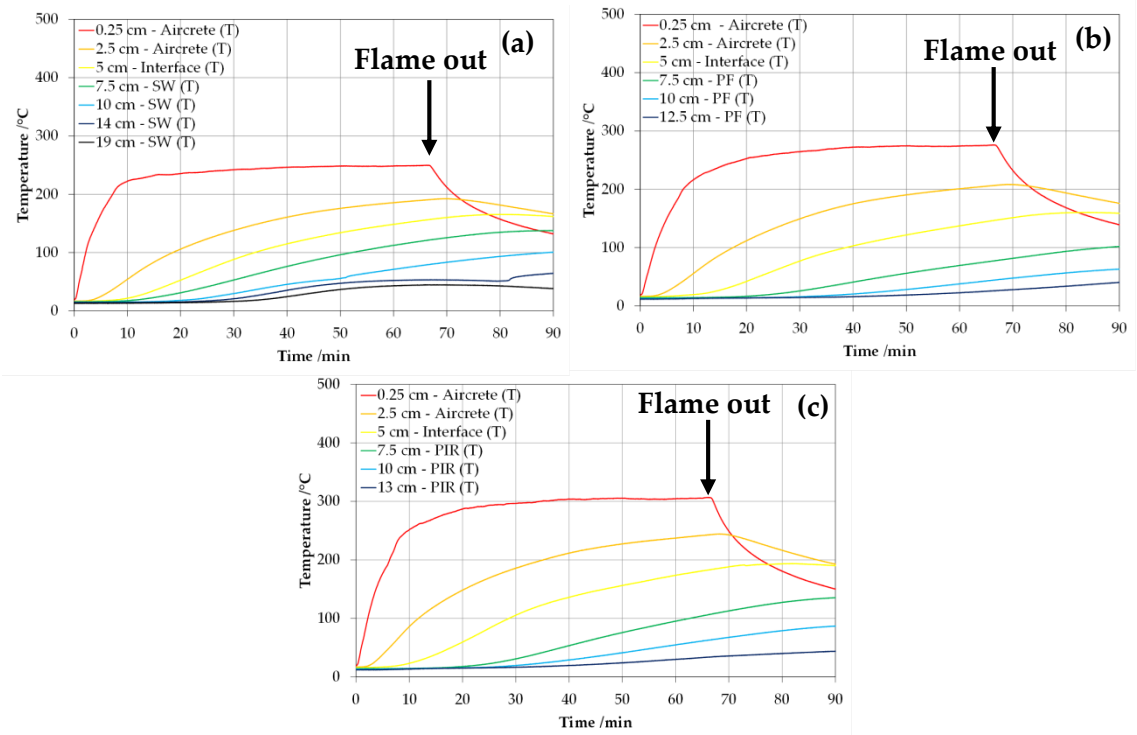

Figure 7.27. Time-history of temperatures within the asseblies W1 (SW), W4 (PF) and W5 (PIR) for experiment GB_05 (static fire with variable ventilation)

The temperature measurements shown for the wall assemblies suggest that the heat exposure during the gas burner experiments is not very severe. Figure 7.28 shows the incident radiant heat flux calculated from the TSCs next to the instrumented walls, and the gas-phase temperature measured by the thermocouples nearby. The incident radiant heat flux to the wall 1 (Figure 7.28a) achieves a maximum heat flux around 10 kW·m^{-2} at 7.5 minutes, continuing to decrease slightly and achieve a quasi-steady state between 5 and 7 kW·m^{-2}. This is also observed by the gas-phase temperature, achieving a maximum of 409°C at 7.5 minutes, when it decreases and achieves a quasi-steady state between 310 and 370°C. The values of gas-phase temperature and incident radiant heat flux are slightly larger for walls 4 and 5 (Figure 7.28b), achieving a quasi-steady state between 340 and 430°C and 8 and 10 kW·m^{-2}. This is consistent with the measured values for surface temperature, with wall 5 being slightly larger than wall 4, and larger than wall 1.

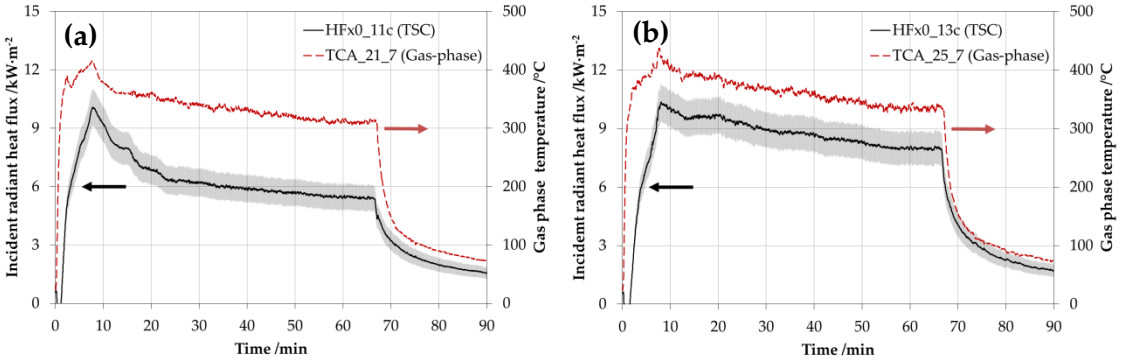

Figure 7.28. Gas-phase temperature and calculated radiant heat flux for TSCs next to (a) the SW assembly and (b) the PF and PIR assemblies for experiment GB_05 (static fire with variable ventilation)

Inverse modelling techniques are applied in order to estimate the net heat flux absorbed by the assemblies noted in Figure 7.27. A case study based on the assembly W5 is presented in Figure 7.29, since the temperature profile achieved by the three assemblies is similar; therefore, similar heat absorption behaviour is expected as this lies on the thermal properties of the barrier. Figure 7.29 shows the model and experimental results for the case study presented in Figure 7.27a, corresponding to the wall W5 (aircrete+PIR) at the top position. Constant thermal properties are assumed for the aircrete, with a conductivity $k = 0.20\ W \cdot m^{-1} \cdot K^{-1}$, density $\rho = 460\ kg \cdot m^{-3}$ and specific heat capacity $c_p = 1100\ J \cdot kg \cdot K^{-1}$. These values are in the range of those found in the literature [17]. A good agreement is found between the experimental results and the model, with the corresponding net heat flux to this thermal profile being as shown in Figure 7.27b. A good qualitative agreement is observed between the incident radiant heat flux presented above and the net heat flux.

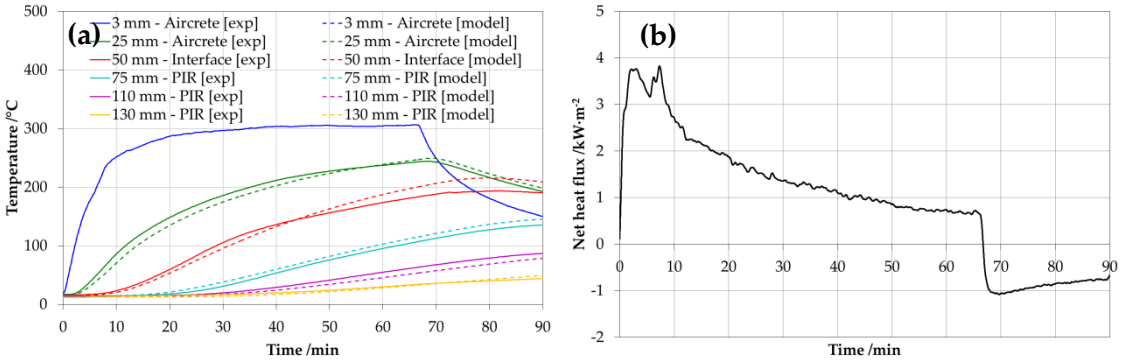

Figure 7.29. Net heat flux obtained by (a) inverse modelling and (b) using levels of irradiance and gas-phase temperature

Figure 7.30 shows the time-history of temperatures within the top position of walls 1, 3 and 5 for the experiment WC_01, where the wood cribs ignited from the right-hand side of the compartment and with all the vents open. The surface temperatures registered for the three configurations show a different transient-state than the one observed for gas burners shown in Figure 7.27. This behaviour is consistent with a fire-growth of the solid fuel of a compartment. The maximum temperatures achieved

by the surface of the aircrete are 424°C, 452°C and 524°C respectively for walls 1, 4 and 5 remaining approximately constant between 30 and 35 minutes, when the fire is extinguished externally with water. The maximum temperature achieved by the aircrete-insulation interface is obtained for times posterior to the fire extinguishment, reaching temperatures not higher than 150°C, therefore lower than the critical temperature of pyrolysis onset. This is indicative of the effectivity of the aircrete barrier, delaying the thermal wave to reach the surface of the insulation board.

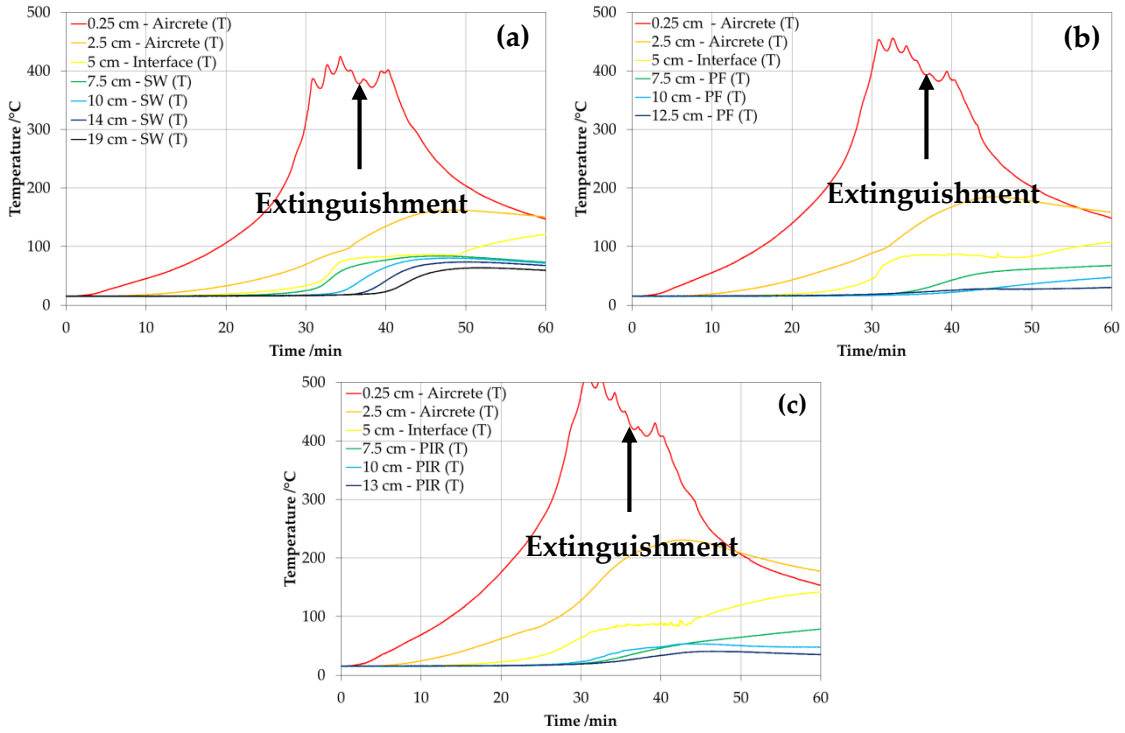

Figure 7.30. Time-history of temperatures within the asseblies W1 (SW), W4 (PF) and W5 (PIR) for experiment WC_01 (wood cribs - full ventilation)

The incident radiant heat flux and gas-phase temperature at the position of TSC next to the location of the studied wall assemblies is presented in Figure 7.31a for the top position of W1, and Figure 7.31b for the top position of walls W4 and W5. The incident radiant heat flux indicates a slow progress of the fire development, with an exponential growth after 25 minutes. The gas-phase temperature however shows a linear growth with a sudden increase from 25-30 minutes. The fire extinguishment is clearly identified after 35 minutes approximately, with values of gas-phase temperature and incident radiant heat flux dropping significantly. The maximum gas-phase temperature for both cases is around 950°C, which is achieved 31 minutes after the initiation of the experiment. The maximum incident radiant heat flux is achieved at the same time, with a value of 63 $kW \cdot m^{-2}$ for the wall W1 and 77 $kW \cdot m^{-2}$ for the walls W4 and W5. However, these are the maximum values that are followed by a reduction and later on an increase as shown in Figure 7.31 below.

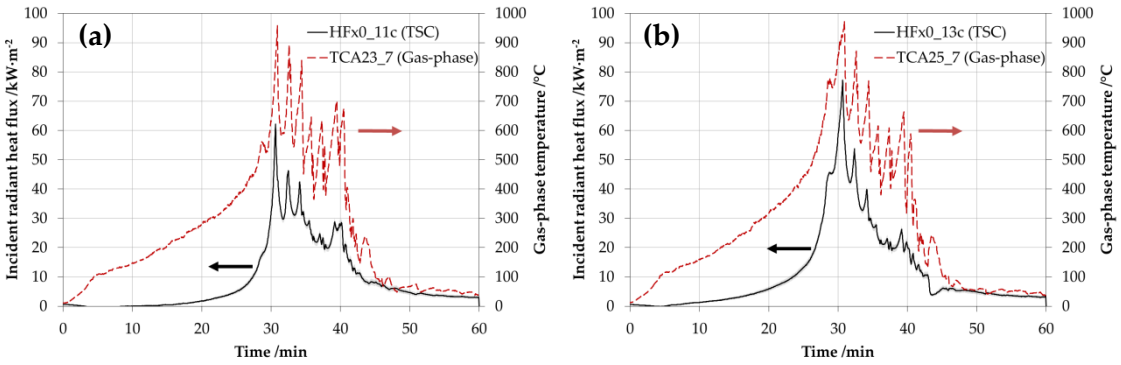

Figure 7.31. Gas-phase temperature and calculated radiant heat flux for TSCs next to (a) the SW assembly and (b) the PF and PIR assemblies for the experiment WC_01 (wood cribs - full ventilation)

Similarly to the experiment GB_05, an inverse model is run in order to predict the time-history of temperatures experienced by the walls. The case study presented in Figure 7.32 corresponds to the top location of wall W5 (aircrete+PIR). The agreement between the experiments and the model is good for the first thermocouples within the aircrete, but not very good for the thermocouple in the interface and back layer of the insulation. However, the temperature profile shown by the thermocouple at the interface is unusual, with a plateau below 100°C after 32 minutes, posterior to actions of fire extinguishment. The net heat flux, corresponding to this thermal profile and thermal properties, is shown in Figure 7.32b.

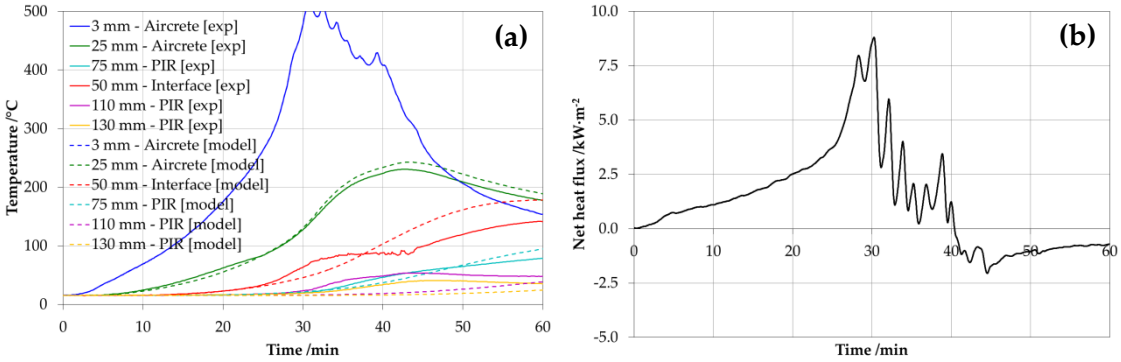

Figure 7.32. Net heat flux obtained by (a) inverse modelling and (b) using levels of irradiance and gas-phase temperature.

7.5.3 Radiant Panel Tests' programme

Some of the radiant panel tests are discussed in this section. The main advantage from these experiments is the known boundary condition, with determined external radiant heat flux given by the calibration of the radiant panels. However, the use of plasterboard as a boundary element includes a series of difficulties for the analysis such as the determination of the net heat flux to the assembly due to exothermic and endothermic reactions that this may experience. In any case, approximated values of the surface temperature are obtained by the use of a thermal camera, the results of which are extracted assuming an emissivity for the plasterboard of $\varepsilon = 0.9 \pm 0.1$ [18–21]. Although no numerical analyses are performed, the net heat flux is estimated by

assessing the energy balance at the surface as noted in Equation (7.1). As will be shown below, the series of observed events in relation to the performance of the insulation can be related to temperature measurements.

7.5.3.1 Plasterboard and stone wool assembly

Figure 7.33 shows the time-history of temperatures for plasterboard-stone wool assemblies under external heat fluxes of 15, 25, 65 kW·m^{-2} and a dynamic rump up to 80 kW·m^{-2}. The surface temperature includes a series of error bars indicating the uncertainty in the emissivity of the plasterboard, inserted as a parameter in the software of the thermal camera.

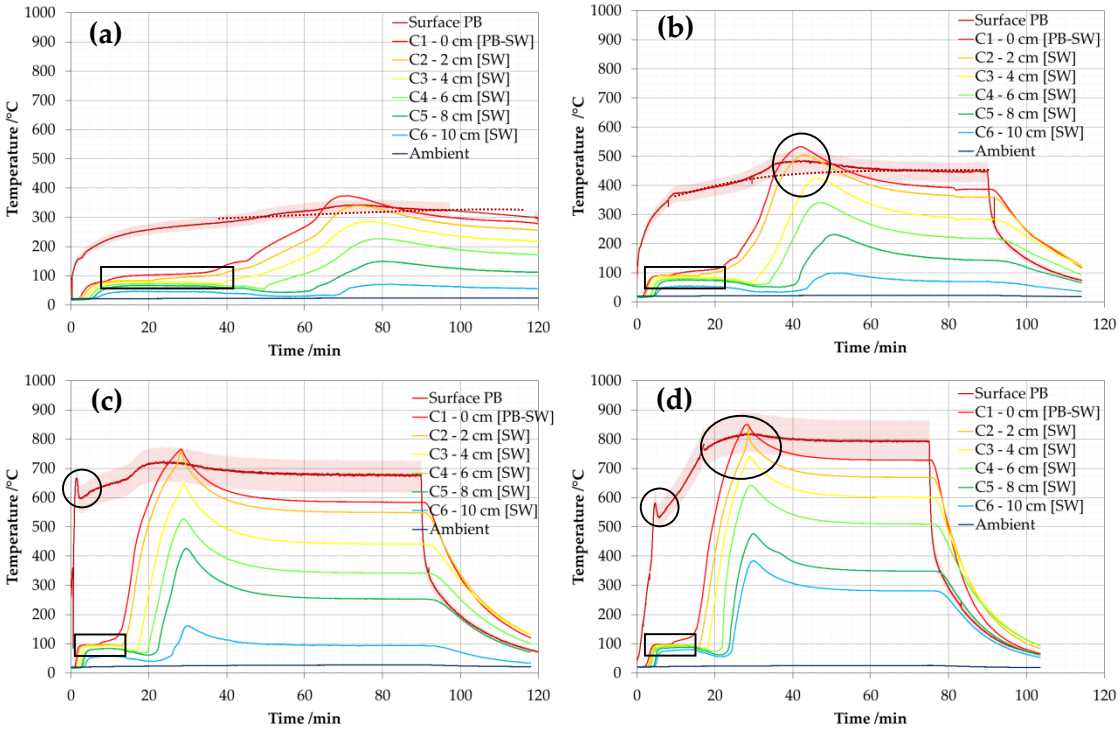

Figure 7.33. Time-history of temperatures within the plasterboard-stone wool assembly tested under external heat fluxes of (a) 15, (b) 25, (c) 65 kW·m^{-2} and (d) dynamic ramp up to 80 kW·m^{-2} Shading indicates sensitivity of the surface temperature to ε=0.9±0.1

Some common observations about these temperature profiles are:

- The surface temperature does not evolve as would be expected from an inert behaviour, with a change in the curvature as shown in Figure 7.33a and Figure 7.33b, where an inert baseline is projected. This increase in the surface temperature is likely due to two effects: the oxidation of the back face render of the plasterboard and the oxidation of the binders from the stone wool. The former effect can be verified in the remains of a test at 15 kW·m^{-2}, presented in Figure 7.34. As noted in Chapter 4, the oxidation processes in the stone wool are observed to start from 350°C, which could indicate a slight contribution from the stone wool oxidation to increase the core temperature.

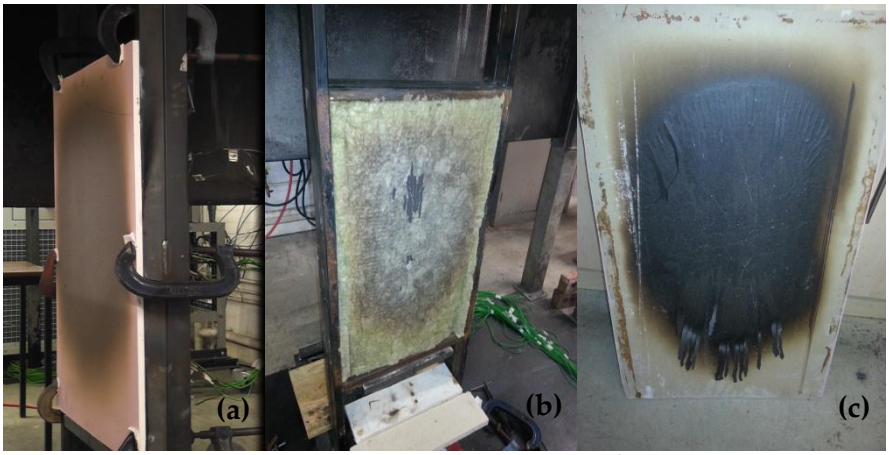

Figure 7.34. Remain of the sample after test at 15 kW·m^{-2}.(a) Exposed face of the plasterboard (b) Stone wool sample within the frame (c) Back face of the plasterboard after test

- A peak on the surface temperature is observed for experiments at 65 kW·m^{-2} and dynamic heating up to 80 kW·m^{-2}. This peak is observed after 1 and 4 minutes of test in Figure 7.33c and Figure 7.33d, with peak temperatures of 650°C and 570°C, respectively. These results are consistent with the visual observations that indicate the oxidation of the front face render of the plasterboard, presented in Figure 7.35 for a series of time steps.

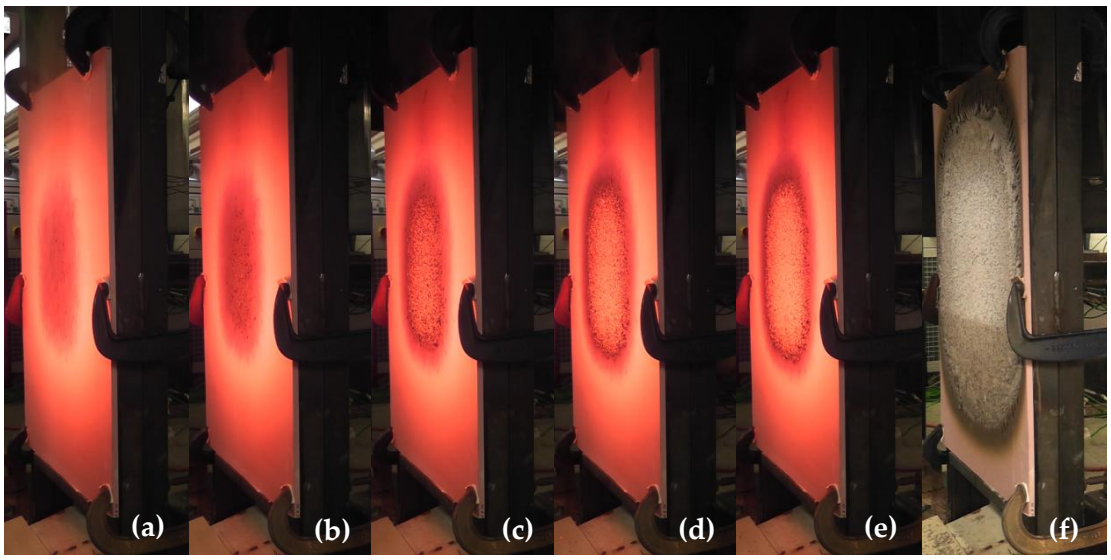

Figure 7.35. Sequence of the front face of the plasterboard during a test at 65 kW·m^{-2}. (a) 1 min (b) 1 min 15 s (c) 1 min 30 s (d) 1 min 45 s (e) 2 min (f) end of test

- A plateau of temperatures around 100°C is observed for the thermocouple at the interface, between the plasterboard and the insulation board, indicating a strong endothermic process taking place during the heating. This plateau, likely due to vaporisation of moisture within the plasterboard, is consistently shorter for larger values of external heat flux.
- During the plateau at the interface, temperatures in the core of the wool start dropping, indicating that the heat losses at the back surface are larger than the heat being conducted through the wool. These heat losses could also be

originated by the internal convection of the wool. This effect was also observed in the experiments results from the Edinburgh Tall Buildings Fire Tests.

- Similarly to the surface temperature, the thermocouples in the core of the insulation register a peak during the transient state, the shape of which is replicated by deeper positions with lower magnitude. The temperature drops after the peak, following a flat profile, indicating that the steady-state in the heat of conduction is achieved. As denoted for the surface temperature, the source of this peak could be due to the combustion of the plasterboard render in the interface or due to oxidation of the binder and additives of the stone wool. In any case, it is observed that a series of oxidative events alter the inert behaviour of the time-history of the solid phase. These events only contribute to self-heating, since no flaming or release of pyrolysates is observed.

Figure 7.36 shows the curves of estimated net heat flux for the experiments presented in Figure 7.33. Since the uncertainty in defining the convective heat transfer coefficient, absorptivity and emissivity is high, the approach to calculate the net heat flux is based on the following expression:

$$\dot{q}''_{net}(t) = \alpha \cdot \dot{q}''_{inc}(t) + h_T \cdot (T_\infty - T_s) \quad (7.8)$$

where α is the absorptivity, $\dot{q}''_{inc}(t)$ is the external heat flux, h_T is a global heat transfer coefficient of losses, T_∞ is the gas-phase temperature and T_s is the surface temperature. The global heat transfer coefficient is obtained by assuming $\dot{q}''_{net}(t_{ss}) \approx 0$ once the steady-state is achieved. Error bars are provided based on the assumption of a constant heat transfer coefficient (lower limit) and a temperature dependent heat transfer coefficient (upper limit) obtained as regression of the different case studies. A dotted baseline indicating the expected behaviour under inert conditions is provided. The curves of net heat flux for these series of constant radiant heat fluxes drop as a potential function with increases of surface temperature. Indeed, the main losses are due to radiation as explained in previous chapters. Therefore, the curves of net heat flux are expected to decay asymptotically towards zero. The calculations show negative values of net heat flux, which indicate that the surface temperature would have never achieved that temperature under inert conditions. Thus, the energy from oxidation reactions intervenes in the energy balance at the surface of the assemblies.

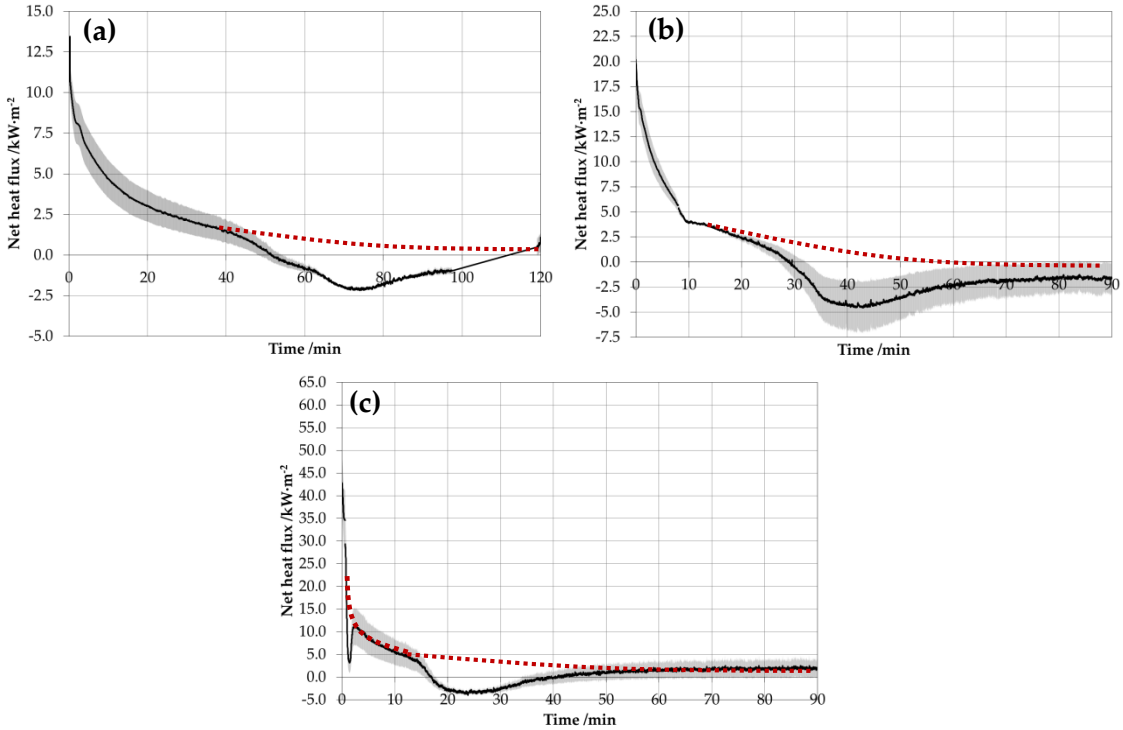

Figure 7.36. Curves of estimated net heat flux (a) 15 kW·m^{-2} (b) 25 kW·m^{-2} (c) 65 kW·m^{-2}

7.5.3.2 Plasterboard and PIRb assembly

Figure 7.37 shows the time-history of temperatures for plasterboard-PIRb assemblies under external heat fluxes of 15, 25 and 65 kW·m^{-2}. The patterns observed in these curves for stone wool tests, such as the oxidation of the interior face and exterior face of the plasterboard and the plateau at the interface at 100°C, are also identified here. The range of temperatures indicating the onset of pyrolysis for PIRb is included in the charts presented in Figure 7.37 as a purple horizontal shade between 300°C and 350°C.

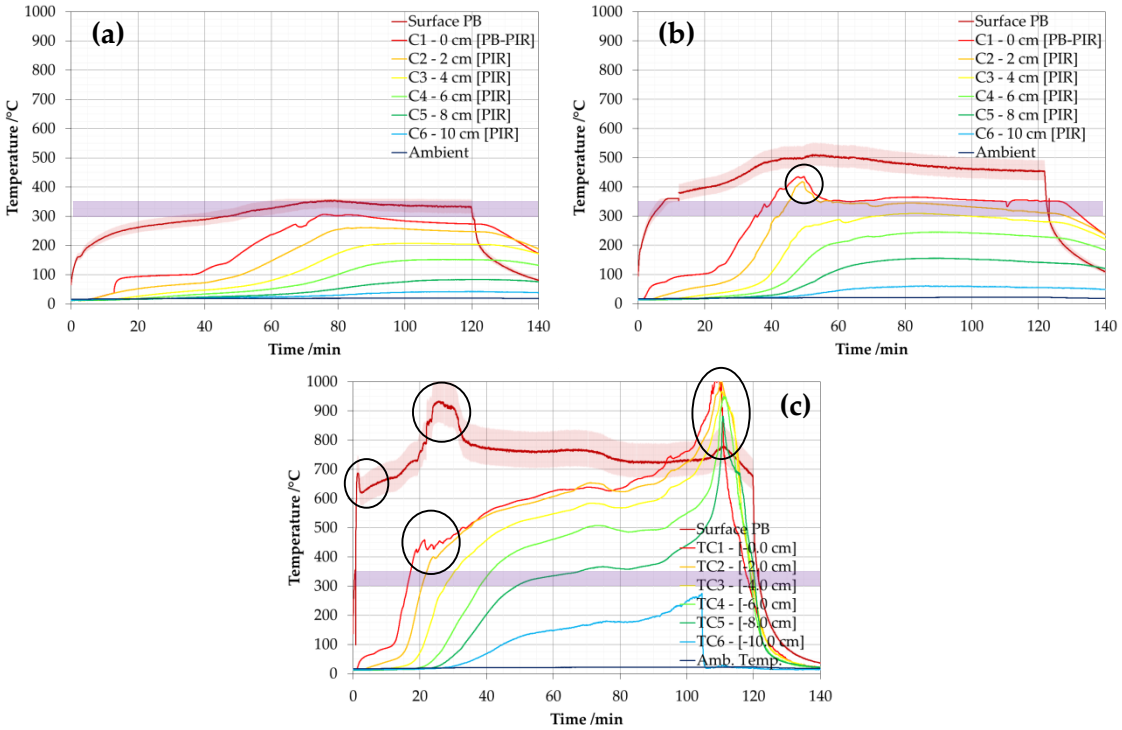

Figure 7.37. Time-history of temperatures within the plasterboard-PIR assembly tested under external heat fluxes of (a) 15 kW·m^{-2}, (b) 25 kW·m^{-2} and (c) 65 kW·m^{-2} Shading indicates sensitivity of the surface temperature to ε=0.9±0.1

Figure 7.37a shows a case study where the surface of the insulation board does not achieve the critical temperature of onset of pyrolysis. Indeed, the surface temperature follows the same trends observed in Figure 7.33, achieving a temperature during the steady-state of approximately 330°C. An irregularity is observed at the thermocouple interface at 20 minutes, indicating a bad positioning of the thermocouple which was later corrected. Some small cracks are observed in the surface of the plasterboard after 70 minutes of test, as well as some expansion of the insulation board after 72 minutes, which seemed to push the plasterboard. Some vapours are observed after 75 minutes of test, coinciding with the time when the interface reaches temperatures near the critical temperature. However, the production of volatiles is minor. The section of the sample residue after the test is presented in Figure 7.41a, indicating some discoloration, cracking and expansion of the thickness up to 1 cm.

Figure 7.37b shows a case study where the surface of the insulation board achieves the critical temperature of onset of pyrolysis after 35 minutes of test. Consistently, release of vapours from the edges of the plasterboard is observed from 36 minutes to approximately 50 minutes. Images from the release of volatiles from the edges are presented in Figure 7.38a. Some cracks are observed in the plasterboard with release of grey-black smoke, leaving a pattern of soot deposition as presented in Figure 7.38c. Additionally, the sample is found to expand 1 cm at the centre from the back of the frame, which is identified by the significant movement of the interface and C2 thermocouple, observed at 49 minutes. Eventually, as noted in Figure 7.37b a steady-state is obtained from 60 minutes. The section of the sample residue after the test is

presented in Figure 7.41b, indicating patterns of discoloration as shown in Chapter 6, several cracks and a residual thickness of approximately 12 cm.

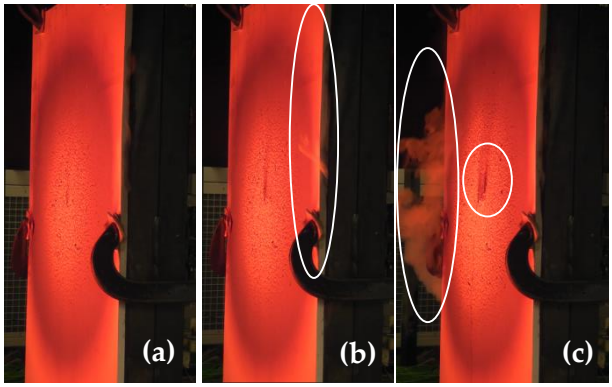

Figure 7.38. Sequence of the front face of the plasterboard during a test at 25 kW·m^{-2}. (a) 37 min 15 s (b) 40 min (c) 45 min 30 s

Figure 7.37c shows a case study where the exterior face of the plasterboard is consumed by surface oxidation after 1 minute of test, as observed during the test with stone wool at 65 kW·m^{-2}. Significant amount of vapours, probably moisture, are released from the plasterboard during the first 5 minutes of the test. Release of volatiles by the edges of the plasterboard is observed after 17 minutes, which is consistent with the interface achieving the critical temperature of 300°C at 16 minutes. After 20 minutes, flaming is observed from the cracks of the plasterboard surface, which is verified by the significant increase of surface temperature (above 900°C) recorded by the thermal camera between 21 minutes and 33 minutes. The thermocouple measurement at the interface shows a drop at 20 minutes, suggesting the expansion of the insulation board, which is confirmed by the 4cm movement of the back layer of the board from its original position and the gap between the plasterboard and the surface of the insulation. A quasi-steady state is observed in the temperatures between 40 and 80 minutes, when a sudden temperature increase is observed for all the thermocouples in the core of the insulation. Dark smoke is observed, suggesting that this rate of temperature increase is due to smouldering of the char within the frame. After 95 minutes, flaming is observed between the edges of the insulation and the top of the frame. The flames finally breakthrough the insulation board and flaming is observed at the back face of the board and top as shown in Figure 7.39. This is represented by virulent increase of temperature shown in Figure 7.37c from 100 minutes until 110 minutes. Large pieces of char that continue to glow (smoulder) remain from the board after the end of the experiments.

Figure 7.39. Evolution of the back face of the insulation board tested at 65 kW·m^{-2}

Figure 7.40 shows the estimated mass per unit area of the sample during the test and mass loss rate per unit area (pyrolysis rate) of the sample for experiments presented in Figure 7.37. It should be noted that since the density of PIRb was measured as 33 kg·m^{-3} and the thickness of the insulation board is 10 cm, the initial mass per unit area of the insulation board is 3.3 kg·m^{-2}. Additionally, the curves are calculated without considering the oxidation of the char, which is why Figure 7.40c shows some mass remaining after 100 minutes. Figure 7.40a confirms that no significant pyrolysates are released during the experiment presented in Figure 7.37a. The minor release of volatiles is calculated between 60 and 80 minutes of test with a maximum of 0.10 g·m^{-2}·s^{-1} around 74-75 minutes, which is in agreement with the visual observations. Figure 7.40b shows that the release of pyrolysates is observed from 30 to 50 minutes, with a maximum rate of 0.8-1.0 g·m^{-2}·s^{-1} from 40 to 47 minutes. Figure 7.40c shows a more severe behaviour, with pyrolysates released from 15 minutes achieving a maximum of 1.0-1.2 kg·m^{-2}·s^{-1} approximately at 21 minutes. The rate of mass loss decreases until being null at 80 minutes, when the rate continues to increase again up to 0.4 kg·m^{-2}·s^{-1}. This increase is explained by the growth of the temperatures in the core due to smouldering combustion with availability of oxygen, displacing the pyrolysis front into the remaining virgin material.

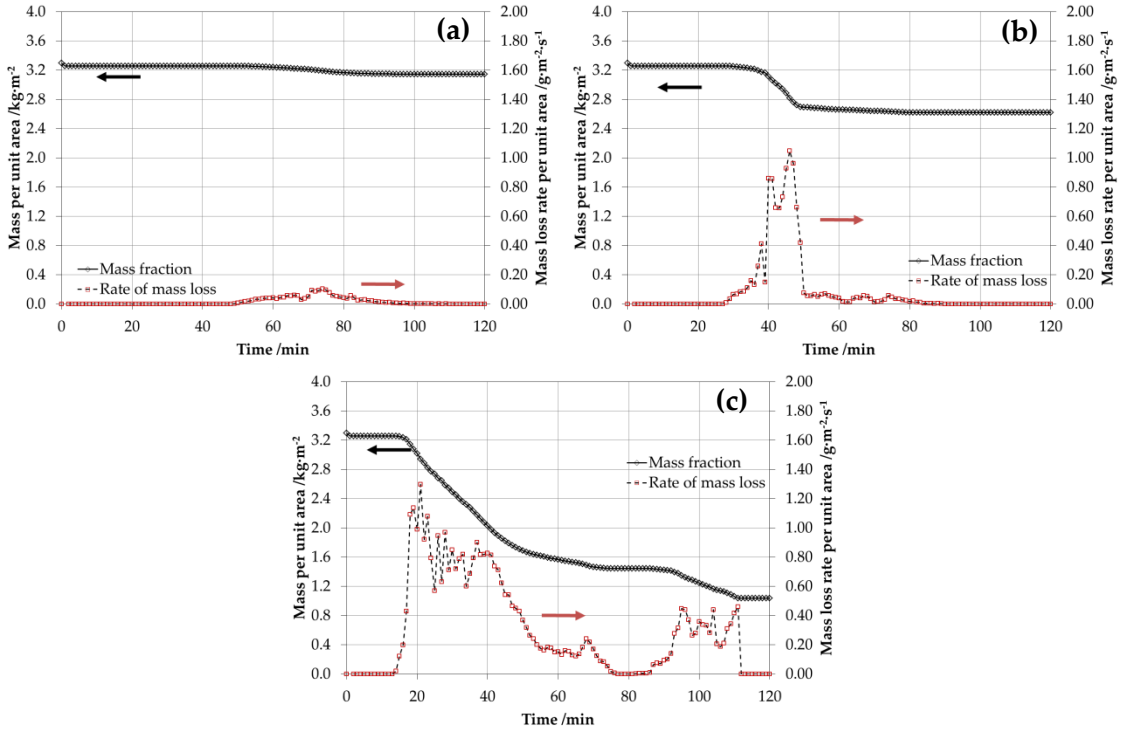

Figure 7.40. Estimated fraction of thermal degradation and pyrolysis rate of PIR for assemblies tested under external heat fluxes of (a) 15 kW·m^{-2}, (b) 25 kW·m^{-2} and (c) 65 kW·m^{-2}

The evolution of the fraction of remaining mass from experiments at 15 kW·m^{-2} and 25 kW·m^{-2} is presented in Figure 7.41, together with sections of the core of the insulation samples, as well as the different rates of thermal degradation and the associated discoloration, which was discussed in Chapter 6.

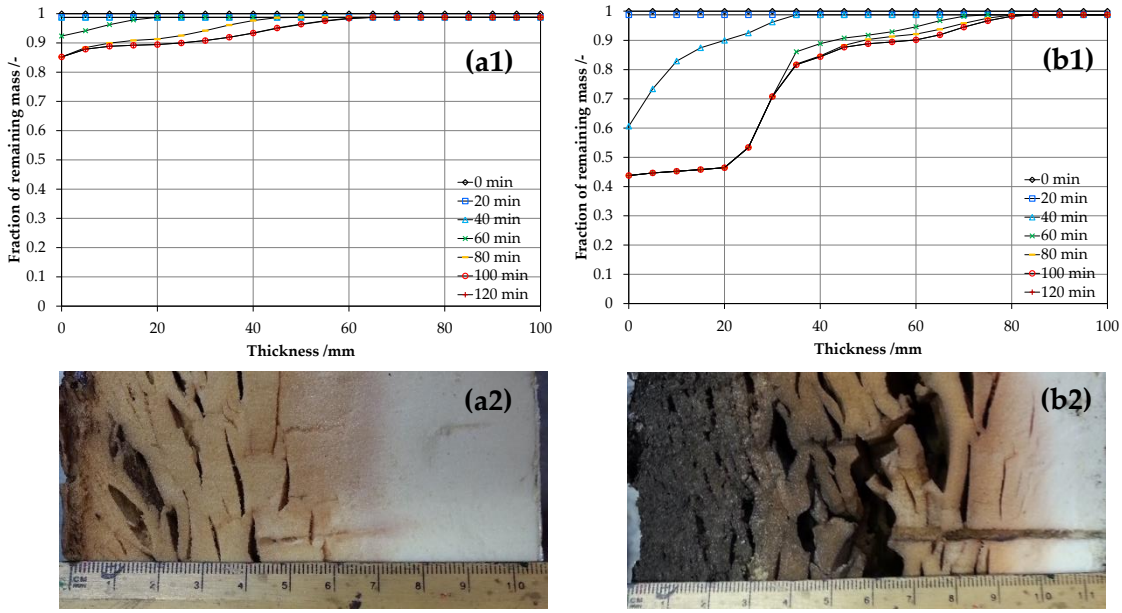

Figure 7.41. Fraction of remaining mass under external heat fluxes of (a1) 15 kW·m^{-2} and (b1) 65 kW·m^{-2} and their residue at the end of the test (a2 and b2)

The curves of net heat flux are equivalent to the ones shown in Figure 7.36. Indeed, the surface temperature of the PIR experiments are found to match the curves presented by the SW experiments, unless flaming is obtained. Therefore, the energy balance can be assumed to be similar.

7.5.3.3 Plasterboard and PF assembly

Figure 7.42 shows the time-history of temperatures for plasterboard-PF assemblies under external heat fluxes of 15, 25 $kW \cdot m^{-2}$ and a dynamic ramp up to 80 $kW \cdot m^{-2}$. Most of the events observed from SW and PIR samples for instance the oxidation of the exterior and interior render of the plasterboard and the pleateu of temperatures at 100°C are applicable here. Additionally, observations related to the onset of pyrolysis of the insulation board, rate of pyrolysis and smouldering of the char are described in a similar way to the previous section. The critical temperature of onset of pyrolysis proposed in previous Chapters between 400-425°C, has been indicated as a purple shade.

Figure 7.42a shows the time-history of temperatures of a case study where the insulation board does not achieve the onset of pyrolysis, since the surface and interface temperature achieve a maximum temperature of 350°C and 386°C, respectively. The temperature profile within the insulation board achieved a quasi-steady state after 80 minutes, however including a slow increase of temperature, likely due to oxidation reactions at the interface. These reactions are probably due to the oxidation of the back face render of the plasterboard as shown previously. After the heating is removed, the temperatures continue to drop, indicating that if smouldering combustion has been produced at the surface of the insulation, this does not progress anymore. No release of vapours is observed during the experiment, but spalling sounds are recorded from 55 minutes until the end of the test, when the temperature at the interface is 190°C and the thermocouple C1 measures 110°C. Additionally, a plateau of temperatures at approximately 100°C is observed. The residue of the sample is shown in Figure 7.44a2, presenting the patterns of discolouration presented in Chapter 6.

Figure 7.42b shows the time-history of temperatures of a case study where the onset of thermal degradation is achieved. Indeed, the interface temperature reaches 400°C 50 minutes after the initiation of the test. Similarly to the previous case, spalling sounds are heard from 25 minutes until the end of the test. The plateau of temperatures is also identified at 100°C. Thermocouples C2 (2 cm) and C3 (4 cm) are found to cross the critical temperature of pyrolysis onset (purple shading) at 65 minutes and 95 minutes, respectively, which suggests the release of pyrolysates. The temperature at the interface achieves a quasi-steady state from 60 minutes, but slowly increases to a rate of 1.7°C·min^{-1} which is also observed for the temperatures in the core of the insulation. This heating occurs by smouldering combustion at the surface of the insulation board (interface), which is confirmed by the release of minor amounts of smoke through the formed plasterboard cracks at the front. Then, the radiant panels are turned off at 120 minutes, the temperatures initially drop, but at

130 minutes the temperatures start to increase again without the presence of an external heat source. Visual observations indicate flaming behind the plasterboard at 30 minutes. Eventually, flaming breaks through the insulation and spreads at the back face of the insulation. This is represented by the significant temperature increase observed between 130 and 160 minutes in Figure 7.42b, similar to the behaviour presented in Figure 7.44b. It is thought that this behaviour produced after turning off the radiant panels has helped to cool down the assembly and therefore the pressure to drop and the plasterboard to contract, allowing higher diffusion of air into the assembly. As a result of this, the char from the PF is at sufficient temperature to oxidise.

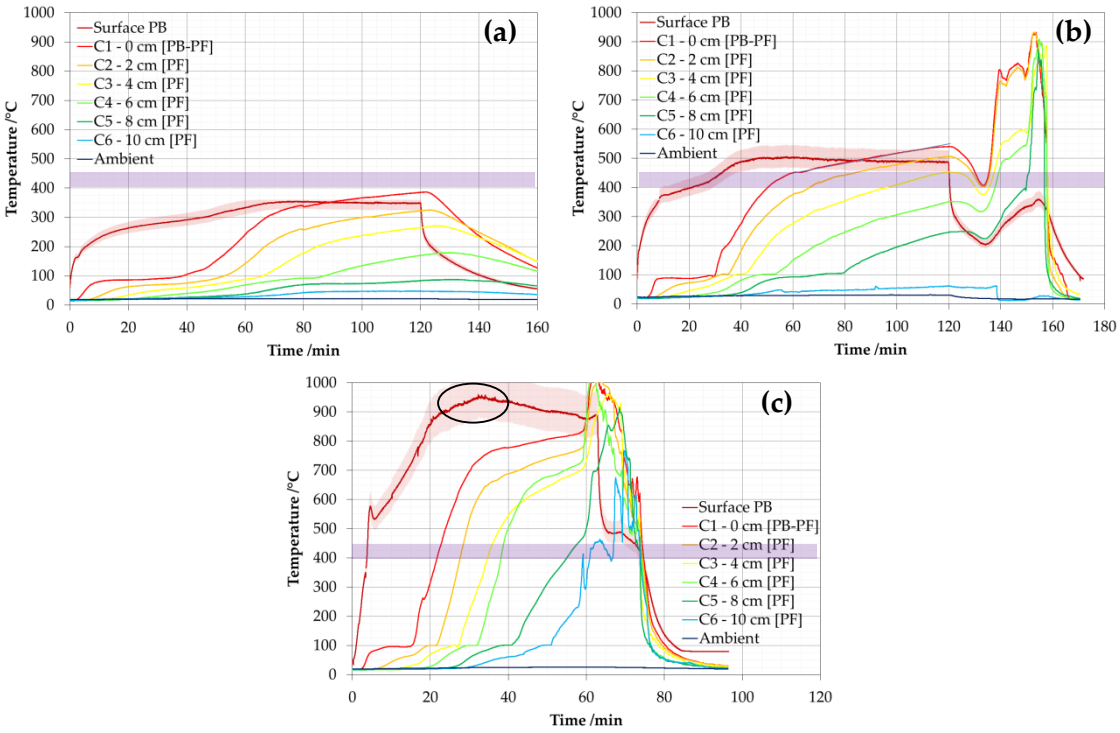

Figure 7.42. Time-history of temperatures within the plasterboard-PF assembly tested under external heat fluxes of (a) 15, (b) 25 kW·m^{-2} and (c) dynamic ramp up to 80 kW·m^{-2} Shading indicates sensitivity of the surface temperature to ε=0.9±0.1

Figure 7.42c shows a case study under a heat exposure with a dynamic ramp up to 80 kW·m^{-2}. The critical temperature of onset of pyrolysis is achieved at the interface after 22 minutes, while thermocouples C2 (2 cm), C3 (4 cm), C4 (6 cm) and C5 (8 cm) reach this temperature after 28, 34, 38 and 55 minutes. This qualitatively indicates increased release of pyrolysates, which is confirmed by flaming at the surface of the plasterboard from the formed cracks, shown in Figure 7.42c as the temperatures at the surface reaches 900°C. Unlike the experiment at 25 kW·m^{-2}, the flames break through the insulation board before turning the radiant heaters off. As a result, fire spreads at the back surface of the insulation board as shown in Figure 7.44, finally consuming all the insulation, while the remaining chunks of char are consumed by smouldering.

Figure 7.43 shows the estimated mass per unit area of the sample during the test and mass loss rate per unit area (pyrolysis rate) of the sample for experiments presented in Figure 7.42. It should be noted that since the density of PF was found to be 38.1 kg·m^{-3} and the thickness of the insulation board is 10 cm, the virgin mass per unit area of the insulation board is 3.81 kg·m^{-2}. Figure 7.43a and Figure 7.43b indicate that the maximum release of pyrolysates is moderate, achieving a maximum of 0.1 and 0.2 kg·m^{-2}·s^{-1} at 67 and 46 minutes, respectively. Figure 7.43c shows a maximum between 1.0 and 1.4 kg·m^{-2}·s^{-1} between 29 and 39 minutes. The times when pyrolysis gases are released are consistent with the visual observations noted above.

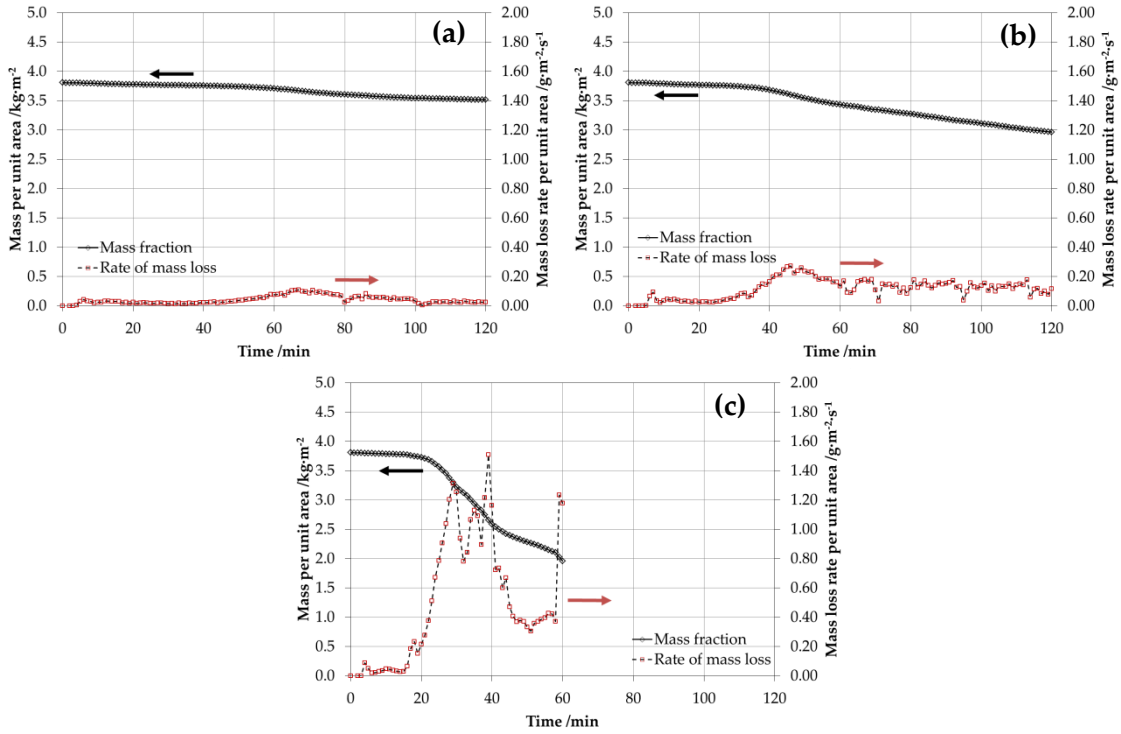

Figure 7.43. Estimated fraction of thermal degradation and pyrolysis rate of PF for assemblies tested under external heat fluxes of (a) 15 kW·m^{-2}, (b) 25 kW·m^{-2} and (c) dynamic ramp up to 80 kW·m^{-2}

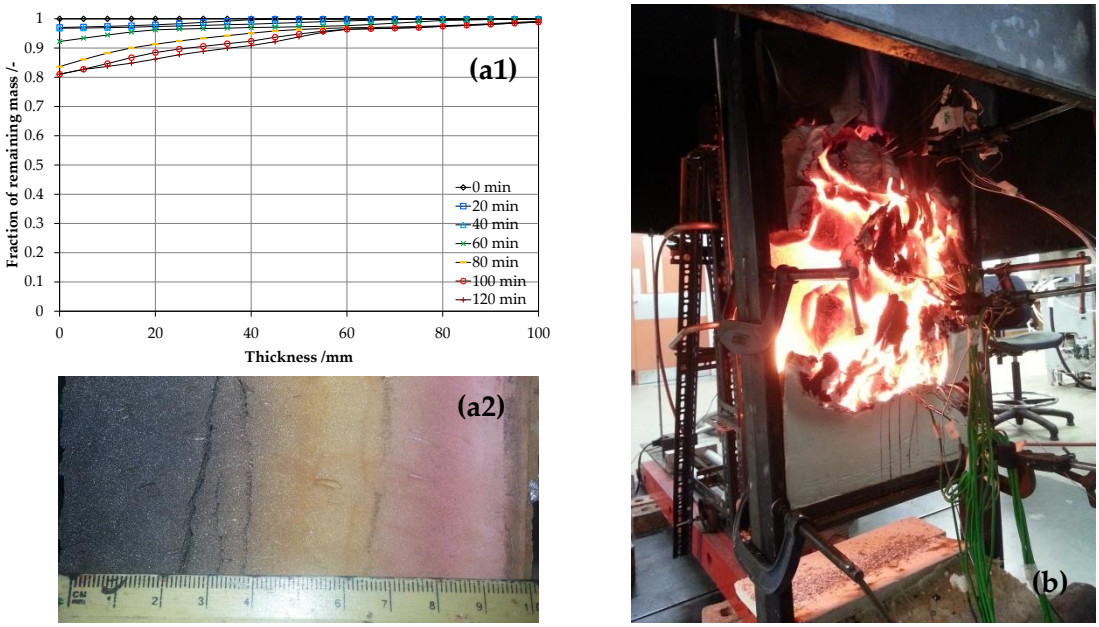

Figure 7.44. Fraction of remaining mass under external heat flux of 15 kW·m^{-2} and the residue at the end of the test (a1 and a2) and combustion of PF after removal of external heat flux of of 65 kW·m^{-2}

As justified for the PIR experiments, the curves of the net heat flux for these experiments are similar to those presented in Figure 7.36. For simplicity in the assessment, the net heat flux curve for the experiment with a dynamic heating curve is not presented.

7.6 Discussion

7.6.1 Evaluation of fire performance

The results obtained by the three experimental programmes have demonstrated the relevance of the boundary element in the performance observed. Then, the design of the barrier for combustible insulation systems is of great importance for the control of their hazards. A quantifiable parameter is required to evaluate their performance and, therefore drive the design of these. The author has proposed throughout this chapter the net heat flux as quantifiable parameter to be considered in the fire performance assessment of these elements. Indeed, the current methodologies for design, based on pass-fail tests (reaction-to fire) and a time-temperature curve (fire-resistance), have been demonstrated to be inadequate for this purpose. This was already suggested by *Harmathy* some time ago for designing boundary and structural elements under fire conditions [22, 23].

The accumulated net heat flux from the case scenarios presented above is correlated to the temperature at the surface of the insulation, i.e. the interface lining-insulation from the wall assemblies. This is presented as a series of plots in Figure 7.45, corresponding to different moments throughout the duration of the tests from the three studied experimental programmes. It should be noted that for the intermediate-scale tests, the absorption of heat was not very precise due to the simplicity of the analysis. Indeed, these did not account for exothermicity behind the

plasterboard or flaming from pyrolysates at the lining's surface. Nevertheless, the estimation of net heat flux prior to these events is considered to be in the right order of magnitude.

Figure 7.45 shows two clearly differentiated regimes:

- A thermally thin regime, corresponding to the plots from the Sandwich Panel Tests (red squares), representing a perfectly linear function with a lower slope.
- A thermally thick regime, corresponding to the plots from the Edinburgh Tall Buildings Fire Tests (green triangles) and from the Intermediate-Scale Tests (blue diamonds), representing a linear function with a larger slope and a final plateau. The final plateau is produced because the surface temperature has achieved the steady-state, with an approximated null value of the net heat flux. In the meantime, the thermal wave keeps propagating through the lining.

It is observed that significantly less energy is required for increasing the surface temperature of the insulation from the sandwich panel assemblies than the assemblies based on plasterboard and aircrete linings. Indeed, this was expected since the heat transfer is governed by the insulation rather than the lining due to the low thickness of the metal skin. As noted in previous chapters, the insulation materials are characterised by their low thermal inertia, thus requiring low amounts of energy to achieve the critical temperature. Additionally, a linear correlation between the absorption of energy from the lining and the temperature at the interface of lining-insulation is found.

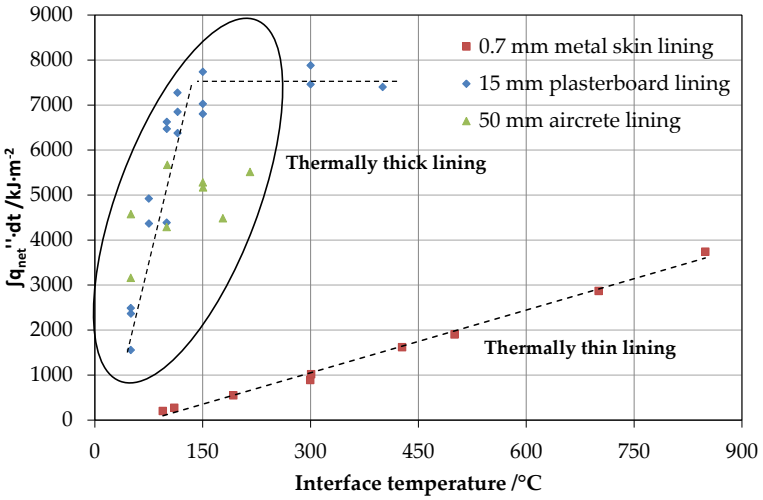

Figure 7.45. Temperature at the surface of the insulation versus integral net heat of the wall assembly

Therefore, the accumulated net heat flux is suggested as quantifiable variable to assess the fire performance of insulation systems. Further study is required in order to evaluate the relationship with the interface temperature, the lining thermal properties and thickness, and adequate it to feasible inputs from real fires. This will be discussed in the next chapter.

7.7 Concluding remarks

The series of experiments and analyses presented above have served the purpose of validation of the bench-scale testing results presented in Chapters 4 to 6; and more importantly the validation of the hazards' map presented in Chapter 3 as framework for the design of insulation materials in buildings.

As noted in Chapter 3, the main hazard from combustible insulation materials is to control the instant at which significant pyrolysis gases are released. The critical temperature of pyrolysis onset was suggested as a quantifiable parameter for the control of this hazard. Plastic foams such as PIR and PF have been found to release significant amount of pyrolysates after the critical temperature is achieved; defined in Chapters 4 through 6 with 300°C for PIR and 400-425°C for PF. However, ignition of the generated pyrolysates is only produced if the correct conditions are found, i.e. the lower flammability limit. Indeed, flaming combustion of the effluent of pyrolysates from edges was found to ignite and later flame out after removal of the pilot igniter. In the case where the radiant panel is moved closer to the plasterboard, the effluent of pyroysates was found to flame continuously, indicating that the lower flammability limit is achieved due to high gas-phase temperature and enough rates of pyrolysis gases. Therefore, once the critical temperature is achieved, prediction of the thermal profile in the solid-phase is crucial to being able to quantify the flammability and toxicity hazards, evaluated by the production rate of pyrolysis gases, which corresponds to the main quantifiable variable to be considered.

Additionally, the importance of the diffusion of oxygen to the already pyrolysed areas of insulation has also been demonstrated, triggering the solid-phase oxidation (smouldering combustion) within the assembly. In some cases, flame spread is produced by the back face of the insulation board, activated by the consumption of mass and heating generated by smouldering.

These results have demonstrated that non-combustible insulation materials such as stone wool with low binder content do not produce enough amount of pyrolysates to sustain flaming, which is consistent with the results presented in Chapters 4 to 6. Therefore, the time for achieving the critical temperature of pyrolysis onset can be assumed as infinite for the methodology proposed in Chapter 3. However, it is shown that the oxidation of the binder may produce self-heating of the wool, which should be considered for heat transfer analyses.

Finally, the importance of the barrier to control the critical temperature and generation of pyrolysis gases has been confirmed, as well as the importance of the non-combustibility of this barrier as shown in the Sandwich Panels Tests' programmes. Therefore, the proper design of the boundary element is vital for the control of any hazard related to combustible insulation materials. The variable total net heat flux absorbed has been shown as a key variable for the design of barriers for the control of the onset of thermal degradation, which is the main and initial hazard of combustible insulation materials.

7.8 References

[1] "ISO 13784-1. Reaction to fire test for sandwich panel building systems. Part 1: Small room test." International Organization for Standardization, Geneva (Switzerland), 2014.

[2] R. J. Crewe, J. P. Hidalgo, M. X. Sørensen, S. Molyneus, M. McLaggan, G. Joomas, S. Welch, J. L. Torero, A. A. Stec, and T. R. Hull, "Fire performance of sandwich panels in a modified ISO 13784-1 small room test: the effect of damage and increased fire load," *Fire Technology (submitted)*.

[3] M. X. Sørensen, "Small and medium scale fire experiments with different insulation materials. (M.Sc. Thesis)," Technical University of Denmark, 2014.

[4] J. P. Hidalgo, M. McLaggan, S. Welch, and J. L. Torero, "Characterisation of fire dynamics in a modification to the Small room test, ISO 13784-1," *(in preparation)*.

[5] J. P. Hidalgo, A. Cowlard, C. Abecassis-Empis, C. Maluk, A. H. Majdalani, S. Kahrmann, R. Hilditch, M. Krajcovic, and J. L. Torero, "Edinburgh Tall Building Fire Tests: Experiment #1," *Fire Safety Journal (submitted)*, 2015.

[6] "BS EN 520. Gypsum plasterboards. Definitions, requirements and test methods." BSI, 2004.

[7] C. Maluk, "Development and Application of a Novel Test Method for Studying the Fire Behaviour of CFRP Prestressed Concrete Structural (Ph.D. thesis)," The University of Edinburgh, 2014.

[8] W. M. Pitts, A. V. Murthy, J. L. de Ris, J. R. Filtz, K. Nygård, D. Smith, and I. Wetterlund, "Round robin study of total heat flux gauge calibration at fire laboratories," *Fire Safety Journal*, vol. 41, pp. 459–475, 2006.

[9] "BS EN 1363-1 . Fire resistance tests - Part 1: General Requirements." BSI, 2012.

[10] J. P. Hidalgo, C. Maluk, and J. L. Torero, "Uncertainty assessment on the use of thin skin calorimeters to measure irradiation from real fires," *(in preparation)*.

[11] J. J. Alston, "Room/Corner Fire Calibration Data: Marine Composite Screening Specimens (M.Sc. thesis)," Worcester Polythecnic Institute (USA), 2004.

[12] A. Amundarain, "Assesment of the Thermal Efficiency, Structure and Fire Resistance of Lightweight Building Systems for Optimised Design (Ph.D. thesis)," The University of Edinburgh. http://hdl.handle.net/1842/2128, 2007.

[13] K. Levenberg, "A Method for the Solution of Certain Non-Linear Problems in Least Squares," *Quarterly of Applied Mathematics*, vol. 2, pp. 164–168, 1944.

[14] D. Marquardt, "An Algorithm for Least-Squares Estimation of Nonlinear Parameters," *SIAM Journal on Applied Mathematics*, vol. 11, no. 2, pp. 431–441, 1963.

[15] C. Lautenberger and C. Fernandez-Pello, "Generalized pyrolysis model for combustible solids," *Fire Safety Journal*, vol. 44, no. 6, pp. 819–839, 2009.

[16] S. R. Wasan, P. Rauwoens, J. Vierendeels, and B. Merci, "An enthalpy-based pyrolysis model for charring and non-charring materials in case of fire," *Combustion and Flame*, vol. 157, no. 4, pp. 715–734, 2010.

[17] *CIBSE Guide A: Environmental Design*, 7th ed. The Chartered Institution of Building Services Engineers London, 2006.

[18] G. Thomas, "Modelling thermal performance of gypsum plasterboard-lined light timber frame walls using SAFIR and TASEF," *Fire and Materials*, vol. 34, pp. 385–406, 2010.

[19] P. Keerthan and M. Mahendran, "Numerical studies of gypsum plasterboard panels under standard fire conditions," *Fire Safety Journal*, vol. 53, pp. 105–119, Oct. 2012.

[20] K. Ghazi Wakili, E. Hugi, L. Wullschleger, and T. Frank, "Gypsum Board in Fire -- Modeling and Experimental Validation," *Journal of Fire Sciences*, vol. 25. pp. 267–282, 2007.

[21] B. H. Jones, "Performance of Gypsum Plasterboard Assemblies Exposed to Real Building Fires," New Zealand, 2001.

[22] T. Z. Harmathy and J. R. Mehaffey, "Normalized heat load: A key parameter in fire safety design," *Fire and Materials*, vol. 6, no. 1, pp. 27–31, Mar. 1982.

[23] T. Z. Harmathy, "The possibility of characterizing the severity of fires by a single parameter," *Fire and Materials*, vol. 4, no. 2, pp. 71–76, Jun. 1980.

Chapter 8.

Design Tool for the Definition of Thermal Barriers for Insulation Materials

8.1 Introduction

The methodology for the performance-based design of flammable insulation systems in buildings presented in Chapter 3, is based on the control of the onset of pyrolysis and requires a series of inputs such as insulation and barrier thermal properties, insulation critical temperature and, more importantly, conditions of heat exposure. The definition of the heat transfer problem consisting of two layers of material (barrier-insulation) with different dimensions and thermal properties is defined in Equations (8.1) to (8.5) below, and schematically represented in Figure 8.1.

$$\dot{q}''_{net}(t) = -k_b(T) \cdot \left.\frac{\delta T}{\delta x}\right|_{x=0^+} \qquad \text{for } x = 0 \qquad (8.1)$$

$$\frac{\partial\left(k_b(T) \cdot \frac{\delta T}{\delta x}\right)}{\partial x} = \rho_b \cdot c_{p,b}(T) \cdot \frac{dT}{dt} \qquad \text{for } 0 < x < L_b \qquad (8.2)$$

$$-k_b(T) \cdot \left.\frac{\delta T}{\delta x}\right|_{x=L_b^-} = -k_i(T) \cdot \left.\frac{\delta T}{\delta x}\right|_{x=L_b^+} \qquad \text{for } x = L_b \qquad (8.3)$$

$$\frac{\partial\left(k_i(T) \cdot \frac{\delta T}{\delta x}\right)}{\partial x} = \rho_i \cdot c_{p,i}(T) \cdot \frac{dT}{dt} \qquad \text{for } L_b < x < L_b + L_i \qquad (8.4)$$

$$-k_i(T) \cdot \left.\frac{\delta T}{\delta x}\right|_{x=L_b+L_i} = \dot{q}''_{loss}(t) \simeq 0 \qquad \text{for } x = L_b + L_i \qquad (8.5)$$

where $\dot{q}''_{net}(t)$ is the net heat flux, k_b, ρ_b, $c_{p,b}$ and L_b are the thermal conductivity, density, specific heat capacity and thickness of the barrier, k_i, ρ_i, $c_{p,i}$ and L_i are the thermal conductivity, density, specific heat capacity and thickness of the insulation behind the thermal barrier respectively, and $\dot{q}''_{loss}(t)$ is the heat loss through the back of the insulation board.

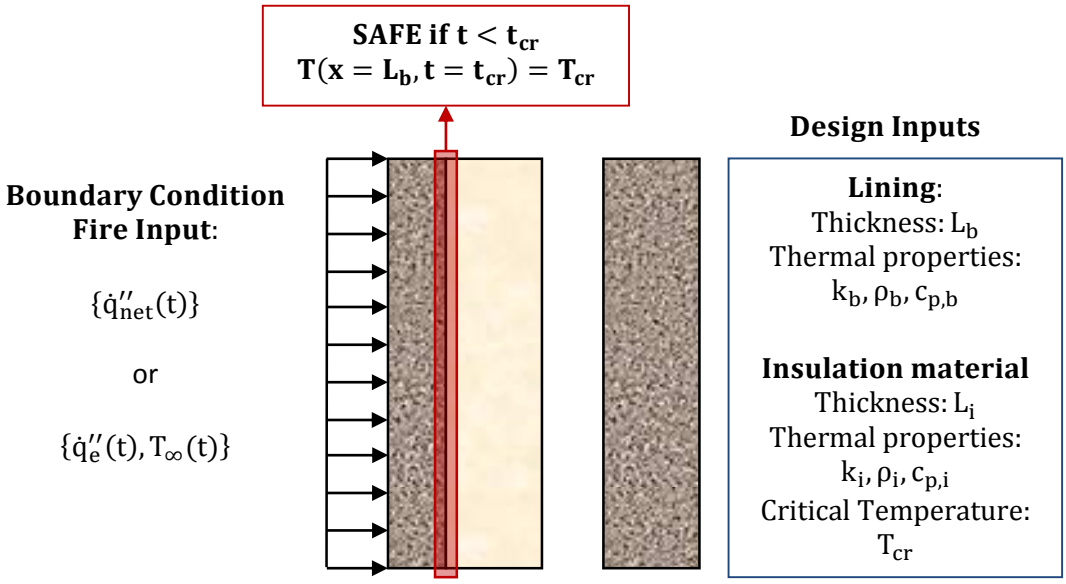

Figure 8.1. Problem definition for the methodology based on the control of pyrolysis onset. Representation of a boundary element consisting of a lining and insulation

This problem can be solved for any particular case of heating and barrier dimensions and properties, by determining the critical time for the onset of thermal degradation. However, since this problem is defined by a series of differential equations and interface conditions, the exact analytical solution cannot be easily obtained. Therefore, a numerical tool based on finite elements or finite differences is required in order to determine the critical time, given certain conditions of heat exposure. An example of the space differentiation used for the finite difference models developed by the author is presented in Figure 8.2, the formulation of which can be found in Appendix D. Despite designers could apply numerical models like this to accurately define optimised dimensions and thermal properties of the barrier element, a simple tool that represents the direct solution of this problem would be ideal due to its simplicity and low computational cost.

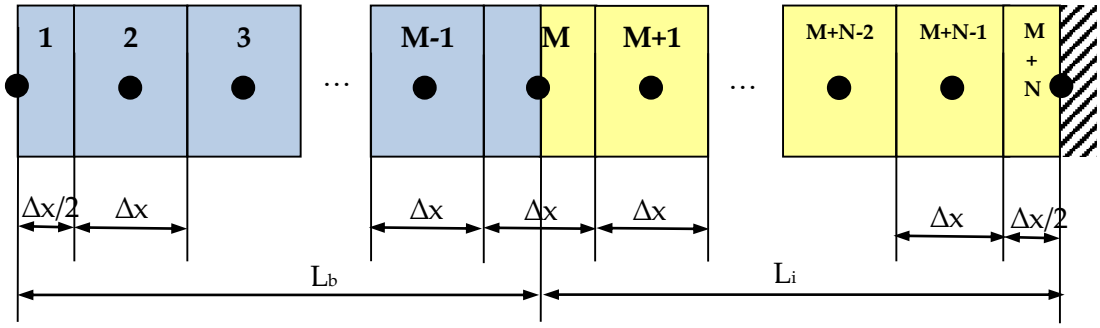

Figure 8.2. Space differentiation for two material layers in the one-dimensional heat transfer analysis of the solid-phase

Hence, the aim of this chapter is to define a series of tools by which designers could easily evaluate suitable solutions to likely fire scenarios without having to solve directly the conduction problem. The approach followed in the following sections is inspired by a concept first introduced by *Harmathy* [1], by which the severity of the fire to the boundaries is assessed by the heat absorption to the elements, rather than the average gas-phase temperature of the fire. This was introduced by *Harmathy and Mehaffey* as the normalised heat load, which was intended to represent a key parameter in fire safety designs, intrinsically related to the prediction of the behaviour of construction elements under fire resistance testing [2].

The application of *Harmathy*'s concept lies on the use of the net heat penetration as the key parameter for design. As presented in the previous chapter, the total heat absorbed by an assembly is related to the time at which the critical temperature is achieved. *Harmathy* showed that for an element embedded in a certain medium, the critical temperature of this element can be expressed as noted in Equation (8.6) for given conditions [1]:

$$T_{cr} \simeq 0.435 \cdot \frac{\bar{q} \cdot \tau}{\rho \cdot c \cdot \Delta x} \qquad 0.8 < \cdot \frac{\Delta x}{\kappa^{1/2} \cdot \tau^2} < 1.2 \qquad (8.6)$$

where T_{cr} is the critical temperature, $\bar{q}$ is the temporal average penetration of heat, τ is the duration of the fire, ρ and c are the density and specific heat capacity of the medium, Δx is the depth of the element and κ is the thermal diffusivity.

This suggests that for the particular case being studied here, the barrier properties, such as thickness thermal properties, could be determined as a function of the total net heat absorbed. This is illustrated in Figure 8.3, representing a design chart in which the designer could choose the right barrier for the selected heat exposure.

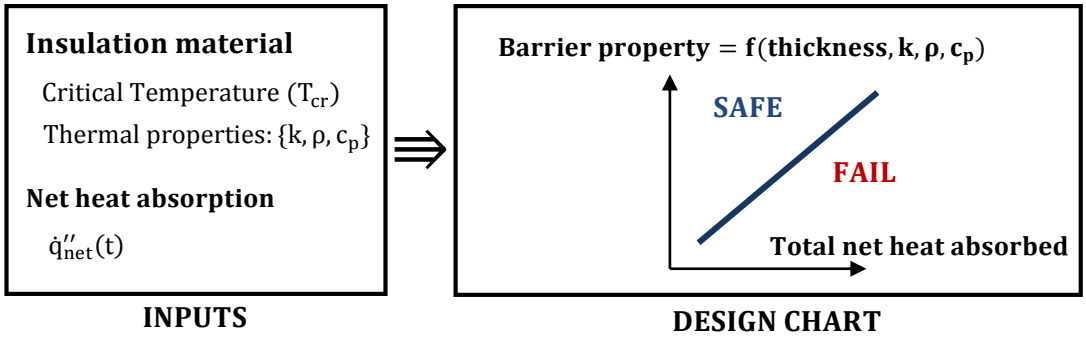

Figure 8.3. Schematic of the design tool based on the total net heat flux absorbed

However, the main disadvantage of the approach based on the integral of net heat flux is related to the phenomenon of heat diffusion through the solid-phase. As will be shown in the following sections, the analysis that sums all the range of solutions based on this parameter is only valid for a specific heat transfer regime, i.e. the thermally thin barrier. The analysis for thermally thick barriers depends on a series of dimensionless parameters defined as a function of the time of heat exposure, material properties and thickness of the barrier. Then, such a tool would be only applicable for thermally thin barriers. These two different regimes and their solutions are discussed below.

Additionally, the use of the net heat flux as an input parameter from the fire would be applicable only to certain conditions. As mentioned in Chapter 3, the classic compartment fire framework defines the evolution of the fire as a pre-flashover (combustible controlled) and a post-flashover regime (ventilation controlled). These regimes have been discussed by *Harmathy* [3] and *Thomas et al.* [4] who described them as *Regime I* (ventilation controlled) and *Regime II* (fuel-surface-controlled). A review for the fire safe design of buildings has been recently presented by *Torero et al.* [5], emphasising the need for understanding the dynamics of fire under *Regime II*. The distinction between these regimes is based on the geometry of the compartment and the mechanisms of mass and energy transfer related to this. The burning rate in *Regime I* is controlled by the static pressure difference within the compartment. For this case, the heat release (burning rate) in the compartment can be assumed to be constant once the thermal equilibrium is achieved and is determined by the available flow of oxygen. The thermal equilibrium will be eventually achieved since the characteristic times of the gas-phase are much shorter than the characteristic times of heat transfer to the boundaries. Then, the temperature in the gas-phase reaches a constant value and thus the variation of energy in the compartment is null. As a result, the net heat to the boundaries can be defined as noted in Equation (8.7), independently of the thermal properties of the material:

$$\dot{q}_{net} = \dot{q}_{fire} - \dot{q}_{smoke,out} + \dot{q}_{air,in} \qquad (8.7)$$

where $\dot{q}_{net}$ is the net heat transferred to the boundaries, $\dot{q}_{fire}$ is the heat release rate inside the compartment, $\dot{q}_{smoke,out}$ is the energy lost by the mass transfer of smoke leaving the compartment and $\dot{q}_{air,in}$ is the energy gained by the mass transfer of fresh air introduced in the compartment. This expression may be obtained by applying the energy conservation equation and assuming the variation of energy within the compartment is null.

However, if *Regime II* is considered, this dynamic pressures generated by the fire dominate over the static differential pressures [5] and therefore, the framework based on classic quasi-cubic compartments is no longer applicable. This fire regime is usually considered as the pre-flashover fire stage for quasi-cubic compartments (<150 m^3), but clearly applicable to compartments with higher volume or low height-floor area ratio, which are more frequently found in modern construction [6, 7]. Then, the transient heat transfer to the boundaries plays an important role and the net heat flux to the boundaries cannot be determined independently of the thermal properties of the boundary element.

If the net heat flux is found as an unsuitable approach, the boundary condition in a real fire should be described as an independent variable from the boundaries. This approach, described in the previous chapters, requires two inputs: the radiant incident heat flux and the gas-phase temperature coupled to a heat transfer coefficient, so as the energy balance can be defined as follows:

$$\dot{q}''_{net}(t) = \alpha \cdot \mathbf{\dot{q}''_e(t)} + \mathbf{h_c} \cdot \left(\mathbf{T_\infty(t)} - T_s(t)\right) - \varepsilon \cdot \sigma \cdot T_s(t)^4 = -k \cdot \left.\frac{\delta T}{\delta x}\right|_{x=0^+} \quad (8.8)$$

where $\dot{q}''_{net}(t)$ is the net heat flux, α is the absorptivity, $\dot{q}''_e(t)$ is the incident radiant heat flux, h_c is the convective heat transfer coefficient, $T_\infty(t)$ is the gas-phase temperature, $T_s(t)$ is the surface temperature, ε is the emissivity, σ is the Stefan-Boltzmann constant, k is the thermal conductivity and $\left.\frac{\delta T}{\delta x}\right|_{x=0^+}$ is the thermal gradient at the surface.

The validity of this definition could be doubted, since the thermal feedback to the fire which could increase the HRR and therefore increase the value of radiant heat flux and gas-phase temperature, is neglected. Despite this being true, it has been mentioned in Chapter 3 that the effect on the thermal feedback is expected to be low if typical linings are used and relegating insulation elements to deeper positions in the boundaries. Indeed, if parametric radiant heat fluxes are obtained and validated experimentally under similar conditions, the thermal feedback would be intrinsically considered.

A simplification of Equation (8.8) may be obtained if the losses or gains by convection and the losses by emitted radiation from the material surface are lumped by using a global heat transfer coefficient, so as the energy balance can be defined as:

$$\dot{q}''_{net}(t) = \alpha \cdot \mathbf{\dot{q}''_e(t)} + \mathbf{h_T} \cdot \left(T_0 - T_s(t)\right) = -k \cdot \left.\frac{\delta T}{\delta x}\right|_{x=0^+} \quad (8.9)$$

where h_T is the global heat transfer coefficient and T_0 is the initial temperature of the surface. This approach gives the opportunity of quantitative and probabilistic analyses that consider different heat insults in the pre-flashover stage, so no contribution to the heat release rate from flammable insulation materials can be guaranteed.

Both approaches are considered for the formulation of guidelines for the design of adequate barriers in order to control the onset of pyrolysis. It is anticipated that further work is required to reduce the uncertainty with regard to input parameters from the fire for the application of performance-based designs, which is out of the scope of this thesis.

8.2 Variables definition and barrier properties review

The required variables for the methodology can be divided into four groups:

- The **fire inputs** such as **net heat flux ($\dot{q}''_{net}$)** or **radiant heat flux with a global heat transfer coefficient of losses ($\dot{q}''_e$, h_T).** These variables characterise the fire scenario for which the barrier is designed. Probabilistic approaches can be incorporated if a wide range of heat exposures are considered.
- The **critical time (t_{cr})** defined as the moment at which the critical temperature of the insulation material is obtained for specific fire inputs.
- The **barrier properties** such as **thickness (L_b), thermal conductivity (k_b), density (ρ_b) and specific heat capacity ($c_{p,b}$)**. These variables can be optimised or simply fixed in order to estimate the critical time at which the critical temperature is achieved for certain conditions of heat exposure (fire inputs).
- The **insulation critical temperature (T_{cr}), thickness (L_i), and thermal properties (k_i, ρ_i, $c_{p,i}$).** These variables are fixed for the definition of the specific tools which are unique to these properties. Indeed, the thermal evolution of the barrier is strongly dependent on the material properties of the insulation layer (back face boundary condition).

Additionally, this study requires knowledge of the common ranges of thermal properties' values which are characteristic of typical linings. Maximum and minimum values for the thermal properties from a selection of materials are listed in Table 8.1.

Table 8.1. Range of thermal properties from a selection of type of materials extracted from CIBSE [8]

Material	Thermal conductivity range /W·m^{-1}·K^{-1}	Density range /kg·m^{-3}	Specific heat capacity range /J·kg^{-1}·K^{-1}
Brick	0.30 – 1.31	1000 – 2000	800 – 921
Cement / plaster / mortar	0.08 – 1.50	350 – 2100	840 – 1340
Ceramic / clay tiles	0.52 – 1.803	1120 – 2000	840 – 850
Concrete blocks / tiles	0.20 – 1.35	620 – 2240	840 – 2040
Concrete, cast	0.08 – 1.70	200 – 2000	840 – 880
Masonry	0.19 – 1.40	470 – 2200	840
Stone	0.35 – 3.49	1300 – 2880	710 – 1470

Chapter 6 and 7 have shown that insulation materials' thermal properties may be considered temperature dependent. The approach is required if precise prediction of the thermal profile is required so as to determine shrinking or pyrolysis rates. However, for the case being studied in this chapter, it is important to represent a consistent boundary condition until the critical temperature is reached at the face of the flammable insulation. Constant values of thermal conductivity showed good prediction of the thermal evolution for temperatures below the critical temperature. Additionally, the temperature dependency showed ranges of thermal conductivity at the critical temperature which are approximated to these constant values. Therefore, the approach suggested in this chapter is to consider constant values of thermal properties as noted in Table 8.2.

Table 8.2. Combustible insulation material properties

Material	Critical temperature /kg·m^{-3}	Conservative thermal conductivity /W·m^{-1}·K^{-1}	Lower density /kg·m^{-3}	Specific heat capacity range /J·kg^{-1}·K^{-1}
PIR (average)	~300-370	~0.060	~31	1500
PF	~400-450	~0.057	~38	1500
EPS	~330-380	~0.067	~10	1500

Since low variability is observed between the thermos-physical properties of PIR and PF, it is suggested to provide a unified design tool for both cases but considering different critical temperature. As shown in previous chapters, the onset of pyrolysis for PF can be considered as a higher temperature than PIR. However, EPS represents a different case since its density is significantly lower than the other materials and the shrinking effect represents a clear limitation for the application of this method. Therefore, it is proposed to consider as a worst case scenario that the EPS does not shrink, and then use a critical temperature given by the range of mass loss rate peaks obtained by thermogravimetry. Despite this hypothesis is fundamentally incorrect, considering that EPS does not shrink represents a more onerous and conservative

scenario, since the air gap created during shrinking provides further thermal resistance for the transfer of heat.

8.3 Thermally thin regime – The lumped capacitance case

8.3.1 Solution for the ideal case of an adiabatic boundary condition

The case of the lumped capacitance method is often referenced for studying thermally thin elements, i.e. elements that meet heating conditions with Biot numbers lower than 0.1. This case has been described in Chapter 6 for the simplification of the boundary conditions in bench-scale testing, and in Chapter 7 for the inverse modelling of heat absorption by sandwich panels. This hypothesis allows considering a uniform temperature through the barrier, and therefore the net heat absorbed by the assembly ($\dot{q}''_{net}$) to be defined as noted below:

$$\dot{q}''_{net}(t) = \rho_b \cdot c_{p,b} \cdot L_b \cdot \frac{dT}{dt} - k_i \cdot \left.\frac{\delta T}{\delta x}\right|_{x=L_b{}^+} \quad (8.10)$$

Equation (8.10) is a non-homogeneous differential equation; thus, an analytical solution is not feasible. A simplified solution can be obtained if an adiabatic boundary condition is assumed, i.e. the heat losses are assumed to be null. Considering the critical time (t_{cr}) at which the critical temperature is achieved (T_{cr}), the relation between the net heat absorbed, thermal properties, thickness and critical temperature can be written as noted in Equation (8.11) below:

$$\int_0^{t_{cr}} \dot{q}''_{net} \cdot dt = \rho_b \cdot c_p \cdot L_b \cdot (T_{cr} - T_0) \quad (8.11)$$

As presented in Chapter 7, the relationship between the temperature and accumulated net heat flux was perfectly linear for the sandwich panels' assembly. Indeed, the boundary element was a thermally thin element (extremely thin metallic plate) and thus this case can be approximated by the relation expressed in Equation (8.11). However, the heat conducted to the insulation is not considered, thus some discrepancies are expected between the numerical and real solution.

8.3.2 Solution for the real boundary condition

In order to identify the exact relationship that generalises the solution for a thermally thin barrier with the real back face boundary condition represented as in Equation (8.10), a series of numerical analyses are performed. The thermal properties and thickness of the insulation material are determined as shown in Table 8.3. A series of parametric studies are conducted according to the range of values noted in Table 8.4.

Since the thermally thin condition is defined by Bi<0.1, the condition that should be satisfied for the analysis is that:

$$h \cdot L_b < 0.1 \cdot k_b \quad (8.12)$$

However, the analysis is based on the definition of a constant heat flux rather than a convective flow; thus, a clear limit for the thickness cannot be evaluated. A range of

thin elements from 1 to 15 mm and an average thermal conductivity of 2.5 $W \cdot m^{-1} \cdot K^{-1}$ is assumed, leading to a limit for the heat transfer coefficient lower than 16.7 $W \cdot m^{-2} \cdot K^{-1}$. The validity of the range of parametric solutions can only be assessed by observing the regressions obtained. If no linearity is observed between the accumulation of heat and the product of density, heat capacity and thickness, a transition to thermally thick regime is produced.

Table 8.3. Properties of PIRa at low temperatures and dimension

Thermal conductivity /$W \cdot m^{-1} \cdot K^{-1}$	Density /$kg \cdot m^{-3}$	Specific heat capacity /$J \cdot kg^{-1} \cdot K^{-1}$	Critical temperature /°C	Insulation thickness /mm
0.06	31	1500	300	100

Table 8.4. Range of values for the parametric analysis

Range of net heat fluxes /$W \cdot m^{-2}$	Barrier thickness /mm	Barrier thermal conductivity /$W \cdot m^{-1} \cdot K^{-1}$	Barrier volumetric heat capacity /$J \cdot m^{-3} \cdot K^{-1}$
1,000 – 5,000 Step: 1,000	1 – 15 Step: 25	2.5	100 · 500 1,000 · 1,000 2,500 · 2,500

Figure 8.4 shows the solution of the parametric analyses presented in Table 8.4. A better correlation for thermally thin barriers with higher volumetric heat capacity is observed, while lower volumetric heat capacities lead to larger dispersion of the results. This is produced because of the low fraction of energy conducted to the insulation in comparison with the energy absorbed by the barrier. Good linearity is found for these cases, suggesting that the thermally thin assumption is valid. However, different constant values of net heat flux lead to the displacement of the linear correlation towards higher amounts of accumulated heat flux.

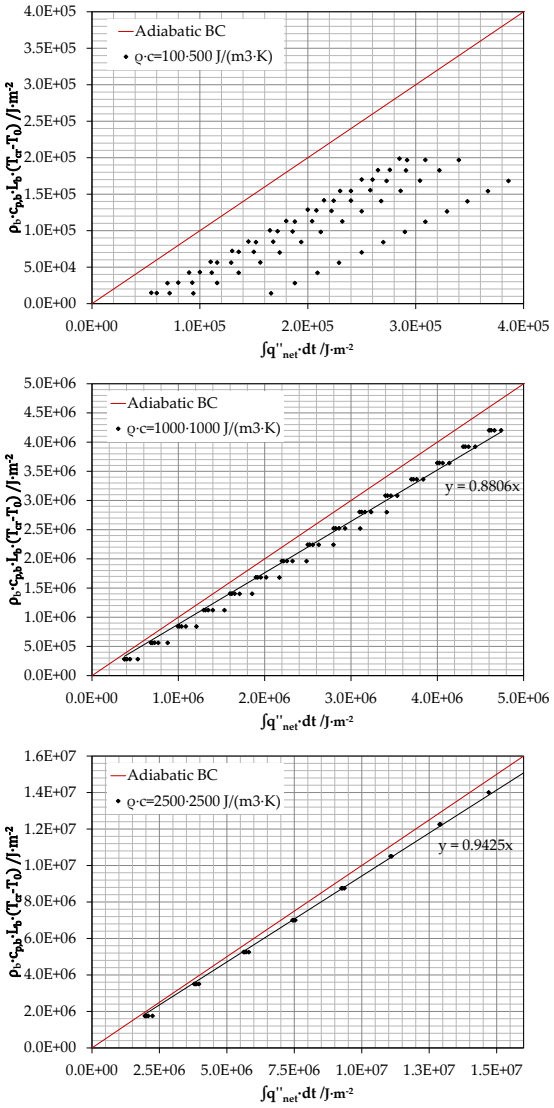

Figure 8.4. Correlation of barrier properties versus accumulated net heat flux

8.4 Thermally thick regime - Non-dimensional solution for a constant net heat flux

8.4.1 Solution for the ideal case of the semi-infinite plate

The exact analytical solution for the temperature distribution within the semi-infinite plate given a constant heat flux is provided by *Incropera et al.* [9], and noted in Equation (8.13) below:

$$T(x,t) - T_0 = \frac{\bar{q}}{k} \cdot \left[\sqrt{\frac{4\kappa t}{\pi}} \cdot \exp\left(-\frac{x^2}{4\kappa t}\right) - x \cdot \operatorname{erfc}\left(\frac{x}{\sqrt{4\kappa t}}\right) \right] \tag{8.13}$$

where x is the position, t is the time, T_0 is the initial temperature, $\bar{q}$ is the constant net heat flux, κ is the thermal diffusivity and erfc is the complementary Gaussian error function defined as:

$$\mathrm{erfc}(w) = 1 - \frac{2}{\pi^{1/2}} \cdot \int_0^w \exp(-u^2) \cdot du \tag{8.14}$$

If a non-dimensional analysis is pursued, the definition of the similarity variable η is required, which is given as:

$$\eta = \frac{x}{\sqrt{4\kappa t}} \tag{8.15}$$

Taking Equation (8.15) and rearranging terms in Equation (8.13), the non-dimensional solution for the temperature at the thickness $x = L_b$ can be expressed as:

$$\frac{k \cdot (T_{cr} - T_0)}{\bar{q} \cdot L_b} = \frac{\exp(-\eta^2)}{\sqrt{\pi} \cdot \eta} - \mathrm{erfc}(\eta) = g(\eta) = g\left(\frac{L_b}{\sqrt{4\kappa t}}\right) \tag{8.16}$$

This non-dimensional solution is represented in Figure 8.5, which corresponds to the assumption of the semi-infinite plate. This solution represents the case of a barrier with the same thermal properties as the insulation being protected.

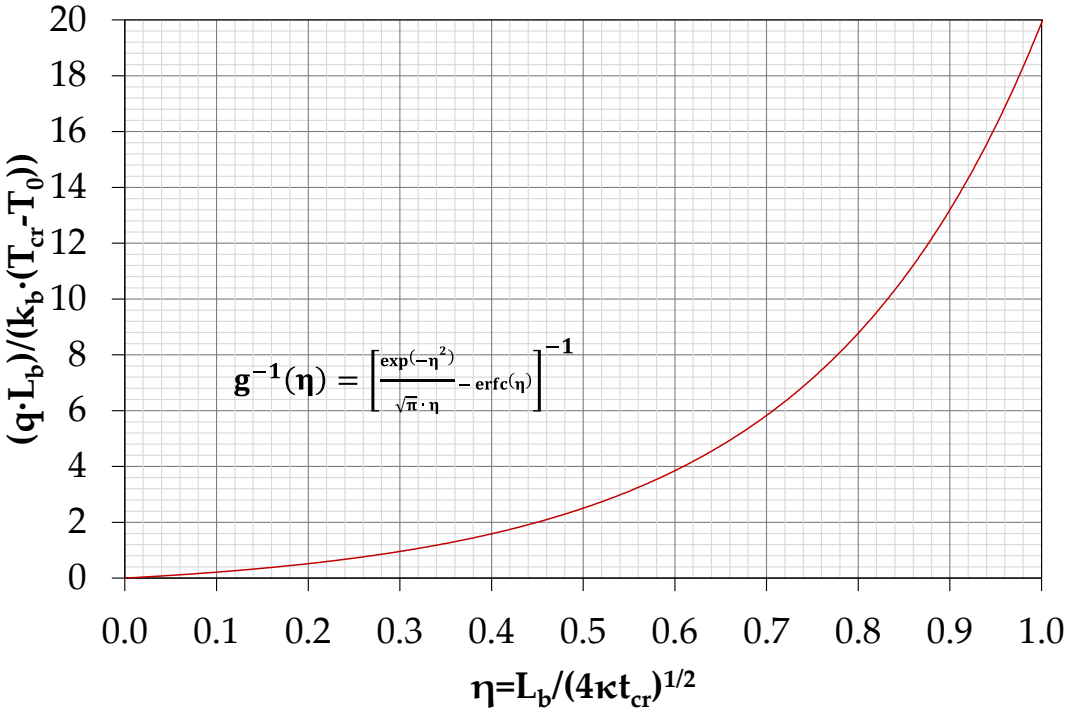

Figure 8.5. Non-dimensional heat transfer solution for a constant heat flux for the semi-infinite plate

8.4.2 Solution for the real boundary condition

The non-dimensional solution for the actual definition of the problem, given by the thickness and thermal properties of the insulation element behind the lining, is expected to be an alteration of the solution for the semi-infinite plate. However, if this correlation is pursued, a series of parametric analyses need to be carried out.

In order to verify the validity of these assumptions, an example is considered herein for PIR, for which the thermal properties and critical temperature are as noted

in Table 8.5. These values are fixed parameters, which are used in order to find the corresponding dimensionless relationship. The net heat flux, barrier thickness, thermal conductivity and volumetric heat capacity are considered here as variable parameters.

Table 8.5. Properties of PIR at low temperatures and dimension

Thermal conductivity /W·m^{-1}·K^{-1}	Density /kg·m^{-3}	Specific heat capacity /J·kg^{-1}·K^{-1}	Critical temperature /°C	Insulation thickness /mm
0.06	31	1500	300	100

Table 8.6. Range of values for the parametric analysis

Range of net heat fluxes /W·m^{-2}	Barrier thickness /mm	Barrier thermal conductivity /W·m^{-1}·K^{-1}	Barrier specific heat capacity /J· m^{-3}·K^{-1}
500 – 100,500 Step: 25,000	5 – 105 Step: 20	0.05 – 4.05 Step: 0.10	31 · 1,500 500 · 500 1,000 · 1,000 2,500 · 2,500

The obtained results are presented in Figure 8.6 as a function of the volumetric heat capacity (the product of density and specific heat capacity). A clear trend equivalent to the analytical solution, but displaced towards higher values of the dimensionless parameter $\eta = \frac{x}{\sqrt{4\kappa t}}$ is observed. The data points from higher volumetric heat capacities seem to converge, while the data points from low volumetric heat capacities (lower than the insulation) have greater dispersion along the η-axis. This dispersion is produced for values of the barrier thermal conductivity in the vicinity of the insulation. Indeed, points on the left of the semi-infinite plate regression correspond to a thermal conductivity lower than that of the insulation board while having the same volumetric capacity.

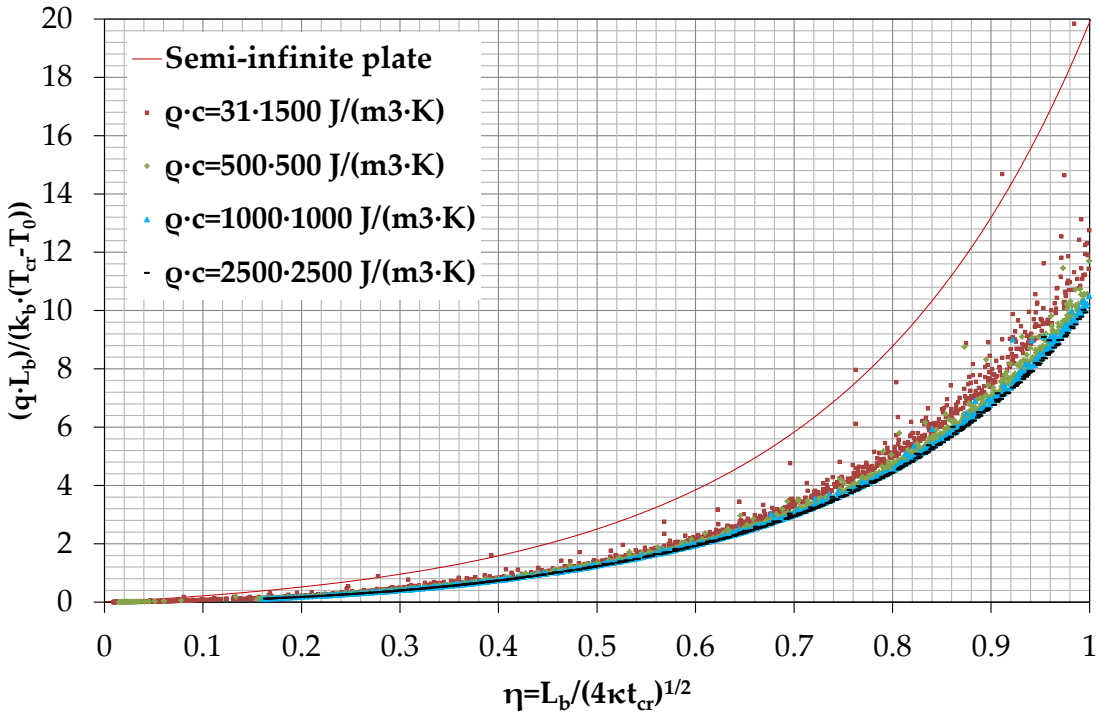

Figure 8.6. Non-dimensional heat transfer solution for a constant heat flux

Therefore, it is important to determine the limits of applicability of the generic solution obtained, which is clearly identified to be a function of the volumetric heat capacity and thermal conductivity.

8.5 Thermally thick regime - Non-dimensional solution for a constant radiant heat flux with a constant heat transfer coefficient of losses

8.5.1 Solution for the ideal case of the semi-infinite plate

The exact analytical solution for the temperature distribution within the semi-infinite plate given a constant radiant heat flux $\dot{q}_r''$ and a heat transfer coefficient h_T as defined in Equation (8.9), is given by the expression noted below provided by Carslaw and Jaeger [10]:

$$T(x,t) - T_0 = \frac{\alpha \cdot \dot{q}_r''}{h_T} \cdot \left[\operatorname{erfc}\left(\frac{x}{\sqrt{4\kappa t}}\right) - \exp\left(\frac{h_T}{\sqrt{\kappa}\sqrt{k\rho c}} \cdot x + \frac{h_T^2}{k\rho c} t\right) \cdot \operatorname{erfc}\left(\frac{h_T \cdot t^{\frac{1}{2}}}{\sqrt{k\rho c}} + \frac{x}{\sqrt{4\kappa t}}\right)\right] \quad (8.17)$$

If a non-dimensional analysis is pursued, the definition of the similarity variable η is required as noted in Equation (8.15), and θ as noted below:

$$\theta = \frac{h_T \cdot t^{1/2}}{\sqrt{k\rho c}} \quad (8.18)$$

Taking Equations (8.15), (8.17) and (8.18), and rearranging terms, the non-dimensional solution for the temperature at the thickness $x = L_b$ can be expressed as:

$$\frac{(T_{cr}-T_0)\cdot h_T}{\alpha\cdot \dot{q}''_r} = \operatorname{erfc}(\eta) - \exp(2\cdot\theta\cdot\eta+\theta^2)\cdot\operatorname{erfc}(\theta+\eta) = g(\eta,\theta) = \\ = g\left(\frac{L_b}{\sqrt{4\kappa t}}, \frac{h_T\cdot t^{1/2}}{\sqrt{k\rho c}}\right) \tag{8.19}$$

The non-dimensional solution depends on two parameters; thus the graphic representation of this is expected to include a combination of both so as to determine the variable $\frac{(T_{cr}-T_0)\cdot h_T}{\alpha\cdot q_r}$. This graphic representation is plotted in Figure 8.7 below. As noted previously, this solution would be applicable for barriers with the same thermal properties as the insulation being protected.

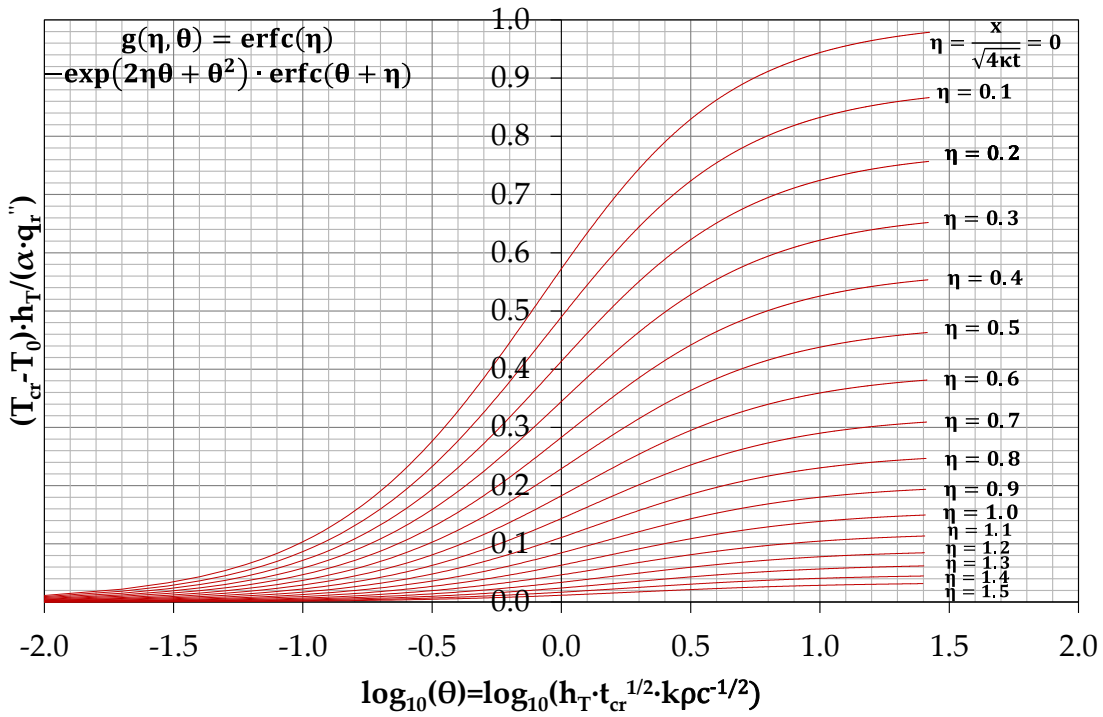

Figure 8.7. Non-dimensional heat transfer solution for a constant radiant heat flux with a heat transfer coefficient

8.5.2 Solution for the real boundary condition

It was found for the previous case of constant net heat flux that the definition of a generic solution for the semi-infinite plate depends on two non-dimensional parameters. Therefore, more complications are anticipated in order to find an equivalent solution for the problem being studied here, due to the existence of two non-dimensional parameters. The approach undertaken is based on forcing the parameter η to be in the range of [0, 1.5] with 0.1 interval fixing the thermal properties and thickness from the barrier and then determining the time of heat exposure.

In the previous section, a generic solution for a constant net heat flux, with a limitation for certain values of the thermal conductivity and volumetric heat capacity was obtained. This phenomenon is also expected to occur for this particular case. In order to determine the limits of applicability of a generic non-dimensional solution,

the effects of the thermal conductivity, volumetric heat capacity as well as the thickness of the barrier are explored.

A series of case studies are considered according to the parameters shown in Table 8.7, which correspond to a value of thermal conductivity similar to the insulation being protected. Figure 8.8 shows the clear dependency of the function $g\left(\frac{L_b}{\sqrt{4\kappa t}}, \frac{h_T \cdot t^{1/2}}{\sqrt{k\rho c}}\right)$ on the volumetric heat capacity, and the convergence to the semi-infinite plate solution if a value of volumetric heat capacity similar to the insulation is chosen. It is observed that for higher volumetric heat capacities the curves from a certain characteristic parameter $\eta = \frac{x}{\sqrt{4\kappa t}}$ are shifted to higher values of $\frac{(T_{cr}-T_0)\cdot h_T}{\alpha \cdot q''_r}$. Then, it is inferred that a generic solution is not feasible for this value of thermal conductivity.

Table 8.7. Range of values for the parametric analysis

Range of net heat fluxes /W·m^{-2}	Range of net heat transfer coefficient / W·m^{-2}·K^{-1}	Barrier thickness /mm	Barrier thermal conductivity /W·m^{-1}·K^{-1}	Barrier volumetric heat capacity /J·m^{-3}·K^{-1}
500 – 100,500 Step: 10,000	0.1, 0.2, …, 1, 2, …, 10, 20, …, 100, 200, …, 1000	5	0.05	100 · 500 500 · 500 1,000 · 1,000 2,500 · 2,500

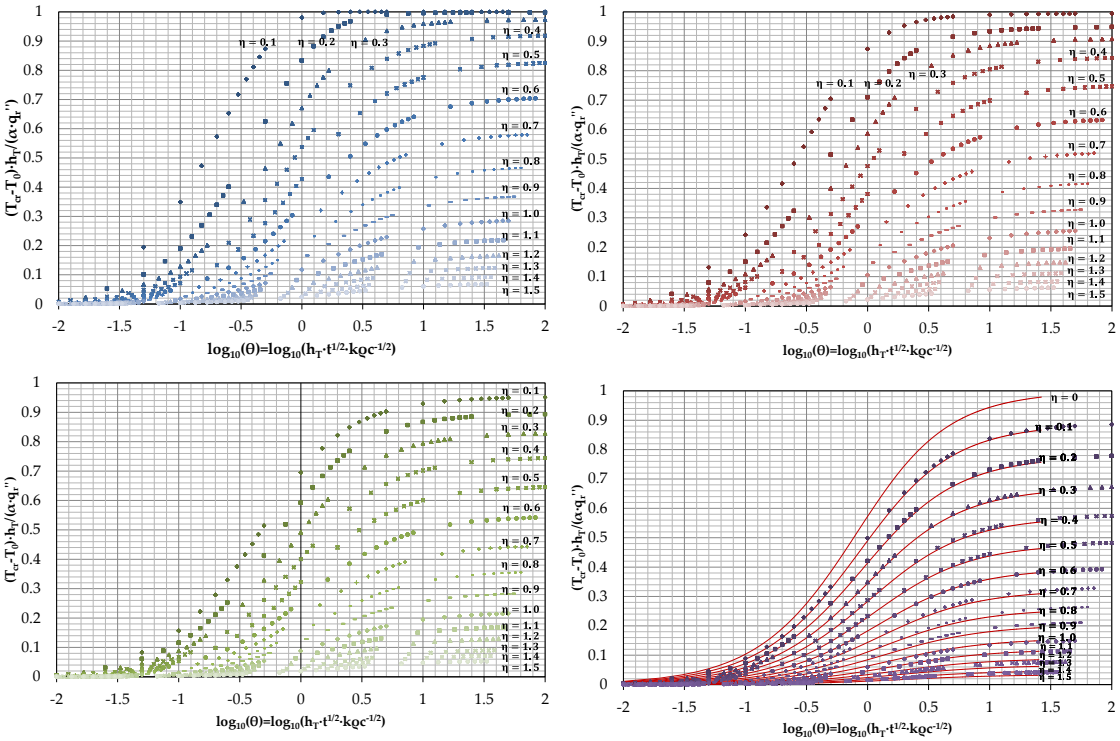

Figure 8.8. Non-dimensional heat transfer solution for a constant radiant heat flux with a cooling/heating coefficient for a thermal conductivity of 0.050 W·m^{-1}·K^{-1}and different volumetric heat capacities (a) 2500·2500 (b) 1000·1000 (c) 500·500 (d) 100·500 J·m^{-3}·K^{-1}

In order to determine the limits of applicability of a possible generic non-dimensional solution, a series of parametric studies are carried out as shown in Table

8.8. Similarly to the previous section, a critical value of thermal conductivity may be found for each volumetric heat capacity. This is represented in Figure 8.9, where two values of volumetric heat capacity are assessed, 500·500 $J \cdot m^{-3} \cdot K^{-1}$ (Figure 8.9a) and 2500·2500 $J \cdot m^{-3} \cdot K^{-1}$ (Figure 8.9b). Several thermal conductivities are considered for each of these cases. As a result, it is found that the convergence for a lower volumetric heat capacity is achieved with values of thermal conductivity larger than 0.20 $W \cdot m^{-1} \cdot K^{-1}$, while the convergence for the highest volumetric heat capacity is achieved almost for every case of thermal conductivity.

Table 8.8. Range of values for the parametric analysis

Range of net heat fluxes /$W \cdot m^{-2}$	Range of net heat transfer coefficient / $W \cdot m^{-2} \cdot K^{-1}$	Barrier thickness /mm	Barrier thermal conductivity /$W \cdot m^{-1} \cdot K^{-1}$	Barrier volumetric heat capacity /$J \cdot m^{-3} \cdot K^{-1}$
500 – 100,500 Step: 10,000	0.1, 0.2, …, 1, 2, …, 10, 20, …, 100, 200, …, 1000	5	0.05, 0.1, 0.2, 0.3, 0.4, 0.5	500 · 500 2,500 · 2,500

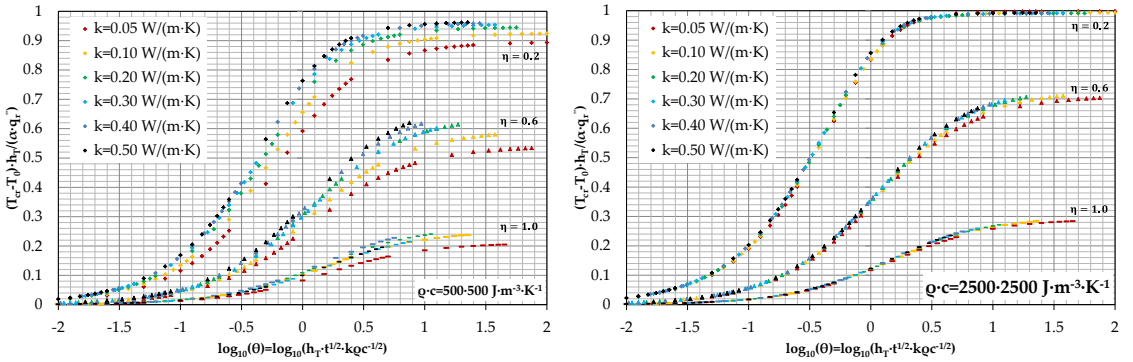

Figure 8.9. Non-dimensional heat transfer solution for a constant radiant heat flux with a cooling/heating coefficient for different thermal conductivities and volumetric heat capacities. (a) 500·500 $J \cdot m^{-3} \cdot K^{-1}$ (b) 2500·2500 $J \cdot m^{-3} \cdot K^{-1}$

8.6 Summary of design charts

Despite that a generic solution cannot be achieved for any thermal property of the barrier due to interaction of the thermal properties from the two layers, a critical value of thermal conductivity and volumetric heat capacity may be identified. A series of design charts are provided for the definition of thermal barriers for each of the flammable insulation materials, based on different quantification of the volumetric heat capacity. Specific ranges of thermal conductivity are indicated for each of these charts, where convergence is observed as the thermal conductivity increase.

8.6.1 PIR and PF

a. Constant net heat flux

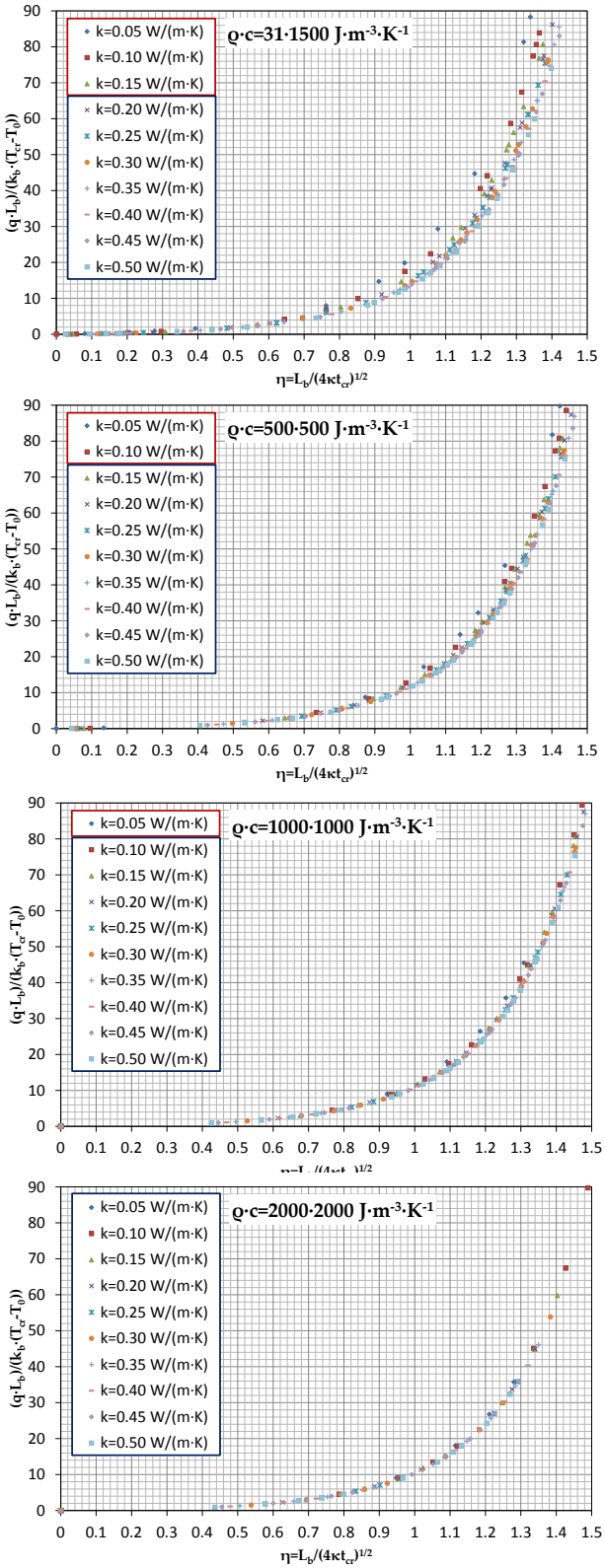

Figure 8.10. Non-dimensional heat transfer solution for a constant heat flux for PIR and PF

b. Constant radiant heat flux with constant heat losses coefficient

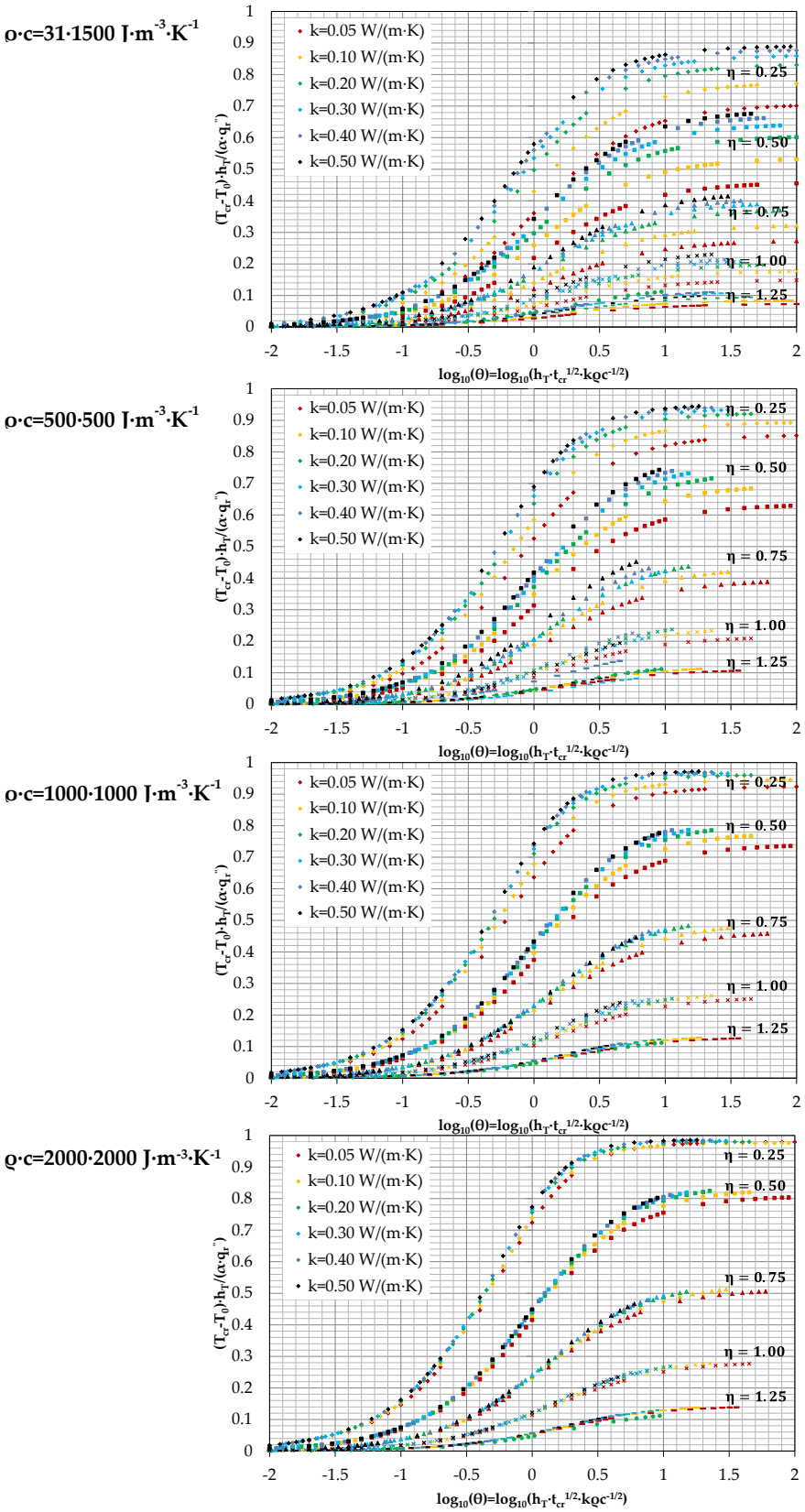

Figure 8.11. Non-dimensional heat transfer solution for a constant radiant heat flux and a heat transfer coefficient for PIR and PF

8.6.2 EPS

a. Constant net heat flux

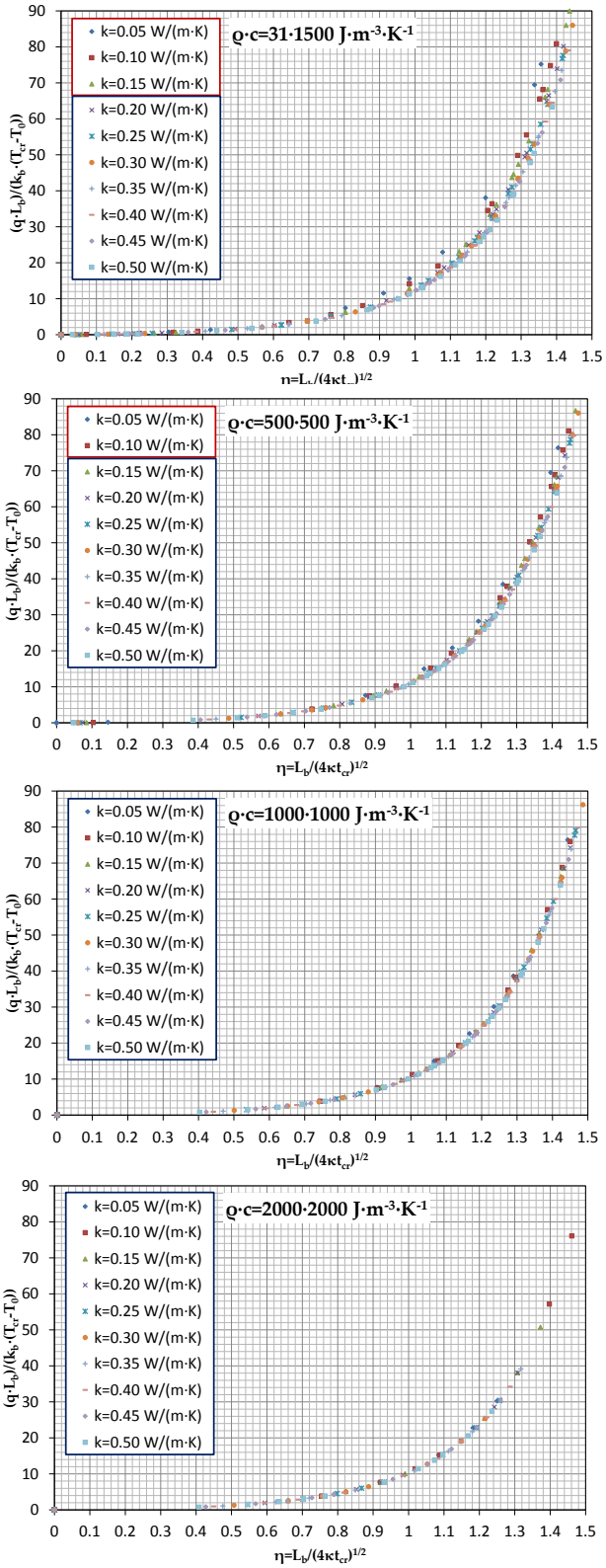

Figure 8.12. Non-dimensional heat transfer solution for a constant heat flux for EPS (assuming no shrinkage)

b. Constant radiant heat flux with constant heat losses coefficient

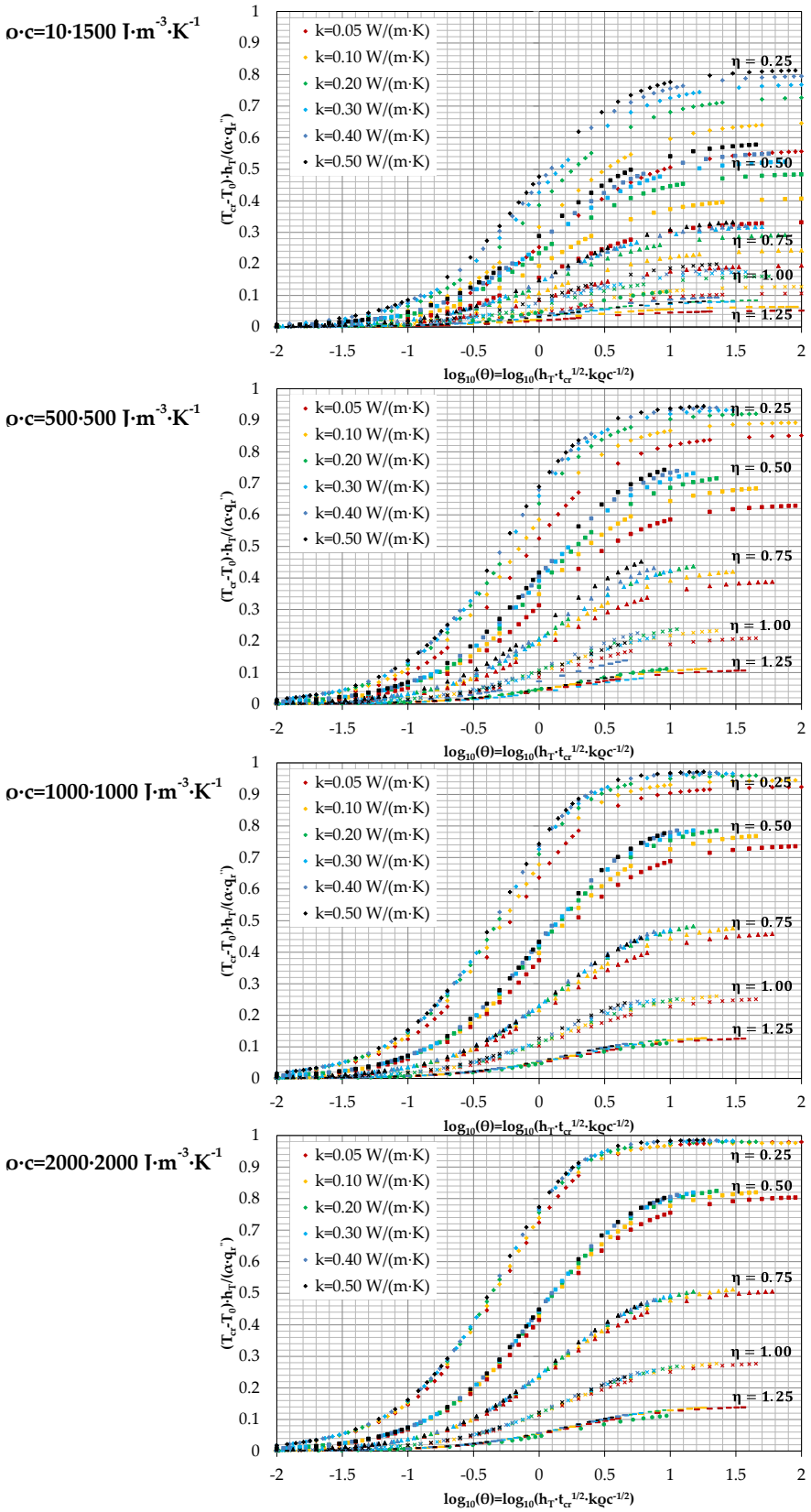

Figure 8.13. Non-dimensional heat transfer solution for a constant radiant heat flux and a heat transfer coefficient for EPS (assuming no shrinkage)

8.6.3 Guidance for the use of these tools

In order to be able to use these design tools, a series of guidelines are provided below. These are presented as schematic logic diagrams in Figure 8.14 for the case of constant net heat flux as input parameter from the fire, and in Figure 8.15 for the case of a constant radiant heat flux and heat transfer coefficient as input parameters from the fire. The input parameters given for these are based on the assumption of the barrier properties and calculating the time at which the critical temperature of pyrolysis onset is reached. This is a simple approach proposed by the author; however, other techniques and analysis processing can be considered for optimisation. In any case, this is not within the scope of this thesis, and further work is required for improving the capabilities of the proposed techniques.

The decision making process is much simpler for the first case of a constant net heat flux, while a series of iterations are required for the case with a radiant heat flux and heat transfer coefficient. This extra complication is introduced by the fact that the latter approach requires two non-dimensional parameters so as to provide a generic solution, considering the range of available parameters.

Another aspect that needs to be clarified is the available range of the non-dimensional parameter $\eta = \frac{x}{\sqrt{4\kappa t}}$ in a specific chart for the case of constant radiant heat flux and heat transfer coefficient. If the obtained non-dimensional parameter is not included in the chart, it is suggested to use interpolation between the two nearest curves as an approximate solution. The inclusion of all the range of available values of η would however complicate the representation of this.

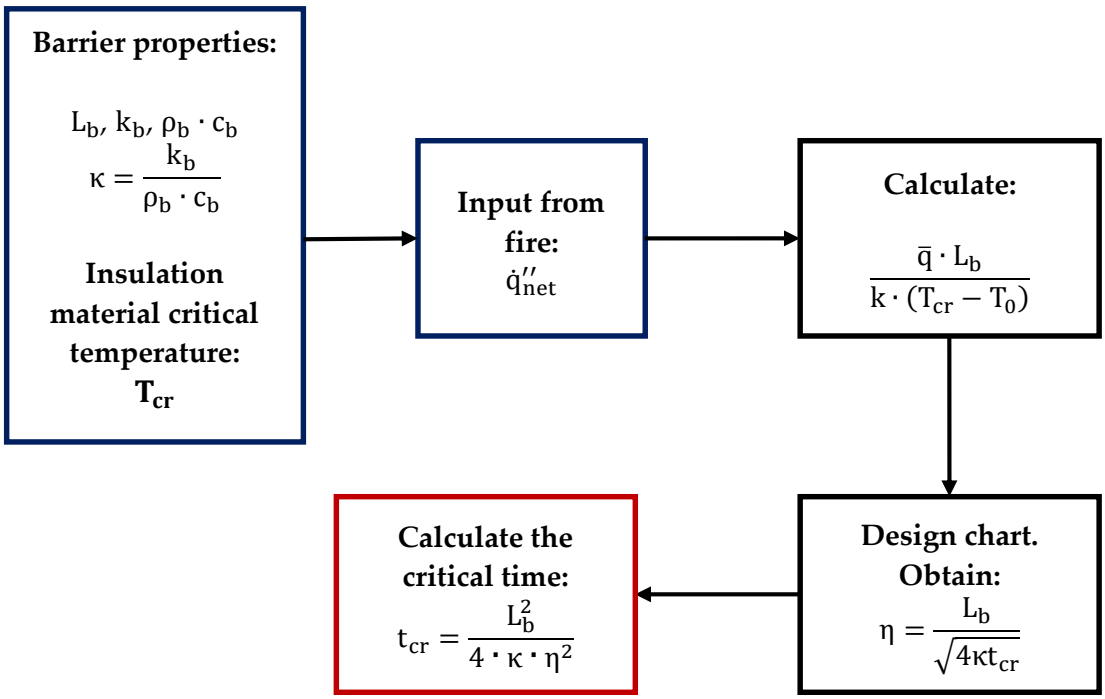

Figure 8.14. Logic diagram for the determination of the critical temperature for a constant net heat flux with known barrier properties

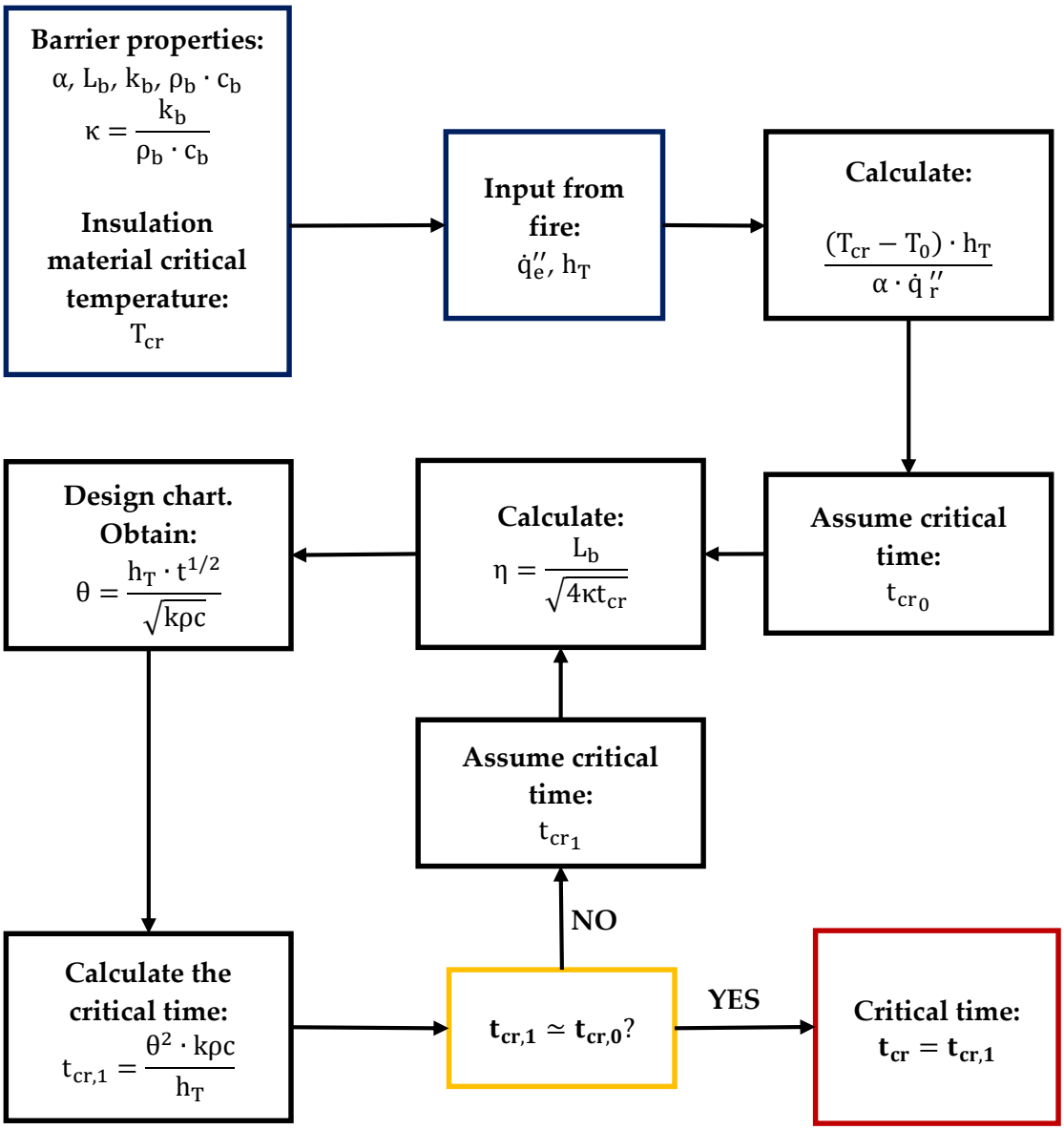

Figure 8.15. Logic diagram for the determination of the critical temperature for a constant radiant heat flux and heat transfer coefficient with known barrier properties

8.7 Application of the methodology for design strategies

The series of design charts introduced in the previous section present the existing relationships among the different variables that control the problem. Understanding these relationships is key to address the design of assemblies incorporating insulation materials. As noted in Chapter 3, the approach presented by the author consists in considering the process of design as a quantitative definition of thermal barriers, based on the specific failure criterion 'pyrolysis onset'. This allows for tailoring assemblies in which an adequate level of fire safety can be guaranteed for a series of fire scenarios.

Then, a design strategy in which no contribution to the heat release of the fire due to the release of volatiles from the insulation is aimed, is then based on assuring that the critical temperature is not achieved by the insulation. This strategy is defined in the time domain as a 'safe time' (herein denoted as critical time) below which it is guaranteed that these events are not achieved. This should be established by the practitioner according to the design objectives.

A specific value of critical time leads to a specific thickness and thermal properties of the barrier, given certain heat inputs. Then, the goal from the design is to optimise the thickness and thermal properties for a given range of fire scenarios, understood as the heat exposure at the surface of the assembly.

This process allows for obtaining a quantifiable design of assemblies with an equivalent level of safety. Indeed, different assemblies incorporating different type of insulation, may not contribute to the fire below a 'safe time' established by the designer for a series of hypothetical heat exposures. From this, it is obviously derived that an insulation material, if flammable, would eventually contribute to the combustion dynamics of the fire, or releasing flammable volatiles, once the 'onset of pyrolysis' is reached.

A logic diagram indicating the design process in which is considered as goal to guarantee that the insulation from the assembly does not contribute to the fire is presented in Figure 8.16 below.

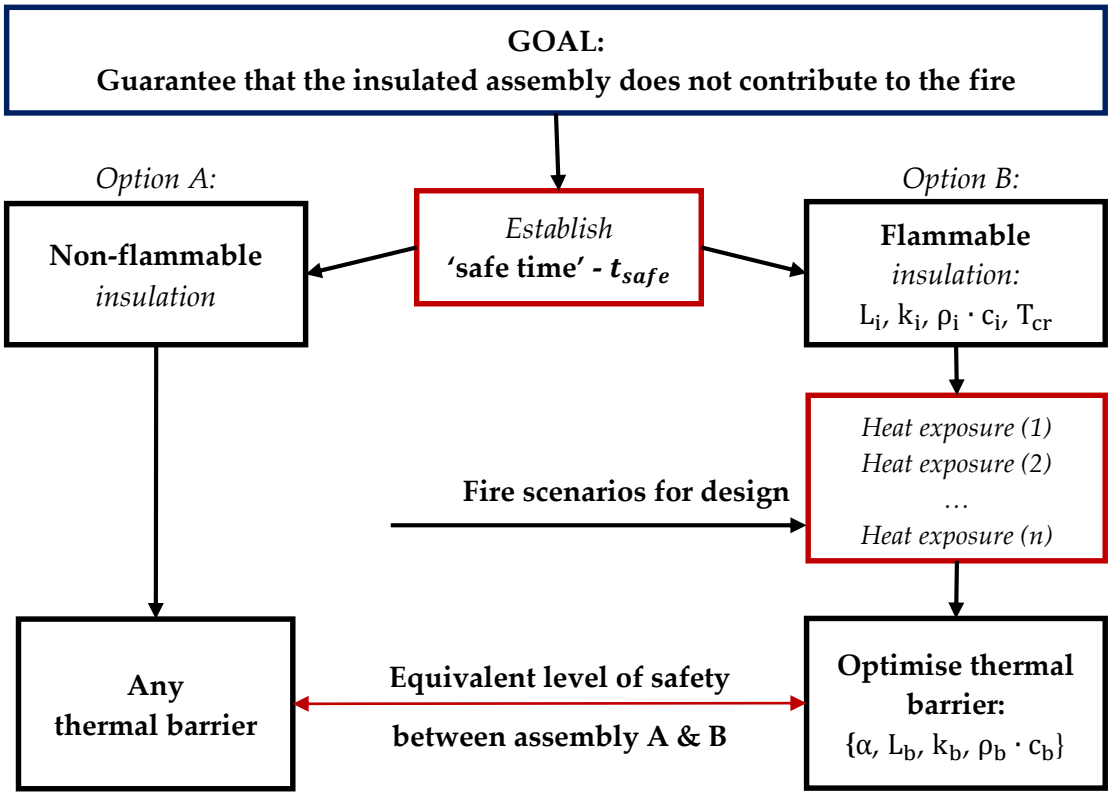

Figure 8.16. Strategy for the design of assemblies including thermal insulation, based on the failure mode 'onset of pyrolysis'

The clear advantage from this method is that a quantifiable risk assessment may be established, and the 'fire variable' may be introduced in an optimisation process by which energy and fire performance are both considered for the definition of building partitions.

8.8 Concluding remarks

A series of tools for the quantification of the critical thickness and thermal properties of barriers for insulation materials has been defined. These tools are provided as a function of different inputs depending on the heat transfer regime (thermally thick or thermally thin barriers) and on different hypotheses of the input parameters from the fire. The input parameters from fires must be referred either to the net heat flux or to a radiant heat flux with heat transfer coefficient of losses. Despite these tools are in early stages of conception (since they refer to constant values of heat flux), approximated quantifiable solutions can be obtained.

Additionally, the dependency of these charts on the thermal properties of the element behind the barrier or lining has been investigated. The singularity of the presented solutions is only applicable for certain range of thermal conductivities, depending on the volumetric heat capacity. However, the impact of these limitations is expected to be low since typical barrier elements generally show values of thermal conductivity higher than the limit. Particular solutions for these cases are provided in the generated tools.

Further work is required in order to identify a lumping factor that could extend the range of application of these solutions into a unique generic solution. Additionally, the extension of this work to variable functions of heat flux is required as well as including endothermicity of the barrier material into the analysis.

8.9 References

[1] T. Z. Harmathy, "The possibility of characterizing the severity of fires by a single parameter," *Fire and Materials*, vol. 4, no. 2, pp. 71–76, Jun. 1980.

[2] T. Z. Harmathy and J. R. Mehaffey, "Normalized heat load: A key parameter in fire safety design," *Fire and Materials*, vol. 6, no. 1, pp. 27–31, Mar. 1982.

[3] T. Z. Harmathy, "A New Look at Compartment Fires," *Fire Technology*, vol. 8, no. 3, pp. 196–217, 1972.

[4] P. H. Thomas, A. J. Heselden, and M. Law, "Fully-developed compartment fires -two kinds of behaviour," *Fire Research Technical Paper No. 18. Ministry of Technology and Fire Offices Committee, Joint Fire Research Organisation, FRS, London, UK*, vol. 18, 1967.

[5] J. L. Torero, A. H. Majdalani, C. Abecassis-Empis, and A. Cowlard, "Revisiting the Compartment Fire," in *11th International Symposium on Fire Safety Science*, 2014.

[6] A. H. Majdalani, "Compartment Fire Analysis for Contemporary Architecture (Ph.D. thesis)," The University of Edinburgh, 2014.

[7] A. Cowlard, A. Bittern, C. Abecassis-Empis, and J. Torero, "Fire safety design for tall buildings," in *Procedia Engineering*, 2013, vol. 62, pp. 169–181.

[8] *CIBSE Guide A: Environmental Design*, 7th ed. The Chartered Institution of Building Services Engineers London, 2006.

[9] F. P. Incropera, D. DeWitt, T. L. Bergman, and A. S. Lavine, *Principles of Heat and Mass Transfer*, 7th ed. John Wiley & Sons, Inc., 2011.

[10] H. S. Carslaw and J. C. Jaeger, *Conduction of Heat in Solids*, 2th ed. 1986.

Chapter 9.

Conclusions and Further Work

9.1 Summary of main conclusions

This thesis has presented a performance-based methodology for the fire safe design of insulation materials in energy efficient buildings. This methodology is based on material characterisation and determination of the main fire hazards from the most common insulation materials used in construction. A redefinition of the set of failure criteria has been proposed, and methods for the quantification of these hazards were provided.

On the basis of the information presented in this thesis, the following primary conclusions can be drawn:

- Energy efficiency and sustainability have become the main drivers in construction during the last decade.
- Extensive requirements on energy performance in buildings have led to the intense use of insulation materials in modern construction.
- Regarding the insulation materials, two main types can be found in the market: non-flammable materials (typically inorganic wools) and flammable materials (mainly plastic rigid foams).
- Current fire safety methods for the design of insulation materials are not suitable for revealing and quantifying the intrinsic hazards related to the intense use of combustible insulation materials in buildings.
- The initiating and main hazard from combustible insulation materials corresponds to the onset of pyrolysis, which can be defined as a critical temperature.
- Subsequent hazards to the onset of pyrolysis are represented by the flammability and release of toxic species from pyrolysis gases, the combustibility of the solid-phase, generation of toxic combustion products from these processes and the breaching of compartmentalisation
- An extended experimental work at different scales has demonstrated that a conservative definition of the critical temperature can be assumed as the main peak of mass loss rate obtained from thermogravimetry at low heating rates, and for materials that not melt. A generic, and conservative, critical temperature of 300°C has been determined for PIR, while for PF a value of 425°C is proposed. The proposed critical temperature for EPS is its melting point, with an approximated value of 240°C.
- The experimental work performed for this thesis demonstrated that the common inorganic wools with low content of binder do not present the onset of pyrolysis as a hazard and thus classical failure criteria may be applied.
- A performance-based design methodology is proposed for the quantitative design of insulation systems in buildings, which is based on the design of thermal barriers for controlling the onset of pyrolysis.

9.2 Detailed summary of the developed work and further conclusions

A number of additional conclusions can be drawn on the basis of the individual chapters contained within this thesis. These are presented in sequence in the following sections.

Chapter 2 discussed the fact that at present, building design can be considered as a multi-objective optimisation problem based on a series of criteria such as, but not limited to, sustainability (energy performance, product life cycle, durability), human comfort (thermal, air purity, acoustical), structural integrity, fire safety and cost of implementation and materials. While many of these criteria may be collaborative (i.e. a better solution for a particular criterion brings a better solution for another criterion), others can be conflicting (i.e. a better solution of a particular criterion deteriorates the solution of another criterion). This may lead to compromised solutions that fail to optimise all of the criteria simultaneously (the 'Pareto frontier'). If these design techniques are to be applied, the considered criteria need to be quantifiable in engineering terms. However, fire safety at present is not usually considered in a quantitative (i.e. performance-based) manner, but rather using a prescriptive approach. Indeed, fire safety is typically established as a material classification based on standard flammability testing (e.g. reaction-to-fire), or as a threshold pass-fail criterion based on standard furnace testing for the design of compartmentalisation elements (i.e. fire resistance). Fire safety cannot therefore be incorporated as a quantifiable variable in the desired multi-objective optimisation design of the built environment. Building energy performance has thus become the main innovation driver in the built environment. As a result, building envelopes with improved thermal performance (lower thermal transmittance) are required for buildings, leading to the ever more intensive use of insulation materials with very low thermal conductivity. Inorganic materials such as stone wool or glass wool, and organic plastic foams such as isocyanurate-based polyurethane foam, phenolic foam or expanded polystyrene, represent 90% of the wide range of insulation materials that can be found in the European market. Since polymer-based insulations generally give better thermal performance, the ever more common situation is that these products represent an optimum for this relevant criterion, as well as for increasing space usage in buildings, while fire safety considerations are often effectively excluded from any serious optimisation analysis or rational performance assessment.

Chapter 3 was interested in an assessment of the suitability of the current methods of design of insulation systems in fire, and the definition of a set of failure criteria representative of the intrinsic fire hazards. Reviews of the literature dealing with the fire performance of insulation materials show inconsistency with regard to their conclusions, depending on the experimental approaches undertaken. This raises the issue that a global understanding of the fire hazards represented by the use of insulation materials is not truly established. Current fire safety methods for the design of particular insulation systems in buildings were shown to be inadequate. The available methods, whilst providing comparative performance of various

systems under specific conditions, were shown to be incapable of revealing the intrinsic hazards from combustible insulation materials, and even less capable of quantifying the risk associated with these hazards. Certainly, the phenomena assessed by standard fire tests do not necessarily correspond to the failure modes that are likely during end-use conditions of the product. The reaction-to-fire framework (BS EN 13501-1) intends to measure fire spread/growth on the surface of a system, however insulation products are rarely used uncovered, rather located behind a lining or render. The fire-resistance framework (BS EN 1363-1) shows a dependency of the fire severity with the thermal properties of the tested element, with this effect being significant due to the characteristic thermal properties of different insulation products. The failure criteria in fire-resistance testing are based on heat transfer assessments that are shown to be inadequate, due to alterations to the heat introduced by the burners in a fire testing furnace, and the interaction from flammable pyrolysis gases being released within the furnace. Therefore, a new set of failure criteria needs to be defined on the basis of the intrinsic hazards from combustible insulation materials.

The definition of the intrinsic hazards requires an assessment of the material behaviour at different scales, so each of the phenomena can be isolated and finally understood globally. Additionally, the definition of these hazards should be quantifiable so as to introduce fire performance as a measurable variable in the design process, i.e. as part of a performance-based approach for the formulation of risk assessments in relation to these specific hazards. A mapping of the fire hazards from combustible insulation products is proposed. A heat transfer analysis on the thermal evolution of combustible insulation materials under severe conditions of heat exposure is presented, which reveals (or rather confirms) that the main hazard is related to their very low thermal inertia. Thus, low amounts of energy input are required to achieve the ignition temperature or onset of pyrolysis. Large-scale tests performed for this thesis demonstrate that the main hazard is represented by the onset of pyrolysis, i.e. the moment when large release of combustible volatiles occurs. Therefore, the main control measure must lie in impeding the insulation surface from reaching the onset of pyrolysis temperature (herein defined as the critical temperature). The subsequent hazards are represented by the flammability and release of toxic species from the pyrolysis gases, combustibility of the solid-phase, release of toxic species from the combustion products, and eventually breaching of compartmentalisation. A series of control measures and quantifiable parameters to define these hazards are proposed for the formulation of a risk assessment. The proposed methodology is based on the design of thermal barriers in order to control the onset of pyrolysis. This is defined as the critical temperature, equivalent to the ignition temperature for solid materials. However, the required inputs for the risk assessment can only be identified with an extended experimental plan. The materials selected for the experimental plan herein were stone wool (SW) as inorganic material, and four types of rigid isocyanurate-based polyurethane foam (PIR), rigid phenolic foam (PF) and expanded polystyrene (EPS) as organic polymeric materials.

Chapter 4 comprised the first stage of the experimental plan which was based on thermogravimetry, so as the heat transfer is isolated from the material behaviour, which was studied in a kinetic regime. Conclusions with regard to the thermal degradation processes from the solid-phase such as pyrolysis and oxidation were obtained for the different insulation materials. Experiments were performed in nitrogen and air atmospheres in order to isolate the pyrolysis and oxidation reactions, and to verify whether oxidative atmospheres affect the process of pyrolysis. Constant heating rates of 2.5, 5, 10 and 20°C·min^{-1} were used to explore the effect on kinetics of the reaction. The main conclusions from these experiments are as follows:

- SW showed very small amounts of thermal degradation, which likely correspond to the decomposition of the binders or additives, with a maximum mass loss less than 2% at 800°C. The main pyrolysis reaction in an inert atmosphere was observed between 200 and 300°C, for which the peak of mass loss rate was at nearly 250°C. The same reaction was observed in an oxidative atmosphere, followed by an oxidation process between 350 and 500°C, and a minor gain of mass likely due to crystallisation after 700°C.
- PIR showed a mass loss of 75-80% at 800°C in an inert atmosphere, with the main process of pyrolysis identified between 250 and 350°C, where the peak was at nearly 300°C for most of the PIR materials studied. The pyrolysis in an oxidative atmosphere appeared in the same range of temperatures, but with a more moderate contribution. Oxidation reactions from the solid phase appeared above 500°C, clearly separated from the end of the pyrolysis. All mass was typically consumed after 600°C.
- PF showed more moderate pyrolysis behaviour than PIR, with a maximum mass loss of 50-55% at 800°C in an inert atmosphere. The pyrolysis was produced in three steps, with the main step being observed between 400 and 500°C. The pyrolysis behaviour seemed to be unaffected in an oxidative atmosphere, but a series of oxidation reactions were observed right after the main pyrolysis step at 450°C, with the main peak of mass loss rate between 480 and 550°C, being larger than that due to pyrolysis.
- EPS showed a single pyrolysis reaction in an inert atmosphere with a peak between 380 and 440°C. The pyrolysis behaviour was found to change in an oxidative atmosphere, shifting it to lower temperatures with the main peak of mass loss between 330 and 380°C.
- Deconvolution techniques based on the Fraser-Suzuki regression and optimisation algorithms were used to assess the effects of oxidative atmospheres on pyrolysis. Furthermore, the complexity of the thermal degradation processes was assessed by identifying the likely number of reactions. While pyrolysis processes from SW and EPS showed simpler kinetics, PIR and PF showed higher levels of complexity, with at least 5-6 different reactions. In any case, modelling of these processes is outside the scope of the current thesis.
- It is proposed to consider the temperature of the main peak of pyrolysis as the critical temperature for the performance-based methodology proposed herein.

However, a flammability assessment is also required to validate this hypothesis, which considers the critical temperature as the solid-phase temperature that provides the highest rate of production of pyolysates beyond the lower flammability limit (flashpoint).

Chapter 5 presented the next stage of the experimental plan which was based on a flammability assessment of the insulation materials by bench-scale testing with the Cone Calorimeter (using a pilot spark). A classical combustibility assessment by gas species calorimetry was also carried out to identify the different regimes of combustion for each material. A number of 100 mm thick samples were tested, and several external heat fluxes were used to identify flammability and combustibility properties, as well as to study the effect of the protective layer from rigid foams. The main conclusions from these experiments are listed below:

- Critical heat fluxes for three types of PIR were found to be in the range of 10-15 $kW \cdot m^{-2}$, with approximate ignition temperatures of 306°C, 337°C, and 377°C, respectively. The critical heat flux for PF was found to be higher than for PIR (22 $kW \cdot m^{-2}$), with an ignition temperature of approximately 453°C. Expanded polystyrene cannot be properly assessed using this methodology due to its melting behaviour; however the ignition temperature was defined between the range 306-389°C. SW was found not to ignite or release sufficient pyrolysis gases to sustain flaming combustion.
- The classical approach for determining the thermal inertia of combustible materials, which considers the pyrolysis time to be much larger than the characteristic time ($t_p/t_c \rightarrow \infty$), was found to provide very large values of thermal inertia. This correlation was found to be inappropriate for materials with low thermal inertia, and the approach that considers $t_p/t_c \rightarrow 0$ was found to provide more reasonable results. This was verified by defining another regression for estimating the thermal inertia. Nominal values of 4500, 6500, 5500 and 4500 $W^2 \cdot s \cdot K^{-2} \cdot m^{-4}$ were obtained for PIRa, PIRb, PIRc and PF, respectively. Values of thermal inertia for SW and EPS were not obtained since SW did not ignite and EPS shrank and melted; therefore the concept of thermal inertia loses relevance.
- Calorimetry calculations for PIR and PF showed the typical shape obtained from charring materials. A peak of heat release rate per unit area (HRRPUA) between 120-170 $kW \cdot m^{-2}$ was observed for PIR, with a decay below 60 $kW \cdot m^{-2}$ represented by the formation of a char layer and the transition of the pyrolysis front towards inner depths. PF peak heat release rate per unit area was observed to be in the range 80-140 $kW \cdot m^{-2}$, with a decay and posterior increase or decrease depending on the external heat flux. EPS showed a heat release rate with a quasi-steady state between 300-450 $kW \cdot m^{-2}$, representing the burning of the melted polystyrene.
- The effective heat of combustion for PIR was found in the range of 13-21 $kJ \cdot g^{-1}$, while for PF was obtained in the range of 15-21 $kJ \cdot g^{-1}$. Expanded polystyrene's effective heat of combustion was obtained in the range of 27-32 $kJ \cdot g^{-1}$.

- Gas analyses demonstrated different stages of the combustion for PIR and PF, i.e. flaming followed by smouldering from the charring materials such as PIR and PF. These phenomena may occur simultaneously.
- The effect of the protective layer that rigid foams use as facing (foil faced foams) is lost above radiant heat fluxes of 35 $kW \cdot m^{-2}$ for PIR, while the layer of PF loses its integrity above 15 $kW \cdot m^{-2}$. The protective layer may slightly contribute to the heat release rate, with slightly larger peaks of heat release rate being obtained when the ignition is obtained with the foil still being attached.
- Comparison between the flammability and thermogravimetric results showed a reasonable agreement between the main peak of pyrolysis observed by DTG and the calculated ignition temperature. Conservative values of critical temperature were proposed as 300°C for PIR and 425°C for phenolic foam. However, other types of PIR showed slightly higher values of ignition temperature (337°C for PIRb and 377° for PIRc). If no specific information is provided with regard to the thermogravimetry of the used foam, a conservative value of 300°C should be used. While the DTG peak for EPS was shown at 330°C, the critical temperature proposed for this material is the melting point.

Chapter 6 was primarily concerned with understanding the thermal evolution and dynamics of the thermal degradation experienced by the studied insulation materials. The subsequent step in the experimental plan was characterisation of the thermal behaviour experienced by the insulation materials when exposed to severe conditions of heat exposure. This stage was based on the use of an external heat source (Cone Calorimeter without spark) to reproduce heating scenarios with different severities. Measurements of temperature within the insulation allowed mapping the different thermal degradation processes, which were identified by thermogravimetry techniques. Measurements of gas species (carbon monoxide, carbon dioxide and oxygen) were also taken to determine whether oxidation processes occurred. The scenarios studied were also used to provide equivalent thermal properties for a simple one-dimensional heat transfer model which was able to predict the thermal evolution of the material relevant for the proposed design methodology; inverse modelling was used to obtain these parameters. The main conclusions from this portion of the experimental programme are listed below:

- A technique based on comparing the eventual thermal discolouration through the thickness of a sample was correlated to the upper edge of the temperature envelopes during the test and the thermogravimetric results. Three clear domains were observed in the thermal evolution of PIR and PF, corresponding to the virgin material, pyrolysis region, and char. SW showed patterns of discolouration indicating loss of the binder. EPS simply showed shrinkage of the surface as it reached the temperature at which the blowing agent was lost (~90-100°C).
- PIR was found to expand in the regions where it was pyrolysing, creating a series of cracks or gaps within the structure of the foam. PF however spalled,

probably due to the loss of chemically bound water, which was evidenced by plateaus of temperature at 100°C.

- A clear effect was observed in the thermal performance of the rigid foams such as PIR and PF when samples were tested with the protective layer attached to the exposed surface. This is related to the reduction of the fraction of absorbed heat flux due to the low emissivity of the protective layer, as well as other effects such as the reduction in the rate of oxidation, avoiding the contact of oxygen with the charred material or the inhibition of a good mixing between air and pyrolysates.
- While the pyrolysis was clearly governed by the thermal evolution of the solid-phase for these charring materials, the rate of oxidation was clearly identified as a diffusion-controlled mechanism. Indeed, values of temperatures higher than those obtained by thermogravimetry were observed within the char. The rate of oxidation of the char was also found to be governed by the external heat flux, which also determined the evolution of the pyrolysis front.
- The proposed heat transfer model showed good agreement with experimental results at low regimes of external heat flux below temperatures where thermal degradation was achieved. Worse agreement was found for experiments at higher external heat flux. This was attributed to the heat losses through the lateral-material, which were expected due to the low conductivity of the tested materials. Despite this model limitation in predicting the thermal evolution at high heat fluxes accurately, the obtained results provide approximate values of thermal properties that estimated the thermal wave in a reasonable way.
- The use of a thin metallic plate as interface for the heat transfer reduced the level of uncertainty in the inverse heat transfer model due to the measurement of surface temperature (a better definition of the boundary condition). Additionally, experiments with a metallic plate helped to isolate this oxidation of the char remaining after pyrolysis, which could not be considered in the simple heat transfer model used.
- A simple heat transfer model was used for several reasons, such as reduction of the level of complexity for predicting the thermal evolution, and controlling the compensation errors often obtained by higher levels of complexity.
- Equivalent value of the thermal conductivity below the temperature of pyrolysis onset for 30-33 $kg \cdot m^{-3}$ PIR and 38 $kg \cdot m^{-3}$ PF is approximately 0.06 $W \cdot m^{-1} \cdot K^{-1}$, considering a specific heat capacity of 1500 $J \cdot kg^{-1} \cdot K^{-1}$. A value of 0.067 $W \cdot m^{-1} \cdot K^{-1}$ can be considered for EPS below the shrinkage temperature.
- Equivalent value of the thermal conductivity below 500°C for PIR and PF can be assumed to be a linear function as $0.018\ (\pm 0.001) + T \cdot 1.24 \cdot 10^{-4} (\pm 1.24 \cdot 10^{-5})$ and $0.044\ (\pm 0.0003) + T \cdot 3.49 \cdot 10^{-5} (\pm 4.6 \cdot 10^{-6})$, respectively for the volumetric heat capacities indicated above, and the temperature (T) in °C.
- Extrapolation of these properties to other conditions than those indicated by the author should be interpreted carefully.

Chapter 7 consists of the last stage of the experimental plan, which was based on two different programmes of large-scale experiments in order to provide the final step

towards the full characterisation and understanding of the performance of insulation materials. The Sandwich Panel Test programme carried out with the University of Central Lancashire (UCLAN) and the Technical University of Denmark in Chorley, UK (2013), and the Edinburgh Tall Buildings Fire Tests carried out by The University of Edinburgh at BRE Watford (2013), were described in this chapter. The first of these tests corresponds to a case study of insulated walls with a thermally thin barrier, while the second corresponds to a case with a thermally thick barrier. These different scenarios highlighted the importance of the thermal barrier in order to control the onset of pyrolysis. An additional programme of intermediate-scale tests based on a typical wall assembly consisting of plasterboard covering an insulation board were tested under controlled environments of heat exposure. These tests have served to validate the material performance observed at lower scales, and more importantly verify the hazards map proposed as framework for the design of insulation materials in buildings. The main conclusions from these experiments are given below:

- Thermally thick barriers allow controlling the onset of pyrolysis with a larger absorption of heat, while thermally thin barriers increase the pyrolysis risk since the amount of energy required to reach the onset of pyrolysis is low.
- Once the onset of pyrolysis occurs, the rate of pyrolysation is vital for quantifying hazards such as contribution to HRR and transport of toxic species. Estimation of the rate of pyrolysation requires predicting the thermal evolution experienced by the solid-phase of the insulation.
- A simple method for estimating the rate of pyrolysation of rigid cellular insulation materials was proposed, which is based on the combination of thermogravimetric analyses and temperature measurements. This approach is valid due to the incapability of air to diffuse through the material, until the barrier loses its integrity (cracks, collapse, generation of gaps, etc.) and allowing air to penetrate into the assembly.
- Surface oxidation (smouldering) from the already pyrolysed material (char) was found to play a crucial role with regard to the later propagation of flaming through the insulation board, representing the breaching of the compartmentalisation.
- It was identified that input parameters from the fire could be correlated to the heat absorption, since a relation between this and the temperature reached by the insulation behind the lining was observed.

Chapter 8 proposes the definition of a simplified tool for the design of thermal barriers for insulation materials. As a result of the extended experimental plan presented in the preceding chapters, a series of inputs from material properties such as critical temperature and thermal properties were generated for the application of a methodology for controlling the onset of pyrolysis. The formulation of this methodology consists of the one-dimensional diffusion equation for solids, but with two layers in contact: (1) the thermal barrier and (2) the insulation. Despite the fact that this problem may be solved by using numerical tools such as finite element or finite difference models, a simpler tool for design has been presented herein. The aim

of this tool is to optimise or select the barrier properties (thickness and thermal properties) for the combustible insulation as a function of the fire inputs, insulation critical temperature, and time of exposure. The net heat absorption was initially proposed as input parameter from the fire, however clear limitations are identified with regard to the application of this approach to thermally thick barriers. Instead, fire inputs could be considered as a net heat flux distribution or as a radiant heat flux and a gas-phase temperature with a certain heat transfer coefficient. The first approach seems suitable if this can be defined independently of the thermal properties of the barrier (which is not applicable in the early stages of a fire), while the second approach can be used as a characteristic boundary condition from the fire, independent from the barrier. Generic solutions based on constant values of net heat flux, radiant heat flux and heat transfer coefficient were proposed in early stages of this work. In order to achieve this objective, the analytical solution for the semi-infinite plate is used as a framework for the definition of design charts. Design charts for thermally thin barriers can be defined by an analysis based on the integral of the net heat flux, this being correlated to the volumetric heat capacity, thickness, and critical temperature for the insulation. However, this approach can only be applied for Biot numbers lower than 0.1, i.e. high thermal conductivities. Design charts for thermally thick barriers require definition of the non-dimensional parameters for achieving a generic solution. A critical value of thermal conductivity was found for defining a unique generic solution. Solutions in-between thermal properties from the insulation and the critical conductivity need to be defined particularly. The limit case represented by a material with same thermal properties as the insulation could be solved by the semi-infinite plate regression. Examples of application were derived, and design charts were produced for the rigid polymeric materials. It is hoped that these tools will play a role in the design of insulation materials under fire conditions in a quantifiable manner, so as to achieve increased fire safety performance in future.

9.3 Recommendations for future work

A series of recommendations to continue and extend the extensive work presented in this thesis are noted below:

- Flammability characterisation of the pyrolysis gases released by the insulation material is required to determine the lower and upper flammability limits.
- Assessment of the dynamics from the oxidation of the char should be further investigated. Indeed, this has shown a clear effect on accelerating the transition of the pyrolysis front of charring materials such as PIR and PF, due to early consumption of the char layer.
- Two-dimensional models could be further developed to verify the thermal properties obtained by the one-dimensional analyses carried out from the bench-scale experiments.
- Assessment of flammability from inorganic materials with higher contents of binder should be further researched, for instance with classic methods such as the Cone Calorimeter.

- Important and urgent work is required in order to define input parameters from the fire as reliable boundary conditions (e.g. net heat flux distributions, or radiant heat flux distributions with convective coefficients and gas-phase temperatures) for the assessment of thermal barriers and compartmentalisation elements, far from the typical small room compartments and the time-temperature approach for characterising fire severity.
- Design charts based on constant heat fluxes should be extended to conditions of variable heat fluxes.
- Further validation of the simple method developed for determining pyrolysis rates for materials such as PIR or PF should be carried out, assessing whether more complex models (e.g. including the chemistry of thermal degradation reactions among other phenomena) are required for predicting the pyrolysis process
- Further work should be focused on understanding the mechanical behaviour of wall assemblies incorporating insulation materials and the interaction between insulation and thermal barrier once the pyrolysis onset is reached.

Bibliography

A

J. G. Abbott, “Standard Laboratory Tests: How Meaningful are they in Assessing Fire Performance of Insulation Materials?,” in Fire and cellular polymers, 1986, pp. 199–218.

Airpacks Ltd. [Online]. Available: http://www.kore-system.com/. [Accessed: 01-Feb-2015].

Airpacks Ltd., “Technical Data Sheet of KORE ICF,” 2012. [Online]. Available: http://cdn2.hubspot.net/hub/299572/file-312283952-pdf/pdf/kore_icf_technical.pdf?t=1422375502661. [Accessed: 08-Jan-2013].

Airpacks Ltd., “Technical Data Sheet of KORE Fill,” 2012. [Online]. Available: http://cdn2.hubspot.net/hub/299572/file-313203405-pdf/pdf/kore_fill_technical.pdf?t=1422375502661. [Accessed: 08-Jan-2013].

Airpacks Ltd., “Technical Data Sheet of KORE Key.” [Online]. Available: http://cdn2.hubspot.net/hub/299572/file-312278167-pdf/pdf/kore_key_technical.pdf?t=1422375502661. [Accessed: 08-Jan-2013].

J. J. Alston, “Room/Corner Fire Calibration Data: Marine Composite Screening Specimens”, M.Sc. thesis, Worcester Polythecnic Institute (USA), 2004.

A. Amundarain, “Assesment of the Thermal Efficiency, Structure and Fire Resistance of Lightweight Building Systems for Optimised Design,” Ph.D. thesis, The University of Edinburgh. http://hdl.handle.net/1842/2128, 2007.

R. Aseeva, B. Serkov, and A. Sivenkov, “Fire Behavior and Fire Protection in Timber Buildings”, Dordrecht: Springer Netherlands, 2014.

F. Asdrubali, C. Baldassarri, and V. Fthenakis, “Life cycle analysis in the construction sector: Guiding the optimization of conventional Italian buildings,” Energy and Buildings, vol. 64, pp. 73–89, Sep. 2013.

K. Ashida, K. Saiki, J. Goto, and K. Sasaki, “Polyisocyanurate foams modified by thermally stable linkages,” in ACS Symp Series, 1997, pp. 669:81–100.

A. Atreya, C. Carpentier, and M. Harkleroad, “Effect Of Sample Orientation On Piloted Ignition And Flame Spread,” Fire Safety Science 1, pp. 97–109, 1986.

“ASTM D3014. Standard test method for flame height, time of burning and loss of mass of rigid thermoset cellular plastics in vertical position.” ASTM International, West Conshohocken, PA, 1999.

“ASTM E1321. Standard Method for Determining Material Ignition and Flame Spread Properties.” ASTM International, West Conshohocken, PA, 2009.

"ASTM E2058. Standard Test Methods for Measurement of Synthetic Polymer Material Flammability Using a Fire Propagation Apparatus (FPA)." ASTM International, West Conshohocken, PA, 2009.

"ASTM D2863. Measuring the minimum oxygen concentration to support candle-like combustion of plastics (oxygen index)." ASTM International, West Conshohocken, PA, 2010.

"ASTM D3801. Standard Test Method for Measuring the Comparative Burning Characteristics of Solid Plastics in a Vertical Position." ASTM International, West Conshohocken, PA, 2010.

"ASTM D1929. Ignition properties of plastics." ASTM International, West Conshohocken, PA, 2011.

"ASTM E1269. Standard Test Method for Determining Specific Heat Capacity by Differential Scanning Calorimetry." ASTM International, West Conshohocken, PA, 2011.

"ASTM Standard E119, "Test Methods for Fire Tests of Building Construction and Materials." ASTM International, West Conshohocken, PA, 2012.

"ASTM E84: Standard Test Method for Surface Burning Characteristics of Building Materials." ASTM International, West Conshohocken, PA, 2014.

"ASTM D635. Standard Test Method for Rate of Burning and/or Extent and Time of Burning of Plastics in a Horizontal Position." ASTM International, West Conshohocken, PA, 2014.

B. Atanasiu (editor), T. Boermans, K. E. Thomsen, J. Rose, S. Aggerholm, A. Hermelink, S. Schimschar, J. Grözinger, and M. Offermann, Principles for Nearly Zero-Energy Buildings: Paving the way for effective implementation of policy requirements. BPIE - Buildings Performance Institute Europe, 2011.

M. L. Auad, L. Zhao, H. Shen, S. R. Nutt, and U. Sorathia, "Flammability properties and mechanical performance of epoxy modified phenolic foams," Journal of Applied Polymer Science, vol. 104, no. 3, pp. 1399–1407, 2007.

B

V. Babrauskas, and W. J. Parker, "Ignitability measurements with the cone calorimeter," Fire and Materials, vol. 11, no. 1, pp. 31–43, 1987.

V. Babrauskas, "Related Quantities: (a) Heat of Combustion and Potential Heat," in Heat Release in Fires, V. Babrauskas and S. J. Grayson, Eds. New York: Elsevier Applied Science, 1992, pp. 207–223.

V. Babrauskas, W. H. Twilley, and W. J. Parker, "The effects of specimen edge conditions on heat release rate," Fire and Materials, vol. 17, no. 2, pp. 51–63, 1993.

V. Babrauskas, "Specimen heat fluxes for bench-scale heat release rate testing," Fire and Materials, vol. 19, no. 6, pp. 243–252, 1995.

V. Babrauskas, “Heat Release Rates,” in SFPE Handbook of Fire Protection Engineering, 3rd ed., P. J. DiNenno, D. Drysdale, C. L. Beyler, W. D. Walton, R. L. P. Custer, and J. M. Watts, Eds. . National Fire Protection Association, Massachusetts, U.S.A., 2002

V. Babrauskas, “The Cone Calorimeter,” in SFPE Handbook of Fire Protection Engineering, 3rd ed., P. J. DiNenno, D. Drysdale, C. L. Beyler, W. D. Walton, R. L. P. Custer, and J. M. Watts, Eds. . National Fire Protection Association, Massachusetts, U.S.A., 2002.

G. Baker, “Performance of expanded polystyrene insulated panel exposed to radiant heat,” University of Canterbury, Christchurch, New Zealand, 2002.

N. Bal and G. Rein, “Numerical investigation of the ignition delay time in black PMMA at high heat fluxes,” Proceedings of the 12th International Interflam Conference. Nottingham, UK, pp. 685–696, 2010.

N. Bal, “Uncertainty and complexity in pyrolysis modelling ,“ Ph.D. thesis, The University of Edinburgh. http://hdl.handle.net/1842/6511, 2012.

E. Bar-Ziv and I. I. Kantorovich, “Mutual effects of porosity and reactivity in char oxidation,” Progress in Energy and Combustion Science, vol. 27, no. 6, pp. 667–697, Jan. 2001.

J. V. Beck, “Thermocouple Temperature Disturbances in Low Conductivity Materials,” Journal of Heat Transfer, vol. 84, no. 2, p. 124, 1962.

R. Berrier, S. Singh, J. Costa, and V. Bonapersona, “Hydrocarbon Blown Rigid Polyurethane Foam for the Boardstock Industry—A Novel Approach,” Journal of Cellular Plastics, 1999.

Craig L. Beyler and M. M. Hirschle, “Thermal Decomposition of Polymers,” in SFPE Handbook of Fire Protection Engineering, 3rd Edition, 3rd ed., P. J. DiNenno, D. Drysdale, C. L. Beyler, and W. D. Walton, Eds. National Fire Protection Association, Massachusetts, U.S.A., 2002

V. I. Blinov and G. N. Khudiakov, “Diffusion burning of liquids. ,” US Army translation, NTIR NO. AD296762, 1961.

H. Biteau, “Thermal and chemical behaviour of an energetic material and a heat release rate,” Ph.D. thesis, The University of Edinburgh. http://hdl.handle.net/1842/4620, 2009.

L. Bisby, J. Gales, and C. Maluk, “A contemporary review of large-scale non-standard structural fire testing,” Fire Science Reviews, vol. 2, p. 1, 2013.

M. Bomberg and S. Klarsfeld, “Semi-Empirical Model of Heat Transfer in Dry Mineral Fiber Insulations,” Journal of Thermal Insulation, vol. 6, 1983.

J. M. Buist, S. J. Grayson, and W. D. Woolley, “Fire and Cellular Polymers,” 1986.

V. M. Brannigan, “The regulation of technological innovation: the special problem of fire safety standards,” in FireSeat “Fire & Building Safety in the Single European Market,” 2008, pp. 20–33.

P. J. Briggs, “Fire Behaviour of Rigid Foam Insulation Boards,” in Fire and cellular polymers, 1986.

S. Brohez, C. Delvosalle, G. Marlair, and A. Tewarson, “Measurement of heat release rate from oxygen consumption in sooty fires,” Journal of Fire Sciences, vol. Vol.18, pp. 327–353, 2000.

“BS 476-15, ISO 5660-1. Fire tests on building materials and structures. Method for measuring the rate of heat release of products.” BSI, 1993.

“BS 8414-1. Fire performance of external cladding systems. Test methods for non-loadbearing external cladding systems applied to the face of a building.” BSI, 2002.

“BS EN 520. Gypsum plasterboards. Definitions, requirements and test methods.” BSI, 2004.

“BS EN 13501-1. Fire classification of construction products and building elements. Part 1: Classification using data from reaction to fire tests.” BSI, 2009.

“BS EN ISO 1182. Reaction to fire tests for products — Non- combustibility test.” BSI, 2010.

“BS EN ISO 1716. Reaction to fire tests for products — Determination of the gross heat of combustion (calorific value).” BSI, 2010.

“BS EN ISO 11925-2. Reaction to fire tests — Ignitability of products subjected to direct impingement of flame. Part 2: Single-flame source test.” BSI, 2010.

“BS EN ISO 13823. Reaction to fire tests for building products — Building products excluding floorings exposed to the thermal attack by a single burning item.” BSI, 2010.

“BS EN 1363-1 . Fire resistance tests - Part 1: General Requirements.” BSI, 2012.

“BS EN 1364-4. Fire resistance tests for non-loadbearing elements. Curtain walling. Part configuration.” BSI, 2014.

N. A. Burley, “Nicrosil/Nisil Type N Thermocouples,” Omega complete temperature measurement handbook and encyclopedia, vol. 28, pp. Z33–Z36, 1992

G. Buxton, “The Montreal protocol on substances that deplete the ozone layer.,” International Negotiation, vol. 1. pp. 231–246, 1988.

C

L. Carmichael, J. Jacobs, and B. H. Sage, “Thermal conductivity of fluids. n-pentane,” Journal of Chemical and Engineering Data, vol. 14, no. 1, pp. 31–37, 1969.

H. S. Carslaw and J. C. Jaeger, Conduction of Heat in Solids, 2th ed. 1986.

R. Carvel, T. Steinhaus, G. Rein, and J. L. Torero, "Determination of the flammability properties of polymeric materials: A novel method," Polymer Degradation and Stability, vol. 96, no. 3, pp. 314–319, 2011.

S. D. Christian, "Legislation — Standards — Polymers," in Fire and cellular polymers, 1986, pp. 93–102.

CIBSE Guide A: Environmental Design, 7th ed. The Chartered Institution of Building Services Engineers London, 2006.

T. G. Cleary and J. G. Quintiere, "NISTIR 4664. Flammability Characterization of Foam Plastics," National Institute of Standards and Technology, 1991.

W. S. Cleveland, "Robust Locally Weighted Regression and Smoothing Scatterplots," Journal of the American Statistical Association, vol. 74, no. 368, pp. 829–836, 1979.

W. S. Cleveland, S. J. Devlin, and S. Cleveland, "Locally Weighted Regression: An Approach to Regression Analysis by Local Fitting," Journal of the American Statistical Association, vol. 83, no. 403, pp. 596–610, 1988.

L. Cody, "Fire Safety Considerations for a Green and Sustainable Future," in IFE AGM and Conference, 2011.

C. A. C. Coello, "20 Years of Evolutionary Multi-Objective Optimization : What Has Been Done and What Remains To Be Done," in Computational Intelligence: Principles and Practice, G. Y. Yen and D. B. Fogel, Eds. IEEE Computational Intelligence Society, 2006, pp. 79–88.

C. C. Coello, "Evolutionary multi-objective optimization: a historical view of the field," IEEE Computational Intelligence Magazine, vol. 1, no. February 2006, pp. 28–36, 2006.

P. Collier and G. Baker, "Improving the fire performance of polystyrene insulated panel in New Zealand," NZFSC, Wellington, New Zealand, 2004.

P. Collier and G. Baker, "The Influence of Construction Detailing on the Fire Performance of Polystyrene Insulated Panels," Fire Technology, pp. 1–17, 2011.

A. Cowlard, A. Bittern, C. Abecassis-Empis, and J. Torero, "Fire safety design for tall buildings," in Procedia Engineering, 2013, vol. 62, pp. 169–181.

R. J. Crewe, J. P. Hidalgo, M. X. Sørensen, S. Molyneus, M. McLaggan, G. Joomas, S. Welch, J. L. Torero, A. A. Stec, and T. R. Hull, "Fire performance of sandwich panels in a modified ISO 13784-1 small room test: the effect of damage and increased fire load," Fire Technology, 2015 (submitted).

C. Croitoru, I. Nastase, F. Bode, A. Meslem, and A. Dogeanu, "Thermal comfort models for indoor spaces and vehicles—Current capabilities and future perspectives," Renewable and Sustainable Energy Reviews, vol. 44, pp. 304–318, Apr. 2015.

A. Cunningham, B. Eling, and D. J. Sparrow, “A study of the low smoke potential, flame resistance and processibility of high index polyisocyanurate rigid foam,” Cellular polymers, vol. 6, no. 6, pp. 42–59, 1987.

D

J. Damsky and J. Gero, “An evolutionary approach to generating constraint-based space layout topologies,” Proc. CAAD Futures, vol. 1, no. Steadman 1983, pp. 855–864, 1997.

“Zero carbon non-domestic buildings. Phase 3 final report,” Department for Communities and Local Government, 2011.

“DIN 4102-17. Fire behaviour of building materials and elements. Determination of melting point of mineral fibre insulating materials. Concepts, requirements and testing.” DIN, 1990.

E. Dominguez-Rosado, J. J. Liggat, C. E. Snape, B. Eling, and J. Pichtel, “Thermal degradation of urethane modified polyisocyanurate foams based on aliphatic and aromatic polyester polyol,” Polymer Degradation and Stability, vol. 78, no. 1, pp. 1–5, Jan. 2002.

R. Dohrn, J. M. Fonseca, R. Albers, J. Kušan-Bindels, and I. M. Marrucho, “Thermal conductivity of polyurethane foam cell gases: Improved transient hot wire cell – data of isopentane + n-pentane mixtures – Extended Wassiljewa-model,” Fluid Phase Equilibria, vol. 261, no. 1–2, pp. 41–49, Dec. 2007.

D. Drysdale, “Fundamentals of the fire behaviour of cellular polymers,” in Fire and cellular polymers, 1986, pp. 61–75.

D. Drysdale, “Fire Science and Combustion,” in An Introduction to Fire Dynamics, John Wiley & Sons, Ltd, 2011, pp. 1–34.

D. Drysdale, “Heat Transfer,” in An Introduction to Fire Dynamics, John Wiley & Sons, Ltd, 2011, pp. 35–82.

D. Drysdale, “Limits of Flammability and Premixed Flames,” in An Introduction to Fire Dynamics, John Wiley & Sons, Ltd, 2011, pp. 83–119.

D. Drysdale, “Steady Burning of Liquids and Solids,” in An Introduction to Fire Dynamics, John Wiley & Sons, Ltd, 2011, pp. 181–223.

D. Drysdale, “Ignition: The Initiation of Flaming Combustion,” in An Introduction to Fire Dynamics, John Wiley & Sons, Ltd, 2011, pp. 225–275.

A. Dunster, “Characterisation of Mineral Wastes, Resources and Processing technologies – Integrated waste management for the production of construction material.” p. 17, 2007.

S. Dyrbøl, “Heat transfer in Rockwool modelling and method of measurement”, Ph.D. thesis, Technical University of Denmark (DTU), 1998.

S. Dyrbøl, S. Svendsen, and A. Elmroth, “Experimental investigation of the effect of natural convection on heat transfer in mineral wool,” Journal of Building Physics, 2002.

E

“Practical refurbishment of solid-walled houses (CE184),” Energy Saving Trust, 2006.

“European Association for External Thermal Insulation Composite Systems.” [Online]. Available: http://www.ea-etics.eu. [Accessed: 01-Feb-2015].

Eurobond Lamintes Ltd. [Online]. Available: http://www.eurobond.co.uk. [Accessed: 01-Feb-2015].

EU, “Directive 2010/31/EU of the European Parliament and of the Council of 19 May 2010 on the energy performance of buildings,” Official Journal of the European Union, pp. 13–35, 2010.

F

M. Fesanghary, S. Asadi, and Z. W. Geem, “Design of low-emission and energy-efficient residential buildings using a multi-objective optimization algorithm,” Building and Environment, vol. 49, pp. 245–250, Mar. 2012.

R. Filipczak, S. Crowley, and R. E. Lyon, “Heat release rate measurements of thin samples in the OSU apparatus and the cone calorimeter,” Fire Safety Journal, vol. 40, no. 7, pp. 628–645, 2005.

R. D. B. Fraser and E. Suzuki, “No Title,” Analytical Chemistry, vol. 38, p. 1770, 1966.

R. D. B. Fraser and E. Suzuki, “No Title,” Analytical Chemistry, vol. 41, p. 37, 1969.

G

P. Gabbot, Principles and Applications of Thermal Analysis. Blackwell Publishing Ltd., 2008, p. 484.

K. Ghazi Wakili, E. Hugi, L. Wullschleger, and T. Frank, “Gypsum Board in Fire -- Modeling and Experimental Validation,” Journal of Fire Sciences, vol. 25. pp. 267–282, 2007.

M. Gilles and T. D. Jensen, “SRI roadshow Paris,” 2011. [Online]. Available: http://www.rockwool.com/files/COM2011/Investor/Presentations/2011/20110610_Paris-SRI-Roadshow_BAML.pdf. [Accessed: 01-Feb-2015].

M. D. Gonçalves, “Insulating Solid Masonry Walls,” Building Envelope Forum. [Online]. Available: http://www.cebq.org/documents/Insulatingsolidmasonrywalls-BEF_000.pdf. [Accessed: 01-Feb-2015].

N. Greeves, “ChemTube3D. The University of Liverpool.” [Online]. Available: http://www.chemtube3d.com/polymer/_PolystyreneF.html. [Accessed: 01-Feb-2015].

S. E. Gustafsson, “Transient plane source techniques for thermal conductivity and thermal diffusivity measurements of solid materials,” Review of Scientific Instruments, vol. 62, pp. 797–804, 1990.

H

R. Hadden, “Smouldering and self-sustaining reactions in solids: an experimental approach,” Ph.D thesis, The University of Edinburgh. http://hdl.handle.net/1842/5587, 2011.

M. Hamdy, A. Hasan, and K. Siren, “Applying a multi-objective optimization approach for Design of low-emission cost-effective dwellings,” Building and Environment, vol. 46, no. 1, pp. 109–123, Jan. 2011.

T. Z. Harmathy, “A New Look at Compartment Fires,” Fire Technology, vol. 8, no. 3, pp. 196–217, 1972.

T. Z. Harmathy, “The role of Thermal Feedback in Compartment Fires,” Fire Technology, vol. 11, no. 1, pp. 48–54, 1975.

T. Z. Harmathy, “The possibility of characterizing the severity of fires by a single parameter,” Fire and Materials, vol. 4, no. 2, pp. 71–76, Jun. 1980.

T. Z. Harmathy and J. R. Mehaffey, “Normalized heat load: A key parameter in fire safety design,” Fire and Materials, vol. 6, no. 1, pp. 27–31, Mar. 1982.

J. P. Hidalgo, A. Cowlard, C. Abecassis-Empis, C. Maluk, A. H. Majdalani, S. Kahrmann, R. Hilditch, M. Krajcovic, and J. L. Torero, “Edinburgh Tall Building Fire Tests: Experiment #1,” Fire Safety Journal, 2015 (submitted).

J. P. Hidalgo, C. Maluk, and J. L. Torero, “Uncertainty assessment on the use of thin skin calorimeters to measure irradiation from real fires,” (in preparation).

J. P. Hidalgo, M. McLaggan, S. Welch, and J. L. Torero, “Characterisation of fire dynamics in a modification to the Small room test, ISO 13784-1,” (in preparation).

HM Government, “Approved Document L - Conservation of fuel and power.” [Online]. Available: http://www.planningportal.gov.uk/buildingregulations/approveddocuments/partl/approved#ApprovedDocumentL1A:ConservationoffuelandpowerNewdwellings. [Accessed: 01-Feb-2015].

HM Government, “The Building Regulations 2010,” Approved Document L1A: Conservation of fuel and power in new dwellings, 2010. [Online]. Available: http://www.planningportal.gov.uk/uploads/br/BR_PDF_AD_L1A_2010_V2.pdf. [Accessed: 01-Feb-2015].

HM Government, “The Building Regulations 2010,” Approved Document L2A: Conservation of fuel and power in new buildings other than dwellings, 2010. [Online]. Available: http://www.planningportal.gov.uk/uploads/br/BR_PDF_AD_L2A_2010_V2.pdf. [Accessed: 01-Feb-2015].

HM Government, “The Building Regulations 2010,” Approved Document L2B: Conservation of fuel and power in existing dwellings. [Online]. Available: http://www.planningportal.gov.uk/uploads/br/BR_PDF_AD_L1B_2011.pdf. [Accessed: 01-Feb-2015].

HM Government, “The Building Regulations 2010,” Approved Document L2B: Conservation of fuel and power in existing buildings other than dwellings. [Online]. Available: http://www.planningportal.gov.uk/uploads/br/BR_PDF_AD_L2B_2011.pdf. [Accessed: 01-Feb-2015].

C. Huggett, “Estimation of rate of heat release by means of oxygen consumption measurements,” Fire and Materials, vol. 4, no. 2, pp. 61–65, 1980.

I

F. P. Incropera, D. DeWitt, T. L. Bergman, and A. S. Lavine, Principles of Heat and Mass Transfer, 7th ed. John Wiley & Sons, Inc., 2011.

Insulating Concrete Formwork Association. [Online]. Available: http://www.icfinfo.org.uk. [Accessed: 01-Feb-2015].

ICF Tech Ltd. ” Insulating Concrete Form structural walling solutions. [Online]. Available: http://www.icf-tech.com/download-brochure/. [Accessed: 08-Jan-2013].

H. Islam, M. Jollands, S. Setunge, and M. A. Bhuiyan, “Optimization approach of balancing life cycle cost and environmental impacts on residential building design,” Energy and Buildings, vol. 87, pp. 282–292, Jan. 2015.

“ISO 9705. Fire tests -- Full-scale room test for surface products.” International Organization for Standardization, Geneva (Switzerland), 1993.

“ISO 13784-1. Reaction to fire test for sandwich panel building systems. Part 1: Small room test.” International Organization for Standardization, Geneva (Switzerland), 2014.

“ISO 22007-2. Plastics -- Determination of thermal conductivity and thermal diffusivity -- Part 2: Transient plane heat source (hot disc) method.” International Organization for Standardization, Geneva (Switzerland), 2008.

J

Jablite. [Online]. Available: http://www.jablite.co.uk. [Accessed: 01-Feb-2015].

Jablite, “Technical Data Sheet of Jabfill,” Jabfill in a Brick & Block Cavity Wall, 2012. [Online]. Available: http://www.jablite.co.uk/products/show/jabfill-system. [Accessed: 08-Jan-2013].

M. L. Janssens, “Measuring rate of heat release by oxygen consumption,” Fire Technology, vol. 27, no. 3, pp. 234–249, 1991.

M. Janssens and W.J. Parker, “Oxygen Consumption Calorimetry,” Heat Release in Fires, edited by V. Babrauskas and S.J. Grayson, vol. Chapter 3, pp. 31–59, 1992.

M. Janssens, J. Kimble, and D. Murphy, “Computer tools to determine material properties for fire growth modeling from cone calorimeter data,” in Fire and Materials. 8th International Conference8th International Conference, 2003, pp. 377–387.

R. Jansson, “Measurement of thermal properties at elevated temperatures – Brandforsk project 328-031,” 2004.

B. H. Jones, “Performance of Gypsum Plasterboard Assemblies Exposed to Real Building Fires,” New Zealand, 2001.

A. Jowsey, “Fire Imposed Heat Fluxes for Structural Analysis (Ph.D. thesis),” The University of Edinburgh. http://hdl.handle.net/1842/1480, 2006.

K

T. Kashiwagi, “Effects of sample orientation on radiative ignition,” Combustion and Flame, vol. 44, no. 1–3, pp. 223–245, 1982.

P. Keerthan and M. Mahendran, “Numerical studies of gypsum plasterboard panels under standard fire conditions,” Fire Safety Journal, vol. 53, pp. 105–119, Oct. 2012.

P. Kiliaris and C. D. Papaspyrides, “Polymer Green Flame Retardants,” in Polymer Green Flame Retardants, Elsevier, 2014, pp. 1–43.

Kingspan Insulation. [Online]. Available: http://www.kingspaninsulation.co.uk. [Accessed: 01-Feb-2015].

Kingspan, “Technical Data Sheet of Thermawall TW50,” 2011. [Online]. Available: http://www.kingspaninsulation.co.uk/getattachment/b08c2d53-474b-4bfd-ad44-d38eb4041dd2/Thermawall-TW50.aspx. [Accessed: 08-Jan-2013].

Kingspan, “Technical Data Sheey of Kooltherm K8 Cavity Board,” 2011. [Online]. Available: http://www.kingspaninsulation.co.uk/getattachment/61f60f6d-8e1f-459e-a533-51e186c775f3/Kooltherm-K8-Cavity-Board.aspx. [Accessed: 08-Jan-2013].

Kingspan, “Technical Data Sheet of Thermawall TW55,” 2011. [Online]. Available: http://www.kingspaninsulation.co.uk/getattachment/e02084f9-9c74-4695-97ea-7877b8e4ea12/Thermawall-TW55.aspx. [Accessed: 08-Jan-2013].

Kingspan, “Technical Data Sheet of Kooltherm K12 Framing Board,” 2011. [Online]. Available: http://www.kingspaninsulation.co.uk/getattachment/fd77d557-97b0-47c1-b0e9-5c12eb237861/Kooltherm-K12-Framing-Board.aspx. [Accessed: 08-Jan-2013].

Kingspan TEK. [Online]. Available: http://www.tek.kingspan.com. [Accessed: 01-Feb-2015].

Kingspan, “Technical Data Sheet of Kingspan TEK Building System,” 2009. [Online]. Available: http://www.kingspantek.co.uk/Products/TEK-Building-System/TEK-Building-System/Introduction-to-TEK-Building-System. [Accessed: 08-Jan-2013].

Knauf Insulation Ltd. [Online]. Available: http://www.knaufinsulation.co.uk. [Accessed: 01-Feb-2015].

Knauf Insulation Ltd., "Technical Data Sheet of Supafil," 2011. [Online]. Available: http://www.knaufinsulation.co.uk/en-gb/products/blown-mineral-wool.aspx#axzz3QslN7ugX. [Accessed: 08-Jan-2013].

H. Komiyama and K. Takeuchi, "Sustainability science: building a new discipline," Sustainability Science, vol. 1. pp. 1–6, 2006.

M. K. Kumaran, "Heat, Air and Moisture Transfer in Insulated Envelope Parts. Final Report, Volume 3, Task 3: Material Properties.," Belgium, 1996.

U. Krause, W. Grosshandler, and L. Gritzo, "The International FORUM of Fire Research Directors: A position paper on sustainability and fire safety," in Fire Safety Journal, 2012, vol. 49, no. 0, pp. 79–81.

L

C. Lautenberger and C. Fernandez-Pello, "Generalized pyrolysis model for combustible solids," Fire Safety Journal, vol. 44, no. 6, pp. 819–839, 2009

K. Levenberg, "A Method for the Solution of Certain Non-Linear Problems in Least Squares," Quarterly of Applied Mathematics, vol. 2, pp. 164–168, 1944.

G. Li and H. Hu, "Risk design optimization using many-objective evolutionary algorithm with application to performance-based wind engineering of tall buildings," Structural Safety, vol. 48, pp. 1–14, May 2014.

J. Lindholm, A. Brink, and M. Hupa, "Influence of decreased sample size on cone calorimeter results," Fire and Materials, vol. 36, no. 1, pp. 63–73, 2012.

Logix. UK. [Online]. Available: http://www.logix.uk.com. [Accessed: 01-Feb-2015].

J. R. Lloyd and W. R. Moran, "Natural Convection Adjacent to Horizontal Surface of Various Planforms," Journal of Heat Transfer, vol. 96, no. 4. p. 443, 1974.

R. T. Long, J. L. Torero, J. G. Quintiere, and A. C. Fernandez-Pello, "Scale and transport considerations on piloted ignition of PMMA," in Sixth International Symposium on Fire Safety Science, 1999, pp. 567–578.

M

B. J. McCaffrey, J. G. Quintere, and M. F. Harkleroad, "Estimating room temperatures and likelihood of flashover using fire test data correlations," Fire Technology, vol. 17, no. 2, pp. 98–119, 1981.

L. Ma and R. Mitchell, "Modeling char oxidation behavior under Zone II burning conditions at elevated pressures," Combustion and Flame, vol. 156, pp. 37–50, 2009.

A. Q. Maani, "Effects of Oxygen Concentration on the Smouldering Combustion of the Rigid PIR Insulation Material, "M.Sc. thesis, The University of Edinburgh, 2013.

A. H. Majdalani, “Compartment Fire Analysis for Contemporary Architecture,” Ph.D. thesis,” The University of Edinburgh, 2014.

C. Maluk, “Development and Application of a Novel Test Method for Studying the Fire Behaviour of CFRP Prestressed Concrete Structural,” Ph.D. thesis, The University of Edinburgh, 2014.

D. Marquardt, “An Algorithm for Least-Squares Estimation of Nonlinear Parameters,” SIAM Journal on Applied Mathematics, vol. 11, no. 2, pp. 431–441, 1963.

The MathWorks Inc., “MATLAB and Optimization Toolbox R2014a.” Natick, Massachusetts, United States.

B. Meacham, B. Poole, J. Echeverria, and R. Cheng, Fire Safety Challenges of Green Buildings. Springer New York, 2012.

D. A. Meikle, “Timber frame wall insulation: A survey of industry practice (2000 - 2011).” (Personal communication), 2014.

M. Modesti, A. Lorenzetti, F. Simioni, and M. Checchin, “Influence of different flame retardants on fire behaviour of modified PIR/PUR polymers,” Polymer Degradation and Stability, vol. 74, no. 3, pp. 475–479, 2001.

M. Modesti and A. Lorenzetti, “Flame retardancy of polyisocyanurate–polyurethane foams: use of different charring agents,” Polymer Degradation and Stability, vol. 78, no. 2, pp. 341–347, 2002.

M. Modesti and A. Lorenzetti, “Improvement on fire behaviour of water blown PIR–PUR foams: use of an halogen-free flame retardant,” European Polymer Journal, vol. 39, no. 2, pp. 263–268, 2003.

A. P. Mouritz and A. G. Gibson, Fire Properties of Polymer Composite Materials. 2006, p. 394.

N

“NFPA 5000 - Building Construction and Safety Code.” National Fire Protection Association, Massachusetts, U.S.A., 2015

The National Institute of Standards and Technology, “The NIST Chemistry WebBook.” [Online]. Available: webbook.nist.gov. [Accessed: 01-Feb-2015].

R. M. Nussbaum and B. A. L. Östman, “Larger specimens for determining rate of heat release in the cone calorimeter,” Fire and Materials, vol. 10, no. 3–4, pp. 151–160, 1986.

O

M. J. O’Neill, “Measurement of Specific Heat Functions by Differential Scanning Calorimetry.,” Analytical Chemistry, vol. 38, pp. 1331–1336, 1966.

G. K. Oral, A. K. Yener, and N. T. Bayazit, “Building envelope design with the objective to ensure thermal, visual and acoustic comfort conditions,” Building and Environment, vol. 39, no. 3, pp. 281–287, Mar. 2004.

B. A. L. Östman, I. G. Svensson, and J. Blomqvist, “Comparison of three test methods for measuring rate of heat release,” Fire and Materials, vol. 9, no. 4, pp. 176–184, 1985.

P

A. M. Papadopoulos and E. Giama, “Design and Development of Innovative Stone-wool Products for the Energy Upgrading of Existing and New Buildings (SAPPEK),” Project Interim Report, Thessaloniki (Greece), 2004.

A. M. Papadopoulos, “State of the art in thermal insulation materials and aims for future developments,” Energy and Buildings, vol. 37, no. 1, pp. 77–86, 2005.

K. T. Paul, “Burning characteristics of materials,” Fire and Materials, vol. 3, no. 4, pp. 223–231, 1979.

K. T. Paul, “Characterization of the burning behaviour of polymeric materials,” Fire and Materials, vol. 8, no. 3, pp. 137–147, 1984.

K. M. Pedersen, “Man-made vitreous fibre products and their use in fire protection systems,” EP 0936060 A1, 1999.

A. Perejón, P. E. Sánchez-Jiménez, J. M. Criado, and L. A. Pérez-Maqueda, “Kinetic analysis of complex solid-state reactions. A new deconvolution procedure.,” The journal of physical chemistry. B, vol. 115, no. 8, pp. 1780–91, Mar. 2011.

L. A. Pérez-Maqueda, J. M. Criado, and P. E. Sanchez-Jiménez, “Combined kinetic analysis of solid-state reactions: a powerful tool for the simultaneous determination of kinetic parameters and the kinetic model without previous assumptions on the reaction mechanism.,” The journal of physical chemistry. A, vol. 110, no. 45, pp. 12456–62, Nov. 2006.

W. M. Pitts, A. V. Murthy, J. L. de Ris, J. R. Filtz, K. Nygård, D. Smith, and I. Wetterlund, “Round robin study of total heat flux gauge calibration at fire laboratories,” Fire Safety Journal, vol. 41, pp. 459–475, 2006.

A. Poulsen and G. Jomaas, “Experimental Study on the Burning Behavior of Pool Fires in Rooms with Different Wall Linings,” Fire Technology, vol. 48, pp. 419–439, 2012.

A. Poulsen and A. C. Bwalya, “An Experimental Study of the Effect of Thermal Radiation Feedback on the Room-Burning Behaviour of Horizontal Slabs of Polyurethane Foam,” Research Report No. 309. NRC Institute for Research in Construction, National Research Council Canada, 2011.

Q

S. Quinn, "Chemical blowing agents: providing production, economic and physical improvements to a wide range of polymers," Plastics, Additives and Compounding, vol. 3. pp. 16–21, 2001.

R

D. J. Rasbash, "Relevance of firepoint theory to the assessment of fire behaviour of combustible materials," International Symposium on Fire Safety of Combustible Materials, pp. 169–178, 1975.

D. J. Rasbash, "Theory in the evaluation of fire properties of combustible materials," Proceedings of the 5th International Fire Protection Seminar (Karlsruhe, September), pp. 113–130, 1976.

G. Rein, "Smouldering Combustion Phenomena in Science and Technology," *International Review of Chemical Engineering*, vol. 1, pp. 3–18, 2009.

P. Reszka, "In-Depth Temperature Profiles in Pyrolyzing Wood," Ph.D. thesis, The University of Edinburgh. http://hdl.handle.net/1842/2602, 2008.

S. J. Ritchie Steckler, K. D., Hamins, A., Cleary, T. G., Yang, J.C. and Kashiwagi, T., "The effect of sample size on the heat release rate of charring materials," Fire Safety Science 5, pp. 177–188, 1997.

Rockwool Limited. [Online]. Available: http://www.rockwool.co.uk. [Accessed: 01-Feb-2015].

"Rockwool factsheet. The way towards Nearly Zero Energy Buildings in EU." Rockwool International A/S Group Corporate Affairs, 2012.

Rockwool, "An introduction to Part L 2010," 2010. [Online]. Available: http://rwiumbracouknew.inforce.dk/media/270255/partl_u_values.pdf. [Accessed: 01-Feb-2015].

Rockwool, "Technical Data Sheet of Rocwool Cavity," 2011. [Online]. Available: http://www.rockwool.co.uk/products/u/2011.product/9838/building-insulation/rockwool%C2%AE-cavity. [Accessed: 08-Jan-2013].

Rockwool, "Technical Data Sheet of Rockwool Energysaver," 2011. [Online]. Available: http://www.rockwool.co.uk/products/u/2011.product/9841/building-insulation/rockwool-energysaver%C2%AE. [Accessed: 08-Jan-2013].

Rockwool, "Technical Data Sheet of HP Partial Fill Cavity Walls," 2011. [Online]. Available: http://www.rockwool.co.uk/products/u/2011.product/9844/building-insulation/hp-partial-fill-cavity-slab. [Accessed: 08-Jan-2013].

Rockwool, "Technical Data Sheet of Rockwool Flexi," 2011. [Online]. Available: http://www.rockwool.co.uk/products/u/2011.product/9908/building-insulation/rockwool-flexi%C2%AE. [Accessed: 08-Jan-2013].

S

P. E. Sánchez-Jiménez, L. A. Pérez-Maqueda, A. Perejón, and J. M. Criado, "Combined kinetic analysis of thermal degradation of polymeric materials under any thermal pathway," Polymer Degradation and Stability, vol. 94, no. 11, pp. 2079–2085, Nov. 2009.

B. Schartel, R. Kunze, and D. Neubert, "Red phosphorus–controlled decomposition for fire retardant PA 66," Journal of Applied Polymer Science, vol. 83, no. 10, pp. 2060–2071, 2002.

B. Schartel, M. Bartholmai, and U. Knoll, "Some comments on the use of cone calorimeter data," Polymer Degradation and Stability, vol. 88, no. 3, pp. 540–547, 2005.

B. Schartel and T. R. Hull, "Development of fire-retarded materials—Interpretation of cone calorimeter data," Fire and Materials, vol. 31, no. 5, pp. 327–354, 2007.

Scottish Government, "Building (Scotland) Regulations 2013: Technical Handbooks (Non Domestic) – Section 2 (Fire)." 2013.

M. J. Scudamore, P. J. Briggs, and F. H. Prager, "Cone calorimetry—a review of tests carried out on plastics for the association of plastic manufacturers in Europe," Fire and Materials, vol. 15, no. 2, pp. 65–84, 1991.

H. Sehaqui, M. Salajková, Q. Zhou, and L. A. Berglund, "Mechanical performance tailoring of tough ultra-high porosity foams prepared from cellulose I nanofiber suspensions," Soft Matter, vol. 6. p. 1824, 2010.

X. Shi, "Design optimization of insulation usage and space conditioning load using energy simulation and genetic algorithm," Energy, vol. 36, no. 3, pp. 1659–1667, Mar. 2011.

S. Singh, M. Ntiru-Karamagi, and M. Ritchie, "Optimizing polyiso blowing agents," in Proceedings of Polyurethanes Expo, 2005, pp. 402–408.

S. N. Singh, S. B. Burns, J. S. Costa, and V. Bonapersona, "Method of increasing the solubility of hydrocarbons and HFCs in polyurethanes raw materials and the effects on the performance and processing characteristics of construction foams," Cellular polymers, vol. 16, no. 6, pp. 444–467.

SIPs Eco Panels Ltd. [Online]. Available: http://www.sipsecopanels.co.uk. [Accessed: 01-Feb-2015].

Sips Industries Ltd.,"Our Strength is our Experience with Ten years in SIPs Manufacturing on three continents," 2012. [Online]. Available: http://www.sipsindustries.com. [Accessed: 08-Jan-2013].

J. Sjöström and R. Jansson, “Measuring thermal material properties for structural fire engineering,” in 15th International Conference on Experimental Mechanics, 2012.

M. X. Sørensen, “Small and medium scale fire experiments with different insulation materials,” M.Sc. Thesis, Technical University of Denmark, 2014.

M. Smolka and Y. Suurenbroek, “Smoke and heat emissions as measures for interaction of tested elements with test environment in fire resistance testing,” Proceedings of the 13th International Interflam Conference. Royal Holloway College, Nr Windsor, UK. 2013.

D. B. Spalding, “Combustion of liquid fuel in gas stream,” Fuel, vol. 29, no. 1, pp. 2–7, 1950.

S. M. J. Spence and A. Kareem, “Data-Enabled Design and Optimization (DEDOpt): Tall steel building frameworks,” Computers & Structures, vol. 129, pp. 134–147, Dec. 2013.

J. E. J. Staggs and R. H. Whiteley, “Modelling the combustion of solid-phase fuels in cone calorimeter experiments,” Fire and Materials, vol. 23, no. 2, pp. 63–69, 1999.

T. Steinhaus, “Determination of Intrinsic Material Flammability Properties from Material Tests assisted by Numerical Modelling,” Ph.D. thesis, The University of Edinburgh. http://hdl.handle.net/1842/3273, 2010.

Structural Insulated Panel Association (SIPA). [Online]. Available: http://www.sips.org. [Accessed: 08-Jan-2013].

B. Sundström, “The Development of a European Fire Classification System for Building Products Test Methods and Mathematical Modelling (Doctoral Thesis),” Lund University, 2007.

T

A. Tewarson, “Heat release rate in fires,” Fire and Materials, vol. 4, no. 4, pp. 185–191, 1980.

A. Tewarson, “Generation of Heat and Chemical Compounds in Fires,” in SFPE Handbook of Fire Protection Engineering, 3rd ed., P. J. DiNenno, D. Drysdale, C. L. Beyler, W. D. Walton, R. L. P. Custer, and J. M. Watts, Eds. NFPA, Quincy MA, 2002.

G. Thomas, “Modelling thermal performance of gypsum plasterboard-lined light timber frame walls using SAFIR and TASEF,” Fire and Materials, vol. 34, pp. 385–406, 2010.

P. H. Thomas, A. J. Heselden, and M. Law, “Fully-developed compartment fires - two kinds of behaviour,” Fire Research Technical Paper No. 18. Ministry of Technology and Fire Offices Committee, Joint Fire Research Organisation, FRS, London, UK, vol. 18, 1967.

W. M. Thornton, “The relation of oxygen to the heat of combustion of organic compounds,” Philosophical Magazine Series, vol. 33, pp. 196–203, 1917.

J. L. Torero, A. H. Majdalani, C. Abecassis-Empis, and A. Cowlard, “Revisiting the Compartment Fire,” in 11th International Symposium on Fire Safety Science, 2014.

J. H. Troitzsch, “How Do Foams Perform Under Fire Conditions?,” in Fire and cellular polymers, 1986, pp. 77–91.

K. Tsai, “Orientation effect on cone calorimeter test results to assess fire hazard of materials,” Journal of Hazardous Materials, vol. 172, no. 2–3, pp. 763–772, 2009.

V

I. Vitkauskienė, R. Makuška, U. Stirna, and U. Cabulis, “Thermal Properties of Polyurethane-Polyisocyanurate Foams Based on Poly (ethylene terephthalate) Waste,” vol. 17, no. 3, pp. 2–6, 2011.

C. Vovelle, R. Akrich, J. Delfau, and S. Gresillaud, “ Influence Of The Thickness On The Thermal Degradation Of PMMA,” Fire Safety Science 1, pp. 473–482, 1986.

W

C. Wade, “Future directions in fire testing of building products,” in Building for a Global Future – Australia’s Built Environment, 2003.

R. N. Walters, S. M. Hackett, and R. E. Lyon, “Heats of combustion of high temperature polymers,” Fire and Materials, vol. 24, pp. 245–252, 2000.

S. R. Wasan, P. Rauwoens, J. Vierendeels, and B. Merci, “Application of a simple enthalpy-based pyrolysis model in numerical simulations of pyrolysis of charring materials,” Fire and Materials, vol. 34, no. 1, pp. 39–54, 2010.

S. R. Wasan, P. Rauwoens, J. Vierendeels, and B. Merci, “An enthalpy-based pyrolysis model for charring and non-charring materials in case of fire,” Combustion and Flame, vol. 157, no. 4, pp. 715–734, 2010.

W. D. Weatherford Jr and D. M. Sheppard, “Basic studies of the mechanism of ignition of cellulosic materials,” Symposium (International) on Combustion, vol. 10, no. 1, pp. 897–910, 1965.

H. R. Wesson, J. R. Welker, and C. M. Sliepcevich, “The piloted ignition of wood by thermal radiation,” Combustion and Flame, vol. 16, no. 3, pp. 303–310, 1971.

S. Welch and P. Rubini, “Three-dimensional Simulation of a Fire-resistance Furnace,” Fire Safety Science, vol. 5. pp. 1009–1020, 1997.

U. Wickström, “Adiabatic Surface Temperature and the Plate Thermometer for Calculating Heat Transfer and Controlling Fire Resistance Furnaces,” Fire Safety Science, vol. 9, pp. 1227–1238, 2008.

R. Wiedermann, “Fire properties of isocyanate based rigid foams,” in Fire and cellular polymers, 1986.

M. Wojdyr, “Fityk: a general-purpose peak fitting program,” Journal of Applied Crystallography, vol. 43, no. 5, pp. 1126–1128, Sep. 2010.

W. D. Woolley, “Are Foams a Fire Hazard?,” in Fire and cellular polymers, 1986, pp. 61–75.

J. R. Wunsch, “Polystyrene – Synthesis, Production and Applications.” iSmithers Rapra Publishing, 2000, p. 15.

X

Xtratherm Ltd. [Online]. Available: http://www.xtratherm.com/. [Accessed: 01-Feb-2015].

Xtratherm, “Technical Data Sheet of CavityTherm,” 2013. [Online]. Available: http://www.xtratherm.com/wp-content/uploads/2013/12/Xtratherm-CT-PIR-12pp-12.13_LOW_RES.pdf. [Accessed: 01-Feb-2015].

Xtratherm, “Technical Data Sheet of Xtratherm Cavity-Plus XT/CWP,” 2012. [Online]. Available: http://www.xtratherm.com/wp-content/uploads/2012/10/Thin-R-XT-CW-4pp-Web-1.pdf. [Accessed: 01-Feb-2015].

Xtratherm, “Technical Data Sheet of Xtratherm Cavity-Plus SR/CW,” 2012. [Online]. Available: http://www.xtratherm.com/wp-content/uploads/2012/06/Xtratherm-SR-CW-4pp-28.6.12.pdf. [Accessed: 01-Feb-2015].

Y

X. S. Yang, Engineering Optimization: An Introduction with Metaheuristic Applications. 2010.

W. Yu, B. Li, H. Jia, M. Zhang, and D. Wang, “Application of multi-objective genetic algorithm to optimize energy efficiency and thermal comfort in building design,” Energy and Buildings, vol. 88, pp. 135–143, Feb. 2015.

Z

M. G. Zabetakis, “Flammability characteristics of combustible gases and vapours,” US Bureau of Mines. Bulletin 627, 1965.

J. Zhang, G.W.H. Silock, and T.J. Shields, “Study of the combustion and fire retardancy of polyarylonitrile and its copolymers by using cone calorimetry,” Journal of Fire Sciences, vol. 13, pp. 141–161, 1995.

Y. Zhang, S. Shang, and X. Zhang, “Influence of the composition of rosin-based rigid polyurethane foams on their thermal stability,” Journal of Applied Polymer Science, pp. 1167–1171, 1996.

R. Zhao and J. Sanjayan, “Test method for concrete spalling using small electric furnace,” Fire and Materials, vol. 34, no. 4, pp. 189–201, 2009.

Appendix A.

Experimental Methods Review

A.1 Sensitivities of bench-scale testing (Cone Calorimeter and Fire Propagation Apparatus)

The Cone Calorimeter [1] and the Fire Propagation Apparatus [2] are established as the most common bench-scale tests for fire science. These instruments are based on an external radiant heat source that transfers energy to the surface of a studied material. The gases produced by the pyrolysis and combustion of the material are collected and analysed. This testing procedure allows examining the flammability and combustibility of materials, as well as how the heat is transferred through the material if temperatures are measured within the solid sample by the use of thermocouples. Although these testing procedures are well established, several sensitivities from each of the elements are accounted.

A review of the main sensitivities associated to the use of the Cone Calorimeter and the Fire Propagation Apparatus are presented below, so as to set a baseline for the analyses and experimental set-ups presented in Chapter 5 and 6.

A.1.1 Heat source

Two factors are analysed in this section: the range of radiant heat fluxes to be used for bench-scale testing and the nature of radiant heat flux imposed.

A.1.1.1 Range of radiant heat fluxes

The radiant heat flux used for bench-scale testing is similar to the heat fluxes produced in real fires in order to test the combustible materials under similar thermal severity. However, as noted in Chapter 5 and 6, the mechanisms of convection in a real fire and in a controlled environment in the lab are different. While the conditions in the lab are characterised by cooling convection with a heat transfer coefficient determined by the orientation and size of the sample, the convection mechanism in a real fire can be characterised as heating or cooling and with a heat transfer coefficient dependent on the velocity of the gas-phase.

Several authors have studied the different range of heat fluxes produced in real compartment fires. The ranges can be classified depending on the stage of the fire, pre-flashover or post-flashover.

Babrauskas et al. [3] identified the value of 25 $kW \cdot m^{-2}$ to be the lower bound of the data studied, with a range of 25-45 $kW \cdot m^{-2}$ being the common heat fluxes on walls. Moreover, *Scudamore et al.* [4] recommended fluxes in the range of 25-30 $kW \cdot m^{-2}$ for developing fires (pre-flashover fires) and 50-75 kW/m^2 for developed fires (post-flashover fires) for wall linings. More recently, *Majdalani* [5] studied the behaviour of post-flashover fires by altering the ventilation factor and modifying the heat released in the compartment. For the worst case scenario, the maximum fluxes that were registered where in the range of 130-180 $kW \cdot m^{-2}$ for walls and ceilings.

During developing fires, low values of the radiant heat flux may represent the situation of fires away from the material, while high values of external heat flux may represent the situation of fire impinging directly the element to be tested.

The radiant heat fluxes to be used for testing of the materials should be similar to those which the materials could receive when tested in a real fire. However, this is a wide range, so different heat fluxes should be analysed in order to study the behaviour of the studied materials. In the same way, it is also important to test different range of heat fluxes in order to obtain flammability parameters such as the critical heat flux and thermal response parameters. Additionally, it should be considered that insulation materials are usually installed covered with a lining product, which means that absorbed heat fluxes obtained by bench-scale testing do not correspond to actual heat absorbed in a real scenario. However, the information obtained by bench-scale testing may be extrapolated if a rigorous heat transfer analysis is undertaken.

If further material characterisation is pursued, the used radiant heat fluxes should cover a range that allows isolation and/or determination of the different phenomena taking place during the exposure of heat. Indeed, different thermal degradation reactions occur at certain temperatures, but this is actually determined by the heat absorbed by the material. Hence, it is important to understand the fundamental mechanisms that govern these phenomena, which are determined by the thermal properties and activation energies of the thermal degradation reactions.

A.1.1.2 Source of radiant heat

The Cone Calorimeter is based on an electrical rod heater while the FPA consists of IR heaters containing tungsten filament tubular quartz lamps. These systems emit radiation at different wavelengths, which might affect the absorption of radiation by the surface of the sample.

Additionally, in-depth absorption (transmission) is not been usually taken into account, assuming that the radiant heat flux is absorbed only by the exposed face of the sample. However, *Bal and Rein* [6] recently studied the importance of in-depth radiation and pyrolysis chemistry in bench-scale testing for translucent materials such as PMMA. Different methods can be used to reduce the in-depth absorption such as the use of black carbon coating referred by the FPA standard [2].

The IR lamps in the FPA assembly present an advantage over the rod of the Cone Calorimeter. Indeed, the lamps of the FPA can impose a time-varying heat flux by controlling the voltage since the response of the system is relatively fast. The voltage can be controlled by computer communication programs. If this is to be achieved by systems such as radiant panels or the rod of the Cone Calorimeter, some modifications must be introduced so as to allow the system to move from its position during the experiments with respect to the exposed surface of the studied material. This approach has been presented by *Maluk* [7], demonstrating the potential of this tool for characterisation of material performance. A similar solution could be achieved for the Cone Calorimeter.

A.1.2 Material

As described in Chapter 2, the thermal decomposition of solids can proceed under different processes depending on the nature of the material, composition and additives such as flame retardants. This determines the burning behaviour observed in bench-scale testing.

The burning behaviour under a system like the Cone Calorimeter, and particularly the behaviour related to the curves of measured heat release rate (HRR) when flaming combustion is produced, has been largely studied. Then, the nature of the material can be classified according to the behaviour observed during the test; however, these also depend on the thickness of the samples. Some of the most common behaviours summarised by *Schartel and Hull* [8] are listed below:

- **Thick and non-charring samples** show a steady-state of HRR after ignition. Then a final peak of HRR is produced before flame extinction, which is due to the reduction on heat losses by conduction during the end of the test.
- **Thick charring samples** show an initial peak of HRR. Then, the HRR and mass loss rate decreases because of the in-depth increase of the char layer.
- **Thick charring samples** can also show an ending peak of HRR due to cracking of the char, likely due to reduction of heat losses by conduction.
- **Thin samples** normally show a peak of heat release rate (pHRR) without a steady-state of burning, which is because all the material tends to burn at the same time.

As noted by *Drysdale* [9], material properties such as thermal inertia ($k\rho c$) also have a significant impact on the fire behaviour. Low values of thermal inertia combined with a large thickness lead to a drastic reduction of heat losses through the in-depth of the material. This is the particular case of the studied materials for this thesis. Therefore, a rapid increase of the temperature at the exposed face is expected, leading to the fast ignition of the material.

With regard to additives such as flame retardants, several studies have been performed. As addressed by *Schartel and Hull* [8], the fire behaviour of materials with and without retardants tends to be different. The presence of fire retardants leads to the formation of char layers in the material. Therefore, the reactions of decomposition are modified or new reactions are included as char formation. *Schartel et al.* [10] studied the behaviour of glass fibre-reinforced polyamide 6.6 (PA66/GF), where they found that for flame-retarded PA66 with red phosphorus, the total heat evolved is reduced, while this effect is diminished when the external heat flux is increased. The relation $pHRR/t_{ig}$ was strongly reduced as well.

Modesti and Lorenzetti [11] studied the fire performance of some polyisocyanurate and polyurethane foams with halogen-free flame retardants. These were tested by the Cone Calorimeter with an external radiant heat flux of 50 $kW \cdot m^2$. The results showed low heat release rate and mass loss rate. In another study developed by *Modesti and Lorenzetti* [12, 13] on flame retardancy of PUR-PIR, they found that the effectiveness of the char layers created by different flame retardants is not the same. Therefore, not

only the fact of having flame retardants in the materials changes the mechanisms of decomposition of the material and heat release rate, but also the concentration which is found to strongly determine the obtained results.

A.1.3 Sample size (surface dimensions)

The suitable size of the sample for bench-scale testing has been studied by different authors, in order to determine a suitable standard size for bench-scale testing, so the results obtained could be extrapolated to real-scale fires.

Babrauskas et al. [14] referenced the study done on pool fires by *Blinov and Khudiakov* [15], in order to explain how the size of the sample can influence the burning rate obtained in bench-scale tests. This study showed that for small pool fires, with a diameter of 1 cm and less, the burning rate is increased and it decreases as the diameter increases until reaching a minimum at approximately 10 cm. After this regime, the burning rate increases with the diameter up to a constant level, where the burning rate becomes independent of the diameter of the pool. This phenomenon, known as the *Blinov and Khudiakov* curve, can be explained in terms of the three different regimes of the pool fire flames (laminar, transition and turbulent regime) where the different mechanisms of heat transfer, convection and radiation, have relative importance [16].

Babrauskas et al. [14] found that some materials could be tested with samples of 7.5 cm x 7.5 cm due to consistency of the results with samples of other dimensions. Nevertheless, other materials showed substantial differences. These results were compared to the results obtained by *Nussbaum et al.* [17] who compared samples of 20 x 20 cm to samples of 10 x 10 cm for the Cone Calorimeter test. The results showed higher HRR per unit area for the largest specimens. *Babrauskas et al.* concluded that specimens of 10 x 10 cm are the suitable size for bench-scale tests such as the Cone Calorimeter as that size corresponds to the minimum of the *Blinov and Khudiakov* curve.

Ritchie et al. [18] studied the influence of the sample size on the heat release rate of charring materials. For sample sizes between 10 cm and 60 cm of diameter the influence to the heat release rate was low with exception of the initial peak of burning rate.

Lindholm et al. [19] recently studied the impact of the sample size in the results of the Cone Calorimeter for different materials (plywood, PP and PU adhesive) in order to verify whether smaller sample sizes are suitable for bench-scale testing. The sizes of the samples studied were 10 cm x 10 cm, 7 cm x 7 cm and 5 cm x 5 cm. It was identified that changing the sample size for rapidly burning materials having a high pHRR, such as PP, strongly affects the results of heat release rate. However, the materials with lower pHRR, such as plywood and PU adhesive, show a stable behaviour when the sample size is decreased. Also, the effective heat of combustion was found not to be influenced by changing the sample size.

Hadden [20] recently studied the effect of the sample size on the smouldering and flaming ignition of polyurethane foam. The analysed sample sizes were 5 cm, 10 cm and 14 cm. The results showed that for larger sample sizes, the critical heat flux is increased for both smouldering and flaming ignition. No measures of heat release rate were taken after ignition.

A.1.3.1 Sample thickness

The sample thickness affects the time to ignition and also the decomposition of the samples to study. As mentioned before, the thermal decomposition and burning behaviour strongly depends on the nature of the material tested.

The time to ignition is governed by the heat losses by conduction through the sample. When time to ignition is independent of the thickness of the sample, the condition of thermally thick solid can be assumed. The assumption of thermally thick, or semi-infinite solid, refers to the condition that the thermal wave does not reach the back face of the sample before ignition is produced at the exposed face. It can be assumed that the thermally thick condition is achieved if the following condition is achieved [21]:

$$L > 4 \cdot \sqrt{\kappa \cdot t} \tag{A.1}$$

where L is the thickness of the sample, κ is the thermal diffusivity of the material and t is the time of exposure.

Some studies showed that the time to ignition is not affected for samples thicker than 50 mm [22, 23]. For particleboards, a minimum thickness above which the material can be assumed to be thermally thick was proposed. This thickness can be calculated using the following expression referred by *Babrauskas and Parker* [24]:

$$L = 0.6 \cdot \frac{\rho}{\dot{q}''} \tag{A.2}$$

where ρ are the thickness and density of the sample respectively, and $\dot{q}''$ is the external radiant heat flux.

Otherwise, the value of time to ignition is affected by the backing material when non-thermally thick materials are tested due to the heat losses by conduction until the top surface reaches the ignition temperature.

Different authors have studied the influence of the thickness of the sample on the results of heat release rate and mass loss rate of certain materials in bench-scale testing. *Vovelle et al.* [25] studied the influence of the thickness on the thermal degradation of a non-charring material as PMMA. For this material, the mass loss rate was found to be dependent on the thickness below a critical thickness.

Filipczak et al. [26] studied the influence of the thickness of PMMA samples on the rate of heat release. The results showed a more stable steady-state of heat release rate for samples with larger thickness. The thinnest samples did not show a steady-state burning, which is consistent with the results obtained by *Vovelle et al.* Moreover, an increased peak of heat release rate followed the steady-state burning for thick

samples, being larger for thinner samples. This behaviour can be explained due to the influence of the rear boundary condition, described in the following sections.

Similar results for a non-charring material (PP-g-MA) were found by *Zhang et al*. [27].For a residue-forming material (HIPS/$Mg(OH)_2$), the time of peak of heat release rate remained constant for different thicknesses.

These studies show that the thickness of the sample strongly affects the heat release rate and mass loss rate of the material. The results obtained by different authors suggest that below a critical thickness, the thermally thick condition is no longer applicable, which leads to a non-steady burning or thermal degradation. Moreover, the nature of the material has been highlighted again. Therefore, an analysis on whether the assumption of thermally thick is applicable to the samples is required, in order to characterise the thermal decomposition of the materials to test. Similar thickness to the end-use condition is also an important factor to be taken into account in order to obtain results to be extrapolated to real conditions.

The end-use condition of the insulation materials in energy efficient buildings has been explored and, for the different typologies of walls, thicknesses larger than 50 mm are expected in order to improve their thermal performance and meet the regulations. Thicknesses up to 200 mm are possible depending on the insulation material used and the use of the building. These thicknesses are much larger than the maximum thickness referred in the standard tests [1, 2] (typically 25.4 mm).

A.1.4 Sample orientation

The suitable orientation of the sample has been largely discussed and studied by different authors. The orientation of the sample in bench-scale testing does not have to be as in the end-use orientation of the product. This is because the results obtained by bench-scale testing have to be understood as apparatus independent. As *Janssen* [28] recognises, none of the two possible orientations, neither horizontal nor vertical, is comparable to the actual situation in real fires, due to convective flows and range of radiant heat fluxes from the flame.

Results obtained using different orientations of the sample can be slightly different. *Atreya et al.* [29] evaluated that ignition times are shorter with the horizontal orientation than with the vertical orientation for mahogany specimens. Similar results were found by *Kashiwagi* [30] for PMMA and red oak. *Östman et al*. [31] developed bench-scale tests of building materials with different sample orientations. This work was reviewed by *Babrauskas and Parker* who reached the same conclusion. Furthermore, specimens of PMMA and redwood were tested with different orientations. Shorter ignition times were only clearly identified for the PMMA. *Babrauskas and Parker*[24] appointed the shorter ignition times with the horizontal orientation of the sample in two reasons:

- A horizontal orientation presents a lower flammability limit than the vertical orientation, while with the vertical orientation the boundary layer is thinner and shows a higher velocity.

- The temperature of ignition is reached earlier in the horizontal orientation because the convective cooling is higher for the vertical orientation.

Therefore, the samples should be tested in a vertical orientation as the thermal feedback from the flame of the sample is lower. *Babrauskas* [32] also recognises that this configuration is preferable for exploratory studies, when the flame needs to be probed and surface temperatures to be measured. Nevertheless, it is recognised that the normal orientation should be the horizontal as most of the products tend to melt and drip. Such phenomena prevent the vertical orientation to be used.

Recently, *Tsai* [33] tested materials such as PMMA, polyurethane foams and wooden products with the Cone Calorimeter in both horizontal and vertical orientations. The horizontal orientation of the sample gave shorter time to ignition, lower peak of heat release rate, identical heat release rate and longer burning time than the vertical orientation. Unlike the recommendations made by *Babrauskas et al.* and the Cone Calorimeter standard [1], *Tsai* recommended the use of the vertical orientation in order to obtain fire performance of materials for regulation of products.

It has been highlighted that despite many authors have reviewed this topic, there is not a single ideal solution. The advantages and drawbacks related to each configuration are listed below:

Table A.1. Summarised advantages and drawbacks for horizontal and vertical set-up

	Advantages	**Drawbacks**
Horizontal set-up	- Ideal for testing materials that melt or drip - Uniform heat transfer by convection.	- Possible not negligible gas phase absorption from the plume. - Shorter times to ignition because of lower heat losses. - Higher thermal feedback from the flames, if flammable tests are carried out. - Convective heat transfer coefficient dependent on the temperature of the cone.
Vertical set-up	- Lower gas phase absorption from the plume. - Vertical flow derives into higher losses by convection and longer times to ignition are reached.	- Difficult to test materials that melt or drip. - Not uniform heat transfer by convention. Higher heat transfer at the bottom (lower gas temperatures), lower heat transfer at the

	- Lower thermal feedback from the flames, if flammable tests are carried out. - An analytical solution for the flow in front of the surface can be determined.	top (higher temperatures of the gas).

A.1.5 Sample holder

An ideal sample holder would be the one which keeps an adiabatic boundary condition on the sides and bottom parts of the specimen to test as well as avoiding mass transfer through these sides. This is because bench-scale testing aims to obtain the heat release rate per unit area of a determined material; therefore this value can be extrapolated into a real-scale where the material burning surface can be understood as the sum of finite elements which behave as the sample tested in bench-scale testing. By assuming that the combustible material is divided into finite elements, it is assumed to have planes of symmetry where no heat or mass transfer can occur. This is the methodology defined by standard flammability tests carried out by the Cone Calorimeter [1] or the Fire Propagation Apparatus [2].

However, this approach is only valid for assessing the flammability of the material and it is difficult to use the obtained results for characterising the thermal degradation of the material as data for advanced pyrolysis models. Hence, this assumption allows obtaining a heat release rate as a value for zone modelling where it is assumed that the material remains physically unchanged and chemically unreactive until the ignition. If the pyrolysis of a material is to be studied, a well-defined rear boundary condition is required as detailed by *Carvel et al.* [34]. Therefore, depending on the objective to be pursued, a different set-up would be appropriate.

Regarding the influence of the sample holder for bench-scale testing, *Babrauskas et al.* [14] studied how specimen edge conditions affect the heat release rate in bench-scale testing. The heat release rate of several materials was analysed with different sample holders, such as aluminium foil layer, aluminium foil layer with a stainless steel frame and luminium foil layer with an experimental insulated edge frame. The results showed that the use of an edge frame is recommended when intumescent or laminated materials are tested; otherwise, the aluminium foil layer seems to suffice. They also recommended the insulation edge frame when accurate results are required, for example, when tasks of fire modelling are pursued.

Other authors found that the set-up of the sample holder affects the thermal feedback of the sample, altering the peak of heat release rate, due to the reduction of the heat losses by conduction during the last stages of burning when an insulator is used at the back of the sample.

Schartel et al. [8, 35] performed some tests on HIPS flammability with a standard and a modified sample holder. The modified sample holder consisted of a copper

plate placed behind the sample. The results showed that the set-up of the sample holder strongly affects the peak of heat release rate, which was significantly reduced in the tests carried out with the modified sample holder.

Staggs et al. [36] performed some modelling work of the combustion of solid-phase fuels in Cone Calorimeter experiments where it was shown that the peak of mass loss rate is strongly affected by the thermal properties of the sample holder and therefore the peak of heat release rate is affected as well.

These results are consistent with those obtained by *Carvel et al.* [34]. A standard and a modified sample holder were used for testing polyamide-6 (PA6; Nylon 6) by using the Cone Calorimeter. The modified sample holder was similar to that used by *Schartel et al.*, consisting of a block of aluminium at the back of the sample and was covered by insulation. A peak of heat release rate was obtained for those tests carried out with the standard sample holder. However, this peak did not appear when the materials were tested with the modified sample holder.

All authors concluded that the peak of mass loss rate or peak of heat release rate is not material characteristic and it depends on the set-up of the tests.

Babrauskas et al. [14] suggested that the peak of heat release rate is associated with surface tension phenomena of the remaining globules of material as they burn out. Thus, this phenomenon cannot be extrapolated to real-scale fires.

Therefore, it has been verified that a sample holder with a heat sink as a metallic block at the back of the sample is an appropriate bench-scale testing methodology, as it prevents the appearance of a peak of heat release rate or mass loss rate and has been proved not to be a material characteristic. Besides, as shown by *Carvel et al.* [34], this methodology allows simplifying the heat transfer problem and applying an improved boundary condition by considering the problem as an unidirectional conductive heat transfer. The metallic block at the back of the sample acts as a heat sink, since the losses by conduction through the insulation sample holder on the sides tend to be negligible compared to those obtained through the metallic block. The heat losses can be quantified as follows:

$$\dot{q}''_{cond} = \frac{1}{A} \cdot \frac{dT_b}{dt} \cdot m_b \cdot c_{p,b} \tag{A.3}$$

where $\dot{q}''_{cond}$ are the heat losses by conduction to the metallic block, A is the surface area of the sample and block, $\frac{dT_b}{dt}$ is the temporal variation of the temperature of the metallic block, and m_b and $c_{p,b}$ are the mass and specific heat capacity of the metallic bloc, respectively.

A schematic representation of the modified sample holder proposed by *Carvel et al.* is presented in the following figure:

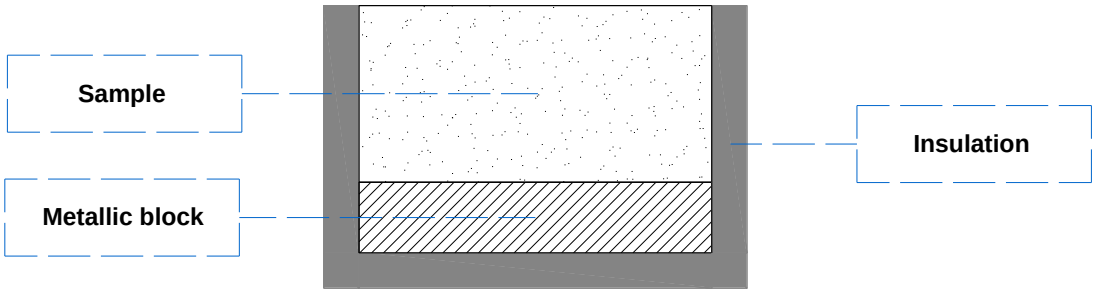

Figure A.1. Modified sample holder presented by Carvel et al. [34]

Nevertheless, the improvement achieved by this procedure is only valid when the sample material conductivity is higher than the insulation at the sides, i.e. $k_{ins\_holder} < k_{sample}$, and the thickness is not too large. In that case, the heat losses at the sides might not be negligible, since the thermal wave would arrive faster to the sides than to the bottom. This is the case of the experiments presented in Chapter 5 and 6, as the studied materials are insulation materials for construction, characterized for presenting significantly low conductivities, lower than the material used as insulation holder. Ceramic fibre paper is usually used as holder in the fire laboratory of the University of Edinburgh, which has a thermal conductivity in the range 0.07 – 0.12 $W \cdot m^{-1} \cdot K^{-1}$, depending on the temperature. In any case, during long processes of heat exposure, the use of the metallic plate allows reducing the uncertainty and determining the rear surface temperature as described in Chapter 6.

A.1.6 Oxygen concentration in the environment

As shown in Chapter 4, the concentration of oxygen plays an important role in the thermal degradation processes experienced by the material. If oxygen depleted atmospheres are used, the processes of thermal degradation are represented by pyrolysis. Nevertheless, if oxidant atmospheres are used (e.g. air), additional reactions of oxidation may occur, and the pyrolysis may be modified.

Some apparatuses like the FPA allow different concentrations of oxygen to be used; however the Cone Calorimeter does not provide this feature. In any case, the possible reduction of the oxidation processes was demonstrated by the use of a metallic plate at the surface so as to inhibit air diffusion onto the surface of the studied materials.

A.2 Calorimetry

A.2.1 Measuring heat release rate - Principles of calorimetry

The heat release rate is the most important variable in order to determine the severity of a fire. Several methods were developed in order to measure the heat release rate produced by the material burning and to provide understanding of the material contribution to a fire. Then, the main objectives of measuring the HRR are:

- To provide information of the fire performance and hazards of a material.
- To determine flammability/combustibility properties of materials that could be used for fire modelling.

Several methods have been developed for measuring the heat release rate in full, intermediate and bench-scale tests. These approaches are presented by *Babrauskas* [37], and a larger description of different methods for bench-scale testing is presented by *Janssens* [28]. Additionally, *Biteau* [38] presented an extended review of the state-of-the-art in calorimetry methods, most of them listed below:

- Sensible enthalpy rise method.
- Substitution method.
- Compensation method.
- **Species evolution approach: oxygen consumption (OC) and carbon dioxide generation methods (CDG).**
- **Mass loss rate approach (MLR).**

The species evolution and the mass loss rate approaches are considered for this review, since these are applied for experimental methods as those applied for this thesis.

A.2.2 Species evolution approach

The species evolution approach is originally based on *Thornton's principle* [39] which assumes that the energy released by the burning of a large amount of different organic materials is proportional to the amount of oxygen consumed by the combustion reaction. *Thornton* found this relation to be valid for different kind of gas and liquid organic materials. Later, *Hugget* [40] found that this assumption is also applicable for solid materials. *Tewarson* [41] also found that a similar principle related to the carbon dioxide generation from a combustion reaction is applicable. Indeed, the energy released in a combustion reaction was found to be proportional to the amount of carbon dioxide generated. Standard average values of these constant energy coefficients are noted in Equations (A.8) and (A.9).

These principles represent the basis of oxygen consumption (OC) and carbon dioxide generation (CDG) calorimetry, which can be expressed as follows:

$$\dot{Q} = \frac{\Delta H_c \cdot M_{fuel}}{\vartheta_{O_2} \cdot M_{O_2}} \cdot \Delta \dot{m}_{O_2} = E_{O_2} \cdot \Delta \dot{m}_{O_2} \tag{A.4}$$

$$\dot{Q} = \frac{\Delta H_c \cdot M_{fuel}}{\vartheta_{CO_2} \cdot M_{CO_2}} \cdot \Delta \dot{g}_{CO_2} = E_{CO_2} \cdot \Delta \dot{g}_{CO_2} \tag{A.5}$$

where $\dot{Q}$ is the heat release rate, ΔH_c is the heat of combustion of the burning fuel, M_{fuel}, M_{O_2} and M_{CO_2} are the molecular weight of the fuel, oxygen and carbon dioxide respectively, ϑ_{O_2} and ϑ_{CO_2} are the stoichiometric coefficients of the combustion reaction for oxygen and carbon dioxide, E_{O_2} and E_{CO_2} are the oxygen consumption and carbon dioxide generation energy coefficients and $\Delta \dot{m}_{O_2}$ and $\Delta \dot{g}_{CO_2}$ are the rate of oxygen consumption and rate of carbon dioxide generation respectively, which can be defined as follows:

$$\Delta \dot{m}_{O_2} = \dot{m}^0_{O_2} - \dot{m}_{O_2} \tag{A.6}$$

$$\Delta \dot{g}_{CO_2} = \dot{m}_{CO_2} - \dot{m}^0_{CO_2} \tag{A.7}$$

where the superscript 0 refers to the incoming air and the variables without superscript refer to the flow of exhaust gases from the burning material.

The fact that the energy coefficients remain approximately constant for a large amount of materials represents the main advantage of this approach, since information about the chemistry reaction is not required. It is also easy to implement this in intermediate or bench-scale tests as the gases can be collected from the exhaust duct used to evacuate the released gases from the combustion and then steered to the gas analysers. Bench-scale tests such as the Cone Calorimeter and the FPA use this methodology.

As noted by *Biteau* [38], *c*ertain assumptions are required if this method is applied:

- The energy or calorimetric coefficients are considered as constants. *Hugget* [40] proposed that the energy generated by the consumption of one unit mass of oxygen is:
$$E_{O_2} = 13.1 \pm 0.7 \text{ kJ} \cdot g_{O_2}^{-1} \quad \text{(A.8)}$$
- *Tewarson* [41] suggested that the energy generated by the generation of one unit mass of carbon dioxide can be considered as:
$$E_{CO_2} = 13.3 \pm 1.5 \text{ kJ} \cdot g_{CO_2}^{-1} \quad \text{(A.9)}$$
- More accurate values can be used if the chemistry of the burning material is known. Otherwise, these assumptions can be assumed as a baseline, and validation can be obtained by comparing results from both methods.
- If the gas species are considered as ideal gases, then the ideal gas law is applied:
$$P \cdot V = n \cdot R \cdot T \quad \text{(A.10)}$$
- The species considered for the calculation are oxygen (O_2), carbon dioxide (CO_2), carbon monoxide (CO), nitrogen (N), water (H_2O) and soot assumed to be carbon (C). The rest of the gases present in air are considered as nitrogen.
- Nitrogen is assumed not to intervene in the chemical reaction of combustion.
- The combustion is assumed to be a one-step reaction, expressed as follows:
$$C_xH_yO_z + \vartheta_{O_2}O_2 + \vartheta_{N_2}N_2 \rightarrow \vartheta_{CO_2}CO_2 + \vartheta_{CO}CO + \vartheta_{soot}soot + \vartheta_{H_2O}H_2O + \vartheta_{N_2}N_2 \quad \text{(A.11)}$$
- The analysed gases are collected when they are well-mixed.
- The flow is laminar in the exhaust duct.
- The measurements are performed in dry basis, i.e. water vapour is removed before the analysis.
- Vapour formed by the combustion is neglected; then water vapour content in the exhaust can be assumed equal to the vapour content in the inflow.
- The time response of the analysers allows obtaining the evolution in the chemistry of the combustion reaction.

A.2.3 MLR approach

This approach is based on assuming that the heat of combustion is an intrinsic property of the material, which is defined as the energy released by a unit mass of the

material in a complete combustion reaction. Its value can be obtained experimentally by means of a bomb calorimeter [42]. Nevertheless, a complete combustion reaction rarely occurs in real fires, where the efficiency of the combustion depends on several factors such as the type of material and the ventilation conditions.

The heat release rate of material involved in a real fire can be expressed as follows:

$$\dot{Q} = \chi \cdot \Delta H_c \cdot \dot{m}_{fuel} \tag{A.12}$$

where ΔH_c is the heat of combustion of the fuel, $\dot{m}_{fuel}$ is the mass loss rate of the burning material and χ is the efficiency of the combustion ($\chi \leq 1$). A value of $\chi = 1$ represents a complete combustion. Some authors usually define the heat release rate as a function of the effective heat of combustion:

$$\dot{Q} = \Delta H_{c,eff} \cdot \dot{m}_{fuel} \tag{A.13}$$

where $\Delta H_{c,eff}$ could be defined as:

$$\Delta H_{c,eff} = \chi \cdot \Delta H_c \tag{A.14}$$

However, the efficiency of the combustion reaction in real fires is lower than one, since many of the species released, such as the carbon monoxide and soot, do not get finally oxidised.

In order to calculate the heat release rate, if the heat of combustion is known, an efficiency of the combustion can be assumed regarding to the state of the material, solid, liquid or gas, as well as the ventilation conditions. Several values for well ventilated conditions can be found in [16, 43, 44]. A range from 0.7 to 1 is common for liquids and gases, while for solids the range is wider, from 0.4 to 0.9. Indeed, the efficiency of the combustion for solid materials tends to be lower than that for liquids and gases because the thermal decomposition of solid materials is characterised for presenting a more complex chemistry.

Another approach is the one explained by *Biteau* [38], by assuming that carbon dioxide, carbon monoxide and water vapour are the major products of the combustion reaction and the ratio of carbon monoxide – carbon dioxide is known. This ratio is expressed as:

$$\xi_{CO/CO_2} = \frac{Y_{CO}}{Y_{CO_2}} \tag{A.15}$$

The effective heat of combustion can be obtained by the following equation:

$$\Delta H_{c,eff} = \chi \cdot \Delta H_c = \frac{\Delta H_c + \xi_{CO/CO_2} \cdot \Delta H_{ic}}{1 + \xi_{CO/CO_2}} \tag{A.16}$$

considering the reactions of complete combustion and totally incomplete combustion yielding to carbon monoxide as noted in Equations (A.17) and Equation (A.18), respectively:

$$C_xH_yO_z + \left(x + \frac{y}{4} - \frac{z}{2}\right) O_2 \xrightarrow[\Delta H_c]{} xCO_2 + \frac{y}{2} H_2O \tag{A.17}$$

$$C_xH_yO_z + \left(\frac{x - z}{2} + \frac{y}{4}\right) O_2 \xrightarrow[\Delta H_{ic}]{} xCO + \frac{y}{2} H_2O \tag{A.18}$$

where ΔH_c and ΔH_{ic} are the heat of the reactions for complete combustion and incomplete combustion of carbon monoxide, respectively.

The mass loss rate approach presented provides a valuable result but requires knowledge on the heat of combustion and thermal decomposition of the material.

A.2.4 Formulation

A.2.4.1 Oxygen consumption (OC)

a. Derivation of the classical formulation

Janssens [28, 45, 46] worked on the formulation of the oxygen consumption principle defined in equation (A.4) when different species are obtained. The derivation of the formulation when only oxygen is measured, and species such as carbon dioxide and carbon monoxide are also obtained, is presented below. The formulation considering the soot generation was proposed by *Brohez* [47]; however, this is not presented.

Only oxygen measured

This formulation is based on the assumption that only oxygen and nitrogen are present in the gases analysed, and the analyses are made in dry conditions and the sample gas is previously filtered. Moreover, the water vapour generated in the combustion is assumed to be negligible. Thus, the following relation is satisfied:

$$X_{H_2O} = X^0_{H_2O} \tag{A.19}$$

Then, the mole fractions of oxygen measured by the analysers in the incoming air and in the exhaust gases are given by the following equations:

$$X^{A0}_{O_2} = \frac{\frac{\dot{m}^0_{O_2}}{M_{O_2}}}{\frac{\dot{m}_{O_2}}{M_{O_2}} + \frac{\dot{m}_{N_2}}{M_{N_2}}} = \frac{n^0_{O_2}}{n^0_{O_2} + n^0_{N_2}} = \frac{n^0_{O_2}}{n_a \cdot \left(1 - X^0_{H_2O}\right)} = \frac{\frac{\dot{m}^0_{O_2}}{M_{O_2}}}{\frac{\dot{m}_a}{M_a} \cdot \left(1 - X^0_{H_2O}\right)} \tag{A.20}$$

$$X^{A}_{O_2} = \frac{\frac{\dot{m}_{O_2}}{M_{O_2}}}{\frac{\dot{m}_{O_2}}{M_{O_2}} + \frac{\dot{m}_{N_2}}{M_{N_2}}} = \frac{n_{O_2}}{n_{O_2} + n_{N_2}} = \frac{n_{O_2}}{n_e \cdot \left(1 - X^0_{H_2O}\right)} = \frac{\frac{\dot{m}_{O_2}}{M_{O_2}}}{\frac{\dot{m}_e}{M_e} \cdot \left(1 - X^0_{H_2O}\right)} \tag{A.21}$$

where n_{O_2}, n_{N_2}, n_e and n_a are the moles of oxygen, nitrogen, exhaust air and incoming air, and the subscript A relates to the measurement by the analyser. The mass flow of oxygen in the incoming and exhaust flow can be obtained from the two equations above, resulting in:

$$\dot{m}^0_{O_2} = \frac{M_{O_2}}{M_{N_2}} \cdot \frac{X^{A0}_{O_2} \cdot \dot{m}_{N_2}}{1 - X^{A0}_{O_2}} = \frac{M_{O_2}}{M_a} \cdot \left(1 - X^0_{H_2O}\right) \cdot X^{A0}_{O_2} \cdot \dot{m}_a \tag{A.22}$$

$$\dot{m}_{O_2} = \frac{M_{O_2}}{M_{N_2}} \cdot \frac{X^{A}_{O_2} \cdot \dot{m}_{N_2}}{1 - X^{A}_{O_2}} = \frac{M_{O_2}}{M_e} \cdot \left(1 - X^0_{H_2O}\right) \cdot X^{A}_{O_2} \cdot \dot{m}_e \tag{A.23}$$

where $\dot{m}_a$ and $\dot{m}_e$ are the flow of gases in the inflow and outflow.

Assuming that the nitrogen does not participate in the combustion reaction, the incoming mass flow of nitrogen is the same as the mass flow of nitrogen after the combustion:

$$\dot{m}_{N_2}^0 = \dot{m}_{N_2} \tag{A.24}$$

Then, the oxygen consumption can be expressed as follows:

$$\dot{m}_{O_2}^0 - \dot{m}_{O_2} = \left[\frac{X_{O_2}^{A0} - X_{O_2}^{A}}{\left(1 - X_{O_2}^{A0}\right) \cdot \left(1 - X_{O_2}^{A}\right)}\right] \cdot \dot{m}_{N_2}^0 \cdot \frac{M_{O_2}}{M_{N_2}} \tag{A.25}$$

Taking Equation (A.4) and substituting (A.20) into equation (A.25), results the following expression for calculating the heat release rate:

$$\dot{Q}_{O_2}^{OC} = E_{O_2} \cdot \left[\frac{X_{O_2}^{A0} - X_{O_2}^{A}}{\left(1 - X_{O_2}^{A}\right)}\right] \cdot \dot{m}_a \cdot \frac{M_{O_2}}{M_a} \cdot \left(1 - X_{H_2O}^0\right) \tag{A.26}$$

The incoming flow of air can be obtained by the expression:

$$\dot{m}_a = \frac{\dot{m}_e}{1 + \phi \cdot (\alpha - 1)} \tag{A.27}$$

where ϕ is the oxygen depletion factor and α is the volumetric expansion factor. This equation is defined by *Janssens* [45], as a simplification of the following equation assuming that the molecular weight of the exhaust flow is the same as the inflow, i.e. $M_e = M_a$. This equation represents the mole/volumetric expansion in a combustion reaction.

$$\frac{\dot{m}_e}{M_e} = \frac{\dot{m}_a}{M_a} \cdot (1 - \phi) + \frac{\dot{m}_a}{M_a} \cdot \alpha \cdot \phi \tag{A.28}$$

Additionally, equation (A.26) is normally represented as a function of the depletion factor. Taking Equations (A.22) and (A.23), the oxygen depletion factor can be defined as the following equation. It must be noted that this form of the oxygen depletion factor is only valid when only oxygen is measured.

$$\phi_{O_2} = \frac{\dot{m}_{O_2}^0 - \dot{m}_{O_2}}{\dot{m}_{O_2}^0} = \frac{X_{O_2}^{A0} - X_{O_2}^{A}}{\left(1 - X_{O_2}^{A}\right) \cdot X_{O_2}^{A0}} \tag{A.29}$$

Finally, the heat release rate by oxygen consumption calorimetry when only oxygen is measured can be obtained using the following expression:

$$\dot{Q}_{O_2}^{OC} = E_{O_2} \cdot \frac{\phi_{O_2}}{1 + \phi_{O_2} \cdot (\alpha - 1)} \cdot \dot{m}_e \cdot \frac{M_{O_2}}{M_a} \cdot \left(1 - X_{H_2O}^0\right) \cdot X_{O_2}^{A0} \tag{A.30}$$

Oxygen, carbon dioxide and carbon monoxide measured

If additional measurements of carbon dioxide and carbon monoxide are considered, two main changes must be taken into account:

- The depletion factor has to be reformulated.

- Equation (A.4) is no longer valid as an incomplete combustion is now considered.

Firstly, the oxygen depletion correction is presented. As noted before, the nitrogen of the incoming air is assumed to be the same in the exhaust flow; hence Equation (A.24) is considered to be valid. If the following relations are considered:

$$X_{N_2}^0 \cdot \frac{\dot{m}_a}{M_a} = \frac{\dot{m}_{N_2}^0}{M_{N_2}} \tag{A.31}$$

$$X_{N_2} \cdot \frac{\dot{m}_e}{M_e} = \frac{\dot{m}_{N_2}}{M_{N_2}} \tag{A.32}$$

The mass flow of the oxygen of the incoming air and the exhaust flow can be expressed as follows:

$$\begin{aligned} \dot{m}_{O_2}^0 &= X_{O_2}^{A0} \cdot \dot{m}_a \cdot \frac{M_{O_2}}{M_a} = X_{O_2}^{A0} \cdot \frac{M_{O_2}}{M_{N_2}} \cdot \frac{\dot{m}_{N_2}^0}{X_{N_2}} \\ &= X_{O_2}^{A0} \cdot \frac{M_{O_2}}{M_{N_2}} \cdot \frac{\dot{m}_{N_2}^0}{\left(1 - X_{O_2}^{A0} - X_{CO_2}^{A0} - X_{CO}^{A0}\right)} \end{aligned} \tag{A.33}$$

$$\begin{aligned} \dot{m}_{O_2} &= X_{O_2}^{A} \cdot \dot{m}_e \cdot \frac{M_{O_2}}{M_e} = X_{O_2}^{A} \cdot \frac{M_{O_2}}{M_{N_2}} \cdot \frac{\dot{m}_{N_2}}{X_{N_2}} \\ &= X_{O_2}^{A} \cdot \frac{M_{O_2}}{M_{N_2}} \cdot \frac{\dot{m}_{N_2}}{\left(1 - X_{O_2}^{A} - X_{CO_2}^{A} - X_{CO}^{A}\right)} \end{aligned} \tag{A.34}$$

Then, by assuming negligible carbon monoxide in the incoming air, $X_{CO}^{A0} \approx 0$, the oxygen consumption can finally be expressed as follows:

$$\Phi_{O_2,CO_2,CO} = \frac{\dot{m}_{O_2}^0 - \dot{m}_{O_2}}{\dot{m}_{O_2}^0} = \frac{X_{O_2}^{A0} \cdot \left(1 - X_{CO_2}^{A} - X_{CO}^{A}\right) - X_{O_2}^{A} \cdot \left(1 - X_{CO_2}^{A0}\right)}{\left(1 - X_{O_2}^{A} - X_{CO_2}^{A} - X_{CO}^{A}\right) \cdot X_{O_2}^{A0}} \tag{A.35}$$

In order to consider an incomplete combustion, the energy coefficient of the combustion reaction to convert carbon monoxide into carbon dioxide, i.e. $E_{CO \rightarrow CO_2}$, has to be considered. Then, the heat release rate can be obtained according to the following expression:

$$\dot{Q}_{O_2,CO_2,CO}^{OC} = \dot{Q}_{tot} - \dot{Q}_{excess} \tag{A.36}$$

where $\dot{Q}_{tot}$ is the heat release rate assuming that a complete combustion is achieved because the carbon monoxide generated is oxidised with certain amount of oxygen, $\left(\Delta\dot{m}_{O_2}\right)_{excess-1}$. This factor can be expressed as follows:

$$\dot{Q}_{tot} = E_{O_2} \cdot \left(\dot{m}_{O_2}^0 - \dot{m}_{O_2} + \left(\Delta\dot{m}_{O_2}\right)_{excess-1}\right) \tag{A.37}$$

and $\dot{Q}_{excess}$ is the heat released by the reaction where the carbon monoxide is converted into carbon dioxide, obtained as:

$$\dot{Q}_{excess} = E_{CO \rightarrow CO_2} \cdot \left(\Delta\dot{m}_{O_2}\right)_{excess-1} \tag{A.38}$$

where $E_{CO \rightarrow CO_2}$is the energy released per unit mass of oxygen for the combustion of carbon monoxide represented by the following reaction:

$$CO + \frac{1}{2}O_2 \rightarrow CO_2 \tag{A.39}$$

Then, the heat release can be obtained as:

$$\dot{Q}^{OC}_{O_2,CO_2,CO} = E_{O_2} \cdot \left(\dot{m}^0_{O_2} - \dot{m}_{O_2}\right) - \left(E_{CO\rightarrow CO_2} - E_{O_2}\right) \cdot \left(\Delta\dot{m}_{O_2}\right)_{excess-1} \tag{A.40}$$

The first term of the right side of the equation can be substituted by Equation (A.30), while the second term depends on the factor $\left(\Delta\dot{m}_{O_2}\right)_{excess-1}$. Considering the oxidation reaction of carbon monoxide expressed in Equation (A.39), the mass flow of oxygen required can be expressed as:

$$\left(\Delta\dot{m}_{O_2}\right)_{excess-1} = \frac{1}{2} \cdot \dot{m}_{CO} \cdot \frac{M_{O_2}}{M_{CO}} = \frac{1}{2} \cdot \dot{m}_{O_2} \cdot \frac{X^A_{CO}}{X^A_{O_2}} \tag{A.41}$$

In order to express $\left(\Delta\dot{m}_{O_2}\right)_{excess-1}$ as a function of the oxygen depletion factor, if Equations (A.27) and (A.29) are considered, the mass flow of oxygen in the exhaust flow can be defined as follows:

$$\dot{m}_{O_2} = (1-\phi) \cdot \dot{m}^0_{O_2} = (1-\emptyset) \cdot \frac{M_{O_2}}{M_a} \cdot \frac{\dot{m}_e}{1+\phi\cdot(\alpha-1)} \cdot \left(1 - X^0_{H_2O}\right) \cdot X^{A0}_{O_2} \tag{A.42}$$

resulting in:

$$\left(\Delta\dot{m}_{O_2}\right)_{excess-1} = \frac{(1-\phi)}{2} \cdot \frac{X^A_{CO}}{X^A_{O_2}} \cdot \frac{M_{O_2}}{M_a} \cdot \frac{\dot{m}_e}{1+\phi\cdot(\alpha-1)} \cdot \left(1 - X^0_{H_2O}\right) \cdot X^{A0}_{O_2} \tag{A.43}$$

Eventually, by substituting equations (A.30) and (A.43) into (A.40), the heat release rate when oxygen, carbon dioxide and carbon monoxide are measured can be obtained as:

$$\begin{aligned}\dot{Q}^{OC}_{O_2,CO_2,CO} = &\left(E_{O_2} \cdot \phi_{O_2,CO_2,CO} - \left(E_{CO\rightarrow CO_2} - E_{O_2}\right) \cdot \frac{\left(1-\phi_{O_2,CO_2,CO}\right)}{2} \cdot \frac{X^A_{CO}}{X^A_{O_2}}\right) \\ &\cdot \frac{\dot{m}_e}{\left(1+\phi_{O_2,CO_2,CO}\cdot(\alpha-1)\right)} \cdot \frac{M_{O_2}}{M_a} \cdot \left(1 - X^0_{H_2O}\right) \cdot X^{A0}_{O_2}\end{aligned} \tag{A.44}$$

b. British Standard 476-13 (ISO 5660) [1]

The British Standard's formula is based on the equation derived by *Janssens* when oxygen, carbon dioxide and carbon monoxide are measured. Then, by considering Equation (A.44) and the following relations:

$$\frac{M_{O_2}}{M_a} = \frac{32g\cdot mol^{-1}_{O_2}}{29g\cdot mol^{-1}_{N_2}} \approx 1.10 \tag{A.45}$$

$$1 + \phi\cdot(\alpha-1) = 1 + \phi\cdot(1.105-1) = (1-\phi) + 1.105\cdot\phi \tag{A.46}$$

$$X^a_{O_2} = \left(1 - X^0_{H_2O}\right) \cdot X^A_{O_2} \tag{A.47}$$

$$\frac{\Delta h_c}{r_0} = E_{O_2} = 13.1\ kJ\cdot g^{-1}_{O_2} \tag{A.48}$$

$$E_{CO\rightarrow CO_2} = 17.6 \pm 0.7\ kJ\cdot g^{-1}_{O_2} \tag{A.49}$$

the heat release rate according to the British Standard 476-13 (ISO 5660) is expressed as:

$$\dot{Q}_{BS} = 1.10 \cdot \left(\frac{\Delta h_c}{r_0}\right) \cdot \dot{m}_e \cdot X_{O_2}^a \left(\frac{\phi_{O_2,CO_2,CO} - 0.172 \cdot \left(1 - \phi_{O_2,CO_2,CO}\right) \cdot \frac{X_{CO}^A}{X_{CO_2}^A}}{\left(1 - \phi_{O_2,CO_2,CO}\right) + 1.105 \cdot \phi_{O_2,CO_2,CO}} \right) \quad \text{(A.50)}$$

A.2.4.2 Carbon dioxide generation (CDG)

a. Derivation of the classical formulation

Tewarson [41] worked on the formulation of the oxygen consumption principle defined in Equation (A.5), but also included the term related to the mass flow of carbon monoxide in the incoming air and exhaust gases flows. Therefore, the heat release rate when carbon dioxide and carbon monoxide are measured can be obtained as:

$$\dot{Q}_{CO_2,CO}^{CDG} = E_{CO_2} \cdot \left(\dot{m}_{CO_2} - \dot{m}_{CO_2}^0\right) + E'_{CO} \cdot \left(\dot{m}_{CO} - \dot{m}_{CO}^0\right) \quad \text{(A.51)}$$

where E_{CO_2} is the energy released per unit mass of carbon dioxide generated and E'_{CO} is the energy released per unit mass of carbon monoxide generated. This coefficient can be calculated by applying the Hess' law, as a function of the energy coefficient for carbon dioxide E_{CO_2}, and the energy released per unit mole of carbon monoxide in a complete combustion ($\Delta H_{CO \to CO_2}$):

$$E'_{CO} = \frac{E_{CO_2} \cdot M_{CO_2} - \Delta H_{CO \to CO_2}}{M_{CO}} \quad \text{(A.52)}$$

If the following values are assumed: $E_{CO_2} = 13.3\ \text{kJ} \cdot g_{CO_2}^{-1}$, $M_{CO_2} = 44\ \text{g} \cdot \text{mol}^{-1}$, $\Delta H_{CO \to CO_2} = 283\ \text{kJ} \cdot \text{mol}_{CO}^{-1}$ and $M_{CO} = 28\ \text{g} \cdot \text{mol}^{-1}$, this coefficient results as:

$$E'_{CO} = 10.793\ \text{kJ} \cdot g_{CO}^{-1} \quad \text{(A.53)}$$

The mass flow of carbon dioxide of the incoming air and exhaust gases can be expressed as follows:

$$\dot{m}_{CO_2}^0 = X_{CO_2}^{A0} \cdot \frac{M_{CO_2}}{M_e} \cdot \dot{m}_a \cdot \left(1 - X_{H_2O}^0\right) \quad \text{(A.54)}$$

$$\dot{m}_{CO_2} = X_{CO_2}^{A} \cdot \frac{M_{CO_2}}{M_e} \cdot \dot{m}_e \cdot \left(1 - X_{H_2O}^0\right) \quad \text{(A.55)}$$

and similar expressions are obtained for the mass flow of carbon monoxide:

$$\dot{m}_{CO}^0 = X_{CO}^{A0} \cdot \frac{M_{CO}}{M_e} \cdot \dot{m}_a \cdot \left(1 - X_{H_2O}^0\right) \approx 0 \quad \text{(A.56)}$$

$$\dot{m}_{CO} = X_{CO}^{A} \cdot \frac{M_{CO}}{M_e} \cdot \dot{m}_e \cdot \left(1 - X_{H_2O}^0\right) \quad \text{(A.57)}$$

Then, the heat release rate can be expressed as given in Equation (A.58):

$$\dot{m} \quad \text{(A.58)}$$

$$\frac{\dot{m}_a}{M_a} \cdot \left(1 - X^0_{H_2O}\right) \cdot E_{CO_2} \cdot M_{CO_2} \cdot X^{A0}_{CO_2}$$

b. ASTM E2058 [2]

The formula derived by the ASTM standard is based on the following expression:

$$\dot{Q}_{chem} = E_{CO_2} \cdot \left(\dot{G}_{CO_2} - \dot{G}^0_{CO_2}\right) + E_{CO} \cdot \left(\dot{G}_{CO} - \dot{G}^0_{CO}\right) \quad \text{(A.59)}$$

where $\dot{G}_{CO_2}$ and $\dot{G}_{CO}$ are the generation of carbon dioxide and carbon monoxide respectively, and the superscript 0 refers to the measurements prior to ignition.

Unlike the formulation developed by *Janssens* and *Brohez*, here the formulation is directly based on the generation of species, i.e. the measurements in the exhaust duct but in different time instants. $\dot{G}_{CO_2}$ and $\dot{G}_{CO}$ represent the generation of carbon dioxide and monoxide after the ignition of the sample, and they can be calculated as:

$$\dot{G}_{CO_2} = \dot{m}_e \cdot \frac{M_{CO_2}}{M_a} \cdot X^A_{CO_2} \quad \text{(A.60)}$$

$$\dot{G}_{CO} = \dot{m}_e \cdot \frac{M_{CO}}{M_a} \cdot X^A_{CO} \quad \text{(A.61)}$$

where $\dot{G}^0_{CO_2}$ and $\dot{G}_{CO}$ are calculated as an average value of the measurements before ignition.

A.3 References

[1] "BS 476-15, ISO 5660-1. Fire tests on building materials and structures. Method for measuring the rate of heat release of products." BSI, 1993.

[2] "ASTM E2058. Standard Test Methods for Measurement of Synthetic Polymer Material Flammability Using a Fire Propagation Apparatus (FPA)." ASTM International, West Conshohocken, PA, 2009.

[3] V. Babrauskas, "Specimen heat fluxes for bench-scale heat release rate testing," *Fire and Materials*, vol. 19, no. 6, pp. 243–252, 1995.

[4] M. J. Scudamore, P. J. Briggs, and F. H. Prager, "Cone calorimetry—a review of tests carried out on plastics for the association of plastic manufacturers in Europe," *Fire and Materials*, vol. 15, no. 2, pp. 65–84, 1991.

[5] A. H. Majdalani, "Compartment Fire Analysis for Contemporary Architecture (Ph.D. thesis)," The University of Edinburgh, 2014.

[6] N. Bal and R. G., "Numerical investigation of the ignition delay time in black PMMA at high heat fluxes," *Proceedings of the 12th International Interflam Conference*. Nottingham, UK, pp. 685–696, 2010.

[7] C. Maluk, "Development and Application of a Novel Test Method for Studying the Fire Behaviour of CFRP Prestressed Concrete Structural (Ph.D. thesis)," The University of Edinburgh, 2014.

[8] B. Schartel and T. R. Hull, "Development of fire-retarded materials—Interpretation of cone calorimeter data," *Fire and Materials*, vol. 31, no. 5, pp. 327–354, 2007.

[9] D. Drysdale, "Fundamentals of the fire behaviour of cellular polymers," in *Fire and cellular polymers*, 1986, pp. 61–75.

[10] B. Schartel, R. Kunze, and D. Neubert, "Red phosphorus–controlled decomposition for fire retardant PA 66," *Journal of Applied Polymer Science*, vol. 83, no. 10, pp. 2060–2071, 2002.

[11] M. Modesti, A. Lorenzetti, F. Simioni, and M. Checchin, "Influence of different flame retardants on fire behaviour of modified PIR/PUR polymers," *Polymer Degradation and Stability*, vol. 74, no. 3, pp. 475–479, 2001.

[12] M. Modesti and A. Lorenzetti, "Flame retardancy of polyisocyanurate–polyurethane foams: use of different charring agents," *Polymer Degradation and Stability*, vol. 78, no. 2, pp. 341–347, 2002.

[13] M. Modesti and A. Lorenzetti, "Improvement on fire behaviour of water blown PIR–PUR foams: use of an halogen-free flame retardant," *European Polymer Journal*, vol. 39, no. 2, pp. 263–268, 2003.

[14] V. Babrauskas, W. H. Twilley, and W. J. Parker, "The effects of specimen edge conditions on heat release rate," *Fire and Materials*, vol. 17, no. 2, pp. 51–63, 1993.

[15] V. I. Blinov and G. N. Khudiakov, "Diffusion burning of liquids.," US Army translation, NTIR NO. AD296762, 1961.

[16] D. Drysdale, "Steady Burning of Liquids and Solids," in *An Introduction to Fire Dynamics*, John Wiley & Sons, Ltd, 2011, pp. 181–223.

[17] R. M. Nussbaum and B. A. L. Östman, "Larger specimens for determining rate of heat release in the cone calorimeter," *Fire and Materials*, vol. 10, no. 3–4, pp. 151–160, 1986.

[18] S. Ritchie, K. Steckler, A. Hamins, T. Cleary, J. Yang, and T. Kashiwagi, "The Effect Of Sample Size On The Heat Release Rate Of Charring Materials," *Fire Safety Science*, vol. 5. pp. 177–188, 1997.

[19] J. Lindholm, A. Brink, and M. Hupa, "Influence of decreased sample size on cone calorimeter results," *Fire and Materials*, vol. 36, no. 1, pp. 63–73, 2012.

[20] R. Hadden, "Smouldering and self-sustaining reactions in solids: an experimental approach (Ph.D. thesis)," The University of Edinburgh. http://hdl.handle.net/1842/5587, 2011.

[21] D. Drysdale, "Heat Transfer," in *An Introduction to Fire Dynamics*, John Wiley & Sons, Ltd, 2011, pp. 35–82.

[22] W. D. Weatherford Jr and D. M. Sheppard, "Basic studies of the mechanism of ignition of cellulosic materials," *Symposium (International) on Combustion*, vol. 10, no. 1, pp. 897–910, 1965.

[23] H. R. Wesson, J. R. Welker, and C. M. Sliepcevich, "The piloted ignition of wood by thermal radiation," *Combustion and Flame*, vol. 16, no. 3, pp. 303–310, 1971.

[24] V. Babrauskas and W. J. Parker, "Ignitability measurements with the cone calorimeter," *Fire and Materials*, vol. 11, no. 1, pp. 31–43, 1987.

[25] C. Vovelle, R. Akrich, J. Delfau, and S. Gresillaud, "Influence Of The Thickness On The Thermal Degradation Of Pmma," *Fire Safety Science*, vol. 1. pp. 473–482, 1986.

[26] R. Filipczak, S. Crowley, and R. E. Lyon, "Heat release rate measurements of thin samples in the OSU apparatus and the cone calorimeter," *Fire Safety Journal*, vol. 40, no. 7, pp. 628–645, 2005.

[27] J. Zhang, G. W. H. Silock, and T. Shields, "Study of the combustion and fire retardancy of polyarylonitrile and its copolymers by using cone calorimetry," *Journal of Fire Sciences*, vol. 13, pp. 141–161, 1995.

[28] M. Janssens, "Calorimetry," in *SFPE Handbook of Fire Protection Engineering*, 3rd ed., P. J. DiNenno, D. Drysdale, C. L. Beyler, W. D. Walton, R. L. P. Custer, and J. M. Watts, Eds. Massachusetts, U.S.A.: National Fire Protection Association, 2002.

[29] A. Atreya, C. Carpentier, and M. Harkleroad, "Effect Of Sample Orientation On Piloted Ignition And Flame Spread," *Fire Safety Science*, vol. 1. pp. 97–109, 1986.

[30] T. Kashiwagi, "Effects of sample orientation on radiative ignition," *Combustion and Flame*, vol. 44, no. 1–3, pp. 223–245, 1982.

[31] B. A. L. Östman, I. G. Svensson, and J. Blomqvist, "Comparison of three test methods for measuring rate of heat release," *Fire and Materials*, vol. 9, no. 4, pp. 176–184, 1985.

[32] V. Babrauskas, "The Cone Calorimeter," in *SFPE Handbook of Fire Protection Engineering*, 3rd ed., P. J. DiNenno, D. Drysdale, C. L. Beyler, W. D. Walton, R. L. P. Custer, and J. M. Watts, Eds. Massachusetts, U.S.A.: National Fire Protection Association, 2002.

[33] K.-C. Tsai, "Orientation effect on cone calorimeter test results to assess fire hazard of materials," *Journal of Hazardous Materials*, vol. 172, no. 2–3, pp. 763–772, 2009.

[34] R. Carvel, T. Steinhaus, G. Rein, and J. L. Torero, "Determination of the flammability properties of polymeric materials: A novel method," *Polymer Degradation and Stability*, vol. 96, no. 3, pp. 314–319, 2011.

[35] B. Schartel, M. Bartholmai, and U. Knoll, "Some comments on the use of cone calorimeter data," *Polymer Degradation and Stability*, vol. 88, no. 3, pp. 540–547, 2005.

[36] J. E. J. Staggs and R. H. Whiteley, "Modelling the combustion of solid-phase fuels in cone calorimeter experiments," *Fire and Materials*, vol. 23, no. 2, pp. 63–69, 1999.

[37] V. Babrauskas, "Heat Release Rates," in *SFPE Handbook of Fire Protection Engineering*, 3rd ed., P. J. DiNenno, D. Drysdale, C. L. Beyler, W. D. Walton, R. L. P. Custer, and J. M. Watts, Eds. Massachusetts, U.S.A.: National Fire Protection Association, 2002.

[38] H. Biteau, "Thermal and chemical behaviour of an energetic material and a heat release rate (Ph.D. thesis)," The University of Edinburgh. http://hdl.handle.net/1842/4620, 2009.

[39] W. M. Thornton, "The relation of oxygen to the heat of combustion of organic compounds," *Philosophical Magazine Series*, vol. 33, pp. 196–203, 1917.

[40] C. Huggett, "Estimation of rate of heat release by means of oxygen consumption measurements," *Fire and Materials*, vol. 4, no. 2, pp. 61–65, 1980.

[41] A. Tewarson, "Generation of Heat and Chemical Compounds in Fires," in *SFPE Handbook of Fire Protection Engineering*, 3rd ed., P. J. DiNenno, D. Drysdale, C. L. Beyler, W. D. Walton, R. L. P. Custer, and J. M. Watts, Eds. Massachusetts, U.S.A.: National Fire Protection Association, 2002.

[42] "BS EN ISO 1716. Reaction to fire tests for products — Determination of the gross heat of combustion (calorific value)." 2010.

[43] A. Tewarson, "Heat release rate in fires," *Fire and Materials*, vol. 4, no. 4, pp. 185–191, 1980.

[44] D. Drysdale, "Fire Science and Combustion," in *An Introduction to Fire Dynamics*, John Wiley & Sons, Ltd, 2011, pp. 1–34.

[45] M. L. Janssens, "Measuring rate of heat release by oxygen consumption," *Fire Technology*, vol. 27, no. 3, pp. 234–249, 1991.

[46] M. Janssens and W. J. Parker, "Oxygen Consumption Calorimetry," *Heat Release in Fires, edited by V. Babrauskas and S.J. Grayson*, vol. Chapter 3, pp. 31–59, 1992.

[47] S. Brohez, C. Delvosalle, G. Marlair, and A. Tewarson, "The Measurement of Heat Release from Oxygen Consumption in Sooty Fires," *Journal of Fire Sciences*, vol. 18. pp. 327–353, 2000.

Appendix B.

Material Fire Properties from the Literature

B.1 PUR and PIR

Table B.1 Properties of different polyurethane foams (PUR) (I)

ID	Thermal properties					
	Ref.	Density (kg/m^3)	Heat Capacity (kJ/kg·K)	Thermal conductivity (W/m·K)	Heat of combustion (kJ/g)	Melting point (ºC)
Polyurethane foams	*Drysdale*, Table 1.2 [1]	Variable	~1.4	Variable	24.4	-

ID	Thermal properties					
	Ref.	Density (kg/m^3)	Heat Capacity (kJ/kg·K)	Thermal conductivity (W/m·K)	α (m^2/s)	Thermal inertia $k\rho c$ (W^{2}s/m^{4}K^2)
Polyurethane foams	*Drysdale*, Table 1.2 [1] *Pitts and Sissom* [2] (0ºC – 20ºC)	20	1.4	0.034	1.2 x 10^{-6}	9.5 x 10^2

ID	Flammability parameters					
	Ref.	Heat of gasification L_v (kJ/g)	Heat flux from flame $\dot{Q}''_F$ (kW/m^2)	Heat losses $\dot{Q}''_L$ (kW/m^2)	Ideal mass loss rate $\dot{m}''_{ideal}$ (g/m^2·s)	Comments
Polyurethane foam (rigid)	*Drysdale*, Table 5.9 [3] *Tewarson and Pion* [4]	1.52	68.1	57.7	45	FPA of FM Global
Polyurethane foam (flexible)		1.22	51.2	24.3	32	FPA of FM Global
FR polyurethane foam (rigid)		1.19	31.4	21.3	26	FPA of FM Global

ID	Burning rate			
	Ref.	Emissivity	$\dot{m}''$ (g/m^2·s)	Comments
Polyurethane foam	*Drysdale*, Table 5.11 [3] *Markstein* [5]	0.17	8.2 ± 1.8	Data were deduced from a spreading fire Emissivity as measured 0.051 m above the fuel bed

ID	Rate of spread of flame				
	Ref.	Density (kg/m^3)	Orientation and direction	Rate of spread (mm/s)	Comments
Polyurethane	*Drysdale* 2nd,	15	0º	3.7	Unknown formulation of polyurethane
		22	0º	2.5	

	Table 7.6 [6] *Paul* (1979)	32	0º	1.6	

Table B.2. Properties of different polyurethane foams (PUR) (II)

ID	Effective flame spread properties					
	Ref.	Ignition temperature T_{ig} (ºC)	Thermal inertia $k\rho c$ (kW^2s/m^4K^2)	Flame spread parameter Φ (kW^2/m^3)	Critical surface temperature $T_{s,min}$ (ºC)	$\Phi / k\rho c$ (mK^2/s)
Polyurethane (S353M)	SFPE Handbook, 3rdEd. Table 2-12.2 [7]	280	-	-	105	82
ID	Critical heat flux and thermal response parameter					
	Ref.	CHF (kW/m^2)	TRP ($kW \cdot s^{1/2}/m^2$)	Comments		
Polyurethane foams	SFPE Handbook, 3rdEd. Table 3-4.2 [7]	13-40	55-221	ASTM E2058 Fire Propagation Apparatus		
ID	Surface Re-Radiation and Heats of Gasification					
	Ref.	Surface re-radiation (kW/m^2)	Heat of gasification L_v (kJ/g) ASTM E2058	Heat of gasification L_v (kJ/g) Cone	Heat of gasification L_v (kJ/g) DSC	Comments
Flexible polyurethane (PU) foams	SFPE Handbook, 3rdEd. Table 3-4.7 [7]	16-19	1.2-2.7	2.4	1.4	Reference 20 & 41 Chapter 3
Rigid polyurethane (PU) foams		14-22	1.2-5.3	5.6	-	
ID	Net Heats of Complete Combustion per Unit Mass of Fuel and Oxygen Consumed and Carbon Dioxide and Carbon Monoxide Generated					
	Ref.	Formula	ΔH_T (kJ/g)	ΔH_O (kJ/g)	ΔH_{CO2} (kJ/g)	ΔH_{CO} (kJ/g)
Flexible polyurethane foam (GM21)	SFPE Handbook, 3rdEd. Table 3-4.13 [7]	$CH_{1.8}O_{0.30}N_{0.05}$	26.2	12.1	11.5	8
Flexible polyurethane foam (GM23)		$CH_{1.8}O_{0.35}N_{0.06}$	27.2	13.7	12.5	9.7
Flexible polyurethane foam (GM25)		$CH_{1.7}O_{0.32}N_{0.07}$	24.6	12.0	11.1	7.5
Flexible polyurethane foam (GM27)		$CH_{1.7}O_{0.03}N_{0.08}$	23.2	11.2	10.4	6.2

Rigid polyurethane foam (GM29)		$CH_{1.1}O_{0.23}N_{0.10}$	26.0	12.6	10.7	6.8
Rigid polyurethane foam (GM31)		$CH_{1.2}O_{0.22}N_{0.10}$	25.0	11.9	10.2	6.1
Rigid polyurethane foam (GM37)		$CH_{1.2}O_{0.20}N_{0.08}$	28.0	12.7	11.2	7.5
ID	Yields of Fire Products for Well-Ventilated Fires					
	Ref.	y_{CO2}	y_{CO}	y_{ch}	y_S	Comment
Flexible polyurethane foam (GM21)	SFPE Handbook, 3rdEd. Table 3-4.14 [7]	1.55	0.010	0.002	0.131	Data measured in the ASTM E2058 fire propagation apparatus. All the data are reported for turbulent fires, that is, materials exposed to higher external heat flux values. (**)
Flexible polyurethane foam (GM23)		1.51	0.031	0.005	0.227	
Flexible polyurethane foam (GM25)		1.50	0.028	0.005	0.194	
Flexible polyurethane foam (GM27)		1.57	0.042	0.004	0.198	
Rigid polyurethane foam (GM29)		1.52	0.031	0.003	0.130	
Rigid polyurethane foam (GM31)		1.53	0.038	0.002	0.125	
Rigid polyurethane foam (GM37)		1.63	0.024	0.001	0.113	
ID	Chemical, Convective, and Radiative Heats of Combustion for Well-Ventilated Fires					
	Ref.	ΔH_T (kJ/g)	ΔH_{CH} (kJ/g)	ΔH_{CON} (kJ/g)	ΔH_{RAD} (kJ/g)	Comment
Flexible polyurethane foam (GM21)	SFPE Handbook, 3rdEd. Table 3-4.14 [7]	26.2	17.8	8.6	9.2	(**)
Flexible polyurethane foam (GM23)		27.2	19.0	10.3	8.7	
Flexible polyurethane foam (GM25)		24.6	17.0	7.2	9.8	
Flexible polyurethane foam (GM27)		23.2	16.4	7.6	8.8	
Rigid polyurethane foam (GM29)		26.0	16.4	6.8	9.6	
Rigid polyurethane foam (GM31)		25.0	15.8	7.1	8.8	

Rigid polyurethane foam (GM37)		28.0	17.9	8.7	9.2	
ID	Stoichiometric Yields of Major Products					
	Ref.	Ψ_O	Ψ_{CO2}	Ψ_{CO}	Ψ_S	Ψ_{HC}
Flexible polyurethane foam (GM21)	SFPE Handbook, 3rdEd. Table 3-4.16 [7]	2.24	2.28	1.45	0.622	0.715
Flexible polyurethane foam (GM23)		2.11	2.17	1.38	0.593	0.682
Flexible polyurethane foam (GM25)		2.16	2.22	1.41	0.606	0.692
Flexible polyurethane foam (GM27)		2.21	2.24	1.43	0.612	0.698
Rigid polyurethane foam (GM29)		2.22	2.42	1.54	0.660	0.721
Rigid polyurethane foam (GM31)		2.28	2.43	1.55	0.662	0.729
(GM37)		2.34	2.51	1.60	0.685	0.753
ID	Critical Mass Loss Rate for Ignition and Kinetic Parameter for Flame Extinction					
	Ref.	Critical mass loss rate ($g/m^2 \cdot s$)	Kinetic parameter	Comments		
Flexible polyurethane foam (GM21)	SFPE Handbook, 3rdEd. Table 3-4.28 [7]	5.6	0.16	Ignition data measured in the ASTM E2058 fire propagation apparatus		
Flexible polyurethane foam (GM23)		5.3	0.17			
Flexible polyurethane foam (GM25)		5.7	0.15			
Flexible polyurethane foam (GM27)		6.5	0.12			
Rigid polyurethane foam (GM29)		7.9	0.10			
Rigid polyurethane foam (GM31)		8.4	0.09			
Rigid polyurethane foam (GM37)		6.9	0.11			
ID	Critical Chemical, Convective, and Radiative Heat Release Rates for Flame Extinction					

	Ref.	Chemical HRR (kW/m^2)	Convective HRR (kW/m^2)	Radiative HRR (kW/m^2)	Comments
Polyurethane foams (flexibe)	SFPE Handbook, 3rdEd. Table 3-4.29 [7]	101	48	53	Critical mass loss rates from the ASTM E2058 fire propagation apparatus, and heats of combustion from Table 3-4.14
Polyurethane foams (rigid)		102	44	58	

Table B.3. Properties of different polyisocyanurate foams (PIR) (I)

ID	Thermal properties					
	Ref.	Density (kg/m^3)	Heat Capacity ($kJ/kg{\cdot}K$)	Thermal conductivity ($W/m{\cdot}K$)	Heat of combustion (kJ/g)	Melting point (ºC)
Polyisocyanurate foams	Drysdale, Table 1.2 [1]	Variable	-	Variable	24.4	chars
ID	Flammability parameters					
	Ref.	Heat of gasification L_v (kJ/g)	Heat flux from flame $\dot{Q}''_F$ (kW/m^2)	Heat losses $\dot{Q}''_L$ (kW/m^2)	Ideal mass loss rate $\dot{m}''_{ideal}$ ($g/m^2{\cdot}s$)	Comments
FR polyisocyanurate foam (rigid, with glass fibre)	*Drysdale*, Table 5.9 [3] *Tewarson and Pion* [4]	3.67	33.1	28.4	9 (peak of burning rate)	FPA of FMGlobal
FR polyisocyanurate foam (rigid)		1.52	50.2	58.5	33	FPA of FMGlobal
ID	Effective Flame Spread Properties					
	Ref.	Ignition temperature T_{ig} (ºC)	Thermal inertia $k\rho c$ (kW^2s/m^4K^2)	Flame spread parameter Φ (kW^2/m^3)	Critical surface temperature $T_{s,min}$ (ºC)	$\Phi / k\rho c$ (mK^2/s)
Polyisocyanurate (5.08 cm)	SFPE Handbook, 3rdEd. Table 2-12.2 [7]	445	0.02	4.9	275	201
ID	Surface Re-Radiation and Heats of Gasification					
	Ref.	Surface re-radiation (kW/m^2)	Heat of gasification L_v (kJ/g)	Comments		
Polyisocyanurate foams	SFPE Handbook, 3rdEd. Table 3-4.7 [7]	14-37	1.2-6.4	ASTM E2058 fire propagation apparatus under nonflaming fire conditions.		
ID	Net Heats of Complete Combustion per Unit Mass of Fuel and Oxygen Consumed and Carbon Dioxide and Carbon Monoxide Generated					
	Ref.	Formula	ΔH_T (kJ/g)	ΔH_O (kJ/g)	ΔH_{CO2} (kJ/g)	ΔH_{CO} (kJ/g)

Rigid polyisocyanurate foam (GM41)	SFPE Handbook, 3rdEd. Table 3-4.13 [7]	$CH_{1.0}O_{0.19}N_{0.11}$	26.2	12.5	10.4	6.4
Rigid polyisocyanurate foam (GM43)		$CH_{0.93}O_{0.20}N_{0.11}$	22.2	10.8	8.9	4.0
ID	Stoichiometric Yields of Major Products					
	Ref.	Ψ_O	Ψ_{CO2}	Ψ_{CO}	Ψ_S	Ψ_{HC}
Rigid polyisocyanurate foam (GM41)	SFPE Handbook, 3rdEd. Table 3-4.16 [7]	2.30	2.50	1.59	0.683	0.740
Rigid polyisocyanurate foam (GM43)		2.25	2.49	1.58	0.679	0.732

Table B.4. Properties of different polyisocyanurate foams (PIR) (II)

ID	Heat Release Rate					
	Ref.	Thickness (mm) Density (kg/m^3)	External heat flux (kW/m^2)	Time to ignition (s)	pHRR (kW/m^2)	Mean HRR from t_{ig} to 180s (kW/m^2)
PIR Foam (Aluminum foil holder)	*Babrauskas et al.* [8]	45 mm - $28kg/m^3$	50	6	83	54
PIR Foam (Steel frame holder)				34	67	27
PIR Foam (Insulated frame holder)				9	74	34

B.2 Phenolic foams

Table B.5 Properties of different phenolic foams (I)

ID	Surface Re-Radiation and Heats of Gasification					
	Ref.	Surface re-radiation (kW/m^2)	Heat of gasification L_v (kJ/g)	Comments		
Phenolic foam	SFPE Handbook, 3rdEd. Table 3-4.7 [7]	20	1.6	ASTM E2058 fire propagation apparatus under nonflaming fire conditions.		
Phenolic foam/FR		20	3.7			
ID	Net Heats of Complete Combustion per Unit Mass of Fuel and Oxygen Consumed and Carbon Dioxide and Carbon Monoxide Generated					
	Ref.	Formula	ΔH_T (kJ/g)	ΔH_O (kJ/g)	ΔH_{CO2} (kJ/g)	ΔH_{CO} (kJ/g)
Rigid phenolic foam	SFPE Handbook, 3rdEd. Table 3-4.13 [7]	$CH_{1.1}O_{0.24}$	36.4	16.8	14	12
ID	Chemical, Convective, and Radiative Heats of Combustion for Well-Ventilated Fires					
	Ref.	ΔH_T (kJ/g)	ΔH_{CH} (kJ/g)	ΔH_{CON} (kJ/g)	ΔH_{RAD} (kJ/g)	Comment

Phenolic foams 1	SFPE Handbook, 3rdEd. Table 3-4.14 [7]	-	10	-	-	Calculated from the data measured in the Cone Calorimeter as reported in References 20 and 39. All the data are reported for turbulent fires, that is, materials exposed to higher external heat flux values. (*)
Phenolic foams 2						
ID	Yields of Fire Products for Well-Ventilated Fires					
	Ref.	y_{CO2}	y_{CO}	y_{ch}	y_S	Comment
Phenolic foams 1	SFPE Handbook, 3rdEd. Table 3-4.14 [7]	-	-	-	0.002	(*)
Phenolic foams 2					-	
ID	Stoichiometric Yields of Major Products					
	Ref.	Ψ_O	Ψ_{CO2}	Ψ_{CO}	Ψ_S	Ψ_{HC}
Phenolic foam	SFPE Handbook, 3rdEd. Table 3-4.16 [7]	2.18	2.60	1.65	0.708	0.773
ID	Critical Mass Loss Rate for Ignition and Kinetic Parameter for Flame Extinction					
	Ref.	Critical mass loss rate ($g/m^2 \cdot s$)	Kinetic parameter	Comments		
Phenolic foam	SFPE Handbook, 3rdEd. Table 3-4.28 [7]	5.5	0.17	Ignition data measured in the ASTM E2058 fire propagation apparatus		

Table B.6 Properties of different phenolic foams (IV)

ID	Thermal properties					
	Ref.	Density (kg/m^3)	Heat Capacity ($kJ/kg \cdot K$)	Thermal conductivity ($W/m \cdot K$)	Heat of combustion (kJ/g)	Melting point (ºC)
Polyisocyanurate foams	*Drysdale*, Table 1.2 [1]	Variable	-	Variable	17.9	chars
ID	Flammability parameters					
	Ref.	Heat of gasification L_v (kJ/g)	Heat flux from flame $\dot{Q}''_F$ (kW/m^2)	Heat losses $\dot{Q}''_L$ (kW/m^2)	Ideal mass loss rate $\dot{m}''_{ideal}$ ($g/m^2 \cdot s$)	Comments

FR phenolic foam (rigid)	*Drysdale,* Table 5.9 [3] *Tewarson and Pion* [4]	3.74	25.1	98.7	11 (peak of burning rate)	FPA of FMGlobal

Table B.7 Properties of different phenolic foams (II)

ID	Fire Parameters									
	Ref.	Thickness - Density	Heat Flux (kW/m^2)	Time to ignition (s)	Mean pHRR$_{max}$ (kW/m^2)	Mean effective heat of combustion (MJ/kg)	Mean specific extinction area (m^2/kg)	Mean HRR from t_{ig} to 180s (kW/m^2)	Mean HRR overall (kW/m^2)	Smoke parameter (MW/kg)
Filled structural foam	*Scudamore et al.* [9]	14 mm - 250 kg/m^3	20	-	-	-	-	-	-	-
			30	31	35	9	14	15	23	1
			40	26	45	12	18	22	27	1
			50	26	44	9	13	31	29	1
			75	-	-	-	-	-	-	-
Insulation foam		50 mm - 37 kg/m^3	20	No well-defined flaming ignition	-	-	-	-	-	-
			30		-	-	-	-	-	-
			40		17	8	30	13	13	1
			50		19	8	30	16	15	1
			75		29	14	-	20	22	-
Glass-faced foam		13.5 mm - 87 kg/m^3 overall	20		-	-	-	-	-	-
			30		19	13	-	-	-	-
			40		66	19	12	14	9	14	0
			50		31	34	16	12	13	15	0
			75		28	17	16	22	21	17	0

Table B.8 Properties of different phenolic foams (III)

ID	Flammability parameters (LIFT)							
	Ref.	Heat Flux (kW/m^2)	Critical flux for spread (kW/m^2)	Ignition temperature T_{ig} (^{0}C)	Thermal inertia $k\rho c$ (kW^{2}s/m^{4}K^2)	Flame spread parameter Φ (kW^2/m^3)	Critical surface temperature $T_{s,min}$ (^{0}C)	$\Phi / k\rho c$ (mK^2/s)
Class I Phenolic Foam 2.6 lb/ft^2	*Cleary and Quintere* [10]	30	28	524	0.11	0.15	509	1.4

B.3 EPS

Table B.9 Properties of different EPS or PS (I)

ID	Thermal properties					
	Ref.	Density (kg/m^3)	Heat Capacity (kJ/kg·K)	Thermal conductivity (W/m·K)	Heat of combustion (kJ/g)	Melting point (^{0}C)
Polystyrene	*Drysdale,* Table 1.2 [1]	1100	1.2	0.11	41.6	240
ID	Flammability parameters					

	Ref.	Heat of gasification L_v (kJ/g)	Heat flux from flame $\dot{Q}''_F$ (kW/m²)	Heat losses $\dot{Q}''_L$ (kW/m²)	Ideal mass loss rate $\dot{m}''_{ideal}$ (g/m²·s)	Comments
Polystyrene (solid)	*Drysdale*, Table 5.9 [3] *Tewarson and Pion* [4]	1.76	61.5	50.2	35	FPA of FMGlobal
FR polystyrene foam (rigid)		1.36	34.3	23.4	25	

Table B.10 Properties of different EPS or PS (II)

ID	Effective flame spread properties					
	Ref.	Ignition temperature T_{ig} (°C)	Thermal inertia $k\rho c$ (kW²s/m⁴K²)	Flame spread parameter Φ (kW²/m³)	Critical surface temperature $T_{s,min}$ (°C)	$\Phi / k\rho c$ (mK²/s)
Polystyrene (5.08 cm)	SFPE Handbook, 3rdEd. Table 2-12.2 [7]	630	0.38	-	630	-
ID	Yields of Fire Products for Well-Ventilated Fires					
	Ref.	y_{CO2}	y_{CO}	y_{ch}	y_S	Comment
EPS	SFPE Handbook, 3rdEd. Table 3-4.14 [7]	1.9	0.054	-	-	(**)
ID	Chemical, Convective, and Radiative Heats of Combustion for Well-Ventilated Fires					
	Ref.	ΔH_T (kJ/g)	ΔH_{CH} (kJ/g)	ΔH_{CON} (kJ/g)	ΔH_{RAD} (kJ/g)	Comment
EPS	SFPE Handbook, 3rdEd. Table 3-4.14 [7]	-	28	-	-	(**)
ID	Critical heat flux and thermal response parameter					
	Ref.	CHF (kW/m²)	TRP (kW·s$^{1/2}$/m²)	Comments		
Polystyrene (PS)	SFPE Handbook, 3rdEd. Table 3-4.2 [7]	13	162	ASTM E2058 Fire Propagation Apparatus		
Polystyrene foams		10-15	111-317			
ID	Surface Re-Radiation and Heats of Gasification					
	Ref.	Surface re-radiation (kW/m²)	Heat of gasification L_v (kJ/g)	Comments		
Polystyrene (PS) foams	SFPE Handbook, 3rdEd. Table 3-4.7 [7]	10-13	1.3-1.9	ASTM E2058 fire propagation apparatus under nonflaming fire conditions.		
ID	Net Heats of Complete Combustion per Unit Mass of Fuel and Oxygen Consumed and Carbon Dioxide and Carbon Monoxide Generated					
	Ref.	Formula	ΔH_T (kJ/g)	ΔH_O (kJ/g)	ΔH_{CO2} (kJ/g)	ΔH_{CO} (kJ/g)

Polystyrene	SFPE Handbook, 3rdEd. Table 3-4.13 [7]	CH	39.2	12.7	12.2	9.2
Expanded polystyrene (GM47)		$CH_{1.1}$	38.1	12.4	11.3	7.7
Expanded polystyrene (GM49)		$CH_{1.1}$	38.1	12.4	11.3	7.7
Expanded polystyrene (GM51)		CH	35.6	11.6	10.8	7.0
Expanded polystyrene (GM53)		$CH_{1.1}$	37.6	12.4	11.3	7.7
ID	Yields of Fire Products for Well-Ventilated Fires					
	Ref.	y_{CO2}	y_{CO}	y_{ch}	y_S	Comment
PS	SFPE Handbook, 3rdEd. Table 3-4.14 [7]	2.33	0.060	0.014	0.164	(**)
Polystyrene foams (GM47)		2.30	0.060	0.014	0.180	
Polystyrene foams (GM49)		2.30	0.065	0.016	0.210	
Polystyrene foams (GM51)		2.34	0.058	0.013	0.185	
Polystyrene foams (GM53)		2.34	0.060	0.015	0.200	
ID	Chemical, Convective, and Radiative Heats of Combustion for Well-Ventilated Fires					
	Ref.	ΔH_T (kJ/g)	ΔH_{CH} (kJ/g)	ΔH_{CON} (kJ/g)	ΔH_{RAD} (kJ/g)	Comment
PS	SFPE Handbook, 3rdEd. Table 3-4.14 [7]	39.2	27.0	11.0	16.0	(**)
Polystyrene foams (GM47)		38.1	25.9	11.4	14.5	
Polystyrene foams (GM49)		38.2	25.6	9.9	15.7	
Polystyrene foams (GM51)		35.6	24.6	10.4	14.2	
Polystyrene foams (GM53)		37.6	25.9	11.2	14.7	
ID	Chemical and Convective Heat Release Parameters					
	Ref.	HRP_{CH} (ASTM E2058)	HRP_{CH} (ASTM E1354)	HRP_{CON} (ASTM E2058)	Comments	
Polystyrene	SFPE Handbook, 3rdEd. Table 3-4.15 [7]	16	19	6	HRP_{CH} (ASTM E1354) is calculated from the data reported in References 20 and 39	
Polystyrene foams (GM49)		19	-	8		
Polystyrene foams (GM51)		18	-	9		
Polystyrene foams (GM53)		20	-	6		
ID	Stoichiometric Yields of Major Products					
	Ref.	Ψ_O	Ψ_{CO2}	Ψ_{CO}	Ψ_S	Ψ_{HC}
Polystyrene	SFPE Handbook, 3rdEd. Table 3-4.16 [7]	3.08	3.38	2.15	0.923	1.00
Polystyrene foams (GM47)		3.10	3.36	2.14	0.916	1.00
Polystyrene foams (GM49)		3.10	3.36	2.14	0.916	1.00
Polystyrene foams (GM51)		3.08	3.38	2.15	0.923	1.00
Polystyrene foams (GM53)		3.10	3.36	2.14	0.916	1.00
ID	Critical Mass Loss Rate for Ignition and Kinetic Parameter for Flame Extinction					

	Ref.	Critical mass loss rate (g/m²·s)	Kinetic parameter	Comments
Polystyrene	SFPE Handbook, 3rdEd. Table 3-4.28 [7]	4.0	0.21	Ignition data measured in the ASTM E2058 fire propagation apparatus
Polystyrene		0.80	0.78	Ignition data measured at the University of Edinburgh, U.K.
Polystyrene foams (GM47)		6.3	0.11	Ignition data measured in the ASTM E2058 fire propagation apparatus
Polystyrene foams (GM49)		4.9	0.14	
Polystyrene foams (GM51)		6.3	0.10	
Polystyrene foams (GM53)		5.7	0.11	

ID	Critical Chemical, Convective, and Radiative Heat Release Rates for Flame Extinction				
	Ref.	Chemical HRR (kW/m²)	Convective HRR (kW/m²)	Radiative HRR (kW/m²)	Comments
Polystyrenes	SFPE Handbook, 3rdEd. Table 3-4.29 [7]	108	44	64	Critical mass loss rates from the ASTM E2058 fire propagation apparatus, and heats of combustion from Table 3-4.14

Table B.11 Properties of different EPS or PS (III)

ID	Flammability parameters (LIFT)							
	Ref.	Heat Flux (kW/m²)	Critical flux for spread (kW/m²)	Ignition temperature T_{ig} (ºC)	Thermal inertia $k\rho c$ (kW²s/m⁴K²)	Flame spread parameter Φ (kW²/m³)	Critical surface temperature $T_{s,min}$ (ºC)	$\Phi / k\rho c$ (mK²/s)
1 PCF FR EPS	*Cleary and Quintere* [10]	15	3.7	376	0.96	49	164	51
2 PCF FR EPS		15	<1.0	376	0.58	-	<60	-
Extruded PS		15	2.7	376	0.91	31	133	35
2 PCF FR EPS (50 mm)		15	2.9	376	0.91	46	139	51
2 PCF FR EPS (37.50 mm)		15	3.0	376	0.71	42	142	59
2 PCF FR EPS (25 mm)		15	4.8	376	0.65	104	194	161
2 PCF FR EPS (12.5 mm)		15	3.8	376	0.69	106	167	153

Table B.12 Properties of different EPS or PS (IV)

ID	Fire Parameters						
	Ref.	Heat Flux (kW/m²)	Time to ignition (s)	pHRR (kW/m²)	THR (MJ/m²)	Average Smoke Extinction Area (m2/kg)
Flame retardant treated EPS covered with steel skin	*Collier and Baker* [11–13]	25	1000	4.8	0.1	692
		26	1000	2.3	0.1	598
		27.5	128	6	0.4	1243
		30	176	217	17.2	1029
		50	83	97	18.6	1004
Flame retardant treated EPS not covered with steel skin		25	1000	3	0.2	842
		26	177	179	13.4	1254
		27.5	115	197.9	15.9	1424
		30	120	193.4	15.4	1351
		50	37	305.6	14.9	1394
Non-flame retardant treated EPS covered with steel skin		15	1400	2	0	110
		20	1000	4.3	0.9	870
		25	335	278	15.3	1232
		30	156	330	17.37	1009
		50	68	476.7	17.3	977
Non-flame retardant treated EPS not covered with steel skin		15	624	289.5	11.3	1139
		20	193	295.5	13.5	1255
		25	109	334.3	17.5	1273
		30	78	319.7	16.4	1261
		50	26	507.3	16.9	1174
Flame retardant treated EPS covered with steel skin a layer of 4.5 mm fibre-cement board between the EPS and the steel skin		30	1000	1.9	0	382
		40	236	64.8	24.1	351
		50	198	76.5	20.2	609
		60	156	91.3	26.8	469
		75	135	144.6	25.9	559

Table B.13 Properties of different EPS or PS (V)

ID	Fire Parameters									
	Ref.	Thickness (mm) Density (kg/m³)	Heat Flux (kW/m²)	Time to ignition (s)	Mean $pHRR_{max}$ (kW/m²)	Mean effective heat of combustion (MJ/kg)	Mean specific extinction area (m²/kg)	Mean HRR from t_{ig} to 60s (kW/m²)	Mean HRR overall (kW/m²)	Smoke parameter (MW/kg)
EPS non-FR	*Scudamore et al.* [9]	25 mm - 15 kg/m³	20	-	-	-	-	-	-	-
			30	73	299	27	1317	146	214	394
			40	28	394	28	1200	173	228	473
			50	18	407	28	1346	158	209	546
EPS FR			20	-	-	-	-	-	-	-
			30	77	238	27	1461	168	93	346
			40	40	321	26	1334	153	110	431
			50	24	379	27	1297	173	119	492

Table B.14 Properties of different EPS or PS (VI)

ID	Fire Parameters				
	Ref.	Effective heat of combustion (kJ/g)	Heat of gasification (kJ/g)	$\dot{Q}_0$ (kW/m²)	THR (MJ/m²)
1 PCF FR EPS (Modified method)	*Cleary and Quintiere* Table D-1 [10]	32.5	2.2	298	21.2
1 PCF FR EPS (Standard method)		31.1	2.5	-69	21.0
2 PCF NFR EPS (Modified method)		35.3	3.9	919	50.1
2 PCF NFR EPS (Standard method)		32.2	2.7	263	45.6
Extruded PS (Modified method)		33.6	2.7	653	33.2
Extruded PS (Standard method)		29.2	2.0	-26	32.8
2 PCF FR EPS 50 mm (Modified method)		32.5	2.0	252	39.4
2 PCF FR EPS 50 mm (Standard method)		30.0	1.9	-32	45.1
2 PCF FR EPS 37.5 mm (Modified method)		34.2	1.9	297	32.3
2 PCF FR EPS 37.5 mm (Standard method)		31.2	2.6	200	33.7
2 PCF FR EPS 25 mm (Modified method)		34.3	3.2	479	20.8
2 PCF FR EPS 25 mm (Standard method)		32.4	2.2	137	21.0
2 PCF FR EPS 12.5 mm (Standard method)		36.6	3.1	64	9.4

B.4 References

[1] D. Drysdale, "Fire Science and Combustion," in *An Introduction to Fire Dynamics*, John Wiley & Sons, Ltd, 2011, pp. 1–34.

[2] D. R. Pitts and L. E. Sissom, *Schaum's Outline Series: Theory and Problems of Heat Transfer*. New York: McGraw-Hill, 1979.

[3] D. Drysdale, "Steady Burning of Liquids and Solids," in *An Introduction to Fire Dynamics*, John Wiley & Sons, Ltd, 2011, pp. 181–223.

[4] A. Tewarson and R. F. Pion, "Flammability of plastics—I. Burning intensity," *Combustion and Flame*, vol. 26, no. 0, pp. 85–103, 1976.

[5] G. H. Markstein, "Radiative properties of plastics," *Proceedings of Combustion Institute*, vol. 20, p. 1055, 1979.

[6] D. Drysdale, "Spread of Flame," in *An Introduction to Fire Dynamics*, John Wiley & Sons, Ltd, 2011, pp. 277–315.

[7] N. F. P. Association and S. of F. P. Engineers, *SFPE handbook of fire protection engineering*. Massachusetts, U.S.A.: National Fire Protection Association, 2002.

[8] V. Babrauskas, W. H. Twilley, and W. J. Parker, "The effects of specimen edge conditions on heat release rate," *Fire and Materials*, vol. 17, no. 2, pp. 51–63, 1993.

[9] M. J. Scudamore, P. J. Briggs, and F. H. Prager, "Cone calorimetry—a review of tests carried out on plastics for the association of plastic manufacturers in Europe," *Fire and Materials*, vol. 15, no. 2, pp. 65–84, 1991.

[10] T. G. Cleary and Quintiere, James G., "NISTIR 4664. Flammability Characterization of Foam Plastics," National Institute of Standards and Technology, 1991.

[11] G. Baker, "Performance of expanded polystyrene insulated panel exposed to radiant heat," University of Canterbury, Christchurch, New Zealand, 2002.

[12] P. Collier Baker, G., "Improving the fire performance of polystyrene insulated panel in New Zealand," NZFSC, Wellington, New Zealand, 2004.

[13] P. Collier and G. Baker, "The Influence of Construction Detailing on the Fire Performance of Polystyrene Insulated Panels," *Fire Technology*, pp. 1–17, 2011.

Appendix C.

Additional Results

C.1 Peak properties from Fraser-Suzuki regression (Chapter 4)

Table C.1. Peak properties from Fraser-Suzuki fitting for SW, PIRa, PF and EPS under nitrogen and air atmosphere

Material	Atmospheric Conditions	Peak	Amplitude a_0	Centre a_1	Width a_2	Asymmetry a_3
SW	Nitrogen	#1	2.48e-05	287.62	123.17	0.457
	Air	#1	7.82e-05	301.32	125.93	-0.105
		#2	0.00010	449.01	97.486	-0.167
		#3	-5.26e-05	768.73	90.118	-0.574
PIRa	Nitrogen	#1	0.00095	79.51	79.51	0.100
		#2	0.00296	320.00	70.498	0.009
		#3	0.00549	336.636	28.599	0.199
		#4	0.00202	408.10	65.321	0.155
		#5	0.00115	481.10	54.237	0.100
		#6	0.00059	556.2	55.388	0.100
	Air	#1	0.00089	201.00	84.584	0.100
		#2	0.00291	316.40	60.661	0.100
		#3	0.00344	339.80	35.206	0.223
		#4	0.00085	421.40	80.000	0.100
		#5	0.00209	544.30	93.1332	0.116
		#6	0.00429	590.70	61.854	0.393
PF	Nitrogen	#1	0.00044	193.70	102.000	0.100
		#2	0.00119	332.11	128.412	0.140
		#3	0.00216	482.634	76.411	0.079
		#4	0.00091	556.52	72.918	0.196
		#5	0.00038	639.10	84.220	0.119
		#6	0.00041	742.90	82.600	0.100
	Air	#1	0.00044	198.70	102.00	0.100
		#2	0.00115	328.80	127.2	0.100
		#3	0.00319	443.80	62.282	0.100
		#4	0.00464	503.93	66.728	0.036
		#5	0.00519	541.00	42.560	0.002
EPS	Nitrogen	#1	0.00597	348.85	55.114	0.075
	Air	#1	0.02695	420.10	31.497	-0.324
		#2	0.01290	373.74	40.890	-0.587

C.2 Summary of flammability and combustibility experimental data (Chapter 5)

Table C.2 to Table C.6 below present the main gross of performed experiments for plastic foams. Time-to-ignition and peak of heat release rate are indicated. Stone wool experiments are not presented since no ignition was achieved for any heat flux.

Table C.2. Summary of results from flammability-combustibility experiments for PIRa

	Material	**Configuration**	**Incident radiative heat flux**	**Ignition Times /s**	**Peak of HRR /kW·m^{-2}**
PIRa.x35.01	Rigid isocyanurate-based foam Manufacturer a) Manufacturer-claimed density: 31 - 34 kg/m^3 Average measured density: 31.0 ± 1.4 kg/m^3	Protective layer Nominal dimensions: 90 x 90 x 100 mm	35	No ignition	-
PIRa.x35.02			35	No ignition	-
PIRa.x45.01			45	228	73.68
PIRa.x45.02			45	49	156.4
PIRa.x55.01			55	34	173.5
PIRa.x55.02			55	42	153.6
PIRa.x65.01			65	14	206.8
PIRa.x65.02			65	28	196.8
PIRa.z07.01		No protective layer Nominal dimensions: 90 x 90 x 100 mm	7	No ignition	-
PIRa.z08.01			8	No ignition	82.0
PIRa.z08.02			8	49	-
PIRa.z09.01			9	No ignition	-
PIRa.z09.02			9	No ignition	-
PIRa.z10.01			10	112	76.1
PIRa.z10.02			10	13	90.8
PIRa.z10.03			10	325	42.2
PIRa.z10.04			10	No ignition	-
PIRa.z10.05			10	No ignition	-
PIRa.z11.01			11	155	93.2
PIRa.z11.02			11	No ignition	-
PIRa.z12.01			12	10	97.0
PIRa.z12.02			12	17	109.5
PIRa.z15.01			15	18	96.8
PIRa.z15.02			15	13	86.5
PIRa.z25.01			25	7	96.1
PIRa.z25.02			25	7	97.4
PIRa.z35.01			35	8	89.3
PIRa.z35.02			35	5	97.8
PIRa.z45.01			45	2 (autoignition)	159.6
PIRa.z45.02			45	3 (autoignition)	116.2
PIRa.z55.01			55	<1 (autoignition)	143.6
PIRa.z55.02			55	<1 (autoignition)	142.2
PIRa.z65.01			65	<1 (autoignition)	178.8
PIRa.z65.02			65	1.5 (autoignition)	155.6

Table C.3. Summary of results from flammability-combustibility experiments for PIRb

	Material	**Configuration**	**Incident radiative heat flux**	**Ignition Times /s**	**Peak of HRR /kW·m^{-2}**
PIRb.x35.01	Rigid isocyanurate-based foam Manufacturer b) Manufacturer-claimed density: 32 kg/m^3 Average measured density: 32.1 ± 1.4 kg/m^3 * Tests performed by different operator: protective layer removed without cutting sample	Protective layer Nominal dimensions: 90 x 90 x 100 mm	35	No ignition	-
PIRb.x35.02			35	No ignition	-
PIRb.x45.01			45	194	60.7
PIRb.x45.02			45	No ignition	-
PIRb.x55.01			55	31	134.5
PIRb.x55.02			55	205-307	
PIRb.x65.01			65	20	132.1
PIRb.x65.02			65	8	138.7
PIRb.z12.01		No protective layer Nominal dimensions: 90 x 90 x 100 mm	12	No ignition	-
PIRb.z12.02			12	311	45.7
PIRb.z15.01			15	151	-
PIRb.z15.02			15	30-35	72.9
PIRb.z20.01*			20	10	124.1
PIRb.z20.02*			20	7	143.8
PIRb.z20.03*			20	6	139.4
PIRb.z25.01			25	6	69.4
PIRb.z25.02			25	9	89.7
PIRb.z30.01*			30	5	130.5
PIRb.z30.02*			30	5	123.9
PIRb.z35.01			35	7	84.1
PIRb.z35.02			35	4 (autoignition)	86.4
PIRb.z40.01*			40	5	136.5
PIRb.z40.02*			40	3 (autoignition)	114.5
PIRb.z45.02			45	5	105.7
PIRb.z45.02			45	4 (autoignition)	101.1
PIRb.z55.01			55	2 (autoignition)	119.5
PIRb.z55.02			55	3 (autoignition)	110.1
PIRb.z65.01			65	3 (autoignition)	118.9
PIRb.z65.02			65	1 (autoignition)	120.8

Table C.4. Summary of results from flammability-combustibility experiments for PIRc

	Material	Protective foil layer	Incident radiative heat flux	Ignition Times /s	Peak of HRR /kW·m^{-2}
PIRc.x25.01	Rigid isocyanurate-based foam Manufacturer c) Manufacturer-claimed density: 30-32 kg/m^3 Average measured density: 32.6 ± 1.1 kg/m^3 * Tests performed by different operator: protective layer removed without cutting sample	Protective layer Nominal dimensions: 90 x 90 x 100 mm	25	No ignition	-
PIRc.x25.02			25	No ignition	-
PIRc.x35.01			35	44	128.1
PIRc.x35.02			35	35	125.7
PIRc.x45.02			45	19	154.0
PIRc.x45.02			45	16	164.7
PIRc.x55.02			55	13	177.5
PIRc.x55.02			55	9	174.1
PIRc.x65.02			65	8	182.9
PIRc.x65.02			65	14	166.0
PIRc.z15.01		No protective layer Nominal dimensions: 90 x 90 x 100 mm	15	No ignition	-
PIRc.z15.02			15	8	69.3
PIRc.z15.03			15	138	-
PIRc.z15.04			15	No ignition	-
PIRc.z15.05			15	No ignition	-
PIRc.z16.01			16	8	74.8
PIRc.z16.02			16	86	-
PIRc.z16.03			16	6	64.8
PIRc.z17.01			17	80	25.6
PIRc.z17.02			17	9	64.1
PIRc.z17.03			17	6	89.5
PIRc.z18.01			18	6	76.2
PIRc.z18.02			18	21	67.8
PIRc.z18.03			18	13	68.7
PIRc.z20.01*			20	13	85.9
PIRc.z20.02*			20	8	87.4
PIRc.z20.03*			20	6	87.9
PIRc.z25.01			25	8	74.5
PIRc.z25.02			25	8	86.9
PIRc.z35.01			35	5	104.2
PIRc.z35.02			35	5	87.1
PIRc.z45.01			45	3 (autoignition)	104.8
PIRc.z45.02			45	4 (autoignition)	107.0
PIRc.z55.01			55	4 (autoignition)	118.6
PIRc.z55.02			55	0 (autoignition)	127.9
PIRc.z65.01			65	0 (autoignition)	144.1
PIRc.z65.02			65	0 (autoignition)	134.7

Table C.5. Summary of results from flammability-combustibility experiments for PF

	Material	Protective foil layer	Incident radiative heat flux	Ignition Times /s	Peak of HRR /kW·m^{-2}
PF.x25.01	Rigid phenolic foam Manufacturer-claimed density: - kg/m^3 Average measured density: 40.3 ± 1.1 kg/m^3	Protective layer Nominal dimensions: 90 x 90 x 100 mm	25	423	52.5
PF.x25.02			25	168	105.4
PF.x35.01			35	13	119.3
PF.x35.02			35	41	142.1
PF.x45.01			45	6	153.1
PF.x45.02			45	34	157.8
PF.x55.01			55	12	142.0
PF.x55.02			55	47	124.0
PF.x65.01			65	5	140.2
PF.x65.02			65	22	176.0
PF.z15.01		No protective layer Nominal dimensions: 90 x 90 x 100 mm	15	No ignition	-
PF.z15.02			15	No ignition	-
PF.z15.03			15	No ignition	-
PF.z15.04			15	No ignition	-
PF.z20.01			20	(flashing – late ignition)	58.6
PF.z20.02			20	(flashing)	24.6
PF.z22.03			22	52	39.9
PF.z22.04			22	27	47.7
PF.z23.01			23	97	39.6
PF.z23.02			23	13	54.2
PF.z23.03			23	14	32.7
PF.z25.01			25	162	49.8
PF.z25.02			25	190	48.0
PF.z25.03			25	9	51.4
PF.z25.04			25	14	73.7
PF.z26.01			26	22	56.7
PF.z26.02			26	69	50.1
PF.z30.01			30	7	94.7
PF.z30.02			30	8	86.0
PF.z35.01			35	5	68.4
PF.z35.02			35	6	70.5
PF.z45.01			45	6	88.2
PF.z45.02			45	6	97.8
PF.z55.01			55	6	102.6
PF.z55.02			55	5	89.3
PF.z65.01			65	6	115.6
PF.z65.02			65	6	95.0

Table C.6. Summary of results from flammability-combustibility experiments for EPS

	Material	Protective foil layer	Incident radiative heat flux	Ignition Times /s	Maximum HRR /kW·m^{-2}
EPS.15.01	Expanded polystyrene foam Manufacturer-claimed density: 15 – 35 kg/m^3 Average measured density: 10.1 ± 0.1 kg/m^3	No protective layer Nominal dimensions: 90 x 90 x 100 mm	15	No ignition	-
EPS.15.02			15	No ignition	-
EPS.16.01			16	544	426.0
EPS.16.02			16	No ignition	-
EPS.16.03			16	No ignition	-
EPS.17.01			17	330	448.8
EPS.17.02			17	404	474.0
EPS.17.03			17	432	373.1
EPS.18.01			18	454	365.6
EPS.18.02			18	No ignition	-
EPS.18.03			18	252	442.6
EPS.18.03			18	258	228.9
EPS.20.01			20	213	334.9
EPS.20.02			20	217	353.1
EPS.25.01			25	115	458.5
EPS.25.02			25	116	433.8
EPS.35.01			35	64	407.7
EPS.35.02			35	58	424.7
EPS.45.01			45	43	428.2
EPS.45.02			45	41	495.9
EPS.55.01			55	34	387.0
EPS.55.02			55	34	415.8
EPS.65.01			65	25	518.7
EPS.65.02			65	25	515.3
EPS.h17.01		No protective layer Nominal dimensions: 90 x 90 x 50 mm	17	288	354.6
EPS.h17.02			17	No ignition	-
EPS.h17.03			17	298	350.6
EPS.h20.01			20	145	320.9
EPS.h20.02			20	164	321.4
EPS.h25.01			25	87	340.9
EPS.h25.02			25	93	401.3
EPS.h35.01			35	50	296.6
EPS.h35.02			35	45	398.0
EPS.h45.01			45	27	364.0
EPS.h45.02			45	27	372.7
EPS.h55.01			55	19	422.1
EPS.h55.02			55	21	429.1

C.3 Extended results from the rest of PIR materials (Chapter 5)

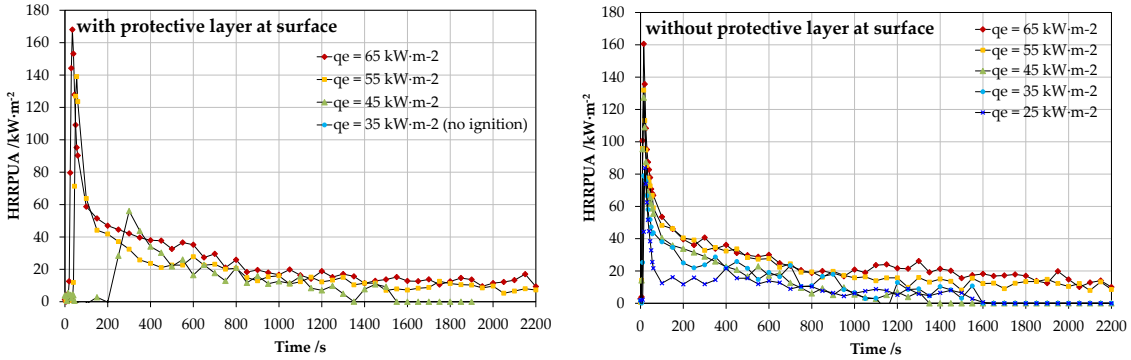

Figure C.1. Heat release rate per unit area of 100 mm thick PIRa samples, with (left) and without (right) protective layer, at different external heat fluxes. ($E_{O_2} = 13.1\ kJ \cdot g_{O_2}^{-1}$). Average from two repetitions

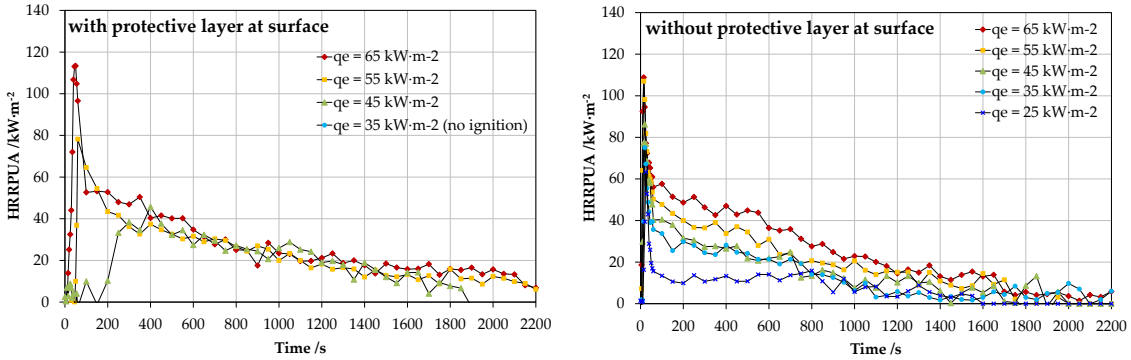

Figure C.2. Heat release rate per unit area of 100 mm thick PIRb samples, with (left) and without (right) protective layer, at different external fluxes. ($E_{O_2} = 13.1\ kJ \cdot g_{O_2}^{-1}$). Average from two repetitions

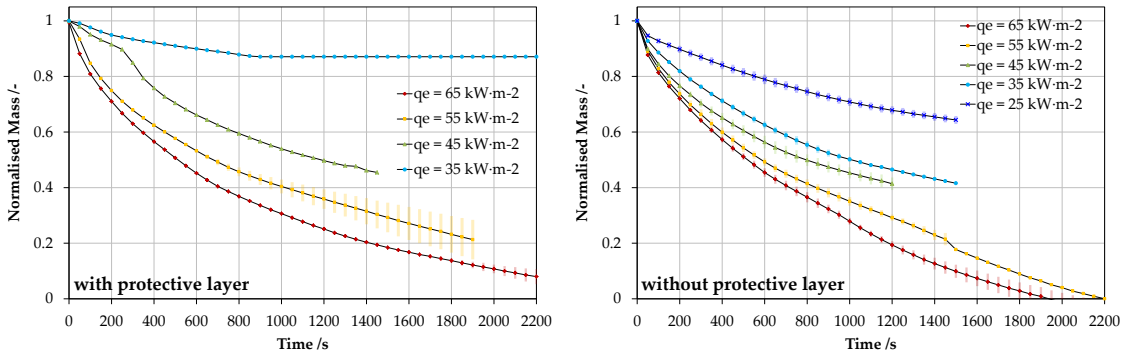

Figure C.3. Normalised mass (m/m_0) of PIRa samples, with (left) and without (right) protective layer, at different heat fluxes. Shading indicates std. dev. from two repetitions

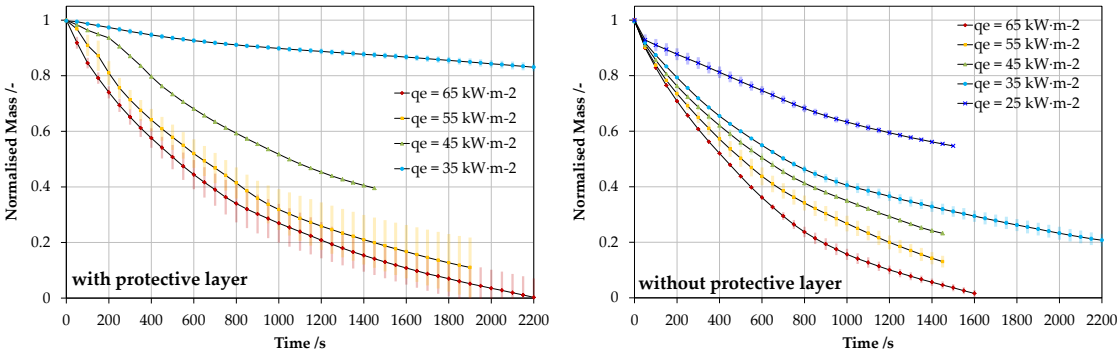

Figure C.4. Normalised mass (m/m_0) of PIRb samples, with (left) and without (right) protective layer, at different heat fluxes. Shading indicates std. dev. from two repetitions

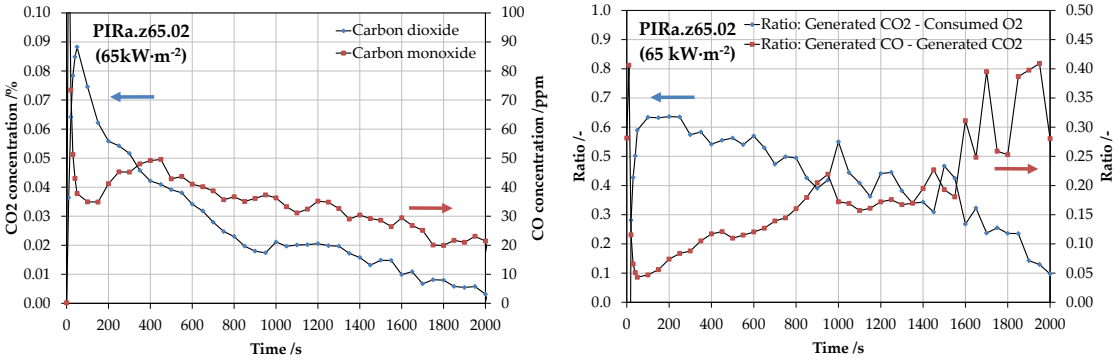

Figure C.5. CO_2 and CO concentrations (left) and ratios of generated CO_2 vs. consumed O_2 and generated O_2 vs. generated CO (right) for PIRa at 55 kW·m^{-2} (test PIRa.z65.02)

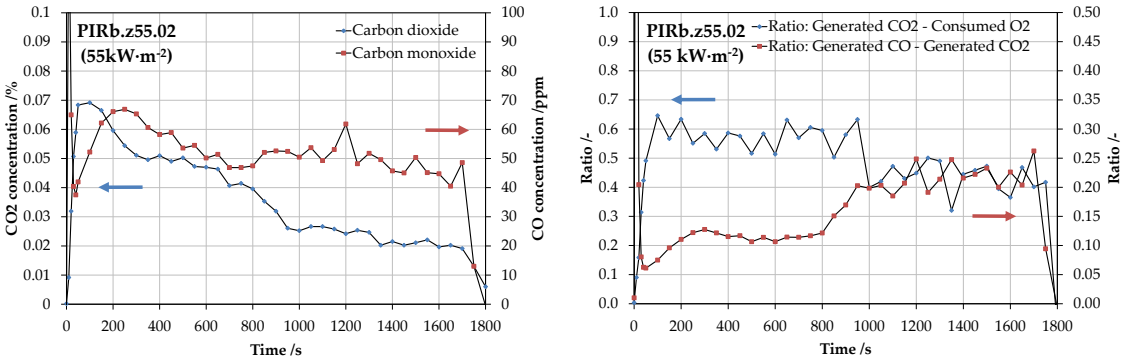

Figure C.6. CO_2 and CO concentrations (left) and ratios of generated CO_2 vs. consumed O_2 and generated O_2 vs. generated CO (right) for PIRb at 55 kW·m^{-2} (test PIRb.z55.02)

C.4 Extended temperature measurements (Chapter 6)

C.4.1 SW

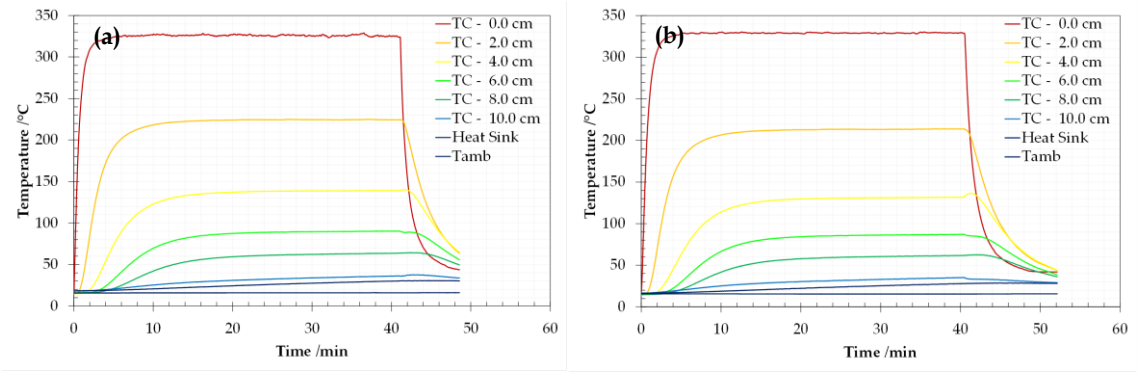

Figure C.7. SW 10 kW·m^{-2} (a) Repetition 1 (b) Repetition 2

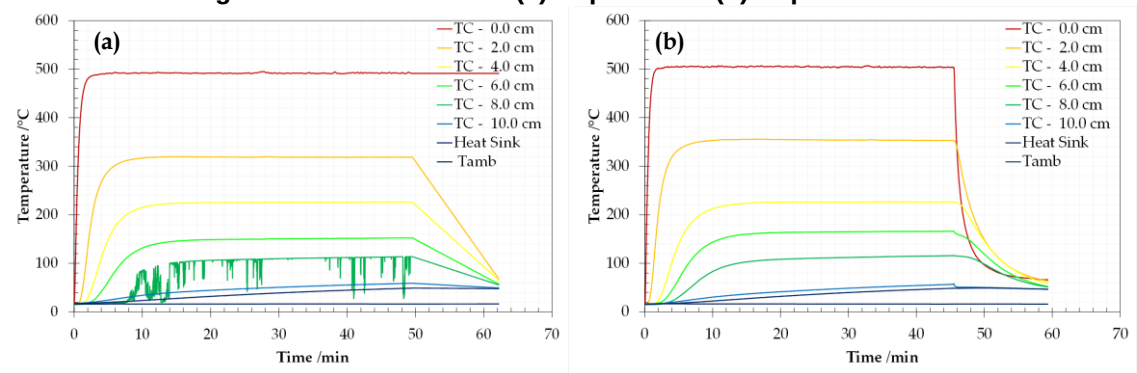

Figure C.8. SW 25 kW·m^{-2} (a) Repetition 1 (b) Repetition 2

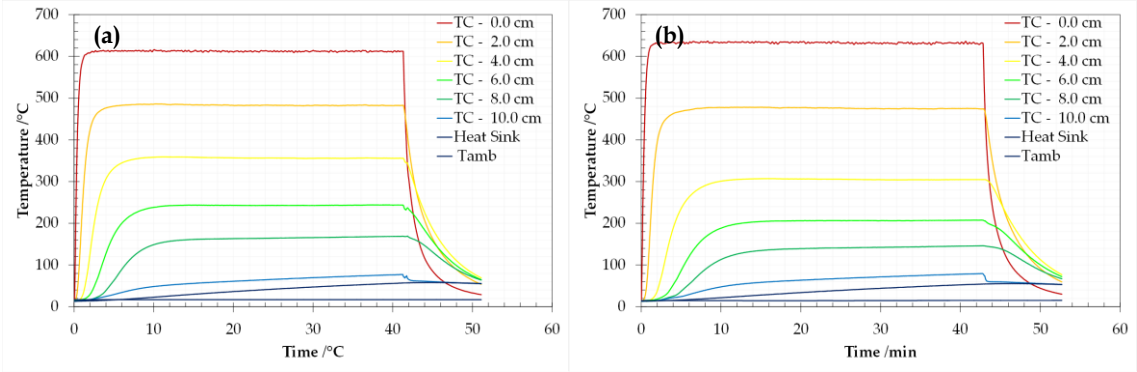

Figure C.9. SW 40 kW·m^{-2} (a) Repetition 1 (b) Repetition 2

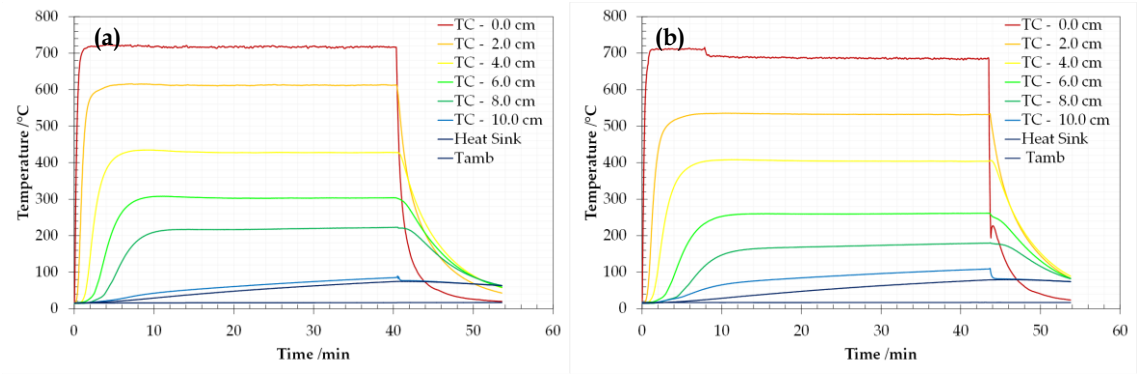

Figure C.10. SW 60 kW·m^{-2} (a) Repetition 1 (b) Repetition 2

C.4.2 PIRa

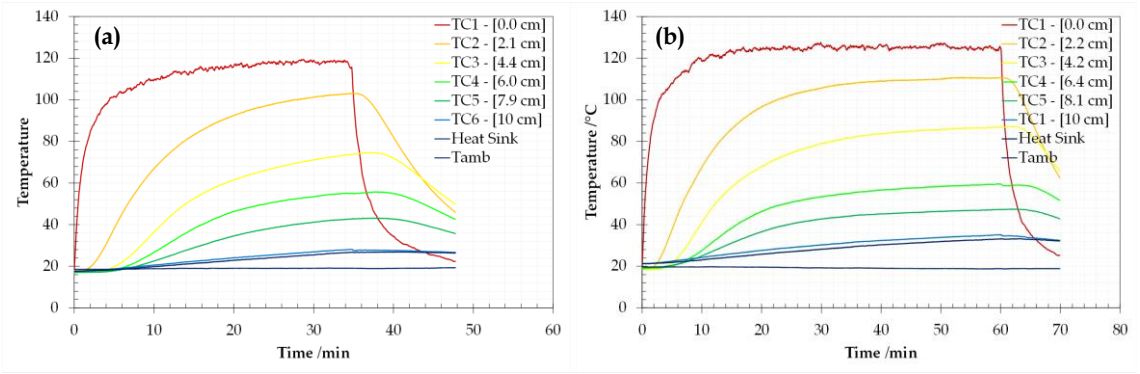

Figure C.11. PIRa 10 kW·m^{-2} with protective layer (a) Repetition 1 (b) Repetition 2

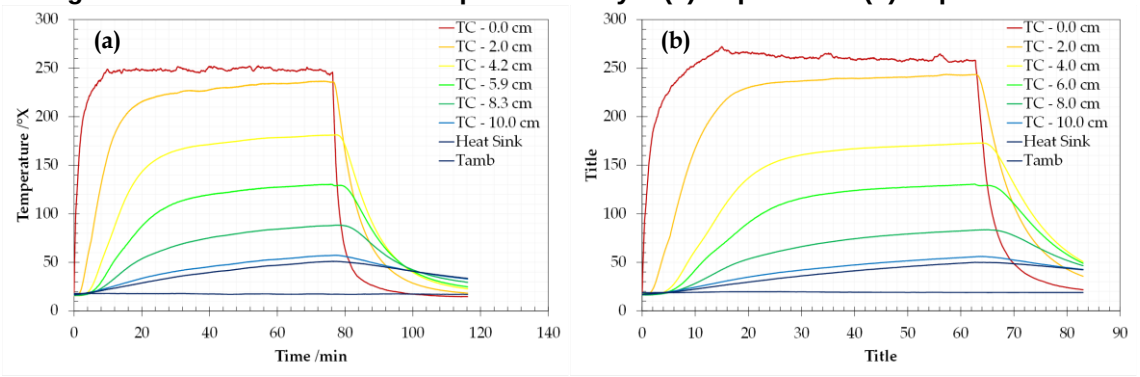

Figure C.12. PIRa 25 kW·m^{-2} with protective layer (a) Repetition 1 (b) Repetition 2

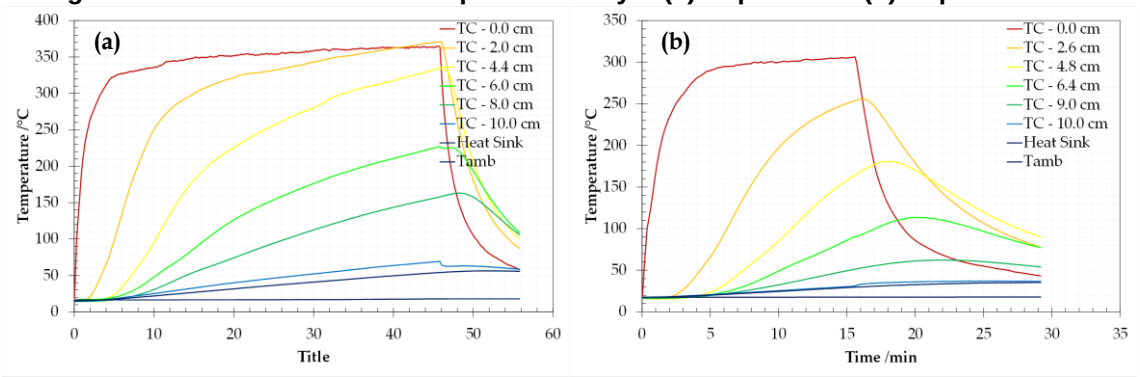

Figure C.13. PIRa 35 kW·m^{-2} with protective layer (a) Repetition 1 (b) Repetition 2

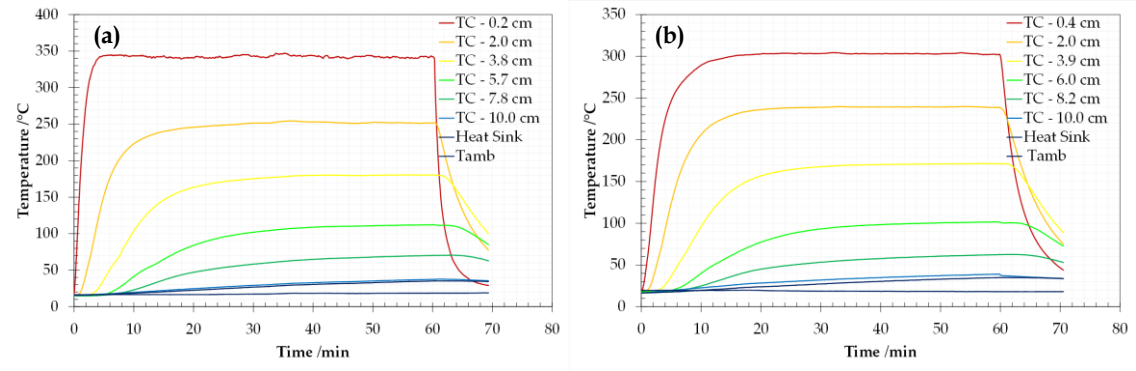

Figure C.14. PIRa 10 kW·m^{-2} without protective layer (a) Repetition 1 (b) Repetition 2

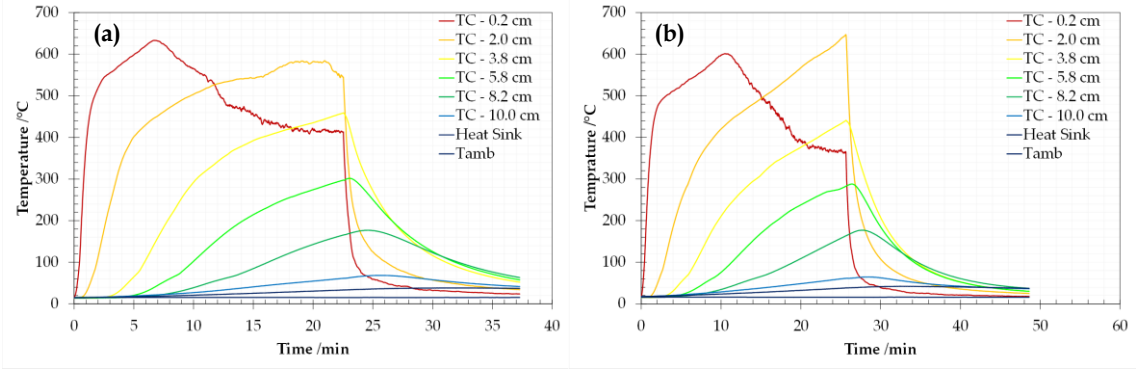

Figure C.15. PIRa 25 kW·m^{-2} without protective layer (a) Repetition 1 (b) Repetition 2

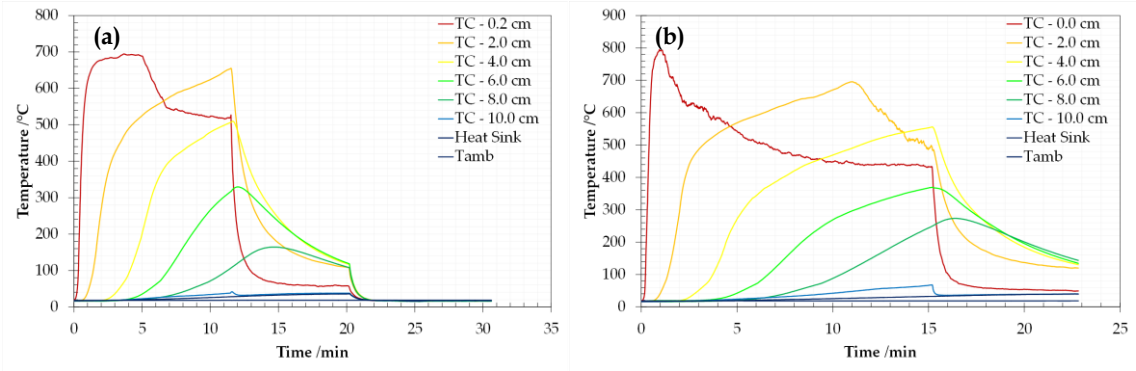

Figure C.16. PIRa 35 kW·m^{-2} without protective layer (a) Repetition 1 (b) Repetition 2

C.4.3 PF

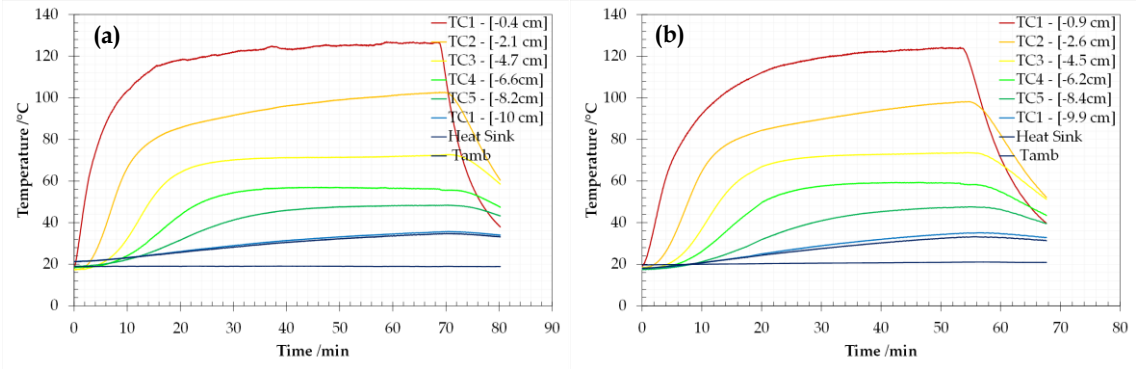

Figure C.17. PF 10 kW·m^{-2} with protective (a) Repetition 1 (b) Repetition 2

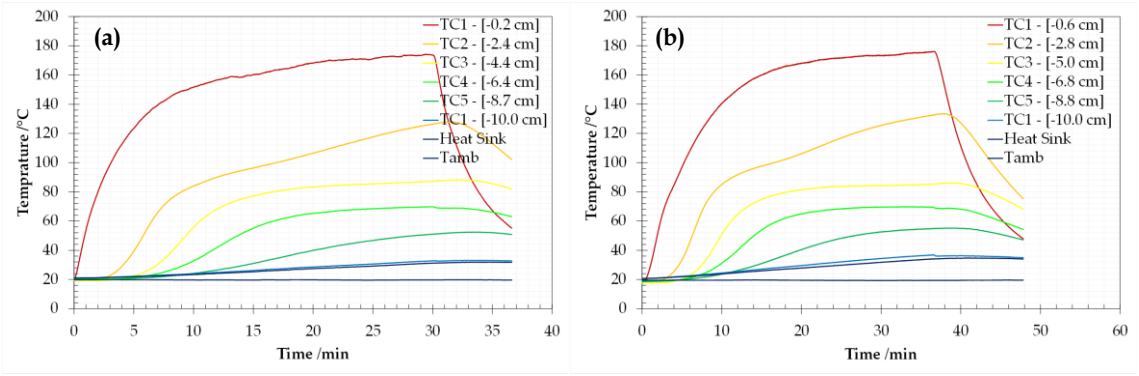

Figure C.18. PF 15 kW·m^{-2} with protective layer (a) Repetition 1 (b) Repetition 2

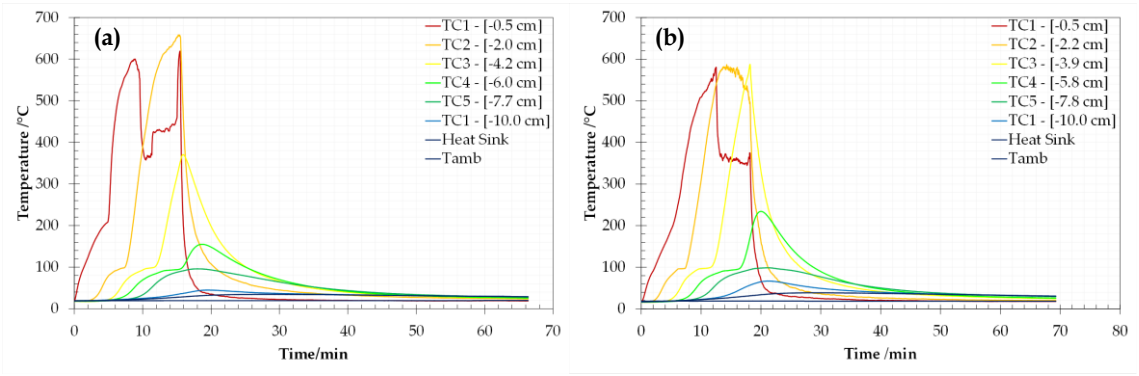

Figure C.19. PF 25 kW·m^{-2} with protective layer (a) Repetition 1 (b) Repetition 2

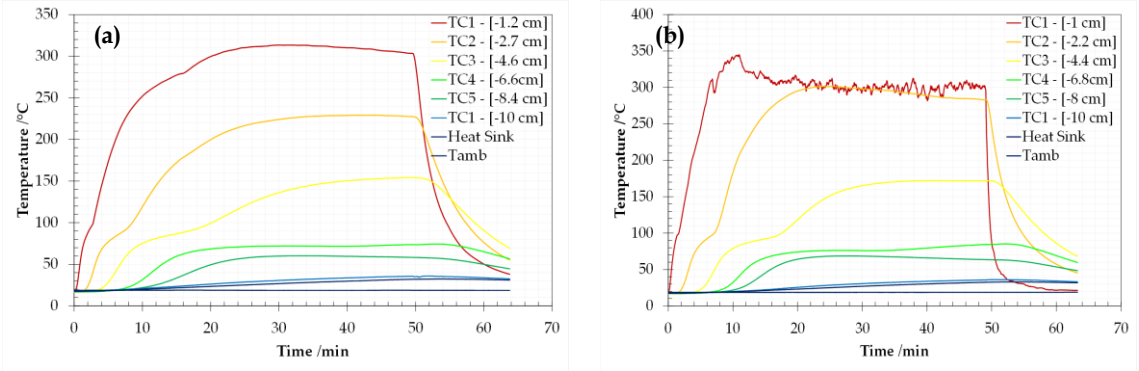

Figure C.20. PF 10 kW·m^{-2} without protective layer (a) Repetition 1 (b) Repetition 2

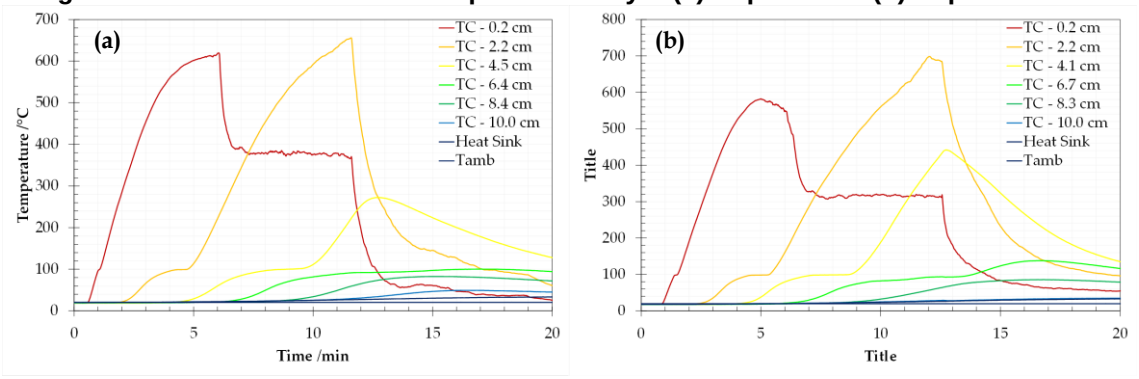

Figure C.21. PF 25 kW·m^{-2} without protective layer (a) Repetition 1 (b) Repetition 2

C.5 Extended temperature measurements from Radiant Panel Tests' programme (Chapter 7)

C.5.1 SW

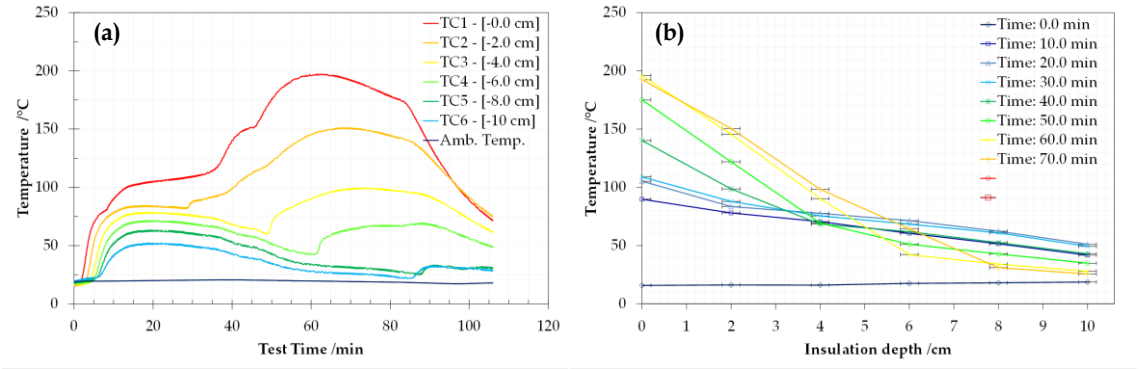

Figure C.22. SW 15 kW·m^{-2} – repetition 2 (failure in propane flow to radiant panels)
(a) Time-history (b) In-depth temperature profile

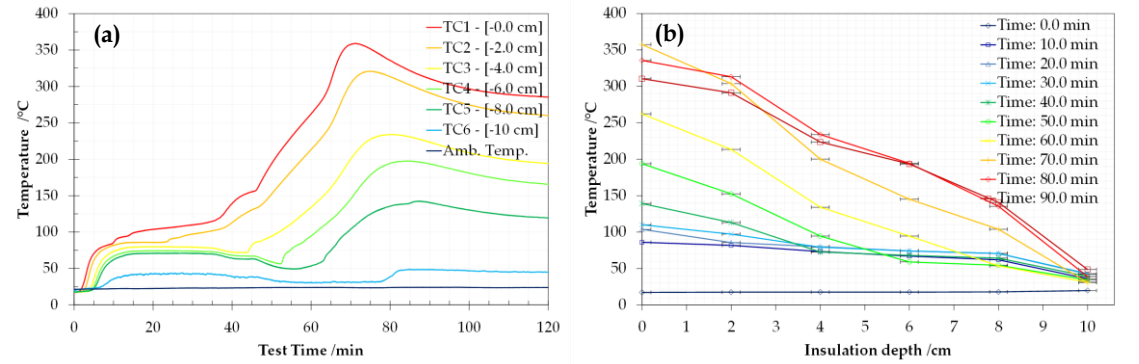

Figure C.23. SW 15 kW·m^{-2} – repetition 3
(a) Time-history (b) In-depth temperature profile

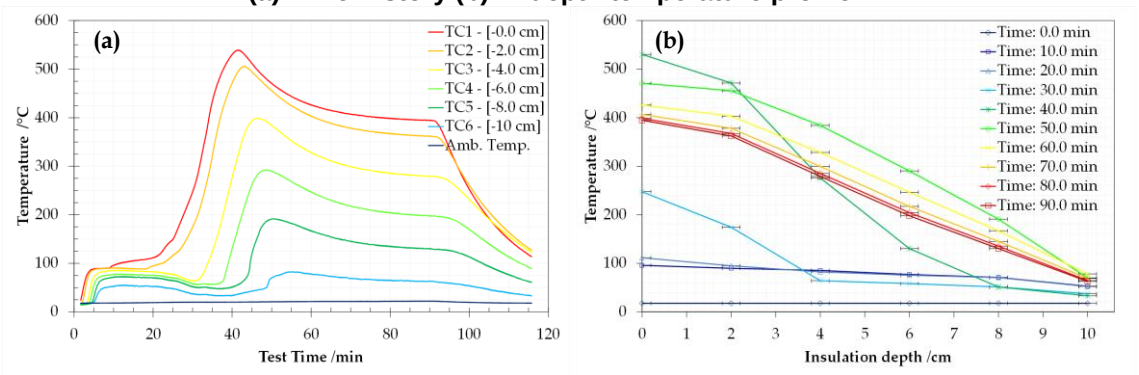

Figure C.24. SW 25 kW·m^{-2} – repetition 1
(a) Time-history (b) In-depth temperature profile

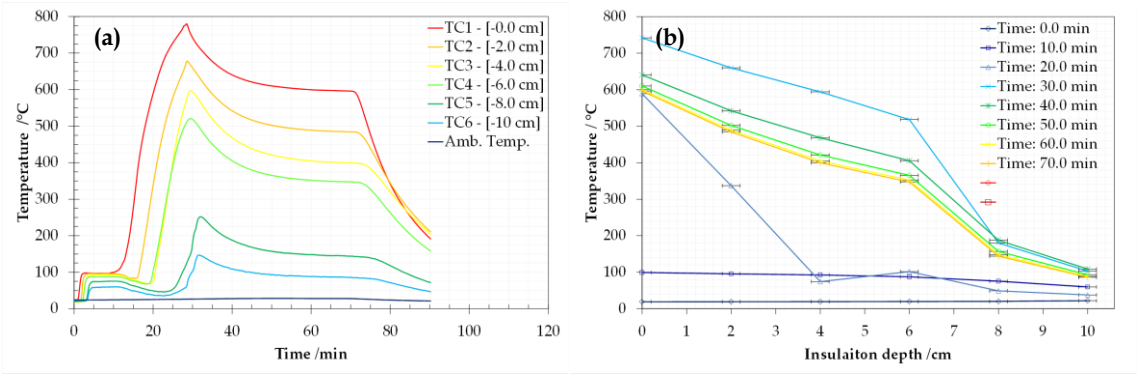

Figure C.25. SW 65 kW·m^{-2} – repetition 2
(a) Time-history (b) In-depth temperature profile

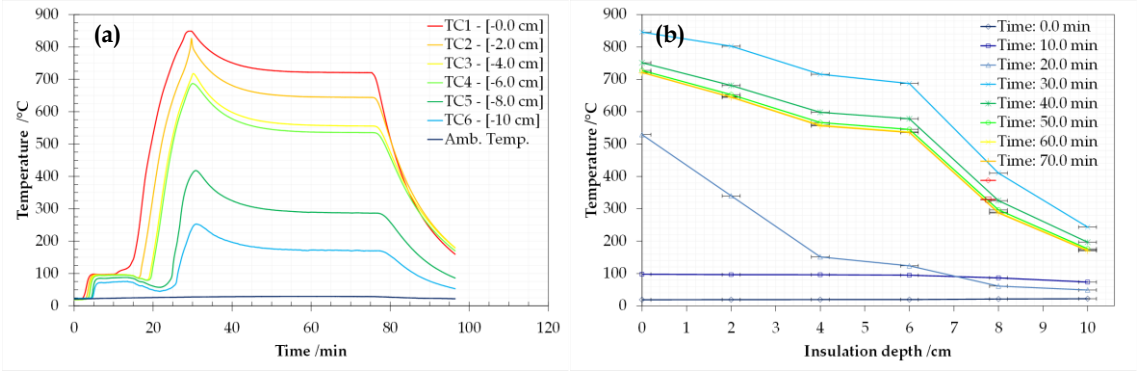

Figure C.26. SW Ramp up to 70 kW·m^{-2} – repetition 1
(a) Time-history (b) In-depth temperature profile

C.5.2 PIRb

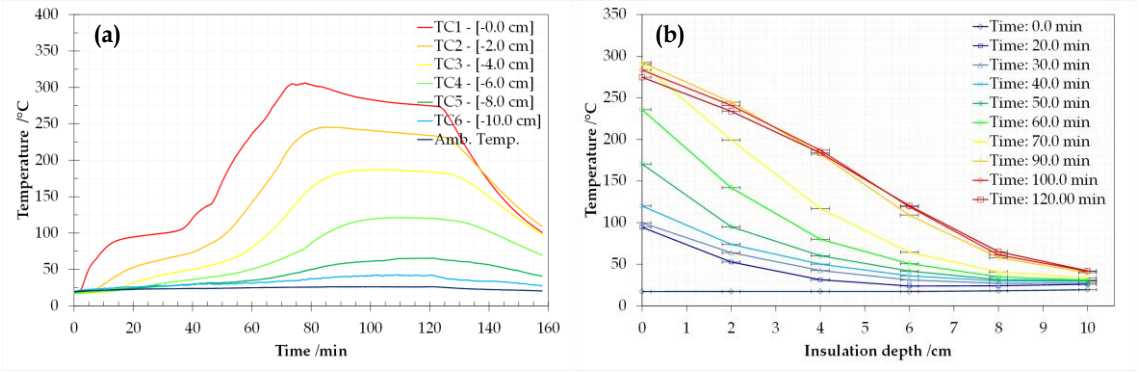

Figure C.27. PIRb 15 kW·m^{-2} – repetition 2
(a) Time-history (b) In-depth temperature profile

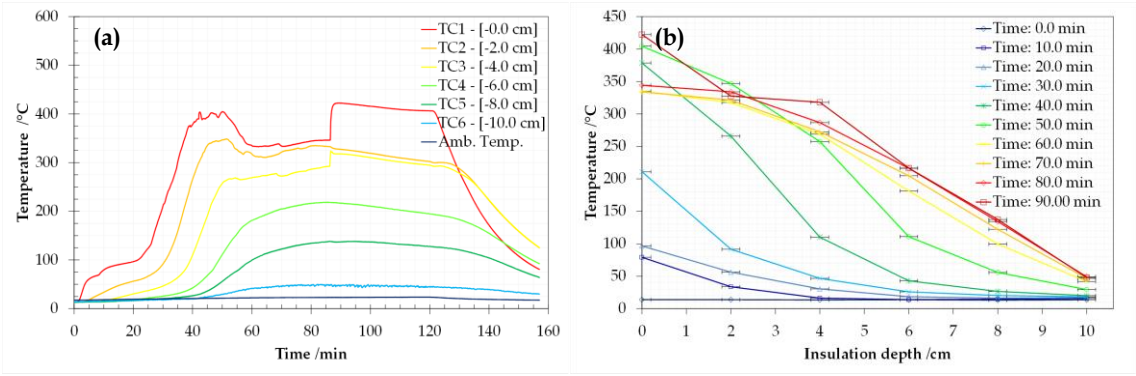

Figure C.28. PIRb 25 kW·m^{-2} – repetition 1
(a) Time-history (b) In-depth temperature profile

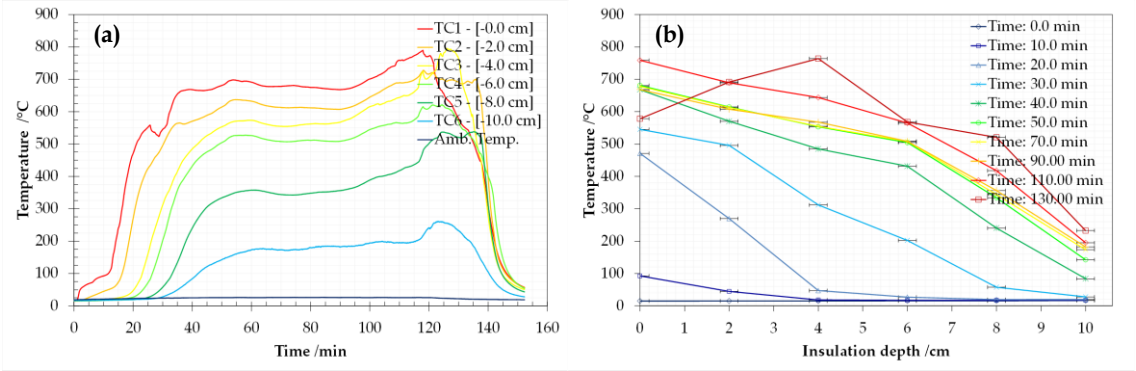

Figure C.29. PIRb 65 kW·m^{-2} – repetition 2
(a) Time-history (b) In-depth temperature profile

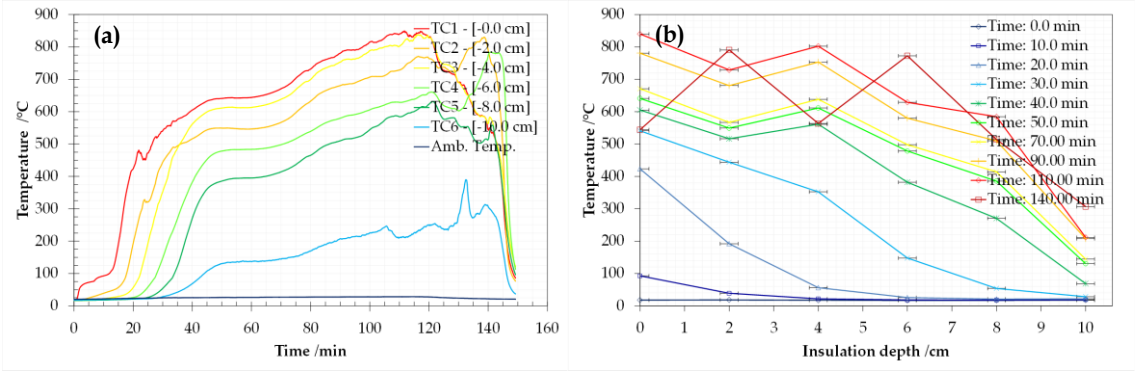

Figure C.30. PIRb 65 kW·m^{-2} – repetition 3
(a) Time-history (b) In-depth temperature profile

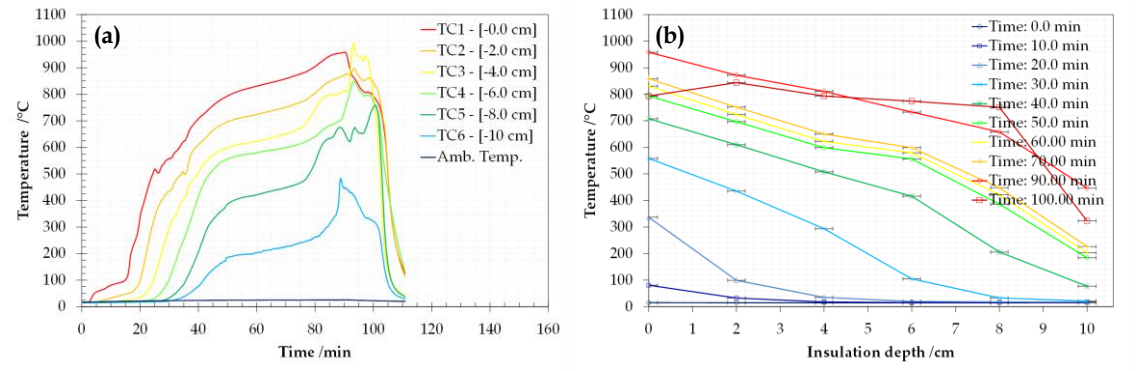

Figure C.31. PIRb Ramp up to 70 kW·m^{-2} – repetition 1
(a) Time-history (b) In-depth temperature profile

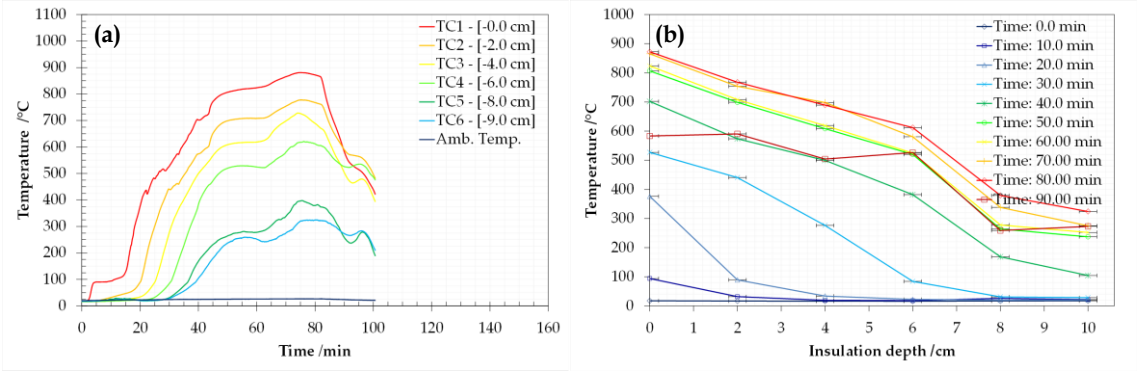

Figure C.32. PIRb Ramp up to 70 kW·m^{-2} – repetition 2
(a) Time-history (b) In-depth temperature profile

C.5.3 PF

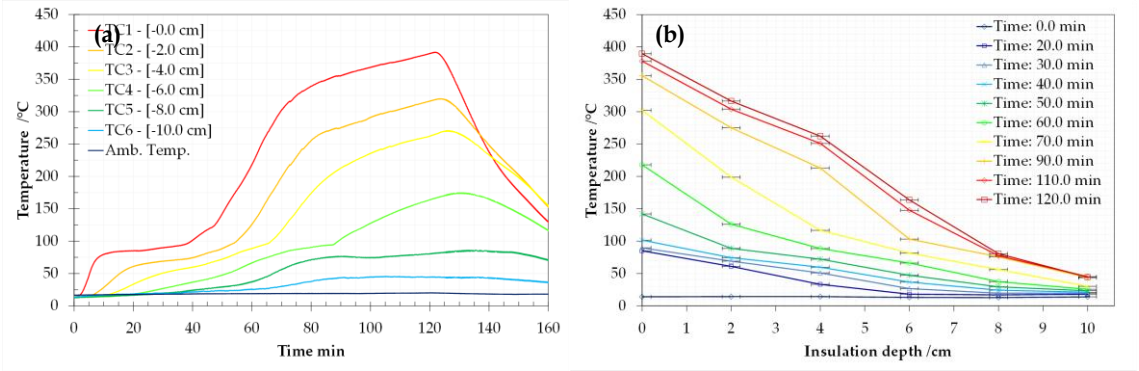

Figure C.33. PF 15 kW·m^{-2} – repetition 1
(a) Time-history (b) In-depth temperature profile

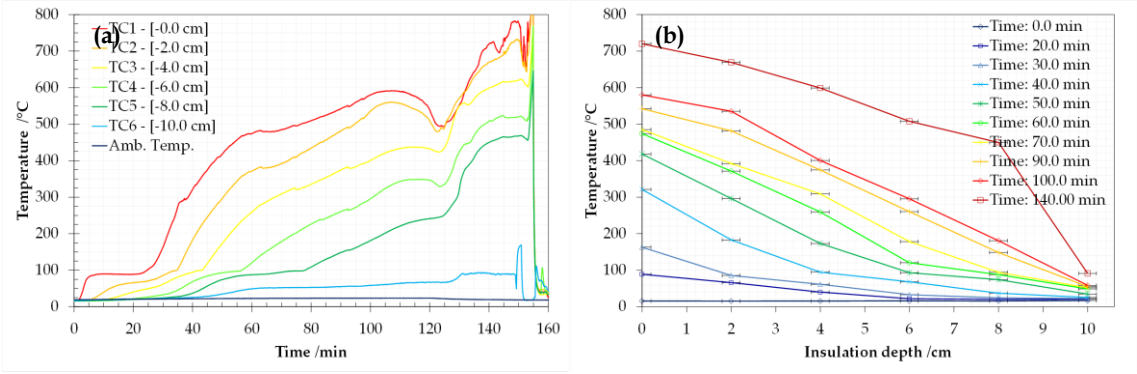

Figure C.34. PF 25 kW·m^{-2} – repetition 1
(a) Time-history (b) In-depth temperature profile

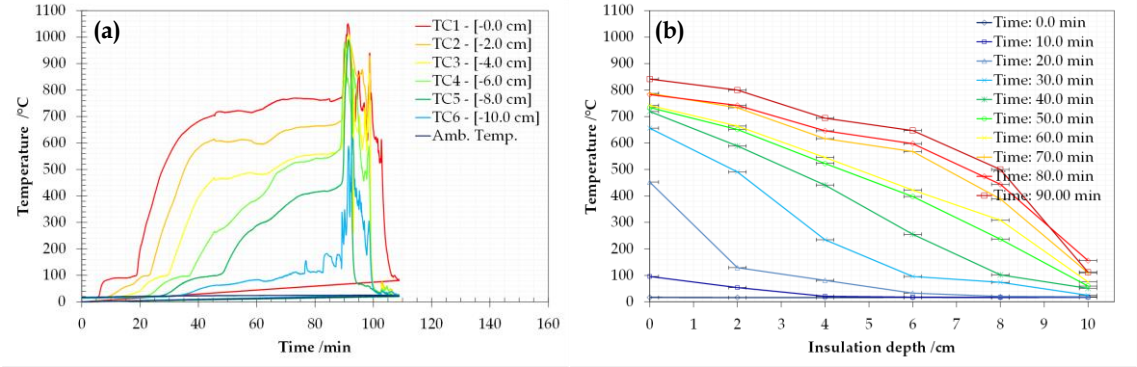

Figure C.35. PF 65 kW·m^{-2} – repetition 1
(a) Time-history (b) In-depth temperature profile

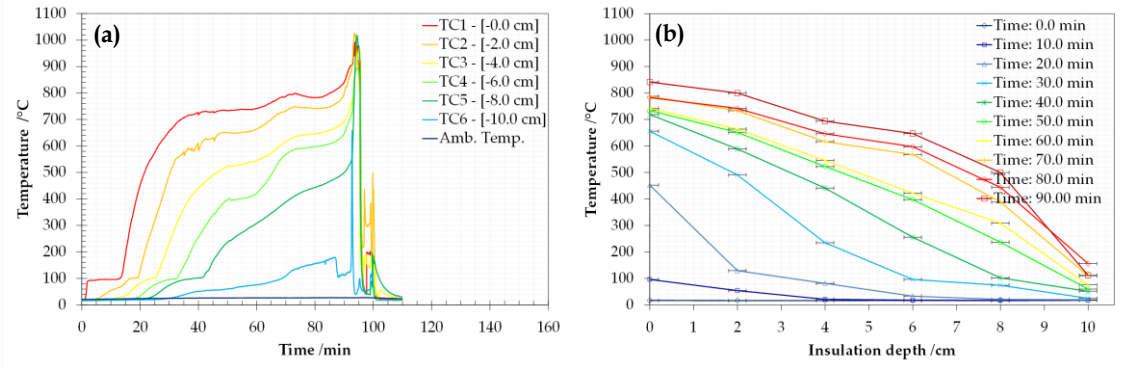

Figure C.36. PF 65 kW·m^{-2} – repetition 2
(b) Time-history (b) In-depth temperature profile

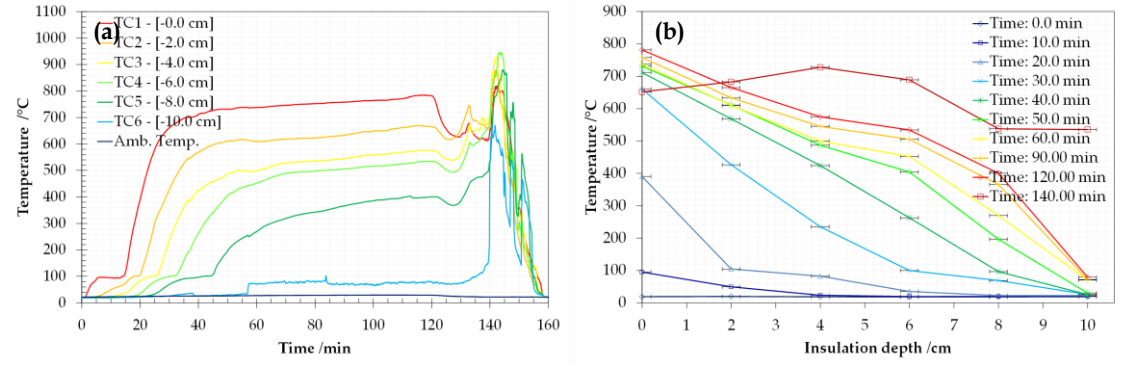

Figure C.37. PF 65 kW·m^{-2} – repetition 3
(a) Time-history (b) In-depth temperature profile

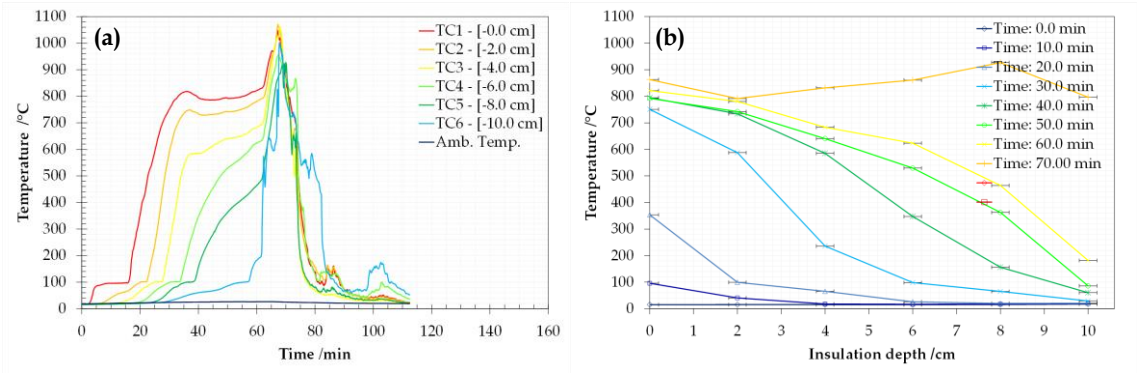

Figure C.38. PF Ramp up to 70 kW·m^{-2} – repetition 2
(a) Time-history (b) In-depth temperature profile

C.6 Cone Calorimeter results from painted skin from the Sandwich Panel Tests' Programme (Chapter 7)

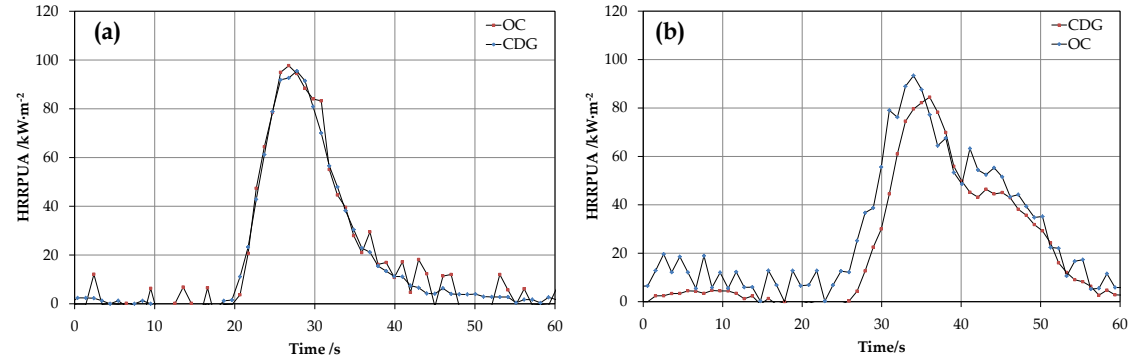

Figure C.39. HRRPUA from painted metal skin from PIR sandwich panel under 35 kW·m^{-2} (a) Repetition 1 (b) Repetition 2

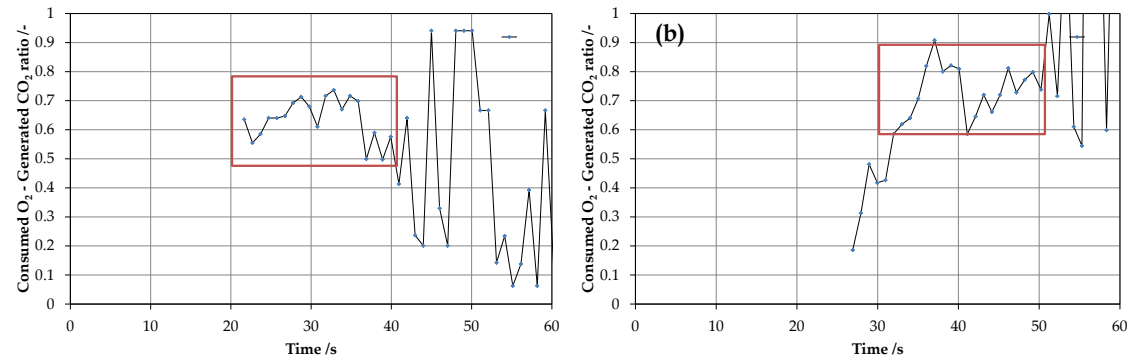

Figure C.40. HRRPUA from painted metal skin from PIR sandwich panel under 35 kW·m^{-2} (a) Repetition 1 (b) Repetition 2

Painted metal skin from SW sandwich panel did not ignite; therefore no HRR or O_2/CO_2 ratios are presented.

Appendix D.

Derivation of the Heat Transfer Formulation for Used Modelling Techniques

The used modelling techniques for solving the conduction heat transfer problem are based on finite differences. The Crank-Nicolson method is the numerical method chosen for solving the one-dimensional conduction equation, which is characterised for being a second-order method in time, implicit in time and numerically stable. The formulation is constructed on the basis of Equation (6.16), used to define a system of N linear equations and N variables (temperatures of each element at the step j+1:

$$T_i^{j+1} = T_i^j + \frac{\Delta t}{2} \cdot \left(\left.\frac{dT}{dt}\right|_i^j + \left.\frac{dT}{dt}\right|_i^{j+1} \right) \tag{D.1}$$

The space domain has been defined in different ways throughout this thesis, depending on the problem considered:

- A single material layer.
- A single material layer with a thermally thin element at the surface.
- Two layers of different material in contact, assuming null contact resistance.
- Two layers of different material in contact, assuming null contact resistance, with a thermally thin element at the surface.

The discretisation of a single material layer of thickness L_A is based on N elements of thickness $\Delta x/2$ for nodes i=1,...,N and thickness Δx for nodes i=2,…,N-1. The schematic representation of the space domain discretisation for this case is represented in Figure 6.28.

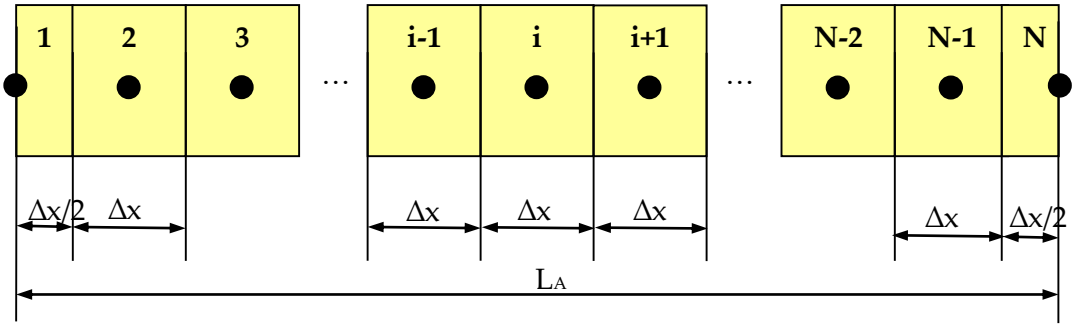

Figure D.1. Discretisation of the space domain for the one-dimensional heat transfer problem consisting of one material layer

The discretisation for a composite sample consisting of two layers of different materials of thickness L_A and L_B is schematically illustrated in Figure D.2. The thickness of the elements of the layer A and the layer B are denoted as Δx_A and Δx_B, respectively. As for a single layer, the thickness of the first and last element corresponds to $\Delta x_A/2$ and $\Delta x_B/2$ respectively, while the thickness of the interface element $i = j$ is $(\Delta x_A + \Delta x_B)/2$. The same approach considered for two layers of material could be applied to any number of layers. Therefore, only the formulation for two layers of material will be presented herein..

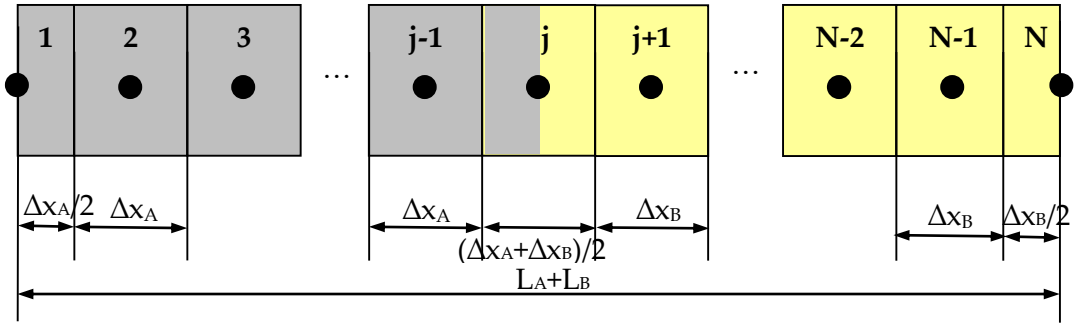

Figure D.2. Discretisation of the space domain for the one-dimensional heat transfer problem consisting of two layers of material in contact

As shown in Equation (6.16), the Crank-Nicolson method requires the derivation of the temperature variation over time $^{dT}/_{dt}$ for each element of the discretisation at the time steps j and j+1. The discretised formulation for each element, related to the one-dimensional heat of conduction equation, is derived below. Principles based on an energy balance and the derivation from the infinitesimal governing equation are considered so as to obtain a system of linear equations that allows solving the temperature of each element within the considered space and the temporal domain. Derivation from the diffusion equation is followed for interior elements, while energy balances are applied for the first and last element based on the possible boundary conditions, which were defined in Chapter 6.

D.1 First element (i=1)

The discretised governing equation for the boundary condition at the surface (first element) at the time step j can be derived from applying an energy balance between the external conditions and elements 1 and 2. This energy balance is illustrated in Figure D.3 and formulated in Equation (D.2):

$$\dot{q}''^{j}_{net} = \dot{q}''^{j}_{st,1} + \dot{q}''^{j}_{cond,1\rightarrow 2} \tag{D.2}$$

where $\dot{q}''^{j}_{net}$ is the net heat flux at the surface, $\dot{q}''^{j}_{st,1}$ is the heat flux stored by the first element and $\dot{q}''^{j}_{cond,1\rightarrow 2}$ is the heat flux conducted from the element 1 to the element 2. Equation (D.2) can be expressed as follows:

$$\dot{q}''^{j}_{net} = \frac{\Delta x}{2}\cdot\rho\left(T_1^j\right)\cdot c_p\left(T_1^j\right)\cdot\left.\frac{dT}{dt}\right|_1^j + k\left(\frac{T_1^j+T_2^j}{2}\right)\cdot\frac{T_1^j-T_2^j}{\Delta x} \tag{D.3}$$

where k, ρ, c_p are the thermal conductivity, density and specific heat capacity of the material respectively.

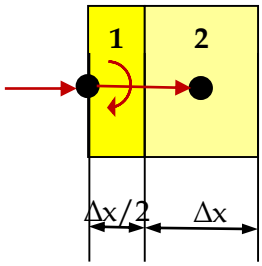

Figure D.3. Energy balance for the first element (i=1)

After rearranging terms, the variation of the temperature over time for the time step j can be defined as:

$$\left.\frac{dT}{dt}\right|_1^j = \frac{2}{\Delta x \cdot \rho\left(T_1^j\right) \cdot c_p(T_1^j)} \cdot \left(\dot{q}''^{\,j}_{net} - k\left(\frac{T_1^j + T_2^j}{2}\right) \cdot \frac{T_1^j - T_2^j}{\Delta x} \right) \tag{D.4}$$

Taking Equation (6.16) , Equation (D.4) and its respective expression for the time step j+1, the discretised governing equation for the first element becomes:

$$\begin{aligned} &\mathbf{T_1^{j+1}} \cdot \left[1 + \frac{k\left(T_1^j\right) \cdot \Delta t}{\rho\left(T_1^j\right) \cdot c_p\left(T_1^j\right) \cdot \Delta x^2}\right] + \mathbf{T_2^{j+1}} \cdot \left[-\frac{k\left(T_1^j\right) \cdot \Delta t}{\rho\left(T_1^j\right) \cdot c_p\left(T_1^j\right) \cdot \Delta x^2}\right] = \\ &= T_1^j + \frac{k\left(T_1^j\right) \cdot \Delta t}{\rho\left(T_1^j\right) \cdot c_p\left(T_1^j\right) \cdot \Delta x^2} \cdot \left(T_1^j - T_2^j\right) + \frac{\Delta t}{\Delta x \cdot \rho\left(T_1^j\right) \cdot c_p(T_1^j)} \cdot \left(\dot{q}''^{\,j}_{net} + \dot{q}''^{\,j+1}_{net}\right) \end{aligned} \tag{D.5}$$

where, it has been assumed for simplicity that the thermal conductivity is approximated to $k\left(\frac{T_1^j+T_2^j}{2}\right) \approx k\left(T_1^j\right)$.

If the net heat flux is known for the step j and j+1, this formulation can be used to calculate the temperature of the elements 1 and 2 for the step j+1. However, if the boundary condition is built as a function of a radiant heat flux ($\dot{q}''_e$) and a heat transfer coefficient of losses ($h_{T,s}$), Equation (D.5) can be expressed as follows:

$$\begin{aligned} &\mathbf{T_1^{j+1}} \cdot \left[1 + \frac{k\left(T_1^j\right) \cdot \Delta t}{\rho\left(T_1^j\right) \cdot c_p\left(T_1^j\right) \cdot \Delta x^2} + \frac{h_T\left(T_1^j\right) \cdot \Delta t}{\rho\left(T_1^j\right) \cdot c_p\left(T_1^j\right) \cdot \Delta x}\right] + \mathbf{T_2^{j+1}} \\ &\cdot \left[-\frac{k\left(T_1^j\right) \cdot \Delta t}{\rho\left(T_1^j\right) \cdot c_p\left(T_1^j\right) \cdot \Delta x^2}\right] = \\ &= T_1^j + \frac{k\left(T_1^j\right) \cdot \Delta t}{\rho\left(T_1^j\right) \cdot c_p\left(T_1^j\right) \cdot \Delta x^2} \cdot \left(T_1^j - T_2^j\right) + \frac{\alpha \cdot \Delta t}{\Delta x \cdot \rho\left(T_1^j\right) \cdot c_p\left(T_1^j\right)} \cdot \left(\dot{q}''^{\,j}_{e} + \dot{q}''^{\,j+1}_{e}\right) \\ &+ \\ &+ \frac{h_{T.s}\left(T_1^j\right) \cdot \Delta t}{\rho \cdot c_p\left(T_1^j\right) \cdot \Delta x} \cdot \left(2 \cdot T_\infty - T_1^j\right) \end{aligned} \tag{D.6}$$

where α is the absorptivity of the material surface and T_∞ is the ambient temperature.

For the case of a thermally thin plate being used at the surface of the sample, the temperature for the element 1 is known for any time step, since it is equal to the plate temperature. Then, the formulation can be written as a function of the unknown heat transfer coefficient and the temperature of the element 2 for the step j+1. For simplicity, instead of using a Crank-Nicolson formulation, an implicit formulation is used to define the governing equation:

$$\mathbf{h}_{\mathbf{T,s}}^{\mathbf{j+1}} \cdot \left[T_1^{j+1} - T_\infty\right] + \mathbf{T}_{\mathbf{2}}^{\mathbf{j+1}} \cdot \left[-\frac{k\left(T_1^{j+1}\right)}{\Delta x}\right] = \\ = \alpha \cdot \dot{q}''^{j+1}_{e} - \dot{q}''^{j+1}_{st,plate} - \frac{k\left(T_1^{j+1}\right)}{\Delta x} \cdot T_1^{j+1} - \frac{\Delta x \cdot \rho\left(T_1^{j+1}\right) \cdot c_p\left(T_1^{j+1}\right)}{2 \cdot \Delta t} \cdot \left(T_1^{j+1} - T_1^{j}\right) \tag{D.7}$$

where $\dot{q}''^{j+1}_{st,plate}$ is the heat stored by the thin plate at the surface at the step j+1 and can be calculated as:

$$\dot{q}''^{j+1}_{st,plate} = \frac{1}{A_{plate}} \cdot m_{plate} \cdot c_{p,plate} \cdot \frac{\left(T_1^{j+1} - T_1^{j}\right)}{\Delta t} \tag{D.8}$$

where A_{plate}, m_{plate} and $c_{p,plate}$ is the surface area, mass and specific heat capacity of the plate respectively.

D.2 Interior element (i):

The discretised equation for an interior element is obtained by deriving the diffusion equation for conduction noted in Equation (D.9):

$$\frac{\delta(k(T) \cdot \delta T)}{\delta x^2} = \rho(T) \cdot c_p(T) \cdot \frac{dT}{dt} + \dot{g}''' \tag{D.9}$$

If the thermal conductivity is temperature dependent, the diffusion equation can be expressed as follows:

$$k(T) \cdot \frac{\delta^2 T}{\delta x^2} + \frac{\delta k(T)}{\delta x} \cdot \frac{\delta T}{\delta x} = \rho(T) \cdot c_p(T) \cdot \frac{dT}{dt} + \dot{g}''' \tag{D.10}$$

which is equivalent to Equation (D.11) below if the second term is multiplied by $\frac{\delta x}{\delta T} \cdot \frac{\delta T}{\delta x}$:

$$k(T) \cdot \frac{\delta^2 T}{\delta x^2} + \frac{\delta k(T)}{\delta T} \cdot \left(\frac{\delta T}{\delta x}\right)^2 = \rho(T) \cdot c_p(T) \cdot \frac{dT}{dt} + \dot{g}''' \tag{D.11}$$

The second derivate of the temperature over the space $\left(\frac{\delta^2 T}{\delta x^2}\right)$ can be expressed by using a central difference method as noted in Equation (D.12), and the square of the derivative of the temperature over space $\left(\frac{\delta T}{\delta x}\right)^2$ can be expressed as noted in Equation (D.13), as the differentiation for the element i and the step j:

$$\frac{\delta^2 T}{\delta x^2} = \frac{T_{i-1}^{j} - 2 \cdot T_i^{j} + T_{i+1}^{j}}{\Delta x^2} \tag{D.12}$$

$$\left(\frac{\delta T}{\delta x}\right)^2 = \left(\frac{T_{i+1}^j - T_{i-1}^j}{2 \cdot \Delta x}\right)^2 \tag{D.13}$$

Then, the discretised equation for element i and step j can be expressed as:

$$k(T_i) \cdot \frac{T_{i-1}^j - 2 \cdot T_i^j + T_{i+1}^j}{\Delta x^2} + \frac{\delta k\left(T_i^j\right)}{\delta T} \cdot \left(\frac{T_{i+1}^j - T_{i-1}^j}{2 \cdot \Delta x}\right)^2 = \rho\left(T_i^j\right) \cdot c_p\left(T_i^j\right) \cdot \left.\frac{dT}{dt}\right|_i^j + \dot{g}_i'''^j \tag{D.14}$$

If the generation/absorption term $\dot{g}_i'''^j$ is neglected, and the thermal conductivity is constant with temperature, the discretised equation for the element i and the step j is given by:

$$k(T_i) \cdot \frac{T_{i-1}^j - 2 \cdot T_i^j + T_{i+1}^j}{\Delta x^2} = \rho\left(T_i^j\right) \cdot c_p\left(T_i^j\right) \cdot \left.\frac{dT}{dt}\right|_i^j \tag{D.15}$$

The same solution may be obtained if an energy balance is proposed for the element i and step j, considering that the incoming heat flux conducted from the element i-1 to the element i has to be equal to the flux stored in the element i plus the flux conducted to element i+1 and the energy generated/absorbed by element i, which is schematically illustrated in Figure D.4 and defined in Equation (D.16):

$$\dot{q}''^j_{cond,(i-1)\rightarrow i} = \dot{q}''^j_{st,i} + \dot{q}''^j_{cond,i\rightarrow(i+1)} \tag{D.16}$$

After substituting terms, the energy balance can be expressed as:

$$k\left(T_i^j\right) \cdot \frac{T_{i-1}^j - T_i^j}{\Delta x} = \Delta x \cdot \rho\left(T_i^j\right) \cdot c_p\left(T_i^j\right) \cdot \left.\frac{dT}{dt}\right|_i^j + k\left(T_i^j\right) \cdot \frac{T_i^j - T_{i+1}^j}{\Delta x} + \Delta x \cdot \dot{g}_i^{j'''} \tag{D.17}$$

which results in Equation (D.15) when rearranging terms and neglecting the energy generation/consumption term.

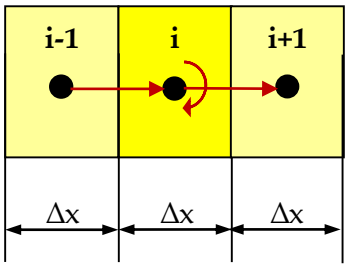

Figure D.4. Energy balance for an interior element (i)

Taking Equation (D.15), the derivative of the temperature over time for the element i and the step j can be expressed as:

$$\left.\frac{dT}{dt}\right|_i^j = \frac{1}{\Delta x^2 \cdot \rho \cdot c_p\left(T_i^j\right)} \cdot \left(k(T_i) \cdot \left(T_{i-1}^j - 2 \cdot T_i^j + T_{i+1}^j\right) - \Delta x^2 \cdot \dot{g}_i^{j'''}\right) \tag{D.18}$$

Equation (6.16), Equation (D.18) and its respective expression for the time step j+1, are considered in order to formulate an expression as a function of the temperature in the elements i-1, i and i+1 for the step j+1 as :

$$\begin{aligned} \mathbf{T_{i-1}^{j+1}} \cdot \left[-\frac{k\left(T_i^j\right) \cdot \Delta t}{2 \cdot \rho\left(T_i^j\right) \cdot c_p\left(T_i^j\right) \cdot \Delta x^2} \right] + \mathbf{T_i^{j+1}} \cdot \left[1 + \frac{k\left(T_i^j\right) \cdot \Delta t}{\rho\left(T_i^j\right) \cdot c_p\left(T_i^j\right) \cdot \Delta x^2} \right] + \\ \mathbf{T_{i+1}^{j+1}} \cdot \left[-\frac{k\left(T_i^j\right) \cdot \Delta t}{2 \cdot \rho\left(T_i^j\right) \cdot c_p\left(T_i^j\right) \cdot \Delta x^2} \right] = \\ = T_i^j + \frac{k\left(T_1^j\right) \cdot \Delta t}{2 \cdot \rho\left(T_i^j\right) \cdot c_p\left(T_1^j\right) \cdot \Delta x^2} \cdot \left(T_{i-1}^j - 2 \cdot T_i^j + T_{i+1}^j \right) \end{aligned} \tag{D.19}$$

It must be noted that Equation (D.19) is only valid if the thermal conductivity is constant with temperature. If this is not the case, a non-linearity is included in the formulation due to the term $\frac{\delta k(T)}{\delta T} \cdot \left(\frac{\delta T}{\delta x}\right)^2$. The non-linearity can be solved by assuming that this term is calculated for the previous step j and checking that the used time step is low enough to provide a good convergence between solutions obtained with different time steps. Then, the formulation to obtain the governing equation for the element i is given in Equation (6.20).

$$\begin{aligned} \mathbf{T_{i-1}^{j+1}} \cdot \left[-\frac{k\left(T_i^j\right) \cdot \Delta t}{2 \cdot \rho\left(T_i^j\right) \cdot c_p\left(T_i^j\right) \cdot \Delta x^2} \right] + \mathbf{T_i^{j+1}} \cdot \left[1 + \frac{k\left(T_i^j\right) \cdot \Delta t}{\rho\left(T_i^j\right) \cdot c_p\left(T_i^j\right) \cdot \Delta x^2} \right] + \\ + \mathbf{T_{i+1}^{j+1}} \cdot \left[-\frac{k\left(T_i^j\right) \cdot \Delta t}{2 \cdot \rho\left(T_i^j\right) \cdot c_p\left(T_i^j\right) \cdot \Delta x^2} \right] = \\ = T_i^j + \frac{k\left(T_i^j\right) \cdot \Delta t}{2 \cdot \rho\left(T_i^j\right) \cdot c_p\left(T_i^j\right) \cdot \Delta x^2} \cdot \left(T_{i-1}^j - 2 \cdot T_i^j + T_{i+1}^j \right) + \\ + \frac{\delta k\left(T_i^j\right)}{\delta T} \cdot \left(\frac{T_{i+1}^j - T_{i-1}^j}{2 \cdot \Delta x} \right)^2 \cdot \frac{\Delta t}{\rho\left(T_i^j\right) \cdot c_p\left(T_i^j\right)} \end{aligned} \tag{D.20}$$

D.3 Last element (i=N):

As for the first element, the discretisation equation for the last element can be derived by applying an energy balance at the rear face, as noted in Equation (D.21) and illustrated in Figure D.5.

$$\dot{q}''^j_{cond,(N-1)\rightarrow N} = \dot{q}''^j_{st,N} + \dot{q}''^j_{loss} \tag{D.21}$$

where $\dot{q}''^j_{cond,(N-1)\rightarrow N}$ is the heat conducted from the element N-1 to the element N, $\dot{q}''^j_{st,N}$ is the heat stored in the element N and $\dot{q}''^j_{loss}$ is the heat lost by the rear face of the element N.

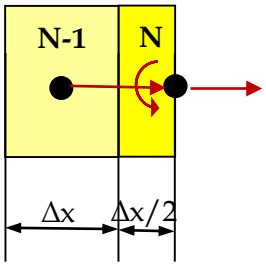

Figure D.5. Energy balance for the last element

Equation (D.21) can be extended as a function of the temperature of the element N-1 and N for the step j+1:

$$T_{N-1}^{j+1}\cdot\left[-\frac{k\left(T_N^j\right)\cdot\Delta t}{\rho(T_N^j)\cdot c_p\left(T_N^j\right)\cdot\Delta x^2}\right]+T_N^{j+1}\cdot\left[1+\frac{k\left(T_N^j\right)\cdot\Delta t}{\rho(T_N^j)\cdot c_p\left(T_N^j\right)\cdot\Delta x^2}\right]=$$
$$=T_N^j+\frac{k\left(T_N^j\right)\cdot\Delta t}{\rho(T_N^j)\cdot c_p\left(T_N^j\right)\cdot\Delta x^2}\cdot\left(T_{N-1}^j-T_N^j\right)+\frac{\Delta t}{\Delta x\cdot\rho(T_N^j)\cdot c_p(T_N^j)}$$
$$\cdot\left(\dot{q}''^{\,j}_{loss}+\dot{q}''^{\,j+1}_{loss}\right) \qquad \text{(D.22)}$$

This equation is valid when the heat losses are measured, e.g. by using a metallic plate at the back of the sample. If the losses can be defined by a heat transfer coefficient $h_{T,s}$, Equation (D.21) can be expressed as:

$$T_{N-1}^{j+1}\cdot\left[-\frac{k\left(T_N^j\right)\cdot\Delta t}{\rho(T_N^j)\cdot c_p\left(T_N^j\right)\cdot\Delta x^2}\right]+T_N^{j+1}$$
$$\cdot\left[1+\frac{k\left(T_N^j\right)\cdot\Delta t}{\rho(T_N^j)\cdot c_p\left(T_N^j\right)\cdot\Delta x^2}+\frac{h_{T,b}\cdot\Delta t}{\Delta x\cdot\rho\cdot c_p(T_N^j)}\right]= \qquad \text{(D.23)}$$
$$=T_N^j+\frac{k\left(T_N^j\right)\cdot\Delta t}{\rho(T_N^j)\cdot c_p\left(T_N^j\right)\cdot\Delta x^2}\cdot\left(T_{N-1}^j-T_N^j\right)+\frac{h_{T,b}\cdot\Delta t}{\Delta x\cdot\rho\cdot c_p(T_N^j)}\cdot\left(2\cdot T_\infty-T_N^j\right)$$

If the boundary condition at the back is defined as an adiabatic condition, i.e. $\dot{q}''^{\,j}_{loss}=0$, the discretised equation can be derived easily from Equation (D.22), resulting in:

$$T_{N-1}^{j+1}\cdot\left[-\frac{k\left(T_N^j\right)\cdot\Delta t}{\rho\cdot c_p\left(T_N^j\right)\cdot\Delta x^2}\right]+T_N^{j+1}\cdot\left[1+\frac{k\left(T_N^j\right)\cdot\Delta t}{\rho\cdot c_p\left(T_N^j\right)\cdot\Delta x^2}\right]=$$
$$=T_N^j+\frac{k\left(T_N^j\right)\cdot\Delta t}{\rho\cdot c_p\left(T_N^j\right)\cdot\Delta x^2}\cdot\left(T_{N-1}^j-T_N^j\right) \qquad \text{(D.24)}$$

If a Dirichlet boundary condition is assumed with a known value of temperature at the rear surface for every time step, i.e. $T_N^j\ \forall\, t$, the discretisation needs to be done for i=N-1 according to the following expression derived from Equation (D.19). For

this case study, the dimension of the system of linear equations becomes N-1, i.e. N-1 unknowns and equations.

$$\begin{aligned} & \mathbf{T_{N-2}^{j+1}} \cdot \left[-\frac{k\left(T_{N-1}^{j}\right) \cdot \Delta t}{\rho\left(T_{N-1}^{j}\right) \cdot c_p\left(T_{N-1}^{j}\right) \cdot \Delta x^2} \right] + \mathbf{T_{N-1}^{j+1}} \\ & \qquad \cdot \left[1 + \frac{k\left(T_{N-1}^{j}\right) \cdot \Delta t}{\rho\left(T_{N-1}^{j}\right) \cdot c_p\left(T_{N-1}^{j}\right) \cdot \Delta x^2} \right] \\ & = T_{N-1}^{j} + \frac{k\left(T_{N-1}^{j}\right) \cdot \Delta t}{\rho\left(T_{N-1}^{j}\right) \cdot c_p\left(T_{N-1}^{j}\right) \cdot \Delta x^2} \cdot \left(T_{N-2}^{j} - 2 \cdot T_{N-1}^{j} + T_{N}^{j} \right) + \\ & T_{N}^{j+1} \cdot \left[-\frac{k\left(T_{N-1}^{j}\right) \cdot \Delta t}{\rho\left(T_{N-1}^{j}\right) \cdot c_p\left(T_{N-1}^{j}\right) \cdot \Delta x^2} \right] + \frac{\delta k\left(T_{N-1}^{j}\right)}{\delta T} \cdot \left(\frac{T_{N-2}^{j} - T_{N}^{j}}{2 \cdot \Delta x} \right)^2 \\ & \qquad \cdot \frac{\Delta t}{\rho\left(T_{N-1}^{j}\right) \cdot c_p\left(T_{N}^{j}\right)} \end{aligned} \tag{D.25}$$

D.4 Interface element between two materials (m):

The derivation of the discretised governing equation for the interface element can be obtained by defining an energy balance as noted in Equation (D.16) and illustrated in Figure D.6.

$$\dot{q}''^{j}_{cond,(m-1)\rightarrow m} = \dot{q}''^{j}_{st,m} + \dot{q}''^{j}_{cond,m\rightarrow(m+1)} \tag{D.26}$$

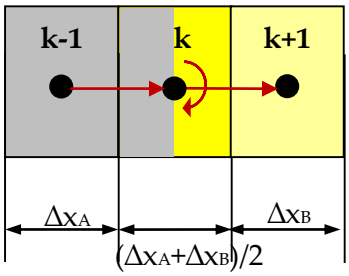

Figure D.6. Energy balance for the interface element

Similarly to previous cases, substituting terms, Equation (D.16) can be expressed as:

$$\begin{aligned} k_A\left(T_m^j\right)\cdot\frac{T_{m-1}^j - T_m^j}{\Delta x_A} &= \frac{\Delta x_A\cdot\rho_A\left(T_m^j\right)\cdot c_{p,A}\left(T_m^j\right) + \Delta x_B\cdot\rho_B\left(T_m^j\right)\cdot c_{p,B}\left(T_m^j\right)}{2}\cdot\left.\frac{dT}{dt}\right|_m^j \\ &+ k_B\left(T_m^j\right)\cdot\frac{T_m^j - T_{m+1}^j}{\Delta x_B} \end{aligned} \tag{D.27}$$

By rearranging terms in Equation (D.27), the derivative of the temperature over time can be expressed as follows:

$$\begin{aligned} \left.\frac{dT}{dt}\right|_k^j &= \frac{2}{\Delta x_A\cdot\Delta x_B\cdot\left(\Delta x_A\cdot\rho_A\left(T_m^j\right)\cdot c_{p,A}\left(T_m^j\right) + \Delta x_B\cdot\rho_B\left(T_m^j\right)\cdot c_{p,B}\left(T_m^j\right)\right)}\cdot \\ &\cdot\left[T_{m-1}^j\cdot\Delta x_B\cdot k_A\left(T_m^j\right) - T_m^j\cdot\left(\Delta x_A\cdot k_B\left(T_m^j\right) + \Delta x_B\cdot k_A\left(T_m^j\right)\right) + T_{m+1}^j\cdot\Delta x_A\right. \\ &\left.\cdot k_B\left(T_m^j\right)\right] \end{aligned} \tag{D.28}$$

By defining the term Fo_m^j as:

$$Fo_m^j = \frac{2\cdot\Delta t}{\Delta x_A\cdot\rho_A\left(T_k^j\right)\cdot c_{p,A}\left(T_k^j\right) + \Delta x_B\cdot\rho_B\left(T_k^j\right)\cdot c_{p,B}\left(T_k^j\right)}\cdot\frac{1}{k_A\left(T_k^j\right)\cdot k_B\left(T_k^j\right)} \tag{D.29}$$

and taking Equation (D.28) and its respective expression for the time step j+1, a function of the temperature in elements m-1, m and m+1 for the step j+1 can be developed:

$$
\begin{aligned}
&T_{m-1}^{j+1} \cdot \left[-\frac{Fo_m^j}{2} \cdot \Delta x_B \cdot k_A\left(T_m^j\right) \right] + T_m^{j+1} \\
&\qquad \cdot \left[1 + Fo_m^j \cdot \frac{\Delta x_A \cdot k_B\left(T_m^j\right) + \Delta x_B \cdot k_A\left(T_m^j\right)}{2} \right] + \\
&\qquad + T_{m+1}^{j+1} \cdot \left[-\frac{Fo_m^j}{2} \cdot \Delta x_A \cdot k_B\left(T_m^j\right) \right] = \\
&= T_m^j + \frac{Fo_m^j}{2} \cdot \left[T_{m-1}^j \cdot \Delta x_B \cdot k_A\left(T_m^j\right) - T_m^j \cdot \frac{\left(\Delta x_A \cdot k_B\left(T_m^j\right) + \Delta x_B \cdot k_A\left(T_m^j\right)\right)}{2} \right. \\
&\qquad \left. + T_{m+1}^j \cdot \Delta x_A \cdot k_B\left(T_m^j\right) \right]
\end{aligned}
\tag{D.30}
$$

D.5 Summary of system matrices

As a summary, the different system of linear equations is written for all the cases noted throughout this Appendix. For simplicity of notation, the Fourier number is defined as:

$$Fo_i^j = \frac{k\left(T_i^j\right) \cdot \Delta t}{\rho \cdot c_p\left(T_i^j\right) \cdot \Delta x^2} \tag{D.31}$$

Similarly, the parameter dFo_i^j is defined as noted in Equation (D.32), so as to solve the non-linearity introduced by temperature dependence on the thermal conductivity:

$$dFo_i^j = \frac{\delta k\left(T_i^j\right)}{\delta T} \cdot \frac{\Delta t}{4 \cdot \rho \cdot c_p\left(T_i^j\right) \cdot \Delta x^2} \tag{D.32}$$

This definition of the Fourier number implies that every time step should be computed for each element of the discretisation.

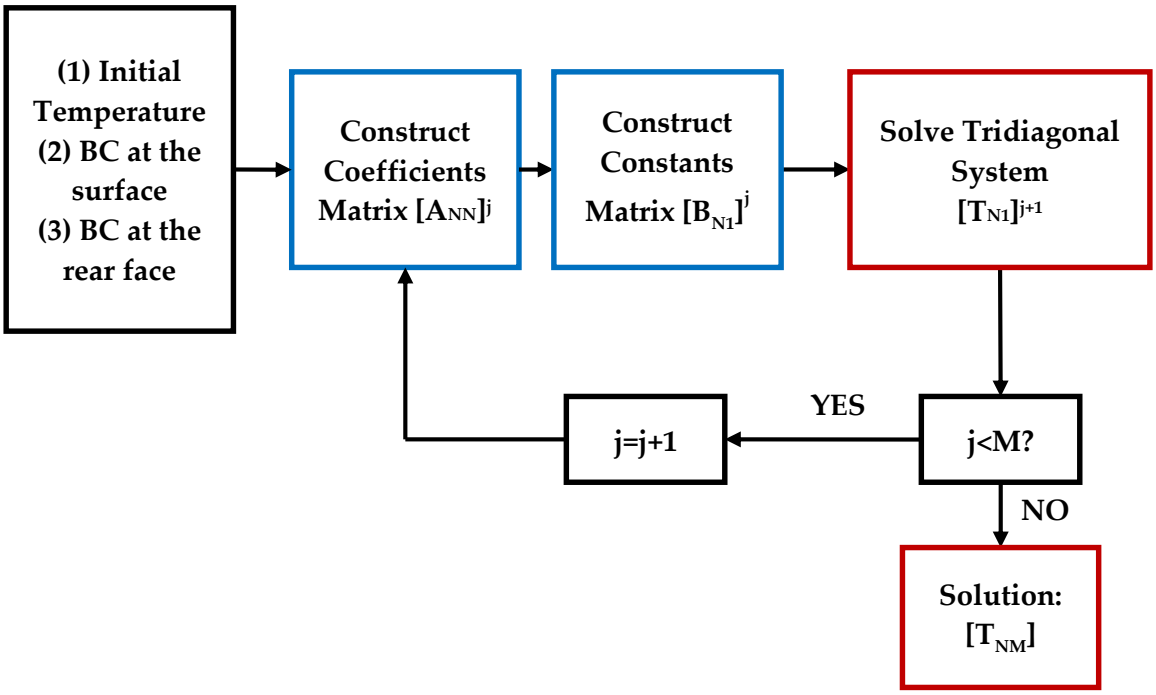

Figure D.7. Logic diagram for the determination of the temperatures' map for a space domain consisting of N elements and a temporal domain consisting of M time steps

D.5.1 Known history of net heat flux ($\dot{q}''_{net}$)

D.5.1.1 Adiabatic BC at the rear face

$$\begin{pmatrix} \left[1+Fo_1^j\right] & \left[-Fo_1^j\right] & & & 0 \\ & \ddots & \ddots & & \\ & \left[-\frac{Fo_i^j}{2}\right] & \left[1+Fo_i^j\right] & \left[-\frac{Fo_i^j}{2}\right] & \\ & & \ddots & \ddots & \\ 0 & & & \left[-Fo_N^j\right] & \left[1+Fo_N^j\right] \end{pmatrix} \cdot \begin{pmatrix} T_1^{j+1} \\ \vdots \\ T_i^{j+1} \\ \vdots \\ T_N^{j+1} \end{pmatrix} = \begin{pmatrix} T_1^j + Fo_1^j \cdot \left(T_2^j - T_1^j\right) + \frac{\Delta t}{\Delta x \cdot \rho \cdot c_p(T_1^j)} \cdot \left(\dot{q}''^j_{net} + \dot{q}''^{j+1}_{net}\right) \\ \vdots \\ T_i^j + \frac{Fo_1^j}{2} \cdot \left(T_{i-1}^j - T_i^j + T_{i+1}^j\right) + dFo_i^j \cdot (T_{i+1} - T_{i-1})^2 \\ \vdots \\ T_N^j + Fo_N^j \cdot \left(T_{N-1}^j - T_N^j\right) \end{pmatrix}$$

D.5.1.2 Heat losses BC at the rear face

$$\begin{pmatrix} \left[1+Fo_1^j\right] & \left[-Fo_1^j\right] & 0 & & \\ \left[-\frac{Fo_i^j}{2}\right] & \left[1+Fo_i^j\right] & \left[-\frac{Fo_i^j}{2}\right] & & \\ & \ddots & \ddots & \ddots & \\ & & \left[-\frac{Fo_i^j}{2}\right] & \left[1+Fo_i^j\right] & \left[-\frac{Fo_i^j}{2}\right] \\ 0 & & & \left[-Fo_N^j\right] & \left[1+Fo_N^j\right] \end{pmatrix} \cdot \begin{pmatrix} T_1^{j+1} \\ \vdots \\ T_i^{j+1} \\ \vdots \\ T_N^{j+1} \end{pmatrix} = \begin{pmatrix} T_1^j + Fo_1^j \cdot \left(T_2^j - T_1^j\right) + \frac{\Delta t}{\Delta x \cdot \rho \cdot c_p(T_1^j)} \cdot \left(\dot{q}''^j{}_{net} + \dot{q}''^{j+1}_{net}\right) \\ \vdots \\ T_i^j + \frac{Fo_1^j}{2} \cdot \left(T_{i-1}^j - T_i^j + T_{i+1}^j\right) + dFo_i^j \cdot (T_{i+1} - T_{i-1})^2 \\ \vdots \\ T_N^j + Fo_N^j \cdot \left(T_{N-1}^j - T_N^j\right) + \frac{\Delta t}{\Delta x \cdot \rho \cdot c_p(T_N^j)} \cdot \left(\dot{q}''^j{}_{loss} + \dot{q}''^{j+1}_{loss}\right) \end{pmatrix}$$

D.5.1.3 Heat losses BC at the rear face with a heat transfer coefficient ($h_{T,b}$)

$$\begin{pmatrix} \left[1+Fo_1^j\right] & \left[-Fo_1^j\right] & 0 & & \\ & \ddots & & & \\ & \left[-\frac{Fo_i^j}{2}\right] & \left[1+Fo_i^j\right] & \left[-\frac{Fo_i^j}{2}\right] & \\ & & \ddots & & \\ 0 & & \left[-Fo_N^j\right] & \left[1+Fo_N^j+\frac{h_T\cdot\Delta t}{\Delta x\cdot\rho\cdot c_p(T_N^j)}\right] \end{pmatrix} \cdot \begin{pmatrix} T_1^{j+1} \\ \vdots \\ T_i^{j+1} \\ \vdots \\ T_N^{j+1} \end{pmatrix} = \begin{pmatrix} T_1^j+Fo_1^j\cdot\left(T_2^j-T_1^j\right)+\frac{\Delta t}{\Delta x\cdot\rho\cdot c_p(T_1^j)}\cdot\left(\dot{q}''^j_{net}+\dot{q}''^{j+1}_{net}\right) \\ \vdots \\ T_i^j+\frac{Fo_1^j}{2}\cdot\left(T_{i-1}^j-T_i^j+T_{i+1}^j\right)+dFo_i^j\cdot(T_{i+1}-T_{i-1})^2 \\ \vdots \\ T_N^j+Fo_N^j\cdot\left(T_{N-1}^j-T_N^j\right)+\frac{h_{T,b}\cdot\Delta t}{\Delta x\cdot\rho\cdot c_p(T_N^j)}\cdot\left(2\cdot T_\infty-T_N^j\right) \end{pmatrix}$$

D.5.1.4 Known temperature BC at the rear face

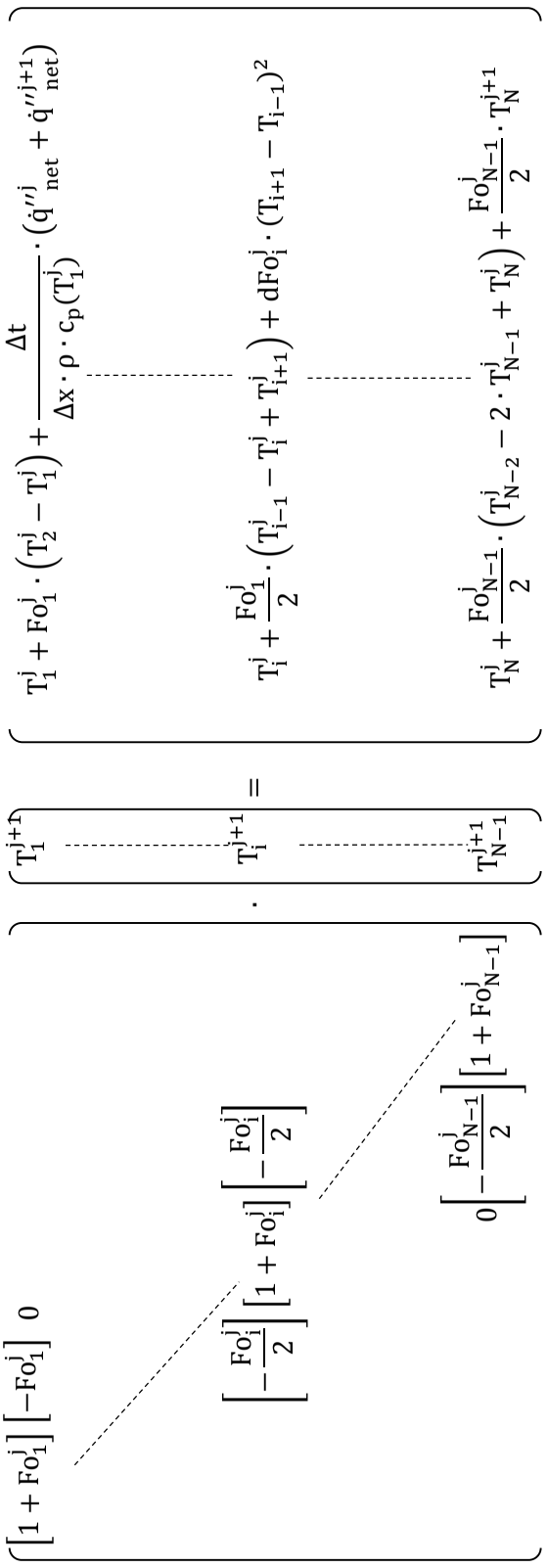

$$\begin{pmatrix} \left[1 + Fo_1^j\right] & \left[-Fo_1^j\right] & 0 & \cdots & \\ \left[-\frac{Fo_i^j}{2}\right] & \left[1 + Fo_i^j\right] & \left[-\frac{Fo_i^j}{2}\right] & & \\ \vdots & & & \ddots & \\ & 0 & \left[-\frac{Fo_{N-1}^j}{2}\right] & \left[1 + Fo_{N-1}^j\right] & \end{pmatrix} \cdot \begin{pmatrix} T_1^{j+1} \\ \vdots \\ T_i^{j+1} \\ \vdots \\ T_{N-1}^{j+1} \end{pmatrix} = \begin{pmatrix} T_1^j + Fo_1^j \cdot \left(T_2^j - T_1^j\right) + \frac{\Delta t}{\Delta x \cdot \rho \cdot c_p(T_1^j)} \cdot \left(\dot{q}''^j_{net} + \dot{q}''^{j+1}_{net}\right) \\ \vdots \\ T_i^j + \frac{Fo_1^j}{2} \cdot \left(T_{i-1}^j - T_i^j + T_{i+1}^j\right) + dFo_i^j \cdot (T_{i+1} - T_{i-1})^2 \\ \vdots \\ T_N^j + \frac{Fo_{N-1}^j}{2} \cdot \left(T_{N-2}^j - 2 \cdot T_{N-1}^j + T_N^j\right) + \frac{Fo_{N-1}^j}{2} \cdot T_N^{j+1} \end{pmatrix}$$

D.5.2 Known history of radiant heat flux ($\dot{q}''_e$) with heat transfer coefficient of losses ($h_{T,s}$)

D.5.2.1 Adiabatic BC at the rear face

$$\begin{pmatrix} \left[1 + Fo_1^j + \frac{h_{T,s} \cdot \Delta t}{\Delta x \cdot \rho \cdot c_p(T_N^j)}\right] \left[-Fo_1^j\right] & 0 & & \\ \left[-\frac{Fo_i^j}{2}\right] & \left[1 + Fo_i^j\right] & \left[-\frac{Fo_i^j}{2}\right] & \\ & & & \\ 0 & & \left[-Fo_N^j\right] & \left[1 + Fo_N^j\right] \end{pmatrix} \cdot \begin{pmatrix} T_1^{j+1} \\ T_i^{j+1} \\ T_N^{j+1} \end{pmatrix} = \begin{pmatrix} T_1^j + Fo_1^j \cdot \left(T_2^j - T_1^j\right) + \frac{\alpha \cdot \Delta t}{\Delta x \cdot \rho \cdot c_p(T_1^j)} \cdot \left(\dot{q}''^j_e + \dot{q}''^{j+1}_e\right) + \frac{h_{T,s} \cdot \Delta t}{\Delta x \cdot \rho \cdot c_p(T_N^j)} \cdot \left(2 \cdot T_{\infty} - T^j\right) \\ T_i^j + \frac{Fo_1^j}{2} \cdot \left(T_{i-1}^j - T_i^j + T_{i+1}^j\right) + dFo_i^j \cdot (T_{i+1} - T_{i-1})^2 \\ T_N^j + Fo_N^j \cdot \left(T_{N-1}^j - T_N^j\right) \end{pmatrix}$$

D.5.2.2 Heat losses BC at the rear face

$$\begin{pmatrix} \left[1 + Fo_1^j + \frac{h_{T,s} \cdot \Delta t}{\Delta x \cdot \rho \cdot c_p(T_N^j)}\right] & \left[-Fo_1^j\right] & & 0 \\ \left[-\frac{Fo_i^j}{2}\right] & \left[1 + Fo_i^j\right] & \left[-\frac{Fo_i^j}{2}\right] & \\ & \ddots & \ddots & \ddots \\ 0 & & \left[-\frac{Fo_N^j}{2}\right] & \left[1 + Fo_N^j\right] \end{pmatrix} \cdot \begin{pmatrix} T_1^{j+1} \\ \vdots \\ T_i^{j+1} \\ \vdots \\ T_N^{j+1} \end{pmatrix} = \begin{pmatrix} T_1^j + Fo_1^j \cdot \left(T_2^j - T_1^j\right) + \frac{\alpha \cdot \Delta t}{\Delta x \cdot \rho \cdot c_p(T_1^j)} \cdot \left(\dot{q}''^j_e + \dot{q}''^{j+1}_e\right) + \frac{h_{T,s} \cdot \Delta t}{\Delta x \cdot \rho \cdot c_p(T_N^j)} \cdot \left(2 \cdot T_\infty - T_1^j\right) \\ \vdots \\ T_i^j + \frac{Fo_1^j}{2} \cdot \left(T_{i-1}^j - T_i^j + T_{i+1}^j\right) + dFo_i^j \cdot \left(T_{i+1} - T_{i-1}\right)^2 \\ \vdots \\ T_N^j + Fo_N^j \cdot \left(T_{N-1}^j - T_N^j\right) + \frac{\Delta t}{\Delta x \cdot \rho \cdot c_p(T_N^j)} \cdot \left(\dot{q}''^j_{loss} + \dot{q}''^{j+1}_{loss}\right) \end{pmatrix}$$

D.5.2.3 Heat losses BC at the rear face with a heat transfer coefficient ($h_{T,b}$)

$$\begin{pmatrix} \left[1 + Fo_1^j + \frac{h_{T,s} \cdot \Delta t}{\Delta x \cdot \rho \cdot c_p(T_N^j)}\right] & \left[-Fo_1^j\right] & & 0 \\ & \ddots & \ddots & \\ & \left[-\frac{Fo_i^j}{2}\right] & \left[1 + Fo_i^j\right] & \left[-\frac{Fo_i^j}{2}\right] \\ & & \ddots & \ddots \\ 0 & & \left[-Fo_N^j\right] & \left[1 + Fo_N^j + \frac{h_{T,b} \cdot \Delta t}{\Delta x \cdot \rho \cdot c_p(T_N^j)}\right] \end{pmatrix} \cdot \begin{pmatrix} T_1^{j+1} \\ \vdots \\ T_i^{j+1} \\ \vdots \\ T_N^{j+1} \end{pmatrix} = \begin{pmatrix} T_1^j + Fo_1^j \cdot (T_2^j - T_1^j) + \frac{\alpha \cdot \Delta t}{\Delta x \cdot \rho \cdot c_p(T_1^j)} \cdot (\dot{q}''^j_e + \dot{q}''^{j+1}_e) + \frac{h_{T,s} \cdot \Delta t}{\Delta x \cdot \rho \cdot c_p(T_N^j)} \cdot (2 \cdot T_\infty - T_1^j) \\ \vdots \\ T_i^j + \frac{Fo_1^j}{2} \cdot \left(T_{i-1}^j - T_i^j + T_{i+1}^j\right) + dFo_i^j \cdot (T_{i+1} - T_{i-1})^2 \\ \vdots \\ T_N^j + Fo_N^j \cdot \left(T_{N-1}^j - T_N^j\right) + \frac{h_{T,b} \cdot \Delta t}{\Delta x \cdot \rho \cdot c_p(T_N^j)} \cdot \left(2 \cdot T_\infty - T_N^j\right) \end{pmatrix}$$

D.5.2.4 Known temperature BC at the rear face

$$\begin{pmatrix} \left[1+\mathrm{Fo}_1^j+\frac{h_{T,s}\cdot\Delta t}{\Delta x\cdot\rho\cdot c_p(T_N^j)}\right] & \left[-\mathrm{Fo}_1^j\right] & 0 & \\ & \ddots & \ddots & \ddots \\ & \left[-\frac{\mathrm{Fo}_i^j}{2}\right] & \left[1+\mathrm{Fo}_i^j\right] & \left[-\frac{\mathrm{Fo}_i^j}{2}\right] \\ & & \ddots & \ddots \\ & 0 & \left[-\frac{\mathrm{Fo}_{N-1}^j}{2}\right] & \left[1+\mathrm{Fo}_{N-1}^j\right] \end{pmatrix} \cdot \begin{pmatrix} T_1^{j+1} \\ \vdots \\ T_i^{j+1} \\ \vdots \\ T_{N-1}^{j+1} \end{pmatrix} = \begin{pmatrix} T_1^j+\mathrm{Fo}_1^j\cdot\left(T_2^j-T_1^j\right)+\frac{\alpha\cdot\Delta t}{\Delta x\cdot\rho\cdot c_p(T_1^j)}\cdot\left(\dot{q}''^j{}_e+\dot{q}''^{j+1}{}_e\right)+\frac{h_{T,s}\cdot\Delta t}{\Delta x\cdot\rho\cdot c_p(T_N^j)}\cdot\left(2\cdot T_\infty-T_1^j\right) \\ \vdots \\ T_i^j+\frac{\mathrm{Fo}_1^j}{2}\cdot\left(T_{i-1}^j-T_i^j+T_{i+1}^j\right)+\mathrm{dFo}_i^j\cdot\left(T_{i+1}-T_{i-1}\right)^2 \\ \vdots \\ T_{N-1}^j+\frac{\mathrm{Fo}_{N-1}^j}{2}\cdot\left(T_{N-2}^j-2\cdot T_{N-1}^j+T_N^j\right)+\frac{\mathrm{Fo}_{N-1}^j}{2}\cdot T_N^{j+1} \end{pmatrix}$$

D.5.3 Thermally thin element at the surface with known temperature (T_1)

D.5.3.1 Adiabatic BC at the rear face

$$\begin{pmatrix} \left[T_1^{j+1}-T_\infty\right] & \left[-\frac{k\left(T_1^{j+1}\right)}{\Delta x}\right] & 0 & & \\ 0 & \left[1+Fo_i^j\right] & \left[-\frac{Fo_2^j}{2}\right] & & \\ & \left[-\frac{Fo_i^j}{2}\right] & \left[1+Fo_i^j\right] & \left[-\frac{Fo_i^j}{2}\right] & \\ & & \ddots & \ddots & \ddots \\ & & & 0 \;\left[-Fo_N^j\right] & \left[1+Fo_N^j\right] \end{pmatrix} \cdot \begin{pmatrix} h_T^{j+1} \\ T_2^{j+1} \\ \vdots \\ T_i^{j+1} \\ \vdots \\ T_N^{j+1} \end{pmatrix} = \begin{pmatrix} \alpha\cdot\dot{q}''^{j+1}_e - \dot{q}''^{j+1}_{st,plate} - \frac{k\left(T_1^{j+1}\right)}{\Delta x}\cdot T_1^{j+1} - \frac{\Delta x\cdot\rho\left(T_1^{j+1}\right)\cdot c_p\left(T_1^{j+1}\right)}{2\cdot\Delta t} \\ T_2^j + \frac{Fo_2^j}{2}\cdot\left(T_1^j - T_2^j + T_3^j\right) + dFo_2^j\cdot(T_3-T_1)^2 + \frac{Fo_1^j}{2}\cdot T_1^{j+1} \\ \vdots \\ T_i^j + \frac{Fo_i^j}{2}\cdot\left(T_{i-1}^j - T_i^j + T_{i+1}^j\right) + dFo_i^j\cdot(T_{i+1}-T_{i-1})^2 \\ \vdots \\ T_N^j + Fo_N^j\cdot\left(T_{N-1}^j - T_N^j\right) \end{pmatrix}$$

D.5.3.2 Heat losses BC at the rear face

$$\begin{pmatrix} \left[T_1^{j+1} - T_\infty\right]\left[-\frac{k\left(T_1^{j+1}\right)}{\Delta x}\right] & 0 & & & \\ 0 & \left[1+Fo_i^j\right] & \left[-\frac{Fo_2^j}{2}\right] & & \\ & \left[-\frac{Fo_i^j}{2}\right] & \left[1+Fo_i^j\right] & \left[-\frac{Fo_i^j}{2}\right] & \\ & & & & 0 \quad \left[-Fo_N^j\right]\left[1+Fo_N^j\right] \end{pmatrix} \cdot \begin{pmatrix} h_T^{j+1} \\ T_2^{j+1} \\ \vdots \\ T_i^{j+1} \\ \vdots \\ T_N^{j+1} \end{pmatrix} = \begin{pmatrix} \alpha \cdot \dot{q}''^{j+1}_e - \dot{q}''^{j+1}_{st,plate} - \frac{k\left(T_1^{j+1}\right)}{\Delta x} \cdot T_1^{j+1} - \frac{\Delta x \cdot \rho\left(T_1^{j+1}\right) \cdot c_p\left(T_1^{j+1}\right)}{2 \cdot \Delta t} \cdot \left(T_1^{j+1} - T_1^j\right) \\ T_2^j + \frac{Fo_2^j}{2} \cdot \left(T_1^j - T_2^j + T_3^j\right) + dFo_2^j \cdot (T_3 - T_1)^2 + \frac{Fo_1^j}{2} \cdot T_1^{j+1} \\ \vdots \\ T_i^j + \frac{Fo_i^j}{2} \cdot \left(T_{i-1}^j - T_i^j + T_{i+1}^j\right) + dFo_i^j \cdot (T_{i+1} - T_{i-1})^2 \\ \vdots \\ T_N^j + Fo_N^j \cdot \left(T_{N-1}^j - T_N^j\right) + \frac{\Delta t}{\Delta x \cdot \rho \cdot c_p(T_N^j)} \cdot \left(\dot{q}''^j_{loss} + \dot{q}''^{j+1}_{loss}\right) \end{pmatrix}$$

D.5.3.3 Heat losses BC at the rear face with a heat transfer coefficient ($h_{T,b}$)

$$\begin{pmatrix} \left[T_1^{j+1} - T_\infty\right]\left[-\frac{k\left(T_1^{j+1}\right)}{\Delta x}\right] & 0 & & & \\ 0 & \left[1 + Fo_i^j\right] & \left[-\frac{Fo_2^j}{2}\right] & & \\ & \left[-\frac{Fo_i^j}{2}\right] & \left[1 + Fo_i^j\right] & \left[-\frac{Fo_i^j}{2}\right] & \\ & & & & \\ & 0 & \left[-Fo_N^j\right] & \left[1 + Fo_N^j + \frac{h_{T,b} \cdot \Delta t}{\Delta x \cdot \rho \cdot c_p(T_N^j)}\right] \end{pmatrix} \cdot \begin{pmatrix} h_T^{j+1} \\ T_2^{j+1} \\ \vdots \\ T_i^{j+1} \\ \vdots \\ T_N^{j+1} \end{pmatrix} = \begin{pmatrix} \alpha \cdot \dot{q}''^{j+1}_e - \dot{q}''^{j+1}_{st,plate} - \frac{k\left(T_1^{j+1}\right)}{\Delta x} \cdot T_1^{j+1} - \frac{\Delta x \cdot \rho\left(T_1^{j+1}\right) \cdot c_p\left(T_1^{j+1}\right)}{2 \cdot \Delta t} \\ T_2^j + \frac{Fo_2^j}{2} \cdot \left(T_1^j - T_2^j + T_3^j\right) + dFo_2^j \cdot (T_3 - T_1)^2 + \frac{Fo_1^j}{2} \cdot T_1^{j+1} \\ \vdots \\ T_i^j + \frac{Fo_i^j}{2} \cdot \left(T_{i-1}^j - T_i^j + T_{i+1}^j\right) + dFo_i^j \cdot (T_{i+1} - T_{i-1})^2 \\ \vdots \\ T_N^j + Fo_N^j \cdot \left(T_{N-1}^j - T_N^j\right) + \frac{h_{T,b} \cdot \Delta t}{\Delta x \cdot \rho \cdot c_p(T_N^j)} \cdot \left(2 \cdot T_\infty - T_N^j\right) \end{pmatrix}$$

D.5.3.4 Known temperature BC at the rear face

$$\begin{pmatrix} \left[T_1^{j+1} - T_\infty\right]\left[-\frac{k\left(T_1^{j+1}\right)}{\Delta x}\right] & 0 & & & \\ 0 & \left[1+Fo_i^j\right] & \left[-\frac{Fo_2^j}{2}\right] & & \\ & \left[-\frac{Fo_i^j}{2}\right] & \left[1+Fo_i^j\right] & \left[-\frac{Fo_i^j}{2}\right] & \\ & & & & 0 \quad \left[-\frac{Fo_{N-1}^j}{2}\right]\left[1+Fo_{N-1}^j\right] \end{pmatrix} \cdot \begin{pmatrix} h_T^{j+1} \\ T_2^{j+1} \\ \vdots \\ T_i^{j+1} \\ \vdots \\ T_{N-1}^{j+1} \end{pmatrix} = \begin{pmatrix} \alpha \cdot \dot{q}''^{j+1}_e - \dot{q}''^{j+1}_{st,plate} - \frac{k\left(T_1^{j+1}\right)}{\Delta x} \cdot T_1^{j+1} - \frac{\Delta x \cdot \rho\left(T_1^{j+1}\right) \cdot c_p\left(T_1^{j+1}\right)}{2 \cdot \Delta t} \cdot \left(T_1^{j+1} - T_1^j\right) \\ T_2^j + \frac{Fo_2^j}{2} \cdot \left(T_1^j - T_2^j + T_3^j\right) + dFo_2^j \cdot (T_3 - T_1)^2 + \frac{Fo_1^j}{2} \cdot T_1^{j+1} \\ \vdots \\ T_i^j + \frac{Fo_i^j}{2} \cdot \left(T_{i-1}^j - T_i^j + T_{i+1}^j\right) + dFo_i^j \cdot (T_{i+1} - T_{i-1})^2 \\ \vdots \\ T_{N-1}^j + \frac{Fo_{N-1}^j}{2} \cdot \left(T_{N-2}^j - 2 \cdot T_{N-1}^j + T_N^j\right) + \frac{Fo_{N-1}^j}{2} \cdot T_N^{j+1} \end{pmatrix}$$